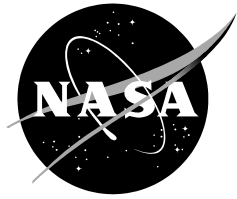
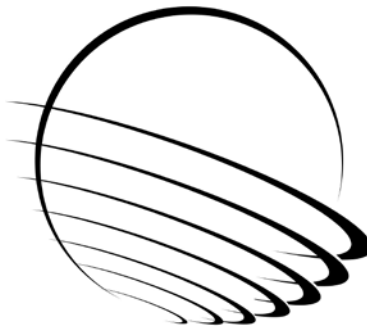


NASA/CP—2016–219090



# 43<sup>rd</sup> Aerospace Mechanisms Symposium

*Compiled/Edited by: Edward A. Boesiger*



Proceedings of a symposium held at  
Biltmore Hotel, Santa Clara, CA  
Hosted by the NASA Ames Research Center and  
Lockheed Martin Space Systems Company  
Sponsored and Organized by the Mechanisms Education Association

May 4-6, 2016

---

**May 2016**





## **PREFACE**

The Aerospace Mechanisms Symposium (AMS) provides a unique forum for those active in the design, production and use of aerospace mechanisms. A major focus is the reporting of problems and solutions associated with the development and flight certification of new mechanisms. Sponsored and organized by the Mechanisms Education Association, responsibility for hosting the AMS is shared by the National Aeronautics and Space Administration and Lockheed Martin Space Systems Company (LMSSC). Now in its 43<sup>rd</sup> symposium, the AMS continues to be well attended, attracting participants from both the U.S. and abroad.

The 43<sup>rd</sup> AMS was held in Santa Clara, California on May 4, 5 and 6, 2016. During these three days, 42 papers were presented. Topics included payload and positioning mechanisms, components such as hinges and motors, CubeSats, tribology, and mechanism testing. Hardware displays during the supplier exhibit gave attendees an opportunity to meet with developers of current and future mechanism components.

The high quality of this symposium is a result of the work of many people, and their efforts are gratefully acknowledged. This extends to the voluntary members of the symposium organizing committee representing the eight NASA field centers, LMSSC, and the European Space Agency. Appreciation is also extended to the session chairs, the authors, and particularly the personnel at ARC responsible for the symposium arrangements and the publication of these proceedings. A sincere thank you also goes to the symposium executive committee who is responsible for the year-to-year management of the AMS, including paper processing and preparation of the program.

The use of trade names of manufacturers in this publication does not constitute an official endorsement of such products or manufacturers, either expressed or implied, by the National Aeronautics and Space Administration.



## CONTENTS

Symposium Schedule .....	viii
Symposium Organizing and Advisory Committees.....	xiii
ATLAS Beam Steering Mechanism (BSM) Lessons Learned .....	1
Ken Blumenstock, Alexander Cramer, Alan Gostin, Claef Hakun, Paul Haney, Matthew Hinkle, Kenneth Lee, Carlos Lugo, Adam Matuszeski, Armando Morell, Nerses Armani, Joseph Bonafede, Molly Jackson, Peter Steigner & Juan Stromsdörfer	
Injection of a Body into a Geodesic: Lessons Learnt from the LISA Pathfinder Case .....	15
Daniele Bortoluzzi, Andrea Zambotti, Stefano Vitale, Carlo Zanoni, Luca Gambini, Hans Rozemeijer, John Conklin, Bengt Johlander, Ingo Koeker, Cesar Garcia Marirrodiga, Philipp Nellen & Blondo Seutchat Tcheungang	
Mechanisms Design for the S5P-TROPOMI Instrument .....	29
Erik Tabak, Jan de Vreugd, Dorus de Lange & Frits van der Knaap	
Tests on the Ductility of Stainless Steel and Titanium Alloy Aerospace Fasteners .....	43
Jarrod Whittaker & Daniel Hess	
Development and Testing of a “Backlash-Free” Gas-Tight High-Precision Sample Dosing Mechanism for the ExoMars 2018 Rover .....	51
Daniel Redlich, Robert Paul, Sebastian Ott, Lutz Richter, Quirin Mühlbauer, Markus Thiel, Tim Tattusch, Harald Weisz, Fabio Musso & Stephen Durrant	
Realization and Testing of the In Field Pointing Mechanism for the Evolved Laser Interferometer Space Antenna .....	67
Gert Witvoet & Jet Human	
Suomi-NPP Mission On-orbit Experience with Toroid Ball Bearing Retainers under Unidirectional and Reversing Motion .....	77
Otto Bruegman, Kamal Thakore, Stu Loewenthal & John Cymerman	
Failure Analysis and Recovery of a 50-mm Highly Elastic Intermetallic NiTi Ball Bearing for an ISS Application.....	91
Christopher DellaCorte, S. Adam Howard & Lewis Moore III	
Ball Bearing Analysis with the ORBIS Tool.....	107
Jacob Halpin	
Extended Life Testing of Duplex Ball Bearings.....	121
Jeffrey Mobley, Michael Robertson & Charles Hodges	
Piezoelectric Actuators and Future Motors for Cryogenic Applications in Space.....	135
Christian Belly, Francois Barillot & Fabien Dubois	
Development of a Self-latching Hold-down RElease Kinematic (SHREK) .....	143
Ruggero Cassanelli	
Challenges of Designing a 13-Hz High-Load Vibration Isolation System with Tight Volume Constraints: Lessons Learnt and Path Forward .....	149
Stella Dearing & Dale Ruebsamen	

Development of a High-Performance, Low-Profile Translation Table with Wire Feedthrough for a Deep Space CubeSat .....	155
Alex Few	
Use of Volute Springs in Space Applications.....	163
Chris Floyd, Ian Bournelis & Cary Clark	
A Multi-Sectioning, Reconfigurable Electromagnetic Hammering Propulsion for Mole Penetrators .....	171
Jerzy Grygorczuk, Bartosz Kędziora, Łukasz Wiśniewski, Marta Tokarz, J. Krasowski, Krzysztof Bieńkowski, M. Drogosz, R. Graczyk & Marcin Dobrowolski	
Development of a Magneto-Resistive Angular Position Sensor for Space Mechanisms .....	177
Robert Hahn, Tilo Schmidt, Klaus Seifart, Bastian Olberts & Fernando Romera	
Cu-Al-Ni Shape Memory Single Crystal Wires with High Transformation Temperature.....	185
Alain Hautcoeur, Florian Fouché & Jacques Sicre	
Prevailing Torque Locking Feature in Threaded Fasteners using Anaerobic Adhesive.....	193
Alan Hernandez & Daniel Hess	
A New Architecture for Absolute Optical Encoders.....	199
Timothy Malcolm, John Beasley & Mike Jumper	
Digital Image Correlation for Performance Monitoring.....	205
Miguel Palaviccini, Dan Turner & Michael Herzberg	
Deployment System for Three Axis CubeSat Electric Field Instrument .....	213
Dana Turse, Larry Adams & Chris Esser	
Degradation of Sputter-Deposited Nanocomposite MoS <sub>2</sub> Coatings for NIRCcam during Storage in Air ...	221
Jeffrey Lince, Stuart Loewenthal & Charles Clark	
The Dynamic Particle Generation of Lubricating Greases for use in Space Mechanisms .....	235
Jason Galary	
APM for a Constellation Intersatellite Link – EM Qualification and Lessons Learned .....	247
Frank Härtel & Horst Kozilek	
Design Development of a Combined Deployment and Pointing System for the International Space Station Neutron Star Interior Composition Explorer Telescope.....	261
Jason Budinoff, Keith Gendreau, Zaven Arzoumanian, Charles Baker, Robert Berning, Todd Colangelo, John Holzinger, Jesse Lewis, Alice Liu, Alissa Mitchell, Chuck Monroe, Richard Pugh & Roger Willey	
Development of Compact Mechanically Driven Systems for High Strain Composite Slit-Tubes .....	269
Bruce Davis & Mark Lake	
James Webb Space Telescope Deployment Brushless DC Motor Characteristics Analysis .....	279
Anh Tran	
Development of a Deployment and Latching Mechanism for a Pointing System on the Neutron Star Interior Composition Explorer (NICER) for Goddard Space Flight Center .....	293
Robert Berning & John Holzinger	

Tape Hinge/Lenticular Strut Hinge Qualification and Evolution .....	303
Donald Gibbons	
Design and Development of NEA Scout Solar Sail Deployer Mechanism .....	315
Alexander Sobey & Tiffany Russell Lockett	
MOPITT Mechanisms – 16 Years In-Orbit Operation on TERRA.....	329
Andrew Gibson, Florian Nichitiu, Dwight Caldwell, John Hackett, Robert Deschambault & James Drummond	
Electrical Noise Performance of Gold-on-Gold Slip Rings.....	345
Ron Hayes, Erik Mumm & Kyle Gotthelf	
Slip Ring Electrical Anomalies Found After Protoflight Vibration Testing .....	359
Troy Nilson, Scott Christiansen & Chad Hebert	
State-of-the-Art Reaction Wheel Optimization for Fine-Pointing Space Platforms: Minimizing Induced Vibration Impacts On Hubble Space Telescope Jitter Performance.....	373
Martin Hasha	
Microspine Gripping Mechanism for Asteroid Capture .....	401
Ezekiel Merriam, Andrew Berg, Andrew Willig, Aaron Parness, Tim Frey & Larry Howell	
Hammering Mechanism for HP3 Experiment (InSight) .....	415
Jerzy Grygorczuk, Łukasz Wiśniewski, Bartosz Kędziora, Maciej Borys, Rafał Przybyła, Tomasz Kuciński, Maciej Ossowski, Wojciech Konior, Olaf Krömer, Tilman Spohn, Marta Tokarz & Mateusz Białek	
Testing and Measurement of Mechanism-Induced Disturbances .....	429
Laoucet Ayari, Michael Kubitschek, Gunnar Ashton, Eric Marquardt & Steve Johnston	
Development and Testing of a High-Precision Position and Attitude Measuring System for a Space Mechanism .....	439
Nikolay Khanenya, Gabriel Paciotti, Eugenio Forzani & Luc Blecha	
Development and Testing of a Bi-Stable Actuator based on a High Transition Temperature Shape Memory Alloy .....	453
Gabriel Paciotti, Jacques-Eric Bidaux, Hervé Girard, Fabrice Rottmeier & Luc Blecha	
Holding Brakes for Space Mechanisms with Minimum Power Requirement .....	465
Ted Hopper, Christoph Stuckmann, Scott Starin & Walter Whitehead	
Lean Development of the Future Actuator .....	473
Mathias Burkhalter, Matthias Schulke, Beny Wüthrich & Oliver Kunz	

## SYMPOSIUM SCHEDULE

### WEDNESDAY, 4 MAY 2016

7:00 Wednesday Presenters' Breakfast – Biltmore San Jose Room

8:00 CHECK-IN AND REFRESHMENTS - Biltmore Atrium

8:15 **INTRODUCTORY REMARKS** – Biltmore Ballroom

William Caldwell, Host Chairman, NASA Ames Research Center, Mt View, CA  
Edward Boesiger, General Chairman, Lockheed Martin Space Systems, Sunnyvale, CA  
David Korsmeyer Engineering Director, NASA Ames Research Center, Mt View, CA

#### 8:30 **SESSION I – MOSTLY INSTRUMENTS**

Steve Koss, Session Chair  
Naval Research Laboratory, Washington, D.C.

- ATLAS Beam Steering Mechanism (BSM) Lessons Learned, Ken Blumenstock et al., NASA Goddard Space Flight Center, Greenbelt, MD
- Injection of a Body into a Geodesic: Lessons Learnt from the LISA Pathfinder Case, Daniele Bortoluzzi et al., University of Trento, Trento, Italy
- Mechanisms Design for the S5P-TROPOMI Instrument, Erik Tabak et al., InnoSpace, Rotterdam, The Netherlands
- Tests on the Ductility of Stainless Steel and Titanium Alloy Aerospace Fasteners, Jarrod Whittaker & Daniel Hess, University of South Florida, Tampa, FL
- Development and Testing of a “Backlash-Free” Gas-Tight High-Precision Sample Dosing Mechanism for the ExoMars 2018 Rover, Daniel Redlich et al., OHB System AG, Oberpfaffenhofen, Germany
- Realization and Testing of the In Field Pointing Mechanism for the Evolved Laser Interferometer Space Antenna, Gert Witvoet & Jet Human, TNO Technical Sciences, Delft, The Netherlands

11:30 **LUNCH** - Lunch for AMS Attendees in the Biltmore Courtyard

#### 12:30 **SESSION II – BEARINGS**

Lionel Gaillard, Session Chair  
ESA/ESTeC, Noordwijk, The Netherlands

- Suomi-NPP Mission On-orbit Experience with Toroid Ball Bearing Retainers under Unidirectional and Reversing Motion, Otto Bruegman et al., NOAA, Silver Spring, MD
- Failure Analysis and Recovery of a 50-mm Highly Elastic Intermetallic NiTi Ball Bearing for an ISS Application, Christopher DellaCorte & S. Adam Howard, NASA Glenn Research Center, Cleveland, OH; Lewis E. Moore III, NASA Marshall Space Flight Center, Huntsville, AL
- Ball Bearing Analysis with the ORBIS Tool, Jacob Halpin, Halpin Engineering LLC, Torrance, CA
- Extended Life Testing of Duplex Ball Bearings, Jeffrey Mobley, Michael Robertson & Charles Hodges, Sierra Nevada Corporation, Durham, NC

**2:30 BREAK**

**2:45 SESSION III – POTPOURRI OF POSTERS & PAPERS**

Scott Starin, Session Chair

Avior Control Technologies, Inc., Longmont, CO

- Piezoelectric Actuators and Future Motors for Cryogenic Applications in Space, Christian Belly, Francois Barillot & Fabien Dubois, Cedrat Technologies, Meylan, France
- Development of a Self-latching Hold-down RElease Kinematic (SHREK), Ruggero Cassanelli, AEREA S.p.A., Turate, Italy
- Challenges of Designing a 13-Hz High-Load Vibration Isolation System with Tight Volume Constraints: Lessons Learnt and Path Forward, Stella Dearing & Dale Ruebsamen, Honeywell Aerospace, Defense and Space, Glendale, AZ
- Development of a High-Performance, Low-Profile Translation Table with Wire Feedthrough for a Deep Space CubeSat, Alex Few, NASA Marshall Space Flight Center, Huntsville, AL
- Use of Volute Springs in Space Applications, Chris Floyd, Ian Bournelis & Cary Clark, Lockheed Martin Space Systems Company, Littleton, CO
- A Multi-Sectioning, Reconfigurable Electromagnetic Hammering Propulsion for Mole Penetrators, Jerzy Grygorczuk et al., Centrum Badań Kosmicznych PAN, Warsaw, Poland
- Development of a Magneto-Resistive Angular Position Sensor for Space Mechanisms, Robert Hahn et al., HTS Hoch Technologie Systeme GmbH, Coswig, Germany
- Cu-Al-Ni Shape Memory Single Crystal Wires with High Transformation Temperature, Alain Hautcoeur & Florian Fouché, Nimesis Technology, Mecleuves, France; Jacques Sicre, CNES, Toulouse, France
- Prevailing Torque Locking Feature in Threaded Fasteners using Anaerobic Adhesive, Alan Hernandez & Daniel Hess, University of South Florida, Tampa, FL
- A New Architecture for Absolute Optical Encoders, Timothy Malcolm, John Beasley & Mike Jumper, BEI Precision Systems & Space Company, Maumelle, AR
- Digital Image Correlation for Performance Monitoring, Miguel Palaviccini & Dan Turner, Sandia National Labs, Albuquerque, NM; Michael Herzberg, National Security Campus, Kansas City, MO
- Deployment System for Three Axis CubeSat Electric Field Instrument, Dana Turse, Larry Adams & Chris Esser, Composite Technology Development, Inc., Lafayette, CO
- Degradation of Sputter-Deposited Nanocomposite MoS<sub>2</sub> Coatings for NIRCams during Storage in Air, Jeffrey Lince, The Aerospace Corporation, El Segundo, CA; Stuart Loewenthal & Charles Clark, Lockheed Martin Space Systems Company, Sunnyvale, CA
- The Dynamic Particle Generation of Lubricating Greases for use in Space Mechanisms, Jason Galary, NYE Lubricants, Fairhaven, MA

**6:30 -10:00 RECEPTION – Biltmore Hotel**

Invited component suppliers display current products and provide tutorials along with FIRST Robotics Team demonstrations and a light buffet meal.

## **THURSDAY, 5 MAY 2016**

7:00 Thursday Presenters' Breakfast – Biltmore San Jose Room

### **8:00 SESSION IV – I LIKE TO MOVE IT**

Rob Kyle, Session Chair

CDA Intercorp LLC, Deerfield, FL

- APM for a Constellation Intersatellite Link – EM Qualification and Lessons Learned, Frank Härtel & Horst Kozilek, Airbus Defence and Space, Friedrichshafen, Germany
- Design Development of a Combined Deployment and Pointing System for the International Space Station Neutron Star Interior Composition Explorer Telescope, Jason Budinoff et al., NASA Goddard Space Flight Center, Greenbelt, MD
- Development of Compact Mechanically Driven Systems for High Strain Composite Slit-Tubes, Bruce L. Davis & Mark Lake, Roccor, Louisville, CO
- James Webb Space Telescope Deployment Brushless DC Motor Characteristics Analysis, Anh Tran, Northrop Grumman Aerospace Systems, Redondo Beach, CA

### **10:00 BREAK**

### **10:15 SESSION V – DEPLOY**

Art Grant, Session Chair

Harmonic Drive LLC, Peabody, MA

- Development of a Deployment and Latching Mechanism for a Pointing System on the Neutron Star Interior Composition Explorer (NICER) for Goddard Space Flight Center, Robert Berning & John Holzinger, Moog Inc. Chatsworth, CA
- Tape Hinge/Lenticular Strut Hinge Qualification and Evolution, Donald Gibbons, Lockheed Martin Space Systems Company, Sunnyvale, CA
- Design and Development of NEA Scout Solar Sail Deployer Mechanism, Alexander Sobey & Tiffany Lockett, NASA Marshall Space Flight Center, Huntsville, AL
- MOPITT Mechanisms – 16 Years In-Orbit Operation on TERRA, Andrew Gibson et al., Canadian Space Agency, Ottawa, Canada

12:15 **LUNCH** - Lunch for AMS Attendees in the Biltmore Courtyard

### **1:15 SESSION VI – "OH THE NOISE!, NOISE!, NOISE! NOISE!"**

Martin Gordinier, Session Chair

Gurley Precision Instruments, Troy, NY

- Electrical Noise Performance of Gold-on-Gold Slip Rings, Ron Hayes, Erik Mumm & Kyle Gotthelf, Honeybee Robotics Spacecraft Mechanisms Corporation, Longmont, CO
- Slip Ring Electrical Anomalies Found After Protoflight Vibration Testing, Troy Nilson, Scott Christiansen & Chad Hebert, Sierra Nevada Corporation, Louisville, CO



- State-of-the-Art Reaction Wheel Optimization for Fine-Pointing Space Platforms: Minimizing Induced Vibration Impacts On Hubble Space Telescope Jitter Performance, Martin Hasha, Lockheed Martin Space Systems Company, Sunnyvale, CA

## 2:45 **BREAK**

### 3:00 **SESSION VII – SMALL SAMPLE OF SAMPLERS**

Erik Mumm, Session Chair

Honeybee Robotics Spacecraft Mechanisms Corp., New York, NY

- Microspine Gripping Mechanism for Asteroid Capture, Ezekiel Merriam et al., Brigham Young University, Provo UT
- Hammering Mechanism for HP3 Experiment (InSight), Jerzy Grygorczuk et al., ASTRONIKA Sp. z o.o., Warsaw, Poland

### 4:00 **INVITED PRESENTATION** - SOFIA and recent accomplishments of the program

Dr. Eric Becklin

Chief Scientist for the Stratospheric Observatory for Infrared Astronomy (SOFIA)

### 6:00-10:00 **BANQUET** – Mountain Winery

Dinner and entertainment at an historic winery in the Santa Cruz Mountains

## **FRIDAY, 6 MAY 2016**

7:30 Friday Presenters' Breakfast – Biltmore San Jose Room

### 8:30 **SESSION VIII – MANUFACTURING/TESTING**

Steve Bauman, Session Chair

NASA Glenn Research Center, Cleveland, OH

- Testing and Measurement of Mechanism-Induced Disturbances, Laoucet Ayari et al., Ball Aerospace & Technologies Corp., Boulder, CO
- Development and Testing of a High-Precision Position and Attitude Measuring System for a Space Mechanism, Nikolay Khanenya et al., Almatech, Lausanne, Switzerland

## 9:30 **BREAK**

### 9:45 **SESSION IX – ACTUATORS**

Lance Werthman, Session Chair

Lockheed Martin Space Systems Co., Sunnyvale, CA

- Development and Testing of a Bi-Stable Actuator based on a High Transition Temperature Shape Memory Alloy, Gabriel Paciotti et al., Almatech, Lausanne, Switzerland
- Holding Brakes for Space Mechanisms with Minimum Power Requirement, Ted Hopper et al., MACCON GmbH, Munich, Germany
- Lean Development of the Future Actuator, Mathias Burkhalter et al., RUAG Space, Zurich, Switzerland

**11:15 SPECIAL PRESENTATION ON NASA AMES**

Jack Boyd, Senior Advisor to the NASA Ames Center Director

**TECHNICAL SESSIONS CONCLUSION**

Stu Loewenthal, Deputy Chairman, Lockheed Martin Space Systems, Sunnyvale, CA

- Herzl Award Presentation – Nadine Herzl-Kraft

**12:15 LUNCH** - Lunch for AMS Attendees in the Biltmore Courtyard

**1:30 – 5:00 TOUR**

1:30 Buses depart hotel for industry tours

5:00 Approximate time buses return to hotel

## **SYMPOSIUM ORGANIZING COMMITTEE**

### **Host Chairs**

**William Caldwell, NASA ARC**

**Fred G. Martwick, NASA ARC**

**General Chairman - Edward A. Boesiger, Lockheed Martin**

**Deputy Chairman - Stuart H. Loewenthal, Lockheed Martin**

**Steven W. Bauman, NASA GRC**

**Jared Dervan, NASA MSFC**

**Michael Dube, NASA NESC**

**Barry J. Dunn, NASA LaRC**

**Carlton L. Foster, NASA MSFC (retired)**

**Lionel Gaillard, ESA/ESTeC**

**Claef F. Hakun, NASA GSFC**

**Christopher P. Hansen, NASA JSC**

**Louise Jandura, JPL**

**Wayne Jermstad, NASA JSC**

**Alan C. Littlefield, NASA KSC**

**Ronald E. Mancini, NASA ARC (retired)**

**Donald H. McQueen, Jr., NASA MSFC**

**Robert P. Mueller, NASA KSC**

**Joseph Pellicciotti, NASA NESC**

**Minh Phan, NASA GSFC**

**Joseph P. Schepis, NASA GSFC**

**Donald R. Sevilla, JPL**

**James E. Wells, NASA LaRC**



# ATLAS Beam Steering Mechanism Lessons Learned

Kenneth A. Blumenstock\*, Alexander K. Cramer\*, Alan B. Gostin\*, Claef F. Hakun\*, Paul G. Haney\*, Matthew R. Hinkle\*, Kenneth Y. Lee\*, Carlos F. Lugo\*, Adam J. Matuszeski\*, Armando Morell\*, Nerses V. Armani\*\*, Joseph Bonafede\*\*, Molly I. Jackson\*\*, Peter J. Steigner\*\* & Juan J. Stromsdörfer\*\*

## Abstract

This paper describes the design, testing, and lessons learned during the development of the Advanced Topographic Laser Altimeter System (ATLAS) Beam Steering Mechanism (BSM). The BSM is a 2 degree-of-freedom tip-tilt mechanism for the purpose of pointing a flat mirror to tightly control the co-alignment of the transmitted laser and the receiver telescope of the ATLAS instrument. The high resolution needs of the mission resulted in sub-arcsecond pointing and knowledge requirements, which have been met. Development of the methodology to verify performance required significant effort. The BSM will fly as part of the Ice, Cloud, and Elevation Satellite II Mission (ICESat II), which is scheduled to be launched in 2017. The ICESat II primary mission is to map the Earth's surface topography for the determination of seasonal changes of ice sheet thickness and vegetation canopy thickness to establish long-term trends.

## Introduction

The primary purpose of this paper is to focus upon “Lessons Learned” that came about during the development of the ATLAS Beam Steering Mechanism (BSM). A secondary purpose is to review the configuration and design features of the BSM, as well as to gain understanding of the reasoning behind some of the design features.

Light, Detection, and Ranging (LiDAR) systems have been used for numerous spaceflight missions. High-powered laser pulses fired from the spacecraft are reflected off the Earth's surface and back to the spacecraft, where they are detected. Measurement time from firing to detection determines the distance to the surface, and signal characteristics reveal additional properties of the atmosphere and surface. ATLAS maps the topography of our planet to monitor seasonal changes in ice sheet and vegetation canopy thickness, which is very important in gaining understanding of long-term trends.

As technology advances, there is always a desire to gain better resolution of measurements. ATLAS has the smallest transmitted beam, smallest receiver field of view, and smallest alignment margin among NASA/GSFC space-borne laser altimeters. This resulted in the stringent requirements imposed upon the BSM, which led to further challenges in verifying that those requirements were met.

## Design

### Overview

An exploded view of the BSM is in Figure 1. Not shown in that figure are both the actuators and the position sensors, which can be seen in the cross sections of Figure 2.

### Mirror

The BSM mirror, which reflects a high-powered laser, required a dielectric coating to provide very high reflectivity at the wavelength of the laser. A metal mirror would not support a dielectric coating, resulting in

---

\* NASA Goddard Space Flight Center, Greenbelt, MD

\*\* Stinger Ghaffarian Technologies Inc., Greenbelt, MD

lower reflectivity, causing more heat on the mirror, thus degrading figure requirements. For a dielectric coating a glass substrate is required, coated on both front and back of the mirror to cancel stresses.

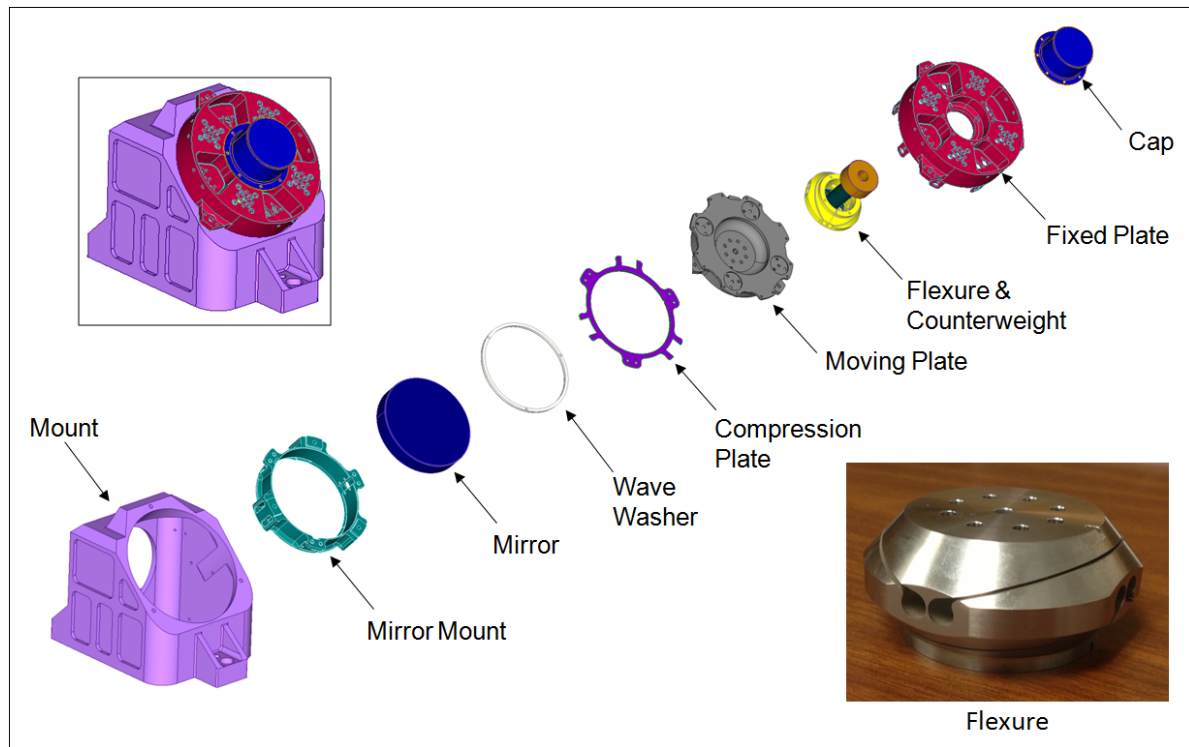


**Figure 1. BSM Exploded View**

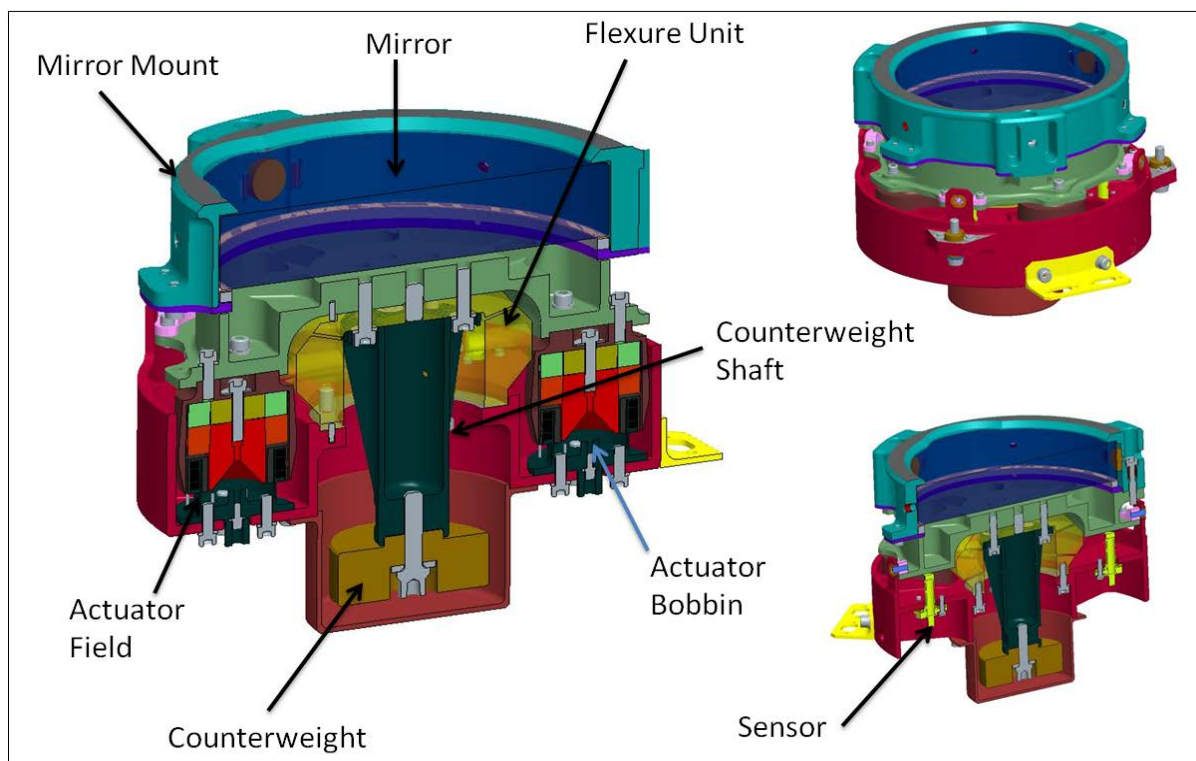


**Figure 2. Cross Sections**

To meet figure requirements, a rather thick mirror was required, resulting in a significant mass. This mirror mass was a significant design driver. An increase in mirror mass results in the need for a larger counterbalance mass, together increasing the total moving mass. The total moving mass is supported by the flexures, which need to survive launch loads without degradation.

#### Flexures

The flexures were electrical discharge machined from conventionally machined titanium. Arrangement of the flexures allows the mirror to rotate about two orthogonal axes. Finite Element Method (FEM) structural and modal analysis was used to trade structural mode frequencies to determine the optimal flexure geometry. Flexures were designed to keep stresses within levels to result in infinite life.

#### Actuators

A pair of voice coil actuators is used to control each axis. The actuators were of an in-house custom design to achieve high efficiency, utilizing a high-performance cobalt-iron alloy along with an arrangement of axial and radial magnets. Cobalt-iron shaping put most of the cobalt-iron near saturation, saving mass. The actuators have redundant windings, with a primary winding in the bobbin center and a secondary winding split inner and outer of the primary winding. This arrangement equalized actuator performance of primary and secondary windings. Equalizing was needed as a result of the air gap magnetic field drop when moving away from the magnet side of the actuator. High damping was incorporated by the inclusion of a copper damping sleeve as a part of each actuator.

#### Damping

High damping adds greatly to the disturbance rejection capability of the system. Disturbances can originate externally, as a result of jitter from momentum wheels and other sources propagating through the spacecraft structure; or internally, from electrical noise or quantization error in the control system. Damping can be provided by closing a velocity loop, which does not have to waste power to overcome the damping during slew operations.

Implementing a velocity loop, however, results in several issues, including the need for a very sensitive velocity sensor to detect low velocities, and could even result in decreased pointing stability as the result of added electronics noise. Such architecture could result in a very large and heavy velocity sensor with very fine, non-robust wire to achieve a high turn count, and might require pre-amplification near the sensor. Deriving velocity from a position sensor also has its limitations, especially when trying to sense low velocities.

Passive damping with a shorted coil, such as a solid copper sleeve, can waste power when slewing. In the case of the BSM, operational mirror velocities are very small, thus there is insignificant impact upon operational power required to overcome shorted coil passive damping. Thus, shorted coil damping was implemented in the BSM actuator design. Figure 3 shows actuator cross section and component views.

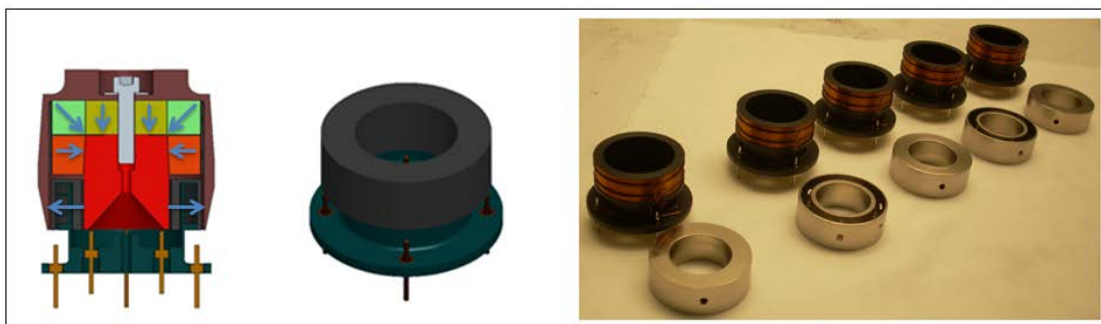


**Figure 3. BSM Actuator Cross Section, Bobbin Assy., and Bobbins with Sleeves**

Damping also proved very useful for minimizing loads during launch. The mirror is free to move until hard stops are contacted. Much of the energy is absorbed by the passive damping. This prevented the need for implementation of a launch lock mechanism.

#### Position Sensors

Differential Impedance Transducer position sensors were chosen from Blue Line Engineering. A pair of sensors was used to sense the angle of each axis. Sensor targets were located on the rotation axes as one function of the aluminum "moving plate," to which the mirror mount assembly attaches. The surface was machined to be planar. Keeping the targets close to the rotation axis minimizes target translation, which is a source of sensor error. Ensuring a planar surface minimizes sensor error that would result from target translation.

#### Modal Considerations

Precision pointing mechanisms require closed-loop control for fast response and required disturbance rejection, which results in the need for high controller bandwidth. It is of critical importance to design the mechanism such that its structural modes are compatible with the controller bandwidth--typically the minimum structural mode must be several times the controller bandwidth frequency. However, high Q modes (high amplitude modal peak) may need to be farther from the controller bandwidth frequency, and lower Q modes could be closer. Also, modes that are in a different direction than the controlled direction might be less of a problem. It is difficult to accurately assess how the structural modes will affect performance until after the hardware is built.

All mechanism components were analyzed for modal frequencies, with the goal of keeping those frequencies to at least four times the controller bandwidth of 70 Hz. In some cases, it was not practical to achieve modal frequencies of four times the controller bandwidth. Most exceptions were modes that analysis showed to be occurring in directions other than in directions that the mirror is controlled.

#### Thermal Stability

Absolute position knowledge required tight thermal stability, dictating the mechanism materials. The BSM Engineering Model had an aluminum structure that mounted onto an aluminum housing. The housing interfaced with a composite bench with titanium inserts. Analysis found thermal instability to be greater than acceptable, so the housing and BSM structure material was changed to titanium for the BSM Flight Model. So, all is titanium up to and including the flexure. The moving side of the flexure comprises the moving plate and the mirror mount, all of which are aluminum. The titanium flexure to aluminum moving plate interface, with its symmetrical and small diameter connection, did not pose any thermal interface issues.

### **Lessons Learned**

#### Overview

Various issues came about during the development of the BSM, as happens with any engineering development. Most issues were resolved in short order. Some of these issues and their lessons learned will be discussed. For this project, verification of requirements was a major focus throughout the development, which will be touched upon.

#### Performance Verification Challenge

Performance verification required a high data sample rate along with highly accurate dynamic measurements over the operating environment, so it was determined that a lab interferometer would be a necessary verification instrument. However, due some measurement non-linearity errors resulting from BSM mirror properties being incompatible with the laboratory interferometer wavelength as well as temperature stability issues of the set-up, static measurements were employed to compensate for these shortcomings. Thus, utilization of multiple measurement instruments along with a data acquisition approach was devised and successful requirements verification was achieved. Pre-planning of the data acquisition approach and the proposed data reduction methods were approved by the project science team early on, paving the way for a very successful outcome.



Verifying the BSM pointing requirements necessitated the use of three separate optical references: a three-axis displacement-measuring interferometer from the Zygo Corporation, a Leviton Inter-target Differential Electronic Autocollimator (IDEA), and a Leica T3000 Theodolite. There was no single metrology solution that could provide high resolution, high accuracy, and absolute position verification over the BSM mirror's full range of motion. Rather, it was necessary to utilize information from multiple reference instruments in order to verify the requirement.

The Zygo interferometer setup consisted of a 3-axis High Stability Plane Mirror Interferometer, driven by a Zygo laser and measured by a Zygo ZMI4100 measurement board (Figure 4). This setup provided both the highest time and spatial resolution, achieving a 10-kHz cadence and having an advertised resolution of just over 20 nanoradians. Unfortunately, its field-of-view (FOV) of  $\pm 3$  milliradians, compared to the 5.6 milliradian range to be measured, resulted in the need to realign the interferometer to capture the full FOV. The pitch axis was prone to significant non-linearity, in part caused by a polarization effect of the BSM mirror's dielectric coating, which was tuned to the 532-nm ATLAS laser, but not the 633-nm Zygo laser wavelength. This non-linearity meant that only the yaw axis data of the Zygo was trusted, and led to inconveniently taking Zygo measurements of both BSM axes using only the Zygo yaw axis. The Zygo has no reference, so is not an absolute, but rather is an incremental sensor. The characteristics of the Zygo made it impractical for TVac testing, but it was extensively used for the bulk of testing.

The IDEA autocollimator has a FOV of roughly  $\pm 10$  milliradians, is very compact and lightweight, has a very high accuracy of 2.5 microradians, and is very stable. IDEA makes use of a reference flat to measure against, which minimizes measurement drift, making it an absolute measurement instrument. No optical adjustments are required to measure the difference between the reference flat and the mirror of interest, which in this case was the BSM Mirror. An aperture select mechanism is required to alternate IDEA's view between the reference flat and the BSM mirror. The IDEA characteristics made it ideal for measuring thermal stability during Thermal Vacuum (TVac) (Figure 5), though it was also used for non-TVac testing. IDEA is a low bandwidth device, able to achieve a maximum cadence on the order of 5 Hz.

The theodolite offered similar performance as IDEA, though large and bulky, but unlike IDEA, it required manual operation for each measurement. Theodolites have significantly more heritage as an optical reference than IDEA, which is a fairly new development not yet commercially available. Measurements taken with a theodolite were used to determine the BSM sensor scale factors and axis orientation.

Optical measurements during TVac were taken using IDEA, whose wider FOV could tolerate gross motion of the BSM mount due to temperature changes in the vacuum chamber. IDEA measurements were used to make temperature-dependent adjustments to the scale factor, determined before TVac. Performance over the full range was quantified using interferometer data which had been post-processed to remove non-linearities. Processing a combination of data from these three instruments verified BSM pointing performance over its full required range of motion and temperature.

The photo of Figure 6 shows optical references used by the measurement instruments. The BSM cube was used by the theodolite as a position reference. The reference flat was used by IDEA as its position reference.

As position knowledge and pointing requirements for similar systems in the future become more demanding, verifying these requirements will require not only the synthesis of measurements from multiple references, but also deep understanding of the limitations of each reference chosen.

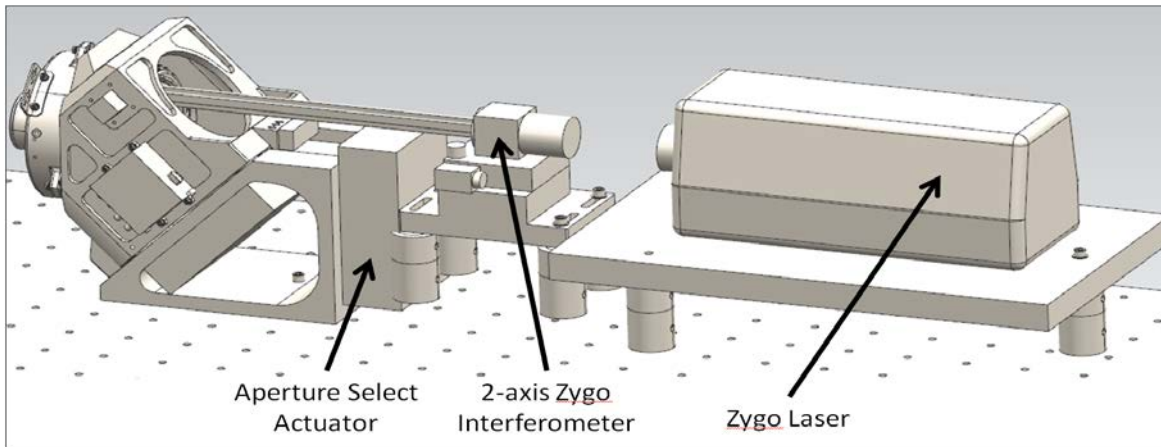


**Figure 4. Interferometer Setup**

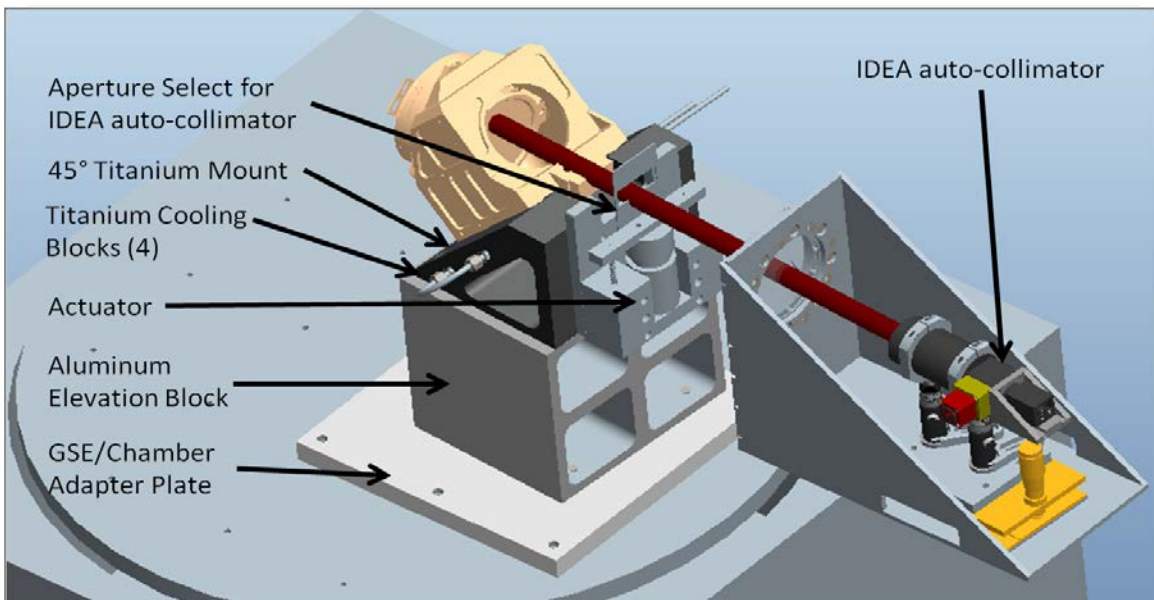


**Figure 5. TVac Configuration Using IDEA**

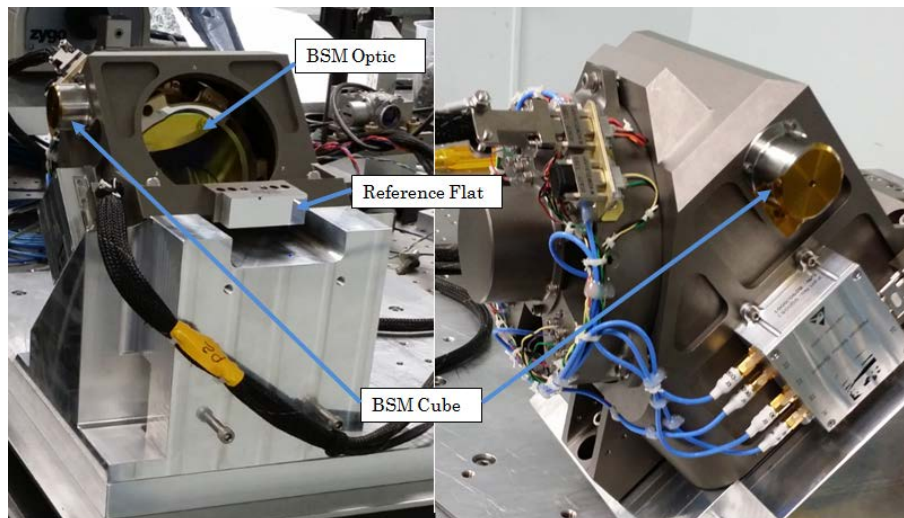


**Figure 6. BSM Optic and Optical References**

### Initial Inconsistent Performance

When the BSM Engineering Model was available for testing, it was mounted to an optical bench and initial frequency response testing was performed. The controls engineers were finding inconsistency upon taking successive frequency responses and it was further found that changing the torque of the mounting hardware changed those responses. Due to the fact that proper hardware for mounting the BSM to the bench was not yet ready, the BSM housing was clamped to the bench using machine tooling. The surface of the honeycomb optical bench is made of a thin section of steel with threaded holes on 1-inch (2.5-cm) centers. There certainly was not concern over the stiffness of the bench that also happened to sit on a very thick granite table, which was floating on a seismic block. However, local attachment threaded holes did not provide adequate stiffness, thus affecting response measurements. The issue was eliminated by adding a half-inch-thick (1.3-cm) aluminum plate between the bench and BSM hardware.

### Undesirable Structural Mode

Measurement of the frequency response found there to be a very undesirable structural mode near 900 Hz. While this frequency was quite far from the controller bandwidth, the mode had a very high Q, which made it troublesome. Very unusual was the wide frequency range of the base of this mode, such that it did not have behavior consistent with that of a structural mode. One of the controls engineers was able to implement filtering in order to deal with this mode, sacrificing some phase margin, but still leaving adequate phase margin.

Careful study was made of the modal analysis to determine the source of this behavior, but it is typical to find that modes revealed in the model do not match the measured modes. Using FEM modal analysis, we were unable to determine the source of this very troubling behavior. The modal analysis software tool does not specify an input location, or an output location. Furthermore, guesses are made to choose damping values for the materials to input into the analysis tool. In the physical world, the frequency response input is the current to the actuators, which becomes localized force inputs, and the frequency response output is the position sensor signal, which is the motion of the sensor targets. So, the modal analysis cannot be expected to give an accurate representation of the measured frequency response. We would be pleased to be made aware of analysis tools that can better predict frequency response for a mechanism with actuators and sensors intended for closed-loop control.

Certainly, management was concerned that effort was being expended to correct this modal behavior issue. The question was posed, "Do we meet requirements?" The answer was that we did on the bench, but the possibility of structural mode behavioral changes after integration, or even on-orbit, requires having capability to deal with such changes. The controls engineer had designed in the capability for a maximum number of poles for filtering, but with the unusual mode, there was risk that filter capability could be insufficient to deal with structural mode changes that might potentially come about.

We hit a dead end using FEM analysis, so we chose a brute force method to find out what was causing the troubling structural mode. The BSM does not have many parts. Trial and error changing of parts with modified parts was the technique implemented. Since the BSM required a rather heavy tungsten counterweight, it was theorized that a lack of stiffness of the titanium counterweight shaft could be responsible. The drawing was revised and parts were put into fabrication. After planned testing of the BSM Engineering Model was completed, the new and stiffer ribbed titanium counterweight shaft was installed. The new frequency response showed that the massive and wide structural mode was replaced by small, typical looking structural modes. Problem solved. The before and after open loop frequency responses (of mechanism and controller together) are shown in Figure 7.

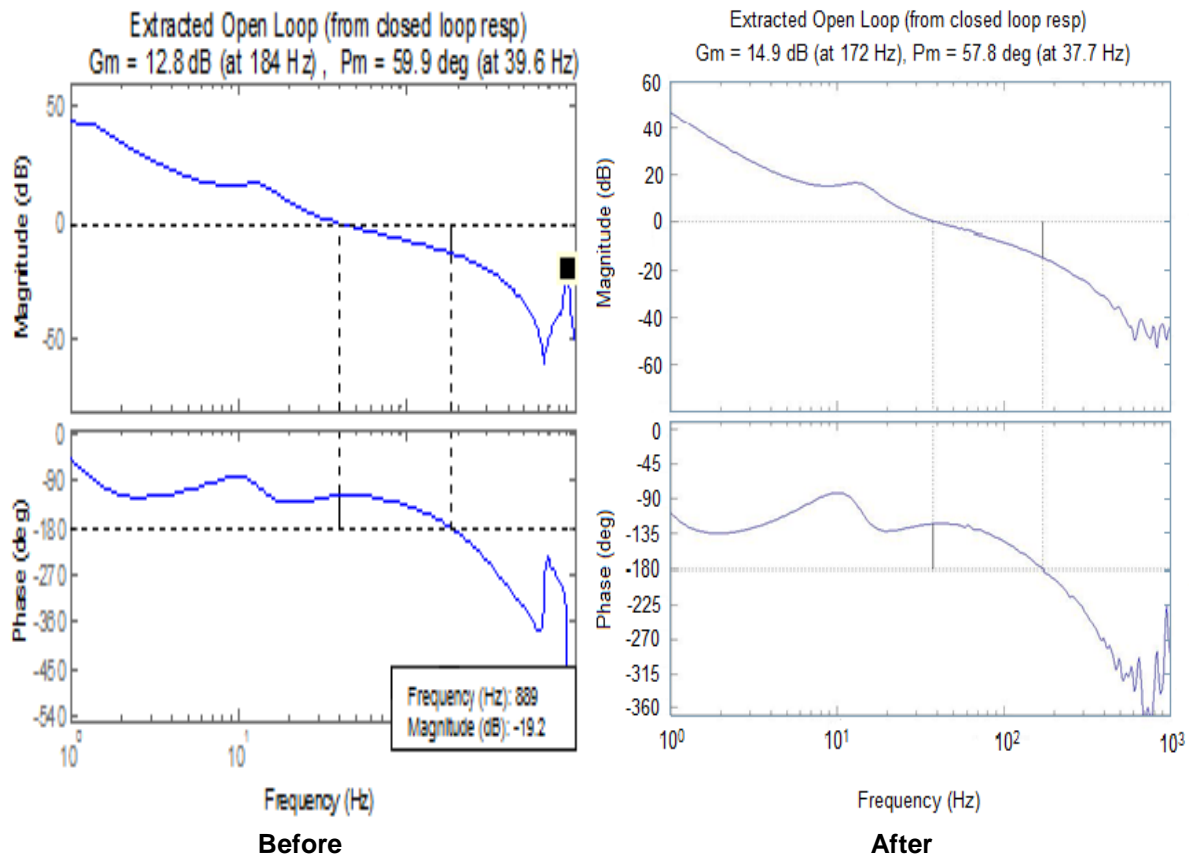


**Figure 7. Frequency Response Before and After Counterbalance Shaft Change**

#### Hipot Overtesting Failure

Qualification of the in-house voice coil actuators required high potential (hipot) and insulation resistance testing to be performed. We referred to one of our test specifications documents, and applied a test voltage of over 1000 volts, which resulted in a failed actuator winding. After investigation, it turned out that our test specifications were really intended to be used for cable and connector testing. Furthermore, we found out that lower voltages were regularly being used for most cable testing, more so for cables with miniature connectors. Since our operational voltage was no more than 12 volts, it was decided to test at 250 volts, after which all hipot and insulation resistance tests were passed without issue. So, the lesson learned is to not blindly follow documentation. We should have surveyed the standard practice for motor winding hipot and insulation resistance testing rather to follow a test specification that was not applicable. Another factor was that we were probably overly confident that our design was bullet proof. It is not prudent to overtest.

#### Undesirable Behavior of the Flight Model

The BSM Flight Model had completed its testing just at the point ready for environmental testing to begin. The controls engineers discovered puzzling behavior of the BSM Flight Model not seen in the BSM Engineering Model. When making mirror motions from one point to another, the trajectory would miss the commanded go-to point and then circle back before arrival to that point. While such behavior was always seen in the BSM Engineering Model, it was not seen at the magnitude observed in the BSM Flight Model. We were privileged to have one of our top technicians perform the assembly of all the BSMs. During our investigation, it was revealed that our technician observed an unusual behavior during the balancing process. The balancing process was dependent upon usage of the highly sensitive internal position sensors. The BSM Flight Model was mounted into a cubical framework that allowed the mechanism to be oriented with gravity in six different directions, two with the counterbalance shaft vertical, and four with the

counterbalance shaft horizontal, with vectors in plus/minus X, Y, and Z (Figure 8). Once balanced, changing the gravity vector direction by 180 degrees should not result in mirror positional changes. However, when checking balance in the X vector, the technician was observing changes in Y, and when checking balance in the Y vector, he was seeing changes in X.

Our technician was advised to not pay attention to changes in the axes he was not balancing since it would only create confusion in the balancing process. That instruction allowed the technician to complete the balancing, but we should have paid attention to the resulting magnitude of the non-gravity-aligned axis. We realized that changing the gravity vector by 180 degrees of what we believed to be a balanced BSM resulted in significant motion in the orthogonal non-gravity aligned axis. This was a very puzzling behavior.

If mirror motions were constrained to flex either one flexure or its orthogonal flexure, axes A and B, that motion would be rotated from the sensor axes X and Y by 45 degrees. The counterweight, its position location Z at the end of the counterbalance shaft, is adjusted by shims to achieve balance. However, flexure rotation locations on Z need to be identical. If flexure rotation locations are different, it is only possible to achieve balance upon one flexure axis or the other. A compromise could be made, such that one flexure axis would be mirror light and the other axis could be equally mirror heavy. The lack of co-alignment of the flexure axes with the sensor axes is important to understanding the behavior observed.

Refer to Figure 9 for the imbalance phenomena explanation that follows. Assume the balance is perfect and the Y axis is aligned with the gravity direction. The mirror will point to position 0 at the origin. Let us move one of the flexure axes in +Z to make the moving assembly mirror light, and then move the other flexure axis in -Z to make the moving assembly mirror heavy. Remember that the flexure axes A and B are such that mirror motion on either flexure axis A and B is constrained to be in a direction that is 45 degrees from the sensor axes. If looking from the back of the mirror along the counterbalance shaft, assume that the mirror light flexure axis A pointed the mirror up and to the right, following the blue arrow to position 1. Motion on the mirror heavy axis B would then be down and to the right, following the red arrow to position 2. The net result is that imbalance did not affect the Y sensor axis in the gravity direction, but rather, the net motion was to the right in the X horizontal, non-gravity-aligned axis, following the purple arrow from position 0 to position 2. It does seem counterintuitive that changing the gravity vector 180 degrees results in motion on an axis that is orthogonal to the gravity vector, yet such motion is an indication of imbalance. Had the flexure axes been aligned with the sensor axes, it would have been apparent that balancing one axis would result in the other axis not being balanced.

The root cause turned out to be that flexure manufacturing tolerances were not met, with the two flexure rotation locations separated in Z by about 0.009 inch (0.23 mm). Inspection reports were incorrect, due to improper fixturing and confusing geometric tolerances. New flexures needed to be manufactured, unfortunately resulting in significant schedule slip. Had there been better awareness of the behavior anomaly, we could have caught the issue sooner.

#### Unknown Pole

An unknown pole of 150 Hz was present in the frequency response, but was accommodated with filtering. The pole is unknown in that a MATLAB/Simulink model of the BSM, based upon the mechanical and electrical specifications, did not reveal such a pole. Similar behavior was observed on the Cassini Composite Infrared Spectrometer (CIRS) Scan Mechanism developed in the early 1990s, which also had damping designed into its custom actuator. Since in both cases, we needed to deliver hardware on a tight schedule and we were able to meet performance requirements with the extra pole, we moved forward. In both cases the project ended without the opportunity to spend the time to fully understand the physics behind the behavior. However, we believe the unknown pole to be the result of coupling between the actuator windings and the damping sleeve, which were arranged coaxially in both projects (Figure 10).

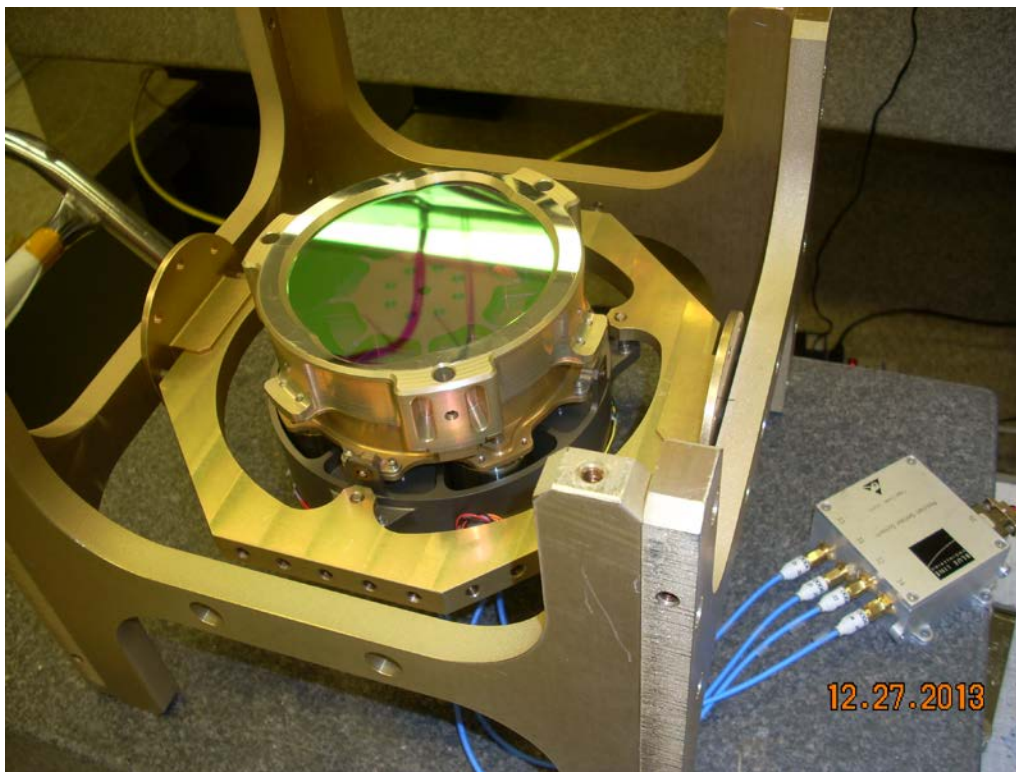


Figure 8. BSM Flight Model Mounted in the 6-Axis Balancing Fixture

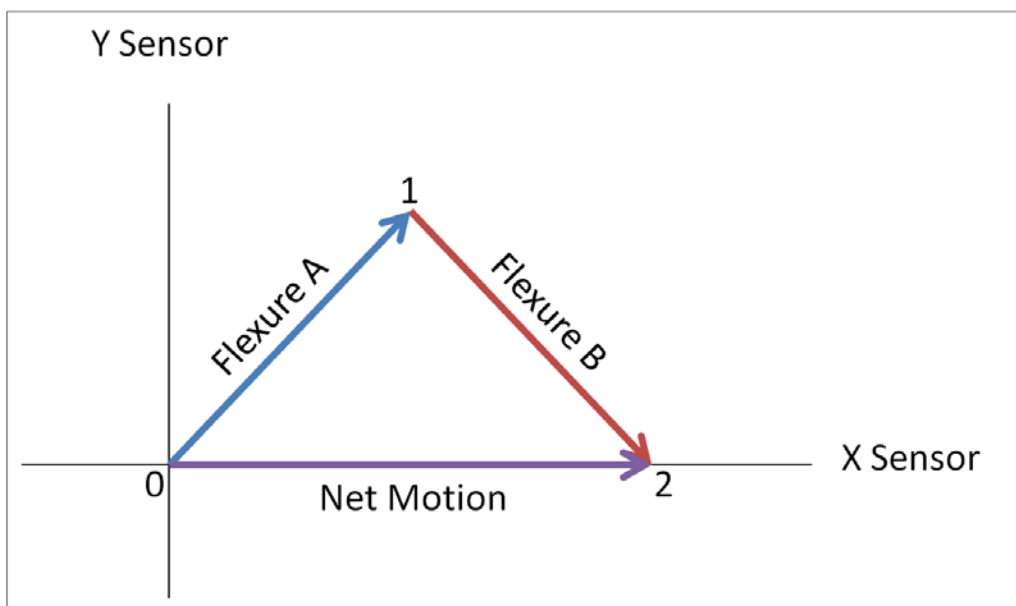


Figure 9. Imbalance Phenomena Explanation Graphic



We did design and fabricate actuator bobbins that separated the windings from the damping sleeves such that they would not be coaxial, but we never had the opportunity to test them. The more prevalent pole was the BSM, and the BSM was designed to have much greater damping than the Scan Mechanism, so it appears that there is a relationship between the amount of damping and the prevalence of the pole. If a non-coaxial design would reduce or eliminate the pole, phase margin could be greater resulting in reduced compensation output, better performance, and increased robustness.

#### Sensor Fabrication Issue

Our Differential Impedance Transducer sensors vendor, Blue Line Engineering, did an excellent job of providing sensors to meet our specifications. The raw sensor behavior is non-linear, so the sensor electronics undergo a tuning process to trade off various performance parameters. The vendor was able to predict very well what they could achieve. We pushed them to the limits of what was achievable for our application and for their technology.

While the vendor certainly was under schedule pressure, there are usually multiple reasons for explanation of any mishap. An error occurred during manufacture of the flight sensors. The epoxy used for potting the cables into the sensor bodies did not cure, which was one of the final steps in manufacturing the sensors. The root cause was an error in computing the mass of the components that were mixed, so the mix ratio was incorrect. It was necessary to build a new set of sensors, resulting in a small schedule slip. The vendor was very responsive and manufactured a new set of sensors very quickly.

While samples of pucks were provided for all epoxy mixes for outgassing testing, this process did not alleviate the risk of an error, but would catch the error after it occurs. Since significant work was at risk if an error in mixing occurred, it would have been prudent to have more checks in place. One possibility could have been to use premixed epoxy stored at cold temperature that had already been tested for outgassing.

A process error such as this can always happen. This lesson is a reminder to elevate checks to prevent such errors, dependent upon the amount of rework that is at stake if a process fails.

#### Schedule Pressure

In more recent times, pressure to meet schedule and budget has come under higher levels of scrutiny than in the past. For this particular project, the in-house engineering team was turned on at the 11<sup>th</sup> hour to produce the entire mechanism from concept to flight. This put us on a tight schedule.

The BSM was initially determined to be supplied from a vendor, but the work was taken in-house after an environmental test failure. The project originally chose the vendor as a cost savings measure since it is more cost effective to buy already developed hardware than it is to develop hardware. However, it turned out that the vendor's hardware had design shortcomings such that flight qualification would require redesign, so the perceived cost savings evaporated. The project further benefited going in-house since BSM requirements were compromised in order to utilize the vendor's hardware, so once the work was brought in-house, optical requirements tightened up significantly.

Being on a tight schedule put us in the spotlight. Management was very concerned and preferred to have hardware sooner than later. Sometimes it is useful to develop some hardware early on to help with the design process if analytical methods lack fidelity, such that the easier path is to build and test. In this case, we determined that any early hardware development would not be of benefit, and also that early hardware development would hurt cost and schedule. Though management desired a quick hardware cycle, we were thankful that the team was permitted to take the necessary time to design and analyze to the degree deemed most efficient.

It takes time and effort to develop hardware. Significant time is expended for procurement and fabrication, followed by time and effort for assembly and testing. The proper approach is to do all your homework and design it right the first time. Ideally, changes to the Engineering Model should be minimal in the Flight Model.

Thus, schedule pressure should not be permitted to result in cutting corners in the design cycle. If by cutting corners in the design cycle, you don't get it right, there is likely not time to do it again. If major changes to the initial configuration are needed, it could result in the need for an additional hardware iteration before the flight build. It could also result in sticking with a troublesome architecture and suffering with performance issues throughout the development and beyond, adding to cost and schedule. Cutting corners in the initial design cycle is a risk not likely to be worth taking. Performing the necessary engineering analyses in the initial design cycle is of key importance in successfully developing hardware efficiently.

### **Conclusion**

The team was very motivated to be tasked with meeting requirements not faced before. In the past, we have developed pointing mechanisms and scanners requiring arcsecond levels of pointing, but we never before developed hardware to meet sub-arcsecond levels of pointing. Pointing requirements were met with margin (Figure 11). If we used the BSM to point a laser from NASA/ARC to San Francisco International Airport, a distance of 40 km, we could keep the center of that beam on a dime.

Various lessons learned have been discussed. Most of the lessons learned dealt with problems that appeared and were in short order, understood and solved. However, throughout the BSM development, verification of pointing was a major focus. In particular, verification of systematic error throughout mission life, full range of motion, and full range of temperature, was extremely challenging. The details of the methodology used for pointing verification go well beyond the scope of this paper, requiring a paper solely on this topic.

Being challenged with each issue that arose, understanding the problem, and finding the solution, is what fulfills us as engineers as each team member can attest. The team is very proud of the BSM development and was recognized by upper management for the outstanding achievements of this very challenging task.

The BSM Flight Model was integrated into ATLAS as shown in Figure 12. The BSM location on ATLAS is identified in Figure 13.

### **Acknowledgements**

Willie E. Barber, Gregory A. Bowers, William G. Bowers, Thomas L. Capon, Gene G. Gochar, Andrea O. Poulin, Joseph P. Schepis, and David S. Schwinger from NASA Goddard Space Flight Center, Eric L. Holt from Stinger Ghaffarian Technologies, Inc., Greenbelt, MD, and Douglas B. Leviton from Leviton Metrology Solutions, Inc., Boulder, CO.



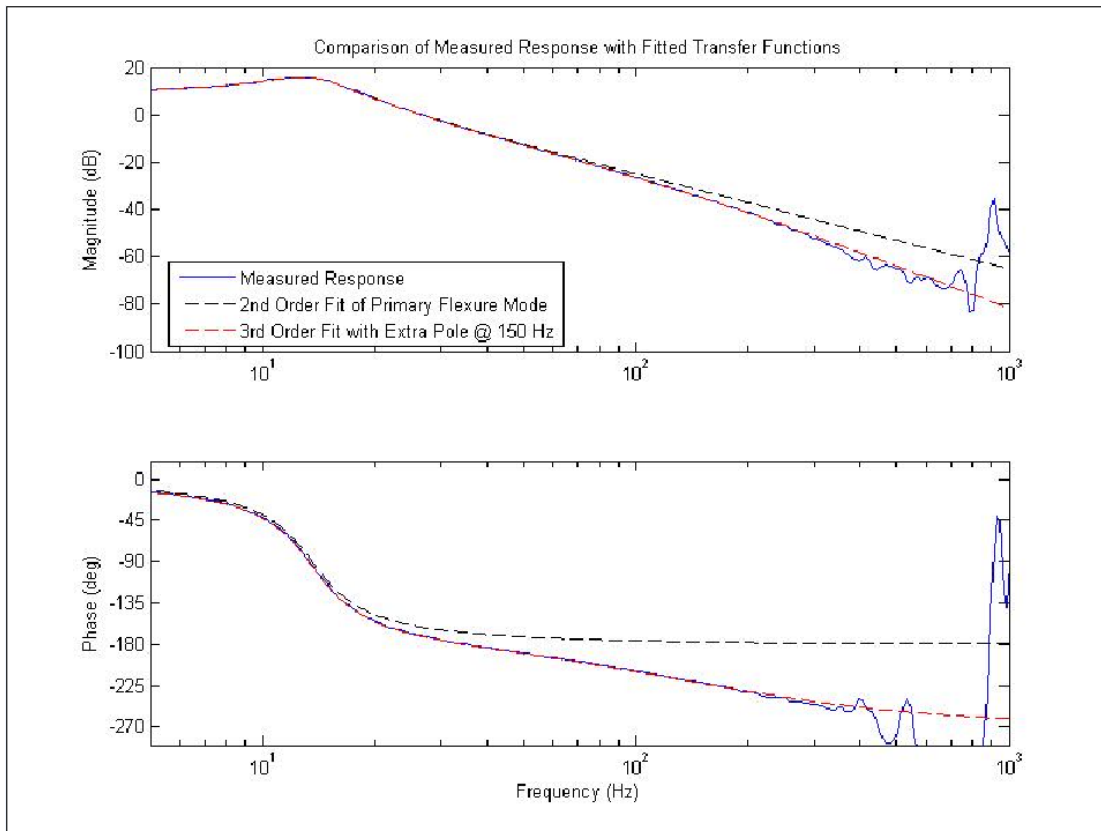


**Figure 10. Unknown Pole**

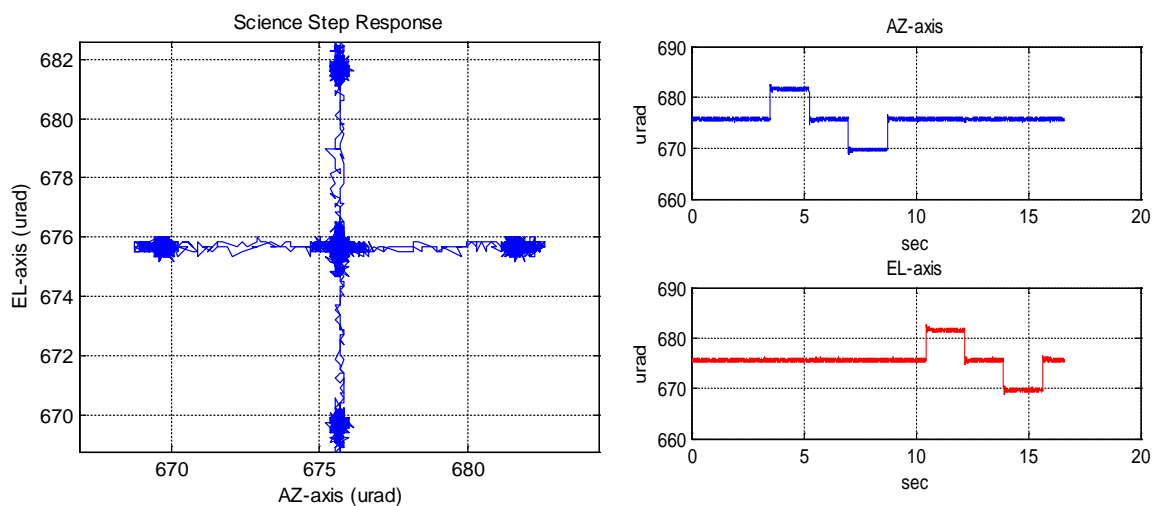


**Figure 11. BSM Pointing Stability**

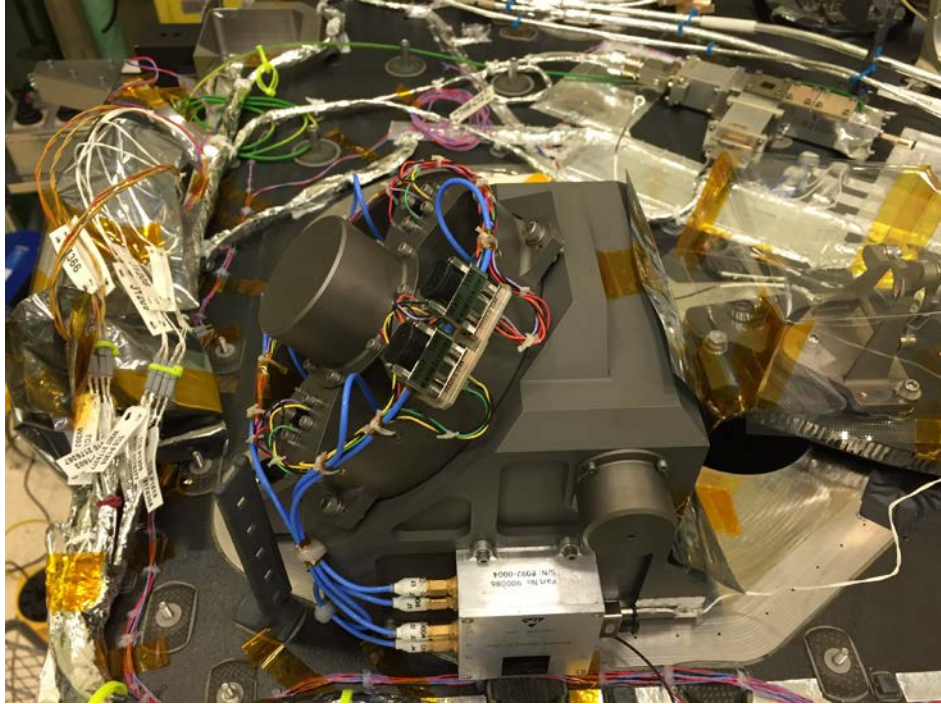


**Figure 12. Initial Integration of Beam Steering Mechanism Flight Model onto the ATLAS Bench**

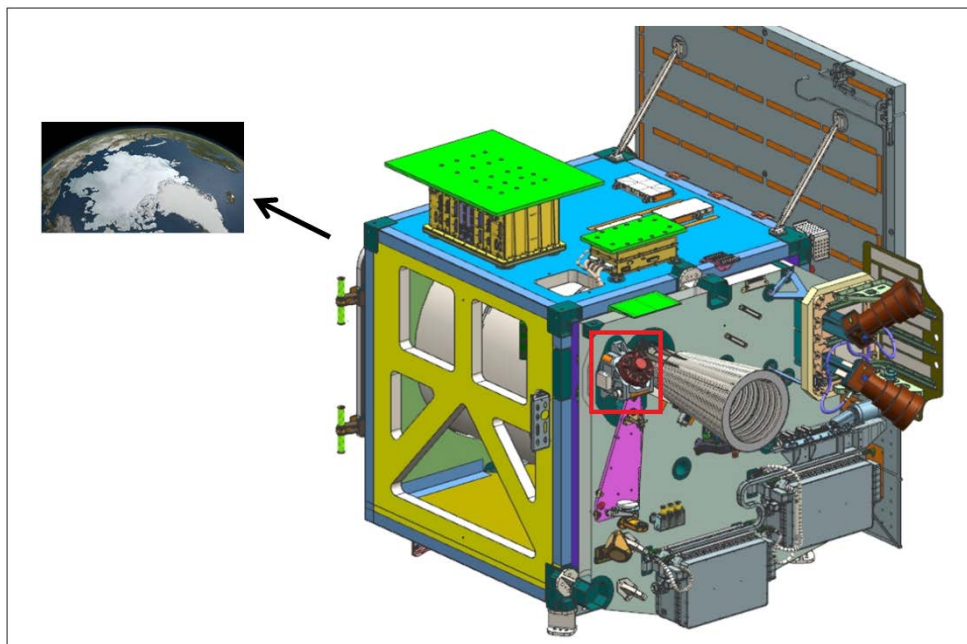


**Figure 13. ATLAS Instrument with a Red Rectangle Indicating the BSM Location**

# Injection of a Body into a Geodesic: Lessons Learnt from the LISA Pathfinder Case

Daniele Bortoluzzi<sup>d</sup>, M Armano<sup>a</sup>, H Audley<sup>b</sup>, G Auger<sup>c</sup>, J Baird<sup>n</sup>, P Binetruy<sup>c</sup>, M Born<sup>b</sup>, D Bortoluzzi<sup>d</sup>, N Brandt<sup>e</sup>, A Bursi<sup>i</sup>, M Caleno<sup>f</sup>, A Cavalleri<sup>g</sup>, A Cesarini<sup>g</sup>, J Conklin<sup>u</sup>, M Cruise<sup>h</sup>, K Danzmann<sup>b</sup>, I Diepholz<sup>b</sup>, R Dolesi<sup>g</sup>, N Dunbar<sup>i</sup>, L Ferraioli<sup>j</sup>, V Ferroni<sup>g</sup>, E Fitzsimons<sup>e</sup>, M Freschi<sup>a</sup>, J Gallegos<sup>a</sup>, L Gambini<sup>d</sup>, C Garcia Marirrodiga<sup>f</sup>, R Gerndt<sup>e</sup>, LI Gesa<sup>k</sup>, F Gibert<sup>k</sup>, D Giardini<sup>j</sup>, R Giusteri<sup>g</sup>, C Grimali<sup>j</sup>, I Harrison<sup>m</sup>, G Heinzl<sup>b</sup>, M Hewitson<sup>b</sup>, D Hollington<sup>n</sup>, M Hueller<sup>g</sup>, J Huesler<sup>f</sup>, H Inchauspe<sup>c</sup>, O Jennrich<sup>f</sup>, P Jetzer<sup>o</sup>, B Johlander<sup>f</sup>, N Karnesis<sup>k</sup>, B Kaune<sup>b</sup>, I Koeker<sup>e</sup>, N Korsakova<sup>b</sup>, C Killow<sup>p</sup>, I Lloro<sup>k</sup>, R Maarschalkerweerd<sup>m</sup>, S Madden<sup>f</sup>, D Mancei<sup>j</sup>, V Martin<sup>k</sup>, F Martin-Porqueras<sup>a</sup>, I Mateos<sup>k</sup>, P McNamara<sup>f</sup>, J Mendes<sup>m</sup>, L Mendes<sup>a</sup>, A Moroni<sup>i</sup>, P Nellen<sup>v</sup>, M Nofrarias<sup>k</sup>, S Paczkowski<sup>b</sup>, M Perreux-Lloyd<sup>p</sup>, A Petiteau<sup>c</sup>, P Pivato<sup>g</sup>, E Plagnol<sup>c</sup>, P Prat<sup>c</sup>, U Ragnit<sup>f</sup>, J Ramos-Castro<sup>q</sup>, J Reiche<sup>b</sup>, J A Romera Perez<sup>f</sup>, D Robertson<sup>p</sup>, H Rozemeijer<sup>f</sup>, G Russano<sup>g</sup>, P Sarra<sup>i</sup>, A Schleicher<sup>e</sup>, J Slutsky<sup>s</sup>, C F Sopuerta<sup>k</sup>, T Sumner<sup>n</sup>, D Texier<sup>a</sup>, J Thorpe<sup>s</sup>, C Trenkel<sup>j</sup>, H B Tu<sup>g</sup>, D Vetrugno<sup>g</sup>, S Vitale<sup>g</sup>, G Wanner<sup>b</sup>, H Ward<sup>p</sup>, S Waschke<sup>n</sup>, P Wass<sup>n</sup>, D Wealthy<sup>i</sup>, S Wen<sup>g</sup>, W Weber<sup>g</sup>, A Wittchen<sup>b</sup>, A Zambotti<sup>d</sup>, C Zanoni<sup>d</sup>, T Ziegler<sup>e</sup>, P Zweifel<sup>j</sup>

## Abstract

Launch lock and release mechanisms constitute a common space business, however, some science missions due to very challenging functional and performance requirements need the development and testing of dedicated systems. In the LISA Pathfinder mission, a gold-coated 2-kg test mass must be injected into a nearly pure geodesic trajectory with a minimal residual velocity with respect to the spacecraft. This task is performed by the Grabbing Positioning and Release Mechanism, which has been tested on-ground to provide the required qualification. In this paper, we describe the test method that analyzes the main contributions to the mechanism performance and focuses on the critical parameters affecting the residual test mass velocity at the injection into the geodesic trajectory. The test results are also presented and discussed.

---

<sup>d</sup> University of Trento, Trento, Italy

<sup>a</sup> European Space Astronomy Centre, European Space Agency, Madrid, Spain

<sup>b</sup> Albert-Einstein-Institut, Hannover, Germany

<sup>c</sup> Universite Paris Diderot, Paris, France

<sup>e</sup> Airbus Defence and Space, Immenstaad, Germany

<sup>f</sup> European Space Technology Centre, European Space Agency, Noordwijk, The Netherlands

<sup>g</sup> Dipartimento di Fisica, Universita di Trento, Trento, Italy

<sup>h</sup> Department of Physics and Astronomy, University of Birmingham, Birmingham, UK

<sup>i</sup> Airbus Defence and Space, Stevenage, UK

<sup>j</sup> Institut fur Geophysik, Zurich, Switzerland

<sup>k</sup> Institut de Ciencies de l'Espai, Bellaterra, Spain

<sup>l</sup> Istituto di Fisica, Universita degli Studi di Urbino, Urbino, Italy

<sup>m</sup> European Space Operations Centre, Darmstadt, Germany

<sup>n</sup> The Blackett Laboratory, Imperial College London, UK

<sup>o</sup> Physik Institut, Universitat Zurich, Zurich, Switzerland

<sup>p</sup> SUPA, Institute for Gravitational Research, University of Glasgow, Glasgow, UK

<sup>q</sup> Department d'Enginyeria Electronica, Universitat Politecnica de Catalunya, Barcelona, Spain

<sup>r</sup> Institut d'Estudis Espacials de Catalunya, Barcelona, Spain

<sup>s</sup> NASA Goddard Space Flight Center, Greenbelt, MD

<sup>t</sup> CGS S.p.A, Compagnia Generale per lo Spazio, Milano, Italy

<sup>u</sup> Department of Mechanical and Aerospace Engineering, University of Florida, Gainesville, FL

<sup>v</sup> RUAG Space, Zurich, Switzerland

## Introduction

In LISA Pathfinder, some of the critical technologies developed for the in-space detection of gravitational waves will be tested [1] [2]. Scope of the mission is to set a 2-kg gold-coated AuPt test mass (TM) into a purely geodesic trajectory, i.e., bring it to free-fall condition inside the spacecraft by reducing any force other than gravity under the level of  $10 \text{ fN/Hz}^{1/2}$  in the measurement bandwidth (1-30 mHz). Such a challenging requirement drove the design of the whole mission. In particular, the Gravitational Reference Sensor hosting the proof mass is internally gold coated and large gaps are present in order to limit the stray forces produced by local sources (i.e., charge patches). The Caging and Vent Mechanism secures the TM during the launch [3], while the Grabbing Positioning and Release Mechanism (GPRM) handles it in orbit and injects it into the geodesic trajectory (Figure 1) [4] [5].

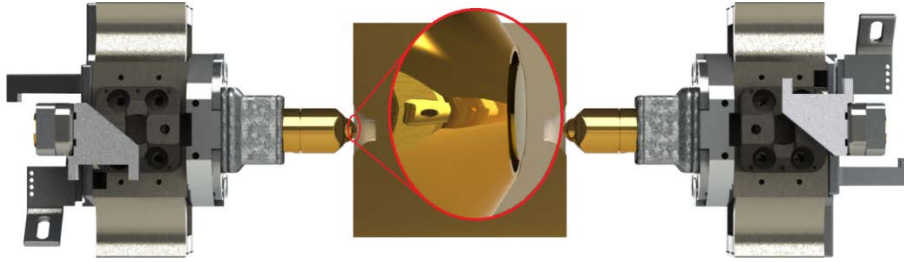


**Figure 1. The Test Mass held by the two opposed GPRMs with detail of the release tip**

We focus here on the latter phase performed by the GPRM, in which the TM is gently held in the center of the Gravitational Reference Sensor electrode housing by two opposed release-dedicated tips and then is left in free fall after their quick retraction. The critical requirement of this phase, determined by the capability of the capacitive control system to catch and re-center the TM after release, is the TM residual velocity, which must be below  $5 \text{ } \mu\text{m/s}$ . The nominal design of the two opposed GPRM release mechanisms provides a symmetric action on both sides of the TM, therefore perfect cancelation of forces and zero residual velocity. However, the ground testing of the release system highlighted some asymmetries. First, adhesive bonds are produced at both TM-release tip contacts [6], whose strength is affected by the surface topography at the microscopic scale, which is not controlled by the conventional machining processes. This converts into a low-repeatable adhesion behavior and high probability of non-cancelation of its effect on the two opposed TM sides (Figure 2 right). Second, some asymmetry is present also on the motion of the tips, which are commanded by two different actuators (for instance, if one of the tips is actuated with a time lag and/or moves with a different velocity, Figure 2 center). Even in the absence of adhesion this asymmetry makes the contact force time history different at the two opposed contacts, with a net contribution of their time integral, i.e., developed impulse. Referring to Figure 2 left, the net impulse is represented by the area enclosed by the two force-time histories, which quantifies the overall level of asymmetry of the two contacts.

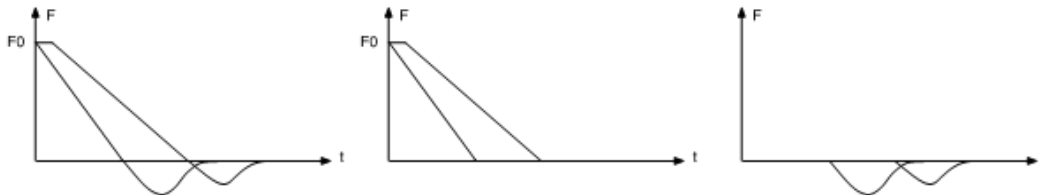


**Figure 2. Asymmetry of contact forces on the TM (positive=pushing), pushing actions (preload) and pulling actions (adhesion)**

The test approach is twofold. The effect of pushing forces (Figure 2 center) is ruled by the behavior of the mechanism (the holding force control level, the repeatability of the retraction) and is quantified by analysis

of the tests of retraction of the piezo and the holding force accuracy level. The effect of pulling forces (Figure 2 right) is ruled by the behavior of adhesion and is quantified by the tests performed with the Transferred Momentum Measurement Facility (TMMF, Figure 3) [7] [8] [9] [10] [11]. The in-flight environment is reproduced by suspending the TM mock up as a pendulum inside a vacuum chamber, and the release experiment consists in the approach and retraction of the tip with subsequent measurement of the swing oscillation produced (i.e., the transferred momentum) [12]. In order to maximize the representativeness of the experiment, in the latest test configuration of the TMMF the EQM of the GPRM is integrated to perform the release phase of the TM.

The two effects may be added since in flight there is no effect of the first effect to the second. This is motivated by the fact that the net velocity produced by the pushing actions (acting first) is negligible with respect to the velocity of retraction of the tip (about three orders of magnitude).

### **In-Flight Release Dynamics**

Tests performed with the previous set-ups and contact mechanics models show that the tip-TM contact persists with relative displacements (from initial penetration under 0.3 N to final elongation at the detachments) of a few microns. By choosing a reference displacement value for the detachment (say 2  $\mu\text{m}$ ), it is possible to quantify the statistic distribution of the time required to obtain the separation of the tip from the TM. If we consider the tests performed by RUAG on the retraction quickness of the tip – unloaded – by restricting the results to the 24 tests performed on the flight models (FM1, FM2, FM3, FM4, nominal and redundant piezos [13]), we obtain a representative dispersion of the time to 2  $\mu\text{m}$  as shown in Figure 4. The mean and standard deviation of the time to 2  $\mu\text{m}$  are 0.04 ms and 0.005 ms respectively.

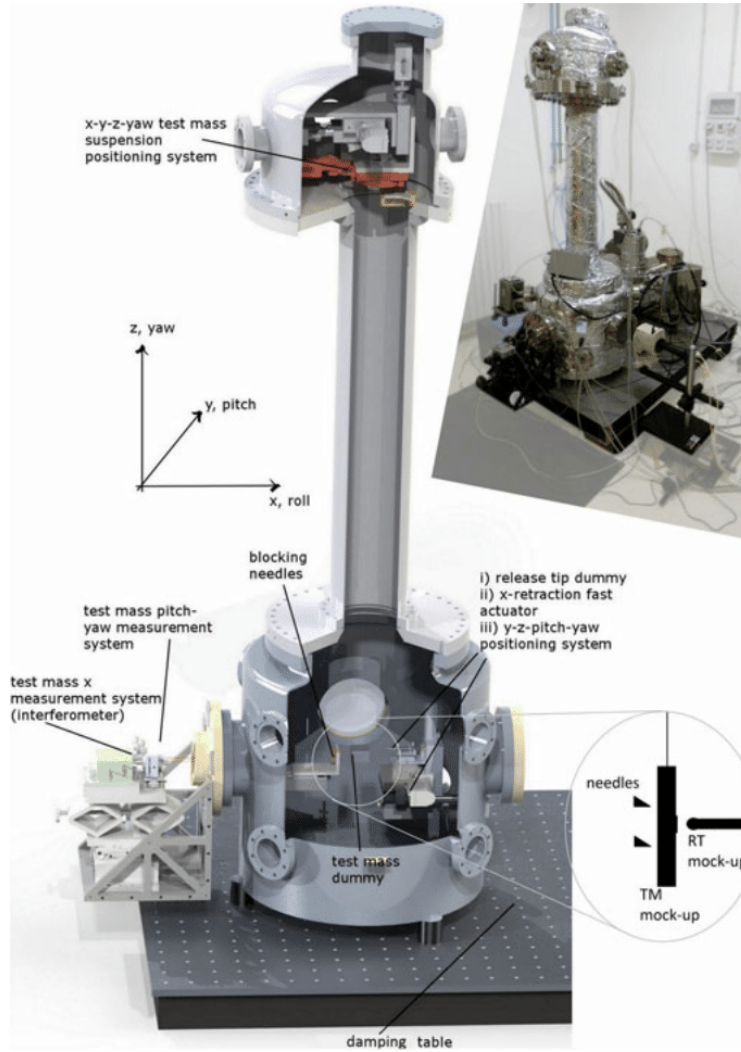


**Figure 3. The Transferred Momentum Measurement Facility**

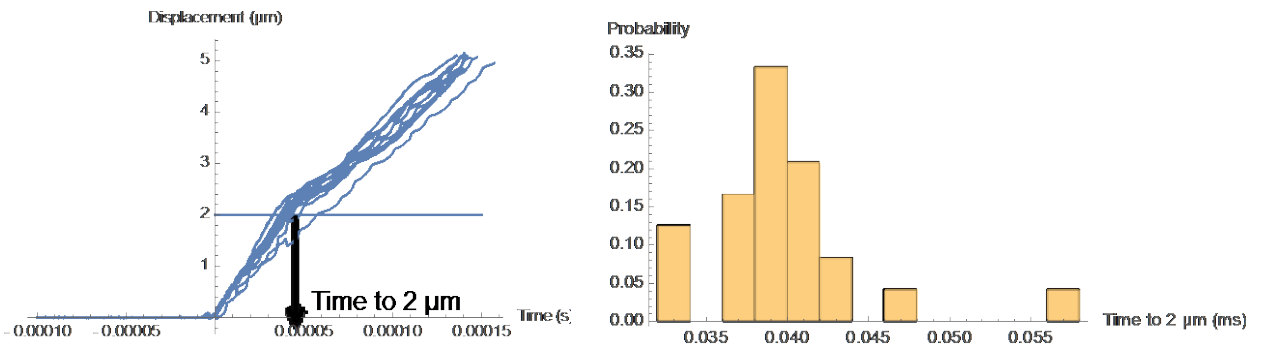


**Figure 4. Time histories of the FM tip retraction (left) - Time to 2  $\mu\text{m}$ , statistical distribution (right)**

Since the pushing force asymmetry is produced by the non-repeatability of the mechanism, we calculate the statistical distribution of the differences among times to 2  $\mu\text{m}$ , which is shown in Figure 5. The standard deviation is about 7  $\mu\text{s}$ .



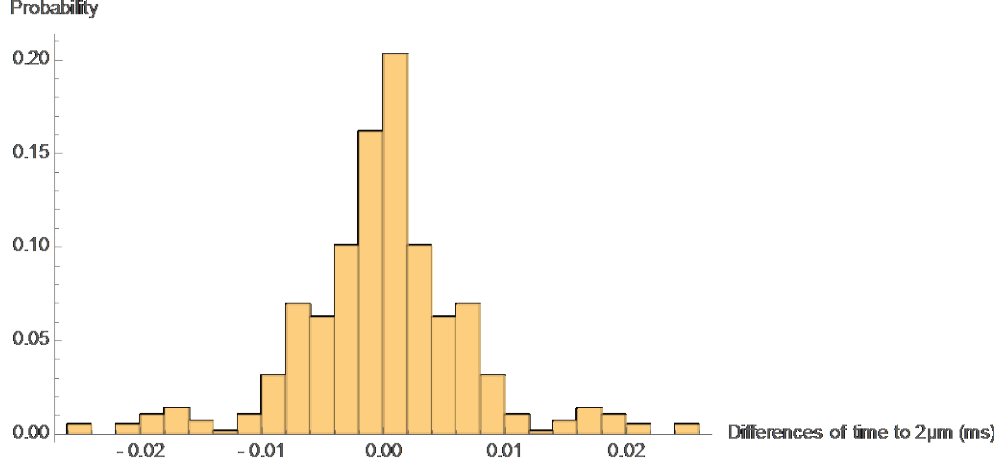


**Figure 5. Statistical distribution of the differences of time to 2μm**

Measurements performed at MAGNA show that the voltage drops 120 V – 0 V commanded by the Caging Control Unit to the two piezo stacks have a fair synchronization but are characterized by a different slope (in particular during the incipient motion), as shown in Figure 6.

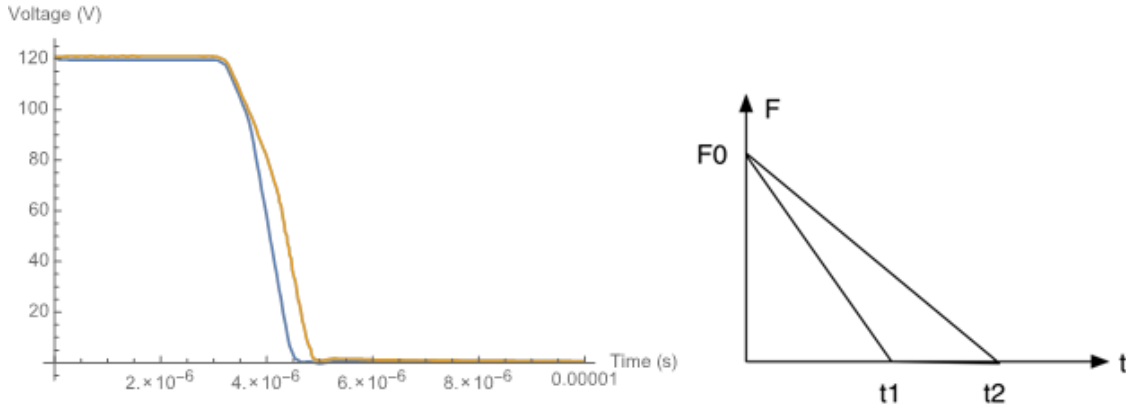


**Figure 6. Caging Control Unit voltages commanded to the two stacks (left, courtesy of MAGNA) - Approximated resulting pushing force profiles (right)**

As a consequence, the time lag between the two force time histories is assumed negligible and their behavior is assumed linear up to the zero level force (Figure 6 right). The net impulse given by such time histories is calculated and the TM velocity produced by the pushing forces can be calculated as follows:

$$v_{F0} = \frac{1}{2} \frac{F0}{m_{TM}} \Delta t \quad (1)$$

where  $F0$  is the initial holding force (about 0.3 N),  $m_{TM}$  is the flight TM mass and  $\Delta t$  is the difference between time  $t2$  and  $t1$  as in Figure 6 right. The resulting statistical distribution of the TM velocity produced by the pushing actions is plotted in Figure 7. The mean is zero (each difference is calculated also with inverted order of the two velocities), while the standard deviation is 0.5 μm/s.



**Figure 7. Statistical distribution of the TM velocity produced by the pushing forces**

If we add the contribution of adhesion to the effect of the pushing forces, the total in-flight velocity is given by the following formula:

$$v_{flight} = \frac{1}{2} \frac{F_0}{m_{TM}} \Delta t + \frac{1}{m_{TM}} \Delta \left( \frac{\Delta U}{v_{RT}} \right) \quad (2)$$

where  $\Delta U$  is the adhesion energy [14],  $v_{RT}$  is the velocity of the release tip at the detachment from the TM,  $\Delta(\Delta U / v_{RT})$  is the difference between the above quantities relative to the two contacts. The object of the TMMF ground testing is the quantification of the second term in Equation 2.

### On-Ground Release Testing

#### The Transferred Momentum Measurement Facility

The past testing activities showed that adhesion occurring at the contacting surfaces produces a pull on the TM due to the retraction of the release-dedicated tip, up to bond failure. In the tests, care must be taken to minimize all environmental effects related to the laboratory, which may affect the adhesion dynamic failure and the developed pulling impulse. In the test set-up of the TMMF, the representativeness of the in-flight TM release conditions is based on the following:

- integration of the GPRM EQM -Z inside the vacuum chamber
- representative vacuum level (around  $10^{-7}$  mbar)
- adoption of representative material of the TM bulk (Au-Pt alloy), machining process (Kugler) and gold coating (Selex Galileo)
- adoption of the same contact load (0.3 N).

The following differences between the test configuration and the flight configuration are present:

- mass of the TM mock-up. Based on the past test campaigns, the intermediate mass configuration (TM mock-up of 0.0883 kg) is chosen. With respect to the heavy (0.844 kg) and light (0.0096 kg) configuration, this allowed for a more detectable adhesion contribution
- cleanliness. The TM mock-up surface has been cleaned by means of isopropyl alcohol with ultrasound bath. A mild baking procedure has been performed in vacuum to enhance outgassing. The whole experiment is located inside an ISO6 (class 1000) clean room
- one sided release. This configuration has been chosen since the early stages of the test activity. The main advantage consists in the absence of cancelation of the two opposed adhesion impulses, maximizing the sensitivity of the experiment to the release velocity
- gold-coated release tip. The GPRM EQM release tip is made of gold-coated TiAlV alloy.



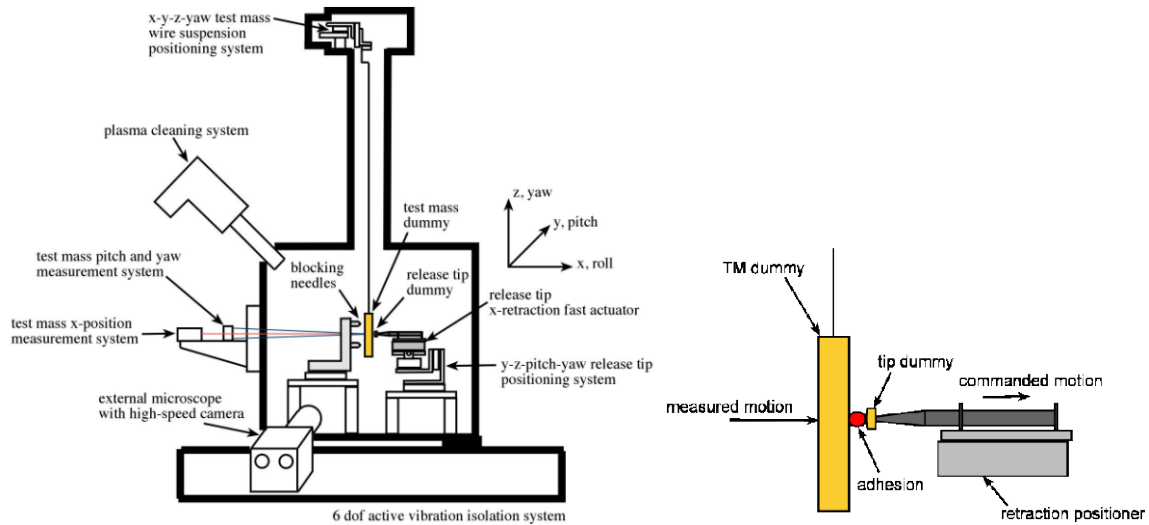


**Figure 8. Old test configuration (before GPRM integration)**

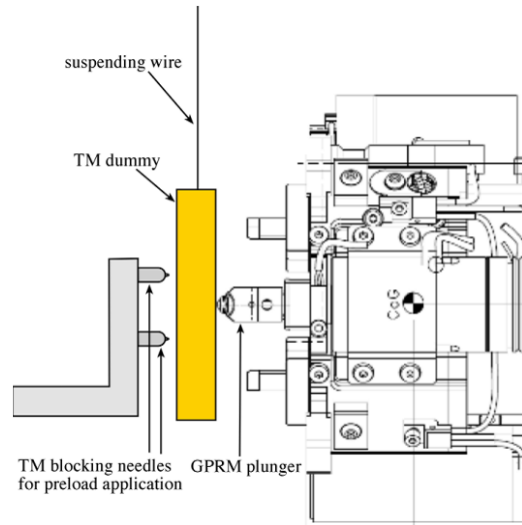


**Figure 9. Test configuration with GPRM EQM -Z**

In Figure 8 the TMMF configuration before the integration of the GPRM EQM is shown. In Figure 9 the test configuration with GPRM EQM is shown: the axis of retraction of the release tip is horizontal, engaging the TM mock-up in the center. The TM x displacement is measured by a laser interferometer, while the TM pitch and yaw angles are measured by a position sensing device through an optical lever system. The GPRM attitude (both pitch and yaw angles) can be adjusted to explore different directions of retraction of the tip. This is used both to search the maximum release velocity and to characterize its statistical distribution when the retraction is repeated with a representative misalignment of that occurring in flight. Pictures of TMMF and GPRM current setup are shown in Figure 10.

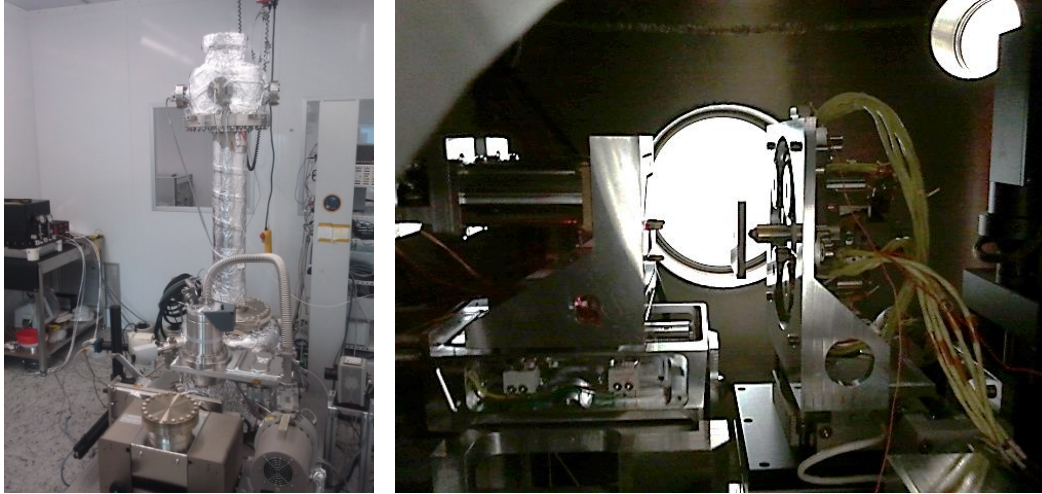


**Figure 10. The TMMF in the clean room (left) – Blocking system, suspended TM and GPRM in the vacuum chamber (right)**

#### On ground release dynamics

During the engagement, the TM mock-up is blocked on its rear side by three needles, which are actuated to adjust their attitude and allow engaging the TM with a minimal variation of its pitch and yaw angles with respect to the equilibrium. According to the tested GPRM handover procedure from the grabbing plunger to the release tip, the tip to TM contact force before the release is set to 0.3 N. This residual holding force is balanced by the blocking needles, which are not retracted during the release and produce an elastic push on the TM when the load is recovered at the retraction of the tip. As a consequence, the measured velocities are affected by this systematic contribution, which following the nominal in-flight procedure (nearly synchronous two-sided release) will be much smaller. The force-time histories plotted in Figure 2 left in the test configuration are modified as shown in Figure 11. The force applied by the release tip starts from  $F_0$  and quickly drops to zero, exerts the adhesive pull and vanishes in a time frame of 0.04 ms, while the push of the blocking needles produce a cosine-like force profile which relaxes in a time frame of about 0.4 ms.

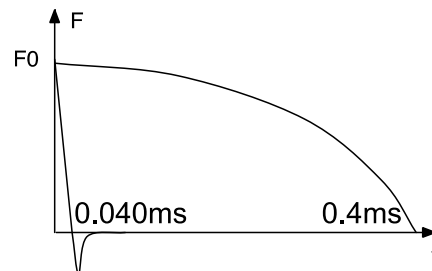


**Figure 11. Force-time histories on the TM in the on-ground configuration**

The stiffness of the blocking system is about  $6 \cdot 10^5$  N/m, which is on the same order of magnitude of the axial stiffness of the GPRM. This means that the tested configuration is representative of an in-flight one-sided release. If the measured velocities are rescaled by the flight TM to mock-up ratio (about 20), they describe the TM velocity produced by a release performed by the retraction of just one tip. The TM velocity produced by the experiment can be calculated as follows:

$$v_{test} = \frac{F0}{\sqrt{m_{mockup} k_{needles}}} + \frac{1}{m_{mockup}} \frac{\Delta U}{v_{RT}} \quad (3)$$

where  $m_{mockup}$  is the mass of the TM mock-up and  $k_{needles}$  is the stiffness of the blocking needles. The control uncertainty of the force  $F0$  is not negligible and the dispersion of the produced velocities is affected also by this variable. From the analysis of the force signal, we assume for the holding force  $F0$  a Gaussian distribution with mean 0.3 N and standard deviation 0.05 N. This is likely to be a worst case assumption. If we consider that the experiment is repeated, the dispersion of the measured velocity (i.e., the differences between pairs of measured velocities) is given both by the dispersion of the applied preload  $F0$  and the dispersion of the behavior of adhesion:

$$\Delta v_{test} = \frac{\Delta F0}{\sqrt{m_{mockup} k_{needles}}} + \frac{1}{m_{mockup}} \Delta \left( \frac{\Delta U}{v_{RT}} \right) \quad (4)$$

Here the term  $\Delta(\Delta U/v_{RT})$  is related to the difference of the behavior of adhesion at the same side between different tests, which is assumed descriptive of the difference of the behavior of adhesion between the two opposed sides. As a worst case, we assume that all the dispersion of the measured velocities is due to adhesion:

$$\Delta v_{test} \approx \frac{1}{m_{mockup}} \Delta \left( \frac{\Delta U}{v_{RT}} \right) \quad (5)$$

Therefore we can calculate:

$$\Delta \left( \frac{\Delta U}{v_{RT}} \right) = m_{mockup} \Delta v_{test} \quad (6)$$

By substituting Equation 6 into Equation 2 we get:

$$v_{flight} = \frac{1}{2} \frac{F0}{m_{TM}} \Delta t + \frac{m_{mockup}}{m_{TM}} \Delta v_{test} \quad (7)$$

Basically, the differences between pairs of measured velocities may be rescaled by the mass ratio and added to the velocity produced by the pushing forces.

### Test Results

During every test, three signals are acquired: TM x-displacement, pitch and yaw angles (Figure 12). At the release, after a quick acceleration phase the TM mock-up moves with almost constant linear and angular (both pitch and yaw) velocities. Angular components of velocity are associated to misalignments of the release tip and the resultant of the forces applied by the three blocking needles with respect to the TM center of mass. However, the amount of kinetic energy due to angular velocities (pitch and yaw) after the release is negligible (0.5%) compared to that associated to the linear velocity. In Figure 13, the TM displacement and linear velocity are shown. The velocity signal is obtained as the discrete time derivative of the sampled displacement, and it is used to estimate the release time interval, after which the velocity can be considered constant. The final velocity is therefore estimated as the slope of the displacement

signal after the release, through a linear least square fit. Fit uncertainty is very small compared to the estimated final velocity.

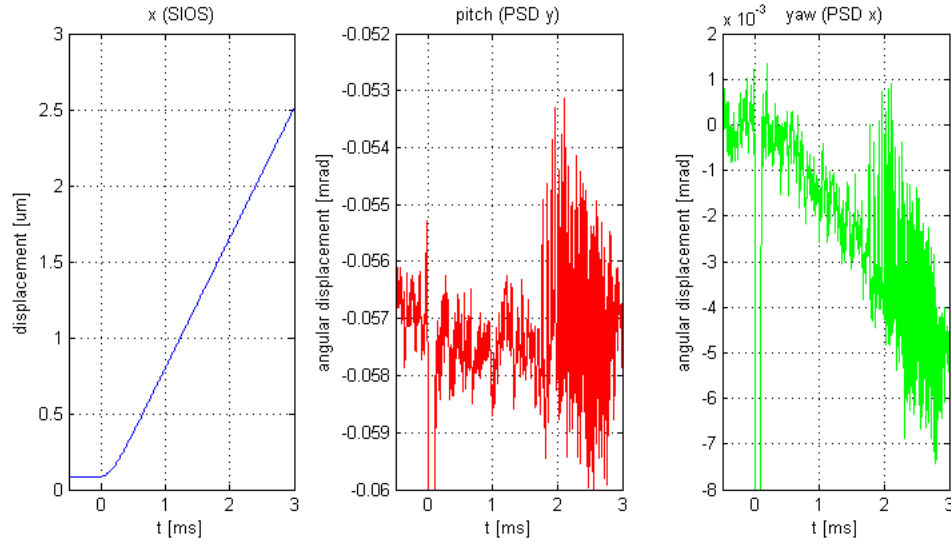


**Figure 12. TM displacement, pitch and yaw signals**

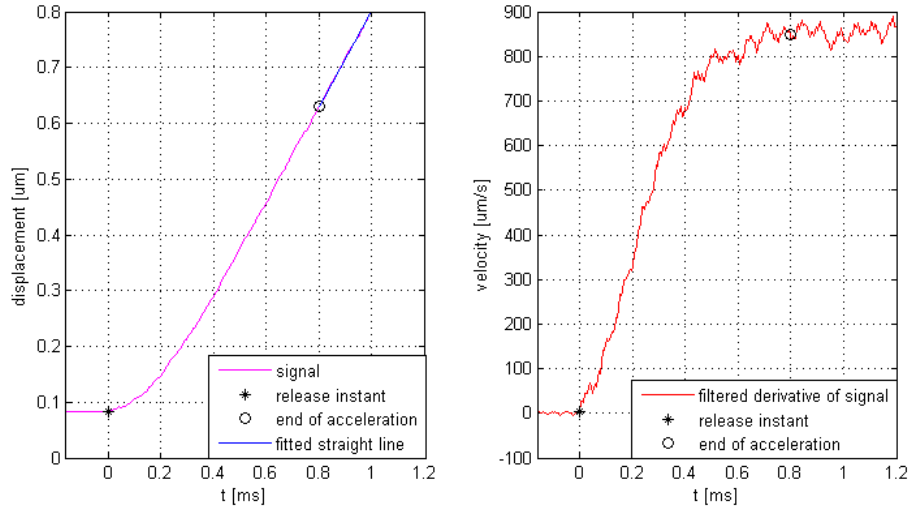


**Figure 13. Example of TM displacement and velocity signal during the release phase, along (0°,0°) direction**

The tests have been performed starting from the nominally aligned direction, searching the maximum release velocity. Across the measured maximum, a release tip misalignment of  $\pm 1.6$  mrad ( $\pm 0.092^\circ$ ) has been explored along both yaw and pitch directions. Ten repetitions have been done along each direction, and test of hypothesis has been performed to check the significance of the difference between the mean of a direction and its neighbors. Two directions are assumed to produce the same mean velocity when the p-value of the test of hypothesis is larger than 50%.

Table 1 shows the 10 measured velocities and their mean value for a single direction. The uncertainty of every estimated velocity is significantly smaller compared to the standard deviation of the direction, confirming that the measurement precision is adequate [15]. The results of the overall test campaign are

reported in Table 2. According to the literature [16][17], a direction of retraction of the tip which is misaligned with respect to the local orthogonal to the surface produces a shear stress which reduces adhesion force. As a consequence, a reduction of the release velocity is expected along the directions of retraction which are locally misaligned. The results show that the peak velocity is reached along two directions, namely  $(-0.3^\circ, 0^\circ)$  and  $(-0.3^\circ, -0.092^\circ)$ . The velocities along the surrounding directions are significantly smaller, such that the hypothesis test rejects the hypothesis of equal mean values. Some of these directions produce velocities that are statistically consistent. The overall behavior of the release velocity is fairly regular and shows just an absolute maximum. Since the absolute maximum is reached along two directions, we assume that the worst-case misalignment of the release tip direction spans of  $\pm 1.6$  mrad ( $\pm 0.092^\circ$ ) around each, covering the yaw interval between  $-0.392^\circ$  and  $-0.208^\circ$  and pitch interval between  $-0.184^\circ$  and  $+0.092^\circ$ . This set of directions covers 120 tests, i.e., 120 values of the release velocity  $v_{test}$  of Equation 3. The distribution of the rescaled (i.e., multiplied by the mass ratio) velocities is plotted in Figure 14: the mean is  $37.7 \mu\text{m/s}$  and the standard deviation is  $1.5 \mu\text{m/s}$ .

**Table 1. Estimated final velocities for one release direction  $(-0.3^\circ, +0.092^\circ)$**

test	final velocity ( $\mu\text{m/s}$ )	fit uncertainty ( $\mu\text{m/s}$ )
1	828.14	0.73
2	863.33	0.79
3	886.09	0.84
4	841.69	0.74
5	790.82	0.61
6	862.65	0.69
7	884.84	0.79
8	878.80	0.80
9	842.54	0.72
10	876.14	0.81
mean	855.50	
standard deviation	30.13	

**Table 2. Mean final velocity ( $\mu\text{m/s}$ ) of release directions. Neighbor numbers in equal colors are statistically consistent. Numbers in gray color have been measured while searching the direction of maximum with a large step ( $0.3^\circ$ )**

	Yaw ( $^\circ$ )					
Pitch ( $^\circ$ )	-0.6	-0.392	-0.3	-0.208	0	+0.3
+0.3					772	
+0.092		848	856	839		
0	820	807	873	843	847	847
-0.092		837	874	847		
-0.184		839	838	859		
-0.3					808	

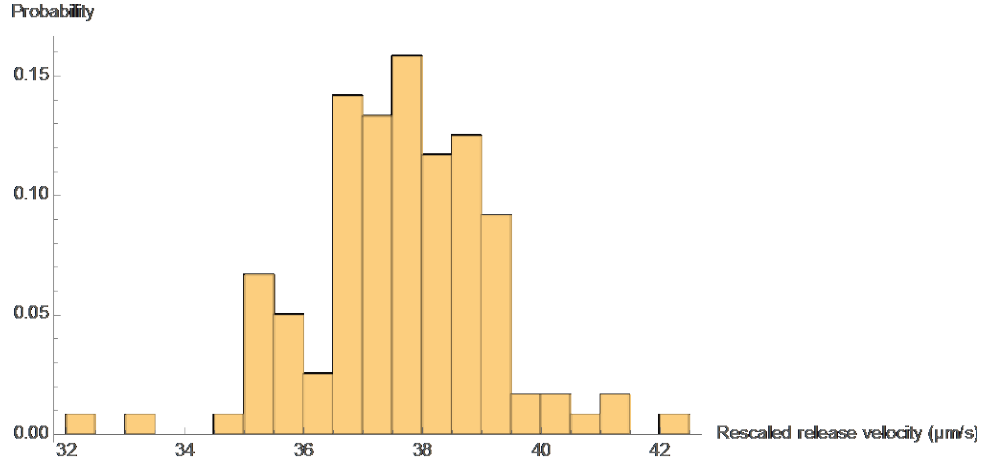


**Figure 14. Rescaled  $v_{test}$  release velocities of 120 tests across the peak direction, covering yaw interval  $(-0.392^\circ, -0.208^\circ)$  and pitch interval  $(-0.184^\circ, +0.092^\circ)$**

The distribution of velocities plotted in Figure 14 is representative of an in-flight one-sided release and are heavily affected by the systematic push of the blocking needles. This contribution cancels out if the differences  $\Delta v_{test}$  between pairs of velocities is calculated. The statistical distribution of the rescaled  $\Delta v_{test}$  variable (second member of Equation 7) is plotted in Figure 15. The mean is zero (similarly to Figure 7) while the standard deviation is 2  $\mu\text{m/s}$ .

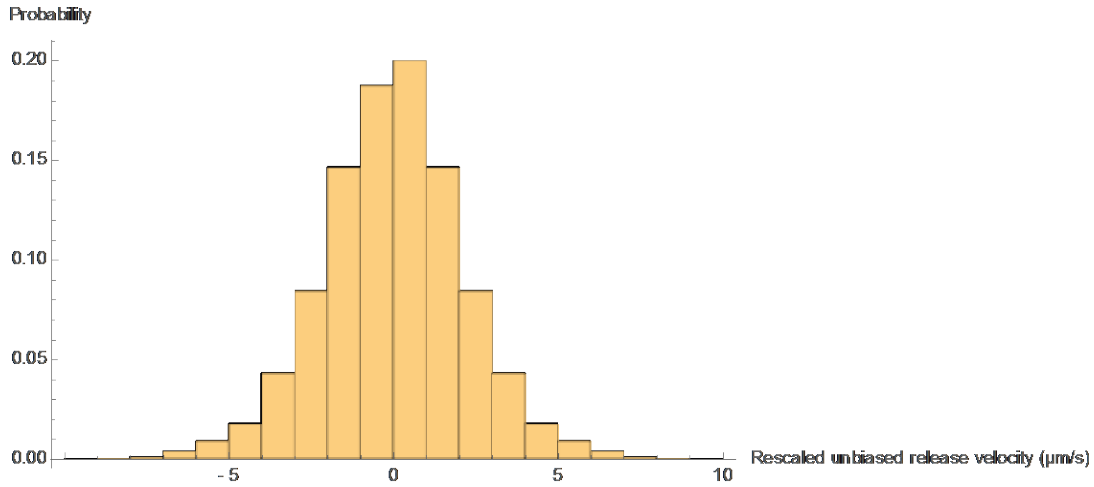


**Figure 15. Rescaled  $\Delta v_{test}$  release velocities**

#### Results synthesis

The results plotted in Figure 7 (effect of pushing forces) and Figure 15 (effect of adhesion) need to be convolved to obtain the resulting release velocity in flight,  $v_{flight}$  of Equation 7. The statistical distribution of the overall release velocity is shown in Figure 16. The mean is zero and the standard deviation is 2.2  $\mu\text{m/s}$ . The probability of a compliant release (magnitude of  $v_{flight}$  less than 5  $\mu\text{m/s}$ ) is 96%. This result is compatible with the previous estimations of the release velocity [18] [19].

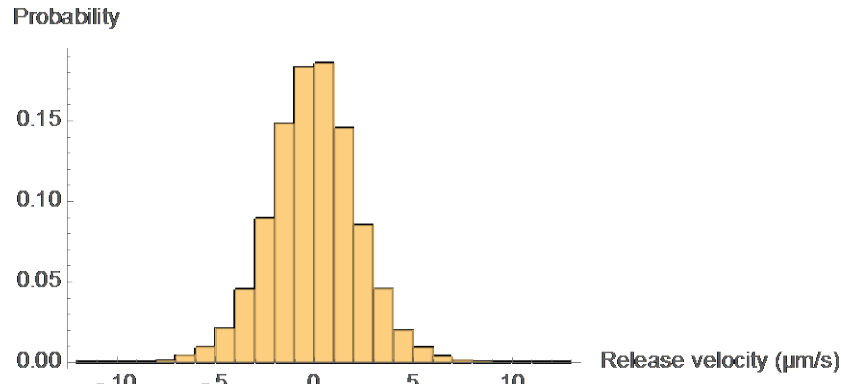


**Figure 16. Overall release velocity in flight**

## Conclusions

The injection of an object into a geodesic trajectory constitutes a relevant space engineering challenge. In this paper we present a ground-based testing approach, which allowed us to provide the qualification of the mechanism designed and developed to perform the injection of a 2-kg gold-coated test mass into a geodesic trajectory of unprecedented purity (LISA Pathfinder). The criticality of the mechanism for its test mass injection into geodesic function mainly relies on the possible asymmetry of the two opposed actions on the test mass. Both the holding forces and following adhesive interaction between the test mass and its holding tips may produce a net impulse at the release, i.e., an excessive test mass residual velocity, when the dynamic behavior of the two opposed contact on the test mass results asymmetric.

The testing method and the test results for the Grabbing Positioning and Release Mechanism developed for the LISA Pathfinder mission are here presented and discussed.

## References

1. F. Antonucci, et al. "The LISA pathfinder mission". *Classical Quantum Gravity*, vol. 29, no. 12, pp. 124014-1–124014-11, 2012.
2. M. Armano et al. "The LISA Pathfinder Mission". *Journal of Physics: Conference Series* Volume 610, Issue 1, 11 May 2015, Article number 012005.
3. B. Zahnd, M. M. Zimmermann, and R. Spörri. "LISA-Pathfinder cage and vent mechanism — Development and qualification". *Proceedings of the 15th European Space Mechanisms and Tribology Symposium*, 2013, pp. 1–7.
4. A. Neukom, R. Romano, and P. M. Nellen. "Testing and lesson learnt of LISA GPRM". *Proceedings of the 13th European Space Mechanisms and Tribology Symposium*, 2009, pp. 1–8.
5. I. Köker, H. Rozemeijer, F. Stary, and K. Reichenberger. "Alignment and testing of the GPRM as part of the LTP caging mechanism". *Proceedings of the 15th European Space Mechanisms and Tribology Symposium*, 2013, pp. 1–7.
6. M. Benedetti, D. Bortoluzzi, M. D. Lio, and V. Fontanari. "The influence of adhesion and sub-Newton pull-off forces on the release of objects in outer space". *J. Tribology*, vol. 128, no. 4, pp. 828–840, 2006.
7. D. Bortoluzzi, M. De Cecco, S. Vitale, and M. Benedetti. "Dynamic measurements of impulses generated by the separation of adhered bodies under near-zero gravity conditions". *Exp. Mech.*, vol. 48, pp. 777–787, 2008.
8. D. Bortoluzzi, M. Benedetti, L. Baglivo, and S. Vitale. "A new perspective in adhesion science and technology: Testing dynamic failure of adhesive junctions for space applications". *Exp. Mech.*, vol. 50, pp. 1213–1223, 2010.

9. D. Bortoluzzi, M. Benedetti, and J. W. Conklin. "Indirect measurement of metallic adhesion force as a function of elongation under dynamic conditions". *Mech. Syst. Signal Process*, vol. 38, no. 2, pp. 384–398, 2013.
10. D. Bortoluzzi, L. Baglivo, M. Benedetti, F. Biral, P. Bosetti, A. Cavalleri, M. D. Lio, M. D. Cecco, R. Dolesi, M. Lapolla, W. Weber, and S. Vitale. "Lisa pathfinder test mass injection in geodesic motion: status of the on ground testing". *Classical Quantum Gravity*, vol. 26, no. 9, pp. 094011-1–094011-11, 2009.
11. C. Zanoni, D. Bortoluzzi, J. Conklin, I. Köker, C. Marirrodiga, P. Nellen, and S. Vitale. "Testing the injection of the LISA-pathfinder test mass into geodesic conditions". *Proceedings of the 15th European Space Mechanisms and Tribology Symposium*, 2013, pp. 1–10.
12. D. Bortoluzzi, M. Benedetti, L. Baglivo, M. De Cecco, S. Vitale. "Measurement of momentum transfer due to adhesive forces: On-ground testing of in-space body injection into geodesic motion". *Rev. Sci. Instrum.* 82, 125107 (2011).
13. D. Bortoluzzi, P. A. Mäusli, R. Antonello, and P. M. Nellen. "Modeling and identification of an electro-mechanical system: The LISA grabbing positioning and release mechanism case". *Adv. Space Res.*, vol. 47, no. 3, pp. 453–465, 2011.
14. M. Benedetti, D. Bortoluzzi, and S. Vitale. "A momentum transfer measurement technique between contacting free-falling bodies in the presence of adhesion". *J. Appl. Mech.*, vol. 75, no. 1, p. 011016, 2008.
15. M. D. Cecco, D. Bortoluzzi, L. Baglivo, M. Benedetti, and M. D. Lio. "Measurement of the momentum transferred between contacting bodies during the Lisa test-mass release phase uncertainty estimation". *Meas. Sci. Technol.*, vol. 20, no. 5, pp. 055101-1–055101-15, 2009.
16. K. Rabenorosoa, C. Clévy, P. Lutz, M. Gauthier, P. Rougeot, *Micro & Nano Letters*, 2009, Vol. 4, Iss. 3, pp. 148–154.
17. A. R. Savkoor and G. A. D. Briggs , *Proceedings of the Royal Society of London. Series A, Mathematical and Physical Sciences*, Vol. 356, No. 1684 (Aug. 15, 1977), pp. 103-114.
18. D. Bortoluzzi, J. W. Conklin, and C. Zanoni. "Prediction of the LISA Pathfinder release mechanism in-flight performance". *Adv. Space Res.*, vol. 51, no. 7, pp. 1145–1156, 2013.
19. C. Zanoni and D. Bortoluzzi. "Experimental-Analytical Qualification of a Piezoelectric Mechanism for a Critical Space Application". *IEEE/ASME Transactions on Mechatronics*, Vol. 20, No. 1, February 2015.



# Mechanisms Design for the S5P-TROPOMI Instrument

Erik Tabak\*, Jan de Vreugd\*\*, Dorus de Lange\*\* and Frits van der Knaap\*\*

## Abstract

TNO developed two mechanisms as a module of the Sentinel 5 Precursor (S5P) TROPOspheric Monitoring Instrument (TROPOMI). The TROPOMI is an advanced absorption spectrometer for Earth observation, developed in The Netherlands under contract to NSO and ESA for the ESA Copernicus Space Component Programme. The TROPOMI will allow continuation of the 15-year satellite data sets started with GOME, OMI and SCIAMACHY. This paper will address all design aspects of the mechanism starting with design considerations and ending with the results of a successful qualification campaign. The design challenges of these mechanisms are: a tight design space, the overall mass, the bearing loads due to both a relatively high carousel mass and vibration launch load (~30g quasi static loading which drives the bearing loads), the relatively high required angular reproducibility, and the thermal constraints (operational temperature range).

## Introduction

TNO has extensive heritage in designing mechanisms for optical space instruments. In this particular case it concerns the two mechanisms within the instrument needed to fulfill different functionality. One of the mechanisms, the Folding Mirror Mechanism (FMM), requires high positional accuracy and reproducibility on one angular position for the mirror, whereas the second mechanism, the Diffuser Mechanism (DIFM), has to provide six distinctive angular positions for the diffuser carousel with sufficient accuracy and reproducibility. The goal has been to use the same bearing and motor type for the two mechanisms. For reliability reasons a redundant winding motor concept is chosen as baseline for both mechanisms.

## Functional description of the Calibration Unit (CU)

The two mechanisms of the Calibration Unit (CU) cooperate to create several optical paths enabling calibration and nadir view. Figure 1 shows the different rotational positions of both mechanisms in section view. The Folding Mirror Mechanism (the smaller mechanism at the right top in the figure) only has one relevant position. It should be able to rotate to enable the slit in the correct position.

The Diffuser Mechanism (DifM) has to be able to rotate the optics in six different positions:

- Solar calibration: this is done in two positions, mutually rotated with 180°
- White Light Source Calibration (90° rotated with respect to the solar calibration)
- Laser diode calibration (180° rotated with respect to the White Light Source calibration position)
- The LED calibration position is rotated with respect to the solar calibration with 45°

The FMM has two positions:

- Reflecting light of any of the six positions of the DifM
- Passing through Earth radiance

---

\* InnoSpace, Rotterdam, The Netherlands

\*\* TNO, Delft, The Netherlands

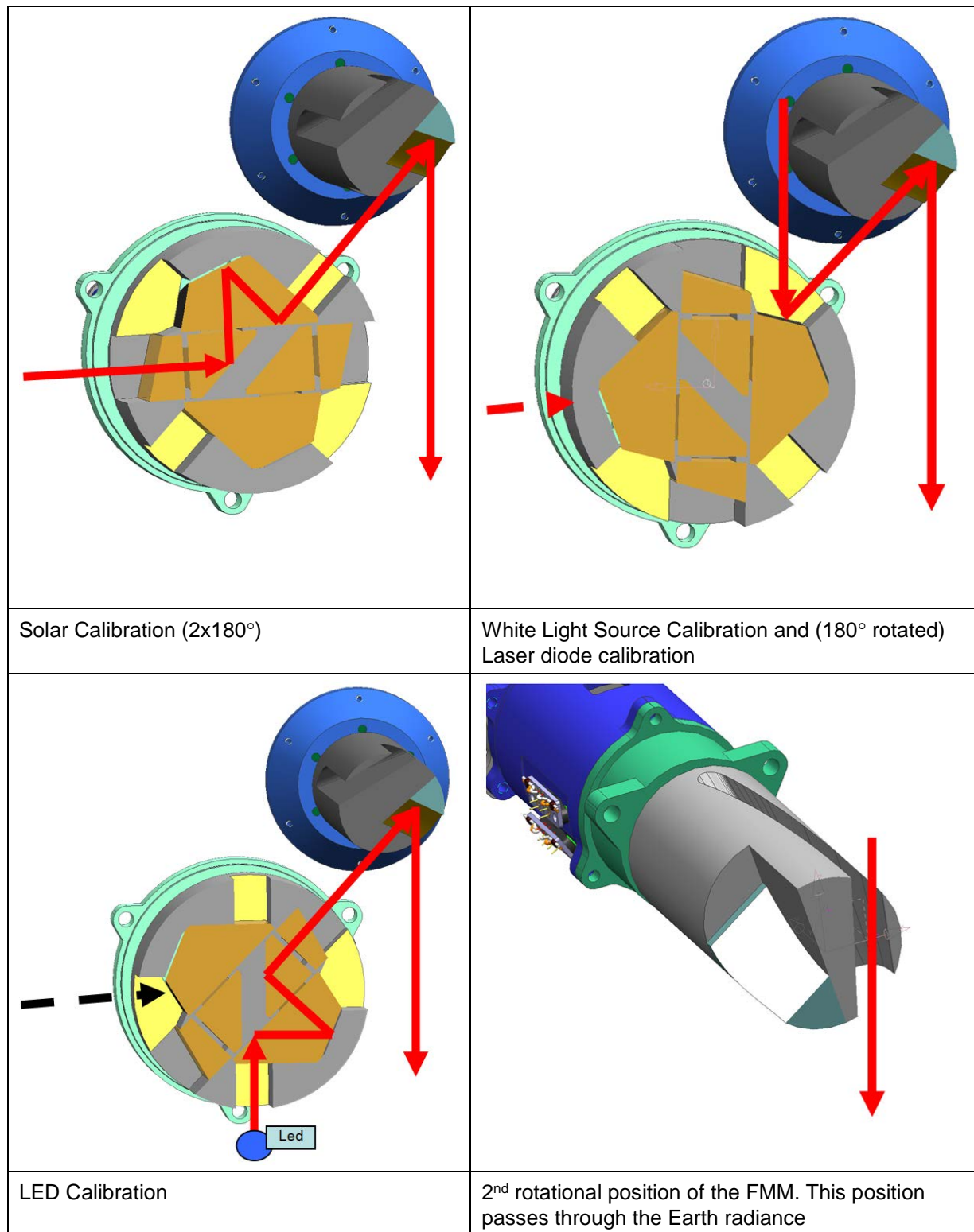


**Figure 1. The different rotational positions of both mechanisms in section view. The arrows indicate the light paths through the mechanisms**

An overview of the driving requirements for both mechanisms is shown in Table 1.

**Table 1. Overview of the driving requirements**

Requirement	Value	Remarks
Reproducibility DifM	$RY \pm 0.42^\circ$	The diffuser carousel shall have a reproducibility of 0.42 degree (zero to peak = $2\sigma$ )
Reproducibility FMM	$RY \pm 0.1^\circ$	The folding mirror shall have a reproducibility of 0.1 degree (zero to peak = $2\sigma$ ).
Testing	-	The folding mirror and the diffuser mechanisms shall be designed to allow complete testing in restricted cleanliness and environmental conditions on ground individually and at spacecraft level.
Number of full rotations in space	30000	The folding mirror and the diffuser mechanisms shall be able to operate for 30000 cycles.
Design survival temperature	$-50^\circ\text{C}$ to $+45^\circ\text{C}$	incl. qualification margin
Design operational temperature range	$+7^\circ\text{C}$ to $+33^\circ\text{C}$	incl. qualification margin
Rotating Mass (carousel)	3.2 kg	incl. 20% design contingency. Applies to the DifM (worst case)
Eigenfrequency	$> 500$ Hz	First eigenfrequency of the mechanisms. It concerns here a design goal
Positions	DifM: 6 positions ( $4 \times 90^\circ$ , $2 \times 45^\circ$ ) FMM: 2 positions	
Oscillation stroke and frequency	$\pm 5$ deg @ 0.5Hz	During a monthly calibration, 3 periods of 10 minutes of oscillations are required
Rotational Speed	$90^\circ$ in 10 s	
Position accuracy	$RY \pm 0.5$ deg	A worst case estimation
Parasitic translations over stroke	$\Delta X, \Delta Y, \Delta Z < 0.1$ mm	A worst case estimation
Parasitic rotations over stroke	$\Delta RX, \Delta RZ < 0.1$ deg	A worst case estimation
Number of full rotations for on ground testing	3000	
QS Design Load	30 g	

## Bearing Design Considerations

Due to the need for relatively large rotations in the mechanisms, the application of bearings is inevitable. This automatically introduces (dominant) tribology in the system, which together with the application in vacuum, is considered as a design driver. For that reason, the design of the mechanism(s) starts with the design of the bearings.

Initially, a design with two angular contact bearings (in combination with a soft preload) would suffice. This provides a relative low complexity design. One end remains fixed whereas the other end is flexible or able to slide in the axial direction (this is in order to minimize the disturbance forces due to thermo-mechanical loads). However, in order to guarantee surface contact in the bearings (during launch loads), the preload needs to be higher than the forces induced by launch. This yields relatively high required preloads. For the mechanisms as described in this article this would yield negative motorization margins. Additionally, the bearing gapping would become unacceptably high. Both the topics motorization margin and the bearing gapping are treated later on in this article.

A solution to the problem of the high preload and large amount of gapping is by applying duplex bearings. A duplex bearing has the advantage that it can be loaded to high loads in both directions while maintaining a relative small preload. A duplex bearing is a bearing set which is prepared to have a dedicated preload, once clamped together. The principle (as shown in Figure 2) is that the width of all the four rings (the inner and outer bearing rings of both bearing) is measured. Next, it is determined by the bearing supplier how much is required to polish from the outer ring of one of the two bearings. Typically this is in the order of microns with a preload of tens of newtons. Next, the bearings are assembled and compressed together in such a way that the outer rings are in contact with each other. The step-by-step procedure is illustrated in Figure 2. The drawback of applying a duplex bearing is the over-constrained system that it results in: the shaft is fixed in four single bearings (two too many). This will be a point of attention when designing the supporting mechanics.

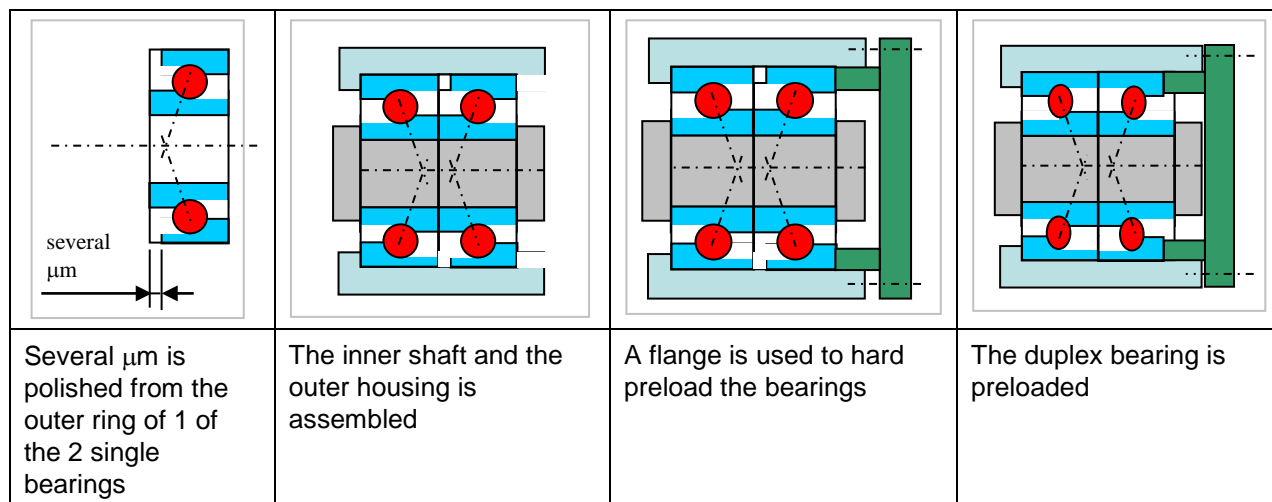


**Figure 2. The principle of a duplex bearing**

The bearing properties are summarized in Table 2. These parameters have been established with the aid of the bearing supplier ADR [1] in cooperation with ESTL [2].

**Table 2. Bearing properties**

Parameter description	Value
<b>Bearing material</b>	Stainless steel 440C
<b>Yields strength bearing material</b>	4000 MPa
<b>Ball diameter</b>	4.762 mm
<b>Loading Configuration</b>	Face-to-face (FF) or X-configuration
<b>Pitch diameter</b>	~ 34 mm
<b>Contact angle</b>	30 ± 2 deg
<b>Ball complement</b>	17 [-]
<b>Width (single bearing)</b>	9 mm
<b>Width (duplex bearing)</b>	18 mm
<b>Compliance (1/Stiffness)</b>	0 m/N ('hard' preloading). This is the setting in the analysis software CABARET. For duplex bearings, the axial stiffness of the bearing determines the compliance of the 'preload spring'
<b>Preload</b>	50 ± 10N
<b>Bearing Center Plane spacing</b>	9 mm
<b>Shaft O.D.</b>	25 mm
<b>Housing I.D.</b>	42 mm
<b>Coefficient of friction (MoS<sub>2</sub> coating, applied on both the races and the balls)</b>	0.05...0.08

### Motor Choice

Each of the mechanisms is driven with a stepper motor of the same type, the Phytron [5] VSS 52.200. The motor is procured as a complete unit, including internal bearings. Table 3 shows the main properties. The redundant motor windings are wound around separate poles. This avoids failure propagation in the windings. The eight poles are clearly seen in Figure 3 (right) and the picture also shows that each coil is wound around separate poles. A photograph of the complete motor is shown on the left in the figure.



**Figure 3. Photograph of the Phytron stepper motor (left) and a photograph of a similar motor (right) provided by Phytron**

**Table 3. Motor properties**

Parameter description	Value	Remarks
<b>Motor Type</b>	VSS 52.200.1.2	
<b>Supplier</b>	Phytron	
<b>Number of teeth</b>	50	
<b>Number of phases</b>	4	With the 50 teeth this results in a full step resolution of $1.8^\circ$ (200 steps/rev)
<b>Number of poles</b>	8	
<b>Windings</b>	“cold” redundant	
<b>Holding Torque</b>	> 0.320 [Nm]	
<b>Running Torque</b>	> 0.220 [Nm]	

### Conceptual Design Description

The design of both mechanisms is optimized to the ability to survive launch loads and having a low friction torque and therefore a high torque margin. Furthermore, the mechanisms are designed as compact as possible to limit the overall mass and volume. The principle of the design baseline is identical for both mechanisms (see Figure 4) and can be roughly divided in the following features:

- A stepper motor drives the carousel of the mechanisms
- The carousel is symmetrically supported by bearings (one duplex at each side)
- The motor and the carousel are coupled through a flexible coupling. This coupling is torsionally stiff, but compliant in all other directions
- The carousel consists of:
  - For the DifM: A set of 6 Fused Silica components (diffusers)
  - For the FMM: A slit and a folding mirror

The left duplex fixes 5 DoF (only  $R_z$  is free), but due to the hinge the  $R_x$  and  $R_y$  are released. The X and Y direction are still constrained since the rotation point of the hinge shaft is placed symmetrically within the duplex bearing. The Z direction is also fixed by the left duplex bearing. The right duplex bearing is fixed in X, Y by the membrane. The Z direction is left free which allows for thermal expansion differences between the carousel (Invar) and the fixed world (aluminium). Hereby, the preload of ~50 N remains approximately the same at large temperature excursions. The  $R_x$  and  $R_y$  of the right duplex are left free due to the membrane. Since both the carousel and the motor shaft are fixed in all except the rotation, a flexible coupling is needed which only transfers the  $R_z$  in a stiff manner.

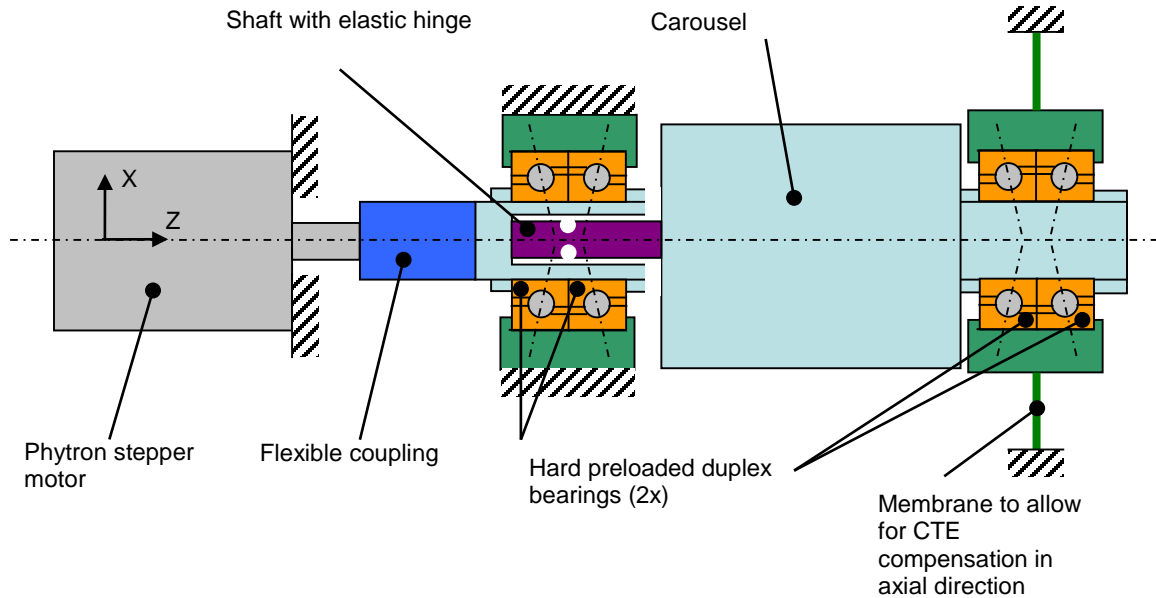


**Figure 4. Schematic overview of the concept design of the mechanism**

### Detailed Design Features

#### Hinge shaft

The elastic hinge is introduced in the design in order to allow for a kinematic design. Therefore, the hinge will ensure that the design is predictable and reproducible even with the presence of tolerance chains within the rotor and relative to the CU housing. The predictability is also guaranteed during the thermal survival and operational range. The following aspects are of importance with respect to the hinge:

- Stresses due to launch loads (30g Quasi-Static load in axial and radial direction)
- Bending effects (stiffness and stresses)
- Stiffness in axial and radial direction (driven by the required  $> 500$  Hz)

Figure 5 shows a side view with the two main parameters: the diameter of the hinge ( $D = 6\text{mm}$ ) and the width ( $h = 4\text{mm}$ ). The shaft is manufactured from Ti6Al4V, which is a close thermal match (CTE match) with the 440C bearings.

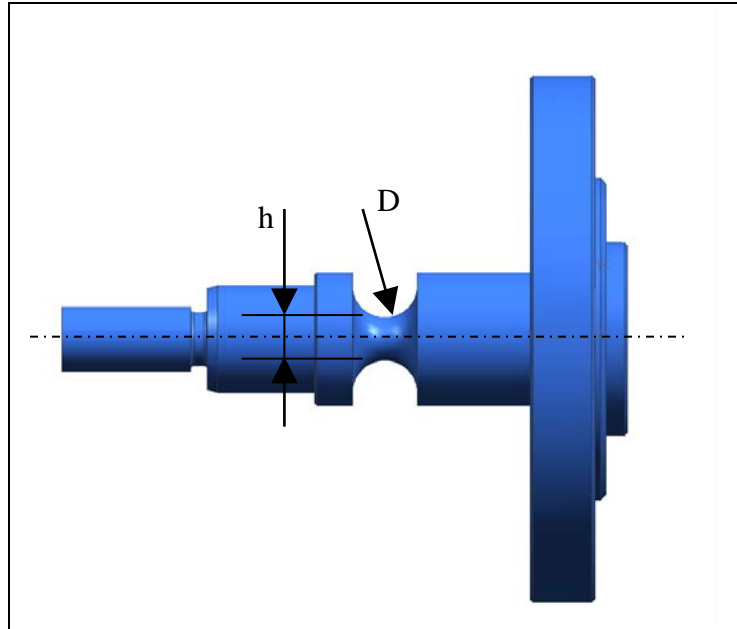


**Figure 5. A side view of the elastic hinge with the two main parameters: the diameter of the hinge ( $D$ ) and the width ( $h$ )**

#### Flexible coupling

The flexible coupling transfers the motor torque to the carousel. Note that this coupling is designed to be torsionally stiff (around the center line) and compliant in the 5 other DOFs. This coupling is needed to enable a kinematic and therefore predictable and reproducible design. Note that the motor is equipped with its own bearings and that the motor housing is rigidly attached to the CU housing. The motor shaft has only one DOF free and that is the rotation around the center line. Also the carousel has only one DOF free, i.e., rotation around the center line. It is therefore essential that the coupling does not add additional stiffness in the remaining 5 DOFs which would result in over-constraining the system. The design of the coupling is illustrated in Figure 6.

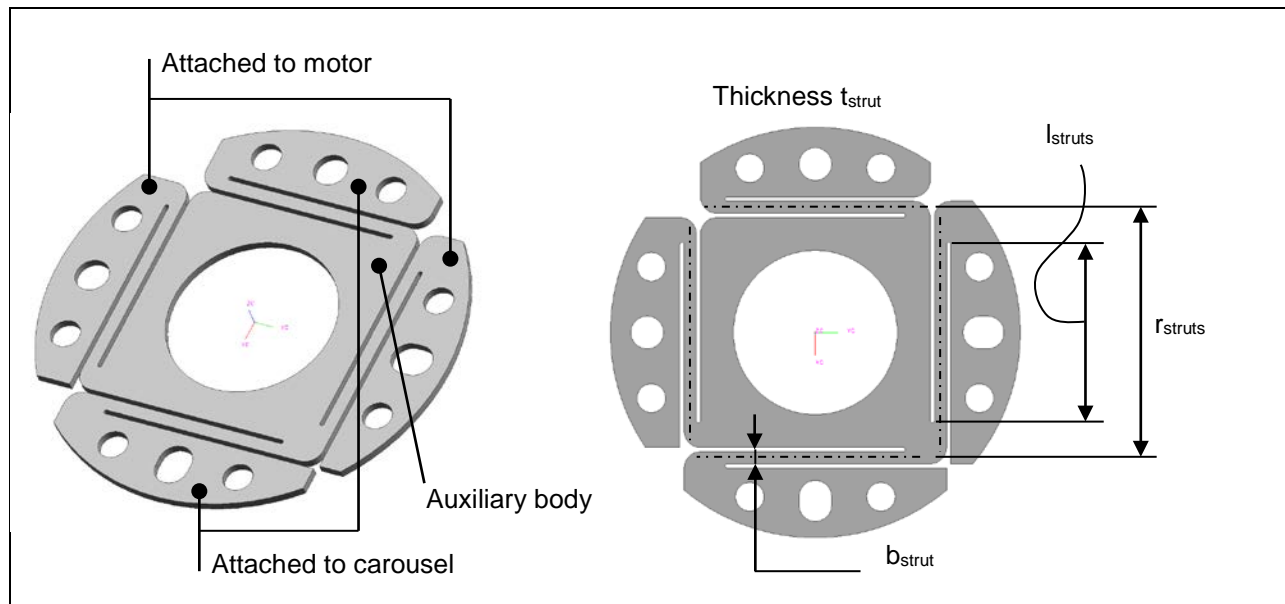


**Figure 6. Flexible coupling used to couple the drive shaft of the motor to the rotor**



The coupling is a monolithic part (Ti6Al4V), manufactured by wire EDM from one single piece of plate. The result is two pairs of flanges, mutually coupled by four struts. One flange pair is rigidly mounted to the motor side. Via one pair of parallel struts, the torque is transmitted through the auxiliary body. Next, through the second pair of parallel struts the torque is transmitted to the carousel. The principle of the coupling is also known as an 'Oldham' coupling in literature.

The only drawback of this coupling is the fact that the auxiliary body is not fixed in axial direction. This stiffness is provided by the lateral stiffness of the struts which is designed to be as low as possible. Special attention is given to keep the first eigenfrequency of this auxiliary body sufficiently high.

### Membrane

One of the two duplex bearings of each mechanism is supported by a membrane (Figure 7). The reason for this is to allow for CTE differences (axially) between the carousel and the CU housing. A membrane will result in a predictable design. An alternative would have been to use a sliding fit. However, this is less predictable and reproducible than an elastic solution with a membrane. The dimensions of the Ti6Al4V membrane are shown in the figure.

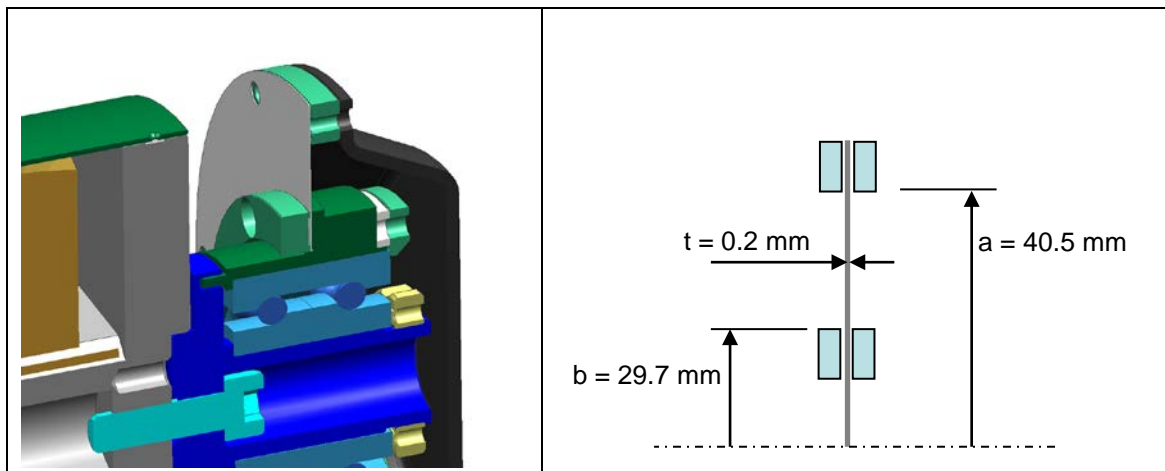


**Figure 7. CAD picture (left) and general dimensions of the membrane**

### End stop

Contrary to the DifM, the FMM is equipped with an end stop. The reason for this is that a higher reproducibility can thereby be achieved for the FMM. Using the detent torque of the stepper motor, a positive torque is exerted against the end stop which enables a stable position with an unpowered motor. The FMM has only two positions: one of the folding mirror (which has to be positioned reproducibly) and one for passing through the Earth's radiance (oversize slot). The end stop is shown in Figure 8.

A cam disc is rigidly attached to the rotating shaft. Additionally, a key or spline is used to prevent mutual rotation. The cam will rest on a Vespel end stop. This end stop, which is clamped to the end stop holder, is adjustable with a shim. This material combination was chosen because:

- Vespel combined with metal avoids cold welding.
- Vespel was used in the Sciamachy and OMI projects, also as an end-stop. Both passed a (comparable) life test.

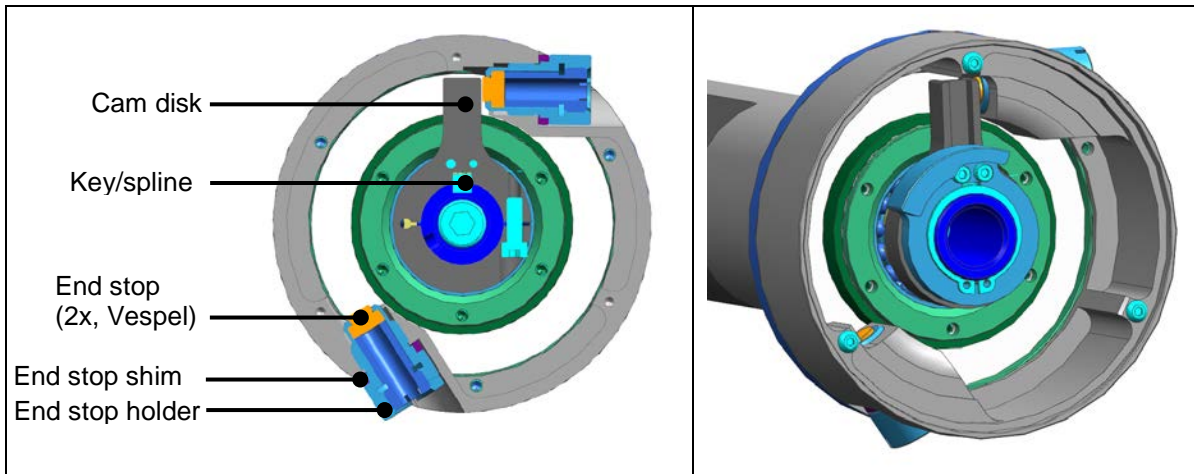


**Figure 8. The FMM is equipped with an end stop in order to guaranty an angular reproducibility < 0.1°. A cam disk will rest on an adjustable Vespel end stop. Note that two stops are incorporated.**

### Bearing analyses

The following analyses are considered to be relevant for assessing the feasibility of the bearing concept:

- Gapping and stress in the bearings due to axial and radial loads (Quasi-Static loads)
- Bearing friction torque due to preload (@ T=20°C)
- Bearing friction torque due to preload (@ worst case operational range)
- Bearing stiffness calculations (radial and axial)

The bearing analyses have been carried with the assistance of the European Space Tribology Laboratory (ESTL) and using the software CABARET. The principle of gapping is explained in Figure 9. Both for radial and axial gapping, an unwanted physical gap will be present. The idea is to minimize this gap. The maximum allowable gapping is set to 20 µm. This is based on the approach followed in the EarthCARE MSI-VNS mission [3] and is based on communication with ESA (European Space Agency) and ESTL. Due to the maturity of the CU design, the design goal for gapping is set to 10 µm.

Figure 10 shows the results for a varying axial load between -2000 to 2000 N. Both the stress and the axial displacements of each of the two bearings are calculated. The axial force for the mechanism is calculated with  $F_{ax} = ma = 3.2 \cdot 30 \cdot 9.81 = 941 \text{ N}$ , where the mass  $m$  of the carousel is 3.2 kg and a 30 g QS load is applied. The bearings start to gap at the point where the Hertzian stress becomes zero. The displacement at this point is 1 µm. The displacement at 941 N is 10 µm. Therefore, the gapping at 941 N is 9 µm. This is within the design goal of 10 µm.

The maximum stress at 941 N is 1800 MPa. With an allowable stress of 4000 MPa, the Margin of Safety becomes  $\text{MoS} = [(4000 / 1.25) / 1800] - 1 = 0.77$  which is > 0 and therefore acceptable.

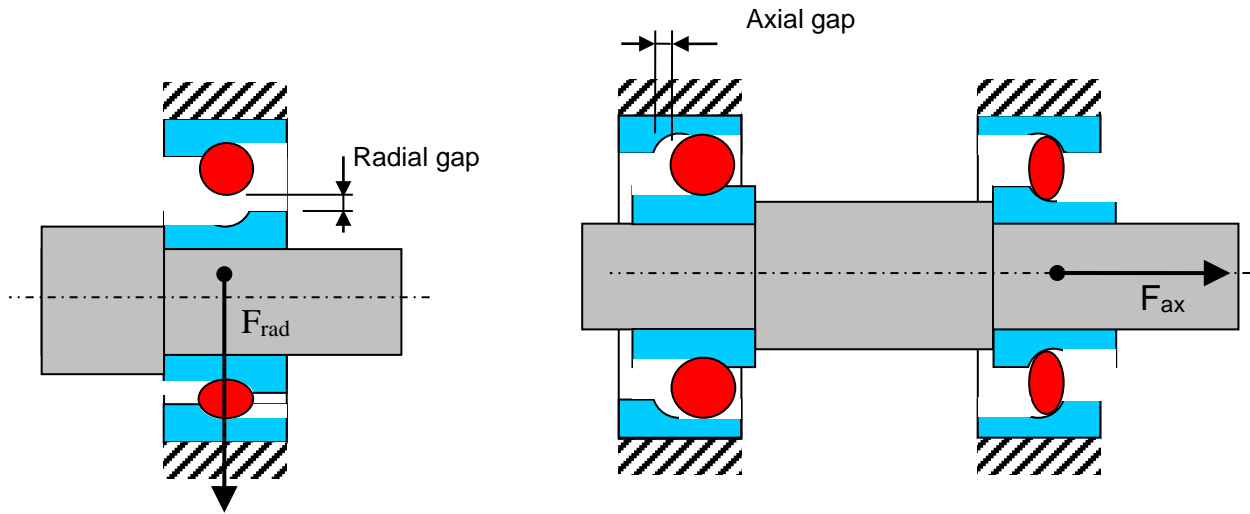


Figure 9. Radial and axial gapping illustrated

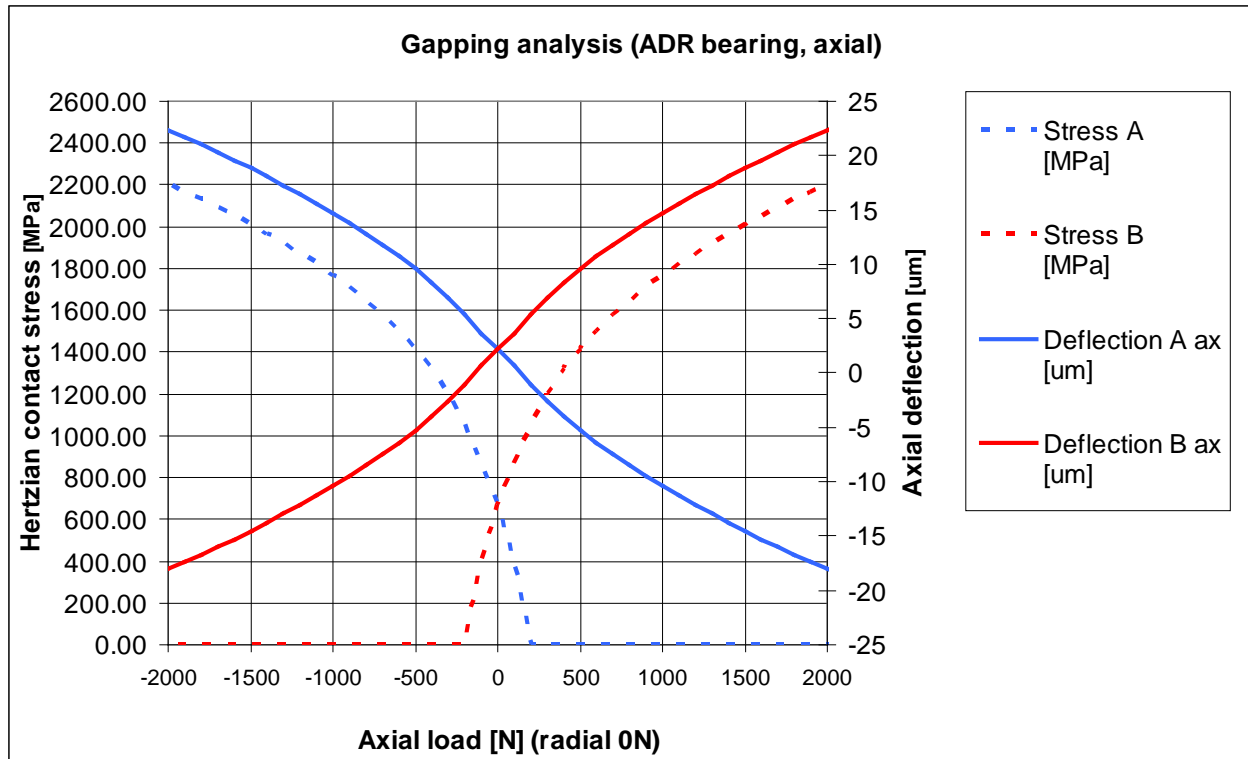


Figure 10. The axial deflection and the Hertzian contact stress in the duplex bearing as a function of the axial load. The preload is set to 50 N.

For two reasons, radial gapping is far less than axial gapping. Firstly, the radial force on the duplex is estimated to be  $941/2 = 470$  N which is half the axial force. Secondly, due to the contact angle, the radial loading is in a much more favorable direction. At 470 N, the radial gap is  $\sim 3 \mu\text{m}$  which is smaller than the axial gap and thereby also below the design goal of  $10 \mu\text{m}$ . This shows that the duplex bearing is considered to be very suited for radial loads.

## Motorization Margin Analyses

The ability of a drive motor to be able to drive a mechanism can be quantified using the Motorization Margin or Torque Margin ( $MoS_{TORQUE}$ ). This margin is defined as  $MoS_{TORQUE} = [ T_{MIN,MOTOR} / T_L ] - 1$ . Herein,  $T_{MIN,MOTOR}$  is the minimal motor torque available and  $T_L$  is torque of the load. The latter is defined as  $T_L = 2 * (FoS_{FRICTION} * T_{FRICTION})$ . Herein,  $FoS_{FRICTION} = 3$  which is the Factor of Safety on friction and  $T_{FRICTION}$  is the torque in bearings. According to ECSS [4], inertia and spring effects should also be taken into account, but for these mechanisms these budgets are considered negligible. The torque margin is calculated for the following load cases:

- At 20°C
- At worst case operational range

The following inputs are elaborated on. The friction torque is calculated with CABARET as described in the previous section. It concerns here a mean friction torque with a worst case coefficient of friction. Next, in order to obtain the maximum (0-peak) friction torque, the mean friction torque is multiplied by a factor of three. This factor is based on empirical data as deduced by ESTL. Next, margins according to [4] are incorporated in the calculations. The resulting margins for both cases are 3.1 and 2.6 respectively, which are both  $> 0$ . From this it is concluded that the motor is suited for the mechanisms.

## Life Test Model Qualification

The Tropomi Life Test Model Calibration Unit has successfully passed the life test program, consisting of:

- Vibration testing (see Figure 11) with a 9.71  $g_{rms}$  input spectrum, resulting in 28.6  $g_{rms}$  on the carousel
- Thermal Vacuum Testing (from -50°C to +45°C) as shown in Figure 12
- On-ground cycles and in-orbit cycles up to 72000 cycles

No change in performance between start and end of the life test program, determined by:

- Pre and Post Vibration resonance search
- Minimum start current (torque margin) during the life test program
- Destructive Physical Analysis

## References

1. ADR, [www.adr.fr](http://www.adr.fr)
2. ESTL, [www.esrtechnology.com/centres/estl](http://www.esrtechnology.com/centres/estl)
3. Tabak, E., de Goeij, B., van Riel, L., Meijer, E., van der Knaap, F., Doornink, J., de Graaf, H. "Design, building and testing of a Sun Calibration Mechanism for the MSI-VNS Instrument on EarthCARE." *ESMATS 2013*.
4. ESA-ESTEC, ECSS-E-ST-33-01C Mechanisms, Requirements & Standards Division Noordwijk, The Netherlands, 6<sup>th</sup> March, 2009
5. Phytron, [www.phytron-elektronik.de](http://www.phytron-elektronik.de)

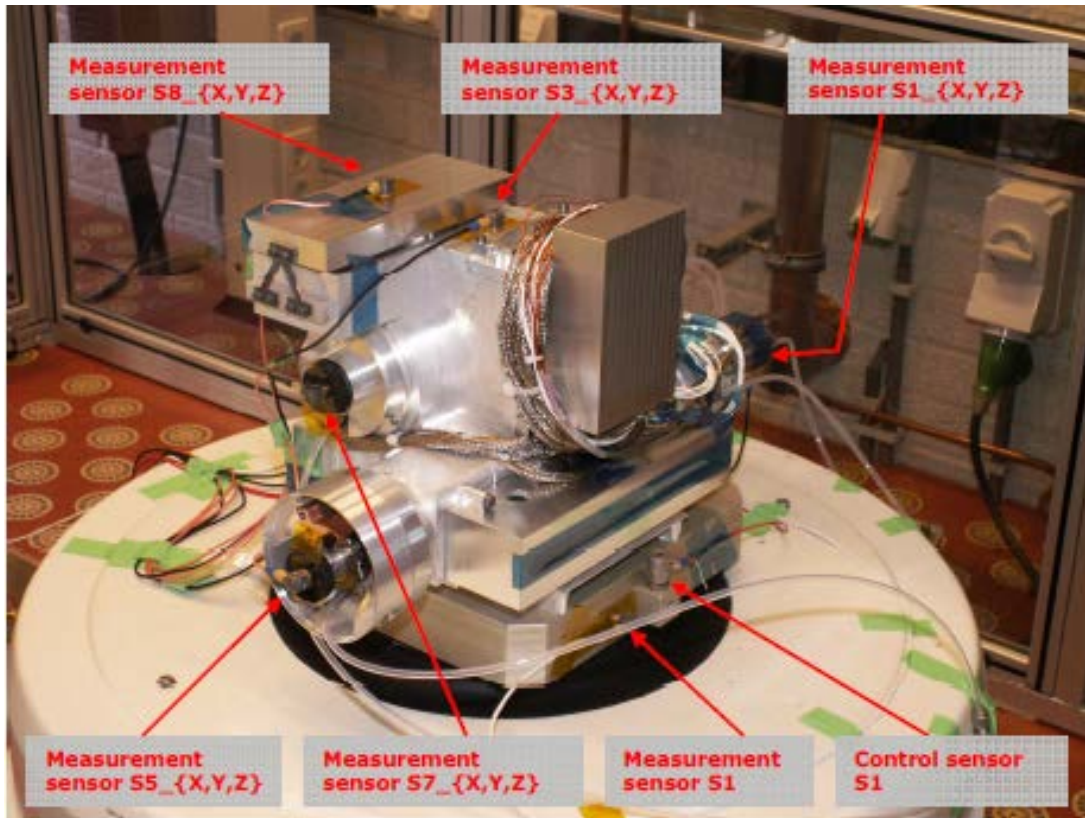


Figure 11. Vibration testing of the CU with a 9.71 g<sub>rms</sub> input spectrum, resulting in 28.6 g<sub>rms</sub> on the carousel

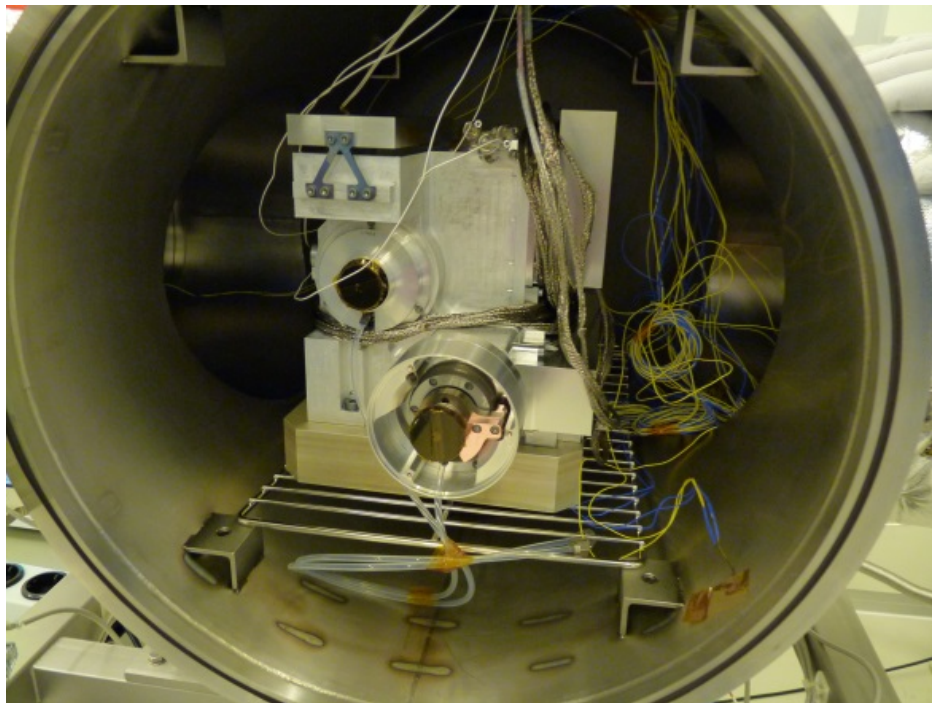


Figure 12. Thermal Vacuum Testing of the CU





# Tests on the Ductility of Stainless Steel and Titanium Alloy Aerospace Fasteners

Jarrold T. Whittaker\* and Daniel P. Hess\*

## Abstract

This paper presents results from tests aimed to assess the relative ductility of titanium alloy Ti 6Al-4V and stainless steel A286 aerospace fasteners of comparable size and tensile strength. A test procedure is developed and tensile tests are performed on test fasteners. All test fasteners fracture in the threaded region. Elastic and plastic deformation at rupture are extracted from the resulting load versus displacement curves and used to compute the ductility index for each test fastener. The ductility index quantifies the relative ductility between the different fastener materials. The average ductility index for the titanium alloy fasteners is about one-tenth the average value for the A286 fasteners. In addition, the fracture surfaces of the titanium alloy test fasteners fracture perpendicular to the axis of tensile loading, whereas the A286 test fasteners fracture across three or four threads which corresponds to about a 45 degree angle. Both the relative ductility index values and fracture surface characteristics indicate much less ductility in the titanium alloy fasteners. These results are not intended to discourage the use of titanium alloy fasteners, but rather to provide additional data for use in proper joint design when the benefits of lower weight or extreme temperature use are required.

## Introduction and Background

Ductility is generally a desirable characteristic for threaded fasteners since tensile stretch is essential for proper fastener function in a preloaded joint. As a result, traditional fastener materials are designed to provide sufficient ductility to help avoid abrupt and potentially catastrophic failure.

Titanium alloy fasteners are currently available for aerospace applications. They provide lower weight and better performance in extreme temperature than traditional aerospace fastener materials such as A286 stainless steel. However, engineers are reluctant to embrace this material due to uncertainty about its ductility and potential catastrophic failure that can result in brittle materials [1-3]. This concern is valid since fasteners by design are often used close to or at yield. Preload and external load uncertainty compound the problem.

This concern was repeatedly raised during recent meetings of the NASA NESC Standard Development for Spaceflight Fastening Systems Team and is the premise for the work reported in this paper [4].

This paper reports on a series of tests performed to assess titanium alloy fastener failure characteristics compared to a more traditional aerospace fastener material with particular interest in quantifying relative ductility. Tensile tests are performed on both titanium alloy and traditional aerospace fasteners of comparable size and tensile strength. Load versus displacement data are obtained. Elastic deformation and plastic deformation at rupture are extracted from the data and used to compute a ductility index [4-6]. In addition, the fracture surfaces of the different fasteners are examined and documented.

While it is found that titanium alloy fasteners are significantly less ductile than A286 stainless steel fasteners, these results are not intended to disqualify the use of titanium alloy fasteners. Rather, the test procedure and/or resulting data from this work can assist in proper joint design with titanium alloy fasteners for safe use.

---

\* University of South Florida, Tampa, FL

This includes appropriate selection of preload with respect to fastener yield and rupture, minimizing or controlling preload uncertainty, and quantifying worse case external load conditions.

A literature search reveals very little published data on this topic. As a result, the data in this paper helps fill an existing void in the literature.

### Test Specimens

The test fasteners used in this work are aerospace bolts made from Titanium 6Al-4V (i.e., Ti 6-4) and A286. Size and thread are ¼-28 UNJF (M6x1) with length of 1.99 in (50.5 mm) for the Ti 6-4 bolts and 2.03 in (51.5 mm) for the A286 bolts. The heads are 12 point for the Ti 6-4 bolts and hex for the A286 bolts. This difference did not affect the test results in this work since all failures occurred in the threaded section of the bolts. The test fasteners were obtained from aerospace fastener suppliers with full certifications [7]. The Ti 6-4 fasteners meet AMS 4928 Rev: R and AMS 4967 Rev: J specifications. The A286 fasteners meet NAS 1004-24A specifications.

Twelve test specimens for each fastener material are tested. This is found to be a more than adequate sample size based on the mean difference in ductility ratio found for the two different fastener materials [7]. Each test fastener is assigned a number as listed in Table 1. The test order or sequence is randomized as listed in Table 2.

**Table 1. Test fastener number**

	Fastener number											
Titanium 6-4	1	2	3	4	5	6	7	8	9	10	11	12
A286	13	14	15	16	17	18	19	20	21	22	23	24

**Table 2 Randomized test sequence**

Test sequence	Fastener number	Material
1	6	Ti 6-4
2	2	Ti 6-4
3	12	Ti 6-4
4	8	Ti 6-4
5	21	A286
6	7	Ti 6-4
7	17	A286
8	20	A286
9	13	A286
10	11	Ti 6-4
11	24	A286
12	5	Ti 6-4
13	9	Ti 6-4
14	15	A286
15	18	A286
16	10	Ti 6-4
17	4	Ti 6-4
18	23	A286
19	14	A286
20	19	A286
21	16	A286
22	1	Ti 6-4
23	22	A286
24	3	Ti 6-4



The twenty-four fasteners were visually inspected, coated with spray-on dry-film MoS<sub>2</sub> lubricant, allowed to dry, and placed in a sectioned container labeled by fastener number. When a test fastener number came up in the test order, it was picked out of the container, tested to failure, and remains placed back into its cell.

### Equipment and Test Procedure

An MTS tensile test machine is used for the testing in this work. The tensile tests in this work consist of a bolt in a tapped fixture rather than a bolt and nut configuration. Figure 1 illustrates a test fastener in the tensile machine. The test fastener head is secured by a high strength steel fastener tensile grip fixture and puck per ASTM F606 [8]. The other end of this fastener tensile grip fixture is threaded into the MTS crossbar head.

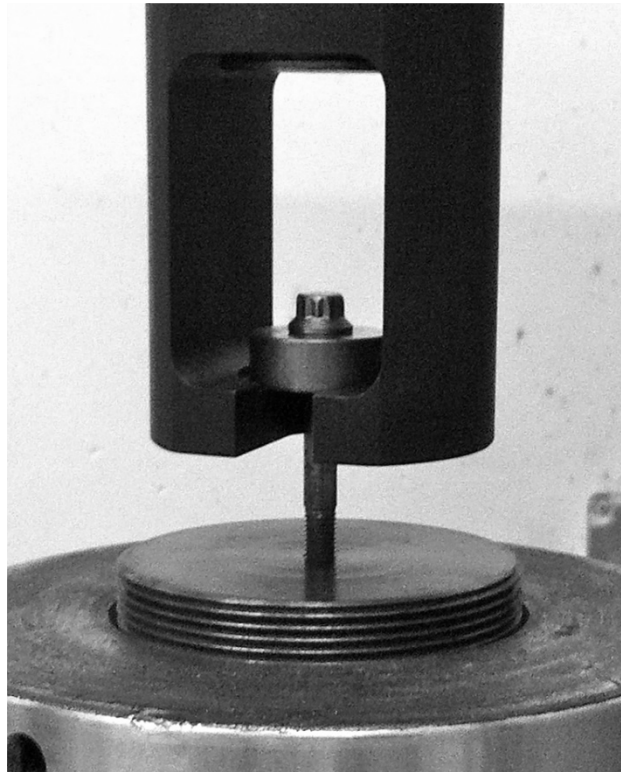


**Figure 1. Sample test fastener in fastener tensile grip with puck and lower test fixture in MTS machine.**

The test fastener threads are secured to the lower steel fixture with a ¼-28 UNJF (M6x1) tapped-hole. This provides ¾ in (9.5 mm) of thread engagement between the test fastener and the lower fixture. The external threads of this lower fixture are threaded into the MTS hydraulic ram.

Once the fixtures are installed on the tensile test machine, the following test setup is performed for each test fastener:

1. The upper crossbar head is adjusted and locked into a position such that the lower hydraulic ram has sufficient range of motion to fracture the test fastener specimen in tension.
2. The test fastener is inserted through the puck and placed into the recessed area of the upper tensile grip fixture.

3. The lower ram is raised up allowing the test bolt to be fully threaded into the lower test fixture in the ram which provides  $\frac{3}{8}$  in (9.5 mm) thread engagement between the test fastener and the lower steel fixture.
4. The ram is slowly lowered until no gap between the washer and head is visible.
5. The ram is further lowered until a 100-lb (445-N) load is placed on the test fastener.

The test procedure for each test fastener is as follows:

1. The ram is lowered at a controlled rate of 2000 lb/min (8.9 kN/min) which is within specification of ASTM F606 [8] for  $\frac{1}{4}$ -28 (M6x1) fasteners.
2. Tensile machine load and displacement are sampled and recorded from onset of test at 4.6 Hz providing over 600 data points per test. Test duration was 130 seconds or greater.
3. Test is run until test fastener failure.

### Test Data and Analysis

A compilation of all twelve A286 test fastener tensile test load versus displacement curves are presented in Figure 2. This reveals minimal scatter in test data across the sample set. The corresponding compilation of all twelve Ti 6-4 test fastener tensile test load versus displacement curves are shown in Figure 3. More scatter is present in this sample set.

Since the displacement scale is different for each fastener material in Figures 2 and 3, sample curves from each fastener material are plotted in Figure 4. This more clearly illustrates the relative displacement to failure of the different fastener materials. The data point at the largest displacement value of each curve corresponds to the test specimen fracture. Since the A286 and Ti 6-4 test fasteners are both  $\frac{1}{4}$ -28 UNFJ (M6x1) and have comparable maximum tensile load, the tensile strength for the test fasteners is also comparable.

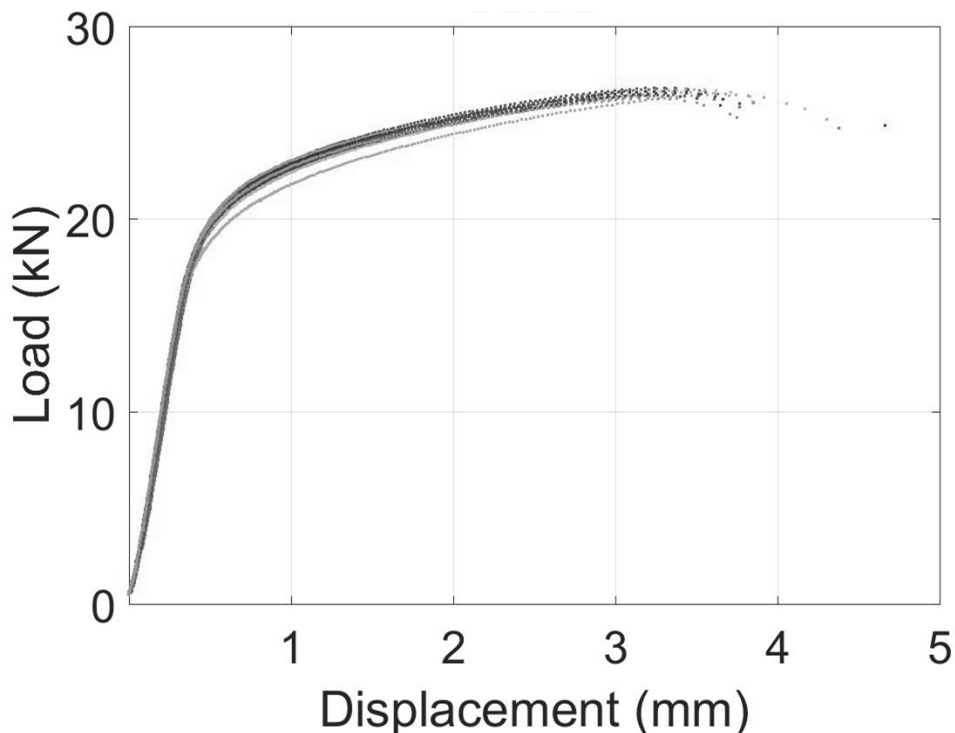


Figure 2. Load versus displacement data for all twelve A286 test fasteners

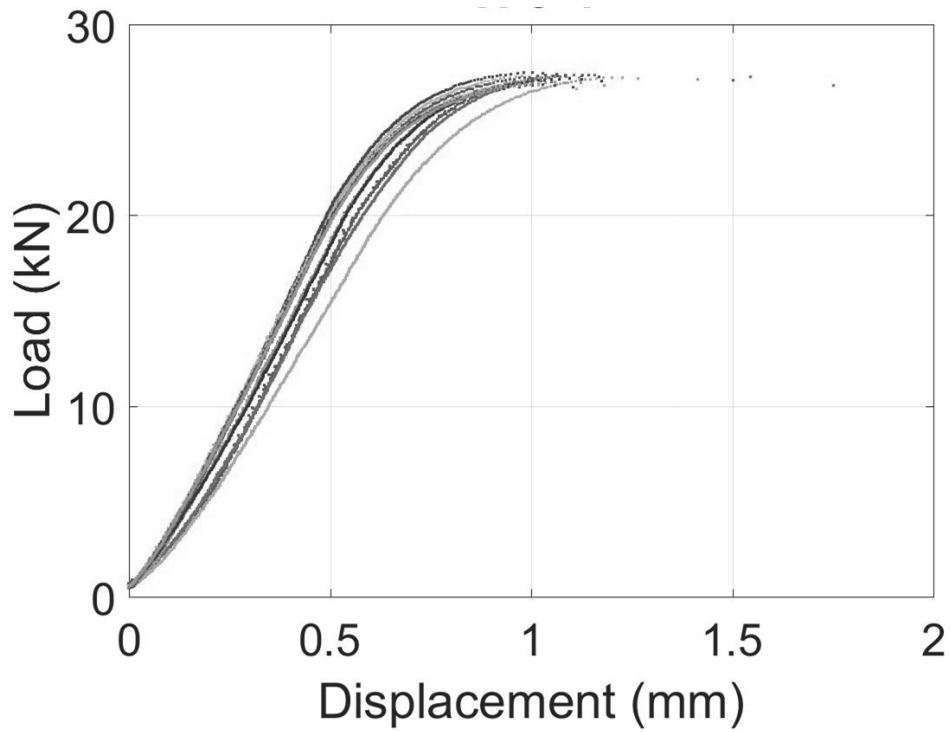


Figure 3. Load versus displacement data for all twelve titanium 6Al-4V test fasteners

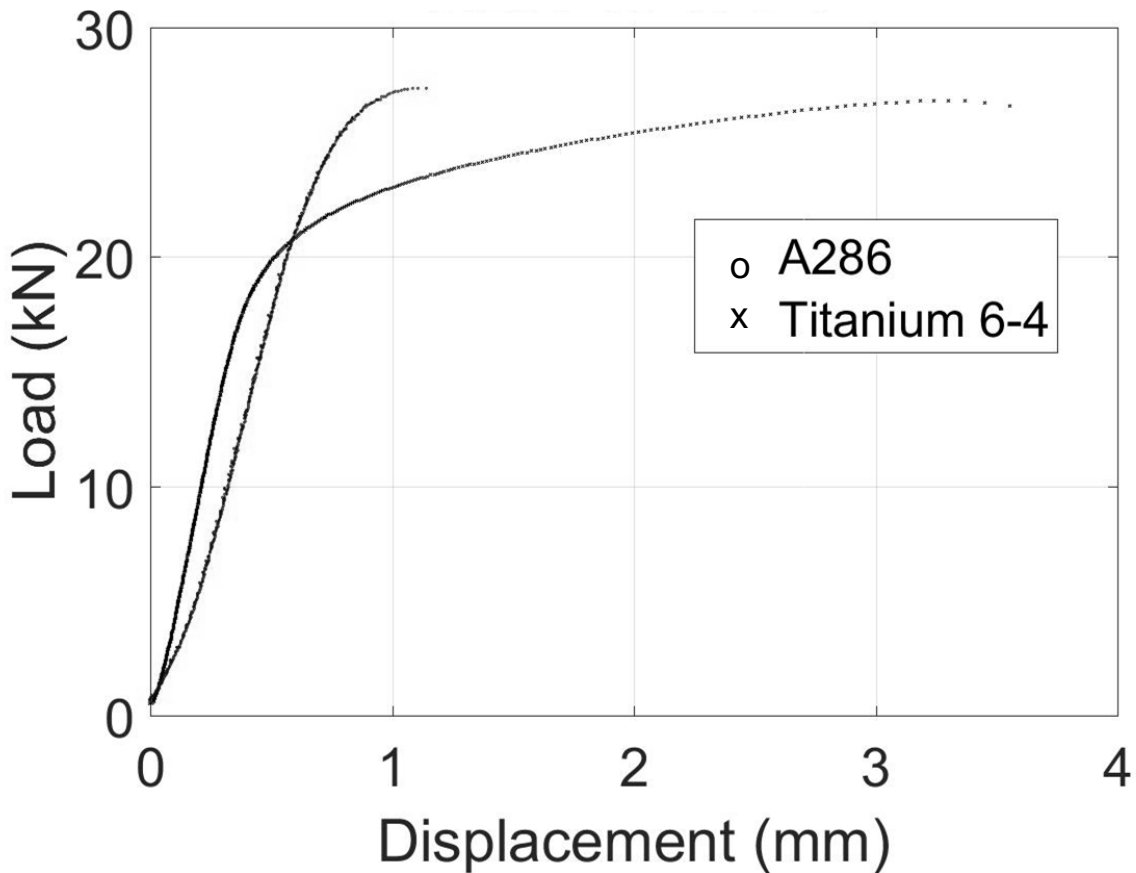
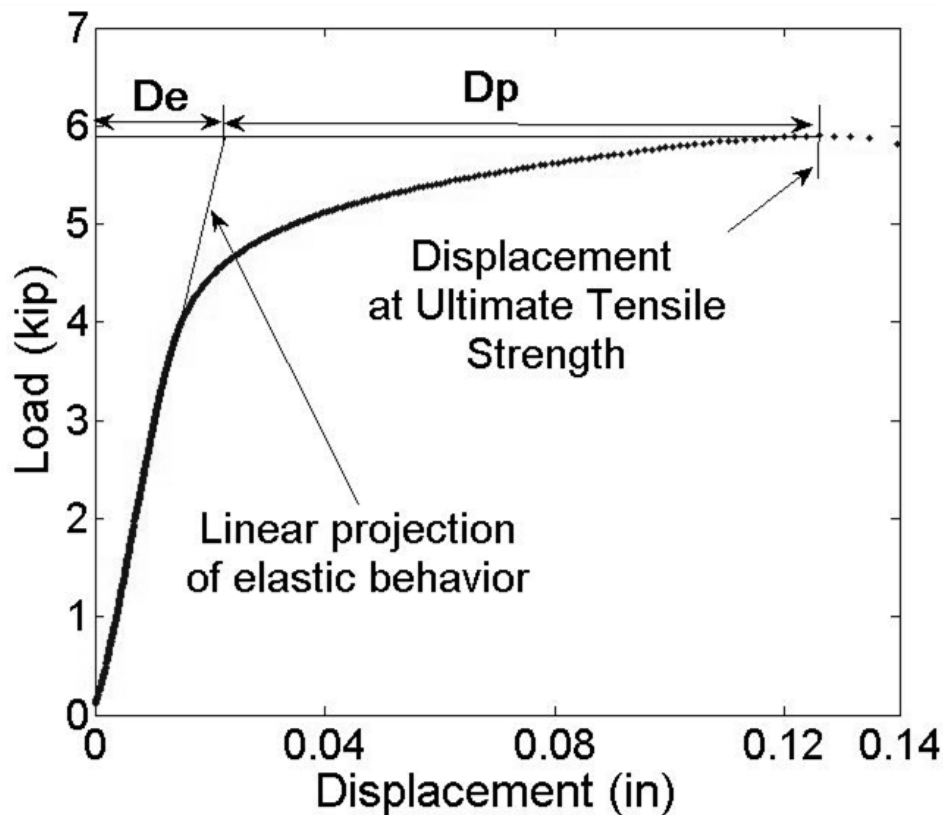


Figure 4. Load versus displacement data for sample A286 and Ti 6-4 test fasteners

Although the tensile strength for the test fasteners is comparable, the displacement from yield to fracture is notably different. The ductility index is calculated to assess this characteristic.

The ductility index is quantified by the ratio of plastic deformation at rupture to elastic deformation at rupture [4-6]. Figure 5 illustrates how the ductility index is determined from a sample load versus displacement curve.  $D_e$  represents elastic deformation and  $D_p$  represents plastic deformation. The ratio of  $D_p/D_e$  is defined as the ductility index. This index is used to quantify the relative ductility in these two test fastener materials in this work. The ductility index provides a means to quantify ductility of product such as full scale fasteners that are not ideal machined tensile test specimens. The test curves with annotation for ductility index parameters for all 24 test fasteners are provided elsewhere [7].



**Figure 5. Calculation of ductility index parameters from sample load vs displacement data**

The ductility index is calculated for all test fasteners. Table 3 lists the ductility index statistics for both the A286 and Ti 6-4 test fasteners. This data reveals that the ductility index for the A286 test fasteners is about ten times larger than the ductility index for the Ti 6-4 test fasteners. In addition, the spread or scatter in the ductility index is modest for each material as indicated by the minimum, maximum and quartile values.

**Table 3. Test fastener ductility index statistics**

	A286	Ti 6-4
Average	5.40	0.53
Minimum	5.05	0.43
25 <sup>th</sup> Quartile	5.12	0.51
75 <sup>th</sup> Quartile	5.65	0.56
Maximum	5.90	0.59

Figures 6 and 7 show fracture surfaces from sample Ti 6-4 and A286 test specimens, respectively. The fracture occurs in the threaded region for all test fasteners as expected. However, the Ti 6-4 test fasteners fracture across only one thread (i.e., nearly perpendicular to the axis of tensile loading which is typical for brittle materials), whereas the A286 test fasteners fracture across three or four threads (i.e., approximately at a 45 degree angle to the axis of tensile loading which is typical for ductile materials).



**Figure 6. Sample Ti 6-4 test fastener failure**



**Figure 7. Sample A286 test fastener failure**

### **Conclusions**

This work assessed the relative ductility of titanium alloy Ti 6-4 aerospace fasteners to stainless steel A286 aerospace fasteners. A test procedure was developed for this assessment. Tests were conducted using an MTS tensile test machine and load versus displacement curves were obtained for 24 test fasteners. The test curves were found to be repeatable for each fastener material, with substantial differences plastic deformation between materials. The tensile strength for the Ti 6-4 and A286 test fasteners were found to be comparable.

Relative ductility was assessed using the ductility index which is the ratio of plastic deformation to elastic deformation from a tensile test. In addition, fracture surfaces of the test specimens were examined for characteristics inherent of ductile and brittle failure.

The results of this work show:

1. The ductility index of the titanium alloy Ti 6-4 aerospace fasteners are about one-tenth of the ductility index of the A286 aerospace fasteners.
2. The average ductility index of the titanium alloy Ti 6-4 aerospace fasteners was found to be 0.53.
3. The average ductility index of the A286 aerospace fasteners was found to be 5.40.
4. The fracture surfaces of the titanium alloy Ti 6-4 aerospace fasteners from tensile testing are perpendicular to the axis of the tensile loading which is characteristic of brittle fracture.

5. The fracture surfaces of the A286 aerospace fasteners from tensile testing are at about 45 degrees to the axis of the tensile loading which is characteristic of ductile fracture.

These results are not intended to discourage the use of titanium alloy fasteners, but rather to provide additional data for use in proper joint design. In cases where weight savings or temperature requirements demand such fasteners, titanium alloy fasteners may be the best option. Proper joint design with titanium alloy fasteners include keeping preloads at or below 65% of yield, minimizing or controlling torque-tension scatter, and accurately quantifying worst case external loads.

### **Acknowledgement**

The authors gratefully acknowledge the funding and support of the NASA Engineering and Safety Center (NESC) and Dr. Michael Dube for this work.

### **References**

1. Gross, F, "Concerns with the Use of Titanium Fasteners," *NASA Materials Engineering Branch Technical Information Paper No. 133*, 2003.
2. Stevenson, M, McDougall, J, Cline, K, "Metallurgical Failure Analysis of Titanium Wing Attachment Bolts," *ASM International - Practical Failure Analysis*, 3 (2003), 75-80.
3. Jha, A, Singh, S, Kiranmayee, M, Sreekumar, K, Sinha, P, "Failure Analysis of Titanium Alloy Ti6Al4V Fastener Used in Aerospace Application," *Engineering Failure Analysis*, 17 (2010), 1457-1465.
4. NASA-STD-5020, *Requirements for Threaded Fastening Systems in Spaceflight Hardware*, .2012
5. Gerard, G, "Structural Significance of Ductility in Aerospace Pressure Vessels," *ARS Journal*, 32 (1962), 1216-1221.
6. Samuel, K, "Dependence of Strength and Ductility Ratios in Austenitic Stainless Steels," *International Journal of Pressure Vessels and Piping*, 83 (2006), 474-476.
7. Whittaker, J, *Ductility and Use of Titanium Alloy and Stainless Steel Aerospace Fasteners*, University of South Florida MS Thesis, 2015.
8. ASTM F606-13, *Standard Test Methods for Determining the Mechanical Properties of Externally and Internally Threaded Fasteners, Washers, and Rivets*, 2013.

# Development and Testing of a “Backlash-Free” Gas-Tight High-Precision Sample Dosing Mechanism for the ExoMars 2018 Rover

Daniel Redlich\*, Robert Paul\*, Sebastian Ott\*, Lutz Richter\*, Quirin Mühlbauer\*, Markus Thiel\*,  
Tim Tattusch\*, Harald Weisz\*\*, Fabio Musso\*\*\* and Stephen Durrant\*\*\*\*

## Abstract

This paper presents the development and testing by OHB System AG of the Powdered Sample Dosing and Distribution System (PSDDS) with specific focus on the bearing and sealing design. The PSDDS is a sample handling mechanism on the Rover of the European Space Agency 2018 ExoMars Mission, a cooperative mission with Roscosmos including a scientific instrument contribution from NASA. It is entirely developed by OHB as a subcontractor to Thales Alenia Space Italia who is the prime contractor for the whole ExoMars program. The PSDDS is the third part of a chain consisting of four individual mechanisms that compose the Sample Preparation and Distribution System (SPDS).

The main task of the PSDDS is to receive powdered samples from a stone mill (Crushing Station) and distribute the samples in defined quantities to two different kinds of receptacles, a refillable container and several one-time use Ovens, which are mounted on a carousel (4th mechanism). The sample distribution is performed by a redundant Dosing Station (DS). As these powdered samples are quite sensitive to cementation, two counter-measures have been implemented. A Piezo to vibrate the Dosing Station and to loosen the sample material as well as a device to bypass the two Dosing Stations which is able to distribute the sample in a more robust way but without the capability to control the amount (Alternative Transport Container (ATC)). Another task of the PSDDS is to clean the refillable container to allow its reuse without cross contaminating the samples (Cleaning Device).

These components and procedures need to be compatible with the Martian environment. This includes sample handling and challenging demands for cleanliness and contamination control resulting in stronger constraints for the mechanism's design and ultimately requiring the development of unique design solutions.

The PSDDS design as well as the results of the qualification test campaign under Mars-like conditions are described in this paper.

## Introduction

Exploring whether life ever existed or is still present on Mars today is one of the most exciting scientific questions of our time. Therefore, ESA together with Roscosmos decided to conduct the ExoMars program, which is divided into two missions: the first mission consists of an Orbiter plus an Entry, Descent and Landing Demonstrator Module to be launched in 2016 whereas the second mission consists of a Lander with a Rover to be launched in 2018. The Rover is equipped with a Drill to take sub-soil samples down to a depth of 2 m, which will then be analyzed in-situ by several instruments dedicated to exobiology and geochemistry research, the so-called Pasteur payload. These instruments are located in the Analytical Laboratory Drawer (ALD) inside of the Rover. These instruments are:

---

\* OHB System AG, Oberpfaffenhofen, Germany

\*\* Weisz, Munich, Germany

\*\*\* Thales Alenia Space Italia S.p.A., Torino, Italy

\*\*\*\* ESA-ESTEC, Noordwijk, The Netherlands

- MicroOmega, a visible and infrared imaging spectrometer
- Raman Laser Spectrometer
- Mars Organic Molecule Analyzer consisting of a Laser Desorption Mass Spectrometer and a Gas Chromatography Mass Spectrometer, including a mechanism to seal Ovens (the so-called Tapping Station)

In order to supply samples to the instruments in a condition allowing an accurate analysis, the Rover is equipped with the Sample Preparation and Distribution System (SPDS), which is also part of the ALD and represents one of the key components of the 2018 mission [1]. It is developed by OHB System AG as subcontractor to the mission prime contractor Thales Alenia Space Italia. To ensure the required cleanliness for the highly sensitive instruments, the ALD and the SPDS form an enclosed volume, the so-called Ultra-Clean Zone (UCZ), which remains pressurized until first opening on Mars.

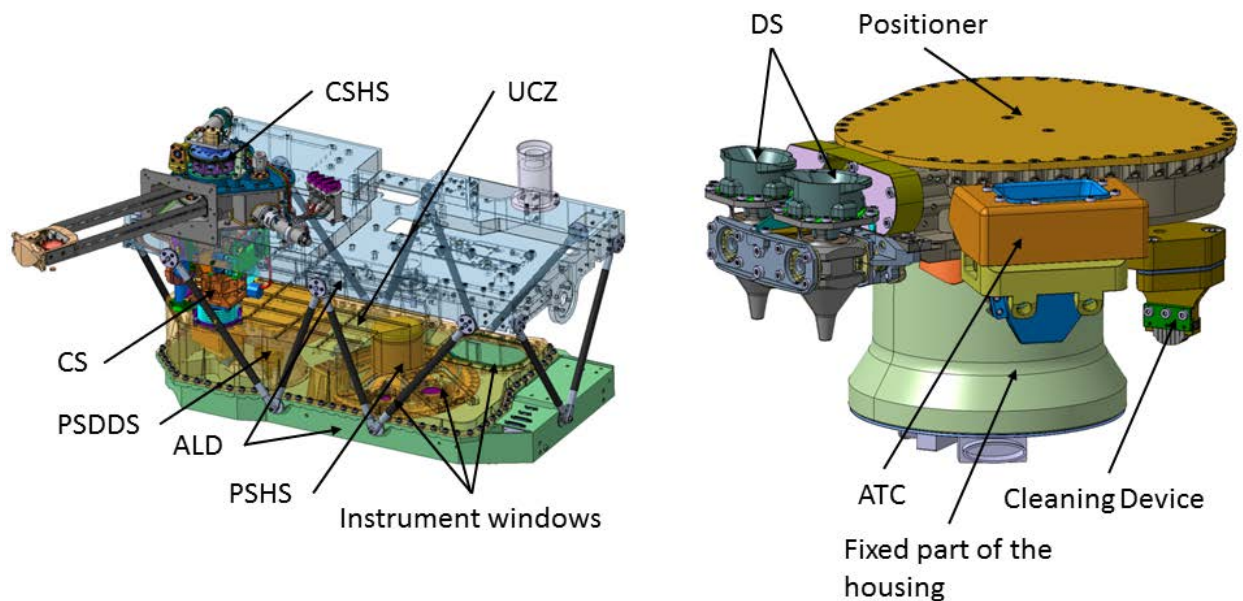


**Figure 1. SPDS (left) and PSDDS (right) Qualification CAD models.**

The SPDS (see Figure 1, left side, integrated into the ALD) consists of four separate mechanisms that interact with each other to transport the sample within the UCZ. The Core Sample Handling System (CSHS) transfers the sample to the Crushing Station (CS) where it is crushed to a certain grain size (50  $\mu\text{m}$ -500  $\mu\text{m}$ ). The PSDDS (see Figure 1, right side) receives the powdered sample and doses it in defined quantities to different sample receptacles, which are subsequently brought to the instruments for analysis by the Powdered Sample Handling System (PSHS) [2].

This sample handling mechanism has three unique design solutions originated by the mission specific challenges:

- Prevent cementation of powdered sample during storage time on Mars
- It is designed to be virtually “backlash-free” to achieve compliance to the positioning requirements originated by sample handover demands of the instruments
- The design is gas-tight to preserve the UCZ pressurized until operation on Mars and to ensure sealing barriers to the Rover’s internal non ultra-cleaned volume, to preventing false measurements of the instruments due to sample contamination originated from the Rover itself.

The paper is structured as follows: In the first section, the main design drivers of the PSDDS are described. This is followed by a detailed description of the PSDDS design. In three sub-sections, special



attention is given to the three main design topics: pre-torque device, bearing concept and dynamic feed-through. In the subsequent section, the test results and lessons learned of the described design topics are presented. The paper concludes with a short summary including an outlook to future activities.

### Design Drivers

The main design drivers can be divided into the following four groups:

- Design drivers derived from the positioning demands for the hand-over of the sample;
- Design drivers originated from Planetary Protection, Cleanliness and Contamination Control requirements preserve Mars and analyzed Martian Samples from Earth contamination;
- Design drivers imposed by the planetary environment on Mars;
- Design drivers created by the behavior of the powdered sample.

The first group of design drivers requires a high radial and angular PSDDS positioning performance in order to be able to dose the powdered sample into the small receptacles accommodated on the ensuing mechanism (PSHS). These receptacles are 32 single-use pyrolysis Ovens plus one multiple use Refillable Container. The pyrolysis Ovens are the most critical receptacles in terms of sample dosing requirements. They have an inlet diameter of few mm and shall be accurately filled with about 0.2 ml of powdered sample. The dosing performance is therefore also dependent upon the relative positioning of the Dosing Station output funnel and Ovens inlet. To ensure that the sample is correctly delivered to the Ovens, the PSDDS shall comply with an absolute position accuracy of approx.  $\pm 0.055^\circ$ . This requirement has been derived from an absolute position accuracy of  $\pm 0.1$  mm of the dosing funnel with respect to the nominal position of the Ovens at the hand-over port, this considering that the dosing funnels are at a distance of 105 mm from the PSDDS rotational axis.

The second group of major design drivers is imposed by Planetary Protection, Cleanliness and Contamination Control requirements. Any kind of contamination originated from Earth could lead to false positives and false negatives findings of the ALD Analytical Instruments while searching for traces of extraterrestrial life on Mars. For this reason, an Ultra Clean Zone (UCZ) has been designed and implemented within which the PSDDS as well as the other SPDS mechanisms operate. A priority requirement is therefore to control and minimize the organic contamination (molecular, particulate and biological) to an extremely small extent, which allows in the end to arrive at a total organic contamination of the whole UCZ of very few tens of nano-grams (ng). Moreover, for Planetary Protection reasons and to preserve UCZ sensitive items from microbial contamination, all UCZ parts are also treated with a rigorous bioburden reduction process (Dry Heat Microbial Reduction) which will bring the UCZ Hardware bioburden to a level of 0.03 spores per square meter maximum. To achieve these very challenging Planetary Protection, Cleanliness and Contamination Control requirements, all UCZ constituent parts are integrated in an ultra-clean environment (ISO3 AMC-9 [or] glove boxes train) and to avoid risk of recontamination the UCZ will be over-pressurized from the moment of its sealing after integration in the ultra-clean environment until the first opening on Mars. Since actuators as well as sensors and other electrical components are a high source of contamination, SPDS electro-mechanics components are not allowed inside the UCZ. This calls for the need of dynamic feed-through that, on the one hand needs to be gas-tight and, on the other hand, need to avoid high parasitic torques to allow smooth motion and a low system weight. These are two contradictory requirements that require the adoption of carefully balanced compromises. Furthermore, all structural parts of the mechanism that enclose the UCZ need gas-tight seals on their interfaces requiring a stiff structure with a minimum number of internal interfaces. Other origins of contamination are different types of materials or coatings. Basically, the only material group that is acceptable inside the UCZ is metals. When unavoidable a very limited use of specific polymers and low temperature grease is allowed. Also the choice of coating is limited by several factors such as its compatibility with the ultra-cleaning processes applied to the parts before entering in the ultra-clean integration environment (which includes bake-outs, ultra-sonic baths with different solvents, bioburden reduction and CO<sub>2</sub> snow-cleaning), chemical compatibility with instruments analysis, and the

demanding small surface roughness ( $R_a = 0.1 / 0.2 \mu\text{m}$ ) for all surfaces in contact with the sample to improve cleaning efficiency and reduce sample contamination by contact transfer.

The third group of design drivers are a result of the environmental conditions on Mars and represents one of the main drivers. The environmental conditions impose several restrictions on the design, such as the operative temperature range of  $-60^\circ\text{C}$  to  $+40^\circ\text{C}$ , and the dry low-pressure  $\text{CO}_2$  atmosphere. Contrary to the sterile vacuum in which most space mechanisms operate, the sample processing produces a very dusty environment, imposing many challenges for the mechanism's tribological elements. The dry atmosphere causes additional triboelectric charging of the particles, which can cause them to stick to all surfaces they come into contact with. The UCZ is thus exposed to an extremely dirty (but uncontaminated) environment during sample handling [2].

Another group of design drivers is concerned with the properties of the powdered sample material. For instance, the cementation of the sample could lead to a blocking and therefore to a loss of a major part of the scientific ExoMars mission. The main reasons for cementation are long storage time and contact of the sample with humidity. Sample cementation can lead to the creation of large agglomerates of sample, which could cause a clogging of the system.

### **Design Description of the PSDDS**

The PSDDS has the following main functions:

- Collection and delivery of sample material to three different points along a circumference
- Delivery of sample into two different receptacle types or waste containers
- Delivery of the sample in defined amounts
- Provide the possibility to store one sample and process a second sample in parallel
- Active prevention of sample cementation
- If the main delivery system has a defect or clogged, the sample delivery system must remain operative albeit possibly with degraded performance
- Provide a system that can remove an entire sample on a specified surface on the next mechanism
- Sealing of the Ultra Clean Zone

The mechanism (see Figure 2, left) is actuated by a brushed DC motor that is modified and qualified by the manufacturer Maxon to work in the environmental conditions on Mars [3]. It is coupled to a gear-box on whose output shaft a pre-torque device is mounted, which divides the torque to two spur gears that are pre-torqued to minimize the mechanism backlash. The counterparts of each spur gear are located on the input shafts of two identical planetary gear-boxes in a parallel arrangement and also developed and adapted by Maxon. The outputs of these two gear-boxes are connected via a gear mechanism to an internal ring gear, which transfers the torque into carousel motion. To allow integration of the drive-train after UCZ closure the entire drive-train and harness are integrated onto their own frame. This allows its introduction as an entire unit into the integrated hub. The motors, potentiometer and piezo, which are placed in the movable part of the mechanism, has to be connected to the harness of the PSDDS. Therefore, the frame also includes a flexible harness (Printed Circuit Board). The rotary degree of freedom (DOF) of the hub is provided by a wire race bearing and incorporates the dynamic feed-through, which guarantees the sealing and encapsulation of the UCZ with the entire drive-train remaining outside of it [2].

The Dosing Station is mounted on the outside of the rotating hub of the PSDDS structure. The central elements for each single Dosing Station (see Figure 2, right) are the dosing wheel and the inlet and outlet funnels. The dosing wheel is part of the dosing shaft, providing two dosing chambers shifted by  $180^\circ$ . The inlet funnel collects the sample from the Crushing Station and guides it into one of dosing chambers. When the dosing wheel is turned the sample falls out of the dosing chamber and the outlet funnel guides the defined sample powder doses to the receptacles on the PSHS. This dosing wheel is driven by a

Motor, which is inside of the housing. The sealing is guaranteed through a dynamic seal to ensure that the UCZ maintains its cleanliness level. To make sure that the dosing works correctly and to avoid cementation of the sample in the inlet funnel, a Piezo vibrator, which is placed inside the PSDDS hub, shakes the complete Dosing Station. To transmit the vibration to the inlet funnels within the UCZ, the Piezo is coupled to a membrane, which guides the vibration to the Dosing Station funnels.

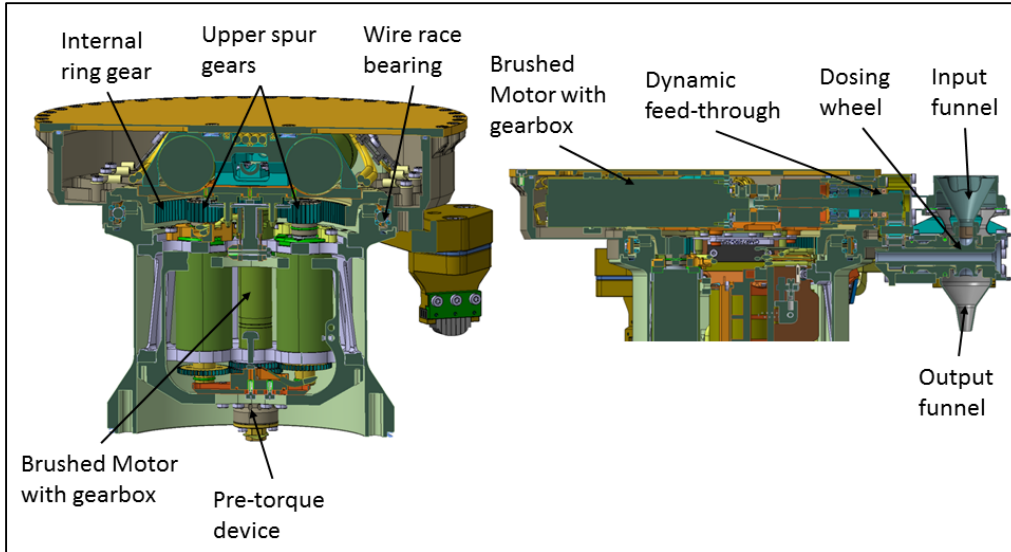


**Figure 2. Cross Section of the PSDDS (left) and Dosing Station (right).**

The Alternative Transport Container (ATC) is a passive mechanism to by-pass the Dosing Station in case both of them have lost their functionalities due to cementation effects. It can only deliver the entire sample at once to the receptacles of the PSHS. Specifically defined dosing quantities as required by the Ovens are not possible. The design of the ATC can be seen in Figure 3. The ATC consists of two hatches that are opened simultaneously by a passive coulisse when the ATC is driven to the PSHS ATC port. The coulisse is located on the PSDDS housing, The ATC is fixed on the moving hub of the PSDDS-Positioner. The position of the ATC was chosen in such a way that an undesired actuation is avoided during nominal PSDDS operation to eliminate this potential single point failure. The ATC is only actuated when commanded to that position and not during other operations. The ATC input is large enough to collect the entire sample that exits the Crushing Station. The outer hatch is pressed against the inner hatch via springs when the ATC is closed during sample acquisition and transport. When the ATC is moved to its interface port with the PSHS, the ball bearing wheel that is connected to the outer hatch is pushed down by the coulisse, so that the hatch rotates around its hinge against the spring pressure. They are coupled via a spur gear pair to ensure both hatches open simultaneously. To protect the mechanism from dust, a dust shield is screwed onto the top of the outer hatch.

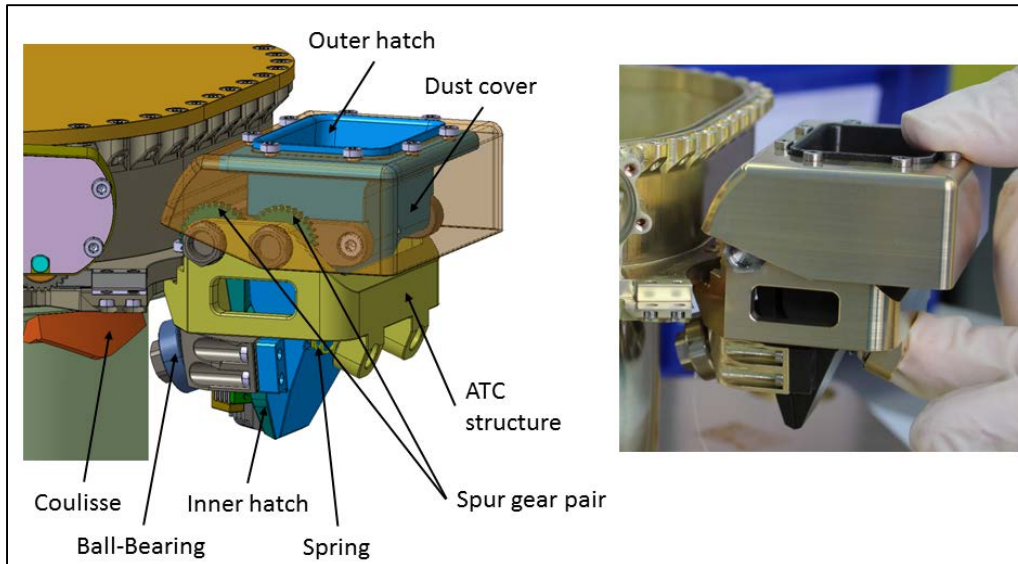


**Figure 3. ATC CAD Modell (left) and ATC integrated (right).**

The last functionality of the PSDDS provides the Cleaning Device, which is placed on the PSDDS hub. Its design and position can be seen in Figure 1. The Cleaning Device consists of a series of four cleaning blades with spacers in between that are all cut into stripes providing enough flexibility to have the effect of a brush. The cuts are shifted from blade to blade to enable the complete cleaning of the entire powdered sample on the Refillable Container of the PSHS and leaving it visibly clean for the next sample. The blades are made of Gylon (a PTFE-based plastic) which provides enough stiffness for the cleaning function without being too stiff to have powder flicked off the Refillable Container through the ALD. Gylon is one of the few plastics that fulfills the requirements for planetary protection and thus avoids contamination risks.

In the next three subsections three particularly noteworthy design solutions are be described.

#### Pre-torque Device

Due to the required high accuracy of the mechanism and the limitation with regards to space, mass and ultra-cleaning, a high-resolution encoder could not be implemented on the last gear stage, as it is usually done if such high accuracy is needed. Instead, a low-resolution encoder (8 quad-counts) has been placed on the rear side of the motor, which provides the advantage of a simpler electronic unit and greater robustness. To achieve the required resolution on the end-shaft, a gear with a high resolution (27228:1) has been installed in between the motor and the end-effector shaft. With this, it is possible to measure a high resolution at the end of the drive train but the resulting problem is the high play in the system. The minimization of this play has been achieved through preloading the gears. This means that the actuator is equipped with two spur gears on its output shaft that are counter-preloaded via a leg spring with a constant torque to minimize the backlash in the following gear stages. The torque is divided by these spur gears into two identical gear-boxes and combined again in the internal ring gear on the positioner end shaft. On each gearbox output shaft, a spur gear is mounted that interfaces with this wheel. Due to the preload, both wheels are in contact with the opposite flanks of the internal ring gear teeth, leading to a large reduction of backlash. When torque is introduced by the actuator, the torque at one spur gear increases in the same way the other reduces to provide the resulting torque to perform the motion. However, the torque is never reduced below zero on any one of the spur gears to maintain the preload to always ensure a reduced backlash.

The moving hub is connected to the fixed positioner by a preloaded wire race bearing.

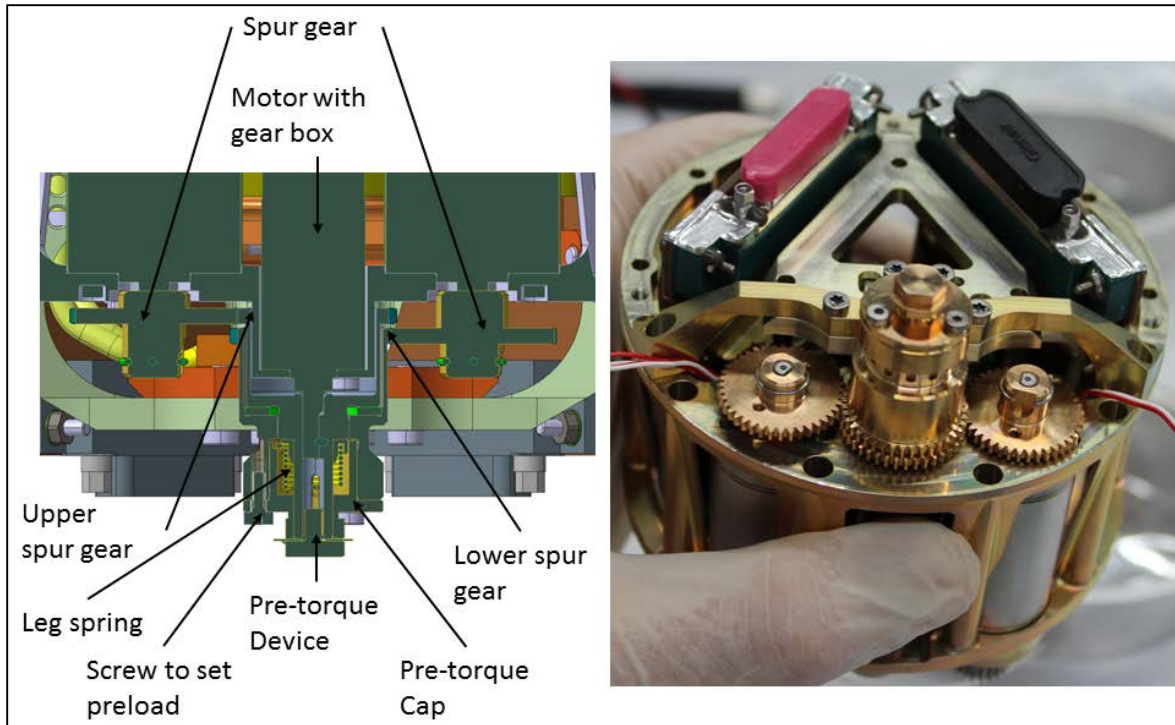


**Figure 4. Pre-torque Device CAD model (left) and hardware (right).**

#### Bearing Concept

The only bearing on the positioner to take the axial and radial loads as well as to provide the rotational DOF is a wire race bearing (see Figure 5). This bearing connects the movable part with the fixed structure of the PSDDS. The balls are guided in a PTFE cage and run on four wire races. The bearing is preloaded to sustain the launch loads and to provide the demanded accuracy. It is dry lubricated via the PTFE cage. The balls and the wire races are made of steel.

It is preloaded via the preload frame that is mounted with screws on the structure. The bearing and the outer two wire races are integrated into the bearing housing and the lower inner wire race in the fixed part of the housing. When the bearing housing is placed onto the fixed part of the housing, the last wire race is installed and pushed down by the preload frame, which is shimmed to adjust the preload. This force eliminates the play in the bearing and induces a preload.

The accuracy of the bearing strongly depends on the surrounding structure that has been optimized according to the recommendations provided by the bearing supplier (Franke).

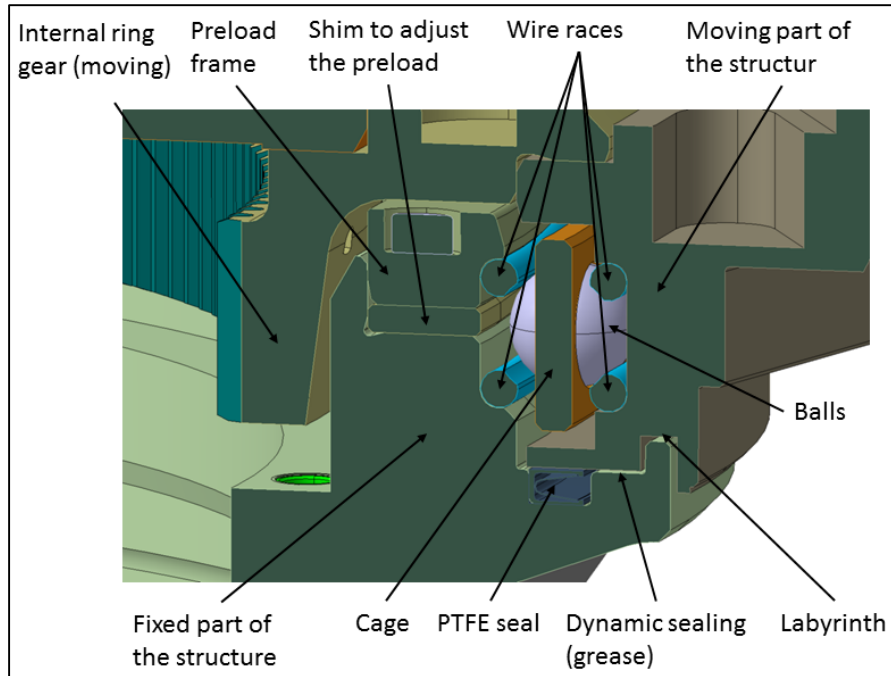


**Figure 5. Wire race bearing and dynamic feed-through of the PSDDS.**

#### Dynamic Feed-through

At the beginning of the ExoMars project, a test campaign has been performed in which different possible rotating shaft sealing technologies have been investigated under a representative environment.

The sealing types examined first were O-rings or other polymeric seals supported by springs. These kind of seals were assessed to be not appropriate because of the inherent strong parasitic torque that is created during shaft rotation and the strict material requirements of the mission. The second sealing type that was subjected to these tests was breakable seals. However, this option had to be discarded because, after the unavoidable breakage of the seal, the volume where the instrument measurements take place would have been exposed to the contamination generated by other components of the Rover. Also, the possibility of using magnetic feed-throughs has been investigated but they failed the qualitative assessment because the envelope and mass that was required to transfer the torque would have exceeded the allowed limits.

These preliminary tests showed that dynamic seals, consisting of a grease barrier which is kept in place by polymeric seals or a so-called grease labyrinth provide a leakage rate (even after motion) of  $6E-7$  mbar·l(He)/s by a seal length of 170 mm and a friction torque not exceeding 950 mNm over a temperature range between room temperature (20°C) and -60°C, which is the worst case operational temperature.

These preliminary tests determined that the dynamic sealing is the option that is to be implemented into the SPDS and practically evaluated in detail. The realization of this concept for the PSDDS can be seen in Figure 5. The sealing function is realized by Braycote 601EF grease that is placed in a labyrinth between the moving and the fixed part of the housing. It is kept in position by one flexible C-shaped sealing ring (which is preloaded by an internal spring) to avoid having the grease pushed out of the sealing over time when the differential pressure of 0.1 bar is applied for a long period or 0.25 bar for a short period (proof pressure). The sealing has a very low stiffness to minimize its frictional torque. This is possible because it does not need to fulfill any sealing function itself.

## Testing and Lessons learned

Due to the challenging manufacturing tolerances and constraints, the integration of PSDDS mechanism had to be shortly postponed, this leading to not being able to complete the full testing program in time for the submission of this paper. However, the three major sub-systems of the PSDDS previously discussed in this paper are also present in the PSHS which has already successfully completed the qualification campaign. Test results and lessons learned of the PSHS are fully valid also for PSDDS and are presented in this paper, together with test results already provided by the ongoing PSDDS qualification campaign. The full PSDDS test results will be presented in the oral presentation at the AMS 2016.

### Pre-torque Device

PSDDS and PSHS are using the same pre-torque device. They are identical.

During this test, the positioning performance of the PSHS has been determined with an external absolute encoder, which can measure the correct position of the PSHS movable part at any time with reference to the fixed part of the housing. This measurement has been performed under ambient condition (20°C and 1bar absolute air pressure) and Mars-like conditions (-60°C and 7 mbar absolute CO<sub>2</sub> atmosphere). For the evaluation of the positioning performance, the following parameters are important:

- Hard-Stop accuracy:
  - Describes the positioning uncertainty introduced by the Hard-Stop parts when they become in contact.
  - Depends strongly on how the Hard-Stop is achieved and on the switch-off criteria of the motor current when the Hard-Stop is reached.
- Mechanism Play:
  - Is the distance the motor has to run until the end-shaft moves again after a direction change?
- Repeatability:
  - Is the spread of the reached positions when the mechanism is operated multiple times in the same conditions?
- Relative accuracy:
  - Is the accuracy that can be achieved when the mechanism is moved from one point to another?
- Absolute accuracy:
  - Is the distance between the actual position and the position measured by the mechanism's sensor?

During the first positioning accuracy tests, a relatively high deviation from the required absolute accuracy was found. After several measurement series, it became obvious that the measured deviation was completely static and thus reproducible. In consequence, it was easy to compensate this deviation with a compensation curve that has been implemented into the control electronics. The fact that the position tolerances of the teeth in the internal ring gear has the same value as the distance between max and min value of the compensation curve suggests that the observed inaccuracy is solely a result of the manufacturing tolerances of this (last) gear stage.

The results show that all accuracy requirements (resolution 20 µm, absolute accuracy 100 µm) are fulfilled under an ambient as well as a Mars-like environment.

### Bearing Concept:

PSHS and PSDDS are using the same kind of wire race bearing. The only difference is that the bearing in the PDDS has a diameter of 110 mm and the PSHS has a diameter of 70 mm. Since the distance between the balls is the same in both systems, the amount of balls in the PSDDS is higher.

The integration procedure for the wire race bearing in PSHS and PSDDS is identical and is performed in the following order:

1. The two bottom rings and the upper outer ring are placed on its dedicated positions
2. The structure is put in position on spacers
3. The cage is inserted
4. All balls are inserted into the pockets of the cage
5. The upper inner ring is inserted
6. The shim and load is inserted
7. The screws are inserted
8. The spacer is removed
9. The screws are tightened

**Table 1. Results of the Positioning and Performance Tests**

	Ambient	Mars-like
<b>Mechanism play</b>		
Min play [ $\mu\text{m}$ ]	33.3	77.6
Mean play [ $\mu\text{m}$ ]	63.6	108.7
Max play [ $\mu\text{m}$ ]	98.5	137.4
Peak-to-Peak value [ $\mu\text{m}$ ]	65.2	59.8
<b>Hard Stop accuracy</b>		
Hard-Stop accuracy $\pm$ [ $\mu\text{m}$ ]	8.8	5.9
Max [ $\mu\text{m}$ ]	-0.3	27.6
Mean [ $\mu\text{m}$ ]	-8.7	20.4
Min [ $\mu\text{m}$ ]	-17.9	15.8
<b>Repeatability</b>		
Repeatability CW $\pm$ [ $\mu\text{m}$ ]	4.3	3
Repeatability CCW $\pm$ [ $\mu\text{m}$ ]	1.1	1.9
<b>Relative accuracy</b>		
Relative accuracy 1deg step $\pm$ [ $\mu\text{m}$ ]	24	15.3
Relative accuracy 0.1deg step $\pm$ [ $\mu\text{m}$ ]	8.4	6
Relative accuracy 0.01deg step $\pm$ [ $\mu\text{m}$ ]	7.6	8.6
<b>Absolute accuracy</b>		
Max value [ $\mu\text{m}$ ]	127.6	103.6
Mean [ $\mu\text{m}$ ]	43	-5.3
Min [ $\mu\text{m}$ ]	-25.5	-60.6
Peak-to-Peak [ $\mu\text{m}$ ]	153.1	164.2
<b>Absolute accuracy only CW</b>		
Max [ $\mu\text{m}$ ]	84.2	0.1
Mean [ $\mu\text{m}$ ]	39.3	-25.5
Min [ $\mu\text{m}$ ]	-25.5	-60.6
Peak-to-Peak [ $\mu\text{m}$ ]	109.7	60.7

The bearing is not self-holding until all the steps are completed. After the integration of the bearing, the rotational torque of bearing preload has to be measured.

The measurement of the bearing torque has to be measured without any other additional torque contribution to achieve a direct conclusion on the torque. The force that is needed to turn the bearing has been measured along a circumference (see Figure 6).



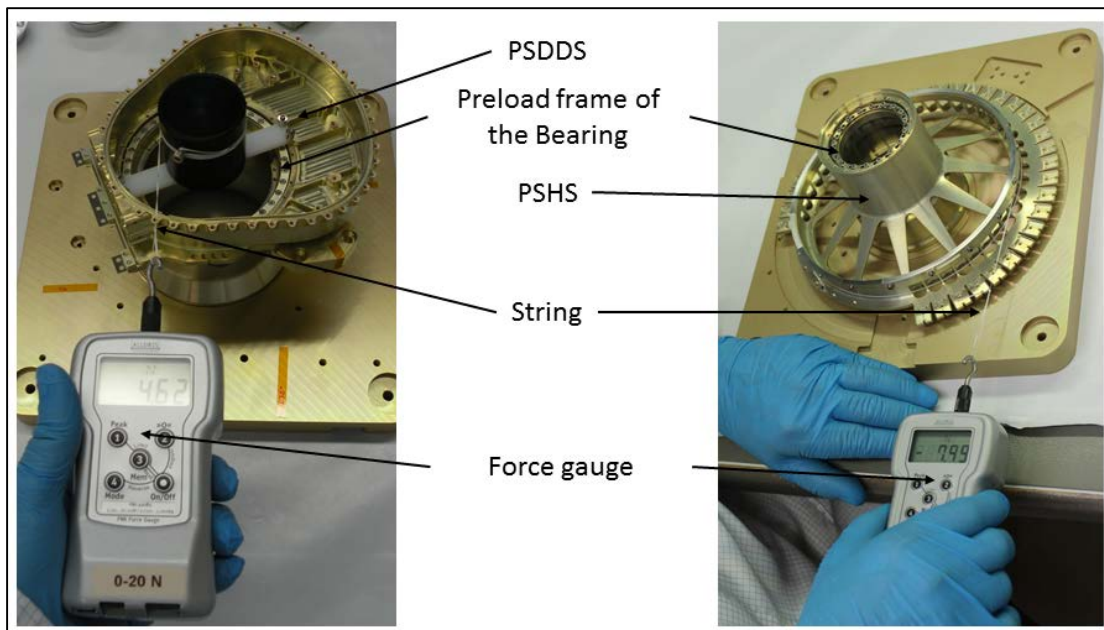


**Figure 6. Test setup to measure the preload torque**

The nominal values have been determined considering the following requirements:

- The preload is required to be high enough to ensure that the bearing balls do not start moving during launch vibration that would result in a gap between balls and bearing wires. This can cause damages on the bearing race wires, reducing accuracy and lifetime of the bearing.
- The torque resulting from the preload is required to be as small as possible to ensure the movement of the bearing. This needs to be guaranteed over the whole operational temperature range.

In a next step, the shim under the preload frame has to be selected, such that the given preload value is met. During the integration, it was observed that the recommended step width between the different shims of 20  $\mu\text{m}$  was too high to meet the required torque. To achieve the defined torque values the shim step width was reduced to 10  $\mu\text{m}$ . A second observation during the integration was that the tightening torque of the screws has a big impact on the preload. This means that the full preload has to be applied to the screws for every test in order to achieve representative results.

An important positioning requirement for both PSDDS and PSHS is the relative radial position of the dosing output funnel (PSDDS) with respect to the Pyrolysis Oven (installed on the PSHS) and radial position of the Pyrolysis Oven (PSHS) with respect to the Oven Tapping Stations (which is an Instrument mechanism that when operated closes the Oven to facilitate analysis with a Gas Chromatographer. It contains the Gas Chromatographer inlet head and a separable connector to the side of the Oven to supply power to the Oven heaters and read the achieved temperature to control the pyrolysis process.

To verify the Oven position performance during the PSHS test campaign, that due to PSDDS-PSHS mechanisms similarity is directly linked to the Dosing Station positioning performance, the PSHS roundness and evenness have been measured. Their deviations are caused only by the manufacturing tolerances of the structure parts and the precision of the wire race bearing. It has to be mentioned that since the bearing only runs on thin and therefore flexible wires, the structure can be considered as part of the bearing and has also an influence on the performance of the bearing. PSHS roundness and evenness were measured via distance laser sensors. The test parameters under which the test has been conducted are the following:

- 4x ambient, no tilt, velocity 2 deg/s
- 6x Mars-like(-60°C, 6 mbar CO<sub>2</sub>), no tilt, velocity 2 deg/s
- 4x ambient, tilt, velocity 2 deg/s
- 4x Mars-like(-60°C, 6 mbar CO<sub>2</sub>), tilt, velocity 2 deg/s

The tilt measurements (see Figure 7) has been performed under an inclination of 10° to the horizontal position, which is the maximal incline under which the measurements will be performed on Mars.

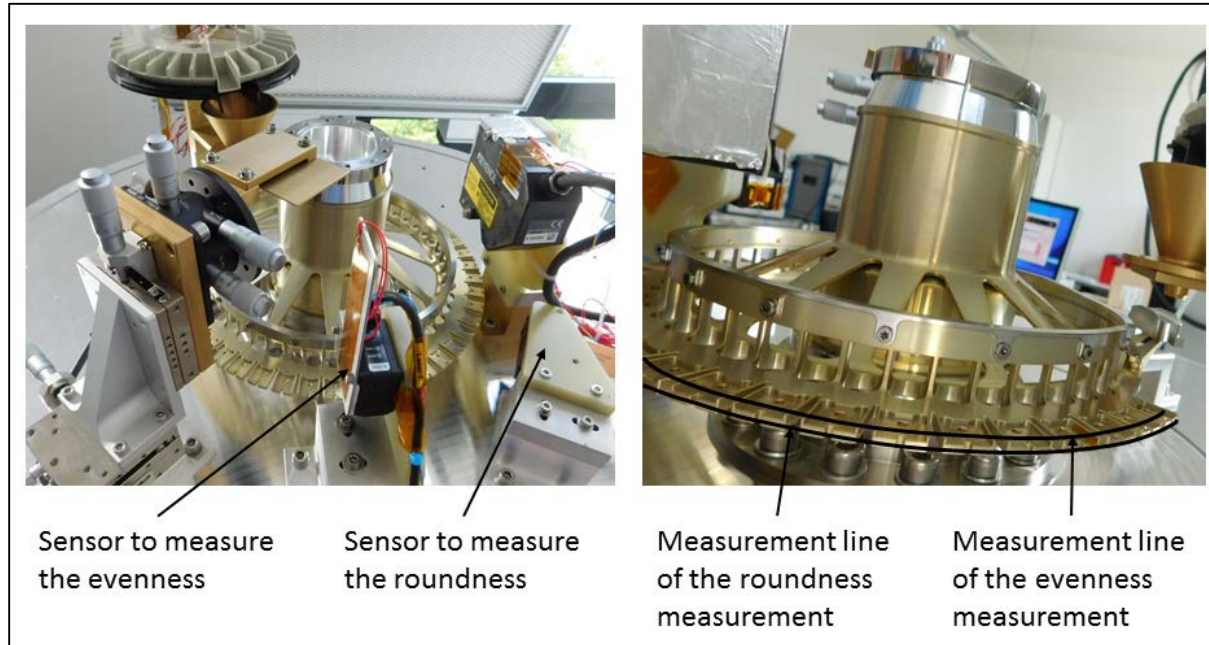


**Figure 7. Test setup for roughness and evenness (left), measurement lines for roughness and evenness (right)**

**Table 2. Results of the Roundness and Evenness Measurements**

<b>Repetition</b>	<b>1</b>	<b>2</b>	<b>3</b>	<b>4</b>	<b>5</b>	<b>6</b>	<b>Maximum</b>
<b>Roundness [µm]</b>							
ambient, no tilt	0.152	0.099	0.133	0.094			<b>0.152</b>
Mars-like, no tilt	0.143	0.089	0.106	0.147	0.122	0.110	<b>0.147</b>
ambient, tilt	0.098	0.120	0.118	0.102			<b>0.120</b>
Mars-like, no tilt	0.107	0.185	0.107	0.164			<b>0.185</b>
<b>Evenness [µm]</b>							
ambient, no tilt	0.083	0.112	0.079	0.117			<b>0.117</b>
Mars-like, no tilt	0.124	0.144	0.122	0.144	0.115	0.154	<b>0.154</b>
ambient, tilt	0.156	0.158	0.158	0.166			<b>0.166</b>
Mars-like, no tilt	0.130	0.118	0.118	0.126			<b>0.130</b>

The results are showing that the maximum radial difference of all measured points along a circle is 0.185 mm (requirement, peak-to-peak 150 µm) and the maximum difference of all measured points along a circle in plane is 0.166 mm (requirement, peak-to-peak 200 µm). The same performances are expected on the PSDDS, this allows precise positioning of Dosing Stations output funnels on the Ovens receptacles for an optimal dosing performance.

#### Dynamic Feed-through (grease seal)

PSDDS and PSHS both have the same type of dynamic feed-through sealing but they are implemented in different ways. While the PSDDS has on one side an axial plastic seal and a labyrinth on the other side to keep the grease in place (see Figure 5), the PSHS has two radial plastic sealings with grease in between (see Figure 8 [2]).

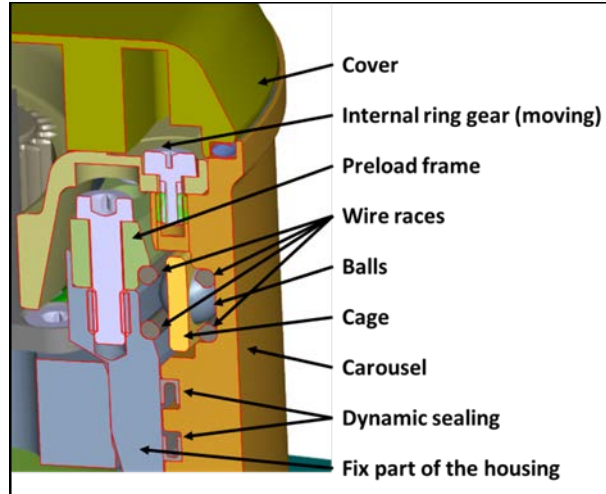


**Figure 8. Wire race bearing and dynamic feed-through of the PSHS**

To fully evaluate the dynamic feed-through, the integration and preload measurement of the wire race bearing was completed. For this the following integration steps were performed:

1. Open bearing and remove all bearing parts
2. Fill the plastic seal/seals with grease
3. Put the sealing's/sealing in there dedicated positions
4. Fill the space between the sealings or between sealings and labyrinths with grease
5. Reintegrate the bearing as described in the section before

The respective torque of both the bearing and the dynamic feed-through has been measured after these integration steps. As the friction torque generated by the bearing was measured in the integration step before, the additional torque resulting from the dynamic seals and the grease can be easily determined. These tests were only performed during ambient conditions (see Figure 6).

**Table 3. Results of the torque measurements**

<b>PSDDS</b>	<b>Max torque [Nm]</b>
Total	0.85
Preload bearing	0.27
Feed-through	0.58
<b>PSHS</b>	<b>Max torque [Nm]</b>
Total	0.86
Preload bearing	0.11
Feed-through	0.75

Compared with the PSHS, the preload in the PSDDS bearing is higher because the step range for the shimming was chosen too high and the required torque of 0.13 Nm could not be met, with either of the shims that have been used. As result, it was decided in co-operation with the supplier of the bearing that the combination with the higher torque will be used because it provides more safety during the vibration test. The only drawback of this solution is that a higher torque has to be provided by the drive-train but

since the feed-through creates less friction torque this effect can be compensated. The lower friction torque of the dynamic sealing can be explained with the fact that in the PSDDS there is only one PTFE sealing, instead of two in the PSHS.

During the PSHS test campaign the leakage of the mechanism has been measured with a Helium leak detector. As the PSHS end-effector reaches into the ALD, the pressure must be applied on the outside of the mechanism. To achieve this, the setup was built in a way that the chamber and the inside of the mechanism are connected with each other and through this it was possible to create a vacuum on both sides at the same time with an additional vacuum pump. After this, the connection needs to be separated and the chamber is filled with 100-mbar Helium. When this condition is reached, the leakage measurement instrument is switched on and the measurement starts. This paper only describes the leakage measurements that were performed after the vibration and shock tests. The leakage measurements were done during qualification thermal cycling of the mechanism. In total, 8 thermal cycles were conducted and during the first, fourth and eighth cycle the leakage measurements were performed. For each cycle (1<sup>st</sup>, 4<sup>th</sup>, and 8<sup>th</sup>), leakage measurements were performed under the following conditions:

1. Ambient temperature, 100 mbar
2. Ambient temperature, 200 mbar
3. Ambient temperature, 100 mbar
4. 70°C, 100 mbar
5. 70°C, 200 mbar
6. 70°C, 100 mbar
7. -60°C, 100 mbar
8. -60°C, 200 mbar
9. -60°C, 100 mbar

The test results are shown in the Table 4.

**Table 4. Results of the PSHS Leak Rate Measurements**

Cycle	Environment	Leak Rate [mbar*I/s]	
	Temperature [°C]	at 100 mbar	after motion and 200 mbar
1st	20	5.6E-7	8.6E-7
1st	-60	2.8E-7	5.0E-7
1st	70	1.1E-6	1.6E-6
4th	20	3.7E-7	6.3E-7
4th	70	4.7E-7	9.8E-7
4th	-60	3.1E-6	3.2E-6
8th	20	7.5E-7	7.9E-7
8th	70	2.0E-6	2.0E-6
8th	-60	1.2E-6	1.4E-6

During these measurements, leakage peaks could be detected which were not present during the characterization test of the chamber without the mechanism. Therefore, it can be concluded that the peaks are caused by the dynamic seal of the PSHS. The peaks can be explained with the following physical effects:

- Helium absorbed or trapped inside the grease
- Helium penetration through the grease (e.g., bubble penetration)

Nevertheless, the peaks are a valid measurement and had to be taken into account for the overall leakage rate. Rates given in this paper are average rates over a measurement time of 30 min including peaks.

## Conclusions and Outlook

The overall concept of the PSDDS presented in this paper and particular design decisions with regards to the three main challenges (pre-torque device, bearing concept, and dynamic feed-through) have proven suitable. The evaluation of the design was supported by test results obtained with the PSHS, which adopts the same design solutions under identical circumstances. The PSHS qualification tests were finished successfully, with satisfying results in all tests. Of special interest were the positioning performance tests, the leakage tests and the results of the roundness and evenness measurement. In the context of the PSHS, all requirements were fulfilled with the proposed design and material solutions, i.e., the PSHS mechanism is ready for the manufacturing of the flight model. Currently, a detailed qualification campaign of the PSDDS mechanisms is being carried out. The results of the PSHS campaign and the preliminary results of the PSDDS tests provide a strong indication that the implemented design choices will lead to a successful PSDDS qualification campaign fulfilling all specific functionality and performance requirements. The final results of the PSDDS qualification campaign will be presented at the AMS.

The four SPDS mechanisms will be sent to the mission prime TAS-I, where they will be completely disassembled and after the replacement of parts worn out by sample material, the extensive ultra-cleaning and sterilization process will be performed with a subsequent mechanism re-integration followed by integration into the ALD-Qualification model with all integration activities taking place inside an ISO3 AMC-9 glove box respectively an ISO7 HC clean room for parts outside the UCZ. After finalization of the integration process, the ALD system qualification campaign is carried out, in which, besides the standard test program (leakage, vibration/shock and thermal-vacuum), several blank samples are processed by the entire SPDS and analyzed by the instruments to investigate the cleanliness and performance of the entire system.

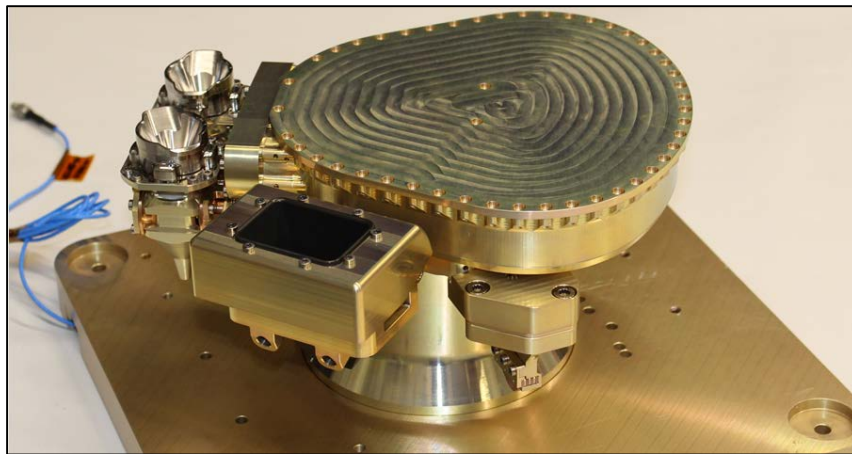


**Figure 9. Final integrated PSDDS**

## References

1. Richter, Lutz., et al. "Progress Report on Development of the ExoMars Sample Processing and Distribution System (SPDS) and Related OHB Sample Handling Studies." *ASTRA 2015*, ESTEC, Noordwijk, The Netherlands, 11-13 May 2015
2. Paul, Robert, et al. "Development and Testing of a „Backlash-Free“ Gas-Tight High Precision Sample Handling Mechanism for Combined Science on the ExoMars 2018 Rover, *ESMATS 2015*, Bilbao, Spain
3. Phillips, Robin., et al. Development of Brushed and Brushless DC Motors for use in the ExoMars Drilling and Sampling Mechanism. *AMS 2012*
4. Kannel, J. W. and D. Snediker. "Hidden Cause of Bearing Failure." *Machine Design* (7 April 1977), pp. 78-82.





# Realization and Testing of the In Field Pointing Mechanism for the Evolved Laser Interferometer Space Antenna

Gert Witvoet\* and Jet Human\*

## Abstract

An active tilt mirror mechanism, meant for correction of the constellation breathing of the evolved Laser Interferometer Space Antenna, has been designed and built. Its open-loop performance has been characterized in both the time and frequency domain. Based on this, a feedback controller has been designed and the resulting closed-loop performance has been assessed. Up to what is measurable in a normal lab environment, these experiments demonstrate compliance with the extreme pointing jitter requirement even when using the internal encoder as feedback sensor.

## Introduction

The evolved Laser Interferometer Space Antenna (eLISA) mission, which is currently under development, is an ambitious project meant to accurately detect gravitational waves [1]. It will consist of three spacecraft flying in a triangular formation mutually  $10^9$  m apart in an Earth-like orbit around the sun, each carrying a free-flying proof mass. Detection of a passing gravitational wave requires measuring the distances between the proof masses with an accuracy of  $10^{-11}$  m, which makes eLISA an extremely high sensitive instrument.

The eLISA mission still faces scientific and technological challenges to be solved before its tentative launch in 2034. One of which is constellation breathing, i.e., how to deal with slight variations in the angle between the interferometer arms over a period of a year due to orbital dynamics. In Telescope Pointing this is accounted for by rotating each of the six complete optical assemblies (two on each spacecraft). As a promising alternative, Airbus Defence & Space has developed the In-Field Pointing (IFP) concept [2], in which only a small tilt mirror, located in an intermediate pupil plane of the telescope, provides the means to steer the beam. IFP comes with a number of advantages over Telescope Pointing, such as actuation of a much smaller mass, possible smaller payload sizes, and possible simpler payload architectures [2, 3].

The feasibility of the IFP concept will be demonstrated in an experiment that Airbus DS is currently developing [3]. One of the critical components in this experiment is the In-Field Pointing Mechanism (IFPM), responsible for actuating the tilt mirror, on which there are high stability requirements. Built upon heritage with the Point-Ahead Angle Mechanism [4], which has similar stability requirements, TNO (Netherlands Organisation for Applied Scientific Research) has successfully carried out breadboard tests and made a design for this IFPM [5]. In this paper we will present the realized IFPM hardware, together with some important test results (in a normal laboratory environment). These tests include open-loop characterizations as well as closed-loop performance validations. Up to what is reasonably measurable in such a lab environment, the results show that the IFPM is indeed compliant with the requirements.

## Hardware Design and Realization

The heart of the IFPM is a 50-mm flat tilt mirror, which needs to rotate  $\pm 2.5^\circ$  in a whole year (equivalent to  $\pm 5^\circ$  beam steering) to accommodate constellation breathing. In science mode it should do so with a maximum pointing jitter of just 5 nrad/ $\sqrt{\text{Hz}}$  over a large frequency range. This combination of large stroke

---

\* TNO Technical Sciences, Delft, The Netherlands

and high accuracy requires the dynamic range of the IFPM to be in the order of  $10^7$  [2]. Moreover, the mirror is not allowed to introduce more than 3 pm/ $\sqrt{\text{Hz}}$  of optical path length (piston) noise.

#### Design concept

In the IFPM design, the rotation of the mirror is guided by two Haberland hinges, which are part of a single monolithic TiAlV structure. Their axis of rotation coincides with the mirror surface, in order to minimize the cross-coupling between the angular motion and optical path length variations. The mirror is connected to a translational actuator module via a stiff lever through the mirror rotation axis; this way the actuation force acts parallel to the mirror surface, which minimizes surface distortions.

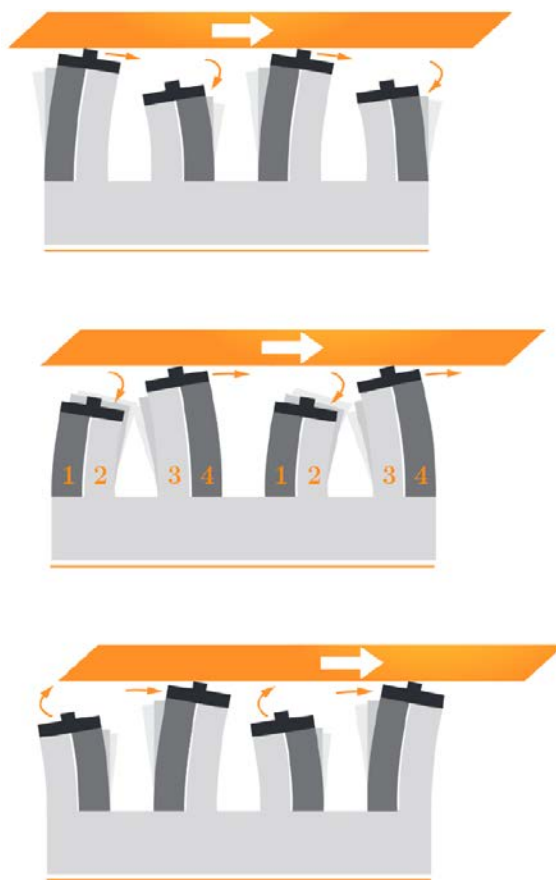


**Figure 1. Operating principle of the walking piezo actuator. Due to the ellipsoidal movement of the tip of the legs, the ceramic rod moves in horizontal direction. The numbers indicate the phases; same-phase piezos are fed with the same voltage. Image courtesy of PiezoMotor®.**

The actuation possibilities are limited for IFPM because of eLISA mission constraints (there are no electromagnetic forces allowed on the optical bench) and the large required stroke. After some successful breadboard tests [5], the Piezo LEGS walking actuator by PiezoMotor Uppsala AB has been selected. The operating principle of this walking piezo actuator is illustrated in Figure 1. Each actuator encompasses two sets of legs (depicted are two times two legs, the used piezostepper has two times three legs), where each leg consists of two pieces of piezoelectric material with a ceramic tip. By applying different voltages to each piezo the legs will elongate and bend. A proper choice of the four driving voltages (phases) can then cause an ellipsoidal movement of the tips of the legs, thereby creating a walking motion. As a result, a ceramic driving rod pushed against the legs with the right preload will move in the horizontal direction.



The piezostepper principle is friction-based and thus relatively stiff, while providing tens of newtons of holding force. The stroke is only limited by the length of the driving rod, and is thus principally infinite; the step size is only limited by the resolution of the DAC generating the voltages for the legs, and can thus be in the order of 0.1 nm or less (one actuator cycle is typically a few  $\mu\text{m}$ ). As such, the complete IFPM assembly utilizes a hard actuator concept, which is both accurate, and stiff enough to potentially withstand launch loads.

### Design improvements

The original IFPM design [5] had an actuator module in which three of such piezosteppers were combined in a triangular orientation, pushing against a triangular driving rod. The choice for three steppers was partly motivated by launch load and redundancy considerations, and partly to combine the guidance of the driving rod and preloading of the piezosteppers in one single component. This actuator module has been manufactured, but thorough testing showed that the nominal preload on the piezosteppers was too high and the distribution of the preload over the different legs was very uneven. It turned out that the performance of the actuator is very sensitive to such preload deficiencies, causing unreproducible irregular open-loop motion, which is why the original design never met its expected performance.

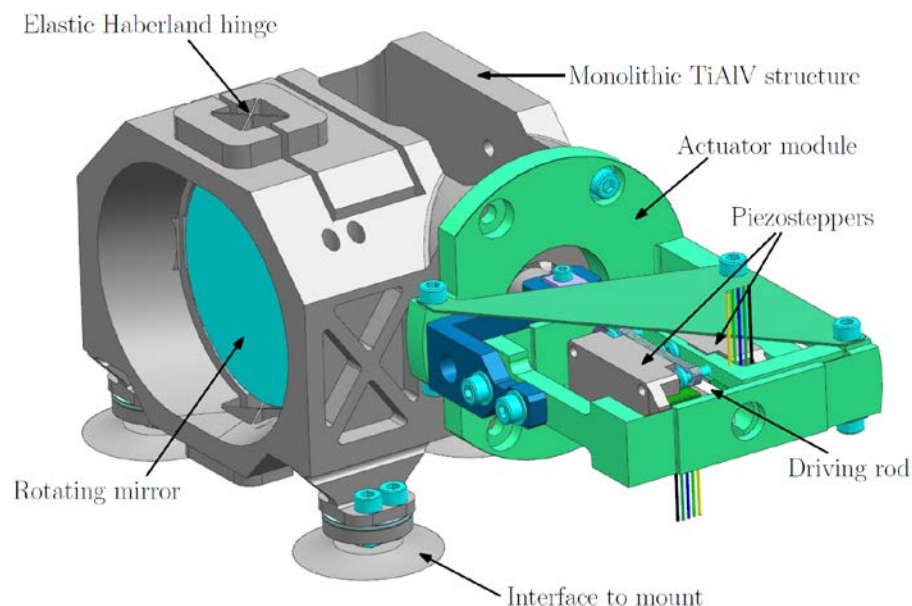


**Figure 2. CAD model of the latest IFPM design.**

It has therefore been decided to loosen the launch load and redundancy targets and focus on the proof-of-concept, by redesigning the actuator module to a two-stepper-concept. In this planar configuration, two piezosteppers are pushed on either side of a rectangular driving rod; the preload distribution along the legs is now much better defined and is tunable via the bolts through the leaf springs with which one of the piezosteppers is connected to the actuator module. Figure 2 shows a CAD model of the updated design.

### Realization

The updated actuator module has been manufactured and assembled, and combined with the previously realized mirror unit. A picture of the complete IFPM assembly is shown in Figure 3. The setup has been tested under normal laboratory conditions (room temperature, atmospheric pressure), the results of which are presented in this paper. In these tests, the mirror rotation has been measured directly via a Renishaw differential interferometer. Both the reference and measurement beam are directed at the mirror; the mirror angle is calculated (with nrad resolution) using the distance between the beams and their optical path length difference. The mechanism is also equipped with a Micro-E incremental encoder and a 20- $\mu\text{m}$

pitch scale, located at a radius of 31.06 mm from the mirror rotation axis. This sensor has a 1.2-nm resolution, which is thus equivalent to 38.6 nrad of mirror rotation. The encoder was originally meant for beam acquisition purposes, but can also be used as a feedback sensor (as an alternative to the external interferometer).

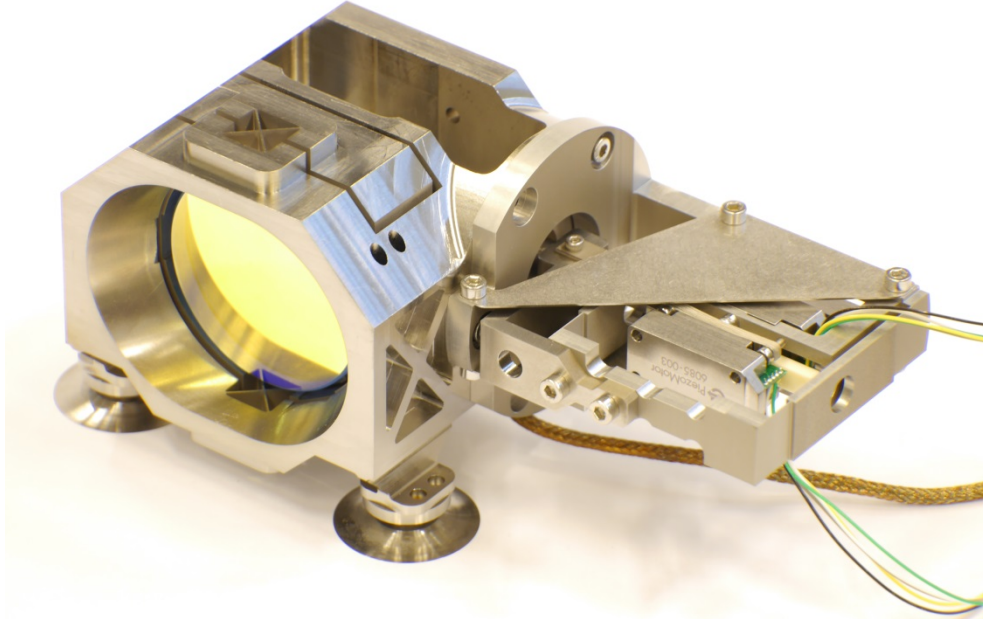


**Figure 3. Picture of the realized two-stepper IFPM. (Photo: TNO / Gert Witvoet)**

The piezosteppers are fed by four high-voltage space-qualified analog amplifiers, one for each of the four phases of the actuators. The voltage waveforms are generated by a dSpace data acquisition system with a 16-bit D/A converter; the encoder (via a 24-bit digital encoder interface) and the interferometer (via a 16-bit A/D converter) are connected to the same dSpace system. This system offers a rapid prototyping environment in MATLAB/Simulink, which provides great flexibility in measurement possibilities and controller design.

### System Behavior

The motion of the legs of the walking actuator is determined by the voltage distribution along the four phases as a function of time. Although the open-loop motion will never be perfectly linear, the exact shape of these voltage waveforms has a large influence on the velocity variations during an actuator cycle [6]. For example, the horizontal and vertical motion of the first set of legs can be approximated by

$$\begin{aligned}x_{p1} &= c_1(u_1(t) - u_2(t)) \\ y_{p1} &= c_2(u_1(t) + u_2(t))\end{aligned}$$

where  $c_1$  and  $c_2$  are motor coefficients and  $u_1(t)$  and  $u_2(t)$  are the voltages applied to phase 1 and 2 respectively [7]. Pure sinusoidal waveforms are known to exhibit zero velocity at the transfer points (i.e., when one set of legs take over from the other), which is undesirable from a performance point-of-view. Therefore so-called asymmetric waveforms [7] have been used, where the voltage of the first phase is defined between 0 and the maximum  $A$  (here 48 V) as

$$u_1(t) = \begin{cases} \frac{1}{2}A + \frac{1}{2}A \sin\left(2\pi \frac{\alpha(t)}{2q}\right), & \alpha(t) \in [0, q] \\ \frac{1}{2}A + \frac{1}{2}A \sin\left(2\pi \frac{\alpha(t)-1}{2(1-q)}\right), & \alpha(t) \in [q, 1], \end{cases}$$

and the other three phases are shifted  $90^\circ$ ,  $180^\circ$  and  $270^\circ$ . The actuator phase  $\alpha(t)$  denotes a specific moment in the waveform cycle, and  $0 < q < 1$  is the asymmetry factor where  $q = 0.5$  is a pure sine wave. After some open-loop testing,  $q = 0.6$  has been chosen, since this value returned the smallest velocity variations during a complete waveform cycle.

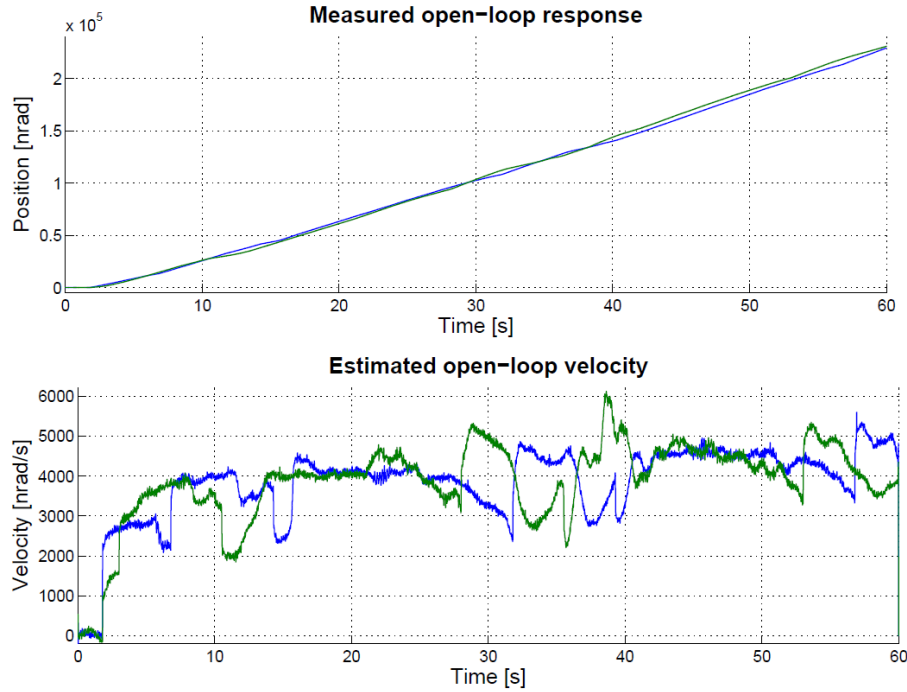


**Figure 4. Measured open-loop mirror rotation and its estimated velocity using a constant 0.02-Hz waveform frequency.**

Two specific open-loop results using these waveforms are shown in Figure 4, depicting the mirror rotation measured by the interferometer and the derived velocity estimate. Both experiments use a constant frequency of 0.02 Hz, i.e. the actuator phase  $\alpha(t)$  increases linearly, so that a complete cycle takes 50 s. Indeed, the mirror rotation is not perfectly linear, but the bottom plot shows that there are no stick-slip effects or reversed directions, which would be show-stoppers for accurate long-stroke closed-loop motion. The velocity variations are at most a factor 3, which are relative easy to account for in a controller design.

#### Frequency response function measurements

Further characterization of the IFPM behavior has been done in the frequency domain, via local frequency response function (FRF) measurements around various actuator operating points [8]. To this end the waveforms have been set at different nominal  $\alpha_{\text{nom},k}$ , around which a small amount of additional noise  $\bar{\alpha}(t)$  has been added, which results in a mirror response  $y$ . The local dynamics around operating point  $k$  can then be calculated as the ratio between the cross-power density  $S_{y\bar{\alpha}}$  and auto-power density  $S_{\bar{\alpha}\bar{\alpha}}$  of the two signals

$$H_k(j\omega) = \frac{S_{y\bar{\alpha}}(j\omega)}{S_{\bar{\alpha}\bar{\alpha}}(j\omega)}.$$

The resulting FRFs for 21 different nominal phases  $\alpha_{\text{nom},k}$  along a full actuator cycle are shown in Figure 5, using either the interferometer or the encoder as sensor for  $y$  (notice the gain difference between the two, since one is expressed in nrad and the other in nm). The latter obviously has a worse coherence and is noisier, since it has a much coarser resolution than the interferometer. Apart from that, both results are very much alike. All FRFs show the same resonances and more or less the same anti-resonances, which implies that the dynamics is nearly constant over a full actuator cycle. The FRFs only differ in their gain, which is particularly clear for low frequencies. These local DC-gain variations of at most 9 dB can directly be linked to the observed velocity variations in Figure 4, since this is roughly a factor 3. Moreover, all FRFs have the same low-frequent phase, which confirms that there are no direction reversals.

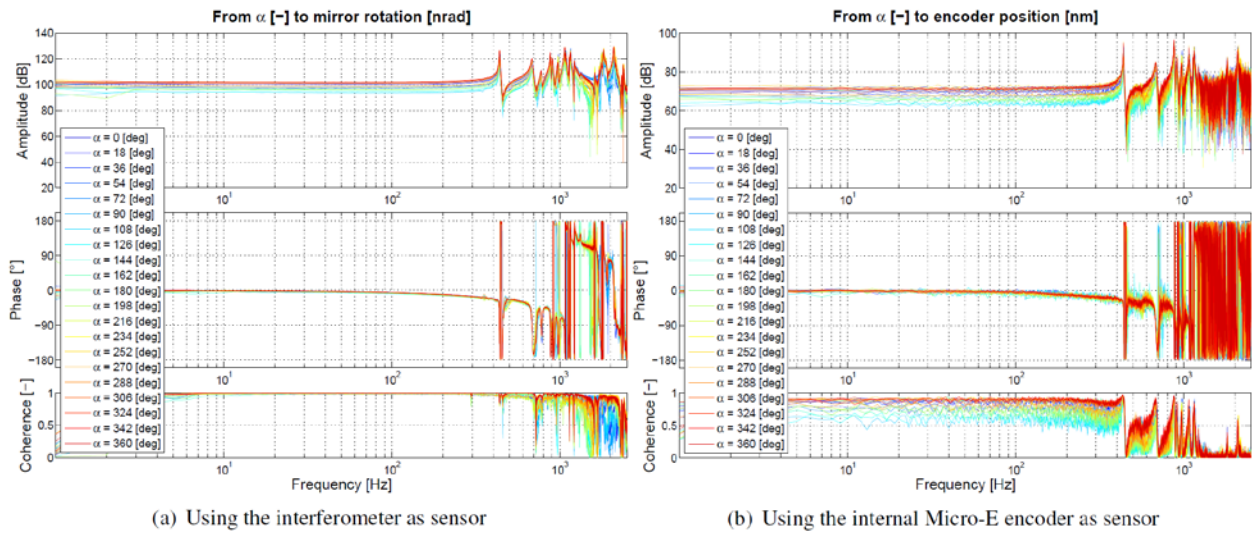


**Figure 5. Measured FRFs as a function of the actuator phase  $\alpha$ .**  
Note that  $360^\circ$  is equivalent to  $\alpha_{\text{nom}} = 1$ .

### Closed-Loop Performance

The friction-based Piezo LEGS actuators are not meant to provide accurate open-loop motion, which is indeed confirmed by the above measurements. Hence, to meet the extreme accuracy requirements, the IFPM has to be operated in closed loop.

#### Controller design

Since the DC-gain variations along the actuator cycle are relatively small, a fixed linear controller can be sufficient to demonstrate the IFPM performance. The foreseen feedback loop is illustrated in Figure 6, where the proposed controller structure encompasses

- a double integrator to allow perfect tracking of linearly increasing setpoints;
- a zero to create phase-lead around the cross-over frequency (i.e. for closed-loop stability);
- a second-order low-pass filter to suppress higher-order dynamics.

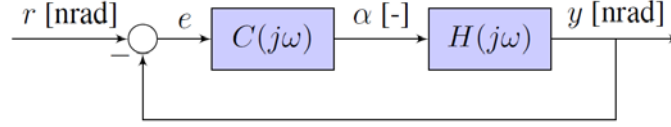


**Figure 6. Feedback loop for controlling the mirror angle  $y(t)$  via the actuator phase  $\alpha(t)$ .**

The controller parameters have been tuned specifically on the measured FRFs in Figure 5(a), i.e., based on the high-resolution interferometer measurements. The parameters have been chosen such that all local FRFs yield a robustly stable closed loop with a high as possible bandwidth. In this case the robustness has been defined by both a maximum phase margin of  $55^\circ$  and a modulus margin (maximum value of the closed-loop sensitivity function) of at most 3.5 dB. The resulting open loops  $H_k(j\omega)C(j\omega)$  are depicted in Figure 7, both as a Bode and a Nyquist diagram. The latter shows that the closed loop is indeed stable for all local FRFs, since all curves are on the right side of the point  $(-1,0)$  [9]. Moreover, all loops indeed satisfy the set modulus margin (black circle) and phase margin (black arc). Figure 7(a) shows that the achieved bandwidth lies between 26 and 62 Hz.

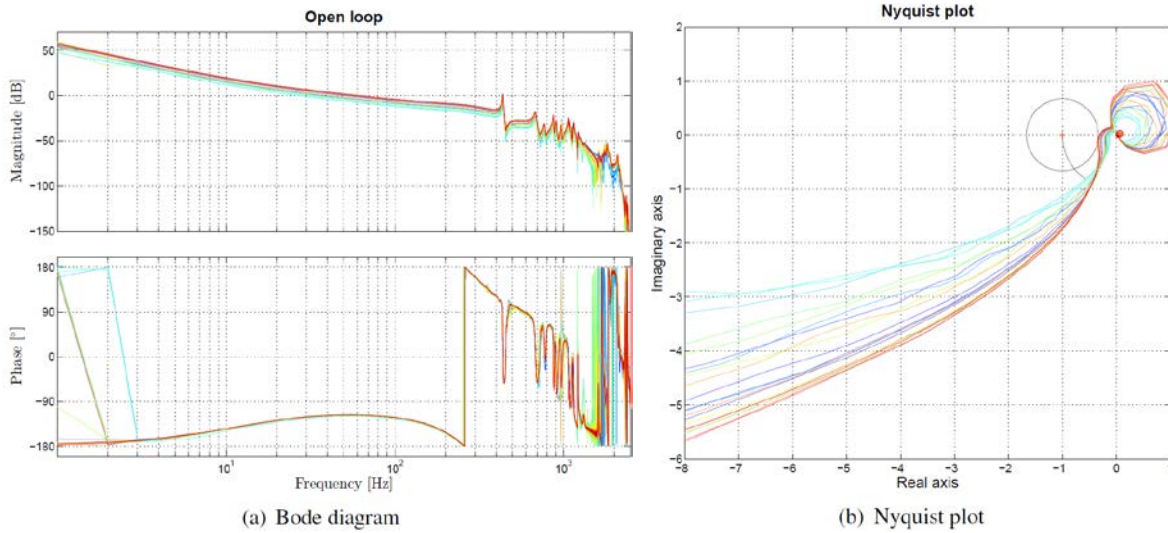


**Figure 7. Frequency domain representations of the open loop  $H_k(j\omega)C(j\omega)$ .**

#### Measured tracking performance

The designed feedback controller has been implemented in the Simulink / dSpace environment, and used to validate the IFPM performance. As was originally the intention, first the external interferometer been selected as feedback sensor.

Figure 8 shows the results in terms of the amplitude spectral density (ASD) of the closed-loop error during various different experiments. The dashed line indicates the  $5 \text{ nrad}/\sqrt{\text{Hz}}$  pointing jitter requirement. During these experiments both forward and backward movements has been carried out with three different velocities ranging from 12.5 nrad/s (specified science mode velocity) to 2250 nrad/s. Strictly speaking the performance does not have to be demonstrated for velocities larger than 12.5 nrad/s, but these are included anyway to demonstrate the IFPM behavior over a larger stroke where the piezosteppers go through a number of cycles. Clearly the requirement is met over all frequencies in all closed-loop experiments.



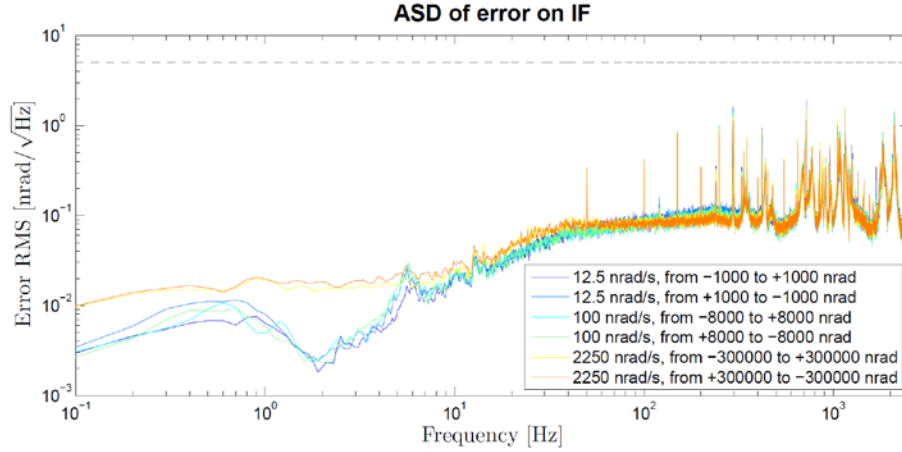


**Figure 8. Measured amplitude spectral density (ASD) of the closed-loop error using the interferometer as feedback sensor.**

However, interferometer measurements are known to be very sensitive to items such as temperature variations and turbulence, which usually results in low-frequency drifts. Hence, when the interferometer is used as feedback sensor, the mirror rotation is actually tracking these drifts. As an alternative, it has therefore been decided to try to close the loop on the Micro-E encoder and use the interferometer as a reference sensor. Since Figure 5 showed that the dynamics are the same for both sensors, the same controller as discussed above can be used for this purpose (only an additional gain of  $1/0.03106$  had to be included to convert the encoder nm-readout to nrad).

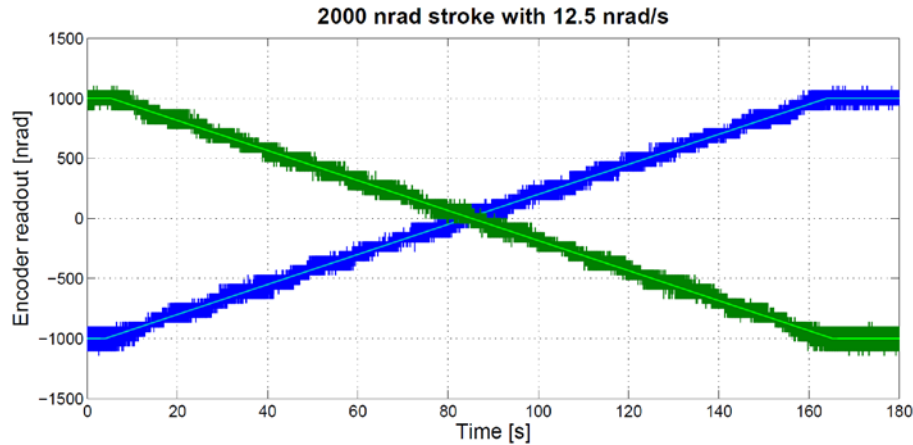
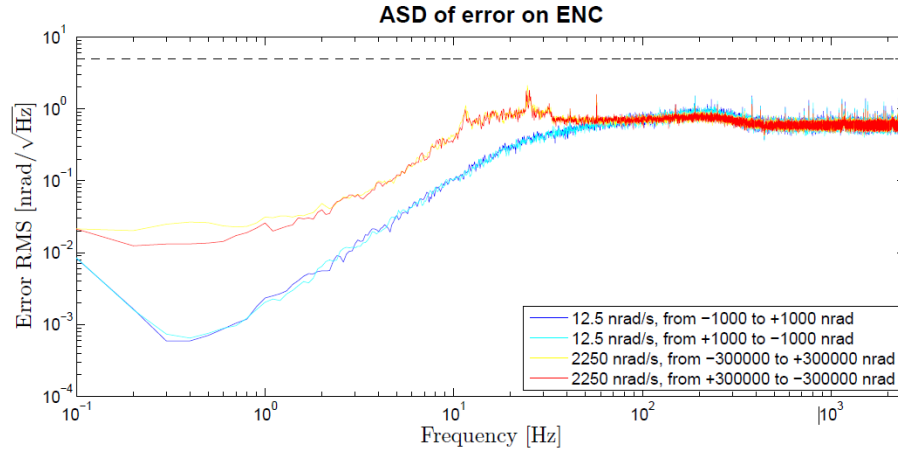


**Figure 9. Two closed-loop responses with 12.5 nrad/s mirror rotation (science mode) using the internal encoder as feedback sensor. The setpoints are drawn on top of the measured rotations.**

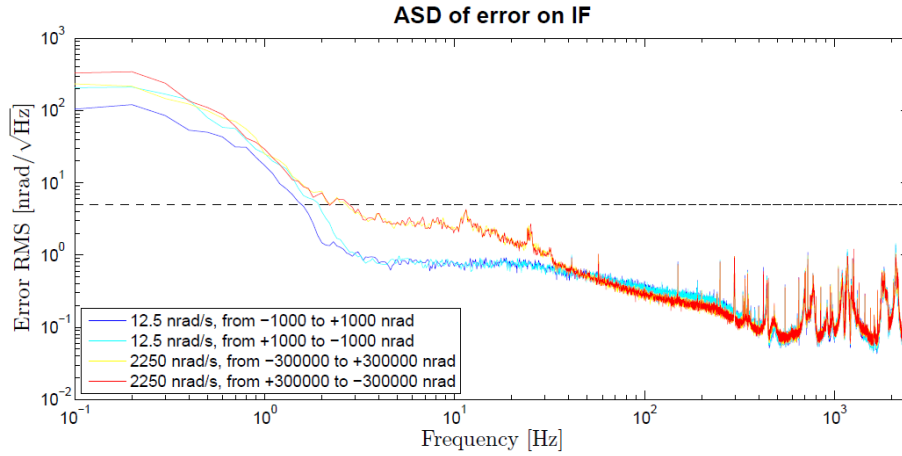
Two specific closed-loop time responses using this approach are depicted in Figure 9. In these experiments the setpoint is changing with the science mode velocity, both forward and backward, which the encoder is tracking successfully. The encoder resolution steps are clearly visible in the response.

The effect of these steps on the ASD of the error (as measured by the encoder) is however very limited, as is shown in Figure 10(a). Due to the coarser resolution, the level of the ASD is much higher than in Figure 8, but still the requirement is met quite easily, both for the science-mode and the large-stroke scenario. This implies that IFPM can be used with high accuracy in a stand-alone configuration, i.e.

independent of any external metrology, which is very beneficial in the current breadboarding phase of the IFP project.



(a) As measured by the encoder



(b) As measured by the interferometer

**Figure 10. Amplitude spectral densities of the closed-loop error using the internal encoder as feedback sensor.**

Notice that the shape of the ASD in Figure 10(a) (especially for the 12:5 nrad/s case) resembles the designed closed-loop sensitivity function

$$S(j\omega) = \frac{1}{1 + H(j\omega)C(j\omega)}$$

which is typically small for low frequencies and constant for high frequencies. In the transition between these two regions the bandwidth can be estimated, which is indeed in the order of 30 Hz.

Figure 10(b) shows the ASD of the interferometer readout for the same experiments. This plot shows a violation of the requirement below 2 Hz. As pointed out before, this could partly be attributed to drift in the reference sensor itself, which is difficult to rule out in a normal unconditioned laboratory environment. As such, we can conclude that the IFPM performs compliant, at least up to what can be measured in a

normal lab. The IFPM performance for very low frequencies will therefore be validated in future environmental tests to be carried out by Airbus DS in their IFP breadboard setup.

## Conclusions

In this paper we have presented the design and realization of the In-Field Pointing Mechanism for the eLISA mission. This mechanism encompasses a tilt mirror guided by Haberland hinges, which is actuated by walking piezo actuators. The redesign of the actuator unit to a planar configuration has improved the open-loop behavior significantly, resulting in local velocity variations of just a factor 3 and nearly constant dynamics over a full actuator cycle.

The open-loop measurements have been taken into account in a robust high-performance controller design. This controller has been combined with both interferometer and encoder feedback; the latter has demonstrated that IFPM can be operated stand-alone with high accuracy. In both cases the resulting ASDs suggest compliance with the maximum allowed pointing jitter.

However, in our unconditioned laboratory the performance could only be guaranteed for frequencies above 2 Hz. For a real validation of the low-frequency performance a better conditioned environment is required. This validation will be carried out by Airbus DS in their environmental tests. In these tests the piston jitter of the IFPM will also be assessed.

## Acknowledgments

The authors would like to thank Dennis Weise, Ewan Fitzsimons and Christina Brugger (Airbus Defence & Space) for the fruitful collaboration within the IFPM project, Per Bendixen (Piezomotor) for his help on improving the actuator module, and former colleagues Joep Pijenburg, Niek Rijnveld and Martijn te Voert for their contributions to the IFPM development.

## References

- [1] K. Danzmann, "LISA mission overview," *Advances in Space Research*, vol. 25, no. 6, pp. 1129–1136, 2000.
- [2] D. R. Weise, P. Marenaci, P. Weimer, H. R. Schulte, P. Gath, and U. Johann, "Alternative opto-mechanical architectures for the LISA instrument," *Journal of Physics: Conference Series*, vol. 154, no. 1, p. 012029, 2009.
- [3] C. Brugger, B. Broll, E. Fitzsimons, U. Johann, W. Jonker, S. Lucarelli, S. Nikolov, M. te Voert, D. Weise, and G. Witvoet, "An experiment to test in-field pointing for LISA," in *Proc. 10th ICSO*, Tenerife, Spain, October 2014.
- [4] N. Rijnveld and J. Pijenburg, "Picometer stable scan mechanism for gravitational wave detection in space," *Proc. SPIE*, vol. 7734, p. 77341R, 2010.
- [5] J. Pijenburg, N. Rijnveld, and H. Hogenhuis, "Extremely stable piezo mechanisms for the new gravitational wave observatory," *Proc. SPIE*, vol. 8450, p. 84500C, 2012.
- [6] R. Merry, M. Maassen, M. van de Molengraft, N. van de Wouw, and M. Steinbuch, "Modeling and waveform optimization of a nano-motion piezo stage," *IEEE/ASME Trans. Mechatronics*, vol. 16, no. 4, pp. 615–626, 2011.
- [7] R. Merry, N. de Kleijn, M. van de Molengraft, and M. Steinbuch, "Using a walking piezo actuator to drive and control a high-precision stage," *IEEE/ASME Trans. Mechatronics*, vol. 14, no. 1, pp. 21–31, 2009.
- [8] R. Merry, J. Holierhoek, M. van de Molengraft, and M. Steinbuch, "Gain scheduling control of a walking piezo actuator," *IEEE/ASME Trans. Mechatronics*, vol. 19, no. 3, pp. 954–962, 2014.
- [9] S. Skogestad and I. Postlethwaite, *Multivariable Feedback Control: analysis and design*. Chichester, UK: John Wiley, 2005.



# Suomi-NPP Mission On-orbit Experience with Toroid Ball Bearing Retainers under Unidirectional and Reversing Motion

Otto Bruegman\*, Kamal Thakore\*\*, Stu Loewenthal+ and John Cymerman++

## Abstract

The Advanced Technology Microwave Sounder (ATMS) instrument scan system on the Suomi National Polar-orbiting Partnership (SNPP) spacecraft has experienced several randomly occurring increased torque 'events' since its on-orbit activation in November 2011. Based on a review of on-orbit telemetry data and data gathered from scan mechanism bearing life testing on the ground, the conclusion was drawn that some degradation of Teflon toroid ball retainers was occurring in the instrument Scan Drive Mechanism. A life extension program was developed and executed on-orbit with very good results to date. The life extension program consisted of reversing the mechanism for a limited number of consecutive scans every day.

## Introduction

The ATMS scan mechanism has been described in references 1 and 2, so only a cursory description is included. This paper is devoted to root identification of the ATMS scan bearing torque events, evaluation of sensor impacts, and mechanism life evaluation by resolving the differences between the ATMS bearing experience vs other more positive on-orbit experience. In addition, part of the paper discusses the implementation of an on-orbit life extension mitigation on the SNPP spacecraft.

Figure 1 depicts the scan mechanism in cross section, which identifies the major components of the assembly. Note that there are two sets of bearings in this assembly. The problem is only observable with the Main Motor bearings for ATMS. The Compensator Motor bearings are identical to the Main Motor bearings, but run at a rate of 1.8X the Main Motor rotation rate and have not shown any misbehavior. At this time, we don't know why the Compensator Motor bearings are acting differently than the Main Motor bearings.

Figure 2 depicts the bearings in question, showing the arrangement of the balls and the retainers. The bearings are an angular contact pair manufactured by Timken. The bearing pairs have an OD of 57.15 mm (2.0 inches), with each bearing having a complement of 38 3.175-mm (0.125-inch) balls and 19 toroids. The nominal contact angle is 20 deg. Bearing preload is 44.5 newtons (10 pounds).

The bearings are lubricated with Nye Rheolube 2000B. The design life of the ATMS instrument is 7 years.

---

\* NOAA, Silver Spring, MD

\*\* NASA Goddard Space Flight Center, Greenbelt, MD

+ Lockheed Martin Space Systems Company, Sunnyvale, CA

++ Aerospace Corporation, El Segundo, CA

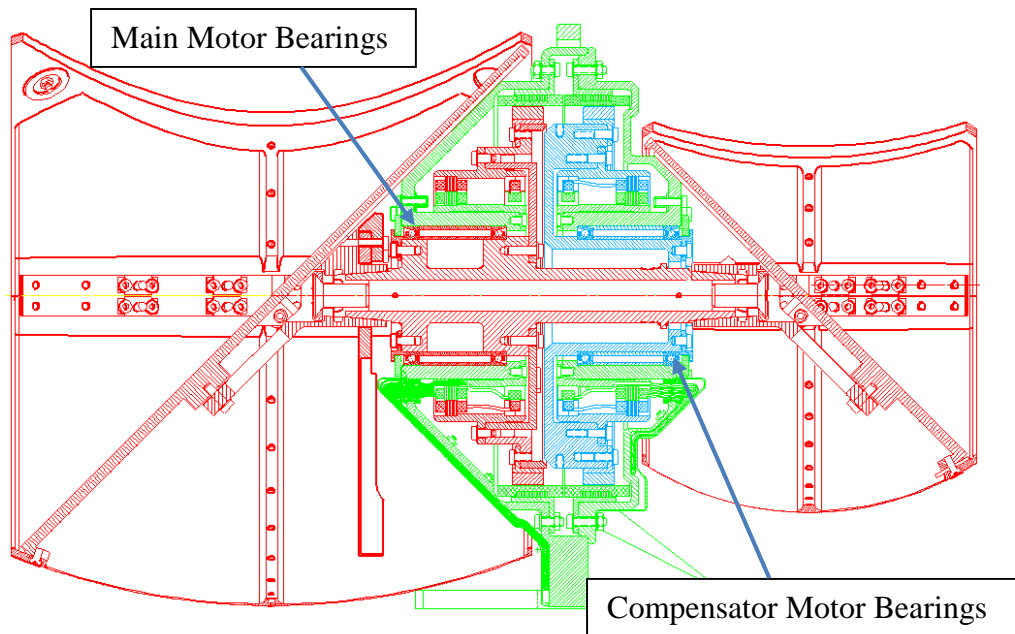


**Figure 1. ATMS Scanner Cross-Section**

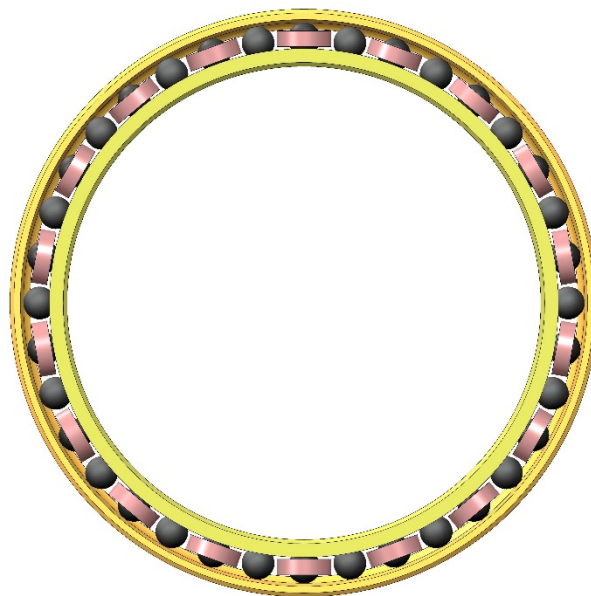


**Figure 2. Nominal ATMS Bearing Configuration**

#### **On-orbit Indications of a Problem**

The SNPP spacecraft was launched on October 28, 2011. The ATMS instrument started operations on Nov 8, 2011 and has since been in continual operations. The instrument experienced its first indications of scanner related problems about a year later. The indications of problems were based on evaluation of main motor current spikes and related motor control telemetry.

Efforts were made to find common ground between the experiences from the bearing life test unit results and the on-orbit flight unit data. This effort was complicated by the fact that the life test units were focused on only the mechanism bearing assemblies and that the on-orbit data were being obtained from a higher level of mechanism assembly. The telemetry obtained for the life test units were not directly relatable to the telemetry available from on-orbit. As an example, the temperature telemetry in the test units was a better indicator of average bearing temperature, while the on-orbit implementation was more of a drive motor temperature. This type of data divergence made the evaluation of the on-orbit motor current spikes much more difficult. We found that the best common data relationship was that of average motor current. We had higher rate motor current data for both the test unit and the on-orbit instrument. However, the data rates were vastly different and the motors were driven by very different control systems. That made any useful comparison of the high rate data from both sources almost impossible. Still, the high rate on-orbit data did provide valuable information on what was going on within the flight mechanism bearing system.

Figure 3 provides some information on the initial on-orbit observation. This shows the main torque trend from the beginning of mission to end of February, 2014. The transient in late 2012 returns to the previous nominal condition on its own with no intervention from the ground or otherwise.

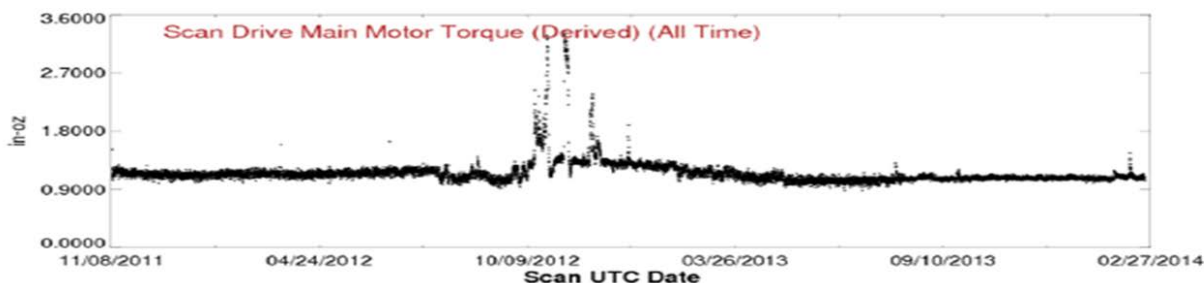


**Figure 3. On-Orbit Main Motor Current – showing the torque spike in late 2012**

### **ATMS Life Test Unit Experience**

The ATMS program initiated a bearing life test program on February 2003 with the first of three bearing test units. This was for the same toroid type separator bearings. All three units went on line by August 2003.

Test unit 2 started experiencing higher torque spikes at about the 5 year mark of its 'operational' life. The torque generated by the unit exceeded limits at the 5.3 year mark of its life (2/20/2009). At this point, the unit was disassembled to inspect the bearings. It was found that the bearing toroids had experienced severe wear. The toroids of one end of the bearing pair were almost totally destroyed and the other bearing showed severe wear of the toroids. The temperature of the test units was initially set at 41 °C as a predicted worst case temperature. In the September 2012 timeframe the temperature was changed to more closely match that of the measured on-orbit values. The test unit temperature was changed from 41 °C to 18 °C. At the time, it was thought that the accelerated wear of the test unit #2 bearings was the result of an overly conservative temperature prediction leading to a premature loss of lubrication.

The higher test temperature did contribute to a very conservative test. The protective elasto-hydrodynamic film thickness between the bearing balls and race differed by a factor of 2X. Also the chemical degradation rate of the lubricant was accelerated by temperature approximately doubling for every 10°C according to the Arrhenius relationship. However the sister unit #1 and #3 test bearings ran approximately twice as long as the #2 bearings so there was yet another unidentified factor present.

Figure 4 shows the wear of the bearing toroids for test unit 2. The left picture shows the 'heater' end bearing and the left shows the 'encoder' end bearing. The 'heater' end bearing was thought to run at a slightly higher temperature than the other, leading to more severe wear.



**Figure 4. Test Unit #2 bearing condition from 2009 disassembly**

The other units (1 and 3) continued to run beyond their 7-year design lives, but test unit #3 exceeded its torque limits on 6/29/2012 and was taken off line. At this point in time, it was decided to switch out the drive motor of the unit to more closely match the torque capability of the flight motor. The original test set motors had a torque capability of 69 in-oz (0.49 N-m) continuous duty, with a 120 in-oz (0.85 N-m) peak capability. While the flight motor had a torque capability of 120 in-oz (0.85 N-m) continuous duty with a 300 in-oz (2.1 N-m) peak capability. The replacement motor chosen for test station 3 closely matched the capability of flight motor. This switch of the motors was completed in March, 2014 and the unit was restarted.

### **Recent Developments**

In late 2014, the SNPP ATMS instrument started to experience some more elevated motor current spikes. This led to the re-institution of the Scanner Drive Working Group. The working group was tasked with the evaluation of the on-orbit situation and to provide recommendations for mechanism life extension mitigations.

This led to a variety of work, starting with a re-evaluation of the work on bearing life prediction, applicability of life test data on other programs, work done in 2009 on the test unit 2 etc.

A re-evaluation of related life test data by Stu Loewenthal of Lockheed Martin suggested that the differences in life test results were the result of mechanism direction of motion. In life test data from other programs that used toroid type bearings, it was noted that the particular mechanism motion profile included periodic and numerous reversals.

A comparison of the Test Station #2 life test bearing with rotation in one direction and a similar life test bearing that rotated equally in both directions is shown in Figure 5. The bi-directional bearing is clearly in much better condition than the ATMS bearing despite achieving six times the number of revolutions.



**Figure 5. Comparison of Test Station#2 bearing with a similar bearing in relatively good condition with equal direction reversals after 6X times the number of revolutions.**

**Left Figure:** ATMS uni-directional test bearing at 63 Mrevs

**Right Figure:** Similar bi-directional bearing at 362 Mrevs

Reversing bearing rotational direction minimizes toroid wear because it reduces the chance for the toroids to get stuck/pinned in one orientation. The toroid that is pinned by the driving ball will tend to rub in one spot causing the lubricant to dry out and also inhibits the supply of fresh lubricant. The photos of the worn toroids from post-test inspection (see the next section) clearly show that the toroids were locked in one orientation forming ball pocket wear divots. From the steel ring-on-block tests reported in Reference 3, the wear rate of unlubricated (dry), PTFE test samples was >1000 times the wear rate of those lubricated. This obviously has a major effect on toroid wear life.

The major benefit from reversing direction is that it allows the toroids to reorient due to clearances between the balls and the release of load during reversal. The unloaded toroids have the opportunity to reorient themselves not only presenting a fresh rewetted surface but also distributing wear more equally around the toroid perimeter.

The ATMS bearing application, by comparison, did not involve any reversals in its operation. The ATMS motion profile is uni-directional for the entire life of the instrument. There are accelerations and decelerations in the ATMS profile, but no opportunities for reversal of motion. A description of the ATMS profile is provided in Figure 6. Note that the primary data collect occurs during the Earth scan at constant speed as does the cold and hot calibrations. In order to minimize revisit time to the required 8/3 of a second per revolution, the scanner must accelerate and brake at extremely high levels (4500 to 5000 deg/s<sup>2</sup>) three times each revolution. At first it was thought that these high acceleration levels were responsible for ball skidding leading to premature life. However subsequent analysis showed that the dynamic loads were very small compared to the bearing preload making skidding unlikely.

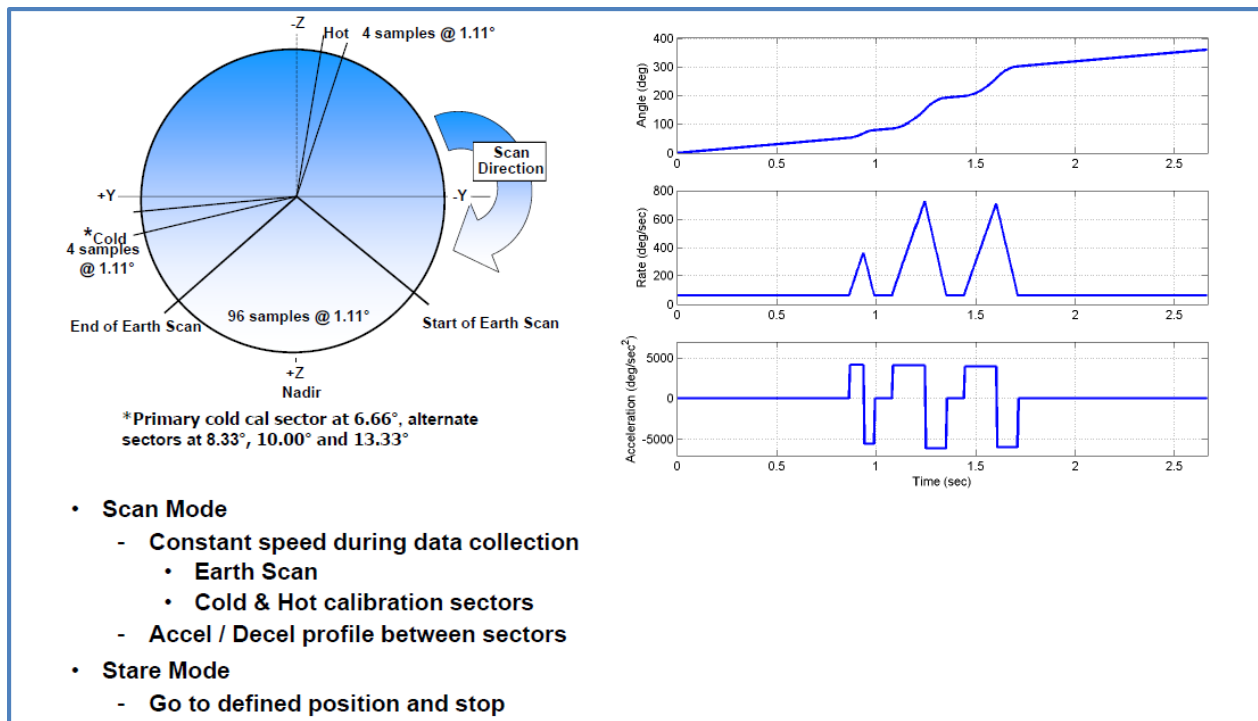


**Figure 6. ATMS Scan Profile Description**

### Test Station Bearing Post-Mortem

To gain insight into the mechanism of the toroid wear seen in the original test station 2 bearings, the bearings were removed from storage for a more detailed inspection. Detailed measurements were taken of the surviving toroids and some 3D modeling was performed to gain insight into the mechanics of the wear phenomena. Figure 7 and 8 present an example of one of the surviving toroids and modeling results showing the configuration of the toroids during the wear process.

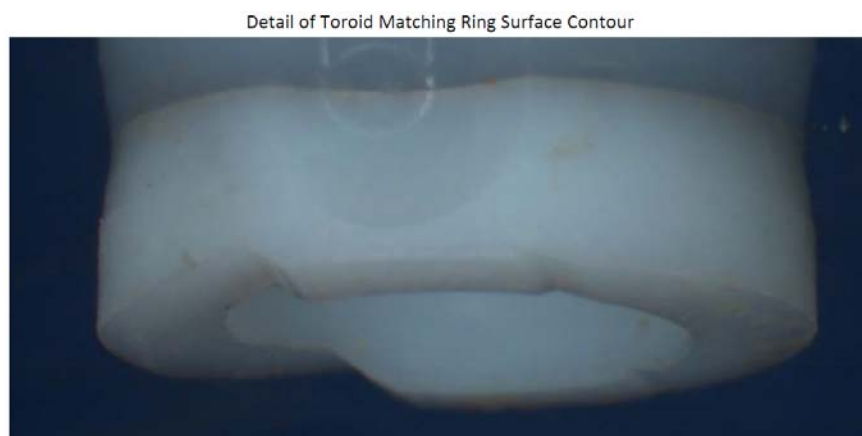


**Figure 7. Sample Bearing Toroid – Test Station #2**



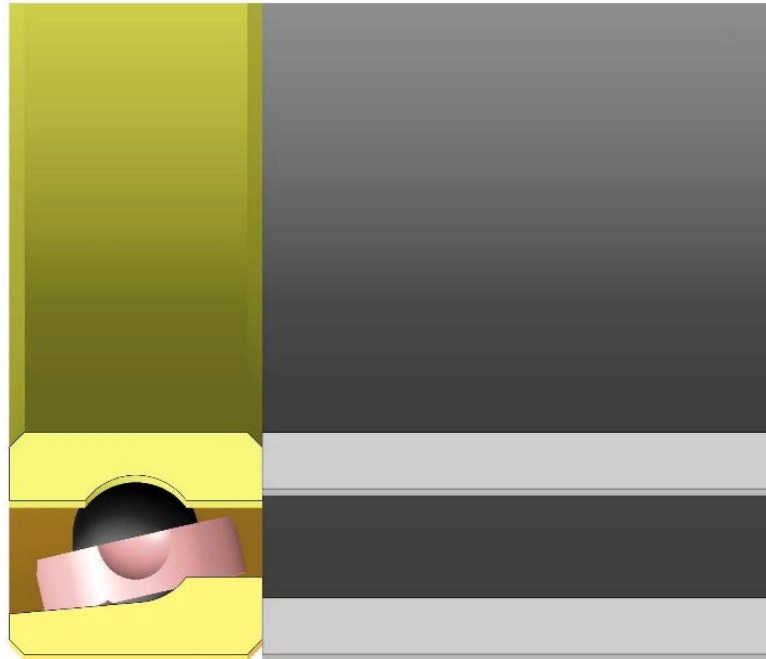


**Figure 8. Modeling of Toroid Wear of Sample Pictured in Figure 7 – Test Station #2**

The wear patterns noticeable in the test station #2 toroids had a variety of configurations, but the one shown above is most telling. It shows that the bearing races had a significant contribution to the wearing of the toroids. However, the major mode of wear that lead to the destruction of the toroids was the one where the balls wore an ever deepening 'dimple' into the toroid that lead to the disintegration of the circular geometry. In other words, the 'dimple' went so deep that the toroid split in two. Subsequently, the toroid halves were ground up by the continuously rotating bearing elements – thereby causing the current spikes that were observed in telemetry. The grinding up of the toroid material lead to the creation of a slurry of Teflon particles and lubricant outside of the bearings. There were no intact toroids in either of the two bearings from test station #1 indicating the test station bearings were run well beyond their useful lives.

Only a slight indication of residual lubrication on rolling elements was observed. There were also indications that lubricant was creeping out of the bearing assembly forming the slurry observed external to the bearing.

Pre-load of the bearing pair was checked and found to be unchanged if not a little higher than from assembly records. This may have been due to measurement uncertainty or to a very thin film of slurry on the metallic surfaces that minutely changed bearing dimensions.

It should be pointed out that it was anticipated that many of the toroids in test stations 1 and 3 were compromised at this point. However, the units were run to gain experience with running damaged bearings and also to see what benefit might be gained from our mitigation strategy of periodically reversing the motion of the scanner.

For the purposes of showing the variety of the wear patterns of the toroids from test station #2, Figure 9 is offered. The first picture shows a concave toroid wear pattern suggesting that this toroid was rotating and distributing wear around the toroid circumference. The remaining pictures show ball wear pockets indicative of toroids that got stuck in one position accelerating wear

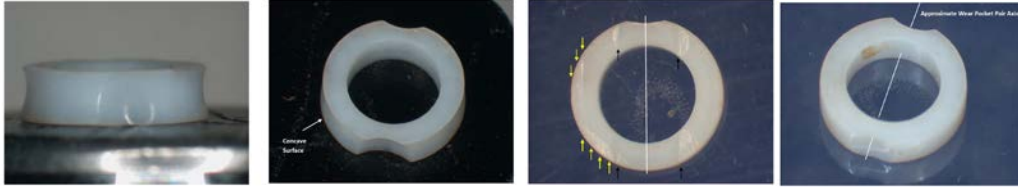


**Figure 9. Toroid Wear Patterns (test station #2)**

### Putting the Puzzle Together

So we had some information suggesting that the on-orbit motor current spikes were similar to the bearing life test station results. Also, we had some 3D modeling results that was able to explain the wear patterns on a sample of the intact toroids. On-orbit motor current data was obtained at a high sampling rate (148 samples/second) that could be used to perform some analyses – including FFT, to get a better understanding of the on-orbit situation. In addition, wear rate analysis was performed that suggested that Teflon wear rate was highly dependent on lubrication of the interfacing surfaces – ball to toroid in this case. Figure 10 shows a sample of an FFT that was obtained from on-orbit data that suggested a response at the Ball Spin Frequency. This was another clue in suspecting an interaction between the bearing ball(s) and its cage (toroid).

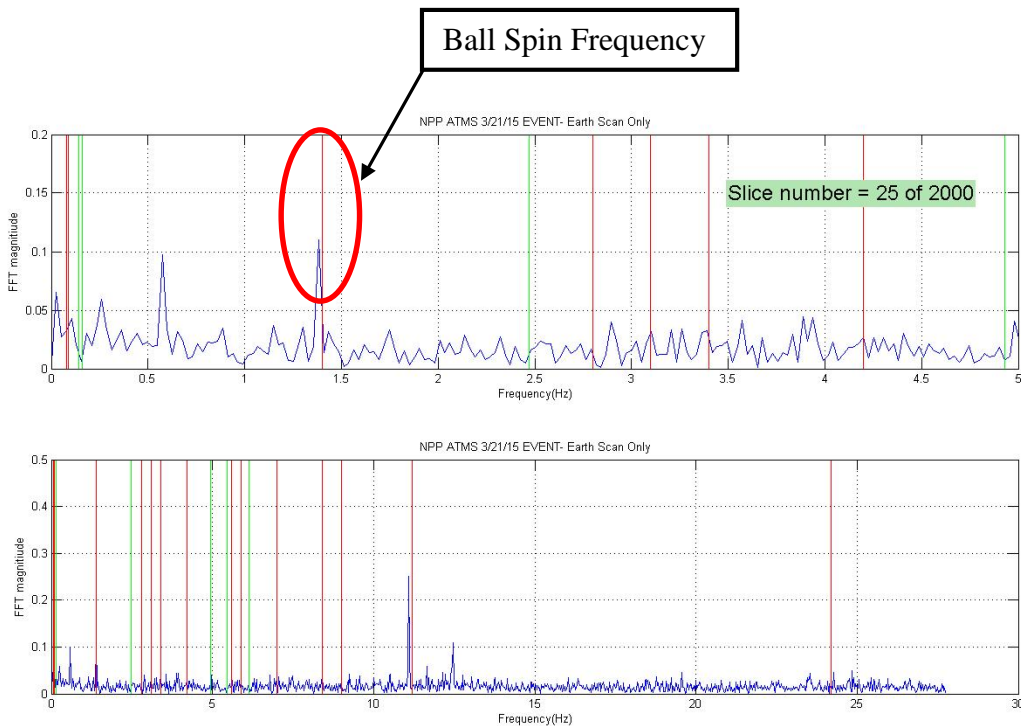


**Figure 10. FFT Results showing Ball Spin Frequency response**

The end result of all the investigation and analysis lead to the conclusion that the ball toroid interface was running dry. The operation of the mechanism in one direction was not allowing for the re-orientation and hence re-lubrication of those surfaces of the toroids. Thus began a rapidly advancing wear of the softer material (Teflon toroids). As the 'pockets' in the toroids got deeper, the harder it was for any re-orientation of the toroids to occur.



Once the wear mechanism was understood, the effort was turned into one of developing a mitigation that could be implemented on-orbit with minimal impact to the science provided by the instrument. With the experience in hand of another program that used the Teflon toroids successfully, it was suggested that a modified scan pattern be implemented to allow for the re-orientation of the toroids. We looked long and hard at new permutations of the instrument scan profile. Eventually, this led to the suggestion of doing some limited number of reversals at a point in the spacecraft orbit that would have negligible impact to science. The SNPP science team came to rescue by suggesting that the instrument science would not be significantly impacted if a limited number of reversals were implemented at a high latitude point in the orbit. Eventually, we settled on doing the reversals above 74 degrees North latitude.

Northrop Grumman was tasked to develop and test a command sequence to have the scanner go in a reverse direction. They came back with an elegant and simple process of uploading a new scan profile table that would perform the desired operation. Once loaded, this new table would be enabled by command at a time desired and then another command would be issued to go back to a normal scan table. Northrop Grumman tested this process on their simulator and also on the sensor Engineering Development Unit. Also, after a number of discussions and some test information from the still running bearing test stations, we settled on doing six contiguous scans in reverse direction once per day above 74 degrees North latitude.

The six reversals per day were tested on two running bearing test stations at different times. At this period of time, both stations were down because both stalled in late 2014 due to high torque and were shut down pending new engineering direction. The reversal testing was started on test station 3 in April 2015 while test station 1 was restarted in March of 2015 running the normal scan profile without reversals. While test station 3 was being used for reversal testing, test station 1 stalled in early August of 2015. At this point in time we needed to develop more experience with reversals, so we decided to restart station 1 doing daily reversals. At first, test station #1 was reluctant to re-start, but eventually did in mid-August 2015. Test station #1 was run with the daily reversals for about a month before its disassembly. At the time of its test termination, test station #1 was past its 2X mission life. Test station #3 continues to run with good results and is almost at its 2X life point as this is being written. Figure 11 shows the motor current data for test station #3 as of December 8, 2015 and Figure 12 shows the motor current for test station #1.

It is anticipated that the toroids in the test station #3 bearings are compromised to some extent, but no definitive statement can be made as to their actual state. It would be logical to expect that the station 3 toroid condition is somewhere between the states of the disassembled test stations 1 and 2.

The reversals on test stations 1 and 3 were successful in giving these bearings new life. However due to the debris generated by the failure of the toroids, some torque spikes are expected to occur. The toroid debris is being ground up by the action of the balls against the races. It is thought that the reversals arrest the further degradation of intact toroids as contact surfaces are being re-wetted with remaining lubricant.

The on-orbit scanner bearing condition is not thought to be in as dire a condition as the test set #2 and certainly not like test station #1 bearings at past its 2X mission life, but it is conceivable that a number of toroids are missing in the flight bearings. So far the scanner on-orbit is still performing within pointing limits and the bearing torque has returned to near mission-start levels after reversal implementation so our expectation is that toroid damage is not too severe.

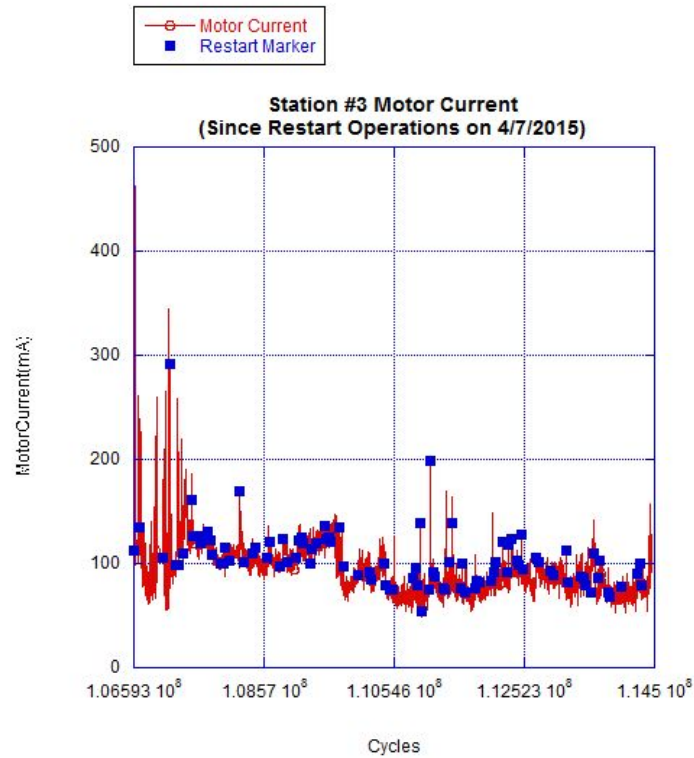


Figure 11. Motor Current of Test Station #3 (12/08/2015) – blue squares indicate reversals

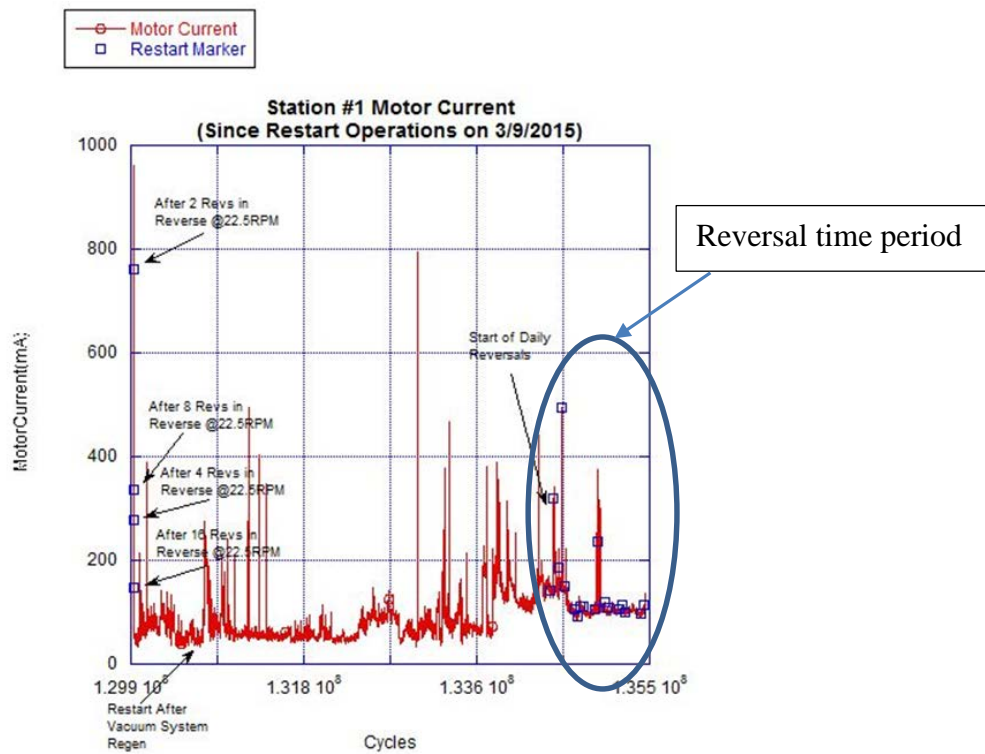


Figure 12. Motor Current of Test Station #1 (9/16/2015) after 11.5 years of equivalent operation prior to disassembly. Note the more stable level of motor current after reversals.

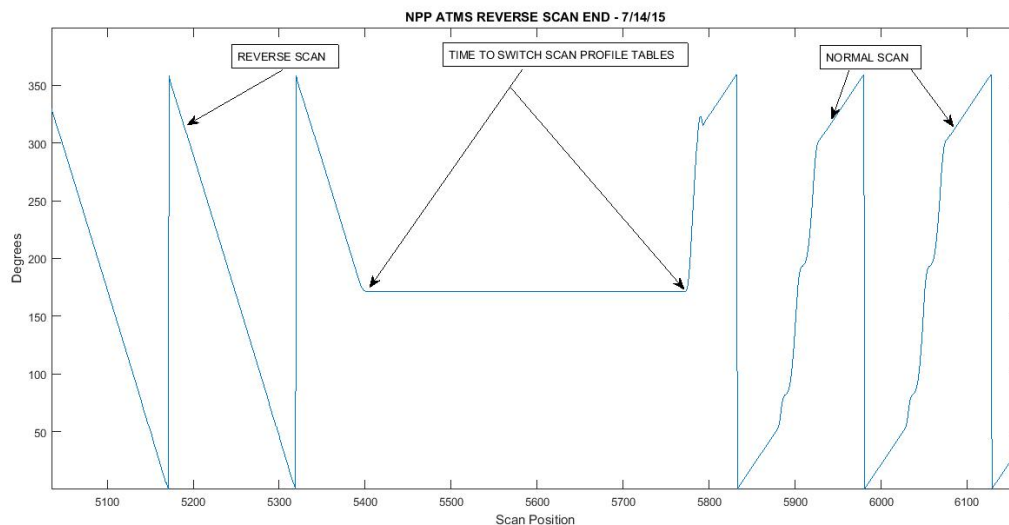
## Life Extension Mitigation Implementation

The on-orbit reversal process was initiated on July 14, 2015. It consisted of a table load and its verification and then followed by the first reversal sequence. The first reversals were done by ground command, which put restrictions on how fast people and command systems can operate. This resulted in approximately 26 reverse direction rotations of the scanner before the return of normal forward scan operation. This reversal resulted in a motor current spike that died away after about 3 days, which is faster than previous 'naturally occurring' current spikes. A result like that was anticipated based on bearing test set reversals. The reversal command process was implemented via the spacecraft Daily Activity Schedule command load on August 24, 2015. This simplified the command implementation and had the effect of implementing the reversals as part of normal spacecraft operation – basically making it seamless. It also had the result of fixing the number of reversals at the desired number of six contiguous reversals per day.

Many thanks go out to the people in the satellite control center for their work in developing and testing of the scripts related to the implementation of the reversals.

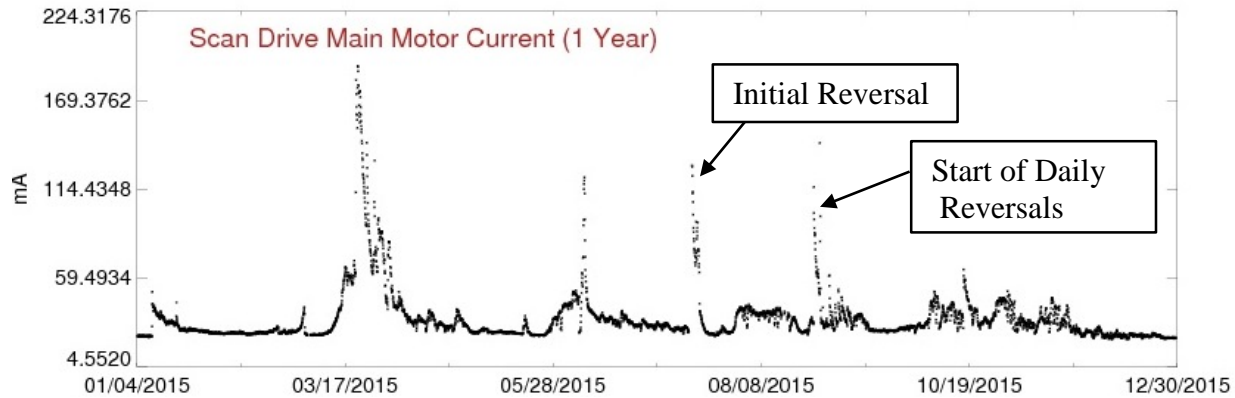
The daily reversals have been performed without interruption since August 24, 2015. Only one noticeable motor current 'event' has occurred since then and that happened early in the process on August 26, 2015. Since then the motor current has been rather stable with only small perturbations.

Figure 13 shows the transition from reverse and then back to normal. The figure shows the scan angle vs scan telemetry sample number of the dataset. There are 148 data samples per complete scan rotation.



**Figure 13. Scanner Recovery from Reverse to Normal Scan**

Figure 14 is provided to capture the scanner main motor current for the past year. It should be noted that the motor current level is now at start of mission values. This would indicate that the reversals are effective in re-lubricating the bearing/toroid surfaces. Also, the reversals may allow the toroids to re-orient themselves exposing freshly lubricated Teflon surfaces to contact the adjacent balls.



**Figure 14. Scan Drive Motor Current 1 Year History**

### **Conclusions**

From the years of effort related to the SNPP ATMS scanner bearing system, the following recommendations and observations can be offered:

- 1) Use of Teflon toroids in space bearing applications has to consider the range of motion of the mechanism. Based on this experience, uni-directional applications for toroid use cannot be recommended. Applications with regular directional reversals may be acceptable and even desirable, but must be based on a good and representative life test program.
- 2) Uni-directional motion will result in eventual dry running of the toroid/ball interface leading to the premature failure of the toroid separators.
- 3) Bearing life test programs must use flight like hardware, not only for the bearings but also for the drive motors, encoders, electrical drivers and telemetry sensors. A flight-like Engineering Development Unit of the mechanism in other words. This would allow for a one to one comparison of life test data to on-orbit telemetry. Not doing so, results in a very difficult analysis task of any on-orbit data when anomalies occur.
- 4) Motion reversals are very effective in preventing or arresting the wear of bearing toroids. It is evident from the bearing test units and on-orbit data that reversals eventually lead to acceptable bearing performance. Depending on the state of toroid wear, initial reversal results may include 'spiky' behavior. However, data shows that eventually the bearings settle down into a near normal state. The SNPP on-orbit torque levels are now subsiding to near early orbit values, although with some spiky behavior.

### **Acknowledgements**

Every successful major project results from the combined efforts of many people. It is with great regret we don't have the space to list all of the many people who contributed time, effort, and talent to the ATMS Scan Drive program. Nonetheless, most of those who participated in the Scan Drive Life Extension program would agree that the following people were key to the success of this effort. Goddard Space Flight Center: Mark McClendon, Chris Hoffman, Robert Lambeck, Bruce Guenther, Jason Sturgis, Tom Manson, Harry Solomon, Tamara Oconnell, Michael Dube, Ed Dobbins, Dan Helfrich; NOAA: Brennan Nowak, Jim Waters, Ninghai Sun; Northrop Grumman Electronic Systems: Mike Landrum, Paul Schan, Victor Jacobo, Kent Anderson; Aerospace Corp: Tina Gentry, Neal Baker, Marc Wigdor, Joe Pope; Lincoln Labs: Vince Leslie

## References

- 1) Advanced Technology Microwave Sounder on NPOESS and NPP, Christina Muth, Paul Lee, Sergey Krimchansky, James Shiue, Allan Webb. NPOES IPO Information center, No. 06125, 06-16-2004, [http://140.90.86.6/IPOarchive/SCI/sensors/ATMSDraftBriefv4\\_AlanWebb.pdf](http://140.90.86.6/IPOarchive/SCI/sensors/ATMSDraftBriefv4_AlanWebb.pdf)
- 2) Design of the ATMS Scan Drive Mechanism, Curtis Allmon, Dave Putnam; Proceedings of the 38<sup>th</sup> Aerospace Mechanisms Symposium, Langley Research Center, May 17-19, 2006
- 3) Zhao-Zhu Zhang, et.al, "Effects of Various Kinds of Fillers on the Tribological Behavior of Polytetrafluoroethylene Composites under Dry and Oil-lubricated Conditions", J. of Applied Polymer Science, V80, #11, Jun 2001, pp. 1891-1897.



# Failure Analysis and Recovery of a 50-mm Highly Elastic Intermetallic NiTi Ball Bearing for an ISS Application

Christopher DellaCorte\*, S. Adam Howard\* and Lewis E. Moore III†

## Abstract

Ball bearings used inside the ISS Distillation Assembly centrifuge require superior corrosion and shock resistance to withstand acidic wastewater exposure and heavy spacecraft launch related loads. These requirements challenge conventional steel bearings and provide an ideal pathfinder application for 50-mm bore, deep-groove ball bearings made from the corrosion immune and highly elastic intermetallic material 60NiTi. During early ground testing in 2014 one 60NiTi bearing unexpectedly and catastrophically failed after operating for only 200 hr. A second bearing running on the same shaft was completely unaffected. An investigation into the root cause of the failure determined that an excessively tight press fit of the bearing outer race coupled with NiTi's relatively low elastic modulus were key contributing factors. The proposed failure mode was successfully replicated by experiment. To further corroborate the root cause theory, a successful bearing life test using improved installation practices (selective fitting) was conducted. The results show that NiTi bearings are suitable for space applications provided that care is taken to accommodate their unique material characteristics.

## Introduction

Bearings, gears and other mechanical components can be made from a wide variety of materials depending upon application requirements that typically include load, temperature, environment and cost [1, 2]. Often, one overriding performance requirement dictates that a specific material be selected. In cases where multiple requirements preclude certain classes of materials, practical designs can become difficult.

For instance, if a bearing must operate at high temperature but also be lightweight neither plastic nor steel would suffice. In such cases, the designer might have to turn to higher cost ceramics. Alternatively, the application requirements could be altered through system design changes to accommodate a lower cost material. A common engineering solution for the aforementioned high temperature example is to employ active cooling which enables the use of low-density plastics or non-ferrous alloys. Such accommodations themselves add cost and complexity and in many aerospace applications are not practical.

Another example where conventional bearing materials fall short are applications that simultaneously require extreme corrosion resistance and tolerance to severe static loads (shock events). Taken separately, these attributes can be found in austenitic stainless steels or superalloys (corrosion resistance) and ceramics or high carbide tool steels (shock load resistance). Taken together, these attributes cannot be provided by existing bearing materials [3].

Over the last decade NASA has been working to develop a new class of bearing materials based upon Nickel-Titanium to address these and other unmet challenges encountered in aeronautics and space mechanism bearing applications [4-6]. As an example, 60NiTi (60 weight% Ni, 40 weight% Ti) is hard, highly corrosion resistant, non-magnetic, electrically conductive, wear resistant, readily machined in the annealed state and exhibits good tribological properties. 60NiTi is also superelastic exhibiting a moderate

---

\* NASA Glenn Research Center, Cleveland, OH

† NASA Marshall Space Flight Center, Huntsville, AL

elastic modulus coupled with an ability to endure large strains elastically. The combination of excellent corrosion resistance and high dent resistance (arising from the high hardness, low modulus and superelasticity) distinguish 60NiTi from the tool steels and ceramics commonly used in bearings. Table I compares bearing relevant properties of 60NiTi to conventional materials.

**Table I. Thermophysical and mechanical properties of 60NiTi and other bearing materials**

Property	60NiTi	440C	Si <sub>3</sub> N <sub>4</sub>	M-50
Density	6.7 g/cc	7.7 g/cc	3.2 g/cc	8.0 g/cc
Hardness	56–62 Rc	58–62 Rc	1300–1500 Hv*	60–65Rc
Thermal Cond. W/m-°K	~9–14	24	33	~36
Thermal Expansion	~11.2×10 <sup>-6</sup> /°C	10×10 <sup>-6</sup> /°C	2.6×10 <sup>-6</sup>	~11×10 <sup>-6</sup> /°C
Magnetic	Non	Magnetic	Non	Magnetic
Corrosion Resistance	Acceptable (in acids)	Marginal	Acceptable	Poor
Tensile/Flexural Strength	~1000/1500 MPa	1900 MPa	600–1200 MPa (Bend Strength)	2500 MPa
Young's Modulus	~90–115 GPa	200 GPa	310 GPa	210 GPa
Poisson's Ratio	~0.34	0.30	0.27	0.30
Fracture Toughness	~20 MPa/√m	22 MPa/√m	5–7 MPa/√m	20–23 MPa/√m
Max. Use Temp	~400 °C	~400 °C	~1100 °C	~400 °C
Elect. Resistivity	~1.04×10 <sup>-6</sup> Ω-m	~0.60×10 <sup>-6</sup> Ω-m	Insulator	~0.18×10 <sup>-6</sup> Ω-m

\*Vicker's hardness, Hv, is a scale used for ceramic materials with hardness values beyond HRC 75.

A NASA application requiring corrosion resistance and high load capacity is inside the International Space Station (ISS) Urine Processor Distillation Assembly [7]. The Urine Processor Distillation Assembly (DA) is a key component of the wastewater treatment system on the ISS. The DA functions as a rotating still that processes waste fluids into steam (gaseous water). Figure 1 shows a cross section of the Urine Processor [8]. It consists of a rotating drum made from titanium alloy supported on a pair of 50-mm ball bearings and is driven by a motor at a constant speed of 200 rpm. The wastewater is introduced into the drum through a feed tube. Through centrifugal action, the rotating motion of the drum forces the wastewater into contact with the drum walls. The drum walls are heated and this boils the wastewater, forming steam that is drawn from the evaporator drum, condensed and then further treated downstream into clean water. The 50-mm bore ball bearings that support the rotating drum are directly exposed to the acidic wastewater and the steam environment and have experienced corrosion problems when made from steel. The use of NiTi is intended to avoid the corrosion problems yet provide good load capacity and wear life.

In a previous test and development program, 60NiTi ball bearings were designed and fabricated for use in the DA centrifuge [9]. Corrosion tests were performed to confirm the chemical compatibility with the wastewater environment and static load experiments were done to show that the bearings would endure anticipated launch loads. As a proof of concept, short-term (~20 hr) bearing tests were run in a simulator test rig that duplicated the load, speed, temperature and moisture conditions found inside the DA, albeit without the low pH acidic fluid nature. These tests were successful and a flight bearing project was initiated.

During the ground test phase of the project, a pair of 60NiTi centrifuge bearings were installed in a fully operational DA and placed into a long-term test program intended to run for up to 2000 hr. After only 200 hr, nickel and titanium particles were observed in the process fluid filtration system. After 235 hr of run time audible bearing noise was emanating from the centrifuge and the test was halted. An inspection revealed catastrophic failure of the hub-side (left side in Figure 1) 60NiTi centrifuge bearing. The second bearing of the pair, which operated on the same shaft on the motor-side of the DA, remained in good condition and showed no signs of distress. In the following sections of this paper, the results of the hub-



side bearing failure investigation are presented along with the development of the likely root cause and failure recovery.

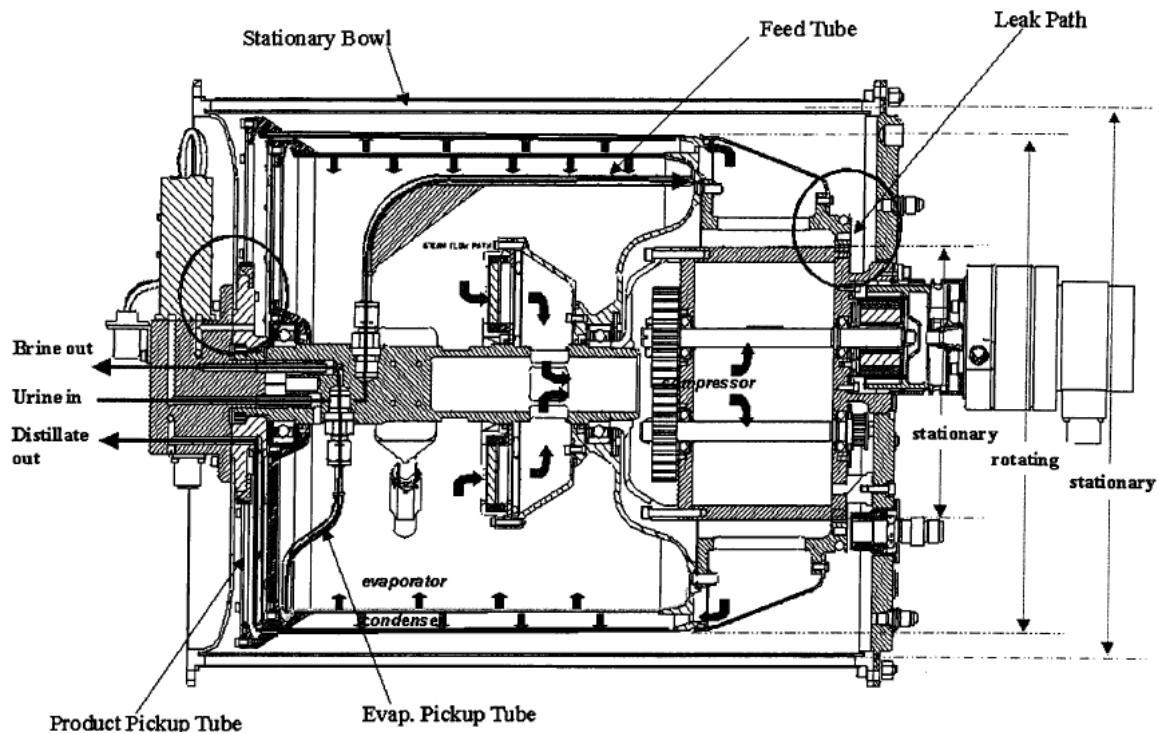


Figure 1. Representative ISS Distillation Assembly cross-section taken from reference 8

### Bearing Design and Operating Conditions

Table II lists the nominal operating conditions and the bearing characteristics for the 50-mm bearings. The load on both bearings comes primarily from the preload wave spring. The outer races use an interference press fit into the drum end walls and the inner races slide over the shaft with a small clearance.

Table II. Representative Application Bearing Parameters and Operating Conditions

Parameter	Value or Condition
Outer Diameter, OD	~80 mm
Inner Diameter, ID	~50 mm
Width, W	~16 mm
Ball Size, D	~9 mm
Ball Material	Si <sub>3</sub> N <sub>4</sub>
Race Material	60NiTi
Cage	Snap fit, polymer
Lubricant	Lithium based grease
Ball-Race Stress Limit	~3.1 GPa
Ball-Race Mean Stress	~1 GPa
Axial Preload	~200 N
Radial Load (terrestrial)	~100 N/bearing
Speed	100-300 rpm
Environment	Warm, highly acidic aqueous solution
Ambient Pressure	Slight vacuum

The operating loads and speeds are low for a 50-mm bearing. In this application, the bearing size was largely dictated by the need to accommodate a large, stationary hollow shaft that houses electrical and fluid flow passageways into and out of the drum assembly. Other than potentially severe vibration loads (~3 g or higher) during a rocket launch, the operating conditions are characterized as mechanically benign and chemically aggressive. Since the 60NiTi alloy had previously been shown to be impervious to the acidic wastewater, the premature bearing failure was unexpected.

### Hardware Observations and Other Forensic Evidence

The presence of nickel-titanium wear debris trapped by the DA filter screens indicated that bearing wear had occurred prior to failure. Following test termination, the hub-side end wall plate of the DA was removed making one face of the bearing visible. Figure 2 shows the view from the hub-side of the DA looking towards the motor-side.

Based upon this image alone, one plausible preliminary failure scenario is that the inner race fractured and caused more generalized damage and wear as the test continued. A close up image of the inner race fracture, shown in Figure 3, offers additional clues to the behavior of the 60NiTi.

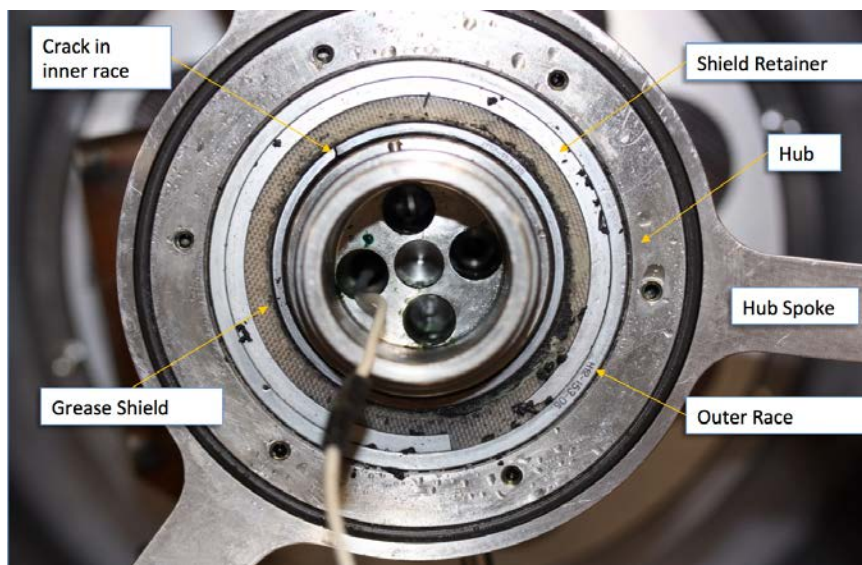


**Figure 2. Hub-side view of failed ISS Distillation Assembly centrifuge bearing. Note cracked inner race and ejected wear debris**

The inner race appears to have sprung radially outward from the DA shaft to the left side of the crack and a significant gap has opened between the faces of the crack. This behavior suggests that the inner ring had been under considerable residual stresses and these may have been a factor in the bearing failure.

Indeed, the bearing manufacturing process for 60NiTi includes a rapid water quench step following heat treatment at 1000 °C [9]. This rapid cooling results in the rise of residual thermal stresses. Unlike steels and other metals in which such residual stresses can be relieved by soaking the parts at elevated temperatures, NiTi has no mechanism for internal atomic level slip. The residual stresses that remain after the quenching step cannot be relieved through additional thermal treatments and these stresses may be a factor in undesirable effects like ring cracks [10, 11].

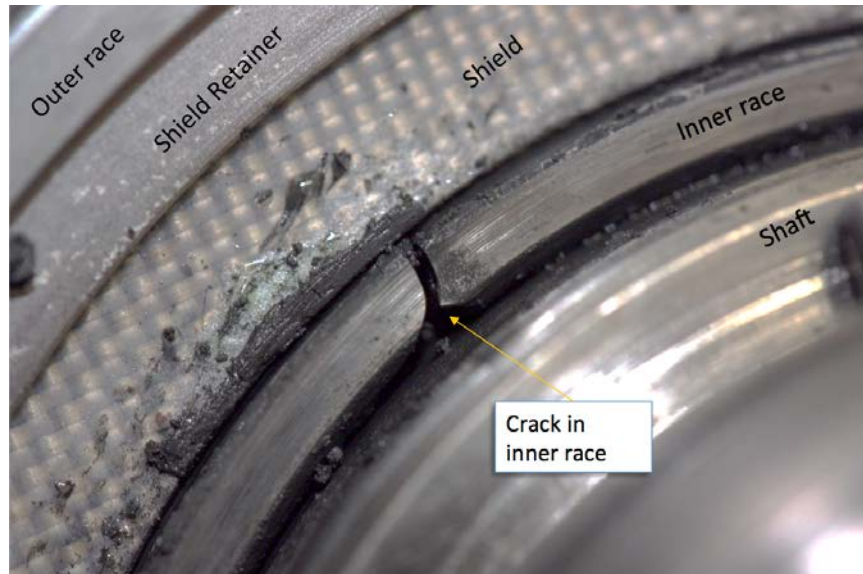


**Figure 3. Close-up view of cracked inner race**

A similar bearing ring crack was observed during prototype bearing development. A bearing had been successfully tested, removed from the test rig and inspected. The bearing was in as-new condition and was placed in storage. Several weeks later, the inner ring developed a crack similar to the one observed in the present case. Figure 4 shows that inner ring crack.

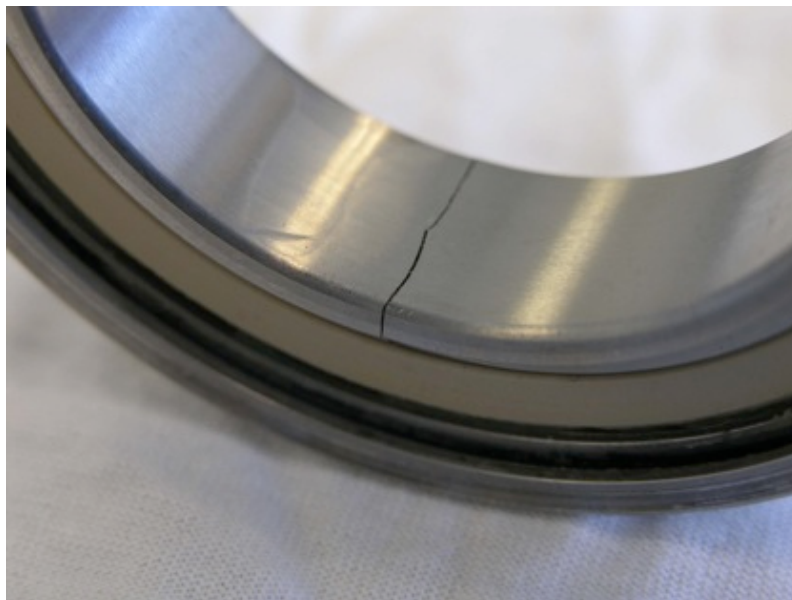


**Figure 4. Photo of an early prototype bearing that developed an inner race crack during post-test storage**

In this instance, forensic analyses showed that the early prototype 60NiTi material used in this bearing contained significant non-metallic inclusions and other internal flaws that could have triggered the crack. In addition, the bearing was damaged during final machining of the inside surface of the inner ring. Adjacent to the fracture location, a low spot and a deep gouge are observed. This damage was a

manufacturing flaw that resulted from the inner ring becoming loose in the machining fixture. Thus this post-test ring crack was attributed to the known material and machining flaws [11].

For the bearing failure that is the subject of the current paper, the material was known to be of the highest quality and absent of similar dimensional errors (low spots) or manufacturing flaws. To fully understand the present bearing failure more detailed information regarding the application and installation are needed.

The bearings were dimensionally characterized two times: once during manufacture by the bearing finisher and once immediately prior to installation by the NASA MSFC Tribology Lab. In general, both bearings were found to be within specification for all major diameters and widths, raceway curvatures and surface finishes. All of the construction materials (balls, cages, race material, etc.) were fully certified for quality. Visual inspection of the bearings revealed no observable flaws and both bearings turned smoothly. The only significant discrepancy between the bearing finisher's dimensions and those from the MSFC lab pertained to the bearings' outside diameter and roundness. The MSFC lab noted that the bearing outer race roundness values were affected by the installation of the grease shield retaining wires. These "C" shaped retaining wires are pre-compressed and then installed in a groove machined in the outer bearing race adjacent to the shield. The wires apply a small expansion load on the outer race causing it to become non-circular (slightly oval). This rather surprising observation is likely the result of the relatively low elastic modulus of the 60NiTi. In any case, the magnitude of the roundness variation was small (less than 0.0002 in or 5  $\mu\text{m}$ ) and deemed unlikely to affect the bearing operation once confined (pressed into) by the DA hub structure.

Unfortunately, the failed bearing could not be removed from the DA intact. Disassembly forces fractured the outer race into several pieces making forensic interpretation of the damage impossible. Further, since the DA was operated long after significant bearing damage (wear debris detection on filters) began; it is difficult to judge the failure mechanism from the severely damaged bearing. The second test bearing (the motor side) that did not fail was in the same condition as prior to test.

Dimensional measurements were then made of the DA bearing-machine interfaces and compared to specifications and to the pre-test bearing dimensions to assess whether the bearing-machine fits were correct. Table III shows the major dimensions of the bearings and their relation to installation fits in the DA.

**Table III. DA Bearing Overall Fit and Housing Dimensional Measurements, inches**

Parameter	Specification	Hub-side bearing	Hub-side bearing fit	Motor-side bearing	Motor-side bearing fit
Outer race outside diameter	3.14960 max 3.14910 min	3.14987	+0.0011 interference	3.14956	+0.0007 interference
Inner race inside diameter	1.9685 max 1.9680 min	1.9681	-0.0007 clearance	1.9681	-0.0005 clearance
Bearing width	0.630 max 0.629 min	0.6296	----	0.6298	----
Radial clearance	0.0014 max 0.0007 min	0.0008	----	0.0008	----

Evaluation of the data in Table III reveals that the failed hub-side bearing's outer diameter was not within specification. Careful measurements were made at two angular locations and at three different width locations. The average is shown in the table. The assembled bearing was under the maximum allowed diameter by approximately 0.0003 in (7.6  $\mu\text{m}$ ) at one angular location and over the maximum by 0.0009 in (23  $\mu\text{m}$ ) at the other location. The averaged diameter of the hub-side bearing was greater than the maximum allowed by approximately 0.0003 in (7.6  $\mu\text{m}$ ). In addition, measurements of the mating DA hub

bore showed that its diameter was undersized by approximately 0.0005 in (13  $\mu\text{m}$ ). As installed, this bearing experienced an interference fit with the hub-side housing bore of 0.0011 in (28  $\mu\text{m}$ ). This heavy interference fit was outside the design range (0.0001 in ( $\mu\text{m}$ )) clearance to 0.0006 in (15  $\mu\text{m}$ ) interference) and may be a contributing factor in the bearing failure.

Like the hub-side bearing, the motor-side bearing also had an outside diameter that varied by approximately 0.0006 inch (15  $\mu\text{m}$ ) but with an average diameter slightly below the maximum allowed. The motor-side bearing housing diameter was larger than the hub-side bearing housing diameter and was within the specified design range. Taken together, the hub-side bearing, which did fail, was substantially tighter in its DA housing than the motor-side bearing, which did not fail. To evaluate whether these bearing fit differences alone contributed to the failure requires a closer examination of the mating hardware and the stresses and deformation that arise from the installed fits. In particular, it is elucidating to examine any other structural differences between the two bearing locations to determine if other differences such as operating loads exist that could have led to one bearing failing while the other performed well.

### **Other Differences between Hub and Motor Side Bearing Locations**

The hub-side bearing is axially loaded against the motor-side bearing using a calibrated wave spring set to approximately 40 lb (178 N). This is the primary bearing load and results in an average Hertz ball-race contact stress level of approximately 180 Ksi (1240 MPa). In ground testing, the weight of the drum rests on the bearings and can add approximately 20 lb (89 N). In addition, a very small radial load (10 lb (44 N)) is imparted by an O-ring drive belt located slightly outboard of the motor side bearing. Taken together, these loads are considered very low for such a large ball bearing. In effect, both bearings experience similar and low loads that are not likely a contributing factor in the failure.

Aside from the differing levels of interference fits, the most obvious difference between the motor and hub-side bearing locations is the structural design of the housings. As shown in Figures 1 and 5, the motor-side bearing housing has an axial symmetric bowl shape while the hub-side bearing housing is comprised of a shallow cylinder supported by a three-spoke flat plate. The spoke design provides ready physical access to the central portion of the drum to enable the installation of piping and other internal elements. Figure 5(c), for example, shows a close-up view of the hub-side of the drum where a fluid pick-up tube is visible. To determine whether the differences between the hub and motor side housing structures were a contributing factor in the bearing failure, a finite element based analysis was undertaken.

### **Bearing Installation Fit Considerations - Structural Analysis**

The interference (press) fit of a bearing into the bowl-shaped motor-side housing results in the circumferentially uniform compression of the bearing outer race. For steel bearing races, the typical rule of thumb is that the bearing diameter will be reduced by approximately 80% of the fit interference [12]. Since the elastic modulus of NiTi is half that of steel, it is expected that the bearing diameter reduction will be at least this amount, or possibly more. For the motor-side bearing which was known to have an interference level of 0.0007 in (18  $\mu\text{m}$ ), we estimate a reduction of about 0.0006 in (15  $\mu\text{m}$ ). This level is slightly less than the bearing's internal clearance (0.0008 in (20  $\mu\text{m}$ )) thus leaving an installed clearance of about 0.0002 in (5  $\mu\text{m}$ ).

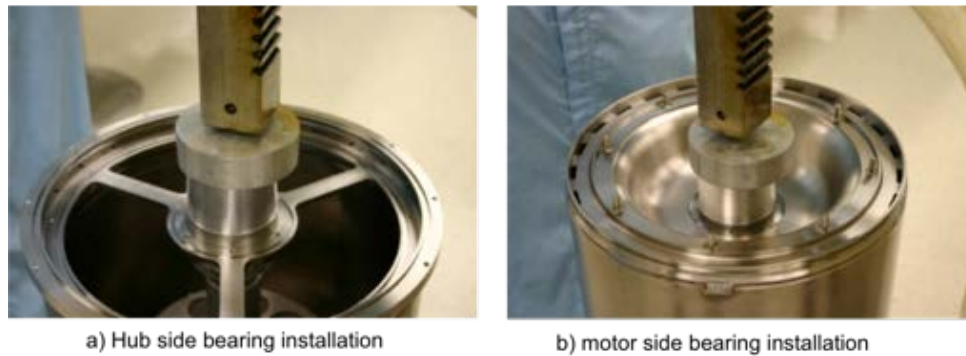


**Figure 5. End views of DA drum shown during bearing installation. Hub side bearing housing structure (a) differs significantly from motor side (b).**



**Figure 5(c). Close up end views of hub-side of DA drum showing how the spoke design allows ready access for assembly. Photo taken from [7].**

For the hub-side bearing the situation is more nuanced. The known interference fit is larger, 0.0011 in (28  $\mu\text{m}$ ). This level of press fit into a circumferentially symmetric and relatively rigid housing would be expected to reduce the bearing diameter by about 0.0009 in (23  $\mu\text{m}$ ). This level is greater than the known bearing internal clearance (0.0008 in (20  $\mu\text{m}$ )) resulting in the bearing having no internal clearance and indeed the balls and the inner race would be under a preload by the outer race. This in itself is an undesirable condition that may factor into the hub-side bearing failure. However, the circumferentially non-uniform spoke structure supporting the hub-side bearing housing may cause additional problems in that the installed bearing outer race may not be compressed uniformly.

To estimate the magnitude of the deformations of the hub-side bearing outer race, a finite element model was developed. Figure 6 displays the model result for the axial deformation of the hub-side three-spoke structure under a greater than normal 200-lb (890-N) axial load. The normal axial load for the DA is only 40 lb (178 N). The 200-lb (890-N) case was run to determine whether axial deformation arising from the spring preload could possibly distort the hub-housing geometry. The result was clear. Even under exacerbated axial load the housing shape remains round. It was noted, however, that significant axial deformation of the spokes occurs even under the 40-lb (178-N) design load. This deformation effectively reduces the axial preload through reduction of the distance between the outer races of the hub and



motor-side bearings. Thus if the wave spring height reduction is used to set preload, it is likely that the installed preload will be lower than expected by about 10%.

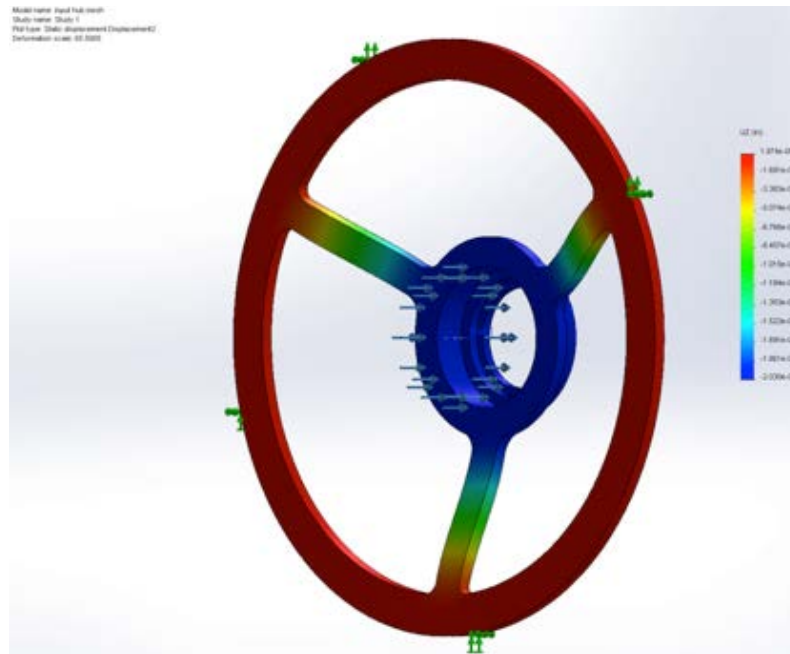


**Figure 6. Finite element deformation of the DA hub side structure in response to a large (200-lb (890-N)) axial load. Note that the hub bore remains round**

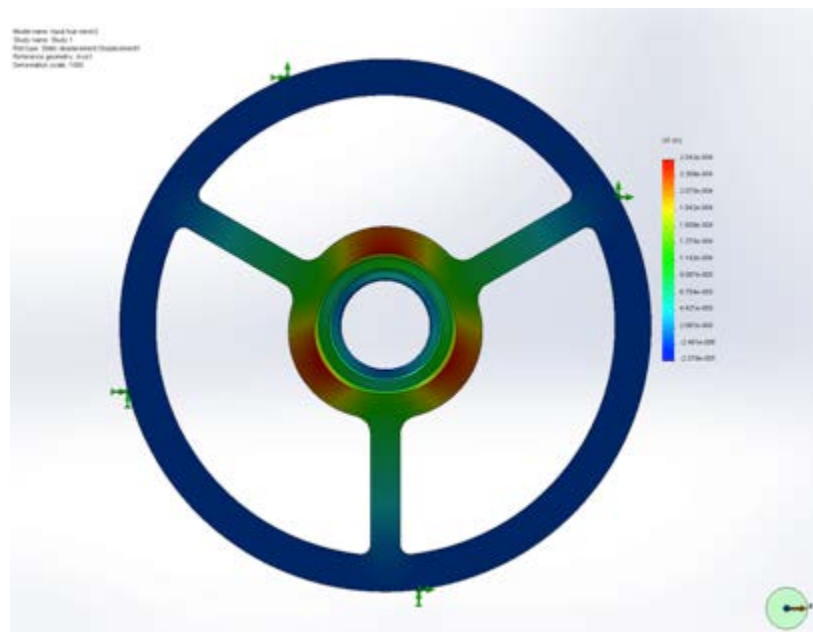


**Figure 7. Finite element deformation of the DA hub side structure into which a bearing is installed with a heavy (0.0011 in/28  $\mu$ m) press fit. Note that the three spoke locations provide high rigidity leading to an irregular bore shape**

The second case examined was for a heavy interference press fit (0.0011 in (28  $\mu\text{m}$ ) diameter difference) of a round bearing into the circular hub-side housing bore. Figure 7 shows the result.

At the spoke locations, the bearing outer race diameter is reduced by approximately the same magnitude as the bearing clearance and the less rigid housing sections between the spokes allows the bearing housing to take on a tri-lobe shape with radial variation of approximately 0.0002 in (5  $\mu\text{m}$ ). Such roundness variation combined with the loss of internal clearance could be responsible for the rapid bearing failure. To corroborate such a root cause theory, however, requires experimental verification.

### **Bearing Testing-Experimental Corroboration of Failure Theory**

The failure of the hub-side bearing in the DA centrifuge after only 200 hr of operation was not anticipated. The operating speed was low (200 rpm) as were the applied external loads. Short-term testing of 60NiTi centrifuge bearings had not surfaced any problems and long-term sub-component 3 ball-on-rod rolling contact fatigue tests suggest infinite life at the design stress levels [13]. However, no long-term life test of a full-scale DA centrifuge bearing had been conducted prior to the failure. Therefore, any bearing tests carried out to corroborate a root cause theory must achieve two goals. First, a bearing test under similar conditions as the failure mode must produce a similar failure in a similar test period. Second, the full-scale, long-term bearing life test under normal design conditions must be done to show that if the factors that contributed to the early failure are ameliorated, long bearing life ensues.

To achieve these two test goals, a series of experiments were conducted in the NASA Glenn DA bearing test rig. This test rig, described in an earlier report on the bearing design and fabrication process, mimics the centrifuge speed, load and other mechanical conditions and can be run continuously and unattended [9]. It does not include the aggressive chemical (wastewater) environment but given 60NiTi's excellent corrosion resistance, the absence of the warm wastewater is not believed to be a failure contributor. The rig is shown in Figure 8.

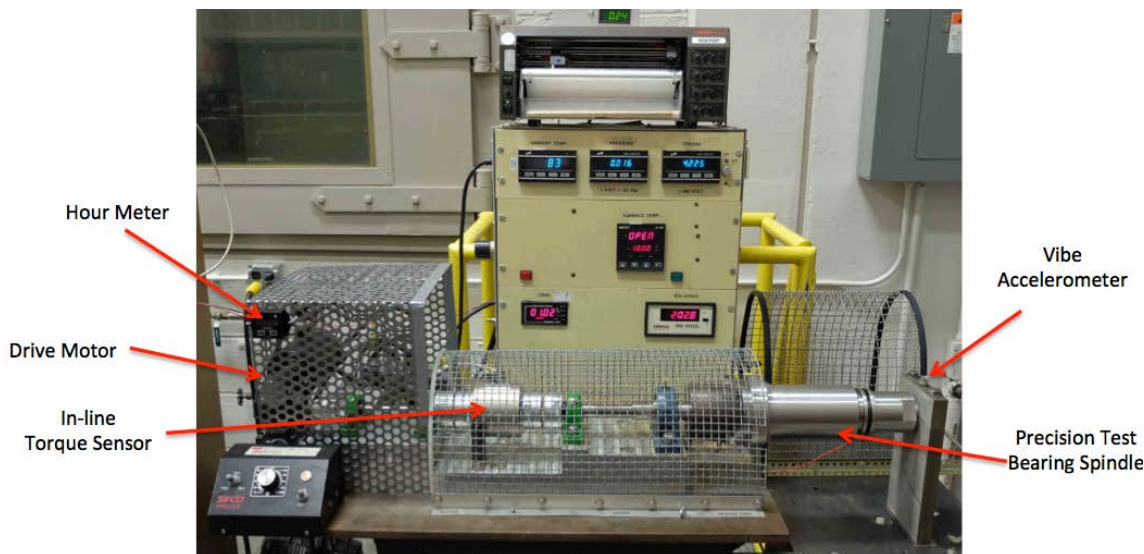


**Figure 8. NASA Glenn's DA centrifuge bearing test rig. The present failure corroboration tests are run without water and heat.**



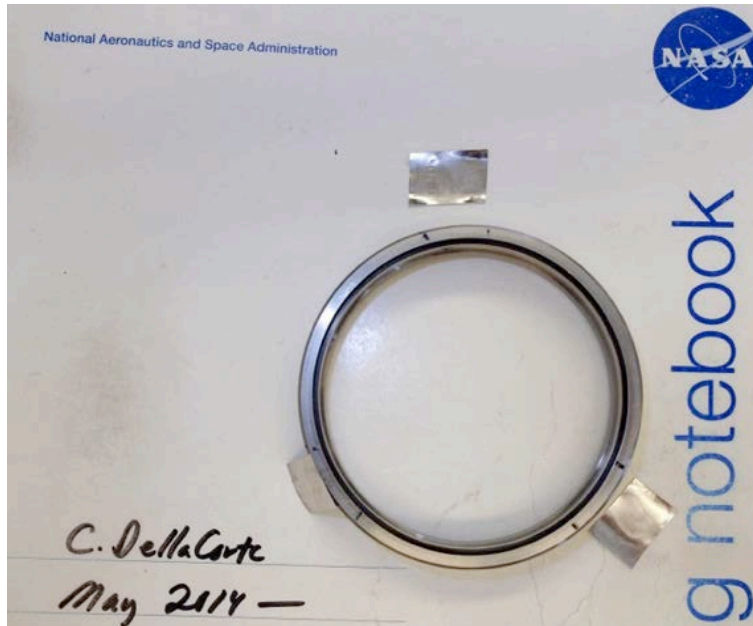


**Figure 9. Shims used to deform the bearing outer race to match operating conditions in the DA that lead to the premature failure**

The first test undertaken was to duplicate the hub-side bearing fit conditions that are believed to have caused the premature bearing failure. This could be achieved by manufacturing a new test rig bearing housing with the same three spoke structure and fit as the DA. Instead, a simplified approach was used that did not require extensive fabrication. The existing cylindrical housing was retained and three small pieces of stainless steel shim stock were placed between the bearing outer race and the housing. These three shims were approximately the same circumferential length and depth as the DA spokes. The shim thickness was selected to deform the bearing outer race approximately the same magnitude as the DA hub side housing. The use of shims is not an exact simulation of the physical race deformations in the DA but it is a fair approximation of the clearance reduction and tri-lobe shape variation. Figure 9 shows a photograph of the bearing outer race and the three shims used for the deformation experiment.

Prior to bearing installation, the shims were affixed to the bearing outside diameter at three equally spaced locations ( $120^\circ$  apart). The bearing housing was warmed to allow a slip fit of the shimmed bearing so as to ensure that the shims were not dislodged. The second test bearing used (simulating the motor-side bearing) was fit normally into the housing with no shims. Despite the shims, the bearings turned smoothly and quietly with low torque. The test began and was monitored for torque once daily.

After 150 hr of test time the bearings continued to turn smoothly. At 157 hr an audible noise was noted and the torque sensor indicated a measurable torque ripple. The test was stopped and the bearings were removed, disassembled and inspected. The shimmed bearing had suffered from fatigue damage. The grease was discolored and wear debris was observed. The fatigue damage resulted in deep raceway pits and spall craters. These were located in the regions that overlapped the shims. The other test bearing that was not shimmed showed no signs of damage. Figure 10 is a close up photograph of the raceway surface of the shimmed outer race after test. Significant surface pitting and spall regions are present. The inner race also showed signs of surface distress (small pits) but it was uniformly distributed around the raceway and less severe.

In the largest spall crater, approximately 4 mm in diameter, cross-race cracks had developed. In some places these cracks had propagated to the outer surface of the race as shown in Figure 11.

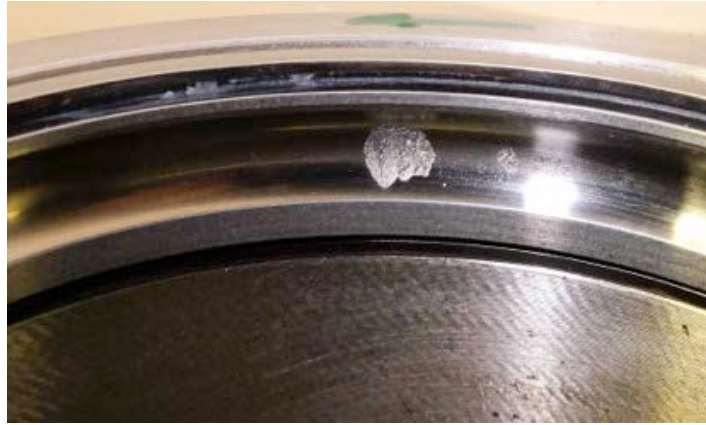


**Figure 10. Raceway pit developed during shimmed bearing test after 157 hr of run-time**

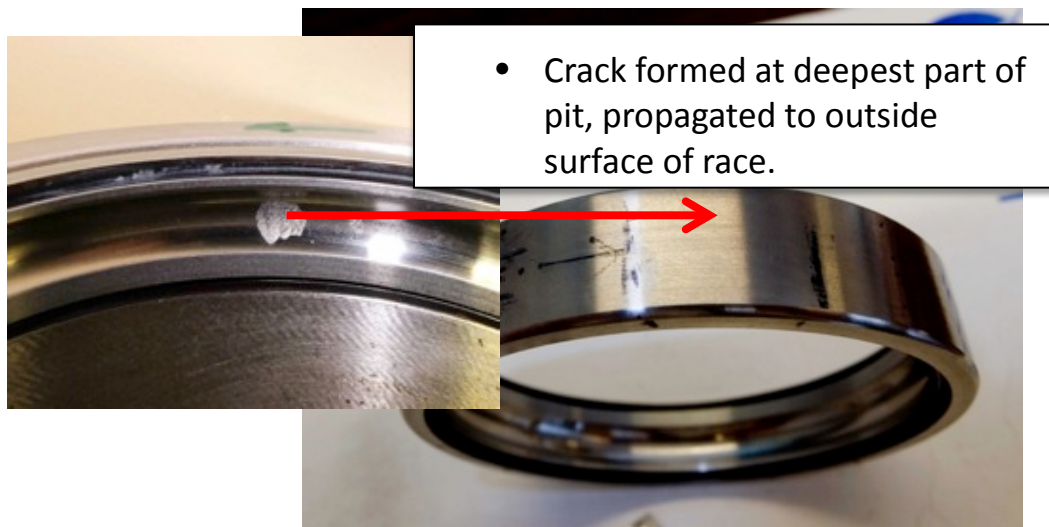


**Figure 11. Crack originating in the fatigue spall on raceway has propagated to the outer surface of the race after 157 hr of run-time**

If this test been allowed to run longer it is reasonable to expect the damage to progress possibly until the race cracked through completely. Upon reflection, it is possible that the failure path for the DA bearing was surface fatigue followed by pit growth, crack formation and propagation and finally, race fracture. At the onset of the investigation, one theory was that the raceway residual stresses had led to ring fracture and subsequent bearing wear and debris generation. Based upon the shimmed bearing experiment, it appears that ring fracture may have been the final step, not the initiation step.

The second test undertaken was to prove that the 60NiTi bearings have the ability to run for a long-term test without failure, providing they are installed with fits and clearances well accepted as good industry practices. To conduct this test, a pair of flight quality 60NiTi bearings was carefully inspected, cleaned and lubricated. The pair was then installed into the NASA Glenn test rig with fits within the specified design range. The inner races had a clearance (shaft to bearing diameter) of 0.0005 in (13  $\mu\text{m}$ ) and the outer races had a slight interference fit of 0.0003 in (7.6  $\mu\text{m}$ ). In our test rig, the outer race housing does not have spokes, thus any outer race deformation is circumferentially symmetric.

In addition, an accelerometer was installed on the stationary inner shaft to monitor the rig vibration. Once each hour the full frequency range (sub-hertz to 100 Hz) is collected and stored. Comparison of these spectra over the course of the test allow for careful health monitoring. Any vibration growth at relevant frequencies (e.g., at the run speed, ball pass frequencies, cage frequency) would be cause for bearing inspection. Figure 12 shows a representative cascade plot of hourly vibration spectra collected over a three-day test period.

The cascade vibration plot provides a convenient visual method to judge bearing condition. Each peak in the spectra corresponds to different aspects of the test rig and test bearing. For example, vibration at the rig speed (3.2 Hz or 200 rpm) would arise from any anomaly associated with the drive motor, couplings or drive shafts. Vibrations generated by the test rig support bearings arise at 22 Hz owing to the number of rolling elements and internal geometry of these bearings. The test rig structure has some activity at 37 Hz. A key test bearing frequency for health monitoring is 24 Hz. This frequency represents the ball pass frequency on the inner race. Slight roundness and other variations will lead to vibration at this frequency. Any significant increase in the amplitude at 24 Hz could signal raceway surface damage in the ball path. Thus the cascade plot serves as a snapshot of bearing health.

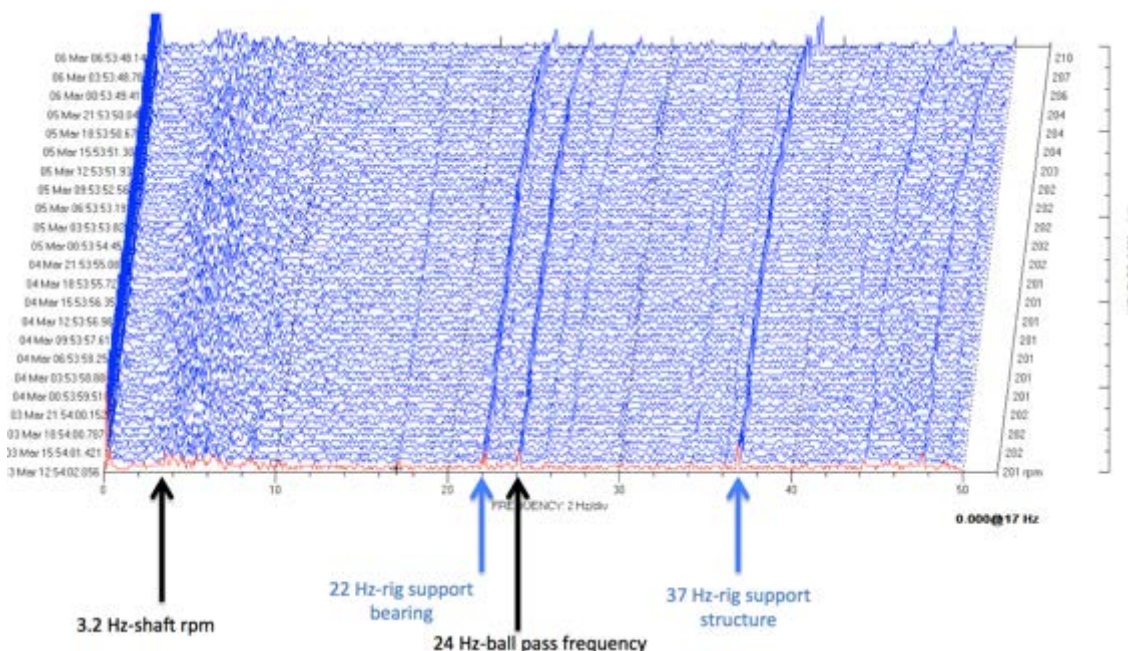


**Figure 12. Cascade plot of hourly test rig vibration spectra captured during a three-day test period. Overall vibrations are very low and consistent**

Prior to the start of this second test, the bearings were disassembled, solvent cleaned, visually inspected, reassembled and greased (30% fill of the free-volume) with a lithium complex synthetic grease. The bearings were then installed into the test rig and the preload spring was adjusted to 90-lb (400-N) preload to match the preload level generally recommended by bearing manufacturers for this size bearing [12]. This preload is higher than the application design preload (40 lb / 178 N) but that lower load level was selected based upon the more modest static load capability of the prior bearing material made from a softer cobalt alloy [9]. Further, the higher load level may offer an acceleration of any fatigue failure modes. Thus, if the bearings indeed survive the life test, the root cause theory and recovery path is better substantiated.

The life test was begun and vibration data collected. At first there was a noticeable torque ripple measured. After a few hours of run time the torque ripple subsided and the cascade plot stabilized



probably because the grease had become more uniformly distributed in the bearing. The life-test period is 5000 hr. Once during test period (1075 hr) a bearing inspection was conducted. Figure 13 shows images of one of the bearings during the interim inspection.

During the inspection the races were examined under 10x optical magnification and appeared to be in excellent condition. They exhibited no surface pits, scratches or wear tracks. Also, the retainer was unworn and the grease color and consistency was the same as the beginning-of-test. Following the inspection, the bearings were solvent cleaned, re-greased and installed back into the test rig. After a few hours of operation the torque ripple subsided leaving a vibration spectra that resembled one from before the inspection.



**Figure 13. Photograph of the test bearing during an interim inspection at 1075 hr. Overall condition of the bearing races, balls and retainer was unchanged from beginning of test. The grease consistency and color was also unchanged**

The life-test concluded at 5000 hr because it met the project requirement. More important, the successful life test helps to corroborate the root cause theory by showing that a set of bearings, when properly fit into the machine structure can operate without failure for long periods.

#### **Root Cause Failure Theory and Recovery Plan**

The forensic examination of the failed bearing, subsequent measurements of the related machine hardware, and corroborative bearing tests supports the root cause theory that an overly tight interference press fit and a non-symmetric housing structure led to surface fatigue damage to the 60NiTi bearing. The

surface damage then progressed until the inner race cracked through its thickness and the operation was suspended. To avoid this failure mode the following remediation steps are indicated.

Selective fitting of the bearings, especially in the hub-side DA housing, should be done to seek a fit in which the bearing outside diameter and the hub bore diameter are as closely matched as possible. The design calls for a range of 0.0001 in (2.5  $\mu\text{m}$ ) clearance to 0.0006 in (15  $\mu\text{m}$ ) interference. Another approach is to manufacture bearings with varying diameters to accommodate future DA machines with less or no interference thus avoiding the deleterious effects of outer race distortion and loss of internal clearance. Furthermore, bearings with larger internal clearances can be used so that any outer race press fit will not result in a significant or even complete loss of internal ball-to-race clearance. Conversely, bearing designs less sensitive to internal clearance variations, such as angular contact bearings, could be considered.

### **Concluding Remarks**

NiTi bearing technology is still relatively immature. Therefore, when problems such as this unexpected bearing failure arise, it is natural to infer that the new material is a cause. Indeed in this case, the low elastic modulus of 60NiTi compared to steel results in more pronounced race deformation due to hub bore interface effects like shape and diameter interference. It is possible that a similarly dimensioned steel bearing would not have failed because the outer race deformations would have been smaller.

For these reasons, it is essential that extra care be taken when using 60NiTi bearings to ensure that all industry accepted engineering and application practices are followed. Going forward, it is likely that the experience base for the use of these materials will grow and this will support the emergence of new best practices. By adopting these practices, the mechanisms community will be able to capitalize on NiTi's excellent corrosion resistance and static load capability properties.

### **Acknowledgments**

The authors wish to thank Anita Howard, Walt Schneider and Mike Perry of the NASA Marshall Space Flight Center for their thoughtful technical input. We thank Walt Wozniak and Steve Miller at the NASA Glenn Research Center for their technical efforts to build the test hardware to corroborate the root cause theory. Finally, we thank NASA Glenn's Penni Dalton for her steadfast project management support and for standing behind our progress despite setbacks and other challenges. We have benefitted from the perseverance and dedication of these colleagues.

## References

1. W.J. Derner and E.E. Pfaffenberger: "Rolling Element Bearings," in CRC Handbook of Lubrication, volume II, pages 495-537, edited by E.R. Booser, CRC Press, Boca Raton, 1983.
2. J.L. Radovich: "Gears", in CRC Handbook of Lubrication, volume II, pages 539-564, edited by E.R. Booser, CRC Press, Boca Raton, 1983.
3. C. DellaCorte: "Novel Superelastic Materials for Advanced Bearing Applications", Presented at 13th International Ceramics Conference of CIMTECH 2014, Montecatini, Italy, June 8-13. Published in Advances in Science and Technology, volume 89 (2014), pp 1-9, 2014.
4. C. DellaCorte, S. V. Pepper, R. D. Noebe, D.R. Hull, and G. Glennon: "Intermetallic Nickel-Titanium Alloys for Oil-Lubrication Bearing Applications," NASA TM-2009-215646, March 2009.
5. S. V. Pepper, C. DellaCorte, R. D. Noebe, D.R. Hull, and G. Glennon: "Nitinol 60 as a Material for Spacecraft Triboelements," ESMATS 13 Conference, Vienna, Austria, September 2009.
6. C. DellaCorte, R.D. Noebe, M.K. Stanford, and S.A. Padula: "Resilient and Corrosion-Proof Rolling Element Bearings Made From Superelastic Ni-Ti Alloys for Aerospace Mechanism Applications," NASA TM-2011-217105, September 2012.
7. D.L. Carter: "Status of the Regenerative ECLSS Water Recovery System", Paper number M10-0762, AIAA International Conference on Environmental Systems; 11-16 July, Barcelona, Spain, 2010.
8. D.W. Holder and C.F. Hutchens: "Development Status of the International Space Station Urine Processor Assembly," SAE 2003-01-2690, 33rd International Conference on Environmental Systems, July 7-10, Vancouver British Columbia, 2003.
9. C. DellaCorte, and W.A. Wozniak: "Design and Manufacturing Considerations for Shockproof and Corrosion-Immune Superelastic Nickel-Titanium Bearings for a Space Station Application", NASA TM 2012-216015, presented at the 41st Aerospace Mechanisms Symposium, Pasadena, CA, May 2012.
10. M.K. Stanford, F. Thomas, and C. DellaCorte: "Processing Issues for Preliminary Melts of the Intermetallic Compound 60-NITINOL," NASA TM-2012-216044, November 2012.
11. M.K. Stanford, W.A. Wozniak, and T.R. McCue: "Addressing Machining Issues for the Intermetallic Compound 60-NITINOL," NASA TM-2012-216027, August 2012.
12. Barden Super Precision Ball Bearings Catalogue, D/SPC/1/USA/113/T, Danbury, CT, 2013.
13. C. DellaCorte, M.K. Stanford, and T.R. Jett: "Rolling Contact Fatigue of Superelastic Intermetallic Materials (SIM) for Use as Resilient and Corrosion Resistant Bearings," Tribology Letters, (2015) 57:26, January 23<sup>rd</sup>, 2015.

# Ball Bearing Analysis with the ORBIS Tool

Jacob D. Halpin\*

## Abstract

Ball bearing design is critical to the success of aerospace mechanisms. Key bearing performance parameters, such as load capability, stiffness, torque, and life all depend on accurate determination of the internal load distribution. Hence, a good analytical bearing tool that provides both comprehensive capabilities and reliable results becomes a significant asset to the engineer. This paper introduces the ORBIS bearing tool. A discussion of key modeling assumptions and a technical overview is provided. Numerous validation studies and case studies using the ORBIS tool are presented. All results suggest the ORBIS code closely correlates to predictions on bearing internal load distributions, stiffness, deflection and stresses.

## Introduction

ORBIS was first released to the public in 2008 and has been actively maintained and enhanced since. The program was developed to modernize the state-of-the-art for bearing codes. Most prior industry standard tools came from the MS-DOS era and required a flat-file type input deck for operation. While these codes pioneered the analytical bearing industry they required a fairly steep learning curve to operate proficiently. With the advent of 64-bit processors in modern computer technology, support for MS-DOS has declined rapidly leaving software programmers with the burden to update their codes. Unfortunately, many developers of the early bearing tools are no longer around to maintain their codes.

The development approach for ORBIS began with selection of the Java programming language for its foundation. Java was initially selected because it runs on a virtual machine that is supported by most computer platforms (i.e., Windows, Mac OS, Unix). Also, the widespread popularity of Java over the internet gave confidence that it would be actively supported for many years to come. Some additional fringe benefits of the Java language that proved particularly useful during the development stages were its object-oriented programming environment and support of multi-threaded processing.

The core bearing model used within ORBIS is based on A. B. Jones' mathematical theory of rolling element bearings [1]; herein referred to as the Jones model. This model provides a nonlinear solution to an entire system of bearings and has been the industry standard for many decades. The primary handicap to the Jones model is its inherent fixed ring assumption. This assumption is generally not tolerable for modern aerospace bearing designs, particularly those that utilize thin section bearings. ORBIS addresses this by including ring compliance algorithms into the core solver. These algorithms determine ring strain during the mounting, preloading, and thermal expansion stages of the solver, thereby greatly improving model accuracy. A more thorough discussion on key bearing modeling assumptions is provided herein.

To validate the ORBIS code a multi-tiered approach is taken. First, the core solver is compared against the A. B. Jones High Speed Ball and Roller Bearing Analysis Program. This comparison study includes twenty-nine different configurations and results such as maximum mean Hertzian contact stresses, bearing row displacements, row reaction forces, and row stiffness components are evaluated. Since these cases must use a fixed ring assumption to match the A. B. Jones program, the next validation step focuses on the ring compliance algorithms. In this study, Alan Leveille's codes BRGS10 and BRGS14 are compared in a case study that was jointly run by Brian Gore from Aerospace Corporation and Steve Koss from Naval Research

---

\* Halpin Engineering LLC, Torrance, CA

Laboratories. The study compares the resolved mounted preload state on a hard preloaded duplex pair of bearings for variations to the bearing fits, contact angles, curvature, temperature and free preload.

The final section presents case studies, based on real bearing analyses found in a literature search, where published results are compared with ORBIS predictions. The first case study is from the 22<sup>nd</sup> Aerospace Mechanisms Symposia proceedings titled “Two Gimbal Bearing Case Studies: Some Lessons Learned” by S. H. Loewenthal. The second case study is from NASA/TP-2014-217906, titled “Analysis of Space Station Centrifuge Rotor Bearing Systems: A Case Study” by J. V. Poplawski, S. H. Loewenthal, F. B. Oswald, E. V. Zaretski, W. Morales, and K. W. Street.

### Technical Model Overview

ORBIS uses numerical techniques to solve the nonlinear elastic behavior of the user-defined system of one or more bearing rows. The model considers each ball-to-race contact for all bearing rows defined in the system, resulting in complete knowledge of the element load distributions and their raceway attitudes. A solution to the system is achieved when the sum of all bearing row reaction forces is sufficiently close to the external applied forces (system equilibrium).

The system model follows the same process necessary to assemble a rotational system: initial conditions are defined, the bearings are fit into the assembly, preload is applied to the bearings, and external loading is finally applied to the mounted and preloaded bearing system. The parameters describing relative ring displacements and internal clearance changes are tracked at each step of the process; ultimately leading to the final state of the bearing system.

Since bearings typically operate with very small internal clearances, it is important to consider the effects of boundary conditions on the races when establishing the mounted state of the bearing system. ORBIS implements a compliance model based on classical thick ring theories to determine the final mounted and preloaded state of the bearing system. The compliance model is also used for assessing thermal strains. Once all mounting, preloading and thermal strains have been considered, the traditional fixed ring theories, as developed by Jones, are applied to assess effects due to external loading.

The compliance model makes a key assumption that in the local vicinity of the bearing, the housing, shaft and bearing rings can be expressed with a series of nested rings. Thick ring theory assumes the representative rings have uniform constant wall thickness and all deflections remain within the linear elastic region of the material. Since the groove side of a bearing race clearly has a non-constant cross section, an equivalent diameter has been developed to represent bearing rings. The equivalence model is shown in (1) and (2), and has been correlated to detailed finite element models. A key benefit to the equivalence model is that it is based on the geometry defining the raceway depth and therefore can account for the general class of raceways. The compliance algorithms also track various sudden changes in the boundary conditions of each nested ring; such as when the fit between a bearing outer diameter (O.D.) and housing inner diameter (I.D.) transitions from clearance to interference due to preload expansion or thermal expansion.

$$D_{IR} = d_{IR_{race}} + 0.68(h_l + h_d) - \frac{2h_l}{d_{IR_{race}}}(h_l - h_d) \quad (1)$$

$$D_{OR} = d_{OR_{race}} - 0.68(h_l + h_d) + \frac{2h_l}{d_{OR_{race}}}(h_l - h_d) \quad (2)$$



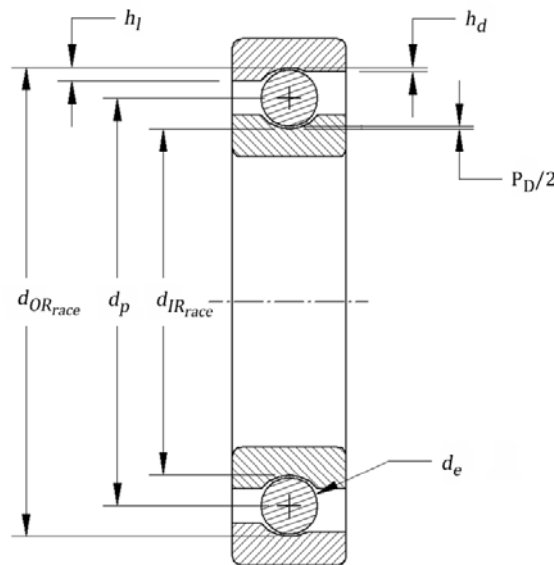


**Figure 1. Bearing nomenclature for equivalent raceway diameter**

### Capabilities and Features

#### Brief overview of ORBIS

The ORBIS main graphical interface is shown in Figure 2. This interface is used to configure/setup the bearing system to be analyzed. ORBIS implements a database approach for definition of key common elements of the analysis, thereby making the setup, and subsequent attainment of results, a fairly quick process. Database features are provided for definition of bearings, materials and lubricants. Once these elements have been defined within the database, the user only needs to assign them to their system from the main interface.

Another noteworthy feature of the main interface is the system sketch (shown in the upper-right quadrant of the interface). This sketch provides a useful means for checking that the setup is as intended. Within the sketch is a drawing of all assigned rows along with their associated contact angle orientation. The bearing rows are labeled with their database name and coordinate position along the shaft. All assigned load points are also included with their defined coordinate positions. Additionally, rows that float on a preload spring are identified with a spring symbol adjacent to the bearing row.

Analytical results are displayed in a separate output window as shown in Figure 3. In addition to displaying tabulated text for the complete set of results, the window contains features to help recognize common results quickly. At the top of the window is a quick reference summary table of maximum values for mean stress, truncation, mounted preload and torque at each bearing row. The bottom region of the results window contains a control panel that allows the user to filter which results to display. Another feature, which is illustrated in the figure, is that all elements with stresses exceeding a predefined threshold are highlighted in red. Additionally, any element found to have truncation is always highlighted.

A more thorough description of the ORBIS software can be found at [2].

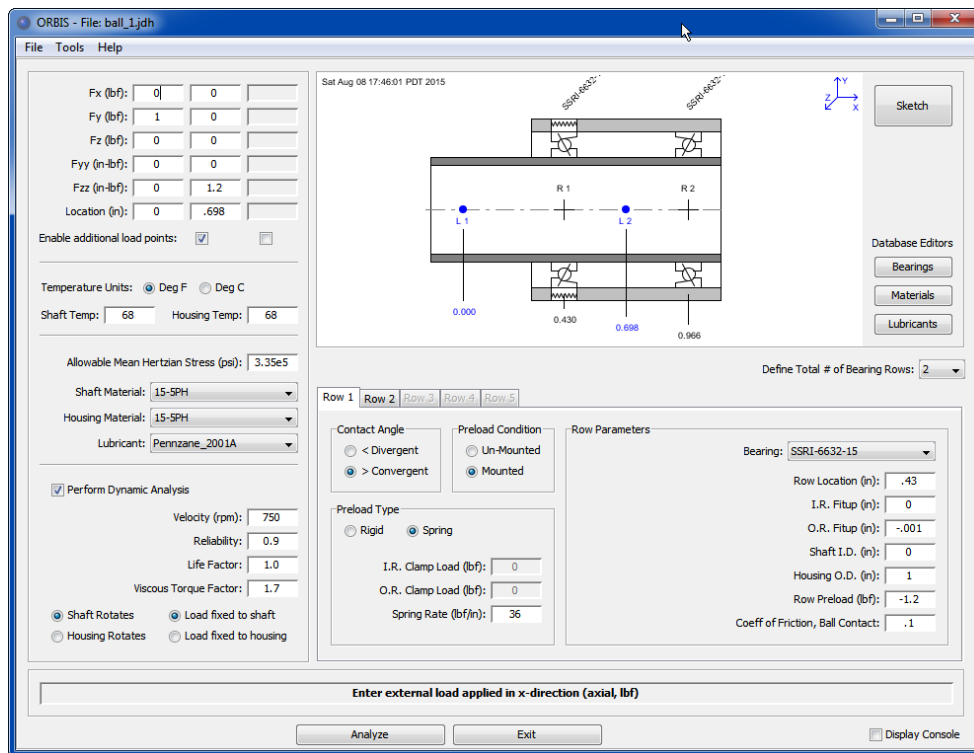


Figure 2. ORBIS main graphical interface

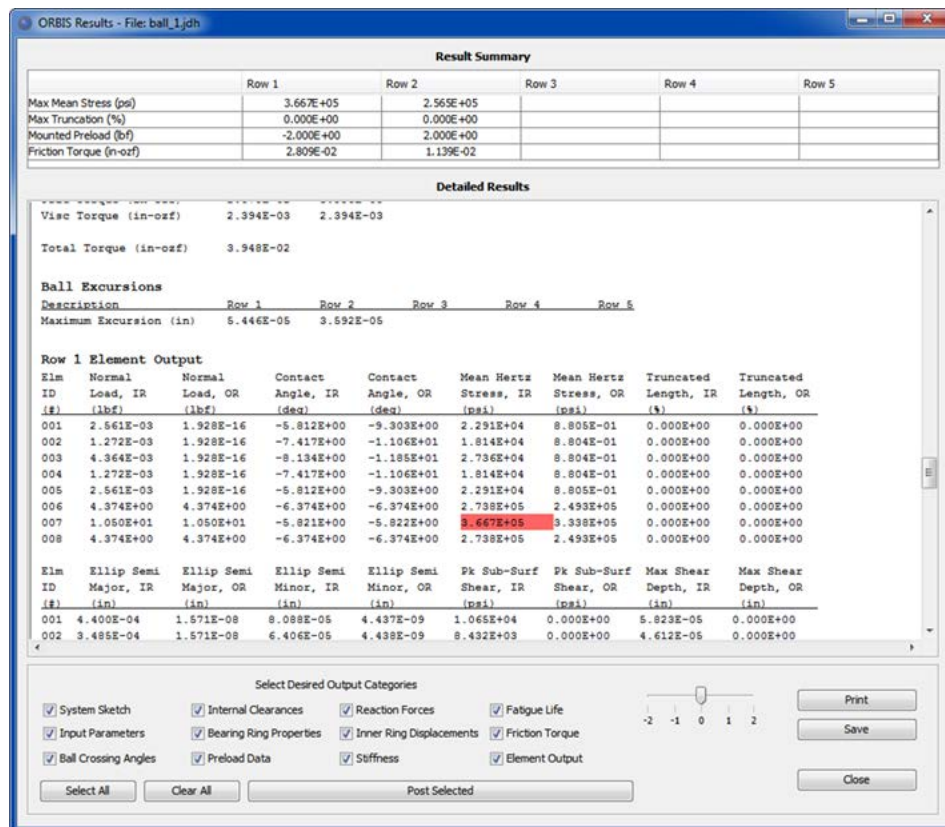


Figure 3. Result output window

## Key Analytical Considerations

Mechanisms that implement rolling-element bearings typically rely on certain performance parameters from the bearings. The most common parameters are load capability, stiffness, torque, and operational life. As it turns out, all of these parameters are dependent on the internal load distributions—meaning normal loads and associated contact angles—within each bearing defined in the system. Given accurate loaded contact angles of each element within a system, Hertzian contact mechanics provide the elliptical contact areas that are the basis for solving stresses, stiffness, primary torque components, and the fatigue life. Hence, the importance of accurately predicting the internal load distributions of a system of bearings should be foremost.

A point often overlooked in the analysis of bearings, which is particularly true for aerospace mechanisms due to their extremely high launch load environment, is that external loads are typically derived by analytical means, such as finite element modeling, and thus the bearing element stiffness is required as an input to the finite element model. This creates a circular process where the bearing stiffness is needed in order to predict the loads on the bearings. Additional complications arise due to the fact that finite element models require a linear stiffness yet bearing stiffness is nonlinear with load. Typically, the best that can be done here is to determine a linear approximation of the bearing stiffness in the vicinity of the load recovery. This may require more than one iteration to establish.

Abstract models of real systems are based on assumptions of the phenomena modeled and it is therefore prudent to review such assumptions. Let's first discuss the inherent assumptions of the mathematical theories derived by A. B. Jones. The Jones model can be summarized as follows. Each raceway's center of curvature is represented with a fixed diameter circle. The outer raceway circles are fixed in space and a local coordinate frame is attached at the center of the inner raceway circles. Inner raceway displacements, which are relative to the fixed outer rings, create differences to the normal approach between the inner and outer circles. The location of the ball center, relative to the fixed outer raceways, and solved at each ball station, is determined by ensuring the ball is in quasi-static equilibrium. A Newton-Raphson search routine then iterates on displacements to the moveable coordinate inner rings. Given the normal approach of the ball center relative to each raceway, classical Hertzian contact analysis is utilized to determine normal loads and elliptical contact areas at each raceway contact point. The vector sum of all ball loads then provides the resultant force reacting on the shaft for a given set of inner ring displacements. Complete bearing equilibrium is achieved when the shaft reaction forces are equal, or sufficiently close, and opposite to the externally applied loads.

The Jones method, which is a very elegant derivation, does rely on the assumption that raceway circles maintain a fixed radius (a.k.a. fixed ring assumption). Should the raceways expand or contract it would change the normal approach to the ball center and could have a profound effect to the internal load distribution. Most traditional bearing materials are intentionally selected to be very hard and stiff and typical normal approach dimensions of the contacting bodies are on the order of 5 micrometers (0.0002 inch). This implies very small changes to the normal approach can have a profound effect on contact angles and normal loads. Such changes should therefore be included in the predictive model to enhance accuracies.

Items such as interference fitting, ring clamping, preloading and thermal expansions will all effect the bearing ring diameters. Most of which, if not all, are inherent in every mechanism containing rolling-element bearings. Before continuing our discussion on key model assumptions lets illustrate some common mounting influences with an example. Figure 4 illustrates a duplex pair of angular contact bearings that are oriented back-to-back. Although not shown in the figure we shall assume the bearings are hard preloaded by some means (perhaps a clamp plate or jam nut). It is well known that such systems as this can be quite sensitive to the mating fits of the bearing. Also, since the bearings are mounted in structure with a higher coefficient of thermal expansion than the bearing material (e.g., aluminum shaft and housing versus 440C bearings), we expect that temperature excursions will also affect the internal load distribution of the mounted bearings.

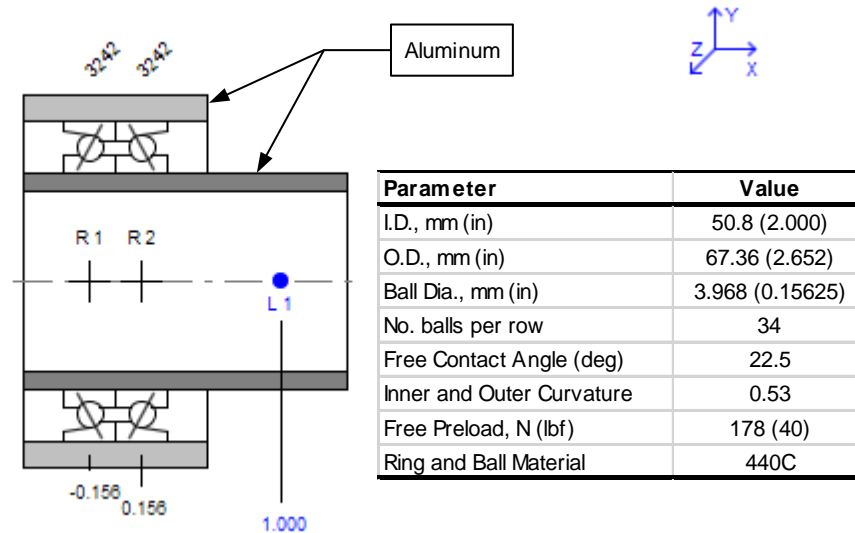


**Figure 4. Example problem**

Using the sensitivity utility in ORBIS allows us to perform parametric studies of inner ring fits and bulk system temperature. This utility takes the user defined system and allows perturbations to an input variable, such as inner ring fit up or bulk system temperature, to be plotted against selected output variables, such as mounted preload and maximum stress.

Figure 5 shows two pairs of plots illustrating the effects of inner ring fit up and bulk temperature of the system on the mounted preload and mean Hertzian stress of the bearings. Figures 5a & 5b illustrate that small amounts of interference at the inner diameter of the bearing cause a rapid increase in the mounted preload. This occurs because the expansion of the inner ring reduces the free contact angle of the bearing; thereby increasing the manufactured preload gap, also referred to as the ring stick-out, between the abutting inner ring faces. With a hard-preloaded system, this gap is forced closed and the balls must react the increased strain.

Figures 5c & 5d show the effects of the aluminum expansion rates on the bearings. The plots illustrate that as the temperature is either increased or decreased from ambient the mounted preload and stress will increase. Initial fits for this example are line-to-line on the shaft and 5  $\mu\text{m}$  (0.0002 in) clearance on the housing. Note that the influence to cold temperature is more pronounced than when the system is heated above ambient. At first glance, this may not seem intuitive since both the shaft and housing are made from aluminum. Hence, as you heat the system above ambient the inner ring fit gets tighter and the outer ring fit gets looser and, adversely, as you cool the system the outer ring fit gets tighter while the inner ring fit gets looser. In either case one ring of the bearing is driven by its boundary condition, however for the bearing to react preload the ball must have equal loads at both raceways. Therefore, the rate of preloading will be a function of the loose ring's hoop stiffness. Since the inner ring has a higher hoop stiffness than the outer ring it will react loads quicker and thus the cold case is more sensitive. Another contribution to why the cold case is worse is the fact that the diameter of the outer ring is larger than the inner ring and, for a given temperature delta from ambient, the magnitude of diametral change for the outer ring will slightly exceed that of the inner ring.

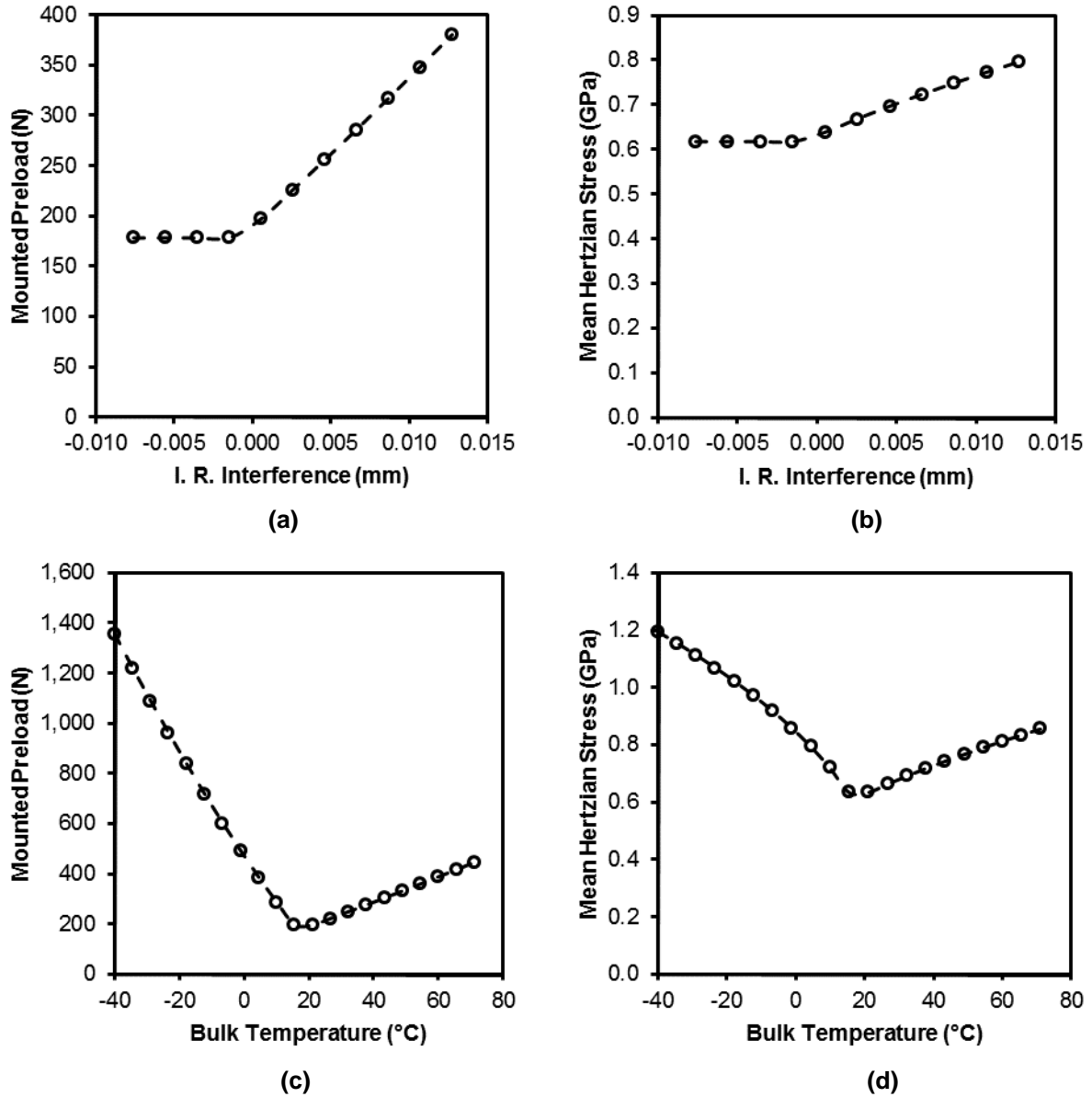


**Figure 5. Effects of inner ring fit up on (a) mounted preload and (b) mean Hertzian stress and effects of shaft and housing bulk temperature on (c) mounted preload and (d) max mean Hertzian stress**

One other noteworthy modeling assumption, which is inherent in the Jones model, is that the contact area between the rolling elements and raceways are always fully contained. When the contact ellipse is not fully contained, it is said to be truncated. A truncated contact area will invalidate the reported stress but also incurs errors to the resolved internal load distribution since the contact stiffness is a function of the contact area. There are some simple methods to de-rate the stress for truncated elements but not the stiffness. Hence, it becomes important to, at a minimum, know when a system has truncation.

## Model Validation

### Core Jones Model

Since ORBIS is based on theories published by A.B. Jones, validation of the core solver can be achieved by comparing identical analysis cases with the A. B. Jones High Speed Ball and Roller Bearing Analysis Program. Numerous test cases were designed to demonstrate that ORBIS maintains accuracy for wide variety of different system geometry. Key results tracked for comparison included maximum mean Hertzian contact stresses, bearing row displacements, row reaction forces, and row stiffness components. These result parameters validate that the nonlinear elastic system solver is correctly determining the internal load distributions and Hertzian contact mechanics for the bearing system.

Twenty-nine test cases were developed for this comparison and are shown in Table 2. The characteristic system consisted of a back-to-back pair of bearings with a single central load point. Note that contact angles, raceway curvatures and material properties were held constant for all test cases. These parameters will be more thoroughly studied in the flexible ring validation cases discussed later. Independent axial, radial and moment loading was studied to verify principal load component accuracy. Combined, or simultaneous loading (all 5 directions), was also studied and included variations in system preload, bearing size, number of balls, ball diameter and bearing row separation.

As shown in Table 1, which summarizes the percent differences between ORBIS and Jones software for all twenty-nine test cases, ORBIS results correlate to the A.B. Jones program within a fraction of one percent. These differences are deemed insignificant and likely relate to either differences in convergence criteria for the Newton-Raphson solver or rounding errors between the two programs (note that ORBIS maintains 64-bit floating point precision while it is believed that the Jones code might only hold 16-bit precision). Figure 6 depicts the Hertzian stress comparisons for each of the test cases.

**Table 1. Comparison of all results**

<b>Comparison Parameter</b>	<b>% Difference</b>		
	<b>Min</b>	<b>Mean</b>	<b>Max</b>
Bearing Row Stiffness Components	-0.1%	0.0%	0.2%
Inner Ring Deflections	-0.3%	0.1%	0.6%
Bearing Row Reaction Forces	-0.2%	0.0%	0.8%
Max Mean Hertzian Contact Stress	-0.5%	-0.3%	0.0%

**Table 2. Test Case Parameters**

<b>Case</b>	<b>Bore (mm)</b>	<b>O.D. (mm)</b>	<b># Balls</b>	<b>Ball Dia. (mm)</b>	<b>Row Span (mm)</b>	<b>Preload (N)</b>	<b>F<sub>x</sub> (N)</b>	<b>F<sub>y</sub> (N)</b>	<b>F<sub>z</sub> (N)</b>	<b>M<sub>y</sub> (Nm)</b>	<b>M<sub>z</sub> (Nm)</b>
1	12.7	19.05	21	1.59	38.10	89	89	89	89	2.26	2.26
2	19.05	25.4	30	1.59	50.8	178	178	178	178	4.52	4.52
3	25.4	34.93	28	2.38	69.85	267	267	267	267	226	226
4	50.8	66.68	34	3.97	133.35	356	445	890	890	452	452
5	76.2	92.08	50	3.97	184.15	445	890	1779	1779	904	904
6	101.6	114.3	80	3.18	228.6	667	1334	3559	3559	1695	1695
7	127	165.1	36	9.53	330.2	890	1779	4448	4448	2825	2825
8	152.4	190.5	42	9.53	381	1112	2669	8896	8896	5085	5085
9	127	165.1	36	9.53	254	890	-	-	-	-	-
10	127	165.1	36	9.53	254	890	2224	-	-	-	-
11	127	165.1	36	9.53	254	890	4448	-	-	-	-
12	127	165.1	36	9.53	254	890	8896	-	-	-	-
13	127	165.1	36	9.53	254	890	1.78E4	-	-	-	-
14	127	165.1	36	9.53	254	890	3.56E4	-	-	-	-
15	127	165.1	36	9.53	254	890	7.12E4	267	-	-	-
16	127	165.1	36	9.53	254	890	-	2224	-	-	-
17	127	165.1	36	9.53	254	890	-	4448	-	-	-
18	127	165.1	36	9.53	254	890	-	8896	-	-	-
19	127	165.1	36	9.53	254	890	-	1.78E4	-	-	-
20	127	165.1	36	9.53	254	890	-	3.56E4	-	-	-
21	127	165.1	36	9.53	254	890	-	7.12E4	-	-	-
22	127	165.1	36	9.53	254	890	-	-	-	113	-
23	127	165.1	36	9.53	254	890	-	-	-	226	-
24	127	165.1	36	9.53	254	890	-	-	-	452	-
25	127	165.1	36	9.53	254	890	-	-	-	904	-
26	127	165.1	36	9.53	254	890	-	-	-	1808	-
27	127	165.1	36	9.53	254	890	-	-	-	3616	-
28	127	165.1	36	9.53	254	890	-	-	-	7232	-
29	127	165.1	36	9.53	254	890	-	-	-	14464	-

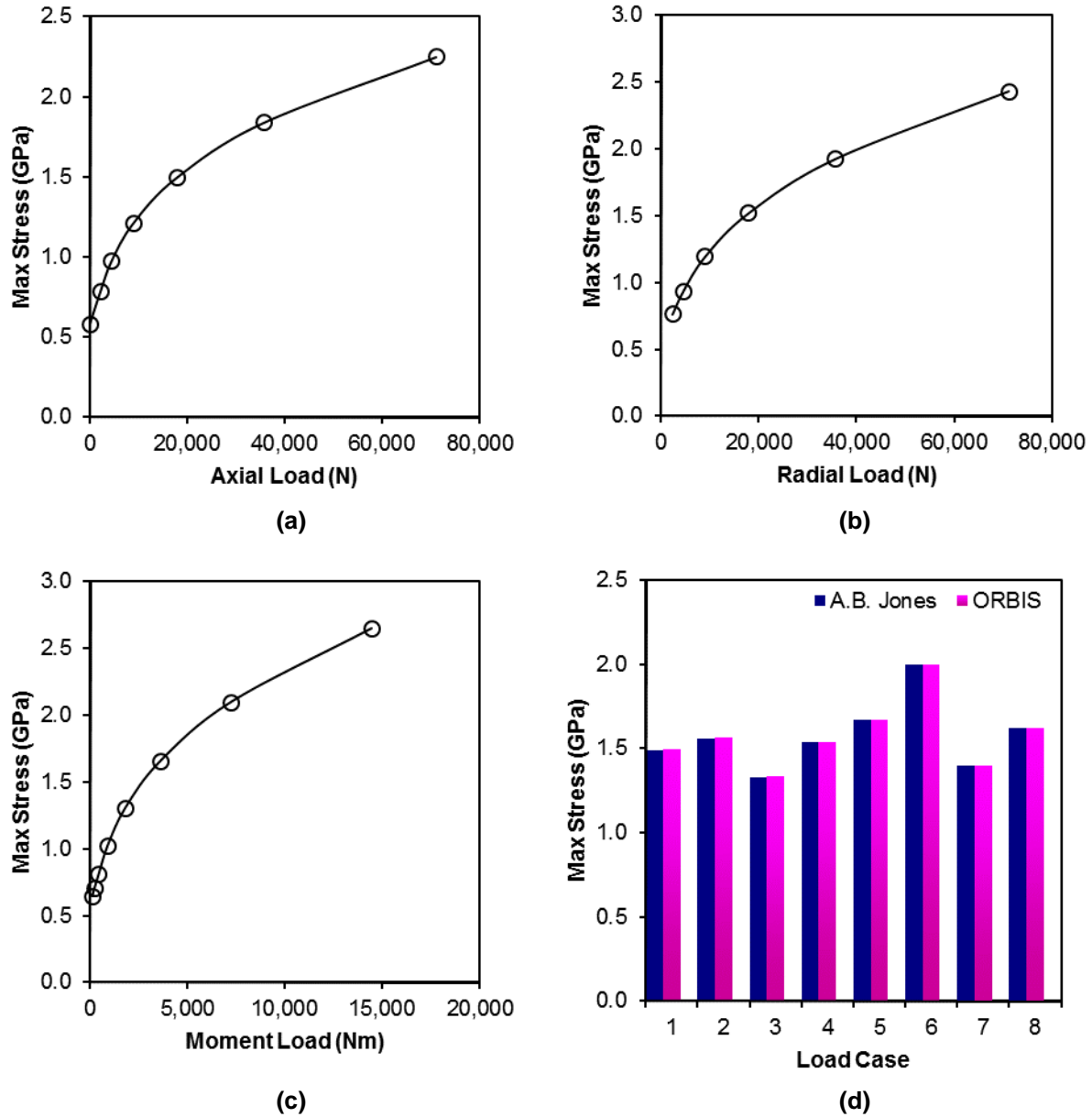


**Figure 6. Comparison of maximum mean Hertzian contact stresses for various loading. ORBIS results denoted with circles and A. B. Jones results shown with solid line. (a) shows axial loading, (b) shows radial loading, (c) shows moment loading and (d) shows 8 combined load cases.**

#### Ring Compliance Model Validation

Since the ring compliance model is used to establish the mounted, or operating, conditions we shall first consider a simple duplex pair of bearings against a well-known code that contains both ring compliance and considers both thermal expansions and ring clamping. The configuration consists of a duplex pair of angular contact bearings oriented back-to-back with a hard preload. The shaft and housing are made from titanium and the bearing rings and balls are 440C. Variations of the free contact angle, raceway curvatures, shaft and housing temperatures, I.D. and O.D. fits, and pre-ground preload are studied. Comparison of the predicted mounted preload are made against two different versions of A. Leveille's code: BRGS10 and BRGS14.



Table 3 shows key setup parameters for the system that were fixed during the study. Table 4 shows the various run cases studied along with the resulting mounted preload condition from all three codes. As shown, ORBIS correlates much closer with BRGS14 than BRGS10. Average difference between ORBIS and BRGS14, for all cases considered, is within 5.3%. It is believed that the earlier version of Leveille's code (BRGS10) does not contain an account for ring clamping, which would explain why it predicts lower mounted preloads. It is not known how Leveille modeled the bearing ring stiffness, particularly the derivation of the equivalent diameter for the grooved side of the races. A common rule of thumb for ring influences is to take approximately 80% of the interference as internal clearance loss in the bearing. This method is not recommended as it assumes a fixed ratio of the stiffness between the boundary and bearing ring.

**Table 3. Setup parameters for mounted preload study**

Parameter	Value	Parameter	Value
Pitch Dia., mm (in)	171.45 (6.750)	Housing O.D., mm (in)	202.18 (7.960)
Ball Dia., mm (in)	9.525 (0.375)	Modulus of Elasticity, Rings & Balls, GPa (psi)	200 (2.90E+07)
No. Balls	42	Poisson's Ratio, Rings & Balls	0.28
Shoulder Height (h/d)	0.206	Coefficient of Thermal Expansion, Rings & Balls, 1/°C	1.02E-05
Dam Height (h/d)	0.011	Modulus of Elasticity, Shaft & Housing, GPa (psi)	112 (1.62E+07)
Row Width, mm (in)	19.05 (0.750)	Poisson's Ratio, Shaft & Housing	0.31
Row Straddle, mm (in)	19.05 (0.750)	Coefficient of Thermal Expansion, Shaft & Housing, 1/°C	8.82E-06
Shaft I.D., mm (in)	134.62 (5.300)		

**Table 4. Mounted preload study results**

Initial Conditions (Free)							Mounted Preload (N)		
Contact Angle (deg)	I.R. & O.R. Curvature	Shaft / Housing Temp (°C)	I.D. Clearance (mm)	O.D. Clearance (mm)	Clamping Force (N)	Ground Preload (N)	BRGS10	BRGS14	ORBIS V2.4.1
22.5	54.5	76/76	0.01397	0.01905	53378	5115	5538	6112	5858
		-10/-10					5373	5133	5084
		66/76					3327	3861	3643
4226	2300					2931	2718		
	2447					3051	2851		
	2331					2954	2749		
	2108					2785	2540		
	2189					2264	2246		
25.0	54.0		0.02286	0.03048		2838	3318	3087	
			0.00508	0.00762					

### Case Studies

This first example is taken from the proceedings of the 22<sup>nd</sup> AMS [3]. Here, we focus on Loewenthal's first case study. The described design consists of a large thin section (12" (30.5-cm) O.D., 11" (27.9-cm) I.D. and 0.250" (6.35-mm) diameter balls) duplex pair of angular contact bearings, oriented face-to-face that is hard preloaded in beryllium structure. The bearing system must operate with fairly large radial thermal gradients. Loewenthal mentions that he found it more expedient to construct a special purpose bearing code to solve this class of problem. In his study, Loewenthal constructed a design plot to show maximum contact stresses versus the radial thermal gradient. Using the Sensitivity Utility within ORBIS and holding the outer race temperature fixed while varying the shaft temperature the maximum contact stresses were solved. These data were then exported from ORBIS for post processing and, as shown in Figure 7,

constructed as a function of gradient along with a few points from Loewenthal's plot. As shown, ORBIS correlates well with Loewenthal's predictions for most of the gradient spectrum considered (note: original units have been converted to SI in accordance with AMS policy). The biggest difference between the two predictions occurs at -20°F (-29°C) case, where ORBIS predicts about twice the stress. Note that this region of bearing stress is highly nonlinear because the contact area is approaching a theoretical point (near zero ball loads).

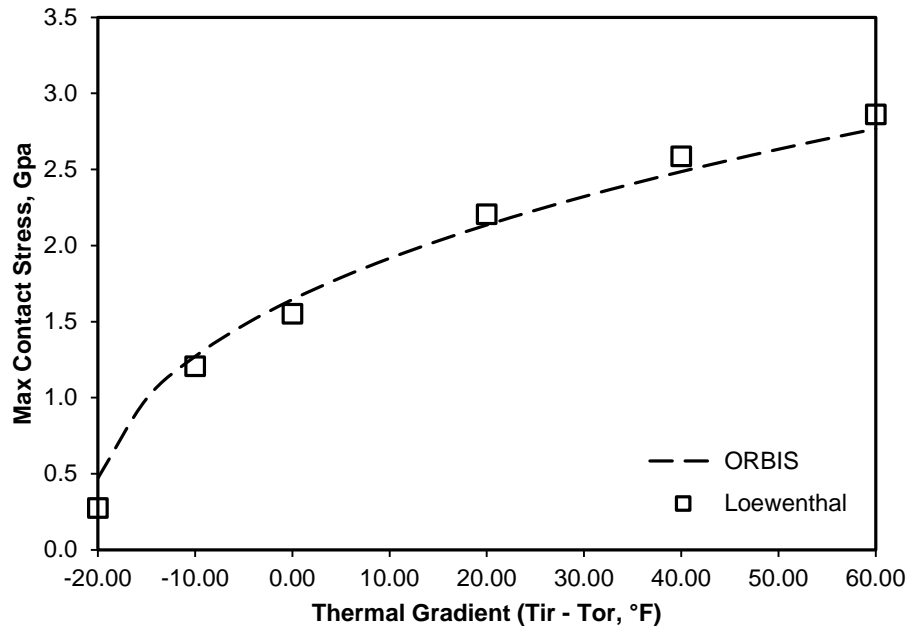


**Figure 7. Comparison of thermal gradient stresses to Loewenthal's paper**

The next example is from an analysis of the space station centrifuge rotor bearing system [4]. In this study, the rotor shaft assembly is analyzed for both bulk temperature loading and thermal gradients. The rotor shaft assembly is comprised of a three-bearing system: a duplex face-to-face pair and deep-groove (Conrad) bearing. The housing and shaft are aluminum 7075-T73 and all bearing rings and balls are 440C stainless. Figure 8 shows the cross section of the rotor shaft assembly. As shown, the system has a fairly large span (~600 mm) and preload springs are located on rows 2 and 3 (where row 1 is the leftmost row in the figure). Due to both the bearing span and fact that the housing and shaft are made from aluminum there are obvious concerns regarding how this bearing will react to both bulk temperature and temperature gradients.

Figure 8 shows the results from ORBIS plotted against the original publication. Here, we have chosen to plot only rows 2 and 3 because row 1 does not differ from row 2 appreciably (row 1 and 2 being the face-to-face pair). As shown, ORBIS matches very closely with the original author for both bulk temperature loading and temperature gradients. Row 3, which is the deep-groove bearing, clearly has the most sensitivity to temperature fluctuations. It should be noted that the ambient shaft fit for row 3 has a fairly profound effect on the contact angle and the publication only mentions a range, or tolerance, for this parameter. The results shown assumed this fit was at its minimum value (0.022 mm). Also, as shown in Figure 8 (right), row 3 has a maximum predicted contact angle that is approximately 2 degrees higher from the publication when the gradient is 20°C. All other points, which are located at both higher and lower gradients, have a much smaller deviation (less than 1° average). This one point appears a bit out of family compared with the other points.

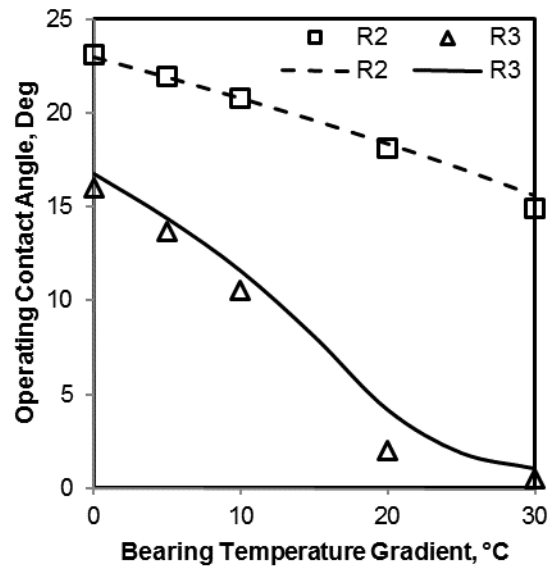
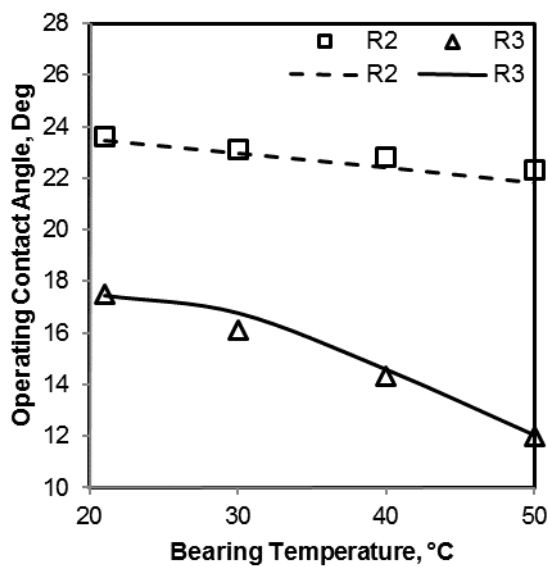
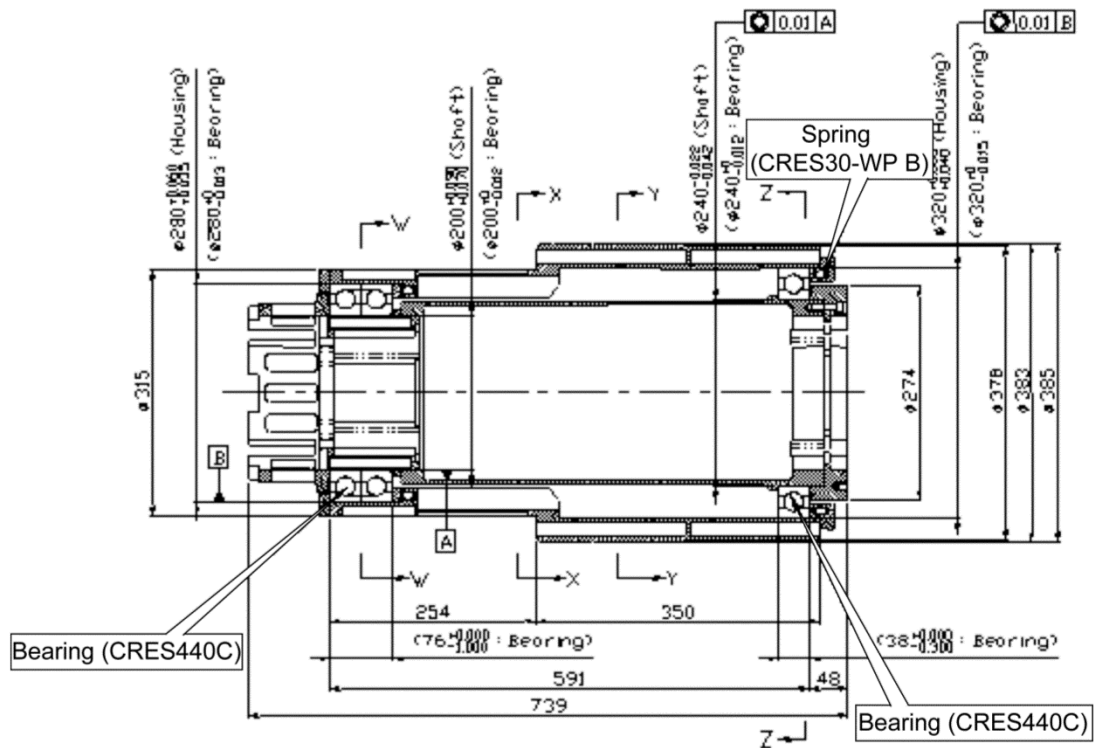


Figure 8. Main rotor assembly cross section (reference Figure 2 in [4]) and comparison of operating contact angle predictions. Left: rows 2 & 3 shown against bulk bearing temperature (reference Figure 3 in [4]). Right: rows 2 & 3 shown against bearing temperature gradient (reference Figure 5 in [4]).

## Conclusion

Many aerospace designs contain bearing rings have been thinned down to minimize weight. They may also utilize dissimilar materials for the bearing support structure. Such systems require ring compliance considerations to accurately determine the internal load distribution of the bearings and, ultimately, the proper performance assessment of the bearings. The ORBIS software tool has been introduced and was developed to account for these effects. Various key technical analysis considerations, including relevant assumptions and a description of the compliant ring modeling, has been discussed. Numerous validation cases, including a few published bearing analysis studies, were performed and all results suggest the code closely correlates to other trusted predictions. In addition to providing reliable results, the tool offers a significant upgrade from the earlier MS-DOS based programs. Forethought has been taken to help ensure ORBIS will provide long-term dependability and robust compatibility with various computer operating systems and machine architectures by using the Java programming language. Moreover, ORBIS strives to eliminate many hand calculations often required with other programs and provides iterative design utilities that allow the user to quickly understand and assess the performance of their bearing system.

## References

- [1] A. B. Jones, "The Mathematical Theory of Rolling-Element Bearings," in *Mechanical Design and Systems Handbook*, New York, McGraw-Hill, 1964.
- [2] J. D. Halpin, "Halpin Engineering - Software," 2016. [Online]. Available: <http://www.halpinengineeringllc.com/software>.
- [3] S. H. Loewenthal, "Two Gimbal Bearing Case Studies: Some Lessons Learned," in *22nd Aerospace Mechanisms Symposium*, Hampton, 1988.
- [4] J. V. Poplawski, S. H. Loewenthal, F. B. Oswald, E. V. Zaretski, W. Morales and K. W. Street, "NASA/TP-20142217906 Analysis of Space Station Centrifuge Rotor Bearing Systems: A Case Study," NASA, Cleveland, 2014.

# Extended Life Testing of Duplex Ball Bearings

Jeffrey Mobley\*, Michael Robertson\* and Charles Hodges\*

## Abstract

Sierra Nevada Corporation's Space Systems performed bearing life testing for the Scan Mirror Motor/Encoder Assembly (SMMA), part of the Scan Mirror Assembly on-board the Aerosol Polarimetry Sensor (APS) on the NASA Glory Spacecraft. The baseline bearing life test duration extended beyond the launch date for the Glory Spacecraft; a risk that the program was willing to undertake with the understanding that if any anomalies or failures occurred before the required life was achieved, then the mission objectives or operating profile could be modified on orbit to take those results into account. Even though the Glory Spacecraft failed to reach orbit during its launch in March of 2011, the bearing life testing was continued through a mutual understanding of value between Sierra Nevada Corporation and our customer; with a revised goal of testing to failure rather than completing a required number of life cycles. Life testing thus far has not only exceeded the original mission required life, but has also exceeded the published test data for Cumulative Degradation Factor (CDF) from NASA/CR-2009-215681 [1]. Many lessons were learned along the way regarding long life testing. The bearing life test has been temporarily suspended due to test support equipment issues.

## Introduction

Since the Aerosol Polarimetry Sensor is a continuous scanning sensor, the SMMA was required to provide a constant rotational speed to the Scan Mirror Assembly while the APS collected earth atmospheric data for analysis. The APS had a design life of 5 years, encompassing a continuously operating mission life of 3 years at 40.69 RPM resulting in 64.2 million shaft revolutions. As the Scan Mirror Assembly was extremely sensitive to torque variation, there were specified requirements on maximum break-away torque, minimum and maximum drag torque, and torque disturbance that had to be met over the lifetime of the mechanism. The bearings were required to meet those torque requirements at the specified operating speed over an equivalent 2X operating mission life equal to 128.4 million revolutions. Based upon the bearing geometry, preload of the bearings, and the number of operating cycles, the lubricant life of the bearing was uncertain when the CDF was evaluated against the data published in NASA/CR-2009-215681 for Pennzane 2001-based lubrication. Since the bearings are a single point failure in the mechanism and could not be qualified through similarity to existing test data, an in depth bearing life test was required to gain mission confidence. The SMMA Actuator is shown in Figure 1.

## Lubricant Lifetime Prediction

As detailed in NASA/CR—2005-213424 [2], the bearing lubricant Cumulative Degradation Factor (CDF) is a method used to determine and compare the relative lubricant lifetime of new applications based upon parameters and test data obtained from heritage programs. The CDF is calculated based on the product of the bearing mean hertzian stress and the number of times a ball passes across a given spot on the raceway and is expressed in units of ball passes•psi (bp•psi). The rotor bearings within the SMMA have a mean hertzian contact stress of 521.7 MPa (75.66 ksi) at nominal bearing geometry and preload. Based upon the bearing geometry, the SMMA rotor bearings experience 22.167 ball passes per shaft revolution. The 1X APS program life requirement of 64.2 million revolutions resulted in a calculated CDF of  $107.7 \times 10^{12}$  bp•psi and the 2X APS program life of 128.4 million revolutions resulted in a calculated CDF of 215.4

---

\* Sierra Nevada Corporation's Space Systems, Durham, NC

$\times 10^{12}$  psi-cycles. Both the 1X and 2X life requirements for the APS program exceed the published lubricant test data from NASA/CR-2009-215681, which showed acceptable life test results up to  $88 \times 10^{12}$  bp•psi. Since the life of the lubricated SMMA rotor bearings could not be verified by comparative test data, a life test was necessary to validate the design against the specific program requirements.



**Figure 1. SMMA Actuator**

#### **Lubrication Film Thickness and Lambda Ratio**

A valid bearing life test needs to operate within the same lubricant regime as the on-orbit conditions to ensure the wear phenomena are similar. As detailed in NASA Technical Memorandum 88875 [3], the lubrication regime can be estimated from the Lubrication Film Parameter ( $\lambda$ ), which is defined as the ratio of the lubrication film thickness divided by the composite roughness of the contacting surfaces. Per STLE SP-34 [4], Lambda ratios less than 1.0 result in Boundary lubrication characterized by a high likelihood of surface asperity contact and resultant wear to the contacting surfaces. This bearing was predicted to have an on-orbit operating temperature primarily in the range of 15°C to 20°C. As shown in Figure 2, the lubrication film parameter at 40.69 RPM is in the boundary lubrication regime with  $\lambda < 1$  for this predicted operating temperature range and above.

With the predicted bearing operation on-orbit occurring in Boundary lubrication, it was determined to keep the predicted Lubrication Film Parameter ( $\lambda$ ) below 1 for the life test in order to stay within that same lubrication regime and replicate the expected wear conditions. Additionally, there was a goal to complete the 1X portion of the life test within 20 months so that the life test results would be available to the program to support modification of on-orbit operating parameters if required. Accomplishing 64.2 million revolutions within 20 months required a life test speed of at least 73.24 RPM. Figure 3 shows that at 74 RPM, the bearings will stay in Boundary lubrication with  $\lambda < 1$  at temperatures of 25°C and above. Lubrication viscous losses increase with bearing speed, generating higher friction torques within the lubricant at 74 RPM, and results in an increase in power and temperature. Since the vacuum chamber was without thermal control, it was predicted that the operating bearing temperature due to frictional self-heating would offset cooling induced by the vacuum chamber cryopump and result in a net steady state bearing temperature of at least 25°C. Any further temperature increase over 25°C would reduce the viscosity of the lubricant and thin the lubricant film, further ensuring that the life test bearings would operate within the Boundary lubrication regime. After evaluating the steady state operating temperature of the bearings in the life test setup, a maximum test temperature limit of 36°C was imposed to limit significant temperature rise while allowing for some environmental temperature fluctuation.

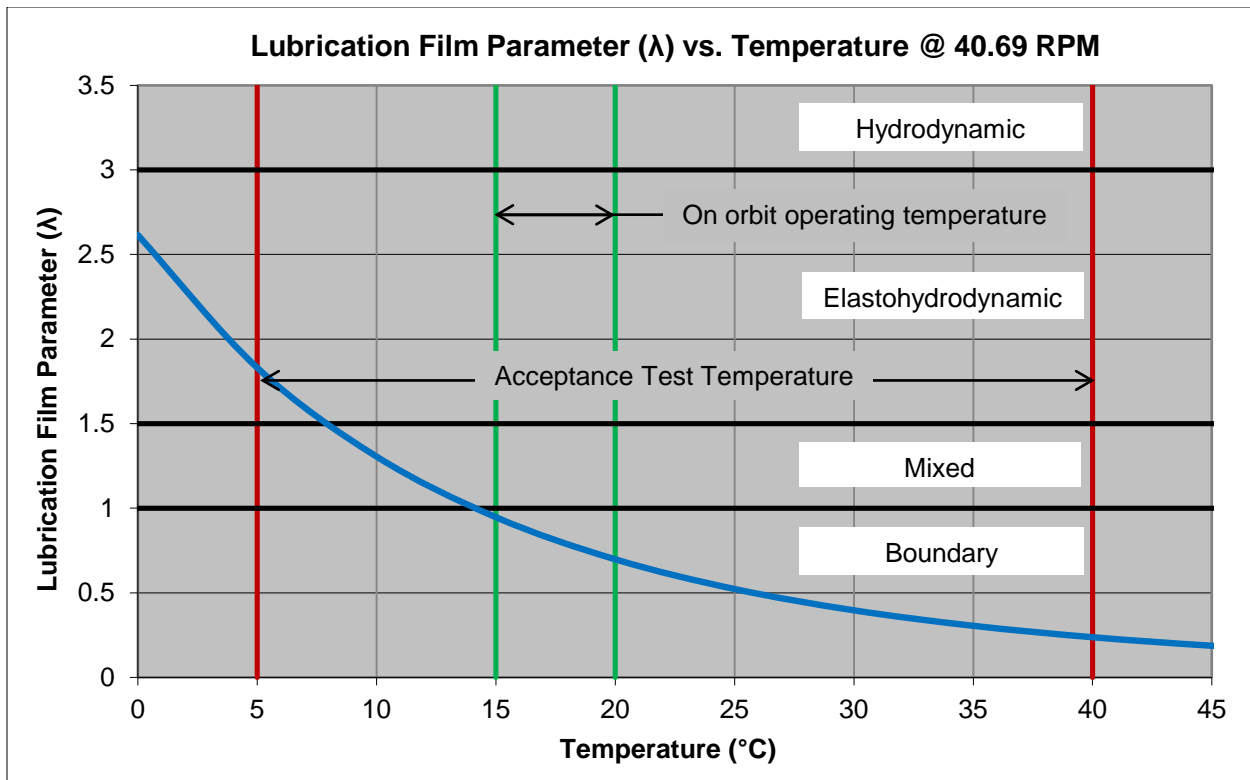


Figure 2. Lubrication Film Parameter ( $\lambda$ ) vs. Temperature @ 40.69 RPM

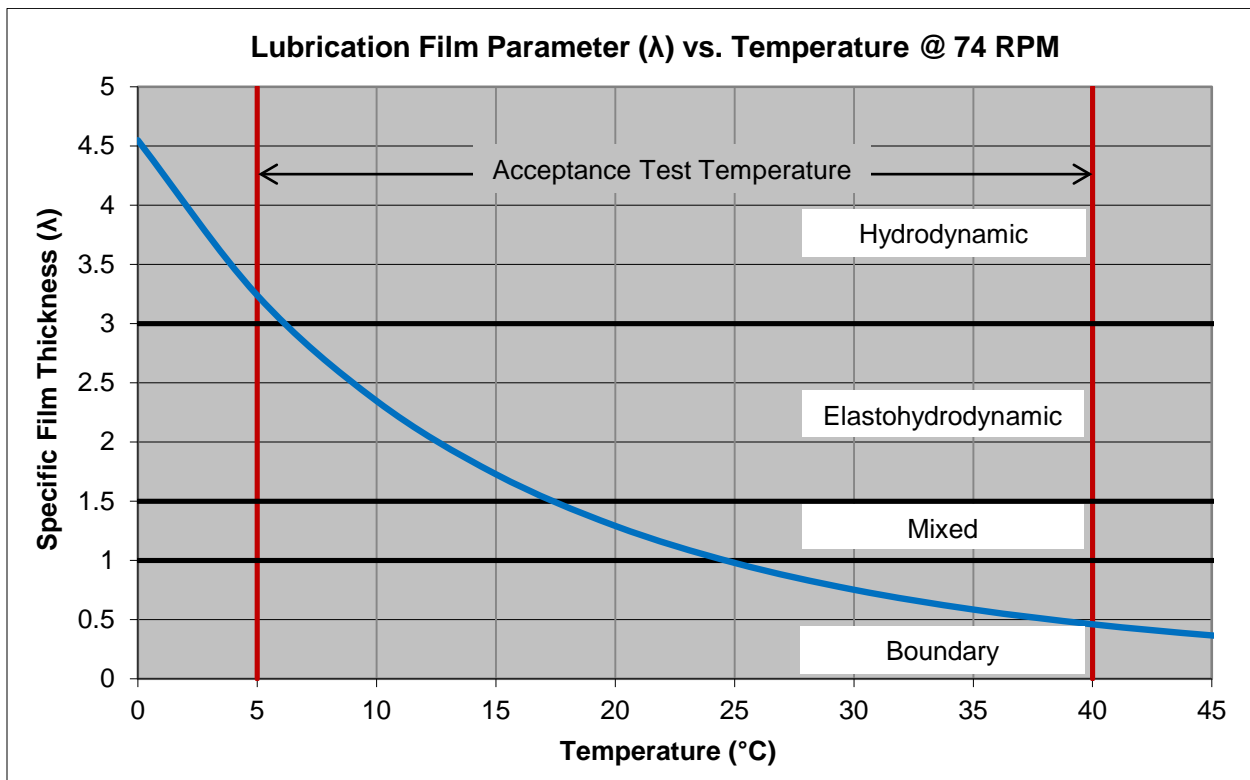


Figure 3. Lubrication Film Parameter ( $\lambda$ ) vs. Temperature @ 74 RPM

## **Design Considerations for Long Life**

In order to achieve extremely long life out of a lubricated bearing, special attention has to be paid to the bearing materials, accuracy, design parameters, lubrication, verification, and mounting techniques.

### Materials

To maximize reliability and minimize the chance of impurities causing surface weakness or contamination, materials should be of the highest purity grade feasible. For this application, Consumable Electrode Vacuum Melted 440C Stainless was chosen for the balls and raceways. Phenolic was chosen as the ball separator material due to its high level of heritage in vacuum operation.

### Accuracy

To minimize inherent torque variation and accuracy error, balls and raceways should be held to the highest accuracy requirements feasible. For this application the raceways were held to ABEC 7 or better and the balls were held to AFBMA Grade 3 or better.

### Surface Roughness

To maximize the lubricant film parameter ( $\lambda$ ), the surface finish of the balls and raceways should be held to the finest finish feasible. For this application, the balls were held to a maximum Ra of .013  $\mu\text{m}$  (0.5  $\mu\text{in}$ ), as controlled by the AFBMA Grade 3 requirements, and the raceways were held to a maximum Ra of .076  $\mu\text{m}$  (3  $\mu\text{in}$ ).

### Lubrication

Finally, lubrication type and amount should be carefully selected to provide the longest life possible within program requirements such as outgassing restrictions and operating temperature range. The program team solicited inputs from several leading lubrication experts within the space industry and concluded that for this application, Pennzane 2001-3PbNp oil was the best candidate for selection. Oil was chosen over grease since the thickeners and other additives in grease tend to create more inherent torque variation over oil alone. Pennzane 2001 was chosen over Braycote 815Z because it has proven to have longer operating life, as can be seen in the CDF data listed in NASA/CR-2009-215681. Pennzane 2001 was deemed acceptable for this application since the cold operating temperature of only +5°C did not get into the realm of significant viscosity increase. Lead Naphthenate was chosen as the high pressure additive to provide an additional layer of wear protection for boundary lubrication. A wettability test was performed on 100% of the raceways and balls to ensure that the surfaces would yield a uniform coating of lubricant with no signs of beading, gaps, or dewetting. The ball separators were desiccated and vacuum impregnated with the same Pennzane 2001-3PbNp oil.

### Component Testing

For bearings with tight requirements on starting torque, running torque, and torque variation; each preloaded bearing pair should be tested for those parameters prior to installation. For this application, the bearing vendor performed those tests on the fully lubricated and internally preloaded bearings and provided that data with each bearing.

### Mounting Techniques

To maintain minimal torque variation and consistent loading in the mounted and assembled bearing configuration, the controlling bearing mounting features have to be precisely controlled. For this application, in addition to applying tight tolerances to the housing and shaft mounting shoulders, the bearing inner and outer races were precisely located and bonded in place to minimize misalignment, wobble, and free play while avoiding the inherent variation and residual stresses resulting from interference fits.



## Life Test Method

In order to simulate on-orbit conditions as closely as possible while balancing total test duration, cost, and setup simplicity; a life test was performed using the following parts, methods, parameters, and criteria.

### Test Articles

Program requirements dictated that the life test bearings be manufactured with the same bearing geometry, ball and raceway material, ball separator material, raceway finishing process, and internal bearing preload as the flight bearings. It was also important to test a large enough sample to be statistically significant. In order to accomplish this most accurately, six duplex bearing sets were taken from the flight procurement manufacturing lot and allocated to the life test. Additionally, all bearings in this lot (flight and life test) were lubricated with the same lubricant lot, quantity, and application method.

### Life Test Mounting

The test bearings are mounted in the same back-to-back duplex arrangement as the flight bearings. The bearing clamping arrangement utilizes comparable stiffness clamps with the same number of fasteners and fastener torque to create the same nominal clamp forces as flight. The tolerances of the fixture mounting diameters and shoulders are held the same as the flight part drawings and the same adhesive shimming procedure is utilized to minimize inner to outer race misalignment and wobble.

### Life Test Parameters:

- Primary Life Test Goal: 64.2 million shaft revolutions (1X Operating Life) within 20 months
- Secondary Life Test Goal: 128.4 million shaft revolutions (2X Operating Life)
- Revised Life Test Goal: Test to failure as defined by termination criteria listed below
- Load: No external load, internal bearing preload of 133.4 N (30 lb) nominal
- Speed: 74 RPM, selected to balance maintaining equivalent film thickness and lubrication regime while reducing test duration as previously described
- Direction: Unidirectional continuous operation
- Pressure: Vacuum of  $6.67\text{E-}4$  Pa ( $5\text{X}10^{-6}$  Torr) or better
- Temperature: No active thermal control, vacuum chamber located in an ambient lab environment, natural self-heating of bearing housings allowed up to the maximum predicted on-orbit operating temperature of 36°C

### Life Test Data Monitoring

The following key parameters were monitored throughout the life test to ensure required conditions were met:

- Torque: Friction torque periodically monitored and recorded using an data logger with a sample rate of once per millisecond for a duration of one minute, collected every hour
- Temperature: Bearing housing temperatures were recorded once an hour
- Revolution Count: Proximity switch counting once per revolution

### Life Test Termination Criteria

Friction torque is the most direct measurement of bearing health available and as such is used as the primary factor in determining when a “test to failure” is completed as follows:

- Friction torque exceeding 125% of the initial setup running torque

Conditions that would warrant pausing the life test in order to determine credibility and impact of the data would be out of family torque conditions such as:

- A sudden increase in bearing friction torque and/or steady state temperature
- An excessively erratic friction torque trace when compared to prior test data or to other bearings under test

## Life Test Setup

As can be seen in Figure 4, the life test is performed inside a vacuum chamber. The selected drive motor is not vacuum compatible and is located outside the chamber. The drive motor is a high quality commercial brush DC motor with a planetary gear output; and drives the bearing shaft through a ferrofluidic feedthrough in the chamber wall. The electrical feedthrough brings out the signals to monitor the load cells and the bearing housing thermocouples. The cryopump maintains the required pressure level inside the chamber as monitored by the vacuum gauge.

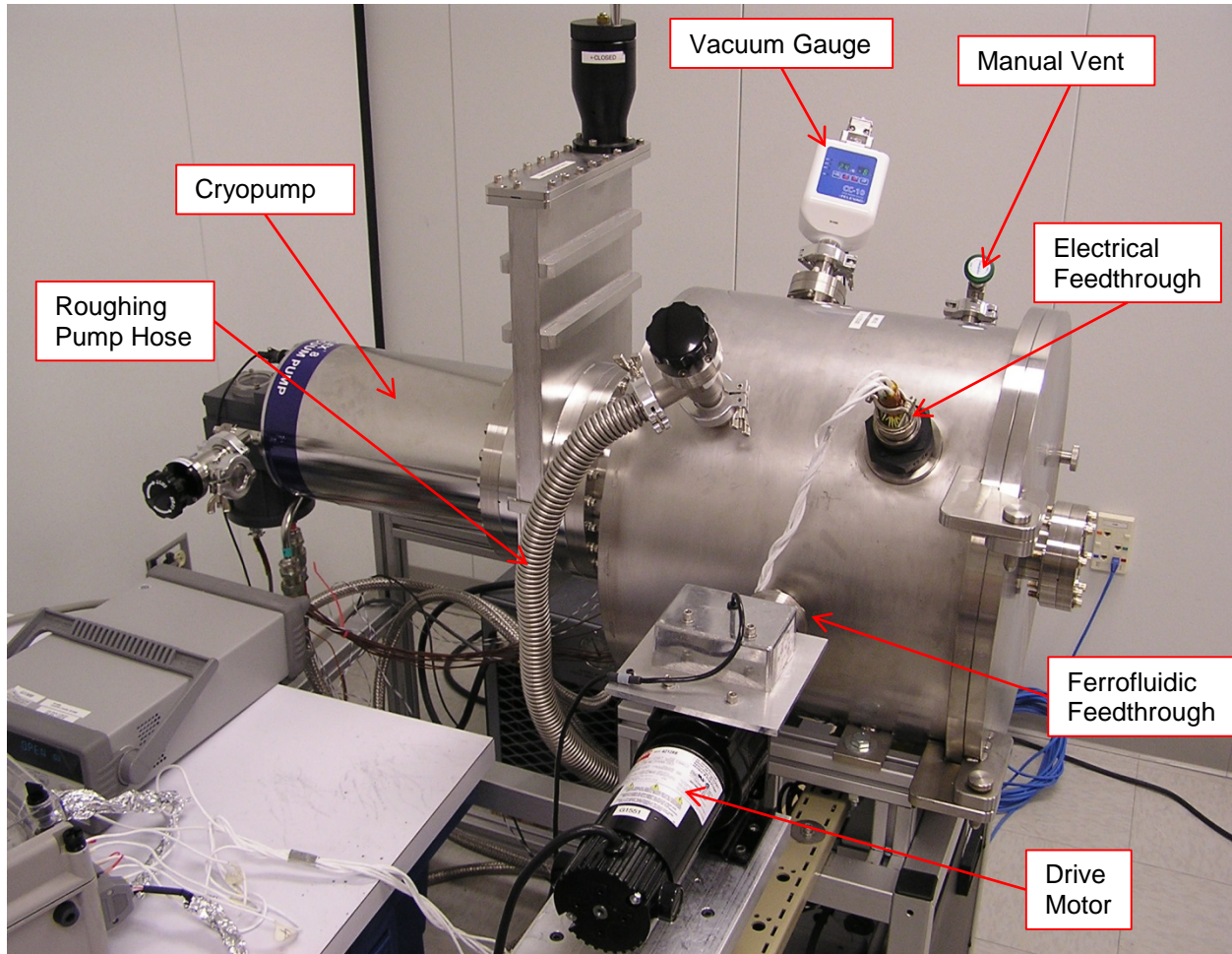


**Figure 4. Vacuum Chamber Setup**

Inside the vacuum chamber is the bearing life test fixture, as shown in Figure 5. Each bearing is mounted and clamped within its own housing and hub in the same manner and with the same tolerances as the flight application. The six bearing housing assemblies are then loaded onto the drive shaft and clamped in place. The drive shaft is supported by redundant fixture bearings which are spring preloaded. A flexible coupling connects the shaft to the ferrofluidic feedthrough in the chamber wall. The bearing housings each have a resistive arm mounted to the housing outside diameter. The resistive arm contacts the load cells through a ball-in-cup arrangement. Based on the force recorded in the load cell and the moment arm length to the spherical contact, the friction torque within the bearing can be monitored. On the opposite side of the bearing housing a counterbalance is mounted to eliminate torque offset due to the weight of the resistive arm. Thermocouples are mounted to each bearing housing to monitor temperature throughout the test. If one bearing experienced increased torque that did not impact the testing of the remaining bearings, then either all bearings could continue to operate without disturbing the setup or the

chamber could be opened up and the load cell for that bearing removed allowing the suspect bearing's housing to spin freely with no resistive load.

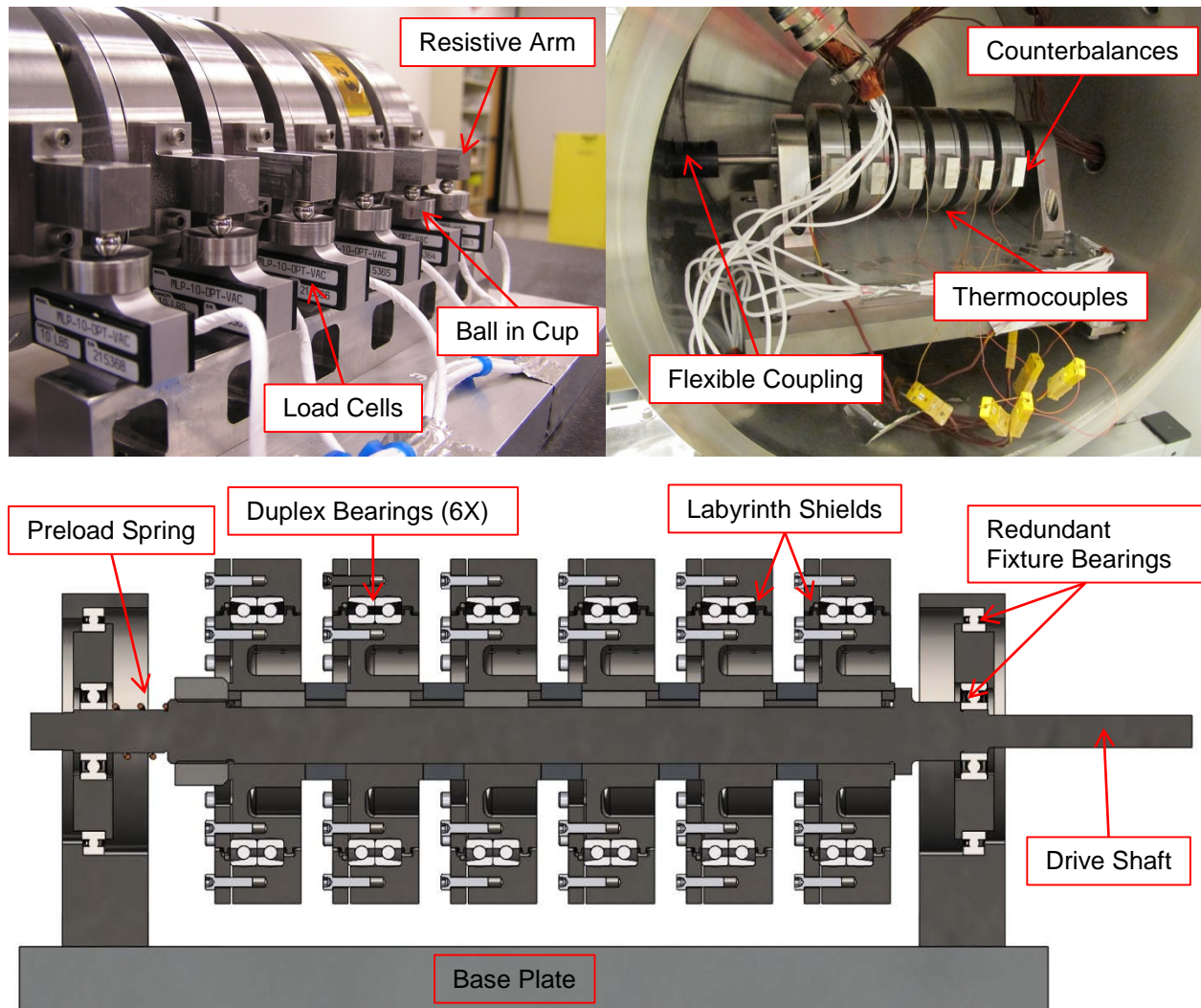


**Figure 5. Bearing Life Test Setup**

## Life Test Results

SMMA Bearing Life testing met and exceeded the 128.4 million revolution requirement for 2X life. The bearings have achieved approximately 202 million shaft revolutions to-date and have not exceeded 125% of the initial setup running torque, nor exhibited credible erratic performance, as defined in the test termination criteria.

### Bearing Friction Torque

From the start of the test, it was noted that bearings 3 and 6 had noisier load cell data than the remainder of the bearings. As seen in the Figure 7, both bearings 3 and 6 had significantly higher fluctuation in load cell output. To determine if those two bearings had significant torque variation or if the load cells were producing erratic output, the temperature plots displayed in Figure 8 were reviewed. Bearing temperature will fluctuate with real changes in friction torque as a component of mechanical power. Since the temperature of bearings 3 and 6 did not follow the torque variation, it was determined that those two load cells were providing erratic output. Per discussions with the customer, it was mutually determined to continue the life test on all six bearings and not subject bearings 3 and 6 to test termination requirements. The team concluded that sufficient life test data could be obtained from the remaining four bearings, and with the life test already extending beyond the launch date, it was not worth the additional schedule to stop the test and replace the faulty load cells. Bearings 3 and 6 were still evaluated for gross changes in performance and will still be subjected to a visual inspection at the end of the life test. As can be seen in Figure 6, none of the remaining four bearings experienced any sudden increases in friction torque and all stayed below 125% of the initial torque measurement. Momentary torque spikes were seen any time the test was paused and restarted due to both the inherent higher starting torque in a lubricated bearing plus the fact that the lubricant had cooled off, thereby reducing its viscosity. Since the on-orbit application operates continuously without starting and stopping, starting torque spikes do not impact on-orbit performance and were not considered against the termination criteria.

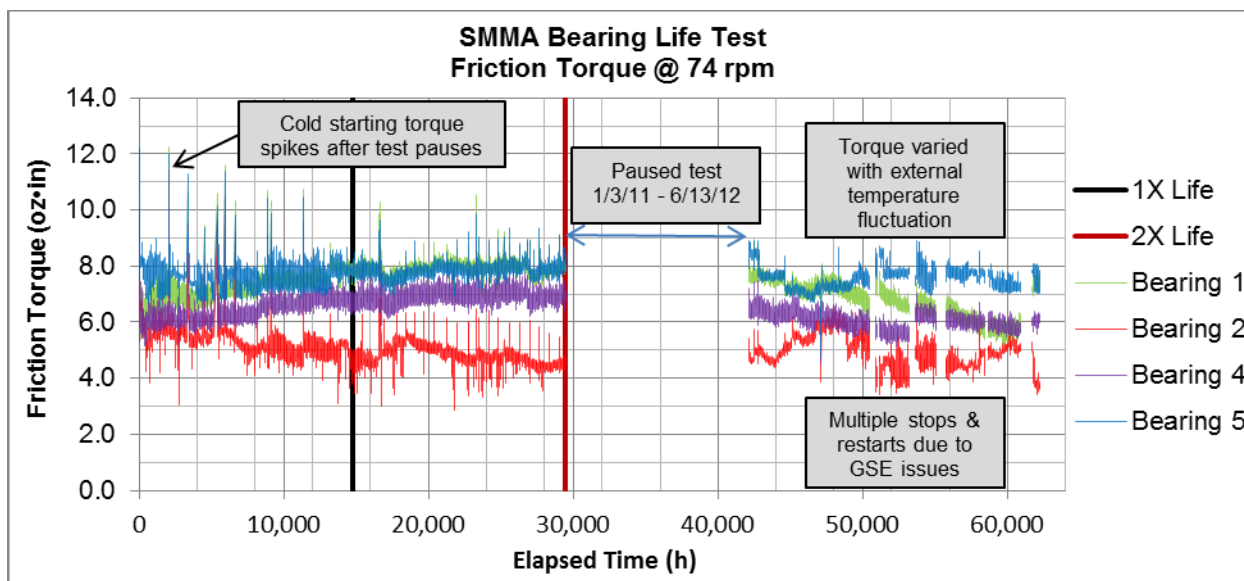


Figure 6. Bearing Friction Torque @ 74 RPM (Bearings 1, 2, 4, & 5)



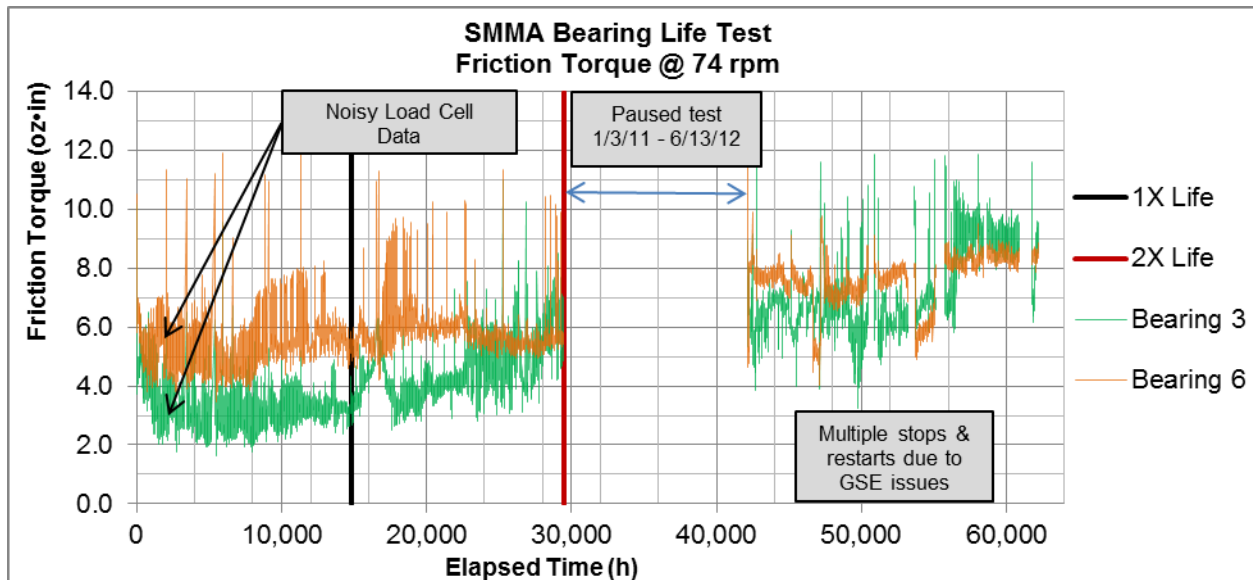


Figure 7. Bearing Friction Torque @ 74 RPM (Bearings 3 & 6)

#### Bearing Temperature

As can be seen in Figure 8, power generated due to viscous losses did heat each of the bearings to a temperature above the 25°C limit to set to achieve Boundary lubrication during steady state operation, while staying below the 36°C upper limit. There were typical daily and seasonal fluctuations in temperature that corresponded to the ambient temperature in the test room, but no upward trends that would correspond with significant changes in internal bearing losses or lubricant degradation. Any time the test was paused, the cryopump would cool the setup resulting in a cold temperature spike. Following a lengthy test pause for maintenance and to negotiate the extended duration, the test setup was repositioned to a different location in the test lab resulting in a higher ambient temperature and a corresponding increase in the temperature of the bearings. The average temperature of the bearings was 28.6°C during the 2X portion of the life test, slightly elevated from the on-orbit typical operating range of 15°C-20°C. This temperature increase results in a conservative test since lubricant life is potentially cut in half for approximately every 10°C rise in temperature as discussed in NASA/CR-2009-215637 [5].

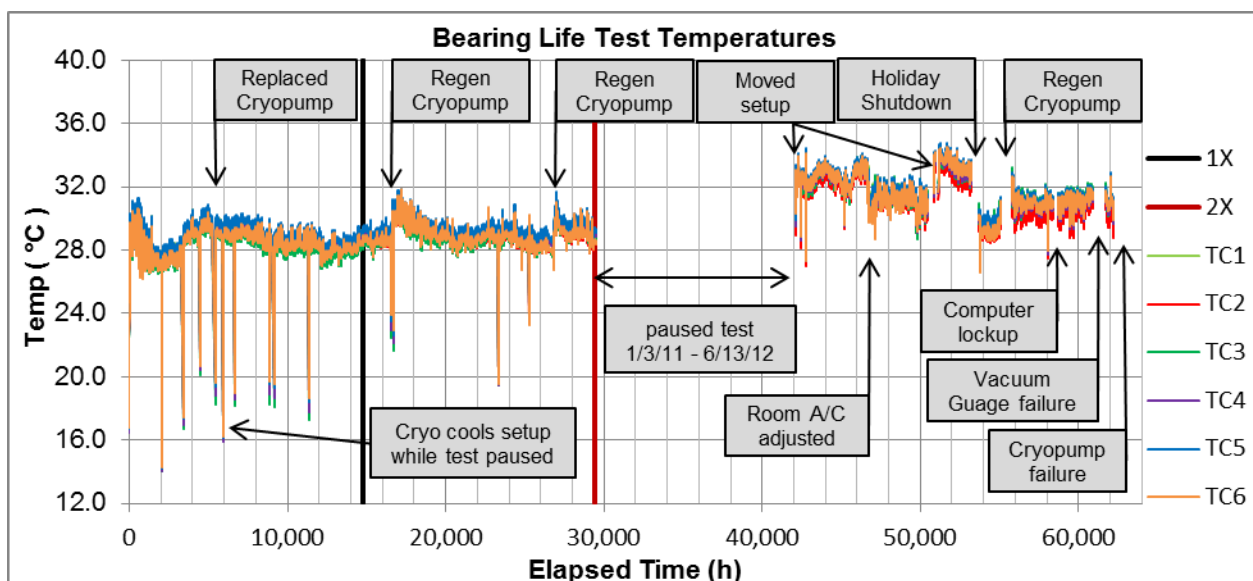


Figure 8. Bearing Temperature

#### Lubrication Film Parameter

Based upon nominal bearing parameters, nominal bearing preload, on-orbit speed of 40.69 RPM, and a nominal on-orbit operating temperature of 17.5°C, the lubricant film parameter ( $\lambda$ ) is calculated to be 0.811. Using those same nominal bearing parameters, nominal bearing preload, life test speed of 74 RPM, and a nominal life test operating temperature of 28.6°C during the 2X portion of the life test, the lubricant film parameter ( $\lambda$ ) is calculated to be 0.810. Since the STLE lubricant life factor [4] changes with  $\lambda$ , even within the same lubrication regime, this close correlation in lubrication regime gives a high level of credence to the life test results.

#### Cumulative Degradation Factor

Taking into account the internal bearing geometry, a mean hertzian contact stress of 521.7 MPa (75.66 ksi) under nominal parameters, and 202 million shaft revolutions; the Cumulative Degradation Factor is calculated to be  $338.8 \times 10^{12}$  bp•psi for this test. This data point significantly exceeds  $88 \times 10^{12}$  bp•psi, which is the highest tested value of CDF published in NASA/CR-2009-215681 [1] for Pennzane-based oil formulation.

### **Lessons Learned**

#### Test Quantity

In order to obtain statistical data more representative of the entire production lot and to cover for any test anomalies that arise with ground support equipment (GSE), it is best practice to test as many articles as feasible. As experienced in this life test, two of the six bearings under test had noisy load cell data. Fortunately, the data sample for this test was large enough to clearly identify that those two setups were outliers allowing them to be sufficiently investigated to determine cause. The investigation benefitted greatly from comparing the abnormal test data to the test data from the remaining four test setups, implicating the load cells. Rather than halt the test and wait for replacement load cells, the life test was able to be continued with the data from the remaining four bearings. If the sample size selected for this test was smaller, noisy data would have likely led to a lengthy and costly investigation, jeopardizing the targeted completion date for 1X life testing. Additionally, higher test quantities increase the likelihood that normal manufacturing variations are accounted for in the test data, further validating the test results.

#### Test Duration

It is highly desirable to test articles to failure whenever possible. Many of the data points listed in the NASA/CR-2009-215681 had the notation "Test Suspension (no failure)" meaning that the bearings/lubricant were functioning normally at the completion of their required life test and could have been operated longer providing better data for future use.

With higher quantities, consider grouping test articles into different life test durations to maximize data usage for future applications. For example, test a portion to 1X mission life, a portion to 2X mission life, and a portion to failure. Multiple test durations are especially important for life test articles that use acceptance criteria that cannot be fully verified during the life test. Such criteria include visual inspection of internal components that require disassembly to perform and measurement of performance parameters which require breaking the life test setup to verify; either of which could jeopardize the validity of additional life testing. In the case of the bearing test described herein, a change in friction torque in the test setup is being used as the pass/fail criteria rather than rely on visual inspection; so testing the bearings to failure results in the most useful data obtainable. Whenever possible, it is preferred to avoid or minimize test pauses so that lubricant temperature and viscosity remain in a steady-state condition and transient data does not have to be rationalized.

#### Test fixture component selection

Ground Support Equipment (GSE) component selection and required maintenance should be carefully evaluated against the life test duration to minimize test interruptions and erroneous data. In reality, not only is the test article undergoing a life test, but every component in the life test setup is undergoing that

same life test. For this test in particular, test equipment was selected based on the initial requirement of 128.4 million shaft revolutions for approximately 40 months. However, once the decision was made to operate the bearings to failure, some of those GSE selections were not sufficient for extended life without additional maintenance, as evidenced by the number of test interruptions seen in Figure 8 after the completion of the 2X portion of the test. Had the life test been planned to operate to failure from the start, then different GSE components may have been selected.

There should be planned maintenance of any test equipment which may fail during the life test and impact the cost and total duration of the test. During this test, there were numerous stoppages resulting from maintenance issues arising with the test equipment.

A DC Brush Motor/Gearhead was selected to drive the bearing test. There is required maintenance to periodically replace the brushes and they were swapped out twice during this life test. Additionally, the entire Motor/Gearbox was swapped out once due to an oil leak between the motor and gearbox causing concerns about insufficient lubrication in the gearbox over the duration of the test. If an indefinite test duration was the original goal, a direct drive motor with closed loop speed control could have been selected to rotate the test shaft due to better control bearing speed over a long duration test, to alleviate concerns about gearhead problems over the duration of the life test, and to minimize rotations on the drive motor bearings.

The cryopump has to be regenerated periodically to clear out collected material in order to be able to maintain the appropriate vacuum level. Regeneration is a fairly quick process, only resulting in a test interruption of approximately 48 hours. Eventually, the cryopump needs to be returned to the manufacturer to be rebuilt resulting in a longer interruption of the test program of approximately 3-4 weeks. Periodic regeneration of the cryopump is inevitable and needs to be factored into the overall test duration. For a longer life test, having a spare cryopump on hand would have reduced the down time due to rebuild.

The vacuum gauge is another maintenance item on vacuum chambers. A cold cathode vacuum gauge was selected over a hot cathode vacuum gauge for this test to obtain longer gauge life at the expense of reduced pressure accuracy. Even so, the cold cathode vacuum gauge had to be replaced after approximately 7 years, well beyond the original planned duration of the life test. Having a spare vacuum gauge on hand would have reduced test down time.

Over time, the weight of the metallic hose from the roughing pump connected to the top of the chamber created a pinhole crack in the feedthrough tube allowing external air to leak inside the chamber. This pinhole was able to be filled with epoxy without breaking the test setup. The leak occurred while the test was halted due to another equipment issue, so the slight drop in vacuum level did not impact the validity of the life test. The roughing pump hose was moved to a more robust feedthrough to prevent recurrence.

The chamber was configured without thermal control as a cost savings feature. Lack of thermal control reduced both the initial cost and schedule of chamber equipment as well as reducing the potential for maintenance issues on the thermal control system. However, the downside to that selection was that the temperature of the bearings under test was at the mercy of self-heating and any temperature variations within the test lab ambient environment. The test chamber also had to be moved midway through the test to a new location within the test facility which resulted in a shift in the external thermal environment that was noticeable in the bearing temperature plots. If the natural self-heating of the bearings from operation combined with the external chamber thermal environment had resulted in a bearing temperature outside of the defined operating condition, then there would have been minimal opportunities for correction without significant delay to add thermal control or significant cost to control the chamber using room ambient temperature.

The length of the subject life test exceeded the calibration due dates on a majority of the test equipment. There was a mutual decision made to not stop the test to calibrate equipment, but rather verify equipment

calibration at the conclusion of the test. There is still a risk of test equipment falling outside of calibration parameters at the end of test with the impact to be assessed at that time.

#### Friction Torque Measurement

When measuring small friction torques in bearings, the test setup must be isolated from external vibration as much as feasible and carefully designed to minimize misalignment loads. Several bearing friction torque measurement issues were discovered during the initial life test setup and validation and had to be resolved prior to starting the life test to ensure recording of accurate data.

Vibration coming from the vacuum chamber equipment created enough noise to appear on the torque readings coming out of the chamber. Rather than continuously collect torque data, the friction torque was captured every millisecond for 60 seconds once each hour with the cryopump and the cryopump compressor turned off during that short period to minimize any torque disturbance.

The weight of the load arm created an offset load which in turn created a zero offset in the friction torque measurements. In order to be able to directly measure friction torque in the bearings without a zero offset, a counterbalance weight, as shown in Figure 9, had to be added to the opposite side of the bearing housing. Additionally, the load cell is very sensitive to off-axis loading. The initial concept of a flat surface contacting a spherical post was not sufficient to provide accurate force measurements. The load arm could not be held exactly parallel to the load cell resulting in a slightly misaligned axis of contact. This misalignment combined with the vertical height of the contact point from the load cell caused a small amount of moment loading into the load cell which produced erroneous values. As can also be seen in Figure 9, the contact was modified to incorporate a ball in a spherical cup to better align the load axis with the load cell, as well as raising the load cell to minimize the vertical moment arm distance. These modifications greatly improved the accuracy of the force measurements from the load cell.

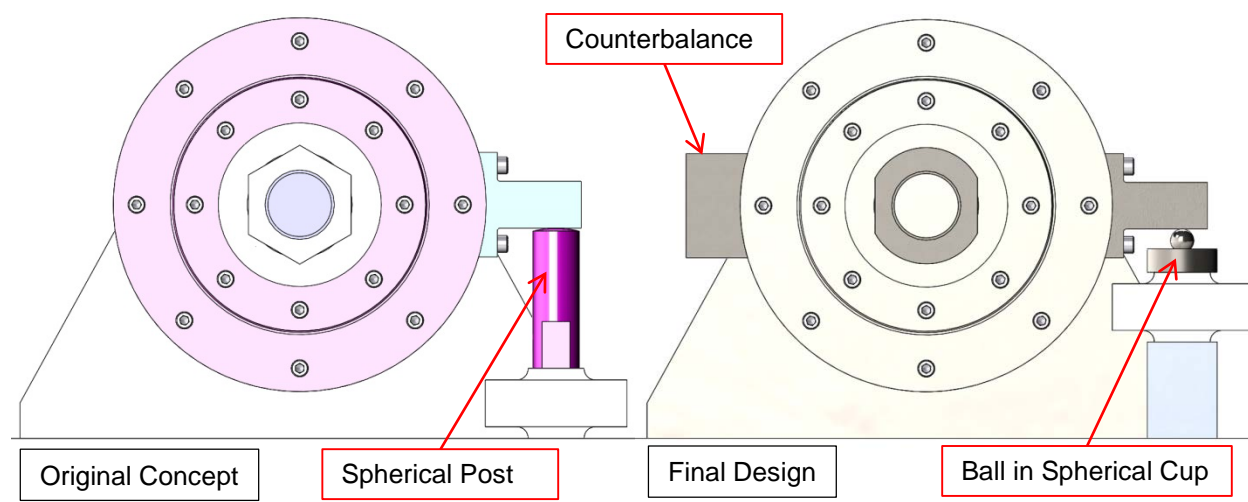


**Figure 9. Test Configuration Changes**

#### Life Test Automation

When running automated life testing, special attention needs to be paid to the computer and software portion of the GSE to minimize test interruptions. Since computers accumulate memory usage over time, the test must be paused periodically for the computer to be rebooted. This allows the automated software to reload and clear the memory cache to prevent unplanned and uncontrolled test interruptions due to automated software crashes. Additionally, other programs running on the computer should be eliminated or minimized as much as possible including virus scans and forced software updates. Several computer crashes were attributed to automatic software updates and their impacts on processor and memory usage. One solution was to minimize computer updates to only those deemed highly critical.



Automated testing over an extended life test also stores a tremendous amount of data (over 6 MB per hour for this test) and maintenance of that data must be considered. The data acquisition computer internal hard drive was not sufficient to store the entire life test data and as such would have to be monitored to ensure the capacity was not exceeded resulting in inadvertent test interruption or loss of data. To free up memory storage space on the internal computer hard drive, the test data was transferred to redundant external hard drives approximately once a month for long term storage and backup. Post-processing of significant amounts of test data for trending summaries and reporting was cumbersome and time consuming. Additional forethought should have been given to utilize different tools to create useful charts and reports with less effort.

Since the test was automated, the test setup was manually checked once per working day to verify that the speed was within tolerance, that the daily rev count was as expected, that the vacuum level was within limits, and that the bearing temperatures were within limits and within expectations. While there were not any occurrences of catastrophic anomalies during the testing performed to date, there would have been an additional level of risk reduction if automated safeties would have been incorporated to safely shut down the test in the event of test parameter exceedances such as torque, temperature, vacuum, or speed. These automated safeties were beyond the budgeted scope of the test.

### **Life Test Conclusions**

The lubricated bearings in this life test not only exceeded the required program life, but also demonstrated the capability to greatly exceed the tested CDF values listed in NASA/CR-2009-215681 [1], showing the possibility to operate bearings for extended lifetimes under closely controlled design parameters and similar operating conditions. For this application, a CDF of  $338.8 \times 10^{12}$  bp-psi has been achieved with no torque degradation seen to date. In order to achieve this life, bearing parameters including bearing geometry, materials, mounting methods, preloading, lubrication, and component screening should be carefully selected and designed in order to optimize contact stress, assembly alignment, and initial torque disturbance. Life testing has been temporarily halted since October 2014 due to maintenance issues with the Vacuum Chamber, but the test articles are being held under rough vacuum in the test chamber. The life test is planned to resume in 2016 with a continued goal of testing until a significant change in bearing torque is witnessed.

### **References**

1. Lo, John C.; et al. "Use of Cumulative Degradation Factor Prediction and Life Test Result of the Thruster Gimbal Assembly Actuator for the Dawn Flight Project." NASA/CR—2009-215681.
2. Jones, William R. Jr and Jansen, Mark J. "Lubrication for Space Applications." NASA/CR—2005-213424.
3. Zaretsky, Erwin V. "Lubricant Effects on Bearing Life." NASA Technical Memorandum 88875.
4. Zaretsky, Erwin V. "STLE Life Factors for Rolling Bearings." STLE SP-34, Park Ridge, IL, 1999.
5. Braza, Joseph; Jansen, Mark J.; Jones, William R. Jr.; "Lubricated Bearing Lifetimes of a Multiply Alkylated Cyclopentane and a Linear Perfluoropolyether Fluid in Oscillatory Motion at Elevated Temperatures in Ultrahigh Vacuum." NASA/CR—2009-215637.



# Piezoelectric Actuators and Future Motors for Cryogenic Applications in Space

Christian Belly\*, Francois Barillot\* and Fabien Dubois\*

## Abstract

The purpose of this paper is to present the current investigation and advancements with piezo actuators or motors in a cryogenic environment especially from the space application point of view. Established performances obtained on cryo-dedicated Amplified Piezo Actuators (APA®) are given and extension of their capabilities is detailed using piezo motors, or Stepping Piezo Actuator. The Stepping Piezo Actuator (SPA) principle is shown in two innovative configurations, fully compatible with a cryogenic environment.

## Introduction

High-precision piezoelectric-based mechanisms have already proven their capability to meet requirements for space applications in common temperature ranges. A new step is now underway to improve their operational range down to temperatures nearing absolute zero. Based on the latest experimental results, this paper presents this emerging capability for piezoelectric-based actuators, motors and mechanisms to meet this need.

First, Amplified Piezo Actuators are presented, and especially their cryo-dedicated version, with measurements down to 40K. Then, APA® integration within a piezo motor is shown, and experimental data, including low temperature (90K) experiments, are presented. After that, two new motor configurations are presented, with ambient behavior explanation before setting the perspectives offered by those newly available technologies.

## Piezo Actuators in a Cryogenic Environment

### Amplified Piezo Actuators

Amplified Piezoelectric Actuators (APA®) are linear actuators offering large deformations (from 1 to 10%) and medium strokes (up to 1 mm) [1]. They have been designed with an efficient mechanical amplifier and a pre-stress applied to the piezo ceramics. This design choice was performed initially to meet space requirements in order to offer a good ability to withstand external vibrations (due to launch). As a consequence of their pre-stress, they can perform the full strokes not only in static conditions but also in dynamic conditions including resonance and fast transient motion. As additional benefit, they are extremely reliable (lifetime is more than  $10^{10}$  cycles), they have passed many aerospace qualifications, and they are selected in many EU and U.S. space missions [2]. Using the ability of APA® for dynamic motions, various mechanisms have been built: fast piezo shutters, fast tool servo, circuit breakers, micro scanners, proportional piezo valves, and piezo generators. APA® samples are visible on Figure 1.

### Cryo Performance of Dedicated Amplified Piezo Actuators

The ability of piezoelectric ceramics and stacks to work in a cryogenic environment has already been shown in previous work [3]. Acquired knowledge has been used in order to design cryo-dedicated actuators, using an ingenious combination of materials in order to control thermos-mechanical behavior. In this study, several actuator characteristics, such as stroke, capacitance and creep are studied versus temperature, in a temperature range going from ambient to 40K. The interest in this knowledge is mainly valuable in terms of cryogenic-dedicated design.

---

\* Cedrat Technologies, Meylan, France

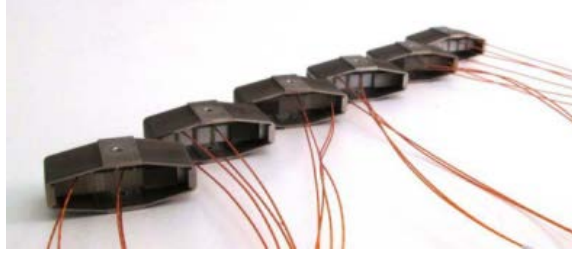


**Figure 1. Cryo-dedicated Amplified Piezo Actuators**

To be compatible with a vacuum and low temperature environment, an interferometric sensor FPS3010 has been used [3]. It provides reliable measurement from ambient to 40K.

Stroke is one of the main performance characteristics of piezo actuators. It is well known that stroke is reduced with low temperature. Stroke is measured using full stroke sinus command. Amplitude is extracted from the interferometer sensor (Figure 2). Full stroke drops from 95  $\mu\text{m}$  to 37  $\mu\text{m}$  (39%) for supplier #1 whereas it decreases from 81 to 17  $\mu\text{m}$  (20%) for supplier#2.

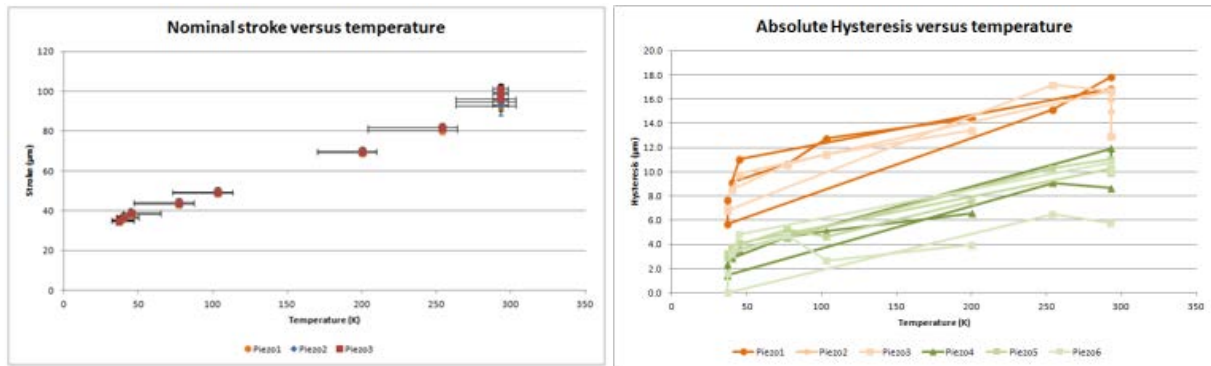


**Figure 2. Stroke and hysteresis versus temperature**

Stroke measurement is also used in order to obtain hysteresis information. Hysteresis is an intrinsic characteristic of piezo actuators. Two suppliers' preloaded stacks are compared at temperatures from ambient (293K) to 35K. It is seen in Figure 2 that hysteresis amplitude is reduced with decreasing temperature. Moreover, supplier #1 actuators are producing higher hysteresis. Supplier #1 actuators reach 20% of full amplitude compared to 10% for supplier #2.

Piezo actuators are assimilated to capacitance from an electrical driver view. The actuator capacitance is determining the bandwidth of the group {electronic + actuator}, due to amplifier current limit. Therefore, this characteristic is important considering driving philosophy or in the case of charge control of piezo actuators. Capacitance versus temperature is plotted in Figure 3. It can be observed that capacitance tends to stabilize at approximately 20% of its ambient value when decreasing temperature.

Position creep is a slow change of actuator position that appears after a constant voltage has been applied. In open loop operation, position is slightly increasing with time, unfavorable to stability. This creep is generally characterized by a logarithmic law [4]. It has been observed, as presented in Figure 3, that creep increases with low temperature. However, this behavior is removed after cycling. Therefore, cycling seems to be good practice before functional actuation of piezo in a cryogenic environment.

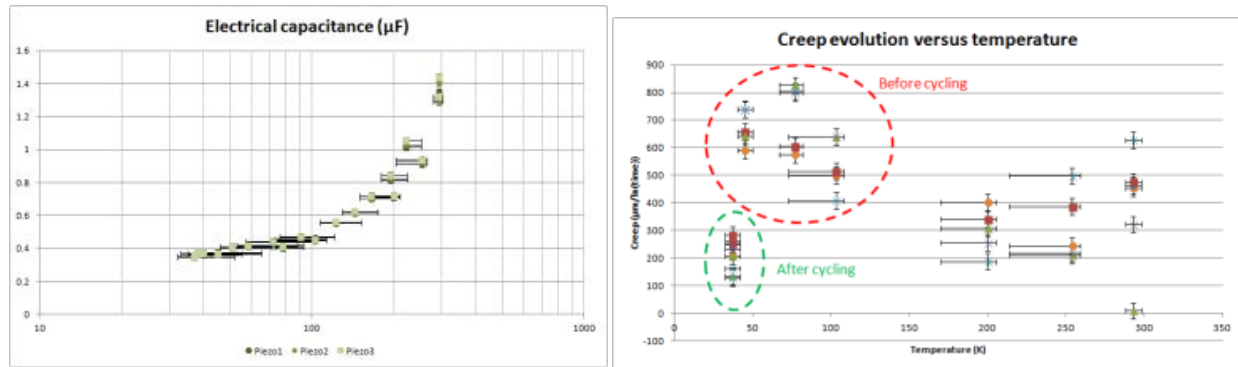


**Figure 3. Capacitance and creep evolution versus temperature**

Reduction of stroke due to temperature limits piezo actuators even more due to their short stroke. Moreover, even if static power consumption is low, position is not kept when power is cut. Therefore, when larger stroke and/or holding force with no power consumption are needed, piezoelectric motors become relevant.

### Piezo Motors

An APA-based piezo motor is presented with its working principle. First, low temperature results are presented, giving a first indication about the technology potential. After that, two innovative linear motors, based on a similar principle are presented.

#### Stepping Piezo principle and low temperature compatibility

Stepping Piezoelectric Actuators (SPA) are long-stroke linear inertial piezoelectric motors for micro/nano positioning applications benefiting from the advantages and the heritage of the APA®. SPA is a way to expand the limited stroke of the APA® to centimeter-length strokes. This feature is achieved using the IDM principle [5].

SPAs are formed of only four parts: the APA®, a front mass, a clamp, and a rod. SPA operates through the accumulation of small steps, using inertial mode, impact forces and stick-slip effects as introduced in [6]. Typically, a slow APA® actuation generates a slow motion of the mass while the rod sits in the clamp. A fast APA® actuation induces a fast motion of the rod slipping in the clamp. This allows getting steps, which gives a long stroke, called the stepping mode (M1). Between each step the actuator is locked in position [7].

The load may be fixed on different positions leading to two different motor capabilities thanks to different modes. In a first configuration offering nano positioning (Figure 4), the load can replace the mass or can be fixed to the mass. So when the long stroke (M1) is performed, the motor can be also operated in a deformation mode (M2) for a fine adjustment. In this case, the stroke is proportional to the applied voltage, which leads to a nanometer resolution and a high bandwidth (limited by motor blocked force). In a second configuration, the load is fixed on the moving rod. In this case, the advantage is a high stiffness, but fine mode is not available.

The long stroke stepping mode (M1) is produced by step accumulation with an appropriate 0-150 V voltage pattern. The short stroke deformation mode (M2) is produced by deformation of the APA®, which is simply proportional to the excitation voltage between -20V to +150V. Only one amplifier channel per SPA is required.

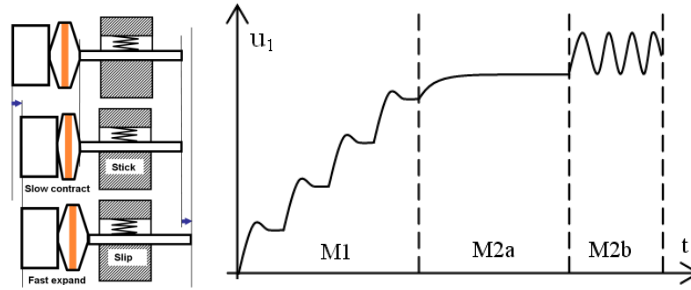


**Figure 4. SPA components and principle: stepping mode (M1) and deformation mode (M2)**

The large deformation stroke of the APA® is also an advantage. It provides a useful deformation stroke mode (M2). It also contributes in getting good speed in long stroke mode (M1); larger steps per cycle compensate for a lower step frequency. Benefits from amplification in the Impact Drive Mechanism have been demonstrated in [8].

Low temperature tests were performed on a SPA40SM (based on middle range APA®) from 0°C to -180°C, the lowest temperature allowed by the test rig. Speed is affected with a linear speed reduction with temperature. This is fully correlated with actuator stroke reduction. The force results are shown in Figure 5. It can be seen that a drive force reduction is observed at lower temperatures, but not lower than 75% of nominal force achieved at ambient temperatures. However, after every temperature cycle, the performance is recovered upon returning to room temperature, showing no continued reduction in performance after periods of exposure to low temperatures under vacuum.

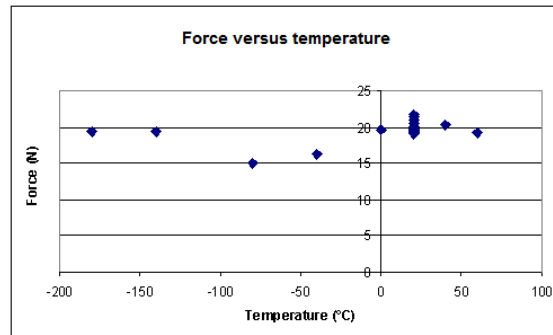


**Figure 5. SPA40SM Force versus temperature [9]**

#### Module Stepping Piezo Actuator

In typical SPA motors, the clamp is moving by friction at a variable distance from the actuator. This creates a limitation in stroke, hyperstatism with potential bearing, reduction of force with the distance, and constraints in new mechanisms design. In comparison, Module SPA (MSPA) frees the rubbing contact so the distance between the friction force and the APA® electromechanical force remains at a constant distance. It is able to drive any type of body by friction in linear or rotary motion depending on the guiding.

First implementation is based on a linear piezo stage. This type of stage is relevant for optics motion, or sample positioning, but is currently limited in stroke. The MSPA configuration is used in order to move a 30x30x10 mm<sup>3</sup> device and is presented on Figure 6. A representative configuration using a dummy lens to simulate an optical zoom or focus system has shown its capability to perform long stroke (200 mm) with a speed of 15 mm/s.

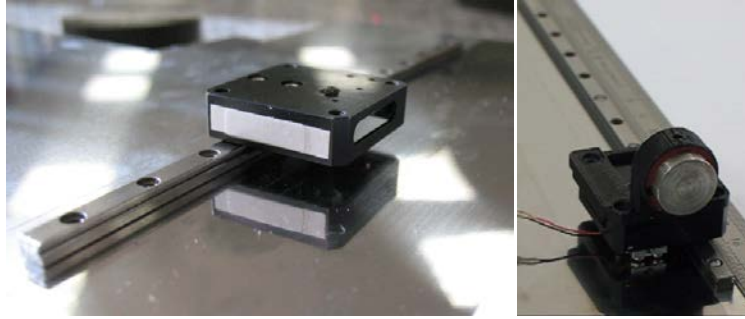


**Figure 6. MSPA combined with 200-mm stroke guiding in linear configuration + with dummy lens**

Another possible requirement is constant speed all along the stroke. MSPA is used to produce a linear displacement and uses inertia principle to disrupt the friction contact and restart a new ramp of displacement. This creates a linear constant speed displacement for the moving module, or moving mass. Figure 7 presents an example of displacement for a few test masses. Linearity of displacement can be observed. For more stringent requirements, a closed-loop solution has been implemented.

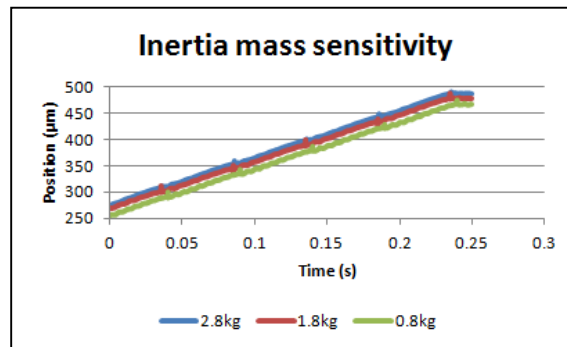


**Figure 7. MSPA displacement example**

#### Force Stepping Piezo Actuator

The second type of configuration is also based on Stepping Piezo Actuators. The internal structure of FSPA (Figure 8) allows decoupling high external forces from actuation mechanism making the motor compatible with high load and high levels of vibration. A prototype has been built to support a more than 600-N external force without losing its position.



**Figure 8. FSPA motor prototype**

Another major advantage of this second configuration is the strong resolution that can be reached. In order to show motor resolution, step-by-step signal is applied and position output is controlled using capacitive sensor. Figure 9 presents the results obtained on the motor. Resolution of steps below 20 nm

is shown. This corresponds to a 1.2  $\mu\text{m}/\text{min}$  speed. The speed reached with a 20 Hz and full voltage amplitude signal is 75  $\mu\text{m}/\text{min}$ .

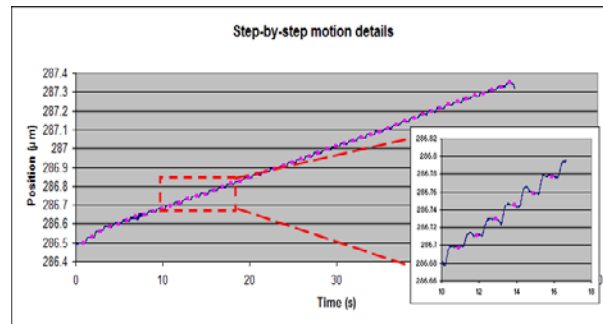


**Figure 9. Motor displacement and resolution (mean step = 20 nm)**

#### Cryo applications and perspectives

The presented configurations and associated results are fully compatible with cryo-dedicated actuators. The impact of temperature on SPA motors are mainly about speed (due to actuator stroke reduction), but not on force. Therefore, performances obtained on MSPA or FSPA should be fully comparable and allow targeting specific cryo needs. One example is the GAIA M2M pointing mechanism, with 70-nm resolution on 550- $\mu\text{m}$  travel in a temperature range from ambient to 100K [10]. Other cryo needs have been identified through the EChO mission [3]. Low temperatures (30K) are combined with high shock levels (2000g), targeted by FSPA usage. Typical 10-100 N actuation force and 200-N to 2000-N holding position force are fully in the field of competence.

#### **Conclusion**

In this paper, results obtained on cryo-dedicated Amplified actuators are shown with respect to temperature influence from ambient to 40K. Compatibility of performances with positioning application is proven but intrinsic limits in terms of stroke have to be overcome; proposed solution is piezo motor. The SPA concept is reviewed and applications within two new configurations are shown. Interesting advantages and performances obtained at ambient temperature are correlated to a cryo-dedicated Actuator in order to give the reader the potential of the combination of technologies.

#### **Acknowledgment**

Cryogenic piezo actuators have been tested within the R&T program from CNES. TV facilities at Toulouse center have been used. The authors want to thank Laurent Cadiergues and Daniel Gervaud for their support.



## References

1. Le Letty R., Claeyssen F., R., New amplified piezoelectric actuator for precision positioning and active damping, *Proc. SPIE Vol. 3041 Smart Structures and Materials*, (1997), pp. 496-504
2. Allegranza C, Gaillard L., Le Letty R., Patti S., Scolamiero L., Toso M., "Actuators for Space Applications: State of the Art and New Technologies", *Proc. Actuator 2014*, Bremen
3. Belly C., Hihoud M., Pages A., Argelaguet H., Moreno J., Mangeot C., "Cryogenic piezo characterisation and integration in Fine Steering Tip/Tilt Mechanism", *Proc. Actuator 2014*, Bremen
4. Junga H., Gweon D., "Creep characteristics of piezoelectric actuators", *REVIEW OF SCIENTIFIC INSTRUMENTS VOLUME 71, NUMBER 4*, (2000), pp. 1896-1900
5. Higuchi, T. "Apparatus and method for effective fine movement by impact force produced by piezoelectric element", (1987) EP0292989
6. Higuchi T., Yamagata Y., Furutani K. & Kudoh K. "Precise positioning mechanism utilizing rapid deformations of piezoelectric elements", *Proc. of IEEE Workshop on Micro Electro Mechanical Systems*, (1990), pp.47-51
7. Claeyssen F., Ducamp A., Barillot F., Le Letty R., Porchez T., Sosnicki O. & Belly C., "Stepping Piezoelectric Actuators based on APAs", *Proc. Actuator 2008*, Bremen
8. Belly C., Charon W., "Benefits of amplification in an inertial stepping motor", *Mechatronics* 22 (2), (2012), pp. 177-183
9. Belly C., Buttery M., Claeyssen F., "THERMAL VACUUM BEHAVIOUR OF A STEPPING PIEZO ACTUATOR", *14th European Space Mechanisms & Tribology Symposium – ESMATS*, (2011)
10. Compostizo C., López R., Rivera L., "GAIA M2M POINTING MECHANISM QUALIFICATION", *14th European Space Mechanisms & Tribology Symposium – ESMATS*, (2011)



# Development of a Self-latching Hold-down Release Kinematic (SHREK)

Ruggero Cassanelli\*

## Abstract

SHREK (Self-latching Hold-down Release Kinematic), is an innovative shape memory actuated hold down and release device, aimed to latch and release solar panels. It is specifically conceived to fit the small satellite market requirements, as well as overcome some recurring shortcomings of existing similar devices. This paper describes SHREK's unique design characteristics and preliminary test results.

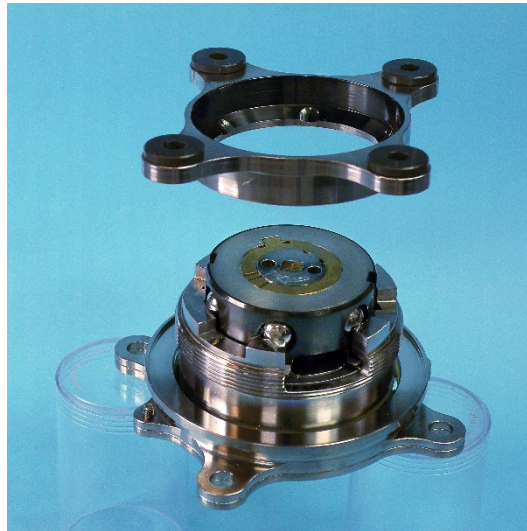


Figure 1. SHREK

## Introduction

Small (mini and micro) satellites represent a rapidly expanding market, which extends the access to space to a number of comparatively small organizations. Its commercial nature brings in requirements that, at no detriment of technical performance, are focused on operability and cost. For this market, AEREA has devised a mechanism for latching and releasing deployables while pursuing the following goals:

- Commercially attractive
- ITAR free
- Automatic manual latching (self-latching)
- Simple manual release
- Remote release with shape memory alloy technology
- Full control over the applied preload
- Ground and flight operable without parts replacement
- On-site ground reset operations without parts replacement
- 50 remote actuations without degraded performance (operating time and shock)
- Functional temperature range: -56°C to +70°C (-56°C to 100°C desirable)
- Disconnection shock: < 300 g's [negligible shock desirable]
- Preload force: up to 5 kN

---

\* AEREA S.p.A., Turate, Italy

- Panel mass: up to 10 kg
- Mechanism mass < 0.5 kg [0.3 kg desirable]
- Nominal power consumption: 15 W
- Actuation time: < 60 s
- Envelope: diameter < 100 mm, height < 40 mm

### SHREK Description

The following is based on an application where the solar panel is hinged to the satellite on one side and held by the SHREK mechanism on the opposite side.

#### Mating principle

The mechanism is composed of a Panel module and a Satellite module. The Panel module is a lightweight metallic ring permanently connected to the internal surface of the panel. The Satellite module is a metallic cylinder 35-mm long and 85 mm in diameter, mechanically and electrically connected to the external surface of the satellite. The two modules are axially mated by interposition of an array of spheres (ball lock concept). The spheres are housed in the Satellite module, where they can be radially displaced in either one of two positions: retracted (Unlatched status) or extracted (Latched status). The position of the spheres is determined by the rotation of a Spool, internal and coaxial to the Satellite module. The Spool has radial pockets which, when aligned with the spheres, allow the spheres to retract.

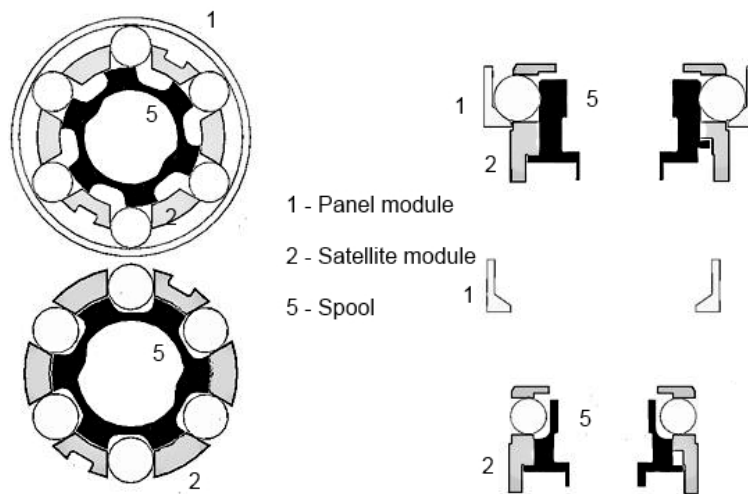


**Figure 2. Mating concept (Top=Latched – Bottom=Unlatched)**

#### Self-latching (reference Figure 3)

This is a unique feature of SHREK, operable by manually pushing the panel against the satellite, and its goal is to simplify installation, integration and ground testing of the mechanism.

The Spool is permanently biased, by a Torsion spring (10), to rotate toward the latched position. The torsion applied to the Spool is reacted by the spheres. The radial components of such reactions permanently push the spheres toward the extracted (Latched) position. In the Unlatched condition, the spheres are kept into the Spool (5) pockets by an external, coaxial, spring-loaded Active sleeve (9) which physically blocks the spheres' passages.

For latching, the Panel module (1) is pushed against the Active sleeve (9), which consequently slides axially toward the base of the mechanism, against the force exerted by the Kick-Off spring (7). At the bottom end of the Active sleeve movement, where the Kick-Off spring reaches its maximum compression, radial motion of the spheres is possible. In this position, the torsion spring rotates the Spool. The rotation of the Spool results in the expulsion of the spheres from their pockets due to the pocket having an angled side that

produces a radial force on the sphere. When the Spool reaches its Latched status, the spheres remain locked between the inside walls of the Panel module and the external surface of the Spool.

#### Preload (reference Figure 3)

The Kick-Off springs force (V), applied to the Panel module through the Active sleeve, is re-introduced through the spheres vertically, into the Satellite module (V), and radially into the Spool (H). Such action removes any residual play between the mated parts. Furthermore, during the unlatching sequence, the Kick-Off force, which is applied all along the demating stroke, provides an additional deployment aid, intended to insure absence of disengagement uncertainties.

The preload introduced by the Kick-Off spring (0.5 kN) is considered adequate for stiff, light panels. Should that be insufficient to ensure continuous contact between Panel and Satellite modules at any point of the operational envelope, the provision of an optional Ring nut (6) to be screwed onto the Active sleeve (9) in order to create further separation force has been provided.

The downward rotation of the Ring nut (6) translates in an upward axial motion of the Active sleeve against the Panel module. With this feature, an additional preload of up to 5 kN can be achieved. The control of the preload is obtained by putting a calibrated preload wave spring (8) between the Ring nut and the Satellite module.

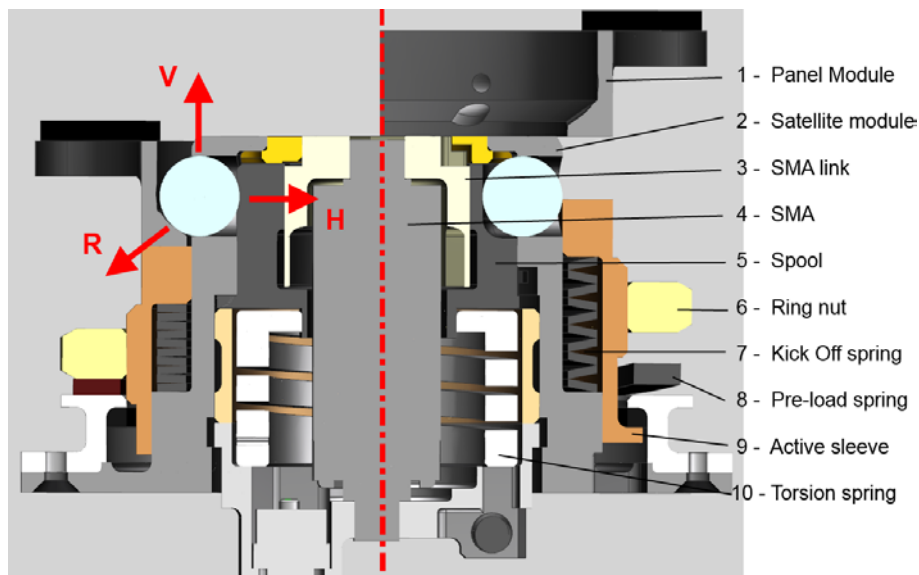


**Figure 3. SHREK section (Left=Latched – Right=Released)**

#### Manual release (reference Figure 3)

On the ground, the Spool can be manually rotated to the Unlatched position through a dedicated operating point accessible from the side of the Mechanism. The Spool rotation ends at a predetermined mechanical stop, where the Spool pockets are aligned with the spheres. In that position, the radial component (H) of the overall force (V), exchanged between Panel and Satellite, drives the spheres into the Satellite module. With the spheres out of the way, the modules are disengaged. The Active sleeve, under the action of the Kick Off spring, slides upward along the Satellite module, forcing the Panel module away and blocking the spheres into their pockets.

#### Remote release (reference Figure 3)

A NiTiNOL bar, enveloped by two redundant heaters, is axially integrated into the Satellite module. The bar is installed in a torsionally deformed martensitic phase with the mechanism in the latched condition.

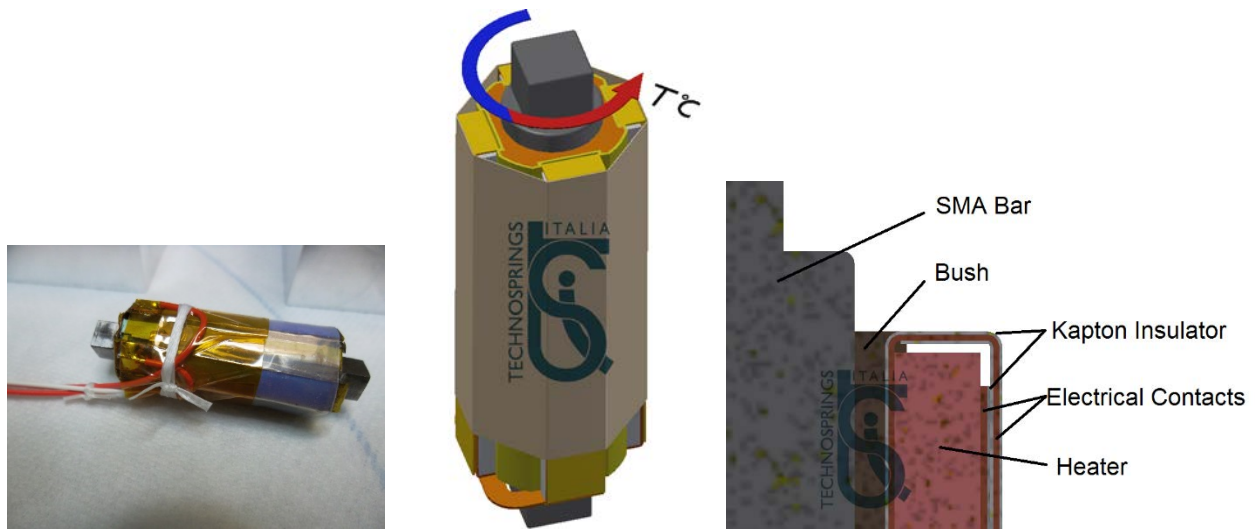


**Figure 4. SMA bar with heater**

The bar has one extremity firmly mated to the Satellite module, while the opposite end is connected to the Spool through the SMA link (3). When heated at a temperature above the austenitic phase transformation, the bar rotates, recovering its original un-deformed shape. The bar rotation, transferred to the Spool by the SMA link, puts the mechanism into the Unlatched status, thus releasing the Panel module.

#### SMA Monolateral spool control

Figure 5 shows the peculiarity of the monolateral constraint between the SMA bar and the Spool, allowing the Spool to rotate without being affected or affecting the SMA bar in the martensitic phase. Conversely, the rotation of the SMA bar in the austenitic phase induces the rotation of the Spool.

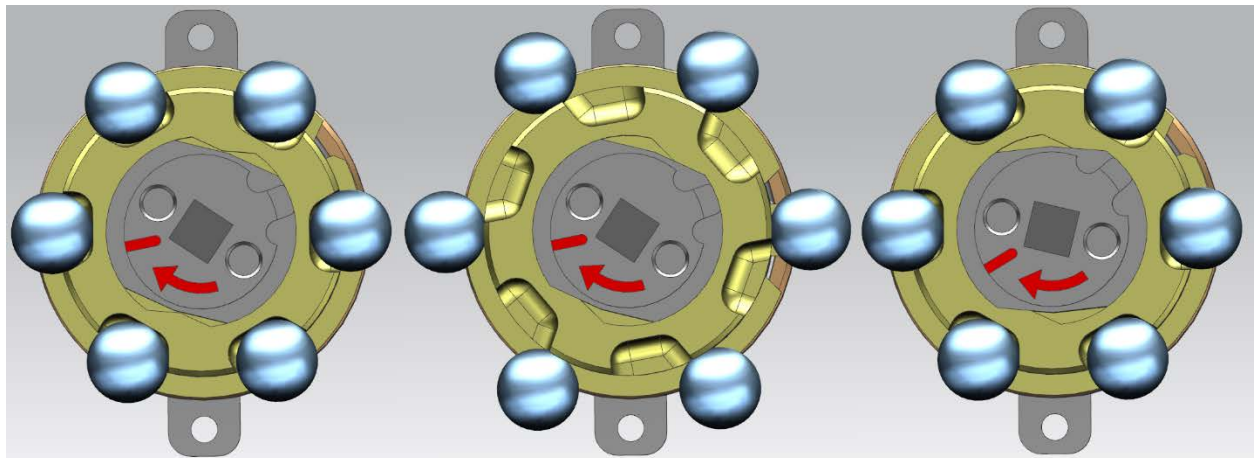


**Figure 5. Spool control**

The central picture of Figure 5 shows the SHREK in closed status. The picture on the left shows the Spool manually rotated in Released status with the SMA bar unaffected by the Spool rotation. The picture on the right shows how the rotation of the SMA bar is transferred to the Spool (remote actuation).

#### Reset after remote actuation

Once the SMA bar is cooled below the martensitic phase temperature, and the mechanism is in the Released condition, the bar can be re-deformed through the operating point located on the top of the

Satellite module (pin wrench interface visible in Figure. 5). Up to 50 reset operations without performance degradation are possible.

## Assessment of Results

### Operability features evaluation

Self-latching, manual Unlatching, Remote actuation and Reset functions have matched the expectations. The additional preloading concept needs to be further improved. The thread pitch is to be enlarged to make it less likely to bind. Smooth manual release requires the Ring nut to be fully screwed down. The use of a relatively large wrench is not seen as appropriate in close vicinity of solar panels. The wave spring effectively allows seeing the applied preload at a glance. Conversely, that spring was revealed to be the single most significant source of shock.

The NiTiNOL bar proved it had more than adequate behavior. In particular, it was ascertained that the actuating time is independent of the preload applied, a good indication of the adequacy of the motorization margin. During development, different alloy compositions and alloy training procedures were tried. It was realized that the functional properties, in terms of torque generation for a given torsion strain, were inversely proportional to the transition temperature. This means that rising the austenitic transition temperature reduces the motorization margin. The selected solution has a transition at about 80°C in 55 seconds. Vacuum tests will probably induce further, hopefully little, adjustments.

### Shock Response Spectrum

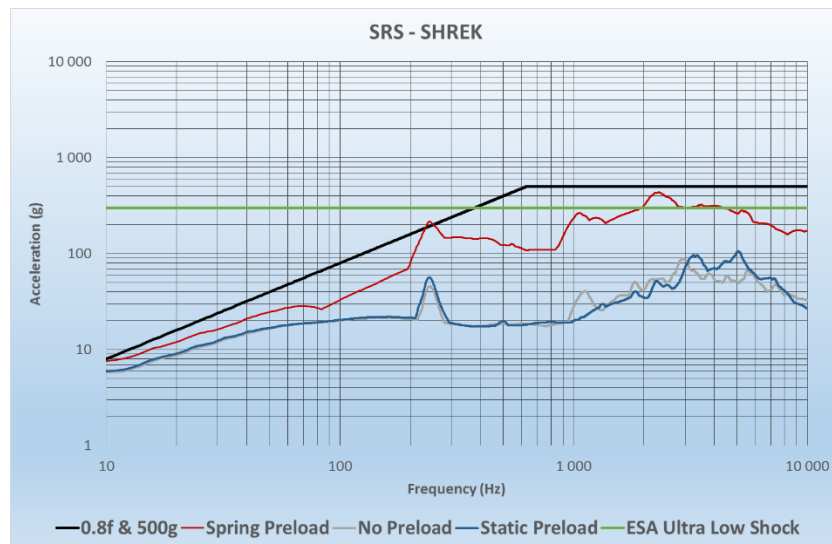


**Figure 6. Preliminary Shock test results**

Within the SHREK mechanism, there are four sources of shock:

- The Spool hitting its mechanical stop under the drive of the torsion spring.
- The spheres hitting the bottom of the Spool pockets driven by the action of the Kick Off spring
- The Active sleeve reaching its mechanical stop driven by the action of the Kick Off spring.
- The release of the energy stored in the preload spring.

Care has been taken to physically separate as much as possible the events associated with shock generation. This has worked well with the first three sources.

From the SRS curves shown in Figure 6, reflecting the Release Shocks in different configurations, it can be seen that the wave spring increases the Shock level, rising it marginally beyond the Ultra-Low Shock acceleration threshold. Replacing such a spring with a standard washer brings back the shock level below

100 g. With the removal of the wave spring, a different method to measure the applied preload needs to be conceived. Integrated strain gauges are under evaluation.

#### Motorization

SHREK concept is based on sliding elements, thus friction plays an important role in performance and motorization factors. Several element tests were performed to support the selection of the materials, the treatments, the roughness and geometry of the contacting surfaces as well as the number and size of the locking bodies.

The torque required to open the mechanism, with a friction coefficient of 0.15 and a preload of 5 kN, is expected to peak at 8 Nm during the initial 5-8 degrees of Spool rotation. After that, the mechanism is expected to become self-propelling with a null driving torque at about 10 degrees and a positive one after that. Actual tests performed in air have shown a max torque of 5 Nm peaking at the same expected rotation point.

The SMA bar is dimensioned with a torque capability of not less than 12 Nm at the beginning of the shape recover and not less than 8 Nm after 20 degrees rotation. Actual motorization factor will be measured in vacuum conditions.

#### Tests

So far, three SHREK prototypes have been manufactured and successfully subjected to Vibration (Sine and Random), Shock, High Temperature and functional endurance tests in air. Thermal Vacuum testing is planned in the first quarter of 2016. Opportunities for an in-orbit demonstration are being actively pursued.

#### Affordability

At a mass of less than 0.4 kg, SHREK is composed of 15 parts, obtained with standard machining processes, a SMA bar with associated heater, plus standard parts. Its assembly takes roughly 20 minutes and the use of two simple special tools. Its manual operation needs one simple, to make and use, special tool. A 30% cost reduction over the average comparative existing mechanisms is expected.

### **Conclusions**

The SHREK mechanism is maturing as a small, simple and reliable mechanism for a specific field of application (solar panels of small satellites). Its unique features, simplicity and economic affordability should grant its adoption on a large scale.

The outstanding future tasks are:

- performance measurement in vacuum environment (actuation time, motorization and life)
- alternative method of preload measurement (strain gauges integration)
- obtain flight experience with an in-orbit demonstration.

The first two tasks are planned to be achieved during first half of 2016.

### **References**

- Patent Pending "Shrek - Domanda di brevetto italiano n. 102015000010459"



# Challenges of Designing a 13-Hz High-Load Vibration Isolation System with Tight Volume Constraints: Lessons Learnt and Path Forward

Stella Dearing\* and Dale Ruebsamen\*

## Abstract

This paper describes the design of a passive isolation system using D-struts® to isolate an optical payload from aircraft-borne jitter with challenging stroke per volume requirements. It discusses the use of viscoelastic-coated D-struts® that meet the customer performance and outgassing specification, NASA-1124. The result was a relatively soft isolation system, (where the first mode was 13 Hz), with each individual strut capable of withstanding loads on the order of magnitude of 623 N (140 lbf), weighing less than 910 g (2 lbf), fitting in a volume 5.1 cm (2 inches) in diameter and 12-cm (4.7-inches) long and capable of performing up to 1000 Hz without nonlinearities.

## Introduction

This paper is a result of a contract to develop a passive isolation system using D-struts® for a high altitude application to isolate an optical payload from aircraft-borne jitter and environmental influences such as temperature, pressure, vibration, and shock loads. The design challenge consisted in meeting a 13-Hz isolation system 1st mode requirement within a limited volume with no permissible non-linearities in the operating range of 0-1000 Hz while experiencing large vibration, shock and static loads. This precluded the use of soft stops and led to a design optimized to minimize length and diameter as well as a strut soft enough to stroke the required amount. This resulted in D-struts® with stroke per unit length and component rotations outside Honeywell's design heritage. It was found that such a soft spring in such a small package resulted in a surge mode, surge mode harmonics and lateral modes at frequencies lower and gains higher than typical designs. This was detrimental to performance out to 1000 Hz and meant a change in modeling approach was required and a low outgassing viscoelastic coating was applied to the main spring to meet the customer specification.

## D-Strut® Background

D-strut® isolation systems have been used consistently in space for the last 25 years for many applications, including satellite launch, momentum control, and payload isolation. They are passive mechanical devices made up of a linear-action machined spring and a fluid damper subassembly including hermetically sealed welded metal bellows. Figure 1 shows the 'MTV' strut with its main components labeled. They are 3 parameter isolators, with a spring in parallel with a series combination of a spring and damper, with 40 dB/decade roll-offs as compared to 20 dB/decade roll-offs from the more traditional two parameter isolators (a spring and damper in parallel). When D-struts® are positioned in a hexapod or octopod configuration they provide six degree of freedom support allowing decoupling between the payload and the supporting structure making them ideal for isolation.

---

\* Honeywell Aerospace, Defense and Space, Glendale, AZ

## The Design Challenge

The 'MTV1' D-strut® is designed to withstand 623 N (140 lbf) axial load, rotate 7° at the main spring and flexure and stroke 0.99 cm (0.389 inch) in compression and 0.68 cm (0.267 inch) in tension, 0.057-0.083 stroke per unit length. More typical designs rotate 3° and stroke 0.025 stroke per unit length. To put this into perspective, the MTV D-strut® is 11.9 cm (4.7 inch) in length with a 5.08 cm (2 inch) diameter and weighs 860 g (1.9 lbm). More typical D-struts® would be 25.4 cm (10 inches) in length with a diameter greater than 7.62 cm (3 inches) and weigh significantly more than 910 g (2 lbm). It was found that such a soft spring in such a small package resulted in a surge mode, surge mode harmonics and lateral modes at frequencies lower and gains higher than desired. This was detrimental to performance out to 1000Hz. Figure 2 shows the actual performance of the hardware prior to applying a low outgassing viscoelastic material ((self-fusing tape (SFT)) and after the application of SFT. With SFT, the strut performance met customer specifications.

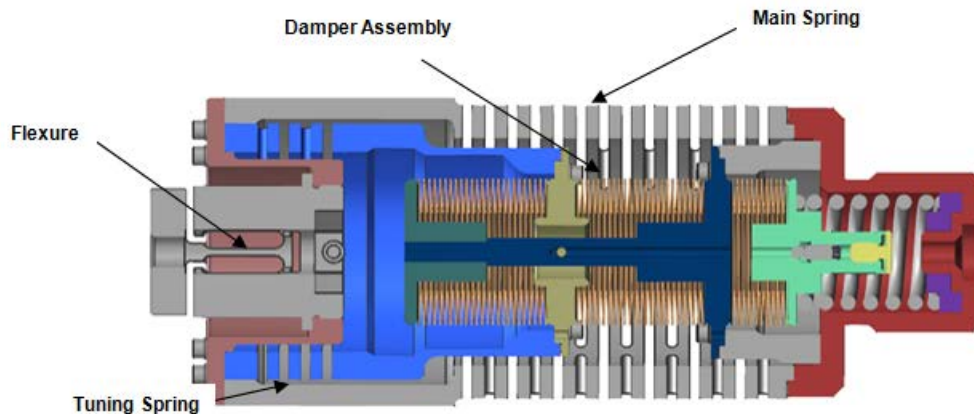


**Figure 1. MTV Isolator Cross Section**

### Application and Test of a Viscoelastic Coating

#### Solution development

A machine spring coated with SFT was used to successfully attenuate undesired modes to acceptable levels of gain and meet performance requirements, as shown in Figure 2. Alternative solutions include the use of a tuned mass damper but this was not viable due to volume constraints and the presence of more than one mode with different excitation directions and frequencies. A complete redesign was out of scope and a coating of some sort was the only way to meet cost and schedule constraints. Several materials were tried and tested: SFT, heat shrink, Sorborthane, RTV Silicone embedded between the strut blades, constrained layer damping, neoprene sleeve, and a silicone coating. It was paramount that any solution applied was able to meet performance and stringent outgassing (max volatile condensable material content of 0.1% and a total mass loss of less than 1.0% by weight) criteria but should require no design modification, not create any particulate, and meet the life requirements of the design. Initial testing showed SFT to be the most promising. ASTM E 595 testing for outgassing was carried out at another Honeywell location (Clearwater) and allowed us to test multiple coatings and iterate on bakeout temperatures and durations in a relatively short time. With bake out, the self-fusing tape met all the requirements and a method to apply the SFT onto the struts consistently and repeatedly was devised.

#### Application of SFT

The material came in 2.5-cm (1-inch) wide tape with backing. A lathe was used to apply the tape onto the main spring with consistent tension, as the tension affected stiffness, and even overlap. Through trial and error the optimum lathe speed and feed rates, drag torque for the tape dispenser, and application angle

---

<sup>1</sup> Honeywell Program Name for this effort

were established. The setup is shown in Figure 3. After the application of the SFT, the units were tested for impedance, to confirm the required stiffness was met. The units were then baked for 40 hours, at 1013.26 Pa (1e-5 Torr) at 204°C (400°F) and impedance testing was repeated. Impedance testing confirms the static stiffness  $K_a$ , measures dynamic stiffness  $K_a + K_b^2$ , and allows the damping magnitude and peak damping frequency to be measured from which the damping coefficient  $C_a$  is determined. Instrumentation measures non-contact displacement at the shaker head vibration input end of the strut and load cell force at the fixed output end of the strut. Based on a sample of 4 struts wrapped in SFT, it was found that the standard deviation of the stiffness ( $K_a$ ), stiffness ( $K_b$ ) and damping coefficient ( $C_a$ ) was 0.62%, 4% and 1.1% of the measured mean respectively and after bakeout these values changed 2.1%, 4.7% and 5% respectively. These values are within the deviation accounted for in Honeywell's systems analysis for  $K_a$ ,  $K_b$ ,  $C_a$ .

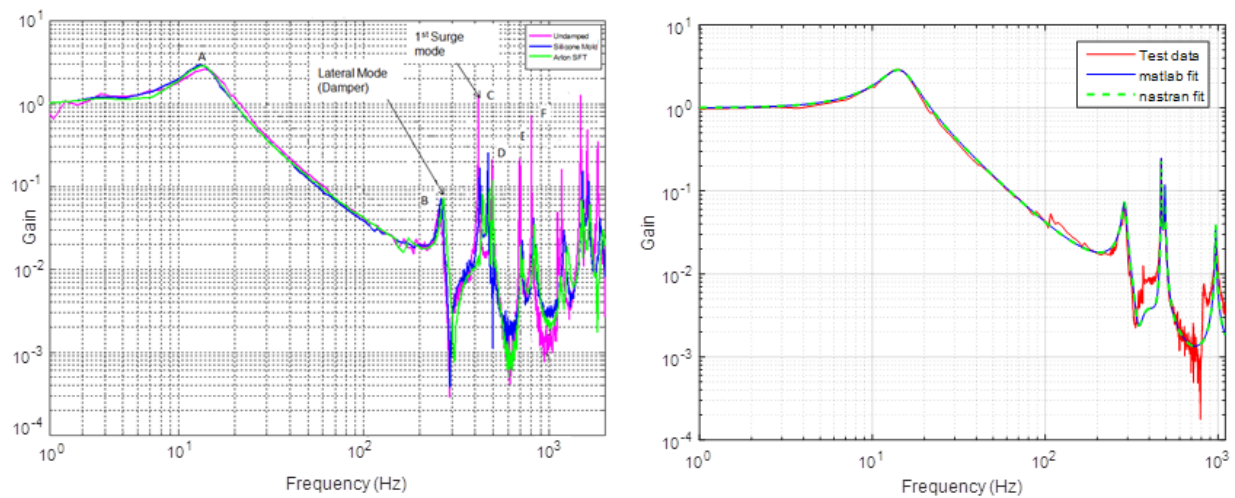


**Figure 2. Left:** Actual Transmissibility of Hardware (prior to coating in magenta, with a silicone mold coating in blue and with SFT coating in green). **A:** Resonant Frequency, **B:** First lateral mode, **C:** First Surge Mode, **D:** Second Lateral mode, **E:** Third Lateral Mode, **F:** Harmonic Surge Mode. **Right:** Bipod Transmissibility Performance of Strut with SFT coating and Model Correlation.



**Figure 3. Left:** Tap Test Set up. **Right:** SFT wrap set up.

<sup>2</sup> Where  $K_b$  is the in-series spring with the damper

### Testing over temperature

SFT has an operational temperature of  $-51^{\circ}\text{C}$  to  $180^{\circ}\text{C}$ . This was well within the temperature requirements, however, thermal cycle testing was carried out to ensure temperature did not affect the material robustness, in terms of life and performance. The MTV isolators were subjected to two survival temperature cycles of  $-40^{\circ}\text{C}$  (cold) to  $71^{\circ}\text{C}$  (hot) and eight non-operational temperature cycles of  $-24^{\circ}\text{C}$  (cold) to  $50^{\circ}\text{C}$  (hot) at cycle rate of  $3^{\circ}\text{C}/\text{minute}$ ; both tests carried out at ambient pressure. The strut was subsequently tested in the bipod transmissibility configuration and it was ascertained that the strut did not show any signs of damage and that performance did not deteriorate. Thermal impedance testing was carried out to evaluate the performance of the SFT during the operational temperature range. Figure 5 shows the results of the test. The temperature shift causes the Ca to decrease and increase as the temperature rises and falls, shifting the Phase Shift peak, left and right. The attenuation of the isolator modes exhibits very little change. The frequency shifts are as expected with viscoelastic behavior: getting stiffer with lower temperature and getting softer with higher temperature. The frequency shift is less than 5%, which is within the variation kept during analysis of the machined parts. This was considered acceptable.

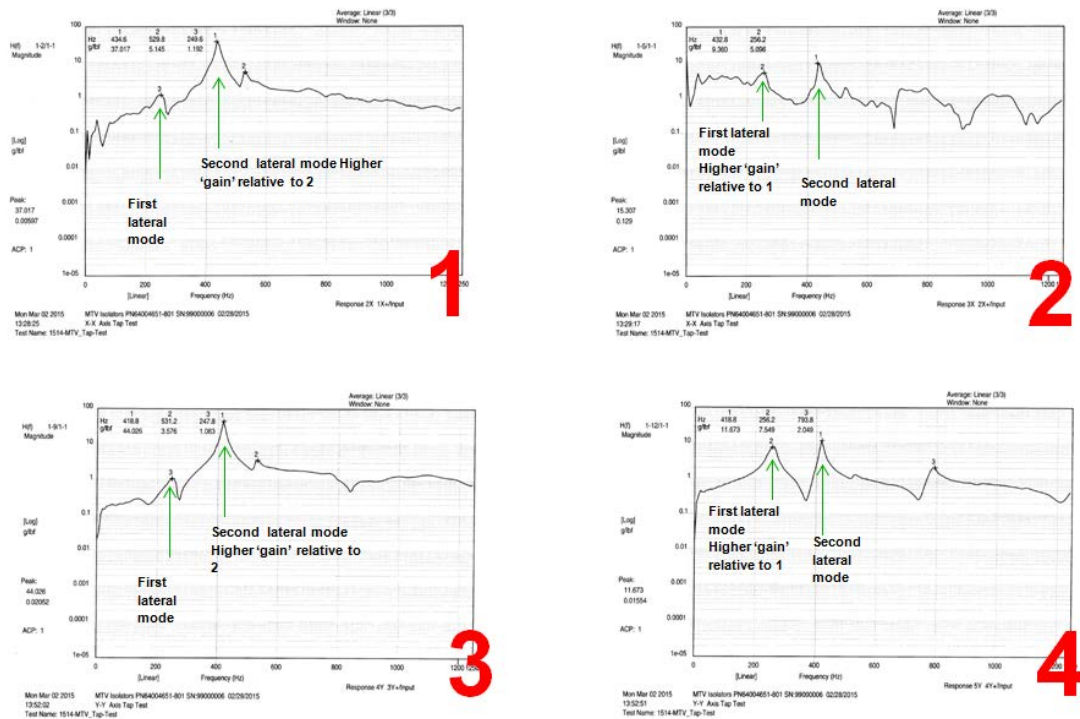
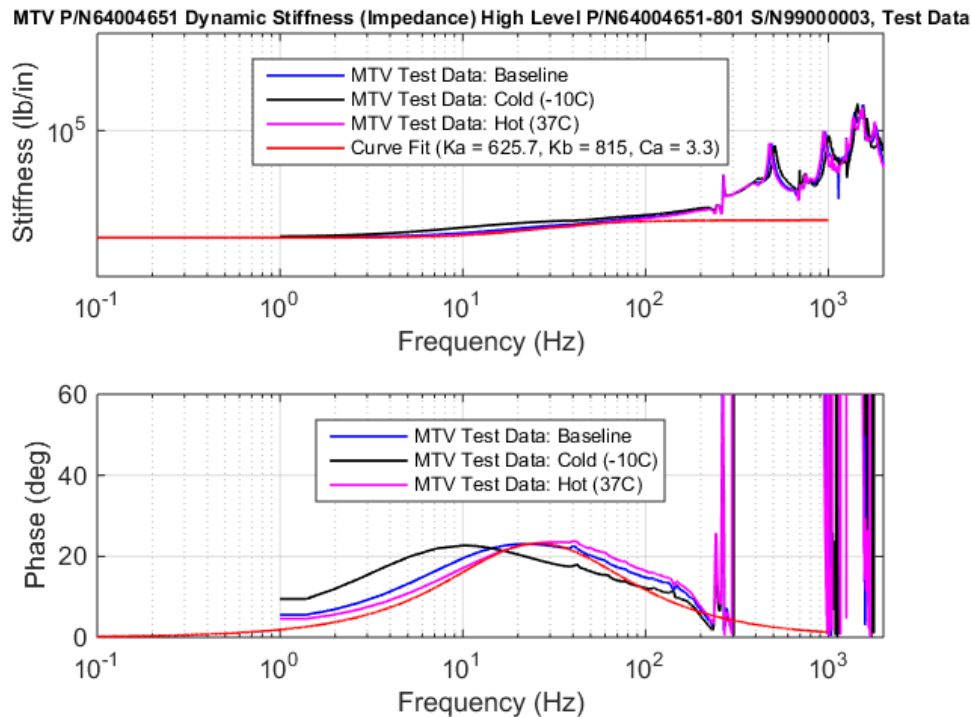


Figure 4. Top: X-X excitation; X axis results. Bottom: Y-Y excitation; Y axis results

### Testing for linearity with forcing and for robustness

High-level and low-level bipod transmissibility testing was also carried out, forcing at random non-op levels and random-op levels. It was found that performance was consistent, such that it was not necessary to consider non-linearities in the range of interest. Life testing included 12 full quasi-static cycles and the full (100-hour) requirement for random non-op and thermal cycle testing. Bipod transmissibility before and the life test was carried to check for any difference in performance. No changes were found and therefore we were confident that SFT was robust to withstand specification environments. The units were subjected to qualification testing. This included single strut & bipod proof load, random survival levels, shock levels and thermal cycle testing. Before and after data from the life test and qualification testing shows that the material had not degraded.



**Figure 5. Thermal Impedance Results.**

#### **D-Strut Model Development and Model Correlation**

Typical applications have operational requirements out to a couple hundred hertz (300 Hz typical) and historically our ability to predict surge modes allows us to design them to be outside the requirement frequency range. In this case, the presence of surge mode harmonics and high gain lateral modes meant the standard approach was not sufficient and more involved testing and modeling correlation was required. Tap testing was carried out on the strut and it was found that the presence of a nested flexure and a male threaded interface meant the lateral modes were sensitive to flexure orientation. The tap test consists of shaking the strut laterally (X & Y direction in Figure 3) with both ends of the struts held and several accelerometers placed on the isolator. Two rows of accelerometers were used, placed at 90 degrees from one another. This allows for lateral modes in the strut to be identified, including differences in modes in X and Y. Figure 4 shows the presence of two lateral modes, with the first lateral mode, associated with the main spring having higher gain closest to the spring (accelerometers 2&4), and the second lateral mode, associated with the flexure having higher gain closest to the flexure (accelerometers 1&3). The frequency<sup>3</sup> of the first lateral mode does not change with excitation direction and is 256.2 Hz for accelerometer locations 2 and 4 (closest to the main spring) whereas the frequency of the second lateral mode is sensitive to excitation direction and change from 434.6 to 418.8 Hz for X-X and Y-Y excitation respectively for accelerometer locations 1 and 3 (closest to the flexure). These results showed that flexure orientation had an effect of lateral mode placement. Subsequent bipod testing showed that the gain of the second lateral mode was dependent on flexure orientation; when flexures were orientated in the same direction the modes constructively interfered producing maximum gain. Based on tap testing and bipod transmissibility data for different flexure orientations, a detailed Simulink model was created and tuned to test data; a good agreement between test data and model data is shown in Figure 2. As mentioned above, it was important to characterize the material used, however, no attempt was made to create a non-linear model of the viscoelastic material as the change in characteristics was within the

<sup>3</sup> N.B. the frequencies reported are lower than those found in transmissibility testing due to the mass of accelerometers. This testing was conducted for mode identification purposes.



predicted performance envelope tolerance due to machine part tolerance and bellows stiffness tolerance. The model, shown in Figure 6, shows the inclusion of a detailed surge model, which is represented by 12 masses simulating the sprung masses of the main spring and damping to control the gains of these modes.

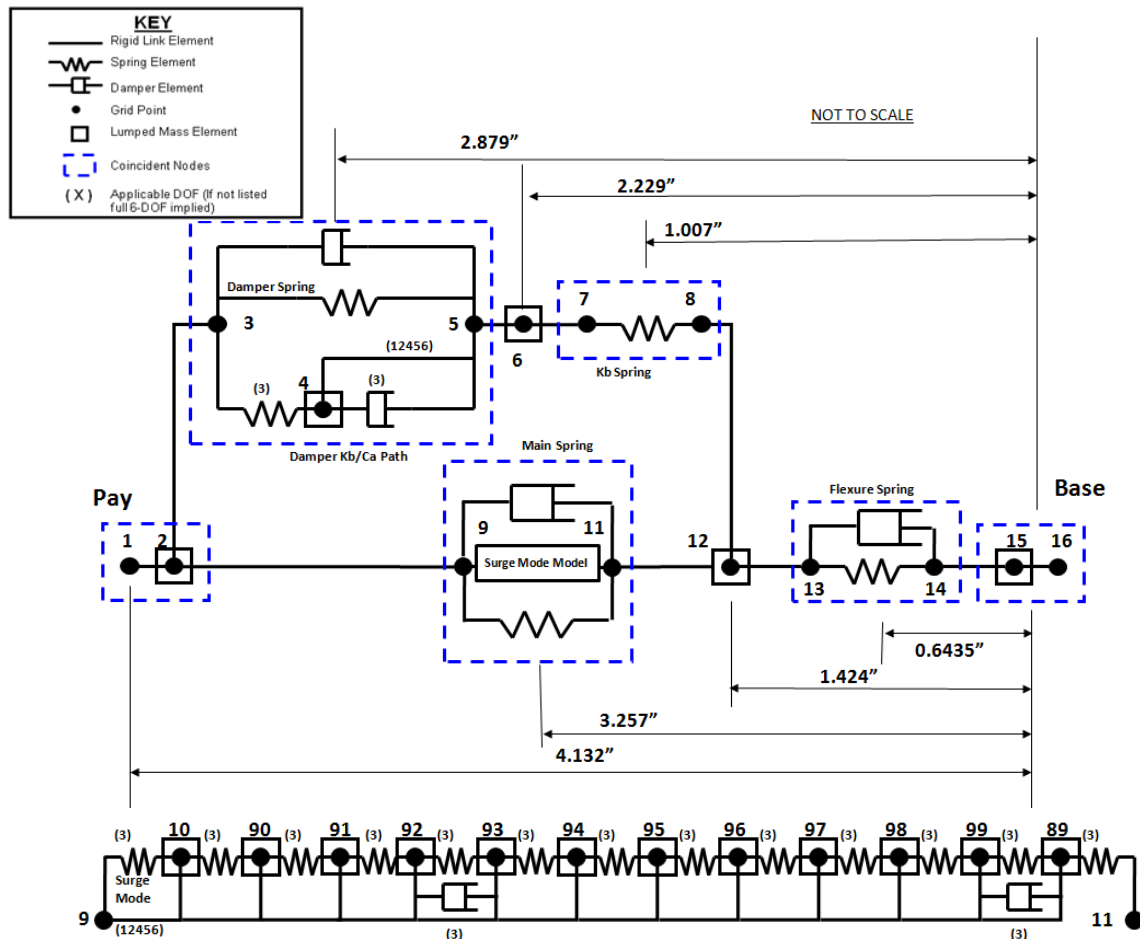


Figure 6. Nastran and MATLAB/Simulink Bipod model

## Conclusions

This paper presents an isolation system comprising of D-Struts®, designed to meet limited volume constraints with a 13-Hz 1st mode requirement with no permissible non-linearities in the operating range of 0-1000Hz, and experiencing large vibration, shock and static loads. It was found that resulting design was susceptible to surge and lateral modes as well as flexure orientation. This required a more detailed approach to strut mode identification and strut model development. A detailed Simulink model was created and tuned to test data providing good agreement between the test data and model data is shown. The model shows the inclusion of the surge model, which is simulated by 12 masses representing the sprung masses of the main spring and damping to control the gains of these modes. A machine spring coated with self-fusing tape, a viscoelastic material, was used to successfully attenuate undesired modes to acceptable levels of gain and meet performance and life requirements. A big concern with viscoelastic materials is their ability to meet life requirements and work repeatedly and predictably. In this paper we detail the tests carried out to ensure robustness and strut performance repeatability was met. The presence of such a solution allows lighter and smaller struts to attenuate to high frequencies, such that challenging program requirements such as the one herein described (13-Hz 1st mode without stops, and high associated loads) can be met.

# Development of a High-Performance, Low-Profile Translation Table with Wire Feedthrough for a Deep Space CubeSat

Alex Few\*

## Abstract

NEA Scout, a 6U cubesat and secondary payload on NASA's Space Launch System Exploration Mission (EM-1), will use an 85-m<sup>2</sup> solar sail to travel about 1 astronomical unit (about  $1.5 \times 10^8$  km) to a near-Earth asteroid for observation and reconnaissance<sup>1</sup>. A combination of reaction wheels, reaction control system, and a slow rotisserie roll about the solar sail's normal axis were expected to handle attitude control and adjust for imperfections in the deployed sail during the 2.5-year mission. As the design for NEA Scout matured, one of the critical design parameters, the offset in the center of mass (CM) and center of pressure (CP) proved to be sub-optimal. After significant mission and control analysis, the CP/CM offset was accommodated by the addition of a new subsystem to NEA Scout. This subsystem, called the Active Mass Translator (AMT), would reside near the geometric center of NEA Scout and adjust the CM by moving one portion of the flight system relative to the other. The AMT was given limited design space - 17 mm of the vehicle's assembly height - and was required to generate  $\pm 8$  cm by  $\pm 2$  cm translation to sub-millimeter accuracy. Furthermore, the design was required to accommodate a large wire bundle and coax cables fed through the center of the mechanism. The bend radius, bend resistance, and the exposure to deep space environment complicated the AMT design and operation and necessitated a unique design to mitigate risks of wire bundle damage, binding, and cold welding during operation. This paper will outline the design constraints for the AMT, discuss the methods and reasoning for the design, and identify the lessons learned through the design, breadboard and test phases for the low-profile translation stages with wire feedthrough capability.

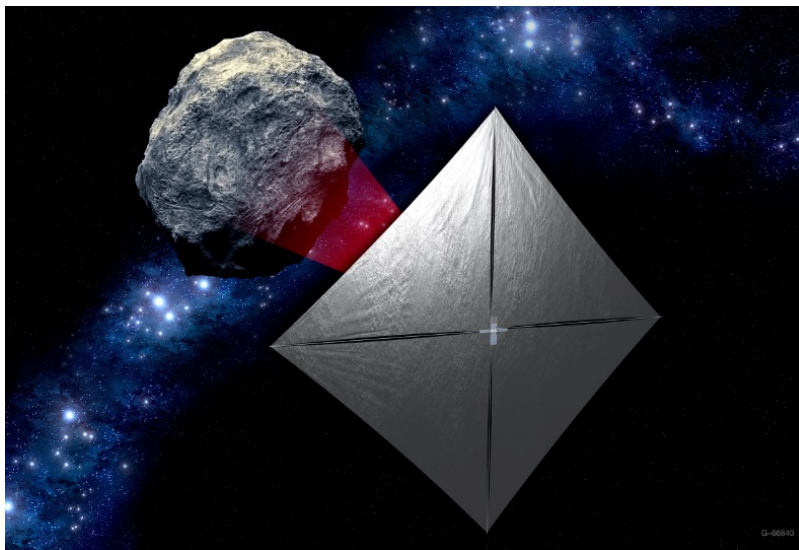


Figure 1. NEA Scout concept design<sup>1</sup>

---

\* NASA Marshall Space Flight Center, Huntsville, AL

## Introduction

CubeSats were developed with the intention to bring spaceflight designs and capabilities to academia. Early in their development, academic institutions composed a majority of the market but a decade later government agencies and large businesses noticed the opportunity to produce big science at low costs. This adaptation of the CubeSat intent required these high-capital entities to compress the form factors of conventional satellites into those outlined in the CubeSat Design Specification. With the growing popularity and development of CubeSats, designers, analysts, and manufacturing specialists noted that the requirements given in the CubeSat Design Specification demanded complicated, miniature systems to accomplish difficult tasks<sup>2</sup>. Numerous CubeSat programs became acquainted with this reality. Thanks to the growing market and development of low-cost launching capabilities for micro- and nano-scale satellites, universities, private industries, and government agencies have maneuvered large programs to take advantage of the CubeSat technology. Many of these CubeSats have the potential to become engineering marvels - they encounter technical issues (thermal, mechanical, and power limitations) similar to larger scale projects, but develop solutions at fractions of the cost. NEA Scout follows this suit. NEA Scout will employ the largest deployed solar sail to date to fly to a near-earth asteroid. The science instrument aboard NEA Scout will then characterize the asteroid by gathering shape, location, inertial properties and compositional information. The collected information will fill strategic knowledge gaps and lay the needed groundwork for future missions and the eventual human exploration of asteroids<sup>1</sup>.

Solar sails create propulsion without propellant, but the physics that makes them excel in efficiency and endurance also limits their ability to accelerate and decelerate quickly. Solar sails produce thrust by reflecting solar radiation with large areas of lightweight material. The reflected light produces solar pressure, which then propels the vehicle with control forces on the magnitude of  $\mu\text{N}/\text{m}^2$  of sail material. The thrust, though miniscule in size, can produce large velocity deltas over a multi-year mission. These small forces also create disturbance torques caused by misalignments in the CM and CP. Although the CM and inertial properties can be easily measured or calculated, the CP of the solar sail is less exact. Guidance, navigation and control engineers have estimated the CP location with considerable margin due to the possibility of sail tears, asymmetry and non-planar shaping. NEA Scout's estimated CP/CM offset is large enough (about 2 cm at beginning of mission and 4 cm at end of mission) to overload the control systems and requires a mechanical system to adjust the center of mass and trim the spacecraft. This mechanical system became the Active Mass Translator (AMT).

## Design Constraints

### Volume, Mass and Power

The AMT's early design activities acquainted the design and analysis team with numerous design constraints and complications. The first few parameters - volume, mass, and power - commonly limit the design space on flight systems and were considered the highest level requirements for the AMT due to the vehicle's size, mission, and risk level. Again, the nuances of the AMT design further complicated these three requirements. First, the AMT could occupy a volume no larger than 22.6 x 10.0 x 1.7 cm (x y z coordinates, respectively). Within this design space, the complete system, including all thermal and electrical components, could weigh no more than 320 grams. This design correlates to less than 5% of the vehicle volume and less than 2.5% of the NEA Scout's mass. As with many other orbiting and deep space vehicles, individual systems' power demands are limited and carefully monitored. The AMT was allowed 0.5 W during standby and 12 W when operating during cruise. The power requirement included the control board, motors, sensing, thermal blankets, and locking mechanisms. These components were chosen accordingly.

### Feedthrough Bundle and Mobility

The next lower level requirements were levied by the AMT's neighboring systems. The AMT resided in between the deployer for the solar sail and booms and the avionics box.



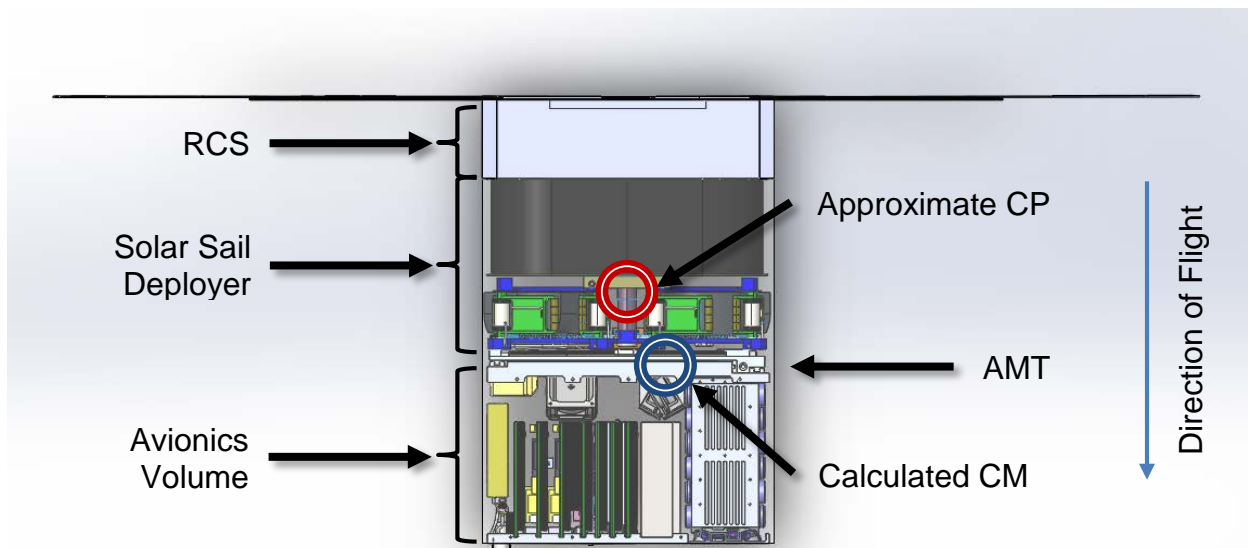


**Figure 2. Current NEA Scout configuration**

Therefore, large power and data wire bundles required passage through the AMT. This wire bundle consisted of an estimated 40 power and data leads and 3 coax cables. Furthermore, they required flexibility and resistivity to radiation and extreme temperatures. The AMT was required to translate  $\pm 8$  cm by  $\pm 2$  cm. The wire bundles had to pass through the AMT as it translated between any two points within the translation envelope. Not only did the dynamic envelope house the wire and cable bundle service loop, but also the connector locations, which had to be positioned so that there was no potential interference or tangling. Thanks to the oversight of many experienced mechanical designers, the feedthrough bundle received much attention in early design stages. The AMT designer was presented with many technical papers regarding the performance and degradation of flexible wire bundles in moving systems, including a previous AMS publication “Lessons Learned to Avoid Coax Cable Failure in Moving Mechanical Mechanisms”, by Sheah Pirnack. This paper suggested what types of coax cable designs were more resistive to cold welding between conductor layers and provided suggestions to cable lots for workmanship and contamination, as these parameters influenced cold welding. Furthermore, the paper discussed when cold welding tends to occur and how to design and test cables accordingly<sup>3</sup>. In turn, the design was modified to include ribbon cables for data and power and accommodate for the largest possible bend radii for the three coax cables. Currently, options are being investigated to route the coax cables outside of the AMT and reduce the probability of cold welding altogether.

#### Locking Mechanism

As with many translating or articulating mechanical systems, locking features are required for launch and some orbiting maneuvers. The AMT was no different. The system presented a clear weak point and introduces more failure modes to the vehicle. During the launch phase of the mission, a locking mechanism was required to create a load path, reduce stress in fasteners, and constrain the translating components of the AMT during the deployment phase of the mission. NEA Scout’s interface to the CubeSat Dispenser is a rail, and due to the discontinuity across the AMT, the interface was held to tight tolerances. The locking mechanism will help control this tolerance. Although this mechanism will operate independently of AMT, it was included as a subcomponent of AMT and therefore be contained within all AMT requirements. This will prove exceptionally difficult as the locking mechanism will inherently reduce the translation ability of the AMT.

## Design Ideology and Testing

### Early Design

Thus far, the AMT is the latest system added to the NEA Scout project. The surrounding systems, the solar sail boom deployer, and avionics box (reference Figure 2), had nearly one year's progress made at the onset of AMT design activities. Therefore, the interfaces for the AMT had some definition and rigidity. AMT had to accommodate the existing designs and make minimal impacts to these two neighboring systems and meet all previously-outlined requirements. Both the avionics box and boom deployer levied requirements for the wire bundle connector locations as well as the mechanical fastening points. In turn, the AMT levied requirements onto these systems regarding the locking mechanism location and fastening. After the interfaces were understood, the mechanical design work commenced.

The NEA Scout design team performed a detailed trade of 20+ concepts of varying TRLs for controlling the CP/CM offset. The concepts included rotation tables, gimbals, and sail tensioning systems, and varying reflectance materials. Each concept was scored according to the estimated ability to meet the AMT design constraints, and the trade concluded that a translation table combined simplicity, heritage, and capability. It quickly became clear that a COTS translation table could not meet the requirements for the AMT. Although many designs exist that can produce high-precision motion in low-profile assemblies (such as those for microscopes and other laboratory optical equipment), few designs could accommodate such a large translation envelope and none could deliver a wire feedthrough capability. Furthermore no space-qualified systems were found that could deliver translation capabilities within the same orders of magnitude as AMT and fit into the given volume. The AMT required an in-house design.

Early design concepts took conventional translation table designs and “inverted” them by moving the motors and transition components from a central location to the periphery of the system. Figure 3 illustrates the “inversion”. Although this concept is not novel, the low mass requirement and translation ability made the concept unique. This modification freed a large internal volume that could be used to house a service loop for the feedthrough bundle, locking mechanisms, and sensing equipment. The design also allowed a small vertical profile, and made the AMT design much more appealing to NEA Scout. The trade, however, complicated the interfaces and required the stepper motors to reside one atop the other. The motors' location and the height requirement only allowed motors of 8-millimeter diameter or less to drive the translation of the AMT. The small motor size constraint required considerable investigation and testing for torque output, margins, and load capacity.

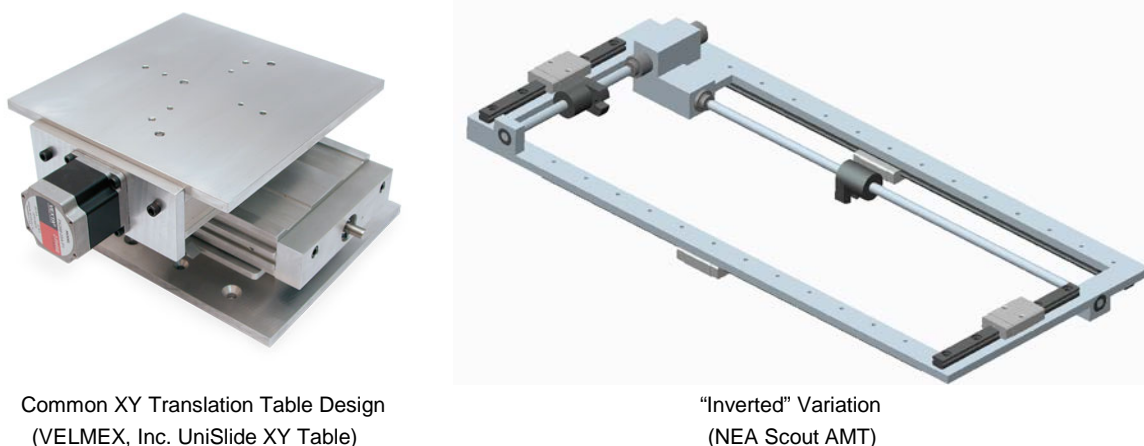


**Figure 3. Comparison of translation table designs**

The main design trade completed during the AMT design was for the driver motors. Stepper motors proved to be the best choice for a number of reasons. First, steppers have flight heritage on many spacecraft deployment mechanisms and solar array gimbals. These heritage systems have similar duty cycles, translation speeds and environments to NEA Scout. Secondly, the stepper motor design allows for microstepping, which when combined with gearboxes and lead screw drive systems, can produce very small, precise steps. Lastly, stepper motors can track motion by counting steps, so long as the detent torque is not exceeded, causing skips. This step counting could replace a positional sensing system as long as the motor is properly sized for the environment and loads<sup>4</sup>.

In order to quantify the required driving torques needed for each of the two motors, the AMT designer used static and dynamic equations to calculate the friction forces and torques in the drive system. These equations combined inertial loads from the driven mass; friction from the bearings, lead screw and nut; motor efficiency; lead screw efficiency; and acceleration. The result produced a torque requirement for a particular set of motors, lead screws, nuts and bearings. These results were then documented and compared to the torque margins required by the organization.

Although the torque outputs for stepper motors and torque requirements for the AMT drive systems were relatively simple to calculate, there were many other elements of the calculations that were assumed (workmanship, degradation, feedthrough wire bending resistance, etc.). Therefore, a drive system test fixture was manufactured to simulate a single axis of the AMT, inertial loads and wire bend resistance. The fixture was then paired with a custom driver board to fine tune motor speed and current supplies. The test assembly is shown in Figure 4.

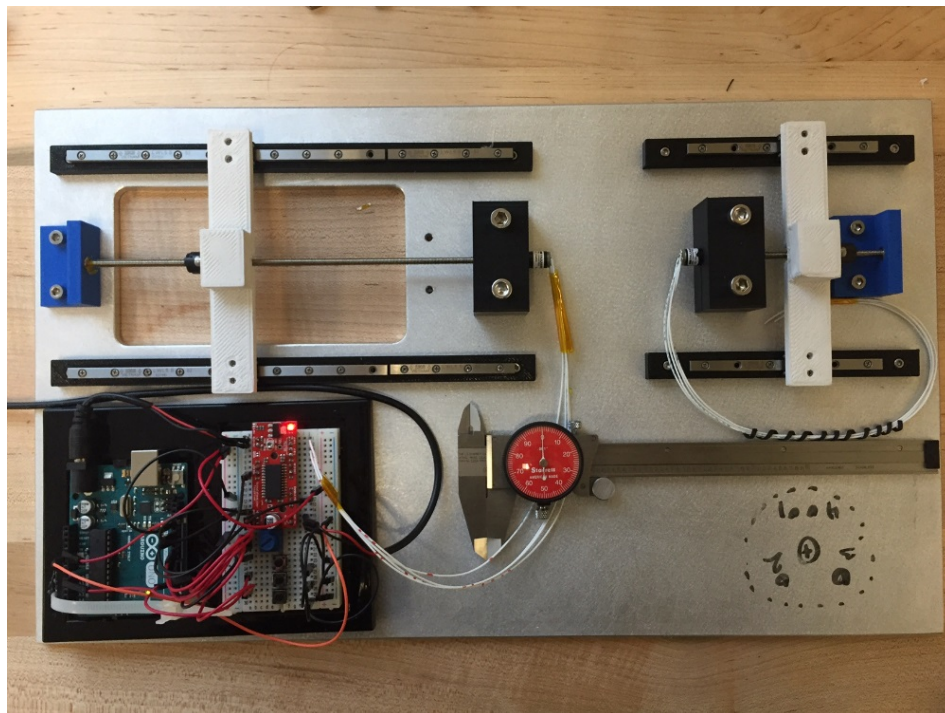


**Figure 4. AMT test assembly**

The test assembly was developed using stock 1/4" (6.35-mm) aluminum plate and 3D-printed components to replicate the X and Y translation axes (the left and right side of the assembly, respectively) of the AMT. The 3D-printed components were designed and manufactured to fit all configurations outlined in Figure 5. The adjustability of this setup allowed for quick interchanging and controlled variations between tests.

### Test Proceedings and Results

Tests were conducted to combine three various motor sizes with two lead screws with varying pitch. The goal was to produce a balance of speed, size, and torque margin. Navigation and control designers required that the AMT move slowly to increase precision and reduce dynamics imparted into the vehicle. The design volume, driven greatly by motor diameter, limited the available height of the AMT. Lastly, the design requirements levied certain torque margins onto the system, which when compounded by conservatism in the preliminary thermal, mechanical and dynamic analysis, yielded driving torques far greater than expected. Nonetheless, the system had to be sized accordingly. Changes to the motor diameter directly affected the AMT vertical size constraint, while combinations of the motor and threads adjusted the speed and torque margins simultaneously. For example, a motor-thread combination could yield acceptable torque margins and size, but produce too rapid of motion. Adjusting to a higher pitched thread would increase the torque margins and reduce the driving speed - a single change benefiting two figures of merit.

A few of the combinations were ruled out by hand calculations. The largest motors (Configurations E and F from Figure 5) were too large for the design volume and had calculated torque margin at beginning of life magnitudes higher than required. Furthermore, when the final two motors were paired with both threaded rods, hand calculations again ruled out two more options. The smallest motor paired with a high pitch thread (Configuration A) and the middle-sized motor paired with the lower pitched thread (Configuration D) produced comparable speeds and margins, but different form factors. The test fixture was used to compare the final two motor and thread combinations and close the trade. The results were as follows:

Configuration Title				
Motor Size [mm]	Thread Pitch [threads/cm]			
	16.4	8.2		
6	A	B		
8	C	D		
10	E	F		

Configuration	Figures of Merit			
	Vertical Height Required	Translation Speed	Torque Required	Torque Available
A	13 mm	0.032 cm/s	1.5 mNm	35 mNm
B	13 mm	0.064 cm/s	2.5 mNm	35 mNm
C	17 mm	0.032 cm/s	1.5 mNm	120 mNm
D	17 mm	0.064 cm/s	2.5 mNm	120 mNm
E	21 mm	0.080 cm/s	1.8 mNm	200 mNm
F	21 mm	0.160 cm/s	4.2 mNm	200 mNm

**Figure 5. Drive system configuration trade**

At the conclusion of the trade, the AMT designer chose Configuration A. This motor-thread combination minimized the vertical profile of the AMT while also minimizing translation speed and retaining an acceptable torque margin. Despite the small motor size, the designer was surprised by the force produced by the system (an estimated 150 N). Originally, the 8-mm diameter motors served as a baseline design, yet this test led to a design change that will reduced the AMT's volume requirement.

Moving forward, there are options to modify the torque output and speeds pending engineering development unit test results. This will be done by modifying the gearboxes and control inputs. According to the tests, all configurations had large torque margins, with configurations E and F clearly oversized for the given application.

As expected, the test setup proved beneficial to the AMT design process. The designer gained confidence in the system's design, particularly with the pairing of the stepper motors, lead screws and rail guides. The motors, despite their small size, were capable to produce driving torques far greater than demanded, even



with the presence of wire bending resistance, gravity, and prototype-level workmanship (it should be noted that many of the components were 3D printed or hand machined).

#### Lessons Learned and Forward Work

The preliminary design activities for the NEA Scout AMT required a significant amount of research and investigation, but in hindsight, too much time may have been spent creating design options and trade spaces. As the design process continued from preliminary sizing into component trades and final down selections, hand calculations and analysis were set aside for bench top testing. This approach proved to be the best use of time. Once the time was spent to design and build the test bed, the results came quickly and were easy to discern. In retrospect, testing should have commenced far sooner to save time and produce hard data. This mindset would have allowed more design iterations and taken advantage of the additive manufacturing capabilities available to the AMT designer. Furthermore, this methodology of “test early and often” would have followed common CubeSat development practices (analysis is less common in CubeSat-sized projects due to cost and staffing constraints).

Earlier testing would have also allowed the test bed to evolve. Once a design parameter - such as the motor size or thread pitch - was determined, another parameter could be tested. The test bed was designed with enough work space to test optical sensing and locking mechanisms, but due to “excessive” research and investigations into space rated components and flight heritage information, time did not allow. This is not to discredit engineering heritages or workmanship, but it is intended to reinforce the point that CubeSats and other micro/nanosatellites have limited heritage. Their comparable mechanical systems are often orders of magnitude different from traditional systems in volume, mass, and cost, thus limiting the comparisons. Other mechanical systems aboard NEA Scout, such as the solar sail and boom deployers, embraced this mindset sooner (partially due to age and design maturity) and the number of design iterations was staggering.

As NEA Scout moves into the next stages of development, the AMT is scheduled to deliver an engineering development unit in May. Before that time, positional sensors and locking mechanisms must be designed and tested. These two subsystems are not trivial and have the potential to greatly alter the current AMT design. It would have been beneficial to baseline structural designs for these components, but that is not the reality. The locking mechanism has numerous single point failure locations. Furthermore, if positional knowledge is lost during cruise, NEA Scout could lose its mission. In retrospect, the locking mechanisms and sensing systems should have been designed and tested in parallel with the linear motion systems. Moving forward, the AMT designer will have to become more flexible and adapt to the creative environment common among microsatellite projects. The designers should embrace a mentality to test, learn, and iterate as often as possible.

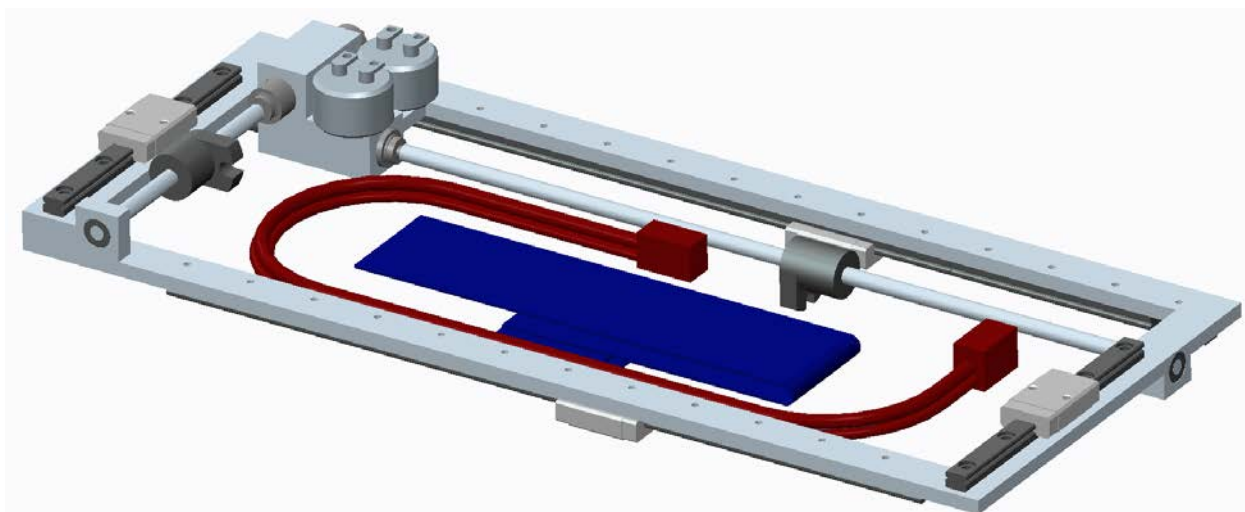


**Figure 6. Current AMT design, and concept wire harnesses (coax cables in maroon, power and data in blue)**

## References

1. "Near Earth Asteroid Scout (NEAScout)." *Jet Propulsion Laboratory*. Web. 19 Jan. 2016.  
<<http://www.jpl.nasa.gov/cubesat/missions/neascout.php>>.
2. Mehrparvar, Arash (February 20, 2014). "CubeSat Design Specification" (PDF). *The CubeSat Program, CalPoly SLO*. The CubeSat Program, CalPoly SLO. Retrieved December 2015.
3. Pirnack, S. (2012). *Lessons learned to avoid coax cable failure in moving mechanical mechanisms*. In *Proceedings of the 41<sup>st</sup> Aerospace Mechanisms Symposium*, NASA JPL, Pasadena, CA, USA.
4. USA. NASA. Glenn Research Center. *NASA Space Mechanisms Handbook*. Ed. Robert L. Fusaro. Linthicum Heights: NASA Center for Aerospace Information, 1999. Print.

# Use of Volute Springs in Space Applications

Chris Floyd\*, Ian Bournelis\* and Cary Clark\*

## Abstract

A volute spring was designed and tested for use in launch restraint assemblies (LRA) on satellite deployables. The volute spring type was chosen because it offers a very compact stowed profile and a relatively long spring stroke compared to conventional wire compression springs. Test results showed that the output force was very predictable with the developed analysis and consistent with negligible change following exposure to thermal cycling, vibration environment, and low cycle life testing. Although the volute spring was ideal for this application, there are several lessons learned that should be considered before using this spring type, including the limited number of vendors willing/able to manufacture custom volute springs, high relative cost per unit, nonlinearity of the spring output force, high weight relative to wire compression springs, the criticality of the spring end configuration (unaltered vs. ground vs. closed) and the how it affected coil-to-coil frictional losses/build-up, and spring lubrication selection and migration during handling.

## Introduction

Springs are a simple and diverse component in many different types of mechanical systems. They can be used as mechanical energy storage devices, dampers, release devices and come in many different materials, shapes, and sizes. Each spring is designed to suit the needs of its system. One particular application for satellites, LRAs, requires a spring with a very compact compressed height and a very long stroke length. The most suitable candidate for this application was a volute spring but the supporting analysis and design background were not available.

## Volute Spring Overview

The volute spring is manufactured from a relatively wide and thin bar or strip of spring material. The bar or strip is coiled around a mandrel such that each coil overlaps the adjacent coil forming a volute or cone. This process forms a tiered inner diameter, shown in Figure 1, which allows each coil to slide past the adjacent coil when the spring is compressed. The result is a spring that can be compressed to the initial width of the spring material regardless of the number of coils or stroke length the spring has. This is very convenient for space applications because it allows for significantly more output force and stroke versatility for a given volume than any leaf, coil, or torsion bar spring. Due to the overlapping strip material configuration, the volute spring also offers more stability than other spring types.



**Figure 1. Volute Spring**

---

\* Lockheed Martin Space Systems Company, Littleton, CO

Volute springs have been used in some terrestrial applications such as vertical and horizontal suspension systems for tanks and smaller tools like garden shears where a compact or self-guided spring is required. Since there are not a wide variety of applications that require the unique characteristics of a volute spring and the relatively high manufacturing cost, there are not as many off-the-shelf configurations that are considered vendor standard parts when compared to wire compression springs. This means that a detailed analysis and custom design is likely required for each application which contribute to the higher unit price of volute springs.



**Figure 2. Terrestrial uses for volute springs**

In general, aerospace applications have much more stringent requirements that require substantially more design margin than terrestrial applications. Custom design parts are frequently employed to meet these requirements as slightly more expensive mechanical piece parts can substantially reduce the system-level cost. One of the most critical requirements, for satellites in particular, is that the overall envelope of the spacecraft fits inside the launch vehicle fairings. The deployables and the LRAs that restrain them are generally at the very perimeter of this overall envelope which makes a compact design a requirement. The volute spring was ideal for this application for that reason.

### **Design and Analysis**

Aerospace parts are upheld to a significantly higher standard than their terrestrial counterparts. Space environments such as extreme temperatures, vacuum, launch loading and payload restrictions often dictate special materials, processes and coatings. Furthermore, mechanical parts often require rigorous analysis to determine both output force margin and internal stress margins to ensure the adequacy of the design. As such, a solid understanding of the spring functions and analysis was required to justify its usage.

During compression, a volute spring essentially takes the applied axial load and bends the centerline of the spring bar downwards. The deflection begins at the largest coil of the spring which has the lowest spring constant. As the spring is compressed, the load is spread through subsequent coils until the point where the largest coil bottoms out, known as the initial bottoming load. After initial bottoming occurs, the load vs deflection curve changes from linear to exponential. This happens because spring force in each subsequent coil increases as the diameter of the coil decreases. This results in a curve that asymptotes at a peak high force at the solid height as shown in Figure 5. The point at which the smallest spring coil bottoms out is called the Final Bottoming Load. The peak of the Load vs Deflection curve is determined by the spring constant of the final coil because it is the stiffest coil in a standard volute spring.

Figure 3 illustrates the key parameters and variables required to perform the volute spring design analysis. The image on the right illustrates an unwound volute spring with ground ends. Based on the spring geometry parameters, the spring load, deflection, and stress can be calculated using the equations in Figure 4. The spring load is used to determine the force that the spring is capable of providing. The spring deflection equations are used to calculate how much the spring compresses axially under a known load. Lastly, the shear stress determines the internal stress in the coils when under an axial load.



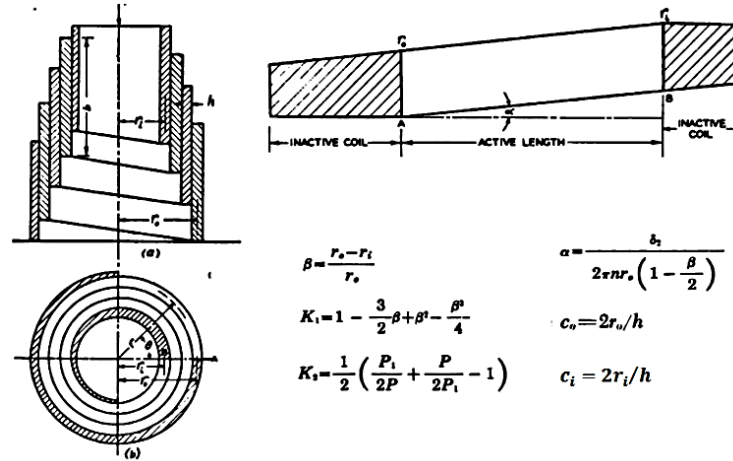


Figure 3. Key Parameters and Variable Definition [1]

	Spring Load	Spring Deflection	Shear Stress
when $P < P_1$	$P = \frac{P_1 \delta}{2\pi n r_o \alpha K_1}$	$\delta = \frac{P}{P_1} (2\pi n r_o \alpha K_1)$	$\tau = \frac{3P(c_o+1)}{2hb \left( 1 - .63 \frac{h}{b} \right)}$
$P = P_1$	$P_1 = \frac{Gbh^3 \alpha \left( 1 - .63 \frac{h}{b} \right)}{3r_o^3}$	$\delta_1 = 2\pi n r_o \alpha K_1$	$\tau = \frac{3P(c_o+1)}{2hb \left( 1 - .63 \frac{h}{b} \right)}$
when $P > P_1$	$P_1 < P < P_2$ P is assumed to solve for deflection	$\delta = \delta' + \delta'' = 2\pi n r_o \alpha \left( \frac{P}{P_1} K_1 - \frac{K_2}{\beta} \right)$	$\tau = \frac{3P \left( c_o \sqrt{\frac{P_1}{P}} + 1 \right)}{2hb \left( 1 - .63 \frac{h}{b} \right)}$
$P = P_2$	$P_2 = \frac{P_1}{(1-\beta)^2} = P_1 \left( \frac{r_o}{r_i} \right)^2$	$\delta_2 = 2\pi n r_o \alpha \left( 1 - \frac{\beta}{2} \right)$	$\tau_2 = \frac{3P_2(c_i+1)}{2hb \left( 1 - .63 \frac{h}{b} \right)}$

$P_1$  = Initial bottoming load

$P_2$  = Fully compressed load

Figure 4. Volute Spring Load (P), Deflection ( $\delta$ ), and Shear Stress ( $\tau$ ) Equations [1]

Figure 5 is a theoretical load versus deflection curve for a volute spring. Initially, the spring has a linear force constant as the coils slide past each other under axial compression. At the point when the largest coil reaches the Initial Bottoming Load, the spring constant becomes exponential. This is because each following coil bottoms out in sequence, increasing the stiffness after each one. Finally, the smallest coil bottoms out and the spring is fully compressed.

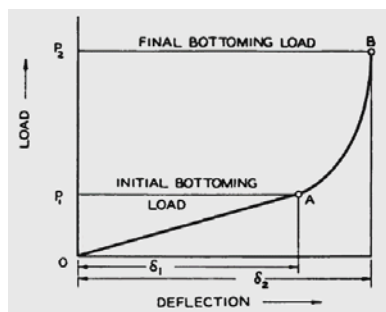


Figure 5. General Load-Deflection Characteristics of Volute Springs [1]

## Test Results

A number of different tests were performed to determine the whether the volute springs were both compliant to drawing requirements and acceptable for use in the spacecraft applications.

### Baseline Spring Force vs. Deflection Test

An Instron fixture with a motorized head (Figure 6) was used to generate the baseline spring force vs. deflection curve. The spring was set up in a simulated containment fixture and compressed to the stowed condition. The spring was then manipulated to relieve any frictional build-up to simulate a post-vibration deployment. The Instron head was then programmed to deploy the spring at a rate of 0.1 in/sec (0.25 cm/sec) to evaluate slip-sticking that may occur during the deployment. Following the deployment, the Instron head then compressed the spring at the same rate to the fully stowed condition. The spring force was recorded throughout this sequence. This test was repeated two more times to evaluate repeatability. As shown in Figure 7, the results proved to be very repeatable.



**Figure 6. Instron Test Fixture for Load vs. Deflection Curves**

### Vibration Testing

The spring was then compressed and subjected to a random vibration environment. Following the vibration environment, the force vs. deflection test was repeated three more times to evaluate the effect of vibration on the spring force. As shown in Figure 7, the results proved to be very repeatable and in family with the baseline test results.

### Thermal Testing

The spring was then compressed and subjected to ten thermal cycles from -100°C to +95°C. Following the thermal cycles, the force vs. deflection test was repeated three more times to evaluate the effect of thermal environment the spring force. As shown in Figure 7, the results proved to be very repeatable and in family with the baseline and post-vibe test results.

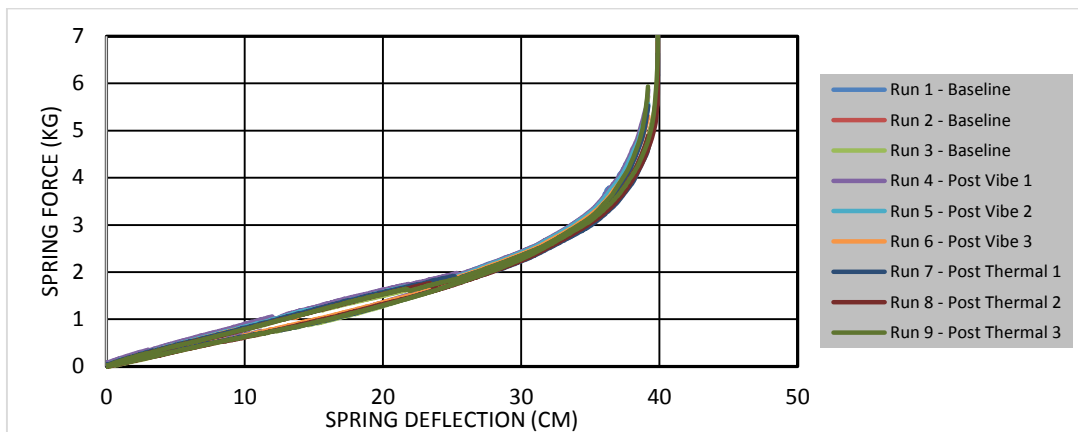


**Figure 7. Volute Spring Force vs. Deflection Data**

## **Lessons Learned**

While the spring proved successful in the end, there were several drawbacks throughout the process that should be noted.

### Vendor Selection

There was a limited selection of vendors that were willing and able to manufacture our custom volute springs. In the production of this spring, multiple requests were submitted but only two vendors were willing to quote. The first vendor lacked extensive experience with volute springs and they did not fully understand how the different spring parameters (inner coil diameter, helix angle, end configuration) affected the final spring force output curve. Their initial batch of springs produced a force vs. deflection curve that was significantly different than what was requested and they were unable to adjust the process or spring parameters to provide a spring that met the design requirements. The second vendor, who also had limited experience but displayed a much better understanding of volute springs, yielded better overall results. The test sample spring as well as the first three batches of springs all satisfied the design requirements with minimal dropout at the vendor.

The vendor's experience and understanding of how the volute spring parameters affect the characteristics of the design is the most critical factor in selecting a vendor. Choosing the right vendor will reduce the dropout rate which will ultimately reduce products overall unit price on future orders as well as the schedule risks associated with having to re-manufacture new springs.

### Manufacturing Process

The process for fabricating standard wire compression springs consists of feeding a wire into an automatic coiler which consistently and accurately sets the pitch and diameter of the spring. The process, which both vendors employed, to fabricate volute springs is much more labor intensive. Due to a lack of standard equipment/tooling, the vendors had to feed the strip material onto the rotating mandrel by hand, which made the process very workmanship dependent. This inherently will reduce the consistency of the spring characteristics on a unit to unit and lot to lot basis.

For large order quantities or anticipated recurring orders, it is strongly recommended that the vendor develops a standard process/procedure and uses the appropriate equipment/tooling to reduce spring variation and overall dropout. For small order quantities or one time purchases, it is recommended that a standard process/procedure is used for manufacturing at a minimum.

### Spring End Configuration

Another critical issue encountered during the development process was the configuration of the ends of springs (unaltered vs. ground vs. closed) and how they affected the spring's overall performance.

The first configuration tested had unaltered ends which caused the spring to have rectangular points on the inner and outer coil (Figure 8) that interfaced directly with the adjacent parts. This resulted in an unstable deployment which caused the adjacent parts to cant. This is an undesirable situation because it makes the final deployed position less stable and less predictable. Another issue observed during testing was that the rectangular point on the end caused the inner, most powerful coil to begin expanding when the spring was being compressed. This caused an increase in friction between the inner coil and the adjacent coil. The increased friction had a negligible effect on output force when the deflection was small but as the spring got closer to the solid height, the impact grew exponentially. When the spring was close to the solid height, the other coils, all fully compressed, forced the inner coil closed to its original diameter. This caused excessive friction between the inner coil and the adjacent coil and the rectangular point on the inner coil and the fitting compressing the spring. This caused false output force readings of ~18 lb (80 N) on a spring with only ~3 lb (13 N) of potential. Although this did not affect the spring to the same degree in the deployment direction, it made it very difficult to get an accurate compressed output force measurement.

The second configuration tested had ground ends which removed the rectangular points that were causing issues with the previous test. This configuration was successful at mitigating the deployment stability issues as the spring now deployed straight and kept the parts oriented properly in the final position. However, while it was improved slightly, the ground-end spring still exhibited an unacceptable frictional build-up by the solid height due to the expanding inner coil.

The final configuration tested had closed ends with a full dead coil at either end (Figure 8). This configuration successfully solved all the issues discovered during testing of the unaltered and ground variants. Ultimately it provided a much more stable and repeatable deployment envelope and there were no indications of frictional changes at any point during the stow or deploy process. The reliability of the output force measurement significantly improved as well.

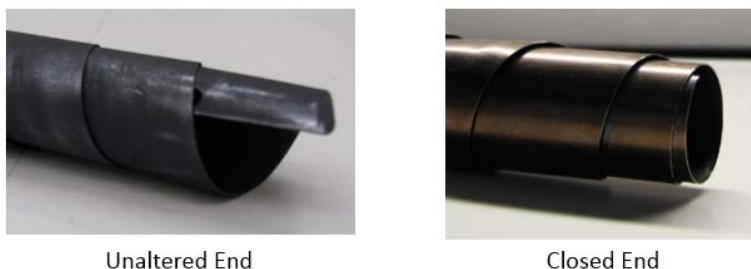


**Figure 8. Unaltered vs. Closed Spring Ends**

Based on the testing performed, it is highly recommended that all future volute spring designs specify that the ends be closed with a single dead coil on either end on the engineering drawing.

#### Spring Lubrication

Two primary concerns from the beginning of the design processes were how the coil-to-coil friction would affect the overall output force of the spring and whether the coils of the spring could cold weld together when the spring is held compressed in a vacuum environment. A trade study was performed to determine the best options for lubricating the spring to reduce the impact and likelihood these concerns. Ultimately a sputtered dry film lubricant was selected since there was less concern of migration associated with wet lubrication and no concern of cracking/chipping/flaking during spring operation associated with hard coatings.

Instron testing was performed to determine deflection vs. spring force curves for both lubricated and unlubricated springs. The resulting data suggests that the lubrication had a minimal effect on the curve under ambient temperature and pressure conditions. Both curves followed their analytically predicted curves and did not show signs of sticking. The unlubricated spring was also functionally tested in a TVAC chamber to evaluate the risk of cold welding. Following thermal cycling from  $-100^{\circ}\text{C}$  to  $+95^{\circ}\text{C}$  in the compressed state, the spring was released at each temperature extreme. The following inspections showed no signs of cold welding.

It is recommended that dry film lubrication be applied on springs to be used for space applications. The testing performed was not comprehensive enough to eliminate the need for lubrication. It did not evaluate the frictional effects on the output force at the temperature, pressure, and humidity of the space environment and it did not evaluate the likelihood of cold welding if the spring was held compressed for vibration/launch then held in a vacuum environment with no release in between.

## **Conclusion**

While the volute spring may not be widely used terrestrially, they are ideal for space applications that require a spring with a very compact compressed height and a very long stroke length. The equations outlined in this paper, which were validated by test data, provide the means to design and analyze this spring and to verify force and stress margins. Testing also verified the volute spring performs consistently after exposure to hostile space environments. For future designs, leverage the lessons learned and recommendations herein to reduce the unit cost and schedule risk and increase the stability and reliability of the spring.

## **References**

1. Wahl, A. M. "Mechanical Springs" *Penton Publishing Company* (1944), Page 359-377.



# **A Multi-Sectioning, Reconfigurable Electromagnetic Hammering Propulsion for Mole Penetrators**

Jerzy Grygorczuk\*, Bartosz Kędziora\*, Łukasz Wiśniewski\*, Marta Tokarz\*, J. Krasowski\*, Krzysztof Bieńkowski<sup>1\*\*</sup>, M. Drogosz\*\*, R. Graczyk\* and Marcin Dobrowolski\*

## **Abstract**

This paper presents a new generation electromagnetic direct drive for low-speed penetrators, which makes them capable of underground mobility within regolith while carrying scientific instruments (such as sampling tools or thermal sensors) in planetary missions, where Mars and the Moon are the mostly foreseen destinations. The propulsion combines new ideas and earlier achievements, both of which had influence on the concept and would demonstrate the technology. A laboratory model device was successively developed and tested. Its principle of operation is based on electromagnets arranged in stock and supplied with high impulse power by rechargeable and dischargeable capacitor.

## **Introduction**

Principle of operation of penetrators is based on interaction of three masses of the device (hammer, casing and counter-mass), between which the energy exchange is performed and as a result hammering action is achieved. Examples of mole-type penetrators include: mole penetrator for the Beagle II mission, HP3 mole penetrator for the Exo-Mars mission (under development), and prototypes of KRET-1 and KRET-2 [1] mole penetrators developed by CBK PAN within ESA PECS projects. All of them have stroke mechanical energy accumulated in their driving springs. EMOLE is the first mole-type penetrator in which the electromagnetic linear drive system has been implemented. Since the mole penetrator has been foreseen as a carrier of a sample return system, electronics and sensors, its power settings regulation has allowed accommodating the power to the concrete soil mechanical properties and in many cases saving sensitive components from higher, more destructive overloads. This was possible through major modification of the previous electromagnetic drive technology introduced in the MUPUS penetrator [2] (40-cm rod) onboard PHILAE for the Rosetta mission, CHOMIK sampling device for Russian Phobos-Grunt and the prototype High Energy and Efficiency Penetrator. Thanks to the EMOLE project, new and more accurate simulations are being performed confirming that the novel concept of splitting a large MUPUS-like coil into stack of small coils is feasible without losing (or possibly even gaining) the energy performance in comparison to mechanical moles.

## **Principle of Operation**

Like in the previously presented solutions, the propulsion principle of operation is based on the interaction of three masses of the device but unlike in all the previously developed mole penetrators, the force is generated by a set of reluctant electromagnets arranged in stock and supplied with high impulse power in sequence rechargeable and dischargeable capacitor.

The major novelty of propulsion concept is twofold – the penetrator has much higher reliability of the drive, and its new drive system is able to have power settings. The first advantage is a consequence of a mechanical simplicity of the drive. Foreseen is only one linear motion of the hammer instead of a number of motions, which are typical for the spring driven systems consisting of an electrical motor, reduction gear box, rollers and screw-shaped surface (based on Gromov idea) or helical screw, nut, special latch

---

\* Centrum Badań Kosmicznych PAN, Warsaw, Poland

\*\* Warsaw University of Technology, Warsaw, Poland

and release clamp (based on CBK PAN idea). An additional common disadvantageous feature of the existing mechanisms is their permanent, maximum stroke setting without gradation of the stroke value. In the proposed electromagnetic drive, equipping it with the power settings function has been realized through electrical power supply.

### Preliminary Tests [3]

The concept's verification test-stand was developed and a single electromagnetic drive section (one coil) was tested on this test-stand. Geometrical and mass proportions are retained in accordance with the actual full design. Velocity of the hammer was measured using a linear encoder and magnetic tape. For the purpose of the tests, the Counter Mass remained fixed, and as the result full stroke energy was transferred to the Hammer Assembly.

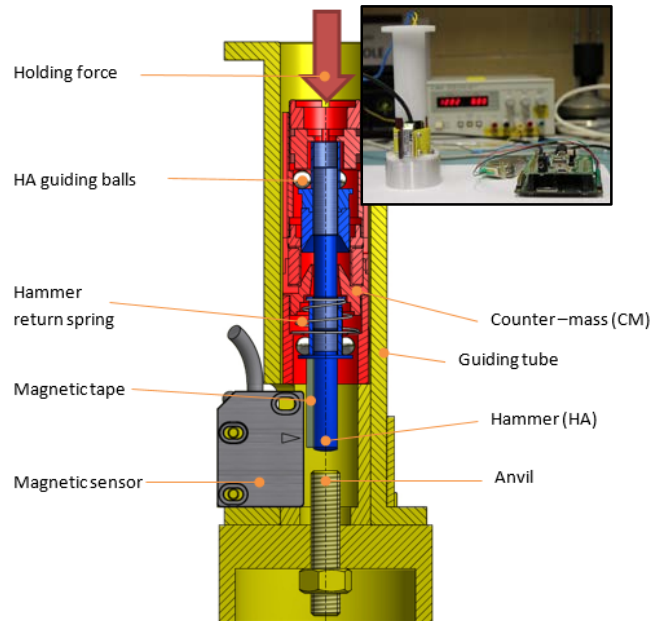


**Figure 1. Verification test-stand, in the top right the actual stand with control electronics.**

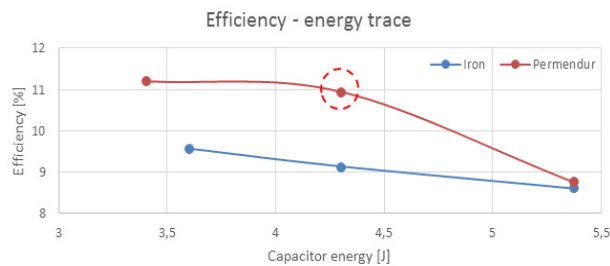


**Figure 2. The system's efficiency as a function of the capacitor's energy for Iron and Permendur 49 coils. Dashed circle indicates optimal capacitor energy.**

Goals of the test campaign on this test-stand were following:

- to see how coil material influences efficiency of the system,
  - to determine the energy fit of the system (meaning at which stored energy the system achieves the highest efficiency),
  - to optimize balance between pair of parameters: capacitance and voltage on the capacitor to achieve the most energetic stroke,
  - to determine optimal initial gap between hammer and counter-mass for the fixed stored energy value,
  - and finally to prove the concept of implementing a coil with 'foot' to the mole-type design and see the outcome of it in comparison to the previously tested concepts.
- For these reasons, a single coil with copper wire of 0.4-mm diameter (147 coil turns) was tested to cover all the above mentioned system configurations.

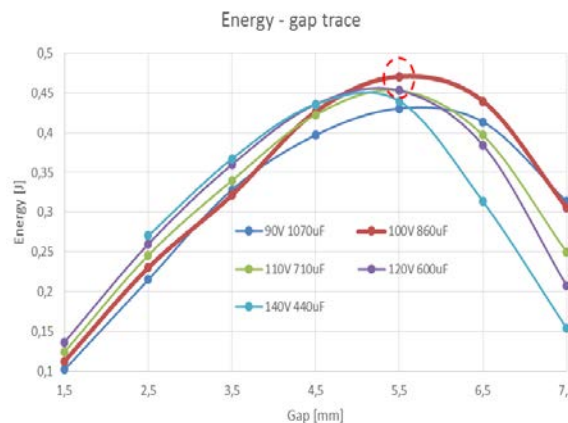


**Figure 3. Optimization of Hammer travel gap. Measured hammer kinetic energy for Permendur 49 coil for 4.3-J capacitor energy level. Dashed circle indicates optimal gap.**



The results and analysis show:

- It is clear that using Permendur 49 can increase the efficiency of the system by 13-20% with respect to the electromagnet made of Iron coil, see Fig. 2.
- There are no radical changes in the resulting hammer's kinetic energy when taking into account different capacitors settings. Nevertheless, a certain optimal setting can be distinguished for Permendur 49 (see Fig. 3.), which is for 100 V/860 uF.
- When it comes to adjusting the energy level to achieve the most efficient system, it is clear from the test results that by lowering energy on the capacitor we get higher efficiency (at least when approaching down to energy of c.a 3.6 J). Nevertheless, it is energy of 4.3 J that is selected as the optimal.
- Optimal travel gap for hammer was also researched for various capacitors' settings. Fig. 3 shows plots for constant capacitor energy of 4.3 J. For most of the cases, the optimal gap is in the range of 4.5-6.5 mm (with full travel freedom of 8 mm). The selected capacitor settings (100 V/860 uF) have an optimal travel gap of 5.5 mm.

### Design Features

#### Mechanical design description

The drive consists of 5 electromagnetic driving sections in which coils, ferromagnetic cores and magnetic separators are concurring to the counter-mass, while armatures of electromagnets with a connection shaft are comprising the hammer. All electromagnetic circuit elements are made

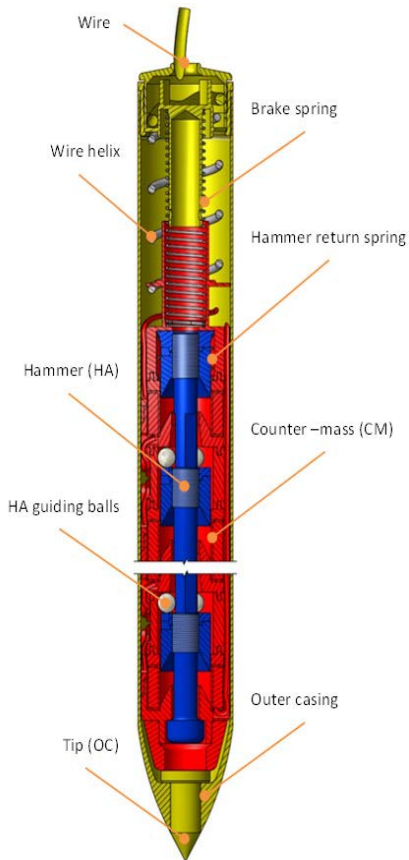


**Figure 4. EMOLE CAD model cross-section.**

of Permendur 49, whereas the magnetic separators are of a tungsten alloy and the connection shaft is made of titanium alloy. The propulsion (counter-mass + hammer) is enclosed in the outer casing assembly and consists of a long, thin wall, titanium sleeve and hardened stainless steel tip.

The hammer is guided by two sets of 3 bearing balls inside the counter-mass which provides low friction losses, while the counter-mass is sliding inside the outer-casing tube. As in all the previous penetrators made by CBK PAN, while the hammers starting position (before hit) is set up by a hammering spring, the position of the counter-mass is determined by a brake spring designed in a way that allows the penetrator to work in a non-gravity environment without any support. A cross-section of a CAD model of EMOLE is shown in Fig. 4.

The EMOLE is 25 mm in diameter and 250 mm length. The mass of the overall assembly is about 700 g, where the counter-mass mass amounts to 520 g and the hammer and the outer casing are of equal weight of about 90 g.



**Figure 5. Outer casing, driving sections and return spring just before final assemblage.**

## Electrical design description [4]

The electrical system consists of three parts: control unit (controller), DC/DC converters unit, and electromagnetic drive placed in penetrator. All three parts are designed to operate separately. Control unit, currently in form of a control panel, is used to set signals to turn on the desired mode of operation of the drive electronic system and therefore to control the penetrators behavior. The control unit's interface is able to turn on and off each of the two DC/DC converters as well as to select one of several “gears” – penetrator stroke energy and actuation frequency.

The DC/DC converter unit consists of two DC/DC converters, both in flyback topology. Each DC/DC converter has an overvoltage protection mechanism ensuring safe operation of the device. High Energy DC/DC (DC/DC HE) converter charges large capacitor, stores the energy, which is then released to the electromagnetic drive when it reaches a certain level, set by device operator. The higher the charge (the energy stored), the lower the actuation frequency.

High Frequency DC/DC (DC/DC HF) converter, operates in a similar way as latter DC/DC converter but operates on the energy level ~200 times lower and two orders of magnitude higher frequency. It is galvanically separated from the system ground to operate totally independently from the state of DC/DC HE.

## Tests [5]

### Actual velocity (and kinetic energy) speed measurements on the finalized assembly

The actual velocity of the hammer with a blocked counter-mass was measured on a test stand. For this purpose, the counter-mass was clamped in the test stand (without the outer casing) and the movement of the hammer was captured on a high-speed camera. The measurement was repeated for all five high energy power settings that the electromagnetic drive possesses. The summary for the achieved velocities, resulting energies and expected efficiencies for each PS are presented in Table 1.

**Table 1. Summary of results**

Power setting	Hit velocity [m/s]	Hit energy [J]	Efficiency [%]
PS-1	3.352	0.49	10.72
PS-2	4.621	0.94	10.62
PS-3	5.774	1.47	11.22
PS-4	6.503	1.86	10.62
PS-5	7.096	2.22	10.28

These results show that the efficiency varies insignificantly between each power setting. The highest efficiency was achieved for the third power setting. Furthermore, this test proved that the stroke energy changes quite equally with the number of the driving sections. It means the amount of sections can be raised or decreased with respect to the direct mission mass or power requirements, and the stroke energy will raise or decrease equally.

### Tests in Syar regolith analogue

After determination of the energy generated by five-coils driving system, the EMOLE penetrator was tested several times, on different power settings, in Syar regolith up to depth of about 50 – 60 cm. The summary of these tests is presented in Figures 6, 7 and 8.

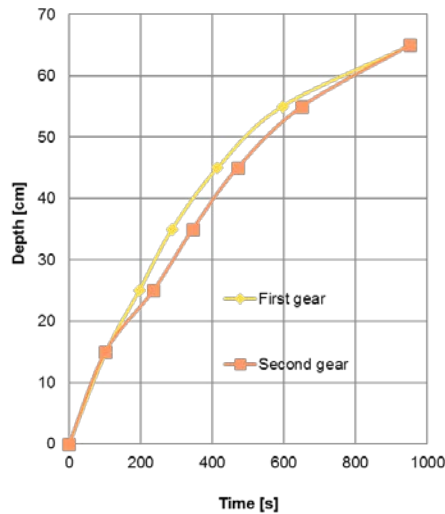


**Figure 6. Dependence of time imbedded from depth in Syar regolith analogue.**

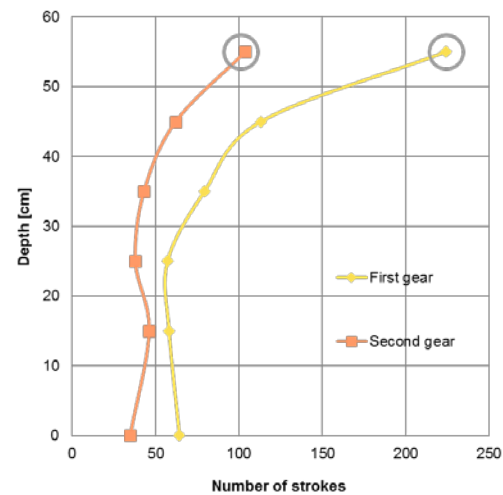


**Figure 7. Dependence of number of strokes from depth in Syar regolith analogue. Numbers of strokes are presented for 10-cm depth sections and only first one is for 15 cm.**

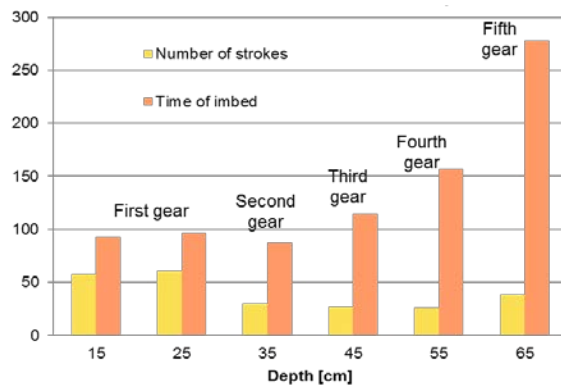


**Figure 8. Dependence of number of strokes and time of imbed from depth for five power settings.**

EMOLE needed more strokes on higher power levels to reach the next ten centimeters because the bottom volumes of the regolith were much more compressed.

### Environmental tests

During the tests conducted in a vacuum chamber, EMOLE was run after degassing ( $p=0.075$  mbar) for about 5 strokes each for all 5 power settings. No problem with launch or any unusual behavior occurred. After gassing the vacuum chamber, the test was repeated again without any problems.

### Vibration tests

The last and the most crucial test concerned durability in regards to vibrations. Thanks to the fact that the propulsion is axially symmetric, tests were performed along two axis: one parallel to the axial symmetric axis and the second one perpendicular to it. In these tests the counter-mass and the hammer were locked. One additional test was performed in which the hammer and the counter-mass were held by an external, permanent magnet. During and after vibration tests with locked counter-mass no problems or difficulties were observed. Afterwards, the drive was run without any problems on all power settings what proves its high resistance against overloads. The preliminary vibration tests with unlocked the counter-mass and the hammer that were held only by magnetic field generated by permanent magnet, showing that this kind of solution is able to prevent the driving sections against damage during vibrations that are generated by a starting rocket.

## Conclusions

A multi-sectioning, reconfigurable electromagnetic hammering propulsion is the first such type of drive to be used in mole penetrator. The main structural novelty, i.e., use of several electromagnets arranged in stock as a direct hammer propulsion, gave twofold improvements. First of all, owing to the fact that the electromagnets do not need any drive transmissions and they do not have any rotating parts (e.g., a DC motor), the whole instrument became much simpler and more reliable. Secondly, the drive has the ability to adjust hit energy during operation, which can contribute to saving energy and to protection of the scientific instruments from damage. Furthermore, to provide an additional mode in which the typical operation is superimposed with a high frequency and low energy mode, a new electronic control was

developed. The simplicity of the direct drive solution, its relevance to the previous flight models of MUPUS (Rosetta), CHOMIK (Phobos-Grunt) and mole penetrator "KRET", along with the experience of CBK PAN, give a path for fast development to a high TRL in a short time.

EMOLE is a low-speed penetrator capable of mobility within the regolith subsurface and is the first mole-type penetrator that employs an electromagnetic linear drive system. Lightweight and compact EMOLE either as a whole device or only its new electromagnetic direct drive, may become flexible solution for space exploration missions providing a wide range of the possible applications, e.g.,:

- carrying sensors (e.g., thermal, miniature spectrometers, cameras) underneath the granular matter of a celestial body
- subsurface ground sampling
- anchoring of lander in microgravity conditions
- anchoring (better coupling with the ground) e.g., seismometers
- act as a special actuator for generating high pulse force (1000-2500 N)

Variable	Value	Comments
Diameter	25,4mm	1in
Length	254mm	10in
Overall mass	704g	Without power supply wire, with the outgoing wire inside the outer casing, brake spring and bearing balls.
Hammer mass	88g	
Counter-mass mass	52g	
Outer casing mass	90g	
Power consumption	4W	12V
Number of coils	5	Can be increased or reduced
Number of wire turns in each coil	147	In each coil
Capacitor parameters	1: 230V; 4,57J 2: 320V; 8,85J 3: 390V; 13,1J 4: 450V; 17,5J 5: 500V; 21,6J	Next power settings in sequence. Discharging voltage and accumulated energy.
Stroke energy, efficiency and duration	1: 0,49J; 10,72%; 1,6s 2: 0,94J; 10,62%; 2,9s 3: 1,47J; 11,22%; 4,3s 4: 1,86J; 10,62%; 6s 5: 2,22J; 10,28%; 7,2s	Next power settings in sequence. Generated on hammer with fixed counter-mass.

**Table 2. Summary of the drive attributes.**

## References

- 1 Grygorczuk, J. et al.: 2011. Advanced penetrators and hammering sampling devices for planetary body exploration. *In proc. of the 11th Symposium on Advanced Space Technologies in Robotics and Automation*, ESA/ESTEC, Noordwijk, the Netherlands.
- 2 Grygorczuk, J. et al.: MUPUS Insertion device for the Rosetta mission. *Journal of Telecommunications and Information Technology*, pp 50-53, 1/2007
- 3 Wiśniewski, Ł., et al.: Pre-testing results and EMOLE's performance. 2015.
- 4 Krasowski, J., et al.: 1. WP5 Electrical Design Description, (*EMOLE – progress report*), 2014.
- 5 Kędziora B, et al.: Report on testing the penetration of a mole and testing the operation of the mole drive in space simulated conditions, (*EMOLE – progress report*), 2015.

# Development of a Magneto-Resistive Angular Position Sensor for Space Mechanisms

Robert Hahn\*, Tilo Schmidt\*, Klaus Seifart\*, Bastian Olberts† and Fernando Romera‡

## Abstract

Magnetic microsystems in the form of magneto-resistive (MR) sensors are firmly established in automobiles and industrial applications. They are used to measure travel, angle, electrical current, or magnetic fields. MR technology opens up new sensor possibilities in space applications and can be an enabling technology for optimal performance, high robustness and long lifetime at reasonable costs. In some science missions, the technology is already applied, however, the designs are proprietary and case specific, for instance in case of the angular sensors used for JPL/NASA's Mars rover Curiosity [1].

Since 2013 HTS GmbH and Sensitec GmbH have teamed up to develop and qualify a standardized yet flexible to use MR angular sensor for space mechanisms. Starting with a first assessment study and market survey performed under ESA contract, a very strong industry interest in novel, contactless position measurement means was found. Currently a detailed and comprehensive development program is being performed by HTS and Sensitec. The objective of this program is to advance the sensor design up to Engineering Qualification Model level and to perform qualification testing for a representative space application.

The paper briefly reviews the basics of magneto-resistive effects and possible sensor applications and describes the key benefits of MR angular sensors with reference to currently operational industrial and space applications. The key applications and specification are presented and the preliminary baseline mechanical and electrical design will be discussed. An outlook on the upcoming development and test stages as well as the qualification program will be provided.

## Introduction

Magnetic microsystems in the form of magneto-resistive (MR) sensors are firmly established in automobiles, mobile telephones, medical devices, wind turbines, machine tools or industrial robots: be it for the measurement of travel, angle or electrical current, or as an electronic compass. Originally developed for data storage applications, the various MR effects open up new measurement possibilities for sensors, not only in terrestrial applications, but also in space applications.

MR sensors are robust, reliable, precise and miniaturized. This combination of features is leading to continuous growth in the application field of MR sensors. The extremely low power consumption of MR sensors make them ideal for wireless, autonomous sensor applications. They present completely new possibilities to the developers of many different types of mechanisms or instruments to measure angle, path, electrical currents, or magnetic fields.

The interest in MR technology from the space community is growing, in particular since the successful application of 40 MR angle sensors to control the motion of electric motors on the Mars Rover "Curiosity" as part of the Mars Science Laboratory Mission [1]. This was not the first application on Mars – MR

---

\* HTS Hoch Technologie Systeme GmbH, Coswig, Germany

† Sensitec GmbH, Lahnau, Germany

‡ European Space Technology Center ESA/ESTEC, Noordwijk, The Netherlands

sensors were already used on the Mars Exploration Rovers Mission to control numerous motors on “Spirit” and “Opportunity”.

All these sensors were designed and manufactured by Sensitec GmbH, located in Lahnu, near Wetzlar, Germany. MR sensors from Sensitec will also be used for the precise positioning of a miniaturized low-mass optical shutter for the MERTIS thermal infra-red imaging spectrometer within the BepiColombo mission to Mercury. Furthermore, MR-based current sensors are likely to be part of the power electronics driving the Thrust Vector Actuators of the Ariane 6 launcher.

Until now the growth in MR applications in space has been opportunistic, with the result that there has been considerable duplication of effort when developing sensor solutions specifically for use in space. In order to focus the effort and to fully exploit the benefits of MR technology for European space mechanisms and applications, HTS GmbH and Sensitec GmbH initiated a close collaboration, leading to dedicated activities for the design and qualification of MR-based angular sensors for space applications. HTS GmbH is located in Coswig, Germany specializing in the development and manufacturing of mechanisms for spacecrafts.

### **Magneto-Resistive Effects and Sensor Application**

The magneto-resistive effect has been known for more than 150 years. The British physicist William Thomson, later known as Lord Kelvin, discovered that the electrical resistance of a conductor changes under the influence of a magnetic field. This effect would first be used industrially more than 120 years later during the late 1970s in combination with thin-film technologies derived from the semiconductor industry. The intelligent arrangement of thin-film structures within a sensor enabled the development of many sensor types for measuring the angle, strength or gradient of a magnetic field. The effect discovered by Thomson was named the “anisotropic magneto-resistive effect” (AMR) and resulted in a resistance change of just a few percent. Nevertheless, this effect was used million-fold in the production of read-heads for hard discs. At the end of the 1980s, the “giant magneto-resistive effect” (GMR) was discovered independently by Prof. Grünberg at the Forschungszentrum Jülich in Germany and by Prof. Fert at the University of Paris in France. Here the resistance change was more than 50%, which opened up even more applications for MR sensors. This discovery was awarded the Nobel Prize for Physics in 2007.

Sensitec manufactures AMR- and GMR-based sensors for industrial and automotive applications and specific terrestrial applications in very harsh environments. The anisotropic magneto-resistive effect may be considered the most obvious and simple effect. It can be observed in ferromagnetic materials such as iron, nickel and cobalt. The specific resistivity  $R$  of these materials is dependent on the angle  $\alpha$  between the current  $I$  and the magnetization vector  $M$ . If the directions of the current and magnetization are in parallel, the resistivity is at its maximum, whereas if the directions are perpendicular, then the resistivity is at its minimum. Based on this relation, illustrated in Figure 1, the resistances  $R$  considering the AMR-effect can be described by the following equation:

$$R(\alpha) = R_m + \frac{\Delta R}{2} \cos(2\alpha)$$

The function  $R(\alpha)$  for  $0^\circ \leq \alpha \leq 360^\circ$  is shown in Figure 1(b). It can be seen from Figure 1 that the resistance  $R$  varies around the mean resistance  $R_m$  as a function of the double angle  $2\alpha$ .

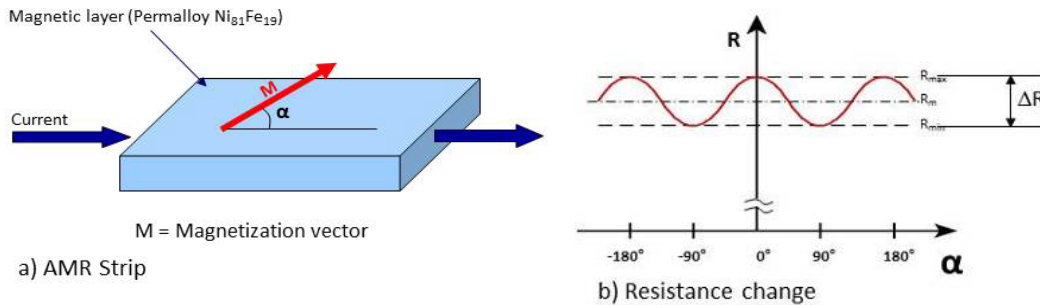


**Figure 1. Anisotropic Magneto-resistive Effect [2]**

The structure of an AMR angle sensor is comparatively simple (see Figure 2). This is one of the reasons that the passive resistive elements are fundamentally reliable. A silicon oxide layer provides the isolation between a silicon wafer (which only acts as a substrate for the thin-film metallic sensor – it has no semiconducting function) and the MR layer. The MR layer consists of a nickel-iron alloy (e.g., Permalloy). This alloy has a high resistivity and demonstrates very low magneto-striction. The next layer comprises an aluminium or gold layer providing the conductors within the sensor as well as the bond contacts. A passivation layer provides protection against the environment in which the sensor chip is applied. Modern production processes in the wafer production, as well as well-matched material pairings allow the temperature coefficients for the output signal amplitude, the offset voltage, and the resistance to be reduced to a minimum. This allows the MR sensor chips to be used in applications at both low and high temperature without significant changes in performance.

To reduce the influences of temperature on the sensor chip even further the sensor structure typically features four resistances connected in a Wheatstone bridge arrangement.

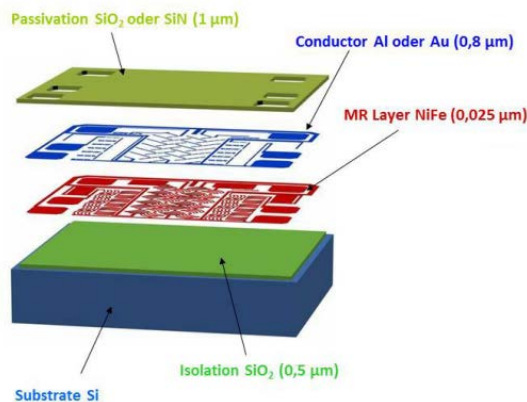


**Figure 2. Structure of Sensitec's AMR Angle Sensor [2]**

In AMR angle sensors, two bridges at an angle of 45° to one another are interlaced in order to generate a sine and cosine output signal as a function of angle. This signal type is generally also known from other angular sensor concepts, e.g., resolvers or optical encoders.

The advantage of the MR sensors is that an unambiguous angular output can be provided even without any signal conditioning. A pre-amplified analog output signal possesses theoretically infinite resolution and could be directly fed into the controller of the application.

However, for the sake of simplicity the sine-cosine output voltage signals are typically pre-processed by means of front end electronics to deliver digital output signals according to the typical interfaces used in industry. For industrial and terrestrial purposes, commercial amplifiers and interpolation ICs are used. For



high performance demands microcontrollers are implemented. However, it is also possible to use passive discrete devices only to provide a digital output, yet knowing that the resolution will be limited. Still this makes the MR sensors ideal candidates for cost efficient position sensors in many space applications where moderate performance is required.

### Sensor Specification

In general, MR-based sensors possess the unique advantage that in order to comply with low or medium performance demands (i.e., up to 11 bit resolution), basically no front end signal conditioning is required to provide the user with a reasonable angular signal due to the intrinsic sine-cosine output signal. In order to achieve discrete (hence TTL compatible) sensor output signal, only a reduced signal processing is required. This is desired by most potential users and makes this concept an ideal candidate for low to medium performance 360° incremental encoders with a reference pulse. Such sensor can be used to replace potentiometers in mechanisms in order to improve reliability, performance and to keep the costs at low level, or to enable closed-loop motor control for improved mechanism performance and reduced microvibrations. Such medium performance encoder could be used for instance for:

- Antenna pointing mechanisms
- Shutter mechanisms
- Calibration mechanisms
- Reaction wheels (e.g., as wheel speed sensors)
- Robotic exploration (e.g., wheel position sensors, as already used in case of the Curiosity Rover [1])

As a baseline for the design of the Magneto-Resistive Angular Sensor for Space Applications (MRS), a dedicated pilot application was selected, and the technical requirements were derived. The baseline specification is given in Table 1.

It is worthwhile to highlight that the AMR and GMR sensors developed and produced by Sensitec allow for various sensor concepts; hence it is also possible to design and qualify mission-specific or user-specific encoders, allowing for true power on absolute angular measurements, or high resolution and high accuracy angular measurement.

**Table 1. MRS Key Requirements Specification**

Requirement	Value
Angular Range	360° (no deadband)
Rotational speed	> 100 RPM
Resolution	> 10 bit (~0.3°)
Repeatability	< 0.5° (goal: 0.1°, TBC)
Measurement type	Incremental with reference pulse
Output signal	Digital ABZ (TTL)
Power consumption	< 150 mW (TBC)
Lifetime	on ground: > 15 years, in orbit operation: > 15 years
Temperature, operational	-50°C ... +100°C
Temperature, non-operational	-60°C ... +110°C
Radiation hardness	> 250 krad
Mass	< 150 g
Mechanical I/F	End of shaft configuration: -shaft diameter: 5 mm -outer diameter: 50 mm -height: 40 mm Alternative hollow shaft configuration: - shaft diameter: 30 mm -outer diameter: 75 mm -height: 25 mm



### Preliminary Sensor Design

Based on the baseline specification, a preliminary MRS design has been developed. In its baseline configuration, the encoder will be attached at one end of the shaft, e.g., at the secondary shaft of an actuator, to allow for closed-loop control. In this configuration, the MRS is most compact and small, yet provided sufficient performance ( $> 10$  bit resolution). This concept is illustrated in Figure 3.

The MRS consists of a magnetic measurement scale (also referred to as pole ring) with a diameter of 45 mm and two parallel magnetic tracks. One magnetic track has 282 magnetic poles that are used for the incremental position measurement. The second magnetic track has one pole pair that is used as a reference pulse, giving precisely the  $0^\circ$  position. The position is measured by an AMR sensor and a GMR sensor for the reference pulse. The MRS is designed to be fully redundant. The MR sensors provide an analog sine-cosine signal. In fact, for each pole pair two full sine-cosine periods are provided.

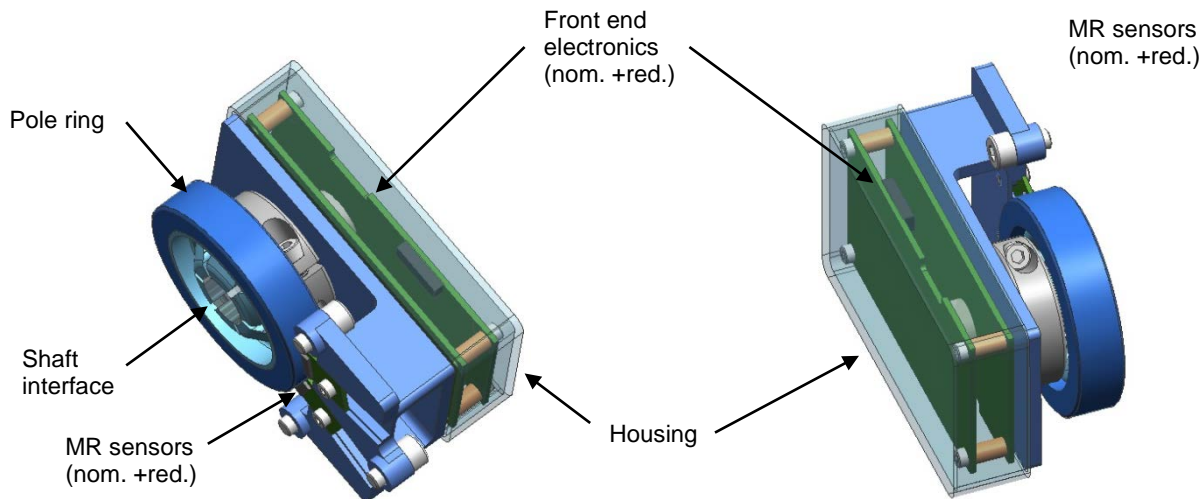


**Figure 3. Preliminary baseline MRS design**

The sensors will be housed in a dedicated LTCC package, conforming to ECSS outgassing and quality standards. The sine cosine signals can directly be delivered to the motor controller. However, often a discrete signal (e.g., TTL signal) is required by the controller. In order to provide this interface, a dedicated front end electronic board is included in the sensor (nominal and redundant), which transforms the sine-cosine signals into a TTL-compatible pulse signal (ABZ, 0 - 5V). This is achieved by a set of comparators and operation amplifiers, which allow to deduce from the pre-amplified sine-cosine signals, a pulsed signal (AB, view Figure 4) with four pulses per pole, resulting in a resolution of about  $0.3^\circ$ . The A and B pulses are phase shifted, allowing determination of the rotation direction.

In the baseline configuration the PCB boards are located in parallel to the pole ring, behind the end of the shaft to minimize the envelope.

A higher resolution can be achieved if a larger measurement scale (i.e., pole ring) is used with the same sensors and front end electronics. In order to reduce the costs of the final product, off-the-shelf ferrite pole rings will be used. The largest off-the-shelf pole rings currently available have an outer diameter of 72 mm (inner diameter 54 mm), giving roughly  $0.2^\circ$  resolution. This enables a hollow shaft configuration, where the electronic boards are attached radially (view preliminary design in Figure 5).

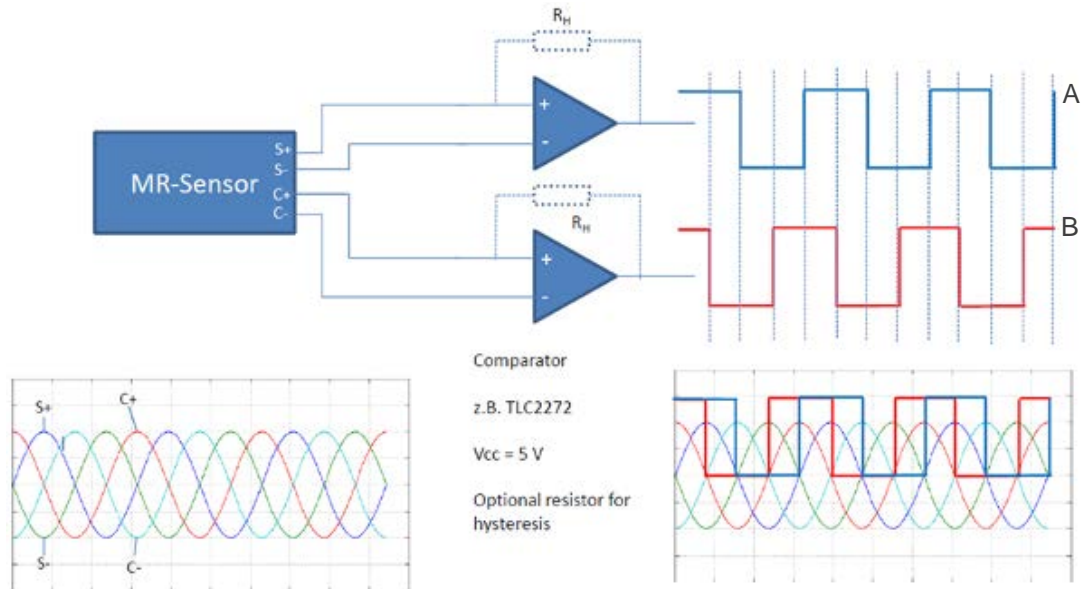


**Figure 4. Signal conditioning approach**

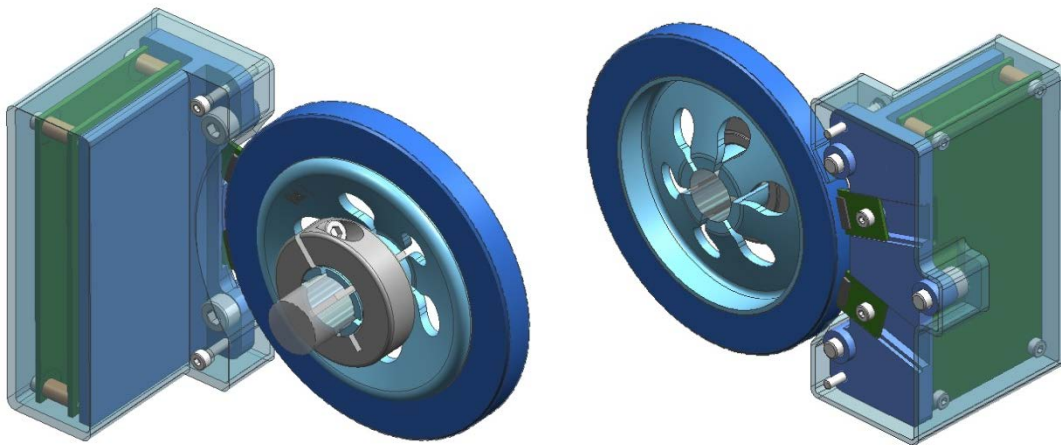


**Figure 5. Alternative hollow shaft configuration of MRS with 72-mm pole ring**

### **Development and Qualification Approach**

The ultimate objective of this development is to develop and qualify an MR-based contactless angular position sensor in order to achieve swift and efficient entry into the market.

The technical requirement specification has already been consolidated and finalized based on a relevant reference application. Currently, the MRS design is further elaborated, and it is planned to build and to test the MRS at breadboard level soon. Breadboard models and several tests are foreseen to validate the measurement and signal conditioning concept. These tests include functional and performance tests of the electronics, as well as full-scale functional and performance tests in reduced and elevated temperature.

Ultimately, Engineering Qualification Models of the MRS will be built and qualification tests shall be performed in order to achieve TRL 6. The qualification tests to be performed include functional performance tests at ambient and thermal vacuum, vibration and shock tests, electro-magnetic compatibility and electro-static discharge tests (EMC, ESD) as well as outgassing tests and radiation tests.

## **Conclusion**

The baseline requirements, pilot applications, and a preliminary flight design of an MR-based contactless angular position sensor dedicated to space mechanisms were completed. Breadboard activities will be initiated to validate the concept. This will be followed by a dedicated qualification test campaign using qualification models in late 2016 / early 2017. It is planned to present the qualified MRS mid 2017.

## **Acknowledgements**

The authors would like to thank ESA for the kind support and technical guidance in this activity as well as all companies and research institutes who provided valuable inputs and information to our market study during the user consultation.

## **References**

1. M.R. Johnson et al.: "The Challenges in Applying Magnetoresistive Sensors on the Curiosity Rover" *12th MR Symposium 2013*, Wetzlar
2. R. Hahn, B. Olberts: "Feasibility Study Magneto-resistive Sensors for Space Applications – Final Report" *MRS-HTS-RP-001, ESA Contract No. 4000109333*



# **Cu-Al-Ni Shape Memory Single Crystal Wires with High Transformation Temperature**

Alain Hautcoeur\*, Florian Fouché\* and Jacques Sicre\*\*

## **Abstract**

CN-250X is a new material with higher performance than Nickel-Titanium Shape Memory Alloy (SMA). For space mechanisms, the main disadvantage of Nickel-Titanium Shape Memory Alloy is the limited transformation temperature. The new CN-250X Nimesis alloy is a Cu-Al-Ni single crystal wire available in large quantity because of a new industrial process. The triggering of actuators made with this Cu-Al-Ni single crystal wire can range from ambient temperature to 200°C in cycling and even to 250°C in one-shot mode. Another advantage of CN-250X is a better shape recovery (8 to 10%) than Ni-Ti (6 to 7%).

Nimesis is the first company able to produce this type of material with its new special industrial process. A characterization study is presented in this work, including the two main sollicitation modes for this material: tensile and torsion. Different tests measure the shape recovery of Cu-Al-Ni single crystals wires during heating from room temperature to a temperature higher than temperature of end of martensitic transformation.

## **Introduction**

Shape memory alloys (SMA) are recognized as reliable and efficient materials particularly to design actuators. The major drawback of these shape memory actuators is the trigger temperature that is lower than 100°C with standard Ni-Ti alloys. The new Nimesis Cu-Al-Ni single crystal wire (Figure 1) shows a transformation temperature higher than 100°C and they are available in round section with a diameter from 0.5 mm to 20 mm. The state of the art and a detailed characterization work made for CNES demonstrated that a Cu-Al-Ni single crystal wire is a very good candidate for space applications that need trigger temperatures between 100°C and 200°C.



**Figure 1. Cu-Al-Ni single crystal Ø2.2-mm wires made with special Nimesis process**

## **Experimental Approach**

Single crystals were produced by a Nimesis special industrial process that is derived from the Bridgman process<sup>(1) (2)</sup>. Dimensions of wires were 2 mm in diameter, and 70 to 300 mm in length. The advantage in using single crystals is that the preferred orientation of these crystals (close to [001]) obtains a maximum

---

\* Nimesis Technology, Mecleuves, France

\*\* CNES, Toulouse, France

reversible strain of about 8 to 10% <sup>(3)</sup> <sup>(4)</sup>. This preferred orientation is due to the high elastic anisotropy of the material.

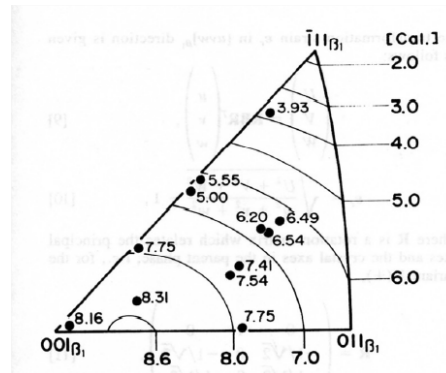


**Figure 2. Relation between transformation strains and crystal orientation <sup>(3)</sup>**

Some Cu 82.4wt%-Al 13.5wt%-Ni 4.1wt% single crystal samples were mainly tested in tensile and torsion mode. The evolution of the deformation during a thermal cycle and with imposed force (shape recovery) was measured. This test was performed for more than 10 thermal cycles. Transformation temperatures were controlled by DSC (Differential Scanning Calorimetry) until 25 cycles.

### Thermomechanical tests

The objective of these tests is to obtain data relative to thermomechanical behavior of the Cu-Al-Ni single crystal wire produced in industrial conditions.

#### DSC tests Results

Table 1 shows the evolution of transformation temperatures ( $A_s$ ,  $A_f$ ,  $M_s$ ,  $M_f$ ) for polycrystalline (before monocrystallization process) and single crystal (after monocrystallization process). There is a small variation of transformation temperatures during the monocrystallization process.

**Table 1. DSC results on Cu-Al-Ni polycrystal and single crystals.**

description	$M_f$ (°C)	$M_s$ (°C)	$A_s$ (°C)	$A_f$ (°C)
Cu-Al-Ni polycrystal	118	152	149	163
Cu-Al-Ni single crystal	134	153	157	163

Figure 3 shows the evolution of temperatures during thermal cycling between 25 to 250°C and between 25 to 200°C. The transformation temperatures are more stable in cycling when the maximum temperature is limited to 200°C.

#### Tensile Test Results

Wire samples are manufactured and tests are done with a tensile testing machine equipped with special grippers and extensometer. Heating is achieved with a direct power supply (Joule Effect) of the sample. Temperature is measured at three different locations: in the center of the sample, just above the extensometer and just below the extensometer. This ensures heating the test zone of the sample homogeneously.

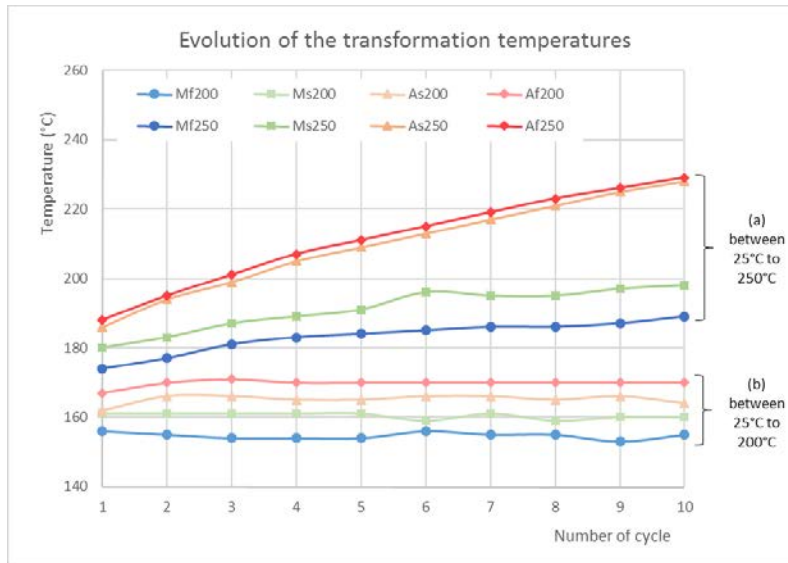


**Figure 3. Evolution of transformation temperatures during thermal cycling (a) between 25 and 250°C, (b) between 25 and 200°C**

Two preliminary tests allowed to evaluate the behavior of the material at room temperature and at 220°C, Figure 4 shows results of tensile tests at room temperature and at 220°C.

Other tests are done with a preload of 150 MPa before heating. Successive thermal cycling from 25°C to 250°C results in measuring evolution of the strain of the martensitic transformation. During the cycling, transformation temperatures were recorded.

Figure 5 presents transformation temperatures and strain as a function of the number of thermal cycles. Contrary to other High Temperature Shape Memory Alloys, deformation and transformation points remain constant until 25 cycles and probably over (test to be done).

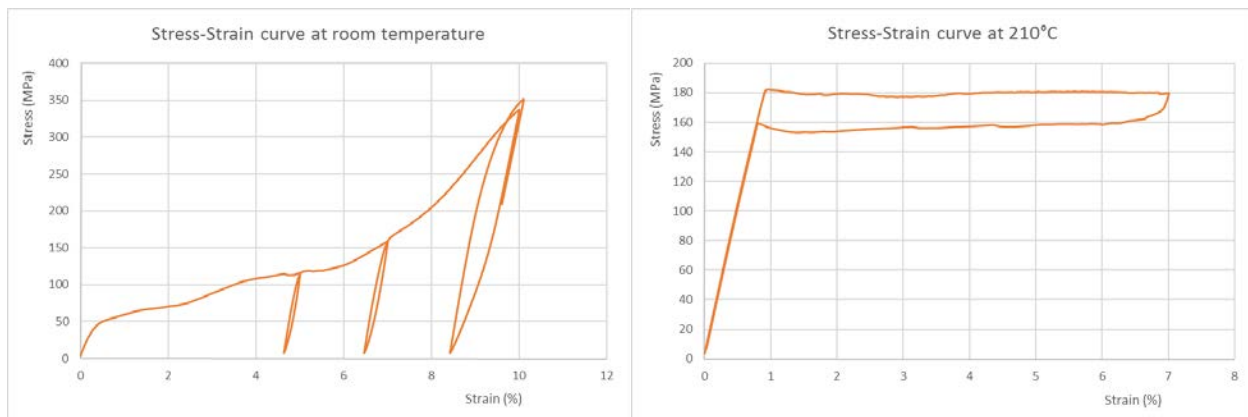


**Figure 4. Tensile tests of Cu-Al-Ni single crystal samples at room temperature (martensitic state) and at 210°C (austenitic state)**

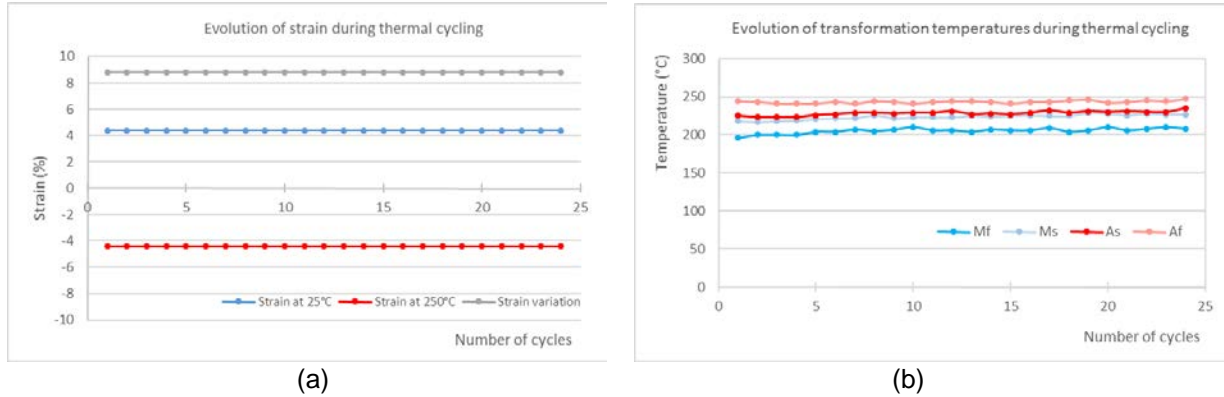


**Figure 5. Evolution of (a) strain and (b) transformation temperatures for a prestressed Cu-Al-Ni single crystal (150MPa) and during thermal cycling from 25°C to 250°C**

#### Torsion tests

Torsion tests were made with Cu-Al-Ni polycrystalline samples, Cu-Al-Ni single crystal samples and Ni-Ti samples for comparison. Length of each sample was 70 mm. Each sample is fastened between one fixed end and one end on which a bulk is set in order to induce a torque. Torque value varies between 0 and 0.5 N-m. Heating is achieved by a heat gun able to reach a temperature up to 200°C. Torsion angle is measured initially at room temperature and then after heating at 200°C after recovery shape. Shear strain  $\gamma$  and shear stress  $\tau$  are calculated from these data. Results of these tests on Ni-Ti are in accordance with those in the literature <sup>(5)(6)</sup>. This establishes a comparison between Ni-Ti and Cu-Al-Ni in torsion. Recovery shape rate is globally the same between Ni-Ti samples and Cu-Al-Ni polycrystalline samples. But  $\Delta\gamma$  is lower for Cu-Al-Ni single crystals.

#### Thermomechanical behavior

Ratio  $d\sigma/dT$  of Ni-Ti ( $\sim 6$  MPa/°C) is higher than the ratio  $d\sigma/dT$  of Cu-Al-Ni single crystal ( $\sim 2.3$  MPa/°C). That means for the same temperature range, and for the same power rate, activation stress of a Ni-Ti actuator will be approximately twice higher than the activation stress of a Cu-Al-Ni single crystal actuator. Furthermore, for the same stress, it takes about twice more heating for a Cu-Al-Ni single crystal actuator than for a Ni-Ti actuator.

#### Electrical behavior

We can heat by Joule Effect Cu-Al-Ni components to change the temperature of the material, as we can heat by Joule Effect Ni-Ti components. That involves taking into account the difference of resistivity between both materials.

**Table 1. Comparison between Ni-Ti and Cu-Al-Ni resistivity**

	Ni-Ti	Cu-Al-Ni
Electrical resistivity $\rho$ (average between austenite and martensite) $10^{-6} \Omega.m$	0.9	0.12



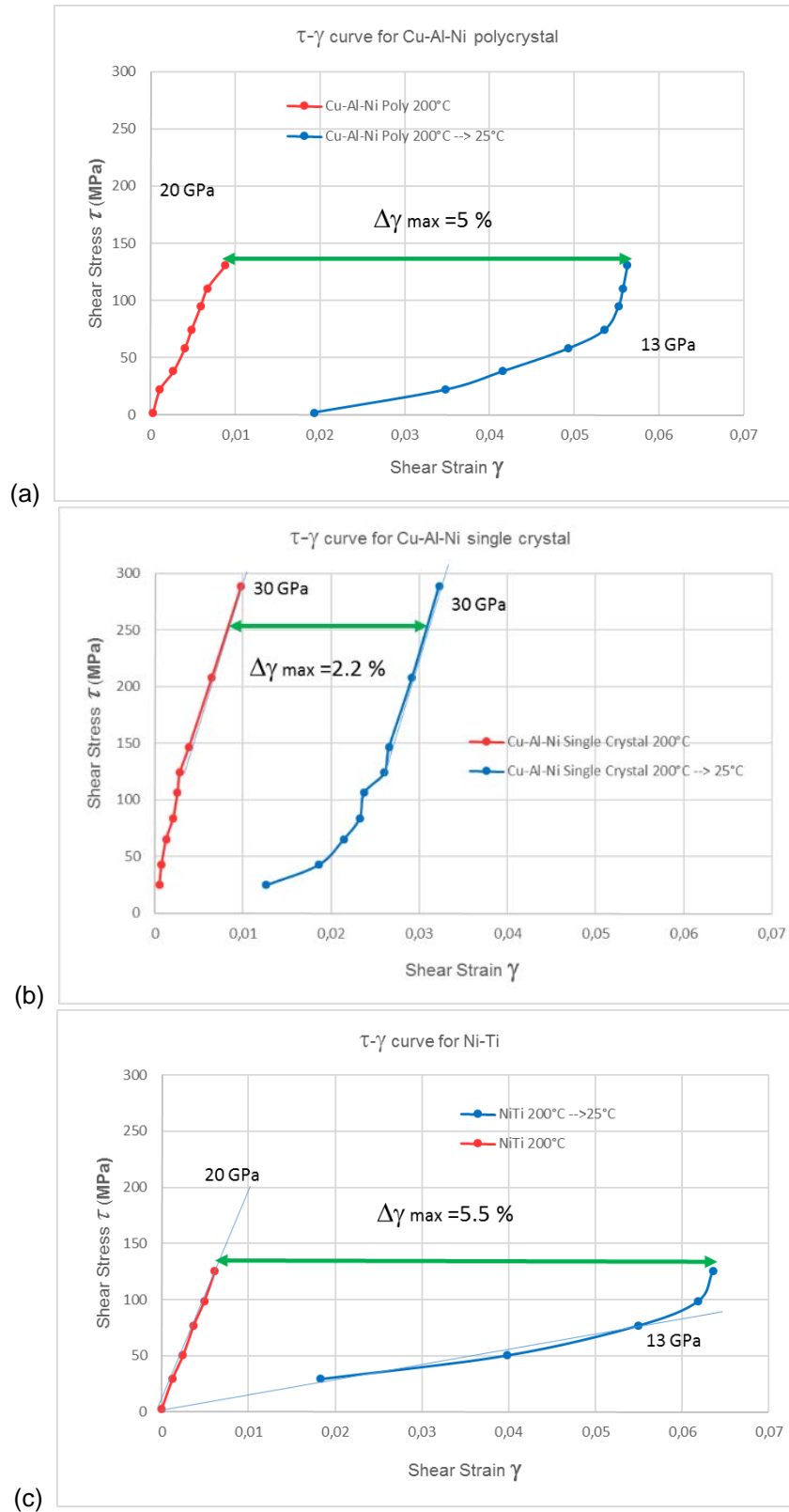
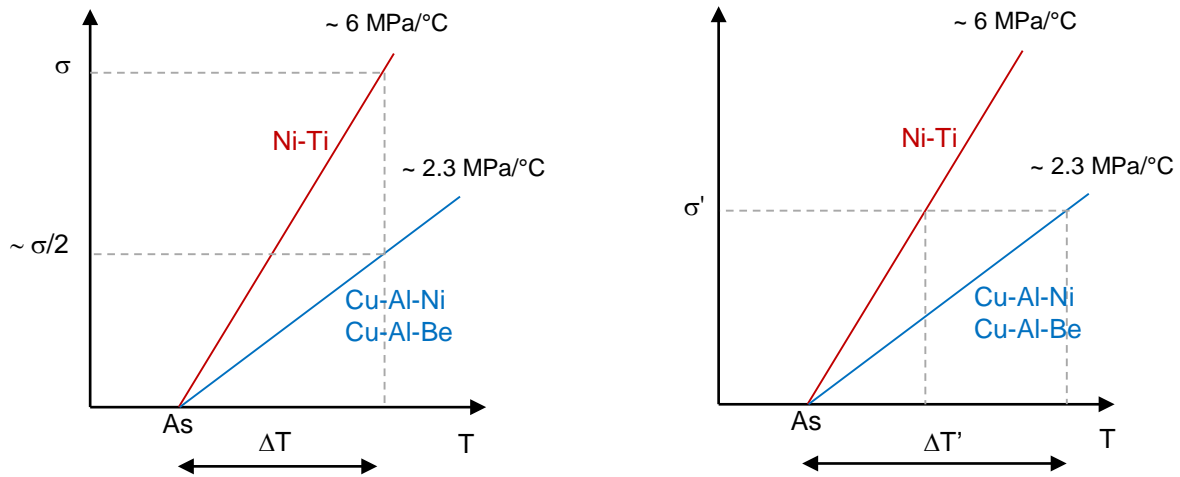


Figure 6. Elements of comparison for (a) Ni-Ti and (b) Cu-Al-Ni polycrystal and (c) Cu-Al-Ni single crystal



**Figure 7. Comparison of Ni-Ti and Cu-Al-Ni  $\sigma$ - $T$  slope and consequences on actuator activation (a) for a given temperature, (b) for a given stress.**

$$\sqrt{\frac{R_{NiTi}}{R_{CuAlNi}}} = \frac{I_{CuAlNi}}{I_{NiTi}} = \frac{U_{NiTi}}{U_{CuAlNi}} \sim 2.7 \text{ to } 3.5$$

For the same dissipated power:

$$I_{CuAlNi} \sim 3 \times I_{NiTi} \quad U_{CuAlNi} \sim \frac{U_{NiTi}}{3}$$

### Conclusion

Results obtained with the new CN-250X by Nimesis showed a very good stability during the thermal cycling in terms of shape recovery (8 to 10%) at 150 MPa for trigger temperature below  $200^\circ\text{C}$ . Higher temperatures (until  $250^\circ\text{C}$ ) can be used for one-shot applications or for applications with a small number of cycles. Cu-Al-Ni single crystal wire seems to be able to be made into high temperature actuators (Figure 8), thermal safety devices, locking-unlocking devices, low shock mechanisms, and deployment mechanisms. Nimesis is now able to manufacture Cu-Al-Ni single crystal wire (diameter between 0.5 to 20 mm) in large quantity with a new patented industrial process, controlling the entire process from alloy casting to wire grinding. This allows supplying High Temperature SMA over the long term.

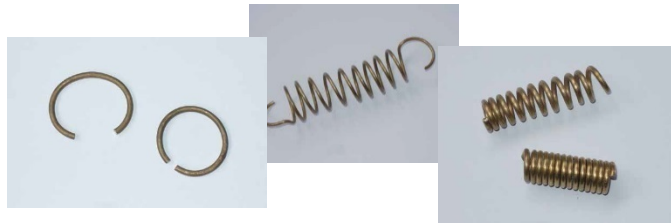


**Figure 8. Examples of actuators made with Cu-Al-Ni single crystal wire**

## References

1. B. Chalmers, Principles of Solidification, 1964
2. K. S. Bagdasarov, Growth of Crystals, 1991
3. H. Horikawa, S. Ichinose, K. Morii, S. Miyazaki, K. Otsuka, Orientation Dependence of  $\beta_1 \rightarrow \beta'_1$  Stress-Induced Martensitic Transformation in a Cu-Al-Ni Alloy : Metall. Trans., 1988, vol. 19A, pp. 915-923
4. Z.G. Wang, Z.F. Zhang, X.W. Li, W.P. Jia, S.X. Li, Orientation dependence of the cyclic deformation behavior and the role of grain boundaries in fatigue damage in copper crystals : Materials Science and Engineering A319–321 (2001) 63–73
5. X P. Sittner, K. Hashimoto, M. Kato, M. Tokuda, Stress induced martensitic transformations in tension/torsion of CuAlNi single crystal tube : Scripta Met. 48 (2003), pp. 1153-1159
6. T.W. Duerig, K.N. Melton, D. Stockel, C.M. Wayman, Engineering Aspects of Shape Memory Alloys, pp. 234-244, 1990



# **Prevailing Torque Locking Feature in Threaded Fasteners using Anaerobic Adhesive**

Alan Hernandez\* and Daniel P. Hess\*

## **Abstract**

This paper presents results from tests to assess the use of anaerobic adhesive for providing a prevailing torque locking feature in threaded fasteners. Test procedures are developed and tests are performed on three fastener materials, four anaerobic adhesives, and both unseated assembly conditions. Five to ten samples are tested for each combination. Tests for initial use, reuse without additional adhesive, and reuse with additional adhesive are performed for all samples. A 48-hour cure time was used for all initial use and reuse tests. Test data are presented as removal torque versus removal angle with the specification required prevailing torque range added for performance assessment. Percent specification pass rates for the all combinations of fastener material, adhesive, and assembly condition are tabulated and reveal use of anaerobic adhesive as a prevailing torque locking feature is viable. Although not every possible fastener material and anaerobic adhesive combination provides prevailing torque values within specification, any combination can be assessed using the test procedures presented. Reuse without additional anaerobic adhesive generally provides some prevailing torque, and in some cases within specification. Reuse with additional adhesive often provides comparable removal torque data as in initial use.

## **Introduction and Background**

Prevailing torque locking features and anaerobic adhesives are used to provide secondary locking in threaded fasteners. The aerospace industry has embraced prevailing torque locking in fasteners, in part, due to the ease in which the feature can be validated during installation. In addition, the industry has well-defined standards and specifications for this type of locking feature [1-6].

Anaerobic adhesives provide excellent locking and can maintain preload in fasteners provided sufficient curing occurs, but this is not always guaranteed. Although validation for this type of locking is possible [7], it is not yet in widespread use in practice.

Recent application of anaerobic adhesive for repair of worn prevailing torque locking in inserts on the Space Shuttle windshield [8, 9] has given rise to the premise of this work. Namely, use of adhesive for providing prevailing torque type locking feature, and quantifying its performance using the well-defined prevailing torque standards and specifications. No published research on this concept currently exists.

Use of anaerobic adhesive for providing prevailing torque locking actually relaxes the usual expectation of adhesive to maintain preload to the common expectation for prevailing torque locking features which is to prevent disassembly.

This paper presents results from tests performed to assess the use of anaerobic adhesive to provide a prevailing torque type locking feature. This work provides much needed test data supporting the use of adhesive in providing prevailing torque locking for repair as well as on fasteners without secondary locking.

Performance of prevailing torque locking fasteners in reuse is required in qualification specifications. However, these requirements are often stated in terms of reuse in unseated rather than seated conditions and this distinction is sometimes missed. This issue has been recently examined through a series of tests

---

\* University of South Florida, Tampa, FL

and presented elsewhere [10]. All prevailing torque features tested [10] exhibit a decrease in prevailing torque with reuse with the largest decrease during first reuse. The effect of seating to preload is a higher loss in prevailing torque (e.g., 10 to 25% loss during initial use) compared to unseated results.

In addition to tests performed to assess initial use of anaerobic adhesives to provide prevailing torque type locking, this paper presents results from tests to assess reuse. Reuse with and without adding additional anaerobic adhesive are tested. It is found in most cases that reuse with additional adhesive performs comparable to the initial use case. The significance of this result is that using anaerobic adhesive to provide prevailing torque locking may have the added benefit of negligible degradation with reuse due to self-repair with additional adhesive.

### **Test Specimens and Equipment**

Tests were performed using ¼-28 (M6x1) threaded fasteners. Three fastener materials were tested including plain grade 8, yellow-zinc grade 8, and aerospace A286. Four low to medium strength anaerobic adhesives (Loctite 290, Loctite 222MS, Loctite 242, and Loctite 243) were tested with each of the three fastener materials. Unseated assembly conditions were tested for all fastener materials and adhesive combinations. Five to ten samples were tested for each combination of fastener material, adhesive and assembly condition for a total of 96 samples. Three tests were performed for each of these samples including 1) an initial use test, 2) a reuse with no additional adhesive, and 3) a reuse with additional adhesive. For each of these tests, torque measurements were obtained at multiple removal angles including 0 (i.e., breakaway), 2-5, 90, 180, 270 and 360 degrees.

The grade 8 test fasteners have ¼-28 UNF (M6x1) threads and the aerospace A286 test fasteners have ¼-28 UNJF (M6x1) threads. All test nuts are hex nuts and all test washers are flat. Specifications for the test fasteners are as follows:

1. Plain grade 8:
  - a. Cap screw: ¼-28 UNF, 1.25-in length (M6x1, 31.75 mm)
  - b. hex nut: ¼-28 UNF, 0.22-in thickness (M6x1, 5.6 mm)
  - c. flat washer: 0.057-in thickness (1.45 mm)
2. Yellow-zinc plated grade 8:
  - a. Cap screw: ¼-28 UNF, 1.25-in length (M6x1, 31.75 mm)
  - b. hex nut: ¼-28 UNF, 0.22-in thickness (M6x1, 5.6 mm)
  - c. flat washer: 0.081-in thickness (2.06 mm)
3. A286 passivated (aerospace):
  - a. NAS1004-1A cap screw: ¼-28 UNJF, 0.6-in length (M6x1, 15 mm)
  - b. hex nut: ¼-28 UNJF, 0.22-in thickness (M6x1, 5.6 mm)
  - c. flat washer: 0.032-in thickness (0.81 mm)

Four types of anaerobic adhesive were used in the tests. These were Loctite 290, 222MS, 242 and 243. Loctite 290 is a medium strength wicking grade which was found to consistently exceed the specification required prevailing torque range of 3.5-30 in-lb (0.40-3.4 N-m) for ¼-28 (M6x1) fasteners, so limited testing was performed with this adhesive. The main characteristics for the other three anaerobic adhesives are as follows:

1. Loctite 222MS is low strength and purple in color.
2. Loctite 242 is medium strength and blue in color.
3. Loctite 243 is medium strength and blue in color. It has activator or primer added to provide better curing and performance with inactive materials such as A286 stainless steel.

Dial torque wrenches were used for measuring the removal and prevailing torque of the threaded fasteners. A torque wrench with a 75 in-lb (8.5 N-m) range and 1 in-lb (0.1 N-m) increments was used for prevailing torque measurements for both seated and unseated tests.

All test fasteners were inspected for smooth assembly and cleaned prior to tests. All test fasteners (i.e., cap screws, nuts and washers) and fixtures were cleaned using an ultrasonic cleaner with methyl ethyl ketone (MEK) solvent for 5 minutes and allowed to air dry before testing.

### **Test Procedures**

Tests include an initial use test, reuse without additional adhesive test, and reuse with additional adhesive test. The preparation procedures for these three tests are different, but the test procedure is the same as listed below.

Preparation for unseated initial use tests:

- 1) Apply 2 drops of anaerobic adhesive to cap screw threads.
- 2) Apply 1 drop of anaerobic adhesive to hex nut threads.
- 3) Assemble cap screw and hex nut until three full threads extend beyond nut.
- 4) Allow adhesive to cure for 48 hours on a lint free paper towel.
- 5) After curing time, wipe any excess adhesive from cap screw threads with a lint free paper towel.

Test procedure for unseated initial use tests, unseated reuse without additional adhesive tests, and unseated reuse with additional adhesive tests:

- 1) Clamp head of cap screw in a vise.
- 2) Use 0-75 in-lb (0-8.5 N-mm) dial-type torque wrench to apply torque to nut in counter-clockwise direction gradually until motion is initiated. Record breakaway torque at the instant of motion.
- 3) Continue applying torque and record torque values at 2-5, 90, 180, 270, and 360 degrees.

Preparation for unseated reuse without additional adhesive tests:

- 1) Remove hex nut completely from cap screw.
- 2) Reassemble hex nut to the same position as in initial use test.
- 3) Allow adhesive to cure for 48 hours on a lint free paper towel.

Preparation for unseated reuse with additional adhesive tests:

- 1) Remove hex nut completely from cap screw.
- 2) Add 2 drops of anaerobic adhesive to cap screw threads.
- 3) Add 1 drop of anaerobic adhesive to hex nut threads.
- 4) Reassemble hex nut to the same position as in initial use test.
- 5) Allow adhesive to cure for 48 hours on a lint free paper towel.

### **Test Data and Analysis**

All the test data has been assembled in plots of measured removal torque in inch-pounds versus removal angle in degrees [11]. The allowable range of prevailing torque for ¼ -28 (M6x1) thread size is between 3.5 and 30 in-lb per specification [1-6]. This is indicated by horizontal dashed lines in the plots for quick assessment of results. Each plot includes data from 5 to 10 test fasteners. Overlap of data points in the plots occurs.

Figure 1 shows three plots for the unseated grade 8 fasteners with Loctite 222MS for the initial use, reuse without additional adhesive, and reuse with additional adhesive. This shows all removal torque measurements were within the specification of 3.5 to 30 in-lb (0.40-3.4 N-m) for initial use giving a 100% pass rate for this fastener and adhesive combination. For reuse without additional adhesive, many torque measurements fall below the specification, whereas for reuse with additional adhesive, only a couple fall below specification. This data shows the effect of reuse with versus without additional adhesive.

An unseated test specimen passes the prevailing torque specification only when the measured removal torque is within the 3.5 to 30 in-lb (0.40-3.4 N-m) range over the entire removal angle range from breakaway to 360 degrees. When all measured removal torque values from all test samples for a combination of fastener material and adhesive are within this range, the test combination has 100% pass rate.

Table 1 lists the pass rates with respect to the 3.5 to 30 in-lb (0.40-3.4 N-m) prevailing torque specification for unseated plain grade 8 threaded fasteners. The first entry in the table shows 100% pass rate for all initial use tests of plain grade 8 fasteners with Loctite 222MS in unseated assembly. Reuse without additional adhesive tests for this case have only a 10% pass rate. An unseated test specimen passes the prevailing torque specification only when the measured removal torque is within the 3.5 to 30 in-lb (0.40-3.4 N-m) range over the entire removal angle from breakaway to 360 degrees. Reuse with additional adhesive tests for this case have an 80% pass rate.

**Table 1. Unseated plain grade 8 specification pass rate**

Plain Grade 8	Loctite 222MS	Loctite 242	Loctite 243
Initial use	100%	90%	10%
Reuse w/o additional adhesive	10%	80%	0%
Reuse w/ additional adhesive	80%	80%	100%

The same analyses has been performed for unseated grade 8 fasteners with Loctite 242 and Loctite 243 [11]. The pass rates for these cases are included in Table 1. This data shows the effect of different adhesives for the same fastener material in the initial use and reuse conditions. Reuse with additional adhesive outperforms reuse without additional adhesive for this fastener material.

Similar results are found for the unseated tests with yellow-zinc grade 8 fasteners and A286 fasteners. The plots for the unseated A286 aerospace fasteners with Loctite 243 adhesive are shown in Figure 2. This combination of fastener and adhesive is shown because A286 is an inactive material and the Loctite 243 has activator or primer included to improve cure. This adhesive performs the best for the unseated A286 fasteners as shown in Table 2 which lists pass rates for all unseated A286 fastener tests. Note that the low pass rate for unseated initial use tests for A286 fasteners with adhesives lacking primer or activator (e.g., 222MS and 242) is due to the fact that A286 material is inactive which inhibits cure.

**Table 2. Unseated A-286 specification pass rate**

A-286	Loctite 222MS	Loctite 242	Loctite 243
Initial use	0%	0%	100%
Reuse w/o additional adhesive	60%	50%	10%
Reuse w/ additional adhesive	78%	78%	100%

The unseated test results reveal several combinations of fastener material and adhesive that provide prevailing torque within specification for initial use and reuse with additional adhesive. This proves using adhesive to provide prevailing torque locking within specification is a viable option.

## Conclusions

This work assessed the use of anaerobic adhesive to provide a prevailing torque locking feature. Test procedures were developed for this assessment that can be used in practice to assess any fastener and adhesive combination and joint conditions. Tests were conducted with different threaded fastener materials and anaerobic adhesives in unseated assembly conditions. Initial use, reuse without additional adhesive, and reuse with additional adhesive cases were tested. A 48-hour cure time was used for all initial use and reuse tests.



Test data were presented as removal torque versus removal angle with required prevailing torque range per specification added for easy assessment. Percent pass rates for the various fastener material, anaerobic adhesive, and assembly condition combinations were tabulated.

The results of this work show:

1. Use of anaerobic adhesive as a prevailing torque locking feature is viable.
2. Not all possible fastener material and anaerobic adhesive combinations provide prevailing torque values within specification. However, any combination can be assessed using the test procedures developed.
3. Reuse without additional anaerobic adhesive generally provides some prevailing torque, and in some cases within specification. Note that a reuse test in this work follows complete disassembly, reassembly and 48-hour cure time regardless of whether additional adhesive is used.
4. Reuse with additional adhesive often provides comparable removal torque data as in initial use.

### **Acknowledgement**

The authors gratefully acknowledge the funding and support of the NASA Engineering and Safety Center (NESC) and Dr. Michael Dube for this work.

### **References**

1. NASM25027, *Nut, self-locking, 250°F, 450°F and 800°F*, National Aerospace Standard, 1999.
2. NASM8846, *Inserts, screw-thread, helical coil*, National Aerospace Standard, 1998.
3. MIL-I-45914A, *Insert, screw thread – locked in, key locked*, Department of Defense Military Specification, 1991.
4. MIL-I-45932/1C, *Insert, screw thread – thin wall, locked in*, Department of Defense Military Specification, 1994.
5. NAS3350, *Nuts, self-locking, 450°F and 800°F, high quality*, National Aerospace Standard, 2006.
6. MIL-DTL-18240F, *Fastener element, self-locking, threaded fastener - 250°F maximum*, Department of Defense Detail Specification, 1997.
7. Hunter, R, Hess, D, "Direct Verification of Threaded Fastener Locking Compounds and Adhesives," *Journal of Failure Analysis and Prevention*, 12 (2012), 724-729.
8. McManamen, J, "Orbiter Window Fastener Issue Summary," NASA SSP presentation, 2008.
9. Roberts, T, "Orbiter Window Installation Fasteners," United Space Alliance presentation, 2008.
10. Zimandy, A, Hess, D, "Effect of Re-use of Locknuts with Prevailing Torque Locking Feature," *Journal of Failure Analysis and Prevention* (featured paper), 13 (2013), 121-127.
11. Hernandez, A, *Use of Anaerobic Adhesive for Prevailing Torque Locking Feature on Threaded Product*, University of South Florida MS Thesis, 2015.

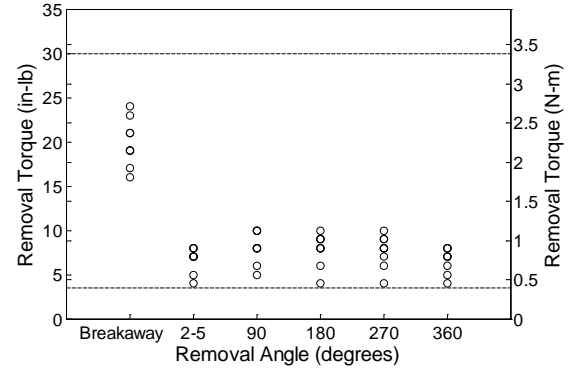
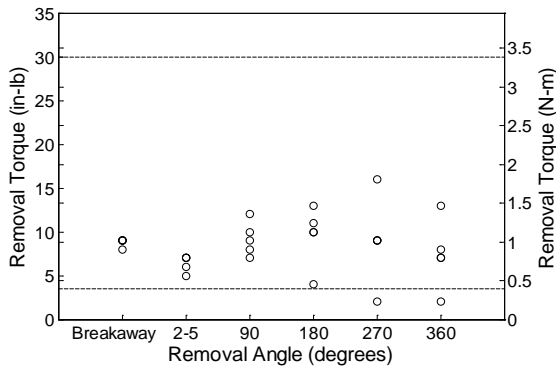
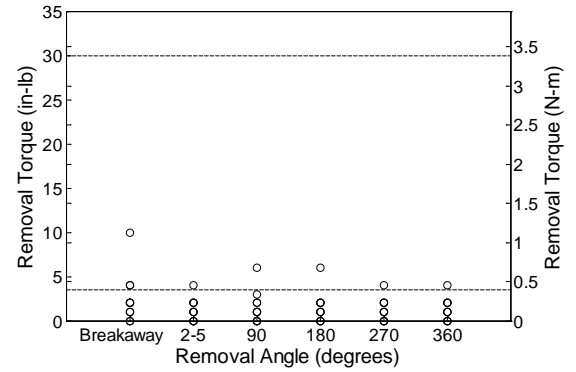
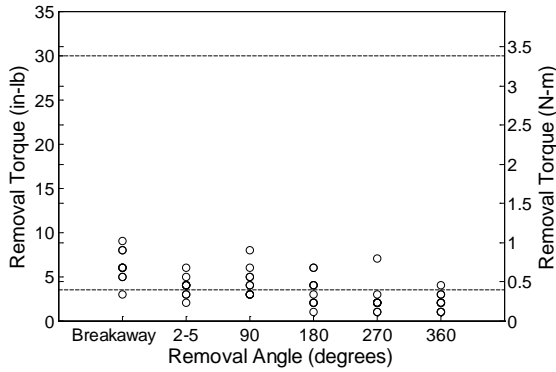
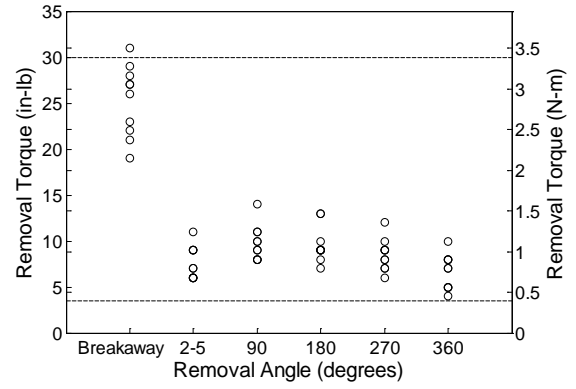
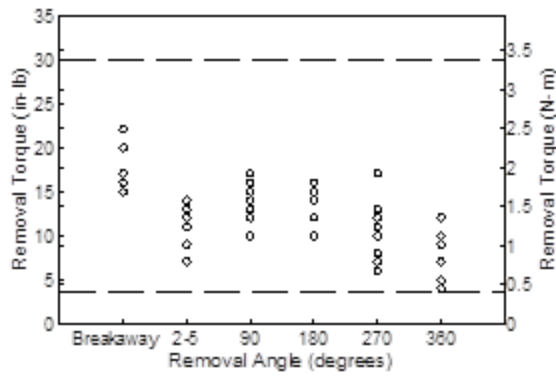


**Figure 1. Unseated plain grade 8 with Loctite 222MS: initial use, reuse without additional adhesive, and reuse with additional adhesive.**

**Figure 2. Unseated A-286 with Loctite 243: initial use, reuse without additional adhesive, and reuse with additional adhesive.**

# **A New Architecture for Absolute Optical Encoders**

Timothy Malcolm\*, John Beasley\* and Mike Jumper\*

## **Abstract**

BEI Precision Systems & Space has developed an encoder technology, nanoSeries, that can calibrate itself in-situ and correct most of the common causes of error in typical encoders. The new nanoSeries ARA design has detailed health and status readouts that can definitively indicate when a re-calibration is in order. The re-calibration process can be done on-orbit if desired. The units can accommodate either full revolutions or limited angle sweeps, and the principles are also applicable to linear encoders.

## **Introduction**

Optical encoders manufactured by BEI Precision Systems & Space (BEI) have been used in space since the earliest days of space flight. The combination of low weight and high resolution relative to electromagnetic resolvers made them an obvious choice for many applications. Optical encoders have typically been of only a few types.

The primary type of optical encoder selected for commercial and industrial applications has been the incremental encoder. This type of encoder requires a return to an index or home pulse to index a counter, which then counts the number of 'incremental' pulses or bits that pass by. This is a very simple and robust concept but it has some disadvantages for space, primarily that if power should go off or the counter upsets, even for a very short time, the encoder does not 'know' where it is until the system moves it back to the home position and it re-acquires the index pulse. A further concern with this type of encoder in space is that Single Event Effects can cause the number of recorded pulses to be in error, or cause a spurious index pulse to reset the counter, and the count will not be corrected until the index is reacquired. Other issues with this type of encoder are that the light source must remain turned on at all times, increasing the power consumption and limiting the lifetime of the source, and that the data rates for high resolution devices can be very high, often resulting in Electromagnetic Interference (EMI) issues.

A second type of encoder could be called pseudo-absolute or chain code. This type of encoder includes a set of tracks encoded with a non-repeating digital code, similar to an endless bar code, plus a set of incremental tracks for timing. This style of encoder does not need to return to zero to reset itself; instead it just needs to read a certain number of sequential bits to know where it is. This design mitigates some of the issues inherent in the typical incremental encoder. However, the Light-Emitting Diode (LED) still must remain on all the time. This sort of encoder has not been used much in space to date.

A third type of optical encoder is the absolute encoder. This style of encoder actually generates a discrete digital code for each of a number of discrete locations encoded on a code disk or scale, and these bits are read simultaneously. Thus, even if power flickers, the encoder recovers immediately and there is no need to return to a home position. Moreover in this type of encoder it is common to pulse the LED to take readings, which has the effect of maximizing the life of the encoder. Of course it is still possible for readings to be in error due to Single Event Effects, but for this type of encoder, the very next sample will correct the error. The simplest versions of this device directly encode the digital patterns on the code disk, but higher resolution types derive the digital data from sine and cosine patterns on the disk.

---

\* BEI Precision Systems & Space Company, Maumelle, AR

## nanoSeries Design

It is important when discussing the relative merits of these various encoding techniques to make a distinction between 'wide angle errors' and 'narrow angle errors', since they arise from different sources.

Wide Angle Error is a term used to encompass all of the low spatial frequency errors that arise as a result of optical pattern alignment to the axis of rotation, i.e., perpendicularity and concentricity, and the repeatable and non-repeatable runout of the spindle bearings. From a kinematic point of view, wide angle errors are those that result from translation of the code pattern relative to the readhead rather than pure rotation. None of the methods discussed above address these geometry-induced errors. Over the years, the primary method of mitigation for these wide angle errors has been the use of multiple read stations. Clearly the use of multiple read stations can cancel the most damaging harmonics of the error at the expense of increasing other less harmful error components. In extreme cases, some larger encoders have had 8, 12, or 16 readheads which dramatically reduce the effects of these geometric errors. As a specific example, consider an encoder with a Total Indicated Runout (TIR) of 2.54 micrometers ( $\mu\text{m}$ ). For a code disk with a radius of 50 mm, the peak once-per-turn error component due to spindle runout would be:

$$Error_{peak} = \tan^{-1}\left(\frac{TIR/2}{R_{Track}}\right) = \tan^{-1}\left(\frac{2.54 \cdot 10^{-6}/2}{50 \cdot 10^{-3}}\right) = 25.4 \mu\text{rad}$$

Adding a second read station located at  $\pi$  radians relative to the first station, properly calibrated, will reduce the error resulting from this particular harmonic to less than  $1.3 \mu\text{rad}$  (95% reduction typically). However, mechanical ball bearing errors are rarely purely sinusoidal. They usually contain many harmonics of the fundamental. In this example, if the twice-per-turn error is 10% of the fundamental (i.e.,  $2.5 \mu\text{rad}$ ), the addition of two readheads can actually double that particular component of the error to  $5.0 \mu\text{rad}$ , as well as doubling every other even harmonic of the error. Adding still more pairs of readheads will reduce other harmonics, at the expense of increasing the higher order residual errors. Clearly this solution to wide angle error is a diminishing returns game, as well as being a distinct cost adder, since each new readhead adds associated circuitry.

In recent times, with the advent of digital signal processors to encoders, it has been found that even without multiple read heads it is possible to remove many of these geometry-induced errors algorithmically. This can be accomplished by adding optical features which make it possible to discriminate which errors arise from wide angle causes and which from narrow angle causes. Since wide angle errors result from translations of the code pattern instead of the expected pure rotation, this change in approach allows mechanical repeatability to be 'finessed' into accuracy. However, it should be apparent that any sort of algorithmic correction can only be as repeatable as the hardware.

The multiple read station approach, although expensive in terms of hardware, is very fast and can usually remove 95+% of the wide angle errors for a high quality spindle. A software approach takes additional processing time, and generally removes somewhat less of the wide angle error. However, there is a large cost advantage to using the software approach. Moreover, as technology advances, the correction algorithms have become more capable, processing hardware is faster, and the disadvantages of the software approach are diminishing. In addition, the software approach does not prefer any harmonic relative to another. In the traditional multiple read head approach the harmonic doubling described above has sometimes resulted in exciting mechanism resonances with servo systems. That sort of problem is very unlikely with the software correction method.

As can be seen in Figure 1, the nanoSeries correction scheme reduces the large once-per-turn harmonic more than 99% while still not doubling the 2<sup>nd</sup> harmonic, and reducing higher order errors. The same raw curve compared to a typical two-head reduction scheme would have indeed reduced the once-per-turn, but the 2<sup>nd</sup> harmonic would have doubled. In this specific case, that would have doubled the residual error!

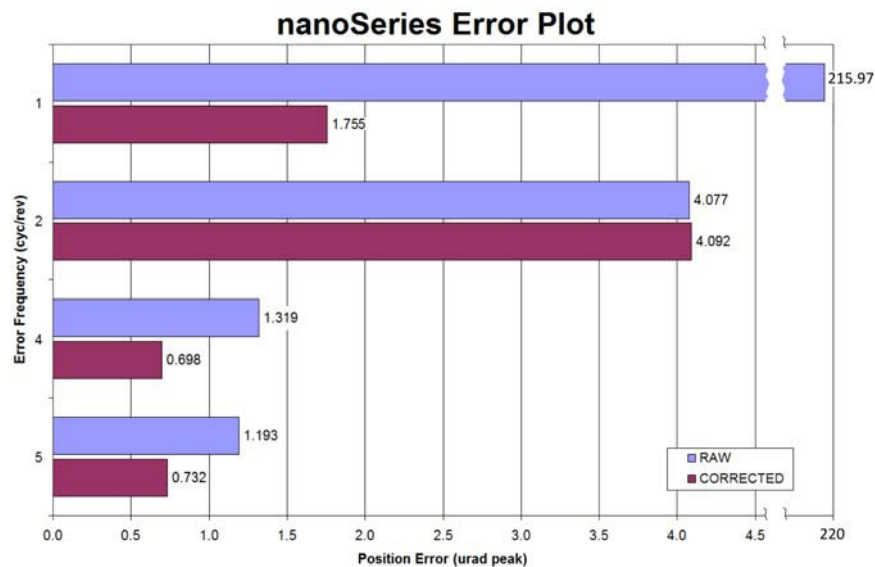


**Figure 1. NanoSeries Error Plot**

Narrow Angle Errors are those which arise from code pattern distortion, interpolation non-linearities, intermodulation, and other sources of noise. These errors are most common at the spatial frequencies of the higher order tiers of data. A few manufacturers have developed test equipment to quantify these harmonics at beginning of life. A properly designed encoder should be capable of measuring and eliminating most of these sorts of harmonics, assuming the mechanical system is robust and repeatable. Of course the patterns printed on the code disk must inherently have a high degree of consistency; otherwise the number of errors that can be removed is limited by the memory available. Modern high-resolution encoders very quickly can outrun the available memory, which is another reason why an algorithmic method of error correction is desirable. In addition, although a static memory map could be made to correct every bit to some ideal number, assuming that an accuracy tester was available, yet the resulting correction would generally not be stable with time, temperature, or life. In fact, the more precise the correction, the more likely it is that subsequent environmental shifts of the axis of rotation will 'break' it. In some cases this can result in much higher error than otherwise would have been observed.

All of these techniques have validity in some area of application. Ideally one would like the simplicity and cost of a single-tier incremental encoder with the resolution and reliability of the multi-tier absolute encoder, and of course all of this achieved in a very small, lightweight, and low power design. Perhaps surprisingly, these goals are all achieved to a large extent in modern space encoders such as the BEI ARA nanoSeries encoders. These absolute optical encoders use a multi-tier design with sine-cosine tracks at several different spatial frequencies to generate all of the code. To minimize the electronic failure rate and reduce the cost, BEI has developed a rad-hard front-end Application-Specific Integrated Circuit (ASIC) which performs all of the chores of managing the LED and photodiode array, and includes simultaneous analog-to-digital conversion of all of the code tracks. This digital data is transmitted to a remote processor in high-speed serial format which includes Error Detection and Correction codes for high reliability. All of the data transmission is done with Low Voltage Differential Signaling (LVDS) drivers and receivers to minimize EMI emission and susceptibility. The remote processor contains the required digital circuitry to correct, merge and assemble the final data words, coordinate multiple readheads (if used), and format and output the final data words to the customer.

All of the circuitry in the BEI Front-End ASIC is silicon gate CMOS, and is rad-hard to more than 100krad (Si). The ASIC also is Single Event Latchup hard (75 MeV-cm<sup>2</sup>/mg), and has a low Single Event Upset hit rate (2.4 x 10<sup>-14</sup> errors/bit-day). The circuitry is all based on switched capacitor CMOS design, so that any sort of upset or error that does occur will rapidly be flushed out. The switched capacitor transimpedance amplifiers

used to convert the small currents from the photodetectors to voltages have programmable gain and other parameters that allow them to be configured ideally for nearly any geometry or technology detector.

The analog-to-digital (A/D) converters in the ASIC are a proprietary design, and provide both fast response and improved DC fidelity for the signals as compared to conventional discrete A/D converters. Since the amplifiers are used primarily for sine-cosine signals that are intended to be ratiometrically compared, common voltage references are used for all of the A/D converters. This assures that the signals all continue to track over time, temperature, and common mode disturbances.

The ASIC also includes the LED pulsing circuitry which is fully selectable for current level, pulse width, repetition rate, and other parameters. Circuitry is also included for monitoring and controlling the LED current. In normal operation, an external transistor is used to switch the LED current, and a small external current sense resistor is also provided to allow for constant current drive. The current drive level is controlled using internal D/A devices to keep the light levels at the detectors at a constant level to end-of-life. Thus at beginning-of-life, the system is set up for robust operation under nominal conditions, and the current through the LED is then varied as required to keep the system margins in place in spite of variations in temperature, radiation, and ageing of components. This sort of scheme nearly doubles the useable life of the LED as it degrades. Moreover, since the LED is pulsed, there is a linear reduction of current-induced degradation of the LED proportional to the duty cycle, allowing very long on-orbit lifetime. The ASIC is procured to a government- controlled SMD at V-quality level which eliminates a lot of concerns about quality and reliability.

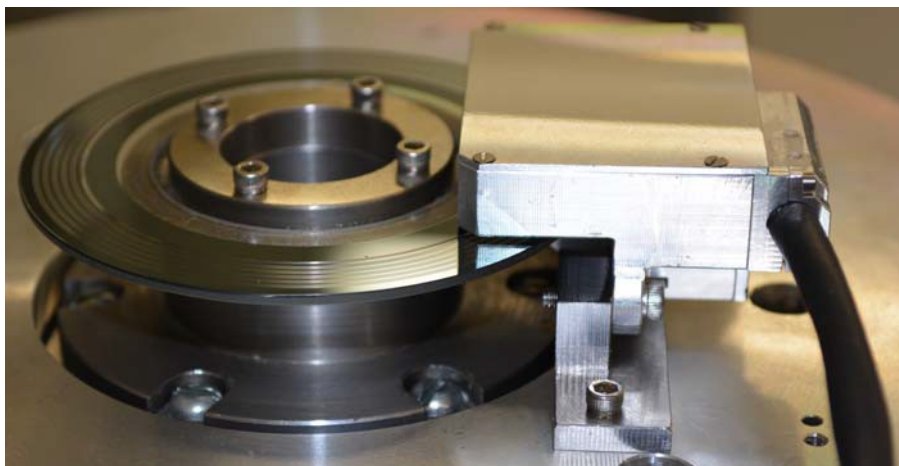


**Figure 2. ARA Space nanoSeries Encoder Readhead**

The new readhead mechanical design is shown in Figure 2. The small readhead (25 x 50 x 46 mm) contains the ASIC, the LED and driver transistor, the photodiode detector with a precision grating, and the optic to collimate and fold the light. The readhead and the code disk hub can be fabricated from titanium, aluminum or stainless steel, depending on the application. The precision code disk (chrome pattern printed on glass) is pre-mounted at the factory to the hub.

The readhead is powered from the remote electronics through a shielded cable with a MicroD connector. All of the signaling wires are using LVDS drivers and receivers and are twisted pairs for low EMI susceptibility and emission.

This design also requires a remote electronics assembly that can process data from 1 to 4 readheads. The small 125 x 125 x 40 mm remote box (not shown) or 3U size remote card (Figure 3) contains a powerful data processor implemented in a rad hard Field Programmable Gate Array with critical portions of the design implemented as a pipelined processor. This processor applies the mathematical algorithms that correct the encoder signals for optimal performance. The details of the algorithms are proprietary to BEI, but the end result is easily demonstrated using BEI test and diagnostic equipment. Research continues to improve the

correction algorithms still further. At some future date, a rad-hard digital ASIC will be obtained with the algorithms internally coded, improving the power consumption, performance, and hardness of the resulting systems.

The system is designed to be relatively straightforward to implement in a customer design. The readhead and code disk/hub are first mounted, usually with pinned or piloted interfaces. Usually it is not necessary to electrically or optically center the code disk. Then the system is connected and powered on and four relatively slow revolutions of the disk are made while the encoder measures the signals. For limited angle systems, such as Az-El gimbal systems often are, four sweeps of the arc to be used performs the same function. Exact rotational speed and/or speed stability are not critical for these sweeps. The preliminary data is then processed and the encoder is calibrated automatically. The processor also provides outputs that verify that the data streams are properly adjusted and merged into one contiguous data word. At this point, the encoder is placed in the normal operational mode and no further calibrations will normally be required. The software corrects for most alignment issues, as well as future component degradation issues on earth or in orbit, including degradation of components with radiation, temperature shifts and most other common issues.

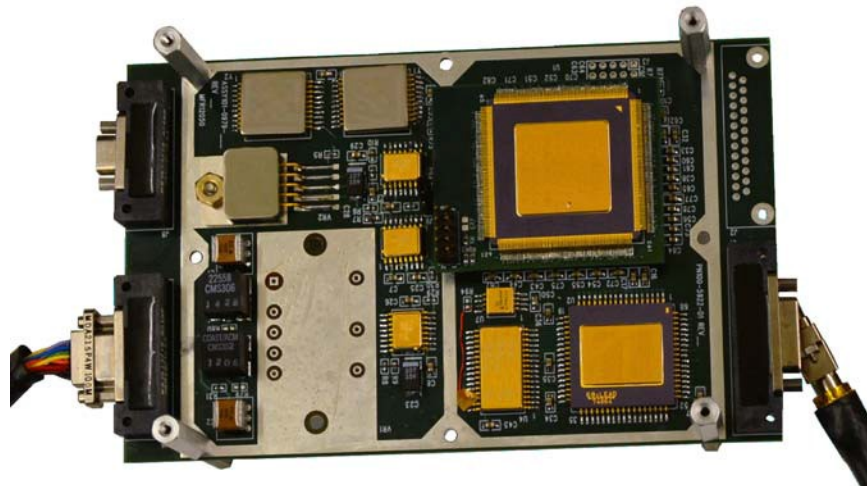


**Figure 3. ARA Space nanoSeries Remote 3U Electronics Card**

The encoder can be queried at any time to verify proper operational margins. The encoder can even be recalibrated on-orbit if required to compensate for unexpected degradation due to either natural or strategic environments.

The standard customer interface to the remote card or assembly is by means of a synchronous serial protocol in which the customer supplies a strobe to initiate a reading and a data clock to shift data out. The primary reason for this non-standard protocol, instead of the more common Synchronous Serial Interface with no strobe, is that many servo systems are sensitive to the delay from the time position data is actually captured to time of receipt of data. A second consideration is that the LED primarily degrades only when current is flowing through it, so reducing the strobe rate to a minimum, consistent with system objectives, is a very good design practice. The standard design also provides a shift clock from the encoder at the same frequency as the clock provided by the customer. In systems with long cable runs or other delays, this provision assures robust capture of the serial data by the customer electronics, even with lengthy cable runs.

There are many advantages to the BEI ARA nanoSeries approach. First is that since most encoders will be very similar in basic design there is a lot of commonality of design and analysis, minimizing the program-specific engineering work required. Second, this design has a minimal number of integrated circuits, none of which are likely to become obsolete. Third is that critical parts like LEDs, photodiode arrays, and ASICs are stocked at BEI to minimize lead time.

The BEI ARA nanoSeries encoders have demonstrated resolutions up to 25 bits and absolute position accuracy less than 5  $\mu$ rad rms over a full revolution at data rates of up to 8 kHz. The power dissipation for the readhead at that rate is just 0.6 watt, while the remote electronics will consume about 3.0 watts with a 5-volt supply and a single readhead, and a little more if the 24-volt option is used. The remote electronics has been designed to handle up to four readheads with no reduction.

BEI can also supply engineering prototype units. Our AIME nanoSeries encoders are industrial temp range encoders that mimic the readhead size of the ARA nanoSeries encoders. These much less expensive units are form, fit and function equivalent to the ARA space encoder readheads, even to using the same test box design. The AIME encoders do not require a remote electronics assembly however, since the complete electronics package can be fit inside the space of the ARA readhead envelope. This allows for cost-effective prototypes and risk reduction units to make system checkout much easier and with much higher fidelity. The AIME encoders are not rad-hard, but are a logical choice for any application that is less demanding. The same code disk sizes and hub/readhead materials are used for both designs.

It is important to know how well a kit encoder is mounted and calibrated and the effects of spindle runout and environments on the encoder during operation. Standard interface and test boxes are available for power, communications and evaluation of the health/status of the ARA and AIME encoders. These test boxes provide the ability to command auto-calibration, normal operation, set output parameters, and evaluate and view in real time the quality and status of each tier of position information and the alignment of all other position tiers internal to the encoder. This information is output in part through health and status bits with each position output word and is valuable in determining if and when re-calibration in-situ may be needed. In-situ calibration can compensate for changes in gravitational loads, component drifts and degradation due to extreme environmental conditions such as radiation, although generally adjustments will not be necessary. The test box software is written in LabVIEW and can support position reporting, analysis, control, and data logging.

For the future, it should be clear that the new ARA nanoSeries space encoder has the potential to dramatically improve performance of space systems, especially when paired with a servo system designed by BEI. BEI has primarily been involved in precision servo systems for only the most demanding applications, such as the pointing systems in the Hubble Space Telescope, or for the Microwave Limb Sounder, one of four instruments on the NASA's EOS AURA satellite. Today's space systems are smaller, lighter, and higher performance than in the past, and BEI can bring our experience in designing space systems to assist you in meeting and exceeding your most stringent program performance requirements.



## Digital Image Correlation for Performance Monitoring

Miguel Palaviccini\*, Dan Turner\* and Michael Herzberg\*\*

### Abstract

Evaluating the health of a mechanism requires more than just a binary evaluation of whether an operation was completed. It requires analyzing more comprehensive, full-field data. Health monitoring is a process of non-destructively identifying characteristics that indicate the fitness of an engineered component. In order to monitor unit health in a production setting, an automated test system must be created to capture the motion of mechanism parts in a real-time and non-intrusive manner. One way to accomplish this is by using high-speed video and Digital Image Correlation (DIC). In this approach, individual frames of the video are analyzed to track the motion of mechanism components. The derived performance metrics allow for state-of-health monitoring and improved fidelity of mechanism modeling. The results are in-situ state-of-health identification and performance prediction. This paper introduces basic concepts of this test method, and discusses two main themes: the use of laser marking to add fiducial patterns to mechanism components, and new software developed to track objects with complex shapes, even as they move behind obstructions. Finally, the implementation of these tests into an automated tester is discussed.

### Introduction

The underlying premise of component health monitoring is to characterize the baseline performance of a unit, allowing for future tests to help identify any mechanical damage caused by environmental loading, as well as future performance of the component as that damage accumulates. In a production setting, the monitoring must be done in quasi real-time, with an automated system that is able to diagnose component fidelity with minimal to no human interaction. The current application focuses on using optical measurements coupled with digital image correlation (DIC) for health monitoring, as opposed to wave propagation, thermal, or other measurement variables that could also be indicative of component health.

The basic process and nomenclature of DIC is given in Ref 1. Displacements are determined by comparing an image of the deformed object to a reference image. Traditionally a square subset is used as the template to match between the reference and deformed image. In most cases, fiducials (the contrast of light and dark within the image) must be applied to the object of interest in a random fashion. The set of fiducials on any given part is often referred to as the speckle pattern.

Square subsets, while mathematically simple, can be challenging to fit onto irregularly shaped mechanism components. Conformal subsets, on the other hand, enable the entirety of the object being tracked to be included in the subset, increasing the information available for tracking and thus increasing accuracy. As a bonus, conformal subsets also enhance the tracking of objects that are partially obscured. This paper briefly discusses the advantages of the newly developed DIC code by Sandia National Laboratories, and how it is currently being used to help extract state of health information from components.

For traditional DIC applications, these random fiducial patterns are often applied using a light dusting of spray paint to the product. In mechanisms work, this can be problematic. When marking a mechanism that is to be fielded, any method that adds organic material or moisture, or alters the shape and mass of the component should be avoided. Additionally, the paint method provides poor control of speckle size

---

\* Sandia National Laboratories, Albuquerque, NM

\*\* National Security Campus, Kansas City, MO

and placement. This paper discusses advances in laser marking techniques, along with material testing on those laser marks, as an alternate solution for adding fiducials on the components to be tracked.

To summarize, traditional DIC methods rely on random contrast fiducials that are either already available on the tracked component or produced by primitive means. For mechanisms, a highly repeatable process consisting of laser marking has been developed. Furthermore, the complex geometry of the mechanisms drove the development of an algorithm that implements conformal type subsets, allowing the tracking of partially obscured objects.

### **DIC for Mechanisms Testing**

DIC, in general, has become a popular means of determining full-field displacements from digital images. While it has also become a vital component in material characterization applications that use full-field information as part of a parameter inversion process, the main usage in mechanism testing is rigid body motion. One commercial package for DIC applications is VIC-2D, from Correlated Solutions. Analyzing motion in VIC-2D begins by defining a square subset with an odd number of pixels. The central pixel is the point of interest, and the surrounding pixels are used as information to help identify the point of interest in the subsequent video frames. This off-the-shelf DIC algorithm operates using the Lucas-Kanade method as a basis. With this, there are underlying challenges for most mechanism testing applications:

1. The image subset must have changes in intensity values in each potential axis of motion. With high-precision mechanisms components, striations from machining are often so fine as to be below the resolution of a high-speed video camera system. This is problematic, as a subset of flat color could move indeterminately within a larger area. Thus, in order to reliably track a component, intensity information must be added to the surface.
2. The second challenge is that motion of the subset must be small between frames – less than a pixel. VIC-2D interpolates the intensity information within the subset by 10x, in order to provide higher positional accuracy. The result is that movements less than 1/10th of a pixel are ideal. This dictates the minimum frame rate for video recording, and helps set camera resolution. For a regularly repeated test in a production setting, increases in frame rate and resolution increase computation time for the DIC process and storage space necessary for the resulting videos.
3. The third challenge is that a subset has a minimum size for effectiveness (about 9x9 pixels), and must be square. The minimum size requirement helps set the required camera resolution and lens, as the smallest tracked component must be capable of containing at least a 9x9 pixel square. With finer resolution, subset size can increase, but the subset must fit on the component. Thus resolution limits the total amount of information available for correlation.

In an effort to help resolve some of the above deficiencies, the tester scope was expanded to include the development of repeatable fiducials applied via laser marking, as well as the implementation of a Sandia-developed DIC software known as DICE.

#### Laser Marking

After an evaluation of potential methods of speckle application, laser marking was selected based on its existing use in the mechanism and low risk of creating debris or residue. Laser marking is, however, not without its concerns. The most obvious is the potential for etching or ablation of material. To address this concern, laser settings were developed in an attempt to minimize dimensional disruption of the surface. The settings must account for part material, but also for part geometry, as heat conductivity becomes more evident in parts at miniature size scales. Avoiding surface melting or ablation is a matter of keeping instantaneous power delivered to the part below a certain threshold. There are many variables involved, but a general approach is to use a defocused beam, increasing the area over which the energy is distributed.

Further discussion requires some understanding of how lasers mark stainless steel. The heating of the surface in an oxygenated environment causes growth in the chromium oxide layer. The oxide layer is naturally transparent, but as its thickness increases, thin film effects begin to occur, and color develops. Thick enough layers absorb much of the light passing through, and appear black.

Even if no material is removed, material properties could change. The oxide layer (the bright white layer on the cross section in Figure 1) essentially behaves like a ceramic, with substantially reduced ductility compared to the surrounding metal. More critically, the laser could heat the underlying material sufficiently to alter or remove heat-treating effects in the bulk of the material. In fact, this laser marking method that avoids etching or ablation is often called ‘anneal marking’ or ‘anneal mode’. Computer simulations predicted minimal change to part properties outside of the marked area. Metallurgical samples show an annealed zone beneath the oxide layer in the range of 1.8-2.5  $\mu\text{m}$ . This is a substantial improvement from initial marking settings, which annealed up to nine times as deep. However, as a precaution, surfaces which contact other parts of the mechanism should be shielded from the laser beam to maintain material integrity. Extensive testing has been performed with marked parts without showing adverse effects.

The second concern stems from the thin film nature of the marking. Thin films are viewing-angle dependent, and can change color and contrast depending on camera and lighting angle. Laser settings that generate surface melt can also create diffraction gratings depending on line spacing. To mitigate these concerns, settings target dark gray to black marks with close line spacing and high spot overlap. Laser vendors do not generally provide all the information needed to calculate settings appropriate for a desired result, so some experimentation is necessary for optimizing settings, particularly when dealing with miniature components.

Regardless of marking method, speckle patterns must take into account the tracking algorithm and camera setup that will be used, and should be optimized to provide the best chances of success.

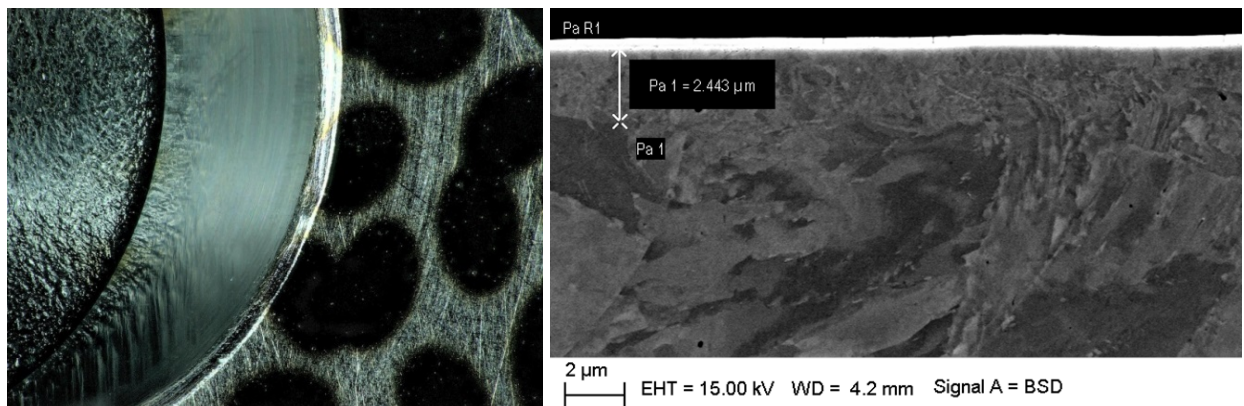


**Figure 1. An example of laser marked surface (left) and a cross-section (right).**

#### Pattern Design

Gradient-based DIC algorithms (like the one used in VIC-2D) perform optimally for speckles with ‘soft’ edges that gradually blend into the background, rather than images with sharp contrast edges which introduce high frequency content in the image. To assist with this, most gradient methods will interpolate pixel values to smooth out transitions or use an image filter. As a result, the pattern must be sized to prevent aliasing. Standard rules-of-thumb have been developed that relate the speckle to pixel size.

For X-Y motion with rotation, speckle should be at least  $2 \cdot 2^{1/2}$  pixels in each dimension. Speckles larger than this size by at least one interpolation step would provide a wider peak, which is preferred. The maximum speckle size is limited by the region of interest (ROI) size. Ignoring strain, for minimum-size

round speckles as above, an ROI would need at least three speckles to be fully constrained. By adding extra dimensions to speckles, it is possible to reduce the number needed to constrain an ROI. For this reason, we use ovals, or clusters of ovals, as the basic shapes for our speckle pattern. A single oval in an ROI limits it to one of two angular orientations. Local solving methods, with frame rates appropriately matched to device motion, should be capable of successfully tracking such an ROI. Global methods (such as DICE, discussed below), or test environments with insufficient framerates, may have more trouble and require more constraint.

This leads to perhaps the ultimate consideration of speckle design, which is the aperture problem. An ROI must be uniquely identifiable within the search area of the algorithm. This implies that it should be non-repetitive over that area. This was accomplished by designing a pattern that extends beyond the intended area of the region of interest. Non-repetition was verified by subjecting it to correlation tests against translated versions of itself.

For certain miniature mechanism components with complex shapes, pattern optimization was not enough to enable robust, automated tracking, and thus drove the development and incorporation of DICE for this purpose.

#### Benefits of DICE as the proposed tracking algorithm

The first and most substantial improvement is that subsets in DICE can be of arbitrary shape. In our application, with irregularly (non-square) regions of interest, this allows the use of more of a component's surface for matching. Conformal subsets are subsets with geometries that correspond to the outline of a particular part or region, therefore including more fiducials/speckles than traditional square subsets. An example of a conformal subset vs. a traditional square subset is shown in Figure 2. This results in an improvement in accuracy since more information is available within each conformal subset. As a bonus, this also enables the tracking of objects that are partially obscured, since even if part of a conformal subset leaves the field of view or becomes blocked by another object, there remains enough pixel information in the subset to successfully correlate.

Note that in Figure 2 it would be possible to place the markings and subsets in such a way that they fall completely within the boundary of the object of interest. If attempting to do that with a traditional square subset, the result would be either a smaller subset (yielding less information to correlate resulting in lower accuracy) or a subset that extends beyond the boundary (leading to possible de-correlation and erroneous tracking).

A second benefit to employing the algorithms in DICE is the ability to use simplex (as opposed to gradient) optimization, providing improved performance in low contrast images. However, this change in matching methods means that patterns optimized for the gradient approach of software like VIC-2D, with as many speckle edges as possible, do not perform as well in the DICE simplex method, which prefers larger areas of constant color. The lack of gradient dependence makes the simplex method useful for data sets that are impossible to analyze with the traditional Lucas-Kanade type algorithms; for example, objects without speckles, images with low contrast, and small subset size. However, the robustness comes at a cost – a substantial increase in processing time when compared to VIC-2D.

The following examples demonstrate the applicability of conformal subsets and illustrate their advantages.

#### Example 1: Synthetic rotation of an oddly shaped object of interest

In this example, an image data set is constructed using a synthetic sequence of images so that the exact solution is known and the error of various methods can be computed. A reference image is synthetically rotated through an angle of 10 degrees. This motion is then tracked using both square subsets and a conformal subset. The synthetic image, subsets, and results are shown in Figure 2. The magenta and green curves show the rotation error for the square subsets vs. the blue line, which shows the conformal subset results. In some cases, for example at a rotation of two degrees, the error in the square subsets is

an order of magnitude higher than the conformal subset. Clearly, the accuracy of the correlation is greatly increased for the conformal subset.

#### Example 2: Partially obscured subsets

In this example, an obstruction is introduced into the data set that blocks a portion of the field of view, as shown in Figure 3. The obstruction is created by removing a strip of each image in the sequence. Results comparing the obstructed subset to the unobstructed results are also shown. The max difference between the two tracked cases is 0.5 degree, which occurs in the frame where the pawl velocity is the highest. In this case, where tracking is performed with DICe, the obstruction can be masked off and the two sections of the pawl are linked together as a single subset, leading to adequate trackable area. Note that performing this correlation using square subsets is not possible because too much of the subset becomes obstructed leading to de-correlation.

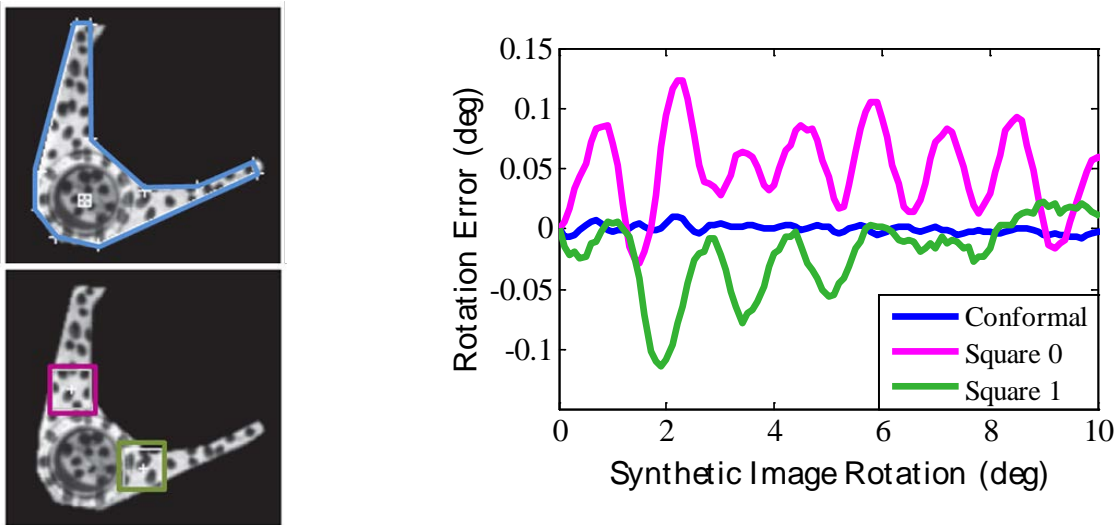


**Figure 2. Synthetic image rotation used to illustrate accuracy difference between conformal and square subsets.**

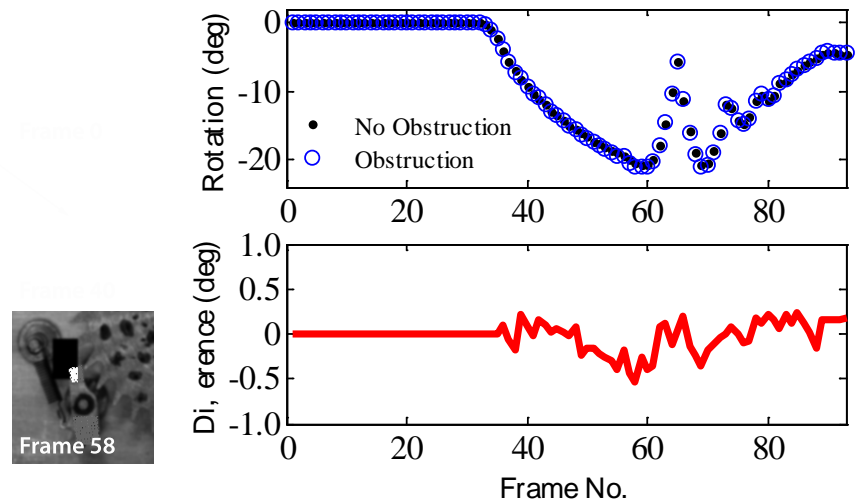


**Figure 3. Rotation error computer for the synthetically generated data set using a conformal subset comparing the unobstructed and obstructed cases**

#### Implementation into an automated tester environment

As previously mentioned, to monitor unit health in a production setting, an automated test system must be created. A system was developed to capture a video of a mechanism in operation, process the video to extract two-dimensional motion information and report results in an automated manner. This provides a statement of health prediction with a high confidence level. An implementation of the system has been in operation for several years undergoing development, and the lessons learned are currently being implemented into a qualified tester.

The tester has four main components. The first is a high speed video camera. For this application, a Phantom v1210 from Vision Research along with a Canon 100-mm f/2.8 macro lens allowed for maximizing field of view within a compact space. Note that camera and lens selection are dependent on mechanism size and motion rate. The second component is a lighting system. As with most vision solutions, the idea is to obtain as much light as possible without casting harsh shadows or creating glare off the surface of the tracked parts. The third component is a signal generator for providing the mechanism drive signals and test start trigger. Finally, a PC to allow sequencing of the test steps and for use to analyze the data as the test is run. The initial test setup was coded in LabVIEW, calling MATLAB scripts for data analysis. To speed execution and reduce maintenance, the code is now in procedural languages.

The basic order of operations is to activate the camera with a rolling frame buffer, feeding it the appropriate resolution, framerate, and exposure settings. The mechanism is then operated, with a trigger signal sent to the camera to begin saving data at the same time the mechanism receives its first drive signal. After the unit is operated, and the video has been captured, the frames are moved from the camera to the data storage folder on the computer. The computer then calls the analysis script, which feeds the video frames and predefined regions of interest to the tracking algorithm. The algorithm outputs 2-D position coordinates and angle for each ROI during each frame. These traces are then analyzed to extract time and duration of various events in the mechanism.

#### **Conclusions and Future Work**

In summary, this paper describes and improved method for analyzing mechanism performance and provides lessons learned when applying DIC to extract useful state of health metrics from components. Specifically, the paper outlines robust and repeatable methods of marking fiducials on parts of interest as well as newly developed ways of extracting information from moving parts using conformal subsets.

Laser marking allows fiducials of controlled dimensions to be added to miniature components, but presents challenges in tailoring settings to part material and shape. Laser marks are conformal for limited strain environments, and do not involve the addition of organics, moisture, or potential conductive debris required for most other conformal marking methods. Further minimizing part heating and developing patterns for low-contrast environments are ongoing topics.

As shown through examples, conformal subsets can be helpful if the tracked object is non-square by allowing more speckles to be included in the correlation. There are also a number of features for conformal subsets that are useful for trajectory tracking. For example, there are ways to enable tracking objects that cross each other's path or become partially obscured by another object. Conformal subsets can also be evolved through an image sequence to build up the intensity profile if the object is not fully visible at the start of a sequence.

With the conformal subset advantages, a price is often paid with regards to computation speed. The simplex solver method in DICe is less efficient, leading to an increase in processing time when compared to gradient-based methods. To combat this weakness, DICe has made several advances to improve parallelization and improving the performance of the simplex method. Methods of in-situ switching between fast optimization methods and more robust ones are also under development.

## References

1. Sutton, M. A., Orteu, J. J., & Schreier, H. (2009). *Image Correlation for Shape, Motion and Deformation Measurements: Basic Concepts, Theory and Applications*. New York, USA: Springer.





# Deployment System for Three Axis CubeSat Electric Field Instrument

Dana Turse\*, Larry Adams\* and Chris Esser\*

## Abstract

To address Heliophysics scientific objectives, CTD is currently developing the deployment system for the CubeSat Electric Field Instrument (CEFI), a 3D vector electric field instrument that can be accommodated on a CubeSat. CEFI is enabled by CTD's deployable composite boom technology that provides lightweight, stiff, straight, thermally stable booms capable of being stowed within a CubeSat form factor. The boom technology will also provide the CubeSat community with the capability to include one or more deployable booms with lengths greater than 5 meters for future CubeSat missions. CTD recently demonstrated this technology through the fabrication and testing of prototypes.

## Introduction

Our present understanding of magnetosphere-ionosphere coupling is limited, partly due to the lack of broad statistical observations of the 3-dimensional (3D) electric field in the altitude region between 300 and 1000 km. This understanding is of national importance not only because of its intrinsic scientific worth, but also because it is a necessary step toward developing the ability to measure and forecast the "space weather" that affects modern technology. Observations from different altitudes and from different magnetospheric activity levels are required to differentiate between spatial and temporal variability. Therefore, the availability of multi-point 3D electric field measurements in this region would greatly improve our understanding of how energy flows and dissipates in the ionosphere.

The high cost of space access and short satellite lifetimes at low altitudes make traditional satellites uneconomical for performing these measurements. Therefore, it is desirable to develop smaller and lower-cost sensor/satellite systems, such as CubeSats, so that the largest possible number of distributed measurements can be economically made in this region. These science objectives can be met using multiple CubeSats in Low Earth Orbit if they each include 3-axis electric field instruments. Therefore, CTD is developing the CubeSat Electric Field Instrument (CEFI), a 3D vector electric field instrument that can be accommodated in less than half of a 6U (10x20x30 cm) CubeSat. This instrument is enabled by CTD's game changing deployable composite boom technology that provides lightweight, stiff, straight, thermally stable booms capable of being stowed within a CubeSat form factor. This technology will also provide the CubeSat community with the capability to include one or more deployable booms with lengths greater than 5 meters for future CubeSat missions.

## CEFI Overview

CEFI will be a 3-axis electric field instrument with six rigid booms packaged into half the volume of a 6U CubeSat. The rigidity of the booms is a key characteristic that enables the instrument to be integrated on a 3-axis stabilized CubeSat platform. A notional 6U spacecraft is shown in Figure 1 with the instrument in both the stowed and deployed configurations. The instrument consists of the internal electronics and six spherical sensors mounted on long rigid graphite composite booms. The opposing sensors can be used to form three orthogonal dipoles or be measured individually depending on the instrument measurement mode. The booms are baselined at 2.5-m long, forming a dipole length of 5 m.

---

\* Composite Technology Development, Inc., Lafayette, CO

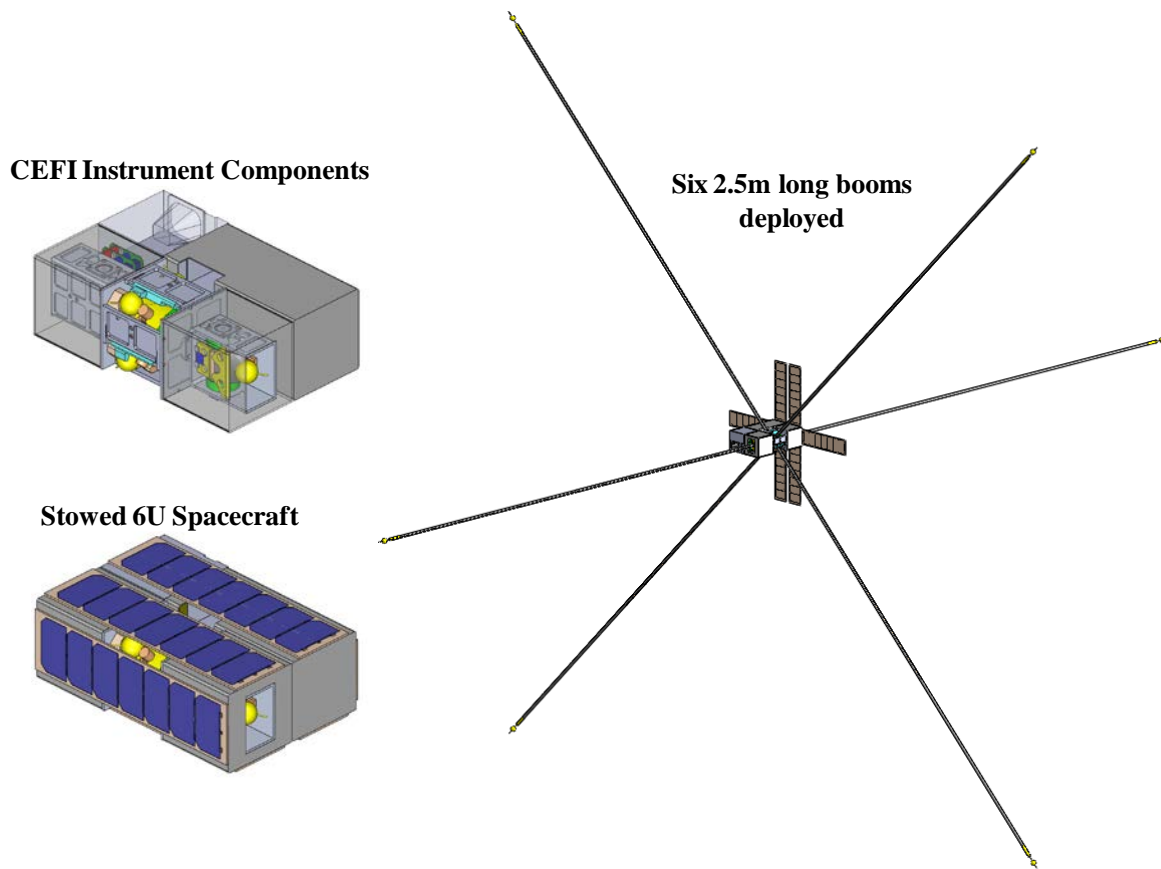


**Figure 1. Notional Spacecraft Incorporating CEFI in Stowed and Deployed Configurations**

This innovative boom system will use three separate mechanisms. The central mechanism will have four booms and sensors wrapped around a single hub (see Figure 2). These four booms deploy 45° to the sides of the spacecraft in a single plane. The remaining two booms deploy from individual mechanisms on each end of the 3U volume. The central four-boom mechanism and the single-boom mechanisms are shown in Figure 2. All six graphite composite booms and their tip sensors will be identical.

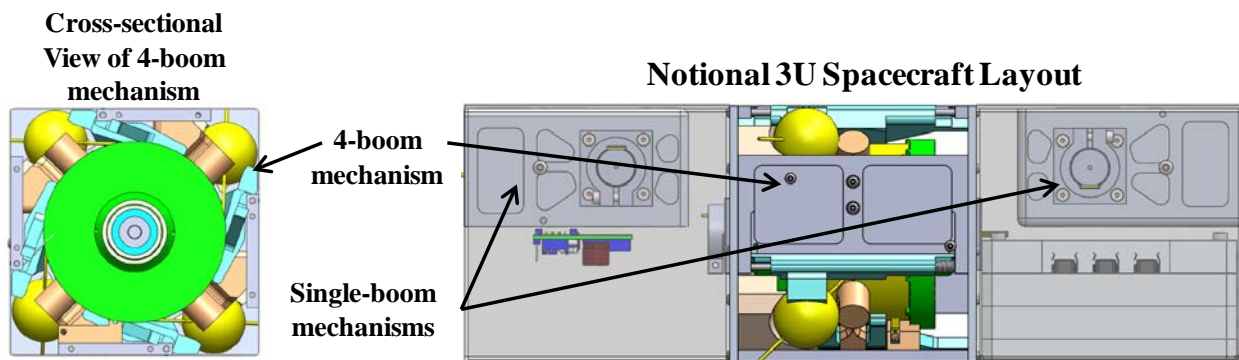


**Figure 2. Notional 3U Instrument Layout**

#### Carbon Fiber Reinforced Composite Booms

The baseline booms are 2.5-m long with a diameter of 1.27 cm (0.5"). Manufactured from graphite composite, these booms are extremely lightweight, stiff and thermally stable. Instrument pointing stability is a key requirement. It is estimated that stability needs to be within 0.1° between orthogonal pairs. The

boom stiffness and thermal stability will enable this requirement to be met. In particular, the booms must have significantly more deployed stiffness than typical CubeSat appendages, such as carpenter's tape springs or conventional slit-tube beams.

One of the main reasons that CTD is capable of providing such a stable sensor platform is the patented Slit-Lock™ technology. Traditional slit-tube booms have low torsional stiffness, as well as reduced bending stiffness and stability due to shear compliance at the seam. To address these issues, CTD has developed Slit-Lock™ technology (US Patent #8863369), which involves the locking of edge features, such as those pictured in Figure 3, as the boom deploys. By locking the edges, the slit-tube attains near closed-section properties, drastically improving stability in both bending and torsion.

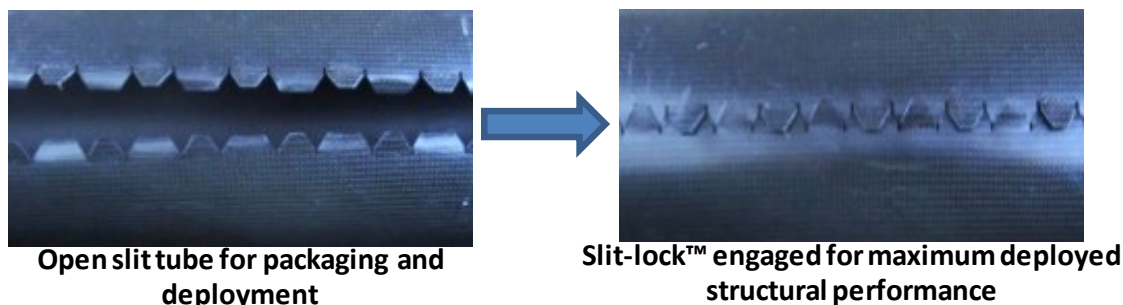


**Figure 3. Slit-Lock™ Technology Used to Improve Boom Structural Performance**

Furthermore, Slit-Lock™ edge features are aligned when the boom is stowed, allowing them to be engaged to keys on the end caps of the spool (see Figure 4). The slot and key engagement guarantees that the boom will spool and unspool at precisely the same rate every time. The engagement also allows much higher forces to be driven from the spool into the boom as it deploys, which increases margin of safety on deployment torque.



**Figure 4. Aligned Slit-Lock™ Edge Features and Matching Keys on End Caps of Stowage Spool**

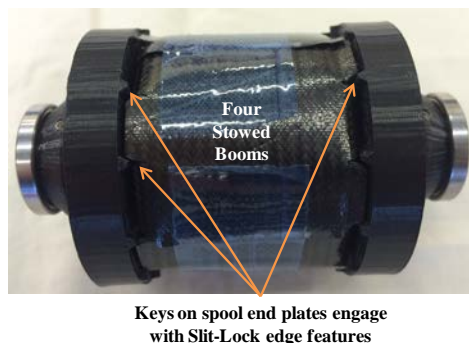


**Figure 5. Keyed Slit-Lock™ Edge Features**

The boom's thermal stability also has a significant effect on the instrument's performance. Solar flux along the boom can result in a temperature gradient across the cross-section of the boom. This is typically problematic for deployable spacecraft appendages, since this gradient can result in significant "thermal bending". Fortunately, graphite composite booms can be designed so that the laminate has a near-zero CTE, which enables pointing accuracy to be maintained despite potentially large on-orbit thermal gradients. The baseline booms developed for CEFI are estimated to experience less than a  $0.1^\circ$  pointing shift as a result of thermal bending.

#### Root-Lock™

CTD's CubeSat boom technology further enhances stability by enabling the boom to regain its full cross-section at the end of deployment, as illustrated in Figure 6. This is referred to as "Root-Lock" (patent pending). This root closure provides for high root stiffness and strength, which is particularly important for maintaining the pointing accuracy of a very long and narrow boom. Typical slit-tube booms have a "transition zone" where the boom transitions from flat (on the spool) to curved, and the cross-section is never able to fully recover, leaving the boom with reduced properties at the root. Spacecraft maneuvers can therefore result in significant bending at the root. In CTD's baseline design, the boom is able to transition off of the spool and clamp down around a root plug, providing the maximum amount of root stiffness to the structure (see Figure 6).

#### **During Stowage/Deployment**

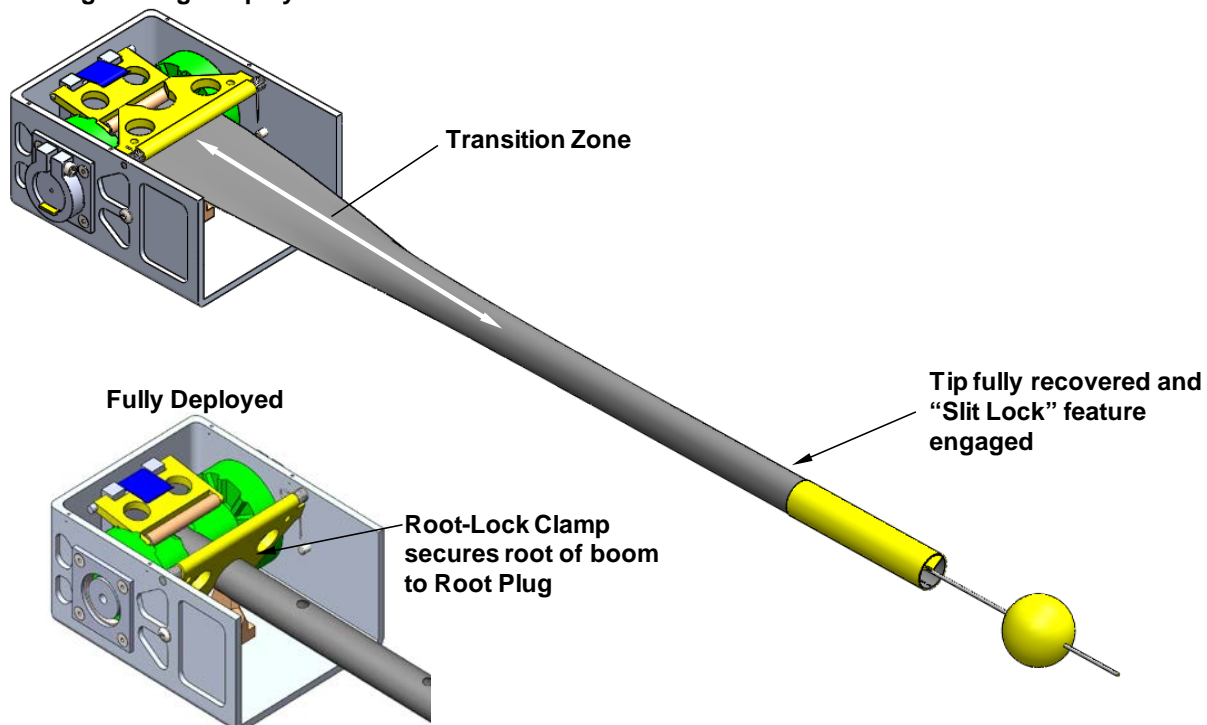


**Figure 6. Root-Lock™ enables boom to regain cross-section at end of deployment, drastically improving root strength and stiffness.**

#### Actuation, Positional Feedback, and Deployment Verification

The baseline design involves driving out the booms with a small motor that is efficiently integrated within the stowage spool of each unit. CTD has demonstrated the use of both stepper and DC motors (brushed and brushless), depending on application requirements. For this application, we have selected a brushed DC motor with a 141:1 gear head and attached encoder. This motor consumes less than 5 W while running at 12 V. Deployment time is expected to be less than 5 minutes, but can be tailored to be faster or slower depending on the application requirements. The motor measures 16 mm in diameter, 45 mm in

length and weighs less than 45 g total (motor, gear head and encoder combined). The attached encoder provides precise positional feedback and deployment verification.

### **Fabrication and Demonstration of Prototypes**

Under NASA funding, CTD recently manufactured and demonstrated prototypes of both the single-boom and quad-boom mechanisms, shown in Figure 7 and Figure 8, respectively. These booms are 1.5-m long and 12.7-mm (0.5-in) diameter. Both mechanisms incorporate Slit-Lock™ and Root-Lock™. These mechanisms have been stowed and deployed several times without failure or anomalous behavior.

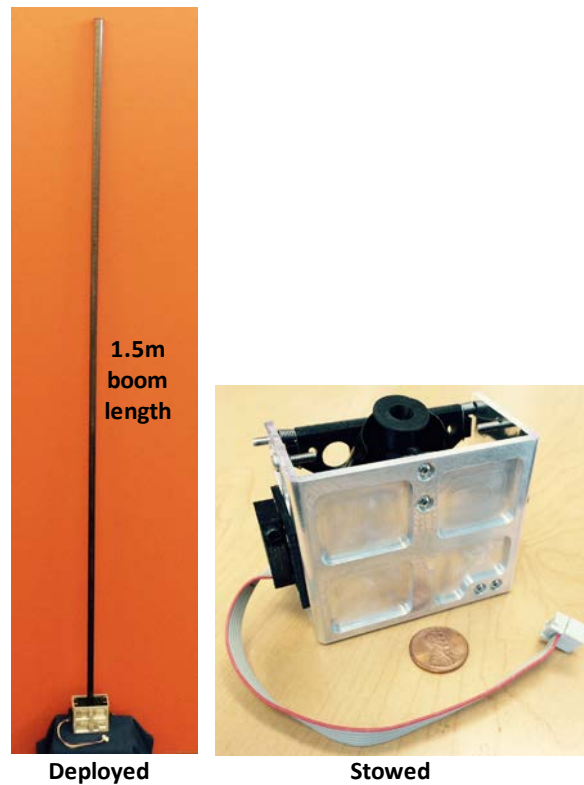


**Figure 7. Single-boom Prototype**

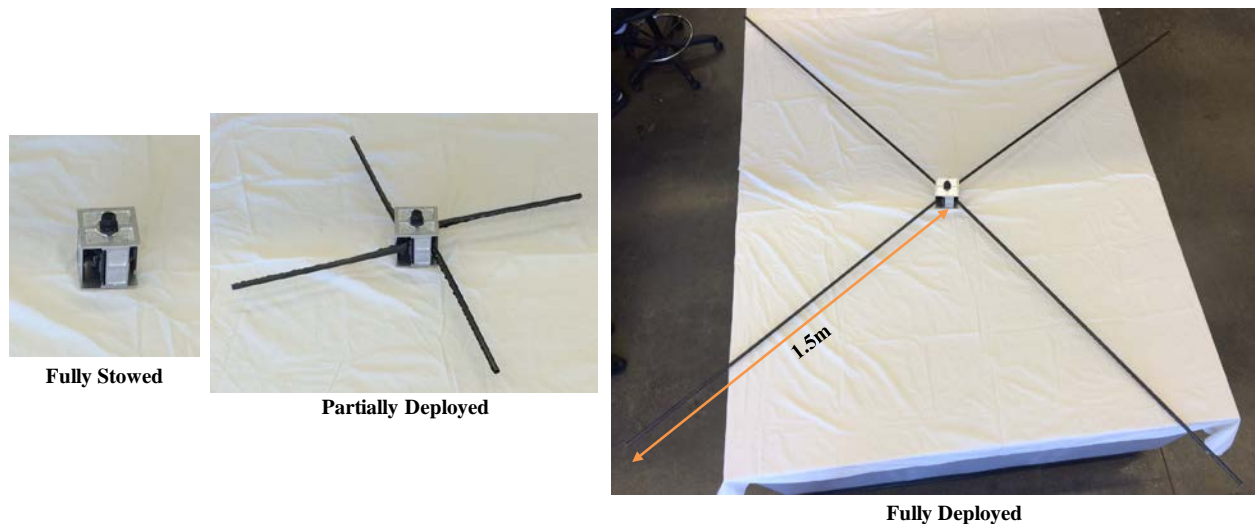


**Figure 8. Quad-boom Prototype**

Both meet the form factor requirement for the CubeSat instrument. Stowed dimensions for each unit are presented in Figure 9 and Figure 10.

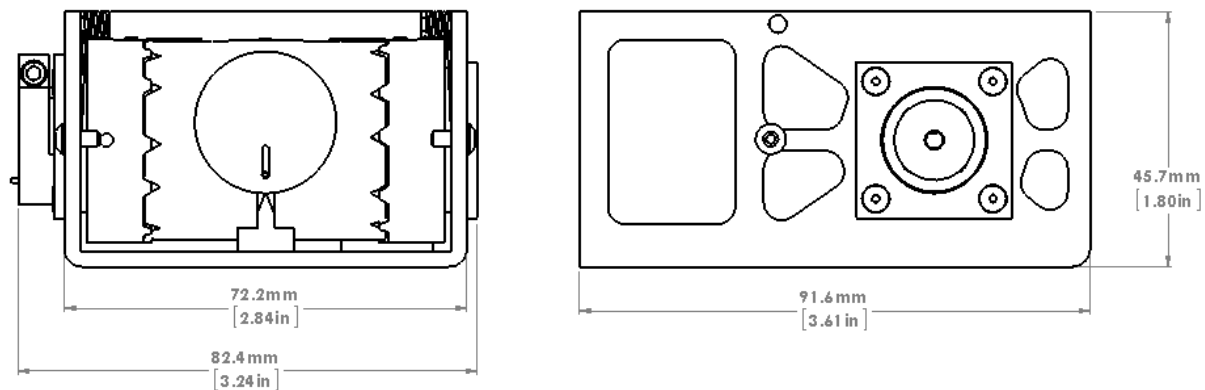


**Figure 9. Single-boom Unit Stowed Dimensions**

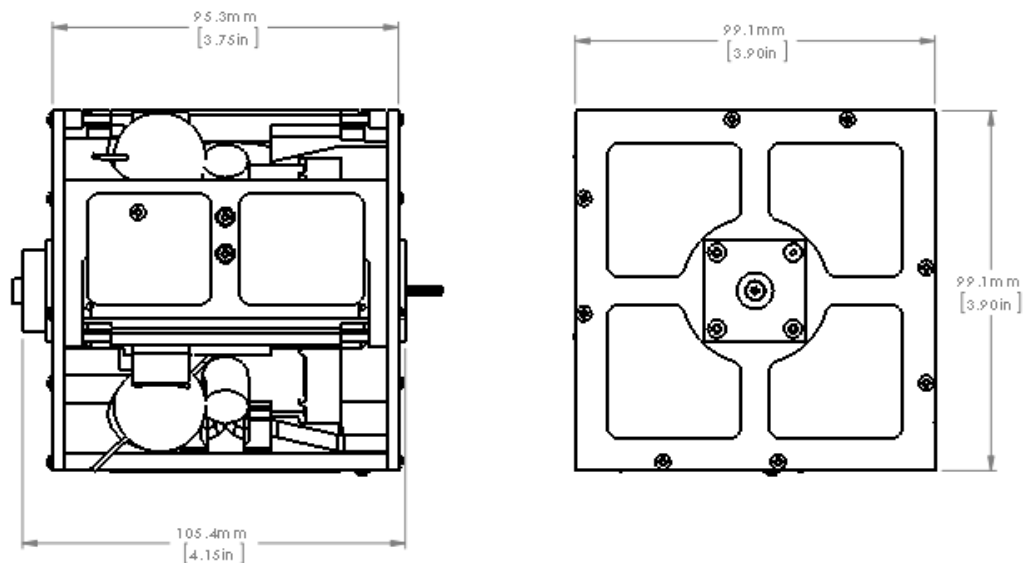


**Figure 10. Quad-boom Unit Stowed Dimensions**

CTD is now working on integrating the tip-mounted sensors into these units. This will involve the installation of an embedded, multi-conductor wire harness along the length of each boom that can be rolled up with the structure. Furthermore, a slip ring will be implemented within the stowage spool of each unit such that sensor signals and power can be transferred across the rotating interface. CTD is also currently developing miniaturized control electronics that can be incorporated into the 3U volume.

## **Conclusions**

Accurate measurements of vector electric fields in the ionosphere are vital to making progress towards our understanding of the physics of the heliosphere. Housing a vector e-field instrument on a CubeSat enables multi-point 3D electric field measurements to be economically made in this region. CTD is therefore developing the deployment system for the CubeSat Electric Field Instrument, which is enabled by CTD's deployable boom technology. Under NASA funding, CTD recently designed, manufactured and successfully demonstrated this deployment system. Next steps for the technology include the implementation of tip-mounted sensors, wiring harness, slip ring and miniaturized drive electronics. This technology has wide applicability to many CubeSat applications, and could also be used as an antenna, instrument boom (magnetometer, Langmuir probe, etc.), gravity gradient boom, or as the deployable structure for a solar array, drag sail, solar sail, etc.





# Degradation of Sputter-Deposited Nanocomposite MoS<sub>2</sub> Coatings for NIRCam during Storage in Air

Jeffrey R. Lince,<sup>\*</sup> Stuart H. Loewenthal<sup>\*\*</sup> and Charles S. Clark<sup>\*\*</sup>

## Abstract

The Focus and Alignment Mechanism (FAM) in NIRCam on the James Webb Space Telescope will be lubricated with nanocomposite sputter-deposited MoS<sub>2</sub> coatings. To respond to concerns regarding how exposure to humid air during storage would affect performance, a study was conducted involving real-time (i.e., unaccelerated) storage of coatings in air at 59% RH for over two years. Pin-on-disk friction testing showed that the endurance of the coatings dropped significantly during storage, but still provided acceptable margin for FAM. The endurance results correlated well with X-ray Photoelectron Spectroscopy results that measured the conversion of MoS<sub>2</sub> to nonlubricating MoO<sub>3</sub> during storage.

## NIRCam Background

Nanocomposite sputter-deposited MoS<sub>2</sub> coatings are being used to lubricate sliding surfaces within the Focus and Alignment Mechanism (FAM) in the Near Infrared Camera (NIRCam); NASA chose NIRCam as one of four science instruments for the James Webb Space Telescope (JWST) (See Figure 1).<sup>1</sup> The three FAMs are linear actuators required to provide micron level positioning in tip, tilt and piston to the Pickoff Mirror that reflects the starlight into the rest of the NIRCam instrument. The FAM, along with the other NIRCam mechanisms such as the filter wheel assembly and pupil imaging assembly, are required to operate at approximately 37K for near infrared imaging during the 5-year JWST mission.<sup>2</sup>

The FAM consists of a fine pitch lead screw driven by 3-phase stepper motor through a high-ratio Harmonic Drive. It was required to pass a cryogenic 2X life test of 200,000 revolutions with repeatable position accuracy of less than 4 microns and with less than a 30% increase in threshold motor current. These demanding requirements and the need to operate at cryogenic temperatures put a high premium on selecting durable solid lubricant films. Sputter-deposited nanocomposite MoS<sub>2</sub>-based coatings manufactured by Hohman Plating, Inc. were chosen for this application.

Because of the high precision nature of the FAM, the plan was to store the flight article in either a vacuum or a dry nitrogen purged environment during ground processing after delivery. This represented a conservative position due to the known sensitivity of the MoS<sub>2</sub> lubricant to humidity. However, providing such an environment proved to be impractical after integration with the next higher assembly, where it will be stored in air with 30 to 60% RH. Although non-reversible degradation of MoS<sub>2</sub> in the coatings to oxides is expected in poorly controlled storage environments, the specific amount of degradation over long periods of time has not been quantified.

Sputter-deposited MoS<sub>2</sub>-based coatings are increasingly being used in spacecraft applications where solid lubricant formulations based on MoS<sub>2</sub> powders are precluded.<sup>3</sup> Sputter-deposited coatings differ from such coatings in that they are thin (i.e., ~0.5–1 μm thick), have smaller crystallite sizes, higher crystalline defect levels, and do not use bonding agents. In their pure form, sputtered coatings exhibit significant sensitivity to oxidation in humid atmospheres. However, improvements in wear life have been achieved by co-sputtering MoS<sub>2</sub> with various species<sup>4-7</sup> to form nanocomposites (as are used in the FAM), or forming multilayer coatings by alternating deposition of a metal with MoS<sub>2</sub>.<sup>8</sup> These mixed coatings should exhibit

---

<sup>\*</sup> The Aerospace Corporation, El Segundo, CA

<sup>\*\*</sup> Lockheed Martin Space Systems Company, Sunnyvale, CA

better resistance to oxidation than conventional sputter-deposited coatings, because the metals increase the density of the coatings, and also "seal" the reactive edges of the MoS<sub>2</sub> crystallites.<sup>8,9</sup> However, quantitative data on the extent of oxidation and its consequent effect on performance is lacking.

The present study was initiated to address the risk of the FAM not being able to perform as required over its mission cycle life due to potential exposure to relative humidity levels up to 60% for extended periods of time. The study was conducted in real-time. We did not accelerate by increasing the temperature or humidity because that would give non-quantitative results that could not be readily applied to real systems. We investigated the effects of storing three types of sputter-deposited MoS<sub>2</sub>-based coatings in air at 59% RH, all manufactured by Hohman Plating, Inc.: Ni-MoS<sub>2</sub>, Au-Sb<sub>2</sub>O<sub>3</sub>-MoS<sub>2</sub>, and Sb<sub>2</sub>O<sub>3</sub>-MoS<sub>2</sub>. Hohman Plating supplies many of the spacecraft contractors in the U.S., including the coatings for the FAM: the Sb<sub>2</sub>O<sub>3</sub>-MoS<sub>2</sub> coating was chosen for the FAM, while the other two coating versions were tested for comparison purposes. Most of the FAM operation (both ground and on-orbit) will occur in inert environments (i.e., N<sub>2</sub> or vacuum); a relatively small amount of testing will occur in air. The testing was conducted in an inert environment (gaseous N<sub>2</sub>) at exceptionally low humidity levels (<0.08% RH) to model these conditions. Although the absolute endurance values may vary slightly from that obtained in vacuum, we are most interested in measuring the relative amount of endurance degradation, which should be valid while testing in N<sub>2</sub>.

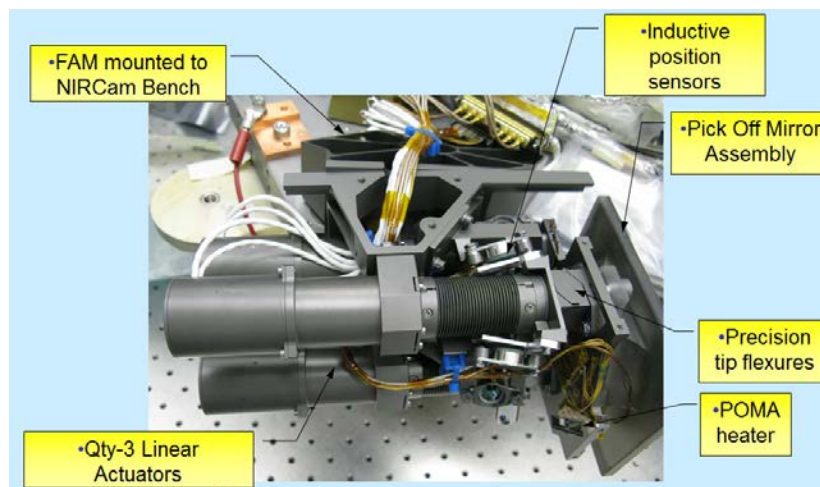
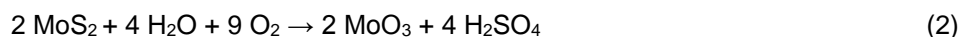
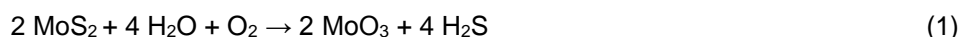


**Figure 1. The Focus and Alignment Mechanism (FAM) provides tip, tilt and piston for NIRCams's Pick Off Mirror (POM)**

### **Previous Studies into MoS<sub>2</sub> Aging and Oxidation**

This section reviews previous work concerning oxidation of MoS<sub>2</sub> solid lubricants due to humid air exposure. MoS<sub>2</sub> can oxidize during exposure to water vapor alone, to oxygen alone, and to water and oxygen together. In general, at ambient storage temperatures, appreciable oxidation is unlikely with water or oxygen alone. For pure oxygen reacting with MoS<sub>2</sub>, oxidation only occurs at temperatures >300°C.<sup>10</sup> The reaction of pure water reacting with MoS<sub>2</sub> has been shown to proceed for temperatures above 780°C,<sup>11</sup> and would probably proceed negligibly at room temperature. However, wear of the films while they are under a partial pressure of H<sub>2</sub>O can accelerate the reaction process. One study showed that H<sub>2</sub>S was produced when rubbing supported MoS<sub>2</sub> films under an atmosphere containing dry nitrogen (N<sub>2</sub>) and H<sub>2</sub>O gases at ambient temperature.<sup>12</sup> As such, either elevated temperature or mechanical wear is required to oxidize MoS<sub>2</sub> in a humid atmosphere without oxygen present.

Oxidation of MoS<sub>2</sub> at ambient temperature is more likely when both water and oxygen are present. In most oxidation scenarios related to storage, both H<sub>2</sub>O and O<sub>2</sub> are present to some degree. There are two reactions that have been proposed to occur:



In one study, H<sub>2</sub>S was detected during wear tests of dry MoS<sub>2</sub> powders in a humid atmosphere.<sup>13</sup> In another study, no detectable sulfates at the surface region of sputter-deposited MoS<sub>2</sub> coatings were found after considerable oxidation of the surface in humid air.<sup>14</sup> The observation of H<sub>2</sub>S production and the lack of sulfates in humid atmospheres indicate that Eq. (1) was active in these cases.

In another study, oxidation in a humid atmosphere was shown to produce sulfate ion and MoO<sub>3</sub> in an approximately 2:1 ratio, and acid was detected after washing the reaction products in water.<sup>15</sup> This suggests that Eq. (2) was occurring. However, no analysis of evolved gases was conducted, so that Eq. (1) might also have been operative, with some production of H<sub>2</sub>S gas.

The presence of H<sub>2</sub>SO<sub>4</sub> is of concern because it can corrode the surfaces of metals such as aluminum and steel. In fact, the production of the acid H<sub>2</sub>SO<sub>4</sub> has caused the establishment of pH limits of aqueous extracts of MoS<sub>2</sub> powders in several specifications.<sup>16</sup>

The presence of H<sub>2</sub>O appears to accelerate the oxidation of MoS<sub>2</sub> in air. The study in Ref. 15 revealed that the rate of oxidation of MoS<sub>2</sub> (as measured by the rate of MoO<sub>3</sub> production) was two to three times higher in an air atmosphere that was saturated with H<sub>2</sub>O compared to a dry air atmosphere. (This experiment was conducted at temperatures of 85°C to 100°C at 1 atm pressure, so that negligible condensation of the H<sub>2</sub>O from the gas phase would be expected.)

Increased humidity has also been shown to degrade tribological properties. Ref. 14 demonstrated decreasing wear life of coatings treated with increasingly humid atmospheres. Ref. 17 showed that the friction coefficient of burnished MoS<sub>2</sub> coatings increased as the humidity increased.

A study was previously conducted at The Aerospace Corporation to better quantify the effects of oxygen and humidity exposure – as well as storage time – on the oxidation of MoS<sub>2</sub>.<sup>18</sup> The study used polycrystalline MoS<sub>2</sub> powders, which are used in fabricating burnished and bonded MoS<sub>2</sub> coatings, and also composites like bearing retainers and slip-ring brushes. The average particle size was 0.7 μm. After washing the powders in aqueous ammonium hydroxide (NH<sub>4</sub>OH) to remove residual MoO<sub>3</sub>, samples were placed into one of three storage environments: air with 4% RH, air with 33% RH, and air with 53% RH. Samples were placed in the bottom of small beakers, forming piles of MoS<sub>2</sub> powder ~1 mm thick. Oxidation of MoS<sub>2</sub> samples was analyzed after 1–3 years of storage by dissolving any MoO<sub>3</sub> present in aqueous NH<sub>4</sub>OH and measuring the resultant Mo content in solution using atomic absorption (AA) spectroscopy.

Analysis gave the fractional amount of MoS<sub>2</sub> that was oxidized to MoO<sub>3</sub>. These values are shown in Figure 2 for each storage atmosphere and storage time. The results for 4% and 33% RH are the same within the error limits, but the amount of oxidation for 53% RH is considerably greater than that for 0% or 33% RH. In addition, the amount of oxidation continues to increase for 53% RH after one year of storage, while the corresponding values for 4% and 33% RH do not.

The similarity of the 4% and 33% curves, and the rapid increase in oxidation between 33% and 53% RH, could indicate a two-step oxidation mechanism: the first step proceeds to completion without requiring substantial H<sub>2</sub>O in the storage ambient, while the second step only proceeds at an appreciable rate for humidities greater than some threshold RH value between 33% and 53%.

As discussed above, the total magnitude of oxidation of the samples to  $\text{MoO}_3$  at 53% RH is ~3%. However, this percentage represents the entire sample, and does not take into account the likelihood that a higher amount of oxidation occurs near the surfaces of the piles of powders. In fact, a whitish color indicative of  $\text{MoO}_3$  was visible on the surfaces of  $\text{MoS}_2$  piles samples stored at 53% RH for 1½ and 3 years, which was not apparent in the region below the surface of the piles.

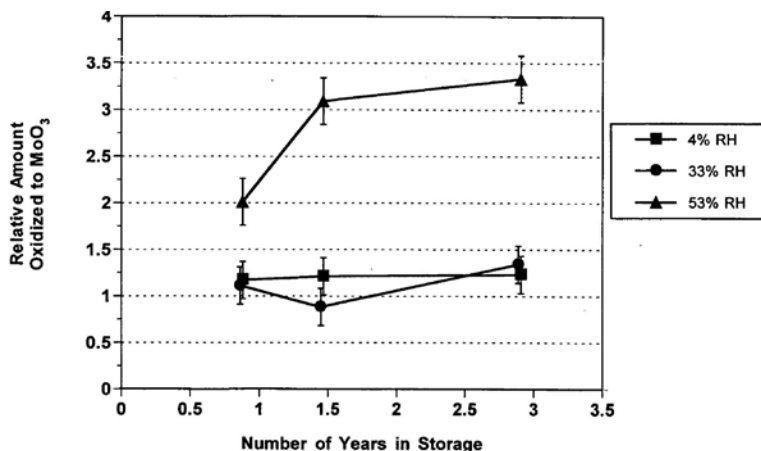


**Figure 2. Relative amount (in percent) of powder  $\text{MoS}_2$  samples that were oxidized to  $\text{MoO}_3$  by exposure to air. Results are shown over 3 years storage for samples stored at three humidities.**

$\text{MoS}_2$  solid lubricant coatings used on spacecraft include burnished films, sputter-deposited coatings, and pressure-sprayed coatings that are considerably thinner than the macroscopic samples evaluated in this earlier study (i.e., 1–10  $\mu\text{m}$  thick). As such, the amount of oxidation *relative to the lubricant thickness* for thin coatings is potentially much greater compared to the more macroscopic samples in the  $\text{MoS}_2$  powder study. In fact, for very thin or porous coatings, a previous study showed that oxidation could be as high as 40–100% throughout the depth of the coating.<sup>18</sup> In less porous coatings, the amount of oxidation might be lower. However, the amount of oxidation would be significant in either case because the oxidation is enhanced at the surface of the coatings, where tribological interactions in lubricated devices occur.

Whether lubricant degradation due to  $\text{MoS}_2$  oxidation adversely affects device performance depends on the application, the type of coating, and the tribological requirements, such as friction/torque and number of duty cycles. Applications involving low numbers of duty cycles and wide friction margins are more robust with respect to such degradation. For example, latches and other release mechanisms will only operate once on orbit (including a few cycles during ground test), and the dominant concern is to ensure that a maximum coefficient of friction (COF) is not reached and to prevent metal-to-metal contact that would cause galling or cold-welding. In such cases, the increase in friction due to partial conversion of the  $\text{MoS}_2$  to  $\text{MoO}_3$  may not be enough to significantly affect deployment. In contrast, scanner and gimbal bearings involve higher contact stresses and must operate for millions of cycles. Also, excessive  $\text{MoO}_3$  production could prevent the bearings from meeting requirements for low torque noise. For these applications, even a small amount of degradation could be significant. For bearings containing self-lubricating retainers, a film of  $\text{MoO}_3$  on the bearing race surfaces could affect the rate of formation and uniformity of transfer films. Poor transfer film formation could result in the appearance of torque noise and lowered lifetime.

The oxidation of  $\text{MoS}_2$  is believed to be many times higher at the more chemically reactive edge plane surfaces of a  $\text{MoS}_2$  crystallite, rather than the relatively unreactive basal plane surfaces.<sup>14</sup> In resin-bonded coatings (containing powdered  $\text{MoS}_2$  as the lubricant), these reactive edge sites are protected significantly from moisture by the surrounding binder matrix. As such, bonded coatings are generally less sensitive to humid air exposure. However, even for these coatings, a thin film of pure  $\text{MoS}_2$  forms on the surface of a burnished/run-in coating, which is then susceptible to oxidation. The result is that there will be initially increased friction until this oxidized surface layer is worn off.

Long term storage life test data for sputter deposited MoS<sub>2</sub> coatings are uncommon. The data available generally involve pure MoS<sub>2</sub> coatings. For example, results reported in the 1980's in Ref. 14 showed that storage of pure sputter-deposited MoS<sub>2</sub> coatings in humid atmospheres (i.e., 84% relative humidity [RH]) resulted in considerably greater oxidation than in dry atmospheres for storage times of 2 weeks to 1 year. Some oxidation increase was even seen for storage in 52% RH compared to dry atmosphere.

Panitz et al. evaluated the friction and wear properties of RF-sputtered MoS<sub>2</sub> coatings after being stored for 150 days in 35%-45% relative humidity followed by over 75 days in either a 2% or 98% relative humidity environment.<sup>19</sup> Two types of coatings were studied, one that was deposited on a heated substrate and subsequently annealed, and another that was deposited on a substrate at ambient temperature and not annealed. The heat-treated coating was more crystalline than the ambient-grown coating as measured by Raman peak intensity (this agrees with X-ray Diffraction results on RF-sputtered MoS<sub>2</sub> coatings that had similar heat-treatment in our laboratory<sup>20</sup>). The coefficient of friction for the MoS<sub>2</sub> coating having a more crystalline structure increased from its initial air tested level of 0.085 to 0.10 after being stored in 98% RH. Its wear life decreased by a factor of 3 when stored the 2% dry environment but dropped by a factor of 10 when stored in the wet environment. The authors point out that this result was consistent with the observation of others that water vapor promotes the conversion of MoS<sub>2</sub> to MoO<sub>3</sub>. On the other hand the less crystalline MoS<sub>2</sub> sample's wear life increased when stored in the wet environment, so microstructure clearly plays a role in oxidation.

Storage tests were conducted by Iwaki et al. on sputter deposited MoS<sub>2</sub> at 40%, 60% and 80% relative humidity for up to 24 months of storage.<sup>21</sup> Wear lives of samples stored for 6 months were relatively unchanged within the scatter of the data except for samples stored at 60% RH which showed improvement. However tests at 1, 1.5 and 2 years showed mixed results with some 60% RH readings showing lower life while others showing essentially no change.

For use in current spacecraft mechanisms, it has been found that greatly improved tribological properties are obtained from cosputtered coatings that consist of MoS<sub>2</sub> mixed with species like Ni and Sb<sub>2</sub>O<sub>3</sub> to form nanocomposites. The higher densities and altered crystalline structure of these cosputtered coatings imply that their sensitivity to storage in humid air should be different also. Storage sensitivity of these mixed coatings is the focus of our study.

### Experimental Approach

Ni-MoS<sub>2</sub>, Au-Sb<sub>2</sub>O<sub>3</sub>-MoS<sub>2</sub>, and Sb<sub>2</sub>O<sub>3</sub>-MoS<sub>2</sub> coatings were deposited onto a series of polished 440C steel disks to a thickness of 400±100 nm. Several of each type of coating were stored in a closed container containing air with humidity controlled to 59% RH by using a saturated solution of NaBr. Samples were periodically removed for testing. Samples not being exposed to humid air were stored in dry, flowing N<sub>2</sub> gas.

Friction/wear testing was conducted using a CSEM Pin-on-Disk Tribometer. The upper specimens for the tests were uncoated 6-mm 440C steel balls (grade 3, R<sub>a</sub>=0.01 μm), cleaned with IPA prior to testing. For all tests, a 3N load was used, and the sliding speed was 20 cm/s. The nominal maximum Hertzian contact stress was calculated as 938 MPa (136 ksi) based on the properties of 440C steel substrate.

Prior to starting the friction/wear tests, the tribometer enclosure was purged with nitrogen gas (99.999% nominal purity, passed through an Aeronex Gatekeeper® getter, which is advertised to reduce oxygen, water, and other impurities to less than 1 ppb) for four hours, and until the relative humidity was reduced to below 0.08% RH. The tests were started, and were run until failure, which is defined as when the COF rose above 0.5. Three tests were conducted on each sample to determine the data uncertainty, but different radii were chosen to ensure that each test was conducted on virgin material; new balls were used for each test.

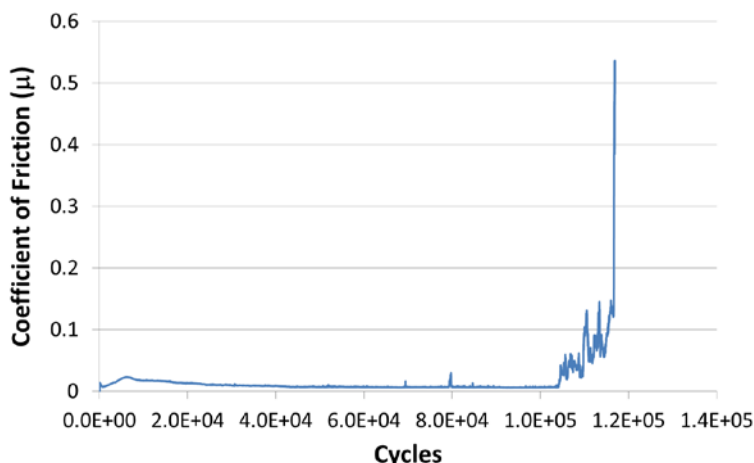
X-ray Photoelectron Spectroscopy (XPS) was used to aid in understanding the chemical changes occurring in the coatings that gave rise to changes in friction and endurance. Our main interest was in the oxidation

state of Mo since the most significant result of storage in humid air is to oxidize the lubricating MoS<sub>2</sub> to nonlubricating MoO<sub>3</sub>, as discussed above. For this study, a Physical Electronics Versaprobe II instrument was used.

In order to determine the composition variation with depth into the coatings, Ar<sup>+</sup> sputtering depth profiles were obtained using a 1 kV accelerating voltage. Ion bombardment has an unpredictable effect on chemical state, and so it is difficult to quantitatively determine relative elemental amounts as well as chemical state with depth. However, it is useful in providing semi-quantitative comparisons between materials.

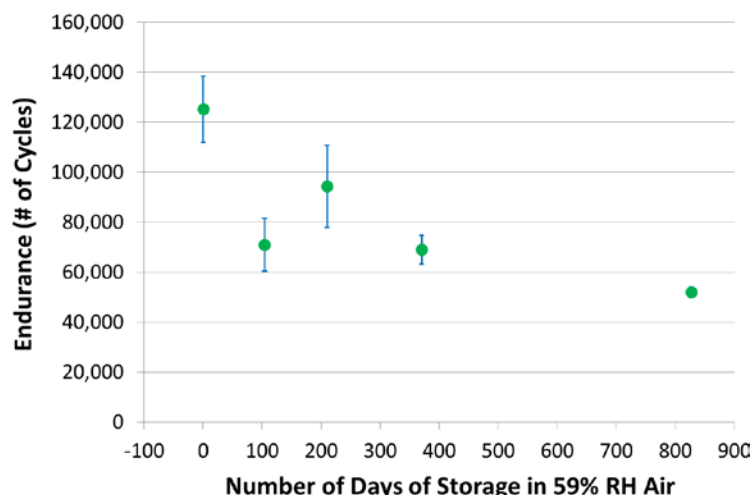
### Friction and Endurance Results

A typical friction trace for a Hohman Plating Ni-MoS<sub>2</sub> coating tested before storing in humid air is shown in Figure 3. The mean endurance for the Hohman Plating Ni-MoS<sub>2</sub> coating prior to humid air storage was 125,000 cycles. In contrast, the endurance for the Au-Sb<sub>2</sub>O<sub>3</sub>-MoS<sub>2</sub>, and Sb<sub>2</sub>O<sub>3</sub>-MoS<sub>2</sub> coatings were 2.2 million and 3.3 million cycles, respectively, or 18 and 26 times the endurance for the Ni-MoS<sub>2</sub> coating. It has previously been shown that the Sb<sub>2</sub>O<sub>3</sub>-containing coatings performed better than the Ni-MoS<sub>2</sub> coating when tested in an air environment.<sup>6</sup> (In that study, tests conducted in dry N<sub>2</sub> were stopped prior to failure for all coatings, so relative lifetimes in an inert environment were not obtained.)



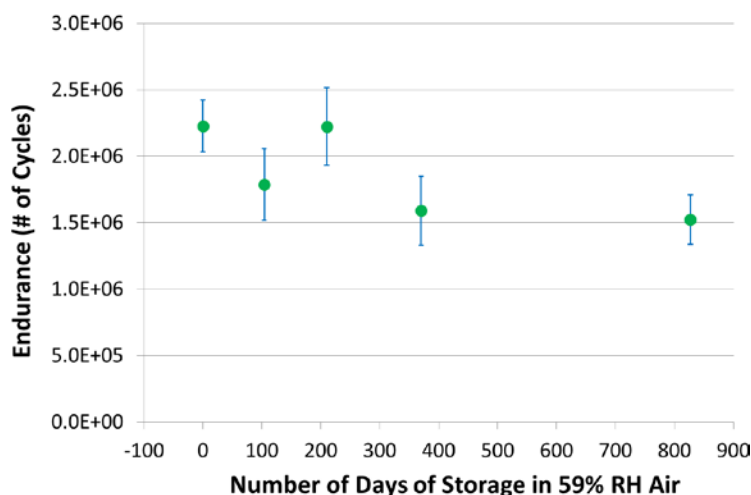
**Figure 3. A typical friction trace for a Hohman Plating Ni-MoS<sub>2</sub> coating tested before storing in humid air. Data were obtained during pin-on-disk testing in a dry N<sub>2</sub> environment.**

Figure 4 shows endurance data for the Ni-MoS<sub>2</sub> coating for various storage times. Even considering the large scatter of the data in the first 200 days, there is a clear reduction in endurance with storage time. The endurance continues to drop for longer storage times up to 827 days (2.3 years), although the rate of decrease appears to slow with increasing storage time. The total reduction over 2.3 years is about 55%, which represents a significant degradation in the performance of this coating.



**Figure 4. Endurance of Hohman Plating Ni-MoS<sub>2</sub> coatings as a function of days stored in 59% RH air. The endurance is defined as the number of cycles for which the COF is below 0.5. Each data point represents the mean of three tribometer runs on one sample; the error bars represent the scatter of the three runs. There is a reduction in endurance of about 55% for a storage time of 2.3 years.**

The endurance data for the stored Au-Sb<sub>2</sub>O<sub>3</sub>-MoS<sub>2</sub> coating is shown in Figure 5. For the early storage data (i.e., ≤200 days), the trend in endurance with storage time is not clear; it is obscured by the scatter in the data. However, over longer storage times (i.e., 1 and 2.3 years), the endurance is clearly lower than the unstored coating. Furthermore, the endurance at 1 year and 2.3 year are comparable, suggesting there is a reduction in the degradation rate of the coatings after 1 year but more data would be needed to confirm this. The total reduction over 2.3 years is about 20%, considerably smaller than for the Ni-MoS<sub>2</sub> coatings. Figure 6 shows corresponding data for the Sb<sub>2</sub>O<sub>3</sub>-MoS<sub>2</sub> coatings. As for the similar Au-containing coating, it also shows a reduction in endurance with storage time, i.e., by 17% over 419 days of storage (1.1 years; this coating was placed into storage later than the other two, and so longer storage times are not available at the time of this writing). Again the data suggests that the endurance may have stabilized.



**Figure 5. Endurance of Hohman Plating Au-Sb<sub>2</sub>O<sub>3</sub>-MoS<sub>2</sub> coatings as a function of days stored in 59% RH air. (See Figure 4 caption.) The endurance has reduced by about 30% for a storage time of 2.3 years.**

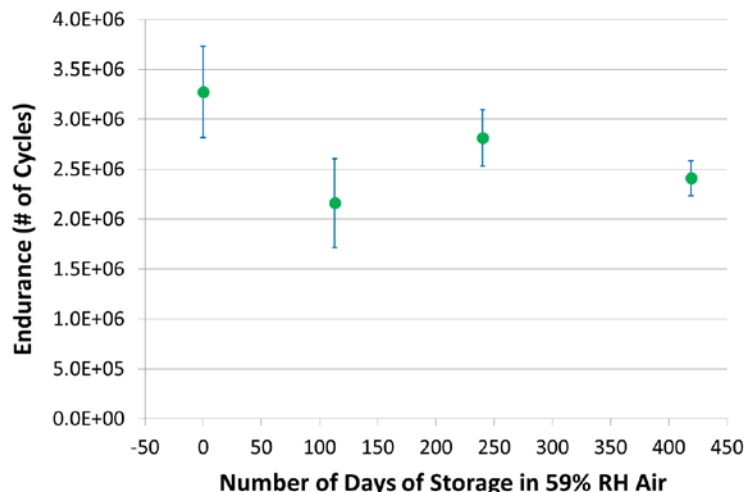


**Figure 6. Endurance of Hohman Plating  $\text{Sb}_2\text{O}_3\text{-MoS}_2$  coatings as a function of days stored in 59% RH air. (See Figure 4 caption.) The endurance has reduced by about 27% for a storage time of 1.1 years.**

Solid lubricant coatings typically exhibit increased friction at the beginning of testing due to the initial coating surface chemical state, morphology, and crystallinity. After steady-state conditions have been reached (i.e., post run-in), the friction is generally at a minimum. Early-life friction was measured during separate (higher data rate) scans for the Ni-MoS<sub>2</sub> and Au-Sb<sub>2</sub>O<sub>3</sub>-MoS<sub>2</sub> coatings stored in N<sub>2</sub> and for storage in air for 2.3 years (these were only run for a few hundred cycles, i.e., not to failure). Results are shown in Table 1. Also shown are the steady-state values obtained from the original endurance runs.

The early-life friction for the Au-Sb<sub>2</sub>O<sub>3</sub>-MoS<sub>2</sub> coating (without air storage) is slightly lower than that for the Ni-MoS<sub>2</sub> coating. After storage for 2.3 years, the early-life friction increases slightly for both types of coatings. For the steady-state values, the friction for the Au-Sb<sub>2</sub>O<sub>3</sub>-MoS<sub>2</sub> coating (without air storage) is lower than that for the Ni-MoS<sub>2</sub> coating. After storage, the steady-state friction does not change significantly for either coating.

**Table 1. Friction Values Obtained from Sputter-Deposited MoS<sub>2</sub> Coatings Before and After Storage in 59% RH Air for 2.3 years (tested in dry N<sub>2</sub>)**

Sample	Maximum COF measured at Start of Test		Steady State/ Minimum COF	
	Stored in N <sub>2</sub>	Stored in Air	Stored in N <sub>2</sub>	Stored in Air
Ni-MoS <sub>2</sub>	0.22 ±.01	0.25 ±.005	.008 ±.002	.007 ±.002
Au-Sb <sub>2</sub> O <sub>3</sub> -MoS <sub>2</sub>	0.18 ±.01	0.22 ±.01	.005 ±.002	.003 ±.001

### Surface Chemical Results

In order to help understand the chemical changes occurring in the coatings that gave rise to the changes in friction and endurance, X-ray Photoelectron Spectroscopy (XPS) was used to study unworn areas of the coatings. Our main interest was in the oxidation state of Mo since the most significant result of storage in humid air is to oxidize the lubricating MoS<sub>2</sub> to nonlubricating MoO<sub>3</sub>, as discussed above.

Figure 7 shows XPS spectra in the Mo 3d region of the Ni-MoS<sub>2</sub> coating that had been stored in dry N<sub>2</sub>, along with one stored for 2.3 years in air with 59% RH. In the spectra, the Mo 3d doublet for MoS<sub>2</sub> overlaps



with that for  $\text{MoO}_3$ , giving a structure that appears to be three peaks. This necessitated using linear least squares deconvolution to determine the molecular ratios of the two species. The ratio of the  $\text{MoO}_3$  to  $\text{MoS}_2$  spectrum indicates the amount of oxidation that has occurred through the detection depth. The two spectra in Figure 7 indicate that some of the  $\text{MoS}_2$  has been oxidized to  $\text{MoO}_3$  at the surface of the coating stored in dry  $\text{N}_2$ . However, significantly more of the  $\text{MoS}_2$  has been oxidized to  $\text{MoO}_3$  for the coating stored in humid air.

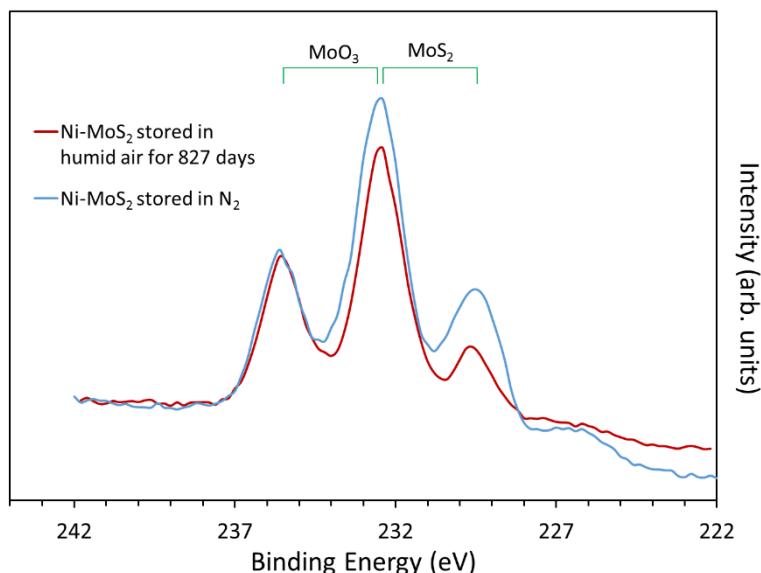


**Figure 7. XPS spectra in the Mo 3d region for Hohman Plating Ni-MoS<sub>2</sub> coatings stored in dry N<sub>2</sub> and stored in 59% RH air for 2.3 years. In the spectra, the Mo 3d doublet for MoS<sub>2</sub> overlaps with that for MoO<sub>3</sub>. The spectra are normalized so that they show equal contributions of MoO<sub>3</sub>. The MoO<sub>3</sub>:MoS<sub>2</sub> ratio is significantly higher for the coating stored in humid air.**

Figure 8 shows corresponding spectra for the Au-Sb<sub>2</sub>O<sub>3</sub>-MoS<sub>2</sub> coating. The two spectra indicate that some of the MoS<sub>2</sub> has been oxidized to MoO<sub>3</sub> at the surface of the coating stored in dry N<sub>2</sub>, although somewhat less than for the Ni-MoS<sub>2</sub> coating. In addition, although some of the MoS<sub>2</sub> in the Au-Sb<sub>2</sub>O<sub>3</sub>-MoS<sub>2</sub> coating has been further oxidized to MoO<sub>3</sub> after storing in humid air, the change is considerably less pronounced than for the Ni-MoS<sub>2</sub> coating.

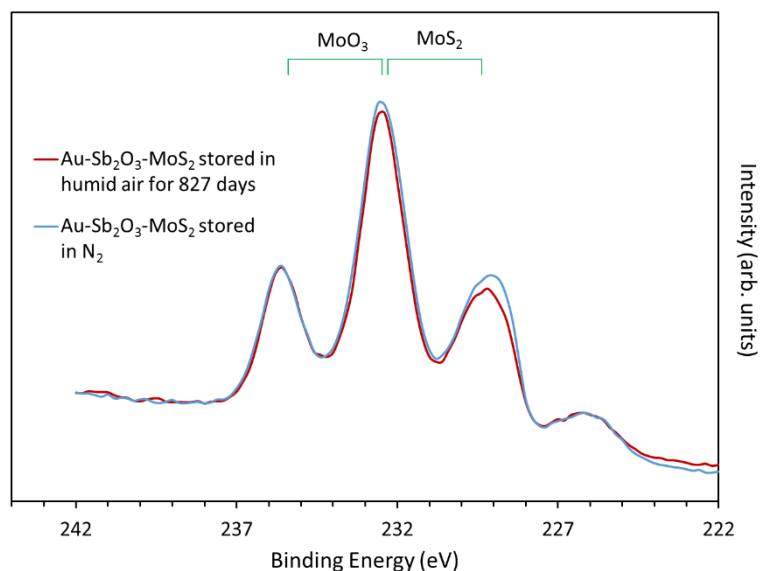


**Figure 8. XPS spectra in the Mo 3d region for Hohman Plating Au-Sb<sub>2</sub>O<sub>3</sub>-MoS<sub>2</sub> coatings stored in dry N<sub>2</sub> and stored in 59% RH air for 2.3 years. In the spectra, the Mo 3d doublet for MoS<sub>2</sub> overlaps with that for MoO<sub>3</sub>. The spectra are normalized so that they show equal contributions of MoO<sub>3</sub>. The MoO<sub>3</sub>:MoS<sub>2</sub> ratio is only slightly higher for the coating stored in humid air.**

Table 2 gives the calculated ratios of MoO<sub>3</sub> to MoS<sub>2</sub> for the spectra shown in Figures 6 and 7. For the Ni-MoS<sub>2</sub> coating stored in N<sub>2</sub>, there is slightly more oxidized material present in the surface region than non-oxidized material, as shown by a MoO<sub>3</sub>:MoS<sub>2</sub> ratio of 1.15. However, after storing in humid air for 2.3 years, the ratio has almost doubled to 2.16, indicating considerable oxidation has occurred during humid air storage.

**Table 2. MoO<sub>3</sub>:MoS<sub>2</sub> Ratios Obtained from XPS Spectra of Sputter-Deposited MoS<sub>2</sub> Coatings**

Sample	Storage Condition	MoO <sub>3</sub> :MoS <sub>2</sub>
Ni-MoS <sub>2</sub>	Stored in N <sub>2</sub>	1.15
	Stored in 59% RH Air for 2.3 years	2.16
Au-Sb <sub>2</sub> O <sub>3</sub> -MoS <sub>2</sub>	Stored in N <sub>2</sub>	1.02
	Stored in 59% RH Air for 2.3 years	1.14

For the Au-Sb<sub>2</sub>O<sub>3</sub>-MoS<sub>2</sub> coating stored in N<sub>2</sub>, Table 2 shows that about the same amount of oxidized material is present in the surface region as non-oxidized material, as shown by a MoO<sub>3</sub>:MoS<sub>2</sub> ratio of 1.02; this represents slightly less surface oxidation than for the Ni-MoS<sub>2</sub> coating stored in N<sub>2</sub>. For the Au-Sb<sub>2</sub>O<sub>3</sub>-MoS<sub>2</sub> coating stored in 59% RH air for 2.3 years, the value of 1.14 indicates that only about 10% greater oxidation has occurred during humid air storage. Storage in air clearly has less of an effect on the Au-Sb<sub>2</sub>O<sub>3</sub>-MoS<sub>2</sub> coating than the Ni-MoS<sub>2</sub> coating.

To investigate oxidation throughout the bulk of the coatings, Ar<sup>+</sup> ion sputter depth profiles were obtained. Figure 9a shows the early stages of the depth profile of the Ni-MoS<sub>2</sub> coating stored in N<sub>2</sub>. At longer sputtering times, about 25 at% O is seen in the coating, indicating that significant oxygen was present in the coating as deposited. This is commonly due to residual water vapor in the chamber during the coating process, which results in the formation of a MoS<sub>x</sub>O<sub>2-x</sub> solid solution, rather than conversion of the Mo to a higher oxidation state.<sup>22</sup> However, the surface of the coating shows that significantly more O is present (55

at%), which as shown in Figure 7, is due substantially to oxidation of the  $\text{MoS}_2$  to  $\text{MoO}_3$ . This probably occurred during brief exposure to the air when not being stored in  $\text{N}_2$ . The region of surface oxidation appears to be about 0.5-nm thick (based on estimates of thickness vs. sputtering time). For the Ni-MoS<sub>2</sub> coating stored in air for 2.3 years, there is more O seen at the surface (65 at%) (see Figure 9b), and in addition, the oxidized layer is about three times thicker than that for the coating stored in  $\text{N}_2$ .

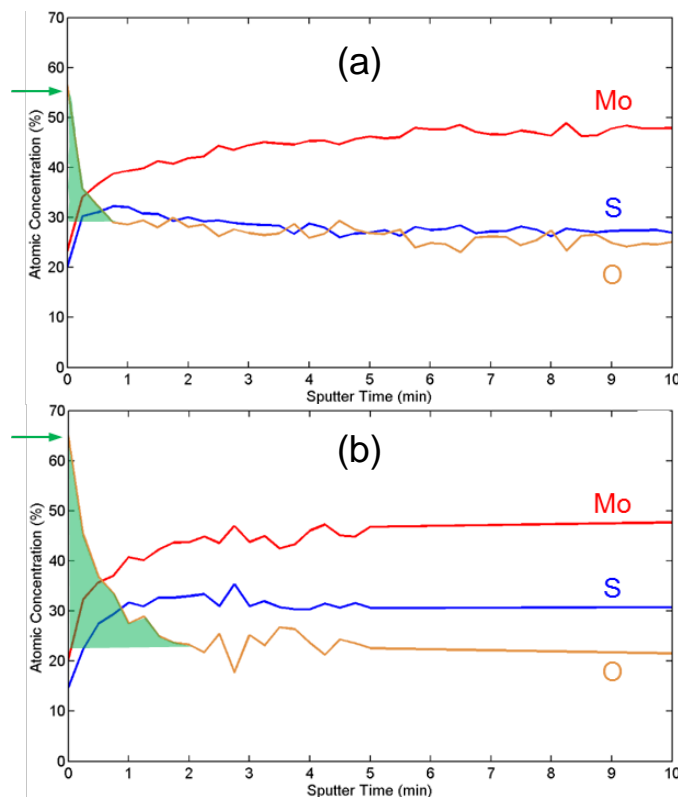


**Figure 9. XPS sputter depth profiles for Hohman Plating Ni-MoS<sub>2</sub> coatings. Profiles are shown for (a) a coating stored in dry  $\text{N}_2$ , and (b) a coating stored in 59% RH air for 2.3 years. (Ni is not shown because of its low intensity.) The profiles show an enhancement in oxygen near the surface (i.e., at low sputtering times) due to surface oxidation of the MoS<sub>2</sub>. The coating stored in humid air for 2.3 years shows a higher level of oxidation at the surface, and a thicker oxidized layer. (Measured atomic percentages after extended sputtering differ from actual bulk values due to preferential sputtering of one element over another.)**

A corresponding depth profile for the Au-Sb<sub>2</sub>O<sub>3</sub>-MoS<sub>2</sub> coating stored in dry  $\text{N}_2$  (not shown) also indicates the presence of oxygen at the surface, but at a much lower level (12 at%) than for the corresponding Ni-MoS<sub>2</sub> coating. The Au-Sb<sub>2</sub>O<sub>3</sub>-MoS<sub>2</sub> coating stored in air for 2.3 years shows increased oxygen at the surface (18 at%), but the thickness of the oxidized layers for the two Au-Sb<sub>2</sub>O<sub>3</sub>-MoS<sub>2</sub> coatings appear similar.

The XPS results correlate with the endurance results during pin-on-disk testing. Specifically, both the Ni-MoS<sub>2</sub> and Au-Sb<sub>2</sub>O<sub>3</sub>-MoS<sub>2</sub> coatings show increased oxidation at their surfaces after 2.3 years of storage in 59% RH air, and both show decreased endurance. The increase in oxidation due to air storage is significantly greater for the Ni-MoS<sub>2</sub> coating compared to the Au-Sb<sub>2</sub>O<sub>3</sub>-MoS<sub>2</sub> coating, and the decrease in endurance is correspondingly greater for the Ni-MoS<sub>2</sub> coating.

## Conclusions

The results of this study demonstrate that the endurance of nanocomposite, sputter-deposited MoS<sub>2</sub> coatings that are typically used on spacecraft can be significantly degraded after storage for two years under typical storage conditions (i.e., storage in air at 59% RH). Specifically, pin-on-disk friction testing showed that sputter-deposited Ni-MoS<sub>2</sub> coatings degrade by 55% over 2.3 years of storage, while Au-Sb<sub>2</sub>O<sub>3</sub>-MoS<sub>2</sub> coatings degrade by 20% over the same period. Sb<sub>2</sub>O<sub>3</sub>-MoS<sub>2</sub> coatings degrade by 17% over 1.1 years of storage.

The reduction in endurance was shown to result from oxidation of lubricating MoS<sub>2</sub> to non-lubricating MoO<sub>3</sub> at the surface of the coatings. This was demonstrated by XPS of the surfaces of the coatings, including Ar<sup>+</sup> ion sputter depth profiles. All coatings exhibited a small amount of oxidation of their surfaces, even those stored in dry N<sub>2</sub> due to brief exposure of the coatings to air. After storage for 2.3 years, a Ni-MoS<sub>2</sub> coating stored in 59% RH air showed significantly greater surface oxidation than a coating stored in dry N<sub>2</sub>, while Au-Sb<sub>2</sub>O<sub>3</sub>-MoS<sub>2</sub> coatings showed a relatively small increase in oxidation stored under the same conditions. These results demonstrate that the degree of oxidation correlates with a decrease in endurance.

Storage effects aside, Au-Sb<sub>2</sub>O<sub>3</sub>-MoS<sub>2</sub> and Sb<sub>2</sub>O<sub>3</sub>-MoS<sub>2</sub> coatings were shown to greatly outperform the Ni-MoS<sub>2</sub> coating, by 18× and 26×, respectively. This may be explained partly by the higher amount of cosputterant in the Sb<sub>2</sub>O<sub>3</sub>-containing coatings relative to the Ni-MoS<sub>2</sub> coating, since a major effect of forming the nanocomposite is to densify the coatings and reduce their crystallinity. Among other effects, this results in a harder, more fracture tough coating that resists wear.<sup>6,9</sup> With respect to oxidation sensitivity, denser, more amorphous coatings would be more likely to resist intrusion of water and oxygen into the coatings, reducing the likelihood of oxidation to nonlubricating MoO<sub>3</sub>.

The results of this study may be used as a guide to storing hardware lubricated with sputter-deposited MoS<sub>2</sub>-based coatings. For devices that require a limited number of cycles (i.e., deployment or release devices), degradation at typical humidities (i.e., <60% RH) will not have a significant effect on performance. However, the degradation must be taken into account for high cycle mechanisms, as endurance can be lowered by 20 to 55% during storage for two years at typical humidities, depending on the type of coating. Storage in dry N<sub>2</sub> or if necessary in air at lower humidities (i.e., <30% RH) can significantly slow the endurance degradation rate.<sup>3,18</sup>

Regarding the FAM storage question, we showed that although the MoS<sub>2</sub> coatings exhibited some degradation in friction performance after the first year of storage, the reduced cycle life of 1.5 million cycles for the Au-Sb<sub>2</sub>O<sub>3</sub>-MoS<sub>2</sub> coating and 2.4 million cycles for the Sb<sub>2</sub>O<sub>3</sub>-MoS<sub>2</sub> coating was more than adequate to meet the NIRCam cycle life requirement.

## References

1. L. G. Burriesci, "NIRCam Instrument Overview," Proc. SPIE 5904, Cryogenic Optical Systems and Instruments XI, 590403 (August 25, 2005).
2. C.S. Clark, "Resolution for Fretting Wear Contamination on Cryogenic Mechanism," Proc. 41st aerospace mechanisms symposium, NASA/CP-2012-217653, pp 399–410 (May 17, 2012).
3. J. R. Lince and P. D. Fleischauer, "Solid Lubricants" Chap. 7: in *Space Vehicle Mechanisms: Elements of Successful Design*, P. Conley, ed., Wiley-Interscience, 1998.
4. T. Spalvins, "Frictional and morphological properties of Au-MoS<sub>2</sub> films sputtered from a compact target," *Thin Solid Films* 118 (1984) 375.
5. B.C. Stupp, "Synergistic effects of metals co-sputtered with MoS<sub>2</sub>," *Thin Solid Films* 84, 257 (1981); B.C. Stupp, "Performance of Conventionally Sputtered MoS<sub>2</sub> versus Cosputtered MoS<sub>2</sub> and Nickel," ASLE SP-14 (1984) p. 217.
6. J.S. Zabinski, M.S. Donley, S.D. Walck, TR Schneider and N.T. McDevitt, "The effects of dopants on the chemistry and tribology of sputter-deposited MoS<sub>2</sub> films," *Tribol. Trans.* 38(4) (1995) 894–904.
7. J. R. Lince, "Tribology of co-sputtered nanocomposite Au/MoS<sub>2</sub> solid lubricant films over a wide contact stress range," *Tribol. Lett.*, 17(3) (2004) 419-428.
8. M. R. Hilton, R. Bauer, S. V. Didziulis, M. T. Dugger, J. Keem, J. Scholhamer, "Structural and tribological studies of MoS<sub>2</sub> solid lubricant films having tailored metal-multilayer nanostructures," *Surface & Coatings Technology* 53 (1992) 13-23.
9. J.R. Lince, M.R. Hilton, and A.S. Bommannavar, "Metal incorporation in sputter-deposited MoS<sub>2</sub> films studied by extended x-ray absorption fine structure," *Journal of Materials Research* 10 (1995) 2091.
10. R. T. K. Baker, J. J. Chludzinski Jr, and R. D. Sherwood, "In-situ electron microscopy study of the reactivity of molybdenum disulfide in various gaseous environments," *Journal of Materials Science* 22 (1987) 3831.
11. D. Kim and H. Y. Sohn, "Intrinsic kinetics of the reaction of molybdenum disulfide and chalcopyrite with water vapor," *Reactivity of Solids* 3 (1987) 273.
12. A. J. Haltner, C.S. Oliver, "Effect of water vapor on the friction of molybdenum disulfide," *Ind. Eng. Chem. Fundam.* 5(3) (1966) 348.
13. G. Salomon, A. W. J. DeGee, and J. H. Zaat, "Mechano-chemical factors in MoS<sub>2</sub>-film lubrication," *Wear* 1 (1964) 87.
14. P. D. Fleischauer and T. B. Stewart (unpublished data); also T. B. Stewart and P. D. Fleischauer, "Chemistry of Sputtered Molybdenum Disulfide Films," *Inorganic Chemistry* 21, 2426 (1982); and P. D. Fleischauer, "Effects of Crystallite Orientation on Environmental Stability and Lubrication Properties of Sputtered MoS<sub>2</sub> Thin Films," *ASLE Transactions* 21 (1984) 82.
15. S. Ross and A. Sussman, "Surface oxidation of molybdenum disulfide," *J. Phys. Chem.* 59 (1965) 889.
16. J. K. Lancaster, "Solid Lubricants," in F. Richard Booser, Ed., *CRC Handbook of Lubrication (Theory and Practice of Tribology)*, vol. II: *Theory and Design*, CRC Press, Boca Raton, 1984.
17. H. F. Barry and J. P. Binkelman, "MoS<sub>2</sub> Lubrication of various metals *Lubrication Engineering* 22 (1966) 139.
18. H. A. Katzman, T. W. Giants, F. Hai, W. D. Hanna, D. J. Chang, C. S. Hemminger, N. Marquez, T. D. Le, M. P. Easton, P. C. Brennan, J. R. Lince, and M. J. Meshishnek, *Spacecraft Aging Program: Final Report -- May 1993 to December 1996*, TOR-97(8504)-2, 15, The Aerospace Corporation, El Segundo, CA, January 1997.

- 
19. J.K.G. Panitz, L.E. Pope, J.E. Lyons, and D.J. Staley, "The tribology properties of MoS<sub>2</sub> coatings in vacuum, low relative humidity and high relative humidity environments," *J. Vac. Sci. Technol. A*, 6(3), May/Jun (1988)
  20. J.R. Lince and P.D. Fleischauer, "Crystallinity of rf-sputtered MoS<sub>2</sub> films," *J. Mater. Res.*, 2 (1987) 827.
  21. M. Iwaki, S. Obara and K. Imagawa, "The Effect of Storage Conditions on the Tribological Properties of Solid Lubricants," *Proc. of 10th ESMATS*, ESA SP-653, (2003)
  22. J. R. Lince, M. R. Hilton, and A. S. Bommanavar, "EXAFS of sputter-deposited MoS<sub>2</sub> films," *Thin Solid Films* 264 (1995) 120.

© The Aerospace Corporation 2016

# **The Dynamic Particle Generation of Lubricating Greases for use in Space Mechanisms**

Jason T. Galary\*

The purpose of this study is to examine the phenomenon of Dynamic Particle Generation in lubricating greases that are used in a variety of critical aerospace mechanisms. Particle Generation occurs in bearings, ball screws, and other mechanical devices where dynamic conditions are present. This should not be confused with outgassing as particle generation is unrelated to the pressure effects on a system. This is a critical factor in many systems as particle generation can contaminate systems or processes causing them to fail. These failures can lead to excessive costs, production failure, and equipment damage.

In this study, several greases made from Multiplyalkylated Cyclopentane and Perfluoropolyether base fluids were tested to evaluate their particle generation properties. This particle generation phenomenon was studied using a custom test rig utilizing a high-precision cleanroom ball screw to simulate true application conditions. The ball screw was tested at speeds from 200, 1,200, and 2,400 RPM to illustrate the effect of speed on the particle generation across different applications. This paper will show the tendencies of different lubricant chemistries to generate particles and which ones present advantages of improved durability and environmental cleanliness for critical processes and applications.

## **Introduction**

Contamination is an element of great concern in regards to mechanisms designed and planned for space flight. While there are many types of contamination including volatile outgassing, residual ions, airborne particulates, etc., the route that the contamination enters the system is just as important. Outgassing has been a well-documented method for contamination in a system and there are many ways to quantify it. Methods like ASTM E-595 and E-1559 are used to generate control limits. The counterpart to outgassing or even the more typical volatile evaporation is called Dynamic Particle Generation which can be as significant of a problem as outgassing. The term Dynamic Particle Generation describes what happens when contaminants are created by being forced from a lubricated ball screw, bearing, or gear system into the operating environment. These contaminants could include base oil constituents, thickener particles, additives, etc. all of which could be volatile or non-volatile.

The manner in which these contaminants are freed from the lubricant system is through dynamic mechanical action whether it be rolling, sliding, or a combination of both. This study will begin to investigate and illustrate that factors like mechanical and chemical compatibility, friction, speed, etc. all have an effect on the amount of contamination generated through particle generation. I will also illustrate that physiochemical effects between lubricating fluids and thickeners play a key factor as well.

Aside from the space application environment, materials can also be contaminated through the manufacturing process even if done in a clean room environment. In these environments, the focus is typically on the quality of the air in the room and it has long been known that lubricants are a source of contamination in cleanroom and vacuum environments. Historically, in order to alleviate the worries of many manufacturers, the solution over the last twenty years has been to ultrafilter<sup>1</sup> the lubricant to reduce the number of particles in the lubricant and the size of them.

---

\* Nye Lubricants, Inc., Fairhaven, MA

There are three levels for cleanliness in a grease:

- Unfiltered grease – Can contain particles larger than 75  $\mu\text{m}$ .
- Filtered or so-called “Clean” grease – For example MIL-G-81322 Aircraft grease cannot have any particles greater than 75  $\mu\text{m}$  and there must be fewer than 1,000 particles/ $\text{cm}^3$  between 24  $\mu\text{m}$  and 74  $\mu\text{m}$ .
- Ultrafiltered or “Ultraclean” grease – Such as MIL-G-81937 must not contain any particles greater than 35  $\mu\text{m}$ . In addition to this it cannot have more than 1,000 particles/ $\text{cm}^3$  between 10  $\mu\text{m}$  and 34  $\mu\text{m}$  in size.

While these processes will certainly help remove or break up bulk and “hard” contaminants which will lead to smoother operation, reduced vibration, and lower noise in bearings, ball screws, and other motion applications, it may have little effect on the amount of particles “shed” or generated from a lubricant in a dynamic condition. So this leaves thoughts about what effect the lubricant truly has on this phenomenon and how does the base fluid, thickener, additive, and manufacturing processes effect this property and ultimately the application environment around it. The first step to investigate this new area of lubricant properties required the construction of a new test apparatus and creation of an accurate and repeatable test method [5].

#### Objective for Testing

The primary purpose of this study was to use a newly developed test method and apparatus that could be used to accurately and repeatedly measure the Dynamic Particle Generation of a lubricating grease. This study centered around two different types of lubricants, Perfluoropolyethers (PFPE), and Multiply-alkylated cyclopentanes (MAC). MAC's are composed of one cyclopentane ring with two to five alkyl groups substituted on the ring. The synthesis is performed by reacting dicyclopentadiene with various chain length alcohols producing a lubricant with a various range of physical properties [7]. PFPE's are produced through the oxidation of hexafluoropropylene and are fully fluorinated oligomers that contain fluorocarbon links containing oxygen atoms. Two PFPE's (Braycote® 601EF and NyeTorr® 6300) as well as three MAC lubricants (Rheolube® 2000, 2000F, and NyeTorr® 6200) were tested in this study

**Table 1. Materials tested in study**

	<b>Braycote 601EF</b>	<b>NyeTorr 6300</b>	<b>Rheolube 2000</b>	<b>Rheolube 2000F</b>	<b>NyeTorr 6200</b>
<b>Base Chemistry</b>	PFPE	PFPE	MAC	MAC	MAC
<b>Thickener</b>	PTFE	PTFE	Sodium	PTFE	PTFE

The key factors of this study will be:

1. To study the particle generation tendencies of different aerospace lubricants evaluated under dynamic conditions.
2. To examine the effect that speed plays on the particle generation of a particular system
3. To examine the profile of the particle generation results plot; that is how the system behaves with respect to time and number of particles generated.

#### **Dynamic Particle Generation Background**

To compare the Dynamic Particle Generation characteristics of various lubricating greases, a custom test apparatus was designed and built to detect, analyze, and classify the products being examined. As this is a newly created test method and fixture, a Design of Experiments was put together to investigate repeatability, variability, and statistical significance [5].

The core of the test apparatus is a high-precision ball screw assembly meant for cleanroom and low outgassing applications. This ball screw design was used due to the fact that when lubricated correctly and under light load, it experiences virtually zero wear on its components. Since a ball screw assembly utilizes



a system of rolling elements, the amount of frictional wear on any components especially under no load is greatly reduced. This allows us to study the particle generation solely based on the lubricant and speed of the test. With the addition of a lubricant that provides a protective film between all surfaces, the main component of wear on the system is the lubricating grease, which then generates the particles being examined in this study. This ensures that the particles generated in the dynamic system are purely generated from the lubricating grease. Please see Figures 1 through 4 for the Dynamic Particle Generation testing apparatus.

In Figure 1, the testing apparatus is illustrated showing the clean air supply that moves over the testing equipment, the ball screw, and tunnel. To supply clean, filtered air to the system, a laminar flow clean air handler supplies clean ISO 2 Class air to the system. The air handler can deliver filtered air at a range of velocities, depending on operator input, but for the sake of repeatability and comparison, a velocity of  $1 \text{ m/s} \pm 0.25 \text{ m/s}$  was used for all testing. This value was decided on after investigating the average volume of clean air turned over in a clean air environment. This filtered air passes over the test system as the ball screw assembly operates for the length of the test.

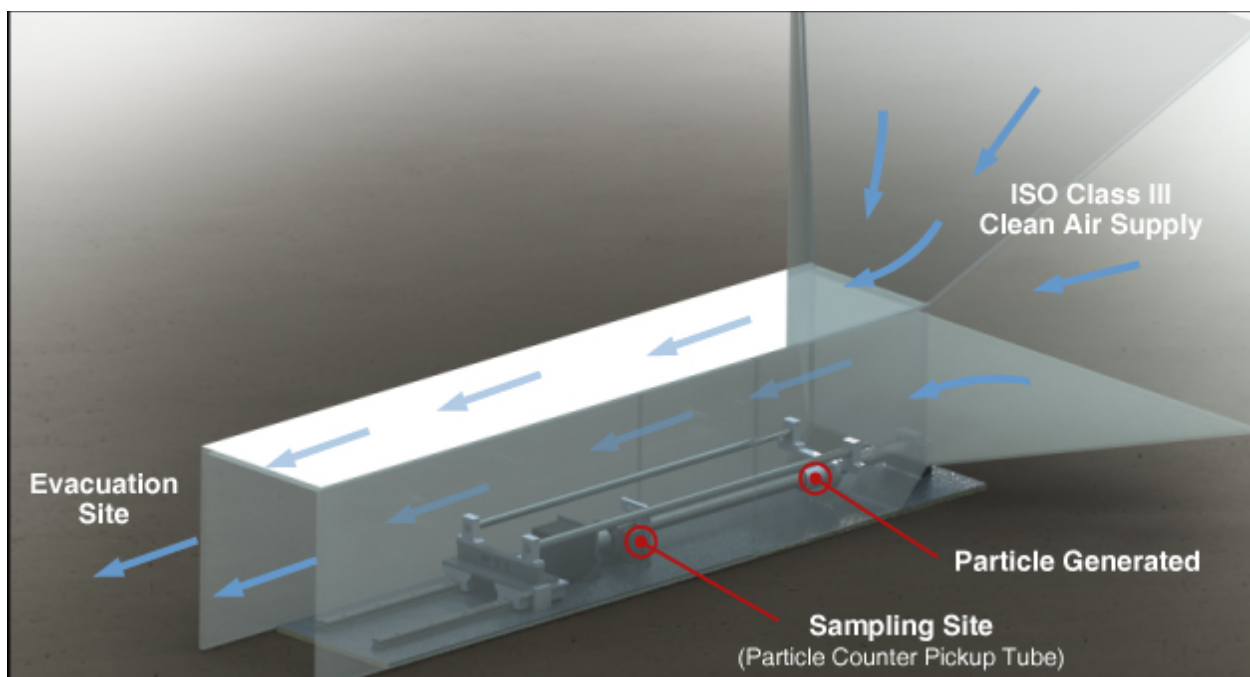


**Figure 1. Dynamic Particle Generating test apparatus**

Figures 2, 3, and 4 shows a more detailed view of the particle generation test unit and components.

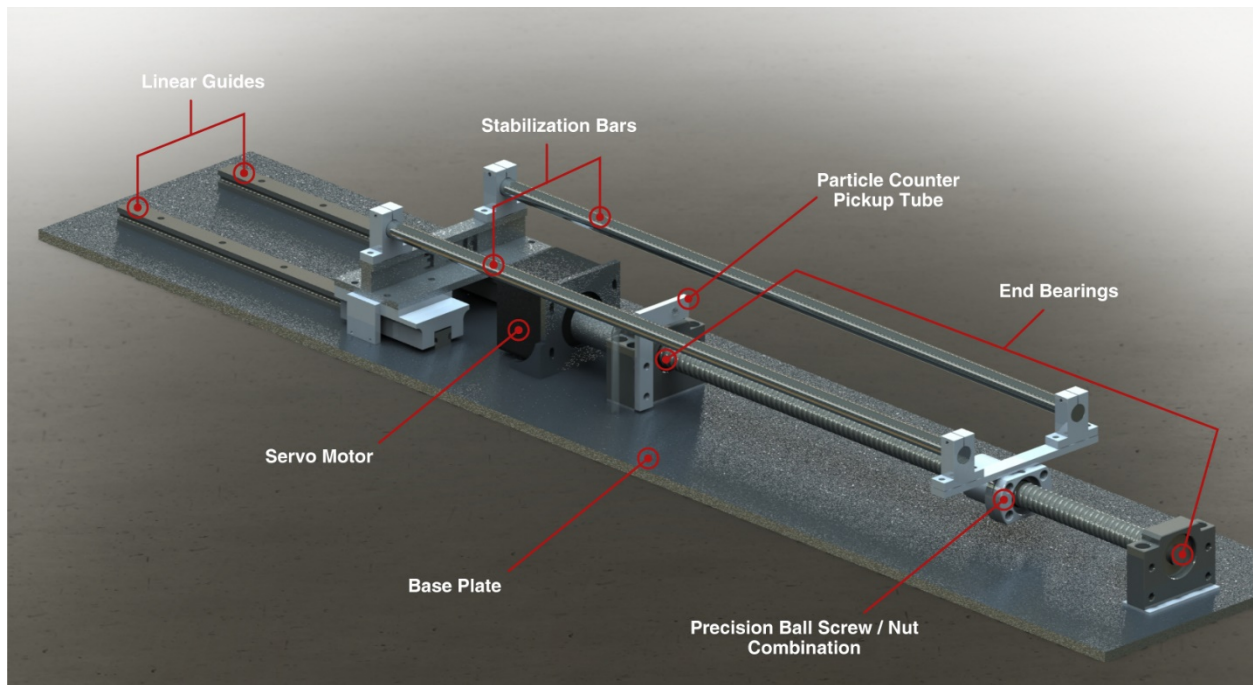


**Figure 2. Dynamic Particle Generating test apparatus**

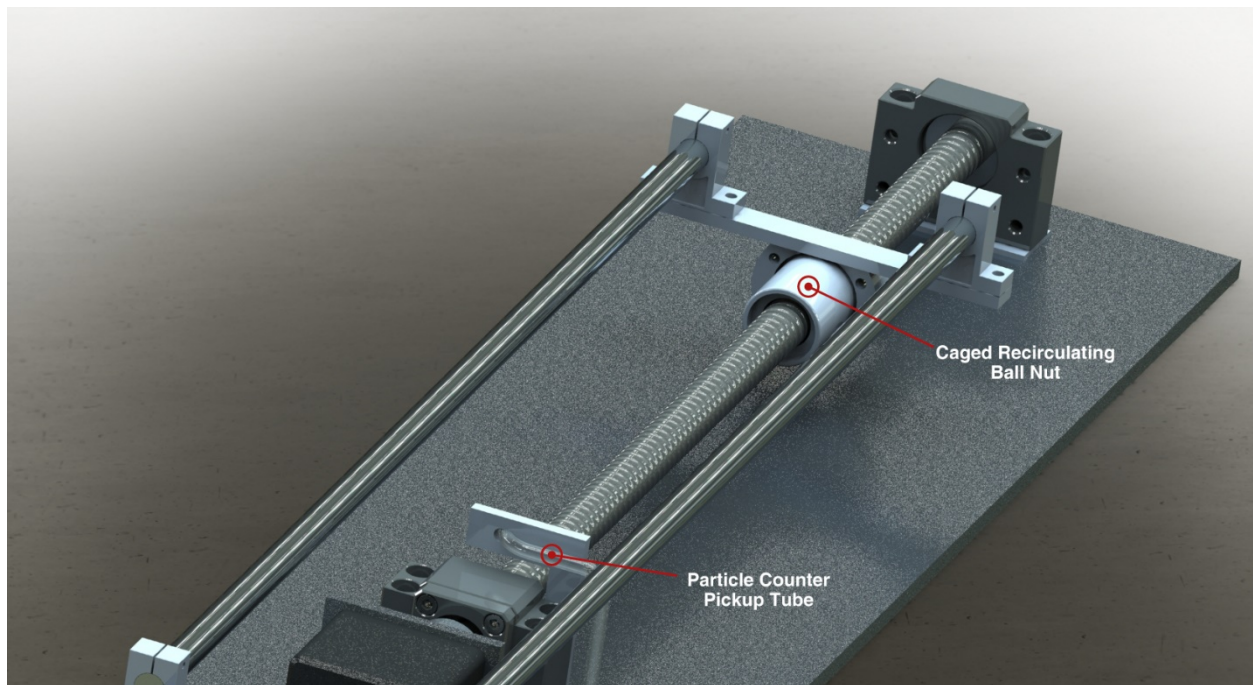


**Figure 3. Dynamic Particle Generating test apparatus**

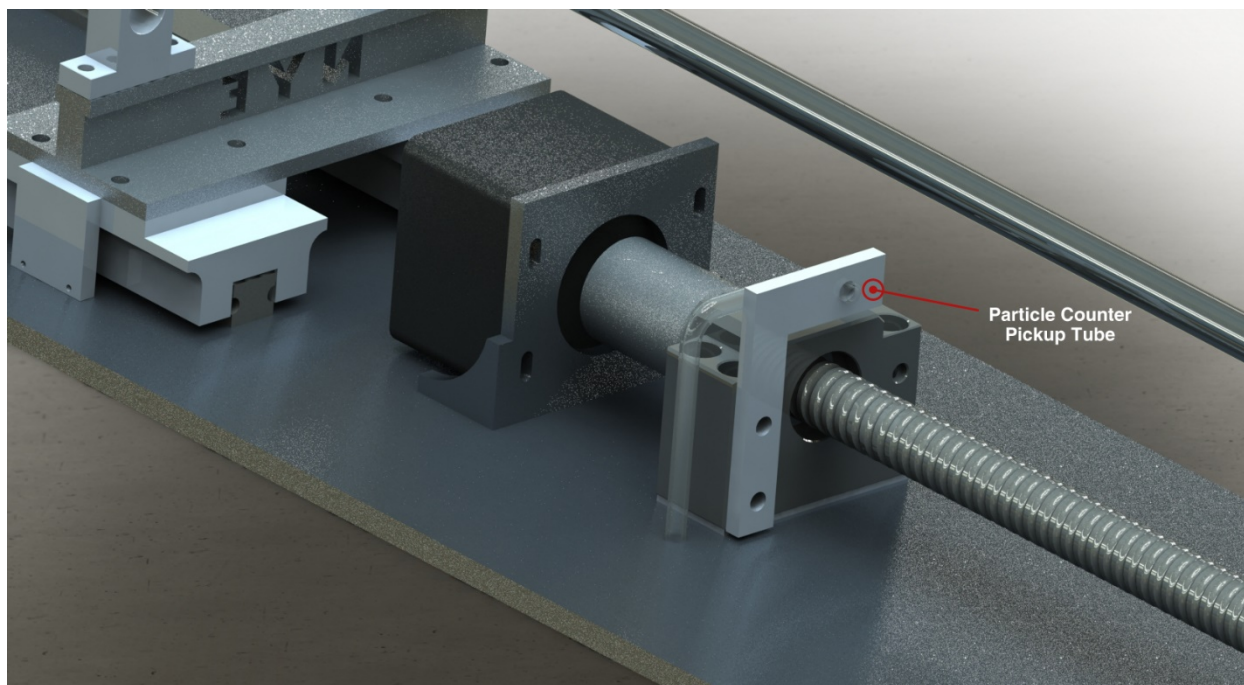


**Figure 4. Dynamic Particle Generating test apparatus**

Particles are collected via an inlet tube mounted at the end of the ball screw assembly (Figure 4.). The location of the pick-up tube is key, as it captures only particles generated by the grease on the ball screw, and none generated by the servo motor, bearings, linear guides, or flex coupling. The pickup tube leads to a Light-scattering Airborne Particle Counter. The particle counter features simultaneous particle measurement of sizes from  $0.1\ \mu\text{m}$  and above all the way to  $5\ \mu\text{m}$  and above via the use of a transverse light-scattering system which provides the most accurate and repeatable measurements available.

During the test, a particle count profile is then constructed, plotting the count of each category vs. test duration. This profile chart is an important asset to have in order to understand the behavior of the grease being run as two greases may share the same cleanliness value (ISO, JIS, or FED), but may have completely different particle distribution profiles over the duration of the test.

The Dynamic Particle Generation test apparatus has the ability to run at speeds from 200 to 2400 RPM but in this study, we looked at 200, 1200, and 2400 RPM respectively. This translates to 0.02, 0.1, and 0.21 m/s of linear velocity, respectively. Comparison between greases should only be conducted at like rotational speeds, as particle generation typically increases as RPM increases.

Grease is applied to the ball screw assembly at 200 RPM with a sample volume of 2 cc being applied via syringe and a 10-cycle run-in to evenly distribute the grease. The test begins with the motor stationary while the particle counter takes a series of background readings. The number of readings taken is user defined. The average of these background readings are subtracted from the particle count under dynamic conditions before ISO, JIS, or Federal Classes are calculated. This ensures that the particles being counted are only those produced by the grease and not the filtered air passing over the system.

At the conclusion of the test, the collected data is compared against the particle classification tables and the ISO, Federal, and JIS classifications are determined. The ISO cleanliness levels are determined by the following formula and Table 2.

$$C_n = 10^N \times [0.1/D]^{2.08} \quad \text{from [2]}$$

Where

$C_n$  = represents the maximum permitted concentration (in particle/m<sup>3</sup> of air) of airborne particles that are equal to or larger than the considered particle size;  $C_n$  is rounded to the nearest whole number

N = ISO class number, which must be a multiple of 0.1 and be 9 or less

D = the particle size in microns

**Table 2. ISO Particle Classifications in Air**

CLASS	Number of Particles per Cubic Meter by Micrometer Size					
	0.1 micron	0.2 micron	0.3 micron	0.5 micron	1 micron	5 microns
ISO1	10	2				
ISO2	100	24	10	4		
ISO3	1,000	237	102	35	8	
ISO4	10,000	2,370	1,020	352	83	
ISO5	100,000	23,700	10,200	3,520	832	29
ISO6	1,000,000	237,000	102,000	35,200	8,320	293
ISO7				352,000	83,200	2,930
ISO8				3,520,000	832,000	29,300
ISO9				35,200,000	8,320,000	293,000

**Table 3. Federal Standard Particle Classifications in Air**

CLASS	MEASURED PARTICLE SIZE (MICROMETERS)				
	0.1	0.2	0.3	0.5	5
1	35	7.5	3	1	
10	350	75	30	10	
100		750	300	100	
1,000				1,000	7
10,000				10,000	70
100,000				100,000	700

#### Repeatability and Statistical Significance

To validate this new experimental test method, materials were tested with a minimum of three replications. Afterwards a statistical analysis of variance was performed on the sample sets to look for any statistically significant differences. Different lots of the same material and different sections of a specific batch were also tested. The results of this statistical analysis can be found in the technical paper entitled "Investigation into the Dynamic Particle Generation of Lubricating Greases" [5].

## Results and Discussion

Table 4 and 5 summarizes the ISO and Federal classifications for the five greases that were studied in this experiment at 200, 1200, and 2400 RPM respectively.

**Table 4. ISO Classification of Aerospace Greases**

	<b>Braycote 601EF</b>	<b>NyeTorr 6300</b>	<b>Rheolube 2000</b>	<b>Rheolube 2000F</b>	<b>NyeTorr 6200</b>
<b>200 RPM</b>	ISO 1	ISO 1	ISO 1	ISO 1	ISO 1
<b>1200 RPM</b>	ISO 4	ISO 4	ISO 4	ISO 2	ISO 4
<b>2400 RPM</b>	ISO 5	ISO 5	ISO 6	ISO 3	ISO 5

**Table 5. Federal Classification of Aerospace Greases**

	<b>Braycote 601EF</b>	<b>NyeTorr 6300</b>	<b>Rheolube 2000</b>	<b>Rheolube 2000F</b>	<b>NyeTorr 6200</b>
<b>200 RPM</b>	Class 1	Class 1	Class 1	Class 1	Class 1
<b>1200 RPM</b>	Class 100	Class 100	Class 100	Class 1	Class 100
<b>2400 RPM</b>	Class 1,000	Class 1,000	Class 10,000	Class 100	Class 1,000

It is apparent from Tables 4 and 5 that at the lowest rotational speeds, all of the lubricants performed equivalently. As the speeds increased as well as friction between the lubricants and the bearings, the materials started performing differently.

The two PFPE greases received identical ISO and Federal ratings so they appear to be equivalent from the perspective of how much particle contamination they generate into the environment. Looking at the particle generation graphs in Figures 5 and 6, a different story is told as the curves are dramatically different at 2400 RPM. While both of these greases are PTFE thickened and made from similar viscosity linear structured PFPE fluids, their tendency to generate particles less than 1  $\mu$  is very different. It is well known that PTFE and PFPE chemistries have weak bonding strengths (Van Der Waals) between the molecules and surfaces during sliding motion [6].

However, the difference seen here between these two materials is most likely the effect of the difference in PTFE used in the material. There are many different grades of PTFE as well as manufacturing processes ranging from emulsion formed polymers to irradiated polymers. These differences in manufacturing processes as well as residuals of surfactants and other chemical processing aids can possibly have a significant effect on the ability of the PFPE and PTFE to bind into a strong lubricant system. This combined with differences in the particle size distribution of the PTFE polymers creates factors that generate more environmental contamination through particle generation.



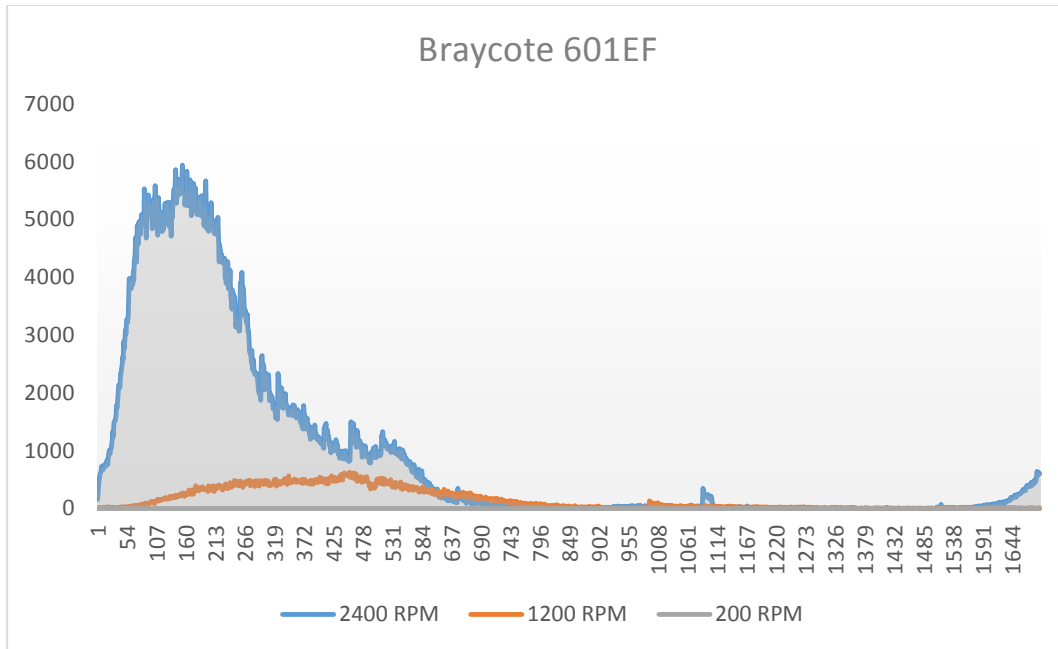


**Figure 5. Dynamic Particle Generation of Braycote 601EF**

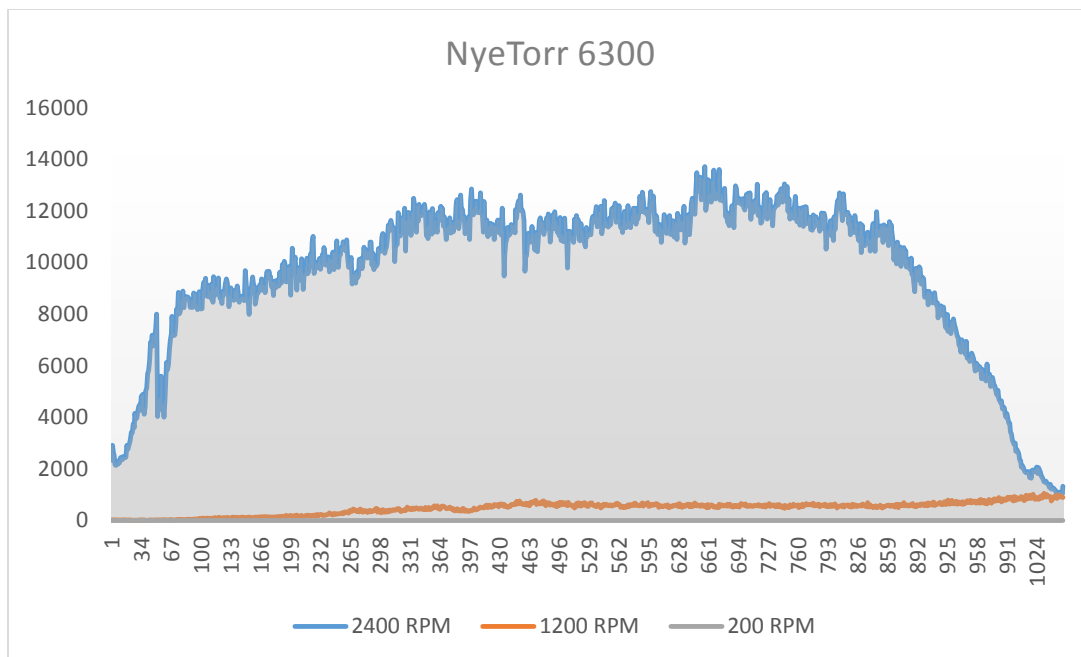


**Figure 6. Dynamic Particle Generation of NyeTorr 6300**

The results for the MAC-based greases showed some potential performance benefits compared to the PFPE lubricants but it did depend greatly on thickener. The Rheolube 2000 and 2000F share the same base fluid while the NyeTorr 6200 utilizes the Pennzane Ultra X-2000 base fluid which is processed additionally to reduce its outgassing. The sodium thickener used in the 2000 grease is apparently sensitive to the shear as the material generates more particles as the rotational speed and sliding friction increases. In Figure 7, the particle generation trend can be seen to continually increase over time. The majority of these particles were small (less than  $1\ \mu$ ) and the continual increase in the amount detected per cubic cm of air is most likely attributed to the processing of the thickener/grease and the bonding strength of the sodium thickener resulting in the ultimate shear stability of the thickener.

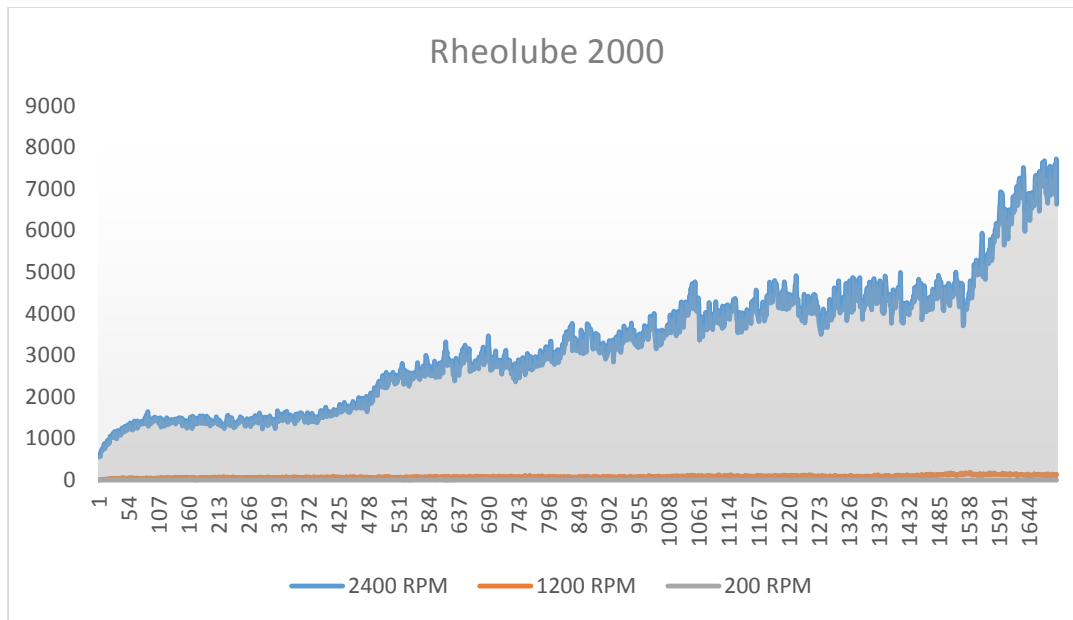


**Figure 7. Dynamic Particle Generation of Rheolube 2000**

As the 2000F and the 2000 grease both share the X2000 base oil and similar additive packages, we can see the direct effect of the thickener of the particle generation. It is well known that the MACs possess superior film strength and adhesion to metal surfaces when compared to PFPE's so we would expect low particle generation as the probability of particles being shed to the air would be lower. With the thickener of the 2000F having strong covalent bonding within the PTFE molecules [6] combined with the strong film strength of the MAC, it showed to be the superior lubricant in this study for particle generation.

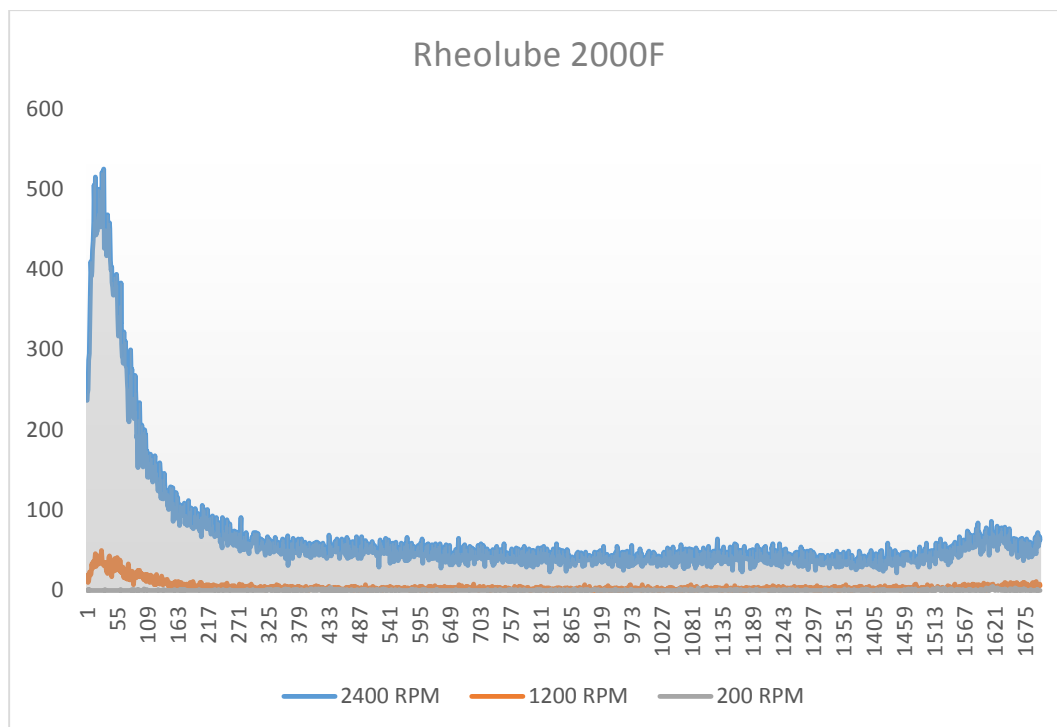


**Figure 8. Dynamic Particle Generation of Rheolube 2000F**

The results in Figure 9 for the NyeTorr 6200 which is made from the X-2000 Ultra (further refined MAC) and PTFE are very interesting as the amount of particle generation trends higher throughout the entire test than the 2000F and is classified one order of magnitude higher in both the 1200 and 2400 RPM tests. Beyond this difference, the NyeTorr 6200 generated ten times the amount of particles less than 1  $\mu$  when compared to the 2000F. Although this is within the allowed error for the Federal Cleanliness standards, it is a significant difference when it comes to space critical applications. The issue is certainly not created by volatility as the X-2000 Ultra has lower ASTM E-595 results as well as Knudsen Vapor Pressures compared to the traditional X-2000 fluids. Since the manufacturing process, additives, and PTFE polymer type are all the same, this leads us to conclude there must be some effect from the X-2000 Ultra on the particle generation of the 6200.

While the X-2000 Ultra contains less volatiles and has demonstrated that it has superior outgassing properties to the standard grade, the particle generation is negatively affected. The reasons for this could be as simple as the refinement of the X-2000 has caused a change in the tribological properties of the fluid which has led increased friction between the fluid, PTFE polymer, and bearing surface. This additional friction could lead to degradation of the lubricant which then leads to shedding of particles from the lubricant system. Another possible cause for this particle generation could also be the removal of something from the X-2000 fluid that helped with the film strength or the compatibility with the PTFE polymer and its removal has promoted the increase in particle generation.

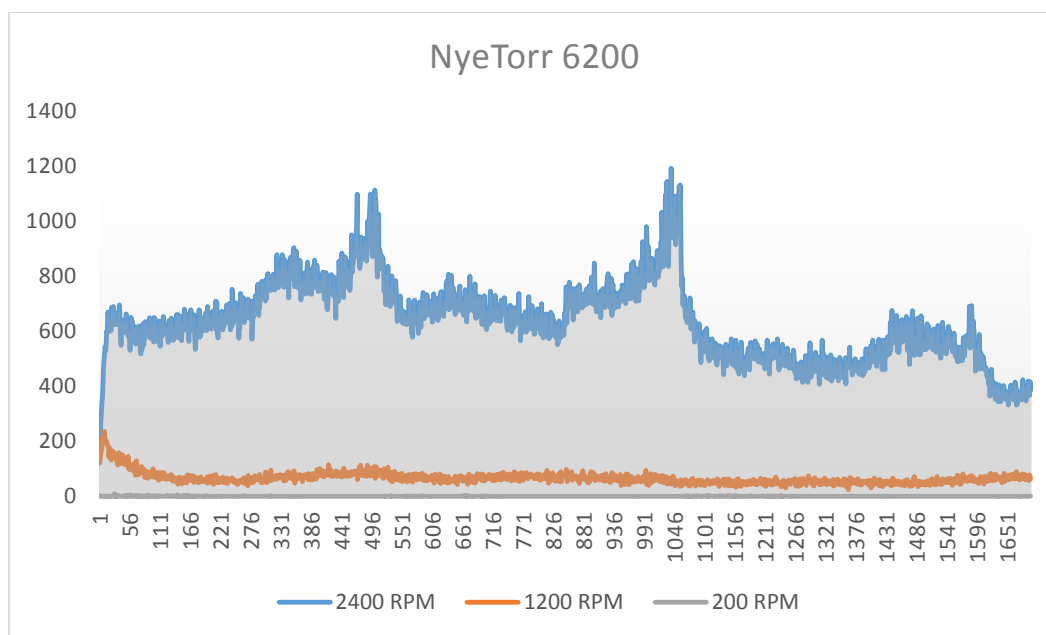


**Figure 9. Dynamic Particle Generation of NyeTorr 6200**



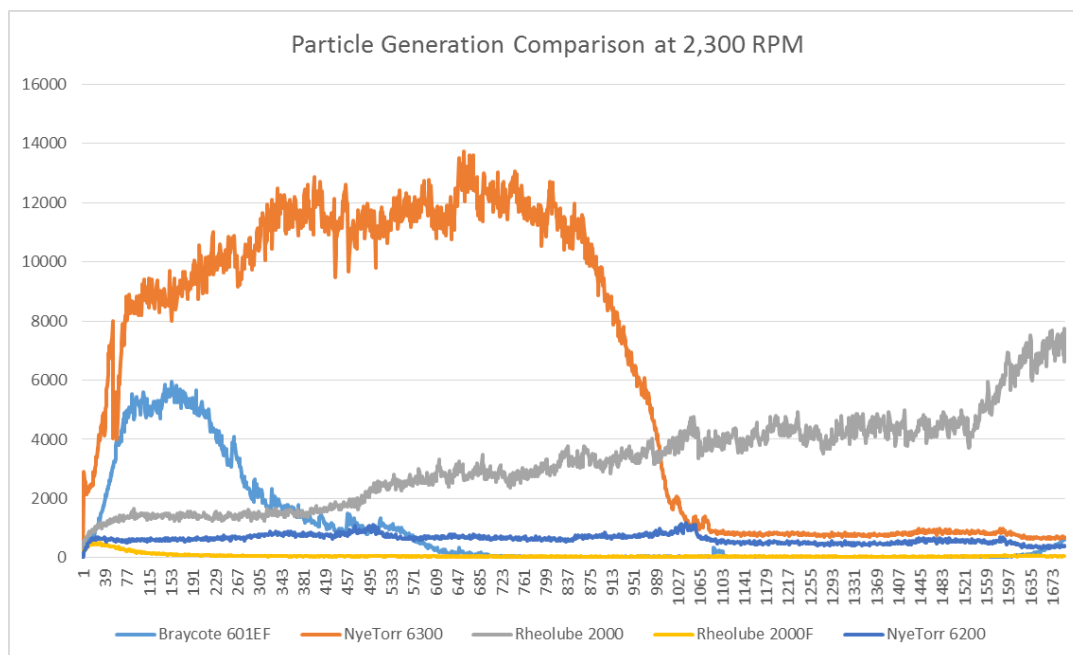


**Figure 10. Comparison of the Dynamic Particle Generation**

In Figure 10, all of the samples tested in this study have been graphically plotted on the same axis to visually illustrate the differences in the particle generation between different materials. The 2000F clearly has the best performance of any of the materials tested.

### Conclusions

Determining the volume of contamination generated from a lubricant through particle generation in dynamic conditions is a new area just starting to be explored. As presented in this study, many factors play into the behavior of a grease in respect to particle generation characteristics. Variables such as run speed, base oil chemistry, and thickening agent properties all play into how much contamination a lubricant will generate through particle generation.

This study has also shown that the 2000F which is a PTFE-thickened MAC grease produced the least amount of contamination due to particle generation as well as the least amount of change in particle generation over speed. It was also illustrated that while MAC lubricants have an advantage over PFPE base ones, it certainly depends on other factors like the thickener, additives, processing, etc. This dependency was clearly seen in the sodium-thickened Rheolube 2000. The organic soap thickener forms a strong matrix of entanglements but at higher speeds it generated more particles as a result of the shear stability of the sodium soap vs. the PTFE-thickened greases. This is due to the fact that PTFE is a very stable molecule with Carbon-Fluorine bonds being one of the strongest known. This combined with the higher RPM creating higher shear on the thickener at the metal surface causing more particles to generate over time. This leads to the conclusion that PTFE is superior to sodium soap in particle generation and based on the differences in thickener stability under the shear conditions of the test.

The ability to plot particle generation over time and see differences in the distributions of various materials, will help us to form hypothesis about particle generation over time using normalized probability. Utilizing this type of analysis can also be used to predict lubricant service life. From these estimations, we could also look into ways to predict saturation by contamination in a space mechanism or the probability for success/failure when using a certain lubricant.

### **Future Work**

The expansion of this work will include using Residual Gas Analysis to determine the molecular weight and chemical species of all contamination materials being generated in the particle generation test. Further research will also be placed on the difference of PTFE polymers, X-2000 Ultra, manufacturing techniques, etc. and how this relates to bonding strength and in turn particle generation. We will also investigate the particle generation of a rolling element bearing system in atmospheric and vacuum conditions. The main goal of this work is to create a model and methodology to be able to predict the failure probability of a mechanism due to contamination when a certain lubricant is used.

### **Acknowledgements**

I would like to thank my colleagues in the Application Development and Validation Testing Lab at Nye Lubricants Inc. who conducted the Dynamic Particle Generation testing, specifically Mason Wood. I would also like to thank William Galary for all of his support and consultation about the Clean Room Industry and its technologies. Finally I would like to thank Gus Flaherty for his work with me on designing and constructing the Dynamic Particle Generation testing equipment.

### **References**

- [1] Galary, William: Ultraclean Grease. Journal of Advancing Applications in Contamination Control 1999; Volume 2, No. 7:23-27
- [2] Cleanrooms and associated controlled environments Part 1: Classification of air cleanliness. ISO 14644-1 1999;
- [3] Classification of air cleanliness for cleanrooms. JIS B 9920 2002;
- [4] Cleanroom and Work Station Requirements, Controlled Environments. Federal Standard 209 1963;
- [5] Galary, Jason and Flaherty, Gus: Investigation into the Dynamic Particle Generation of Lubricating Greases. NLGI Annual Journal, 2016
- [6] Lince, Jeffrey and Fleischauer: Solid Lubricants. Space Vehicle Mechanisms, 1997
- [7] C.G. Venier, E.W. Casserly, Lubricants comprising novel cyclopentanes, cyclopentadienes, cyclopentenenes, and mixtures thereof and methods of manufacture, US 4,929,782 (1990).

# **APM for a Constellation Intersatellite Link – EM Qualification and Lessons Learned**

Frank Härtel\* and Horst Kozilek\*

## **Abstract**

For an Intersatellite Link (ISL) of a future constellation program, a study phase was initiated by ESA to design a mechanism for Radio Frequency communication. Airbus DS Friedrichshafen (ADSF) proposed a design based on the Antenna Pointing Mechanism (APM) family with modifications that met the stated needs of the constellation. A qualification program was started beginning in September 2015 to verify the launch and thermal loads and the equipment performance (Radio Frequency, Pointing, Microvibration and Magnetic Moment). Technical challenges identified with the Engineering Model will be discussed within this paper.

## **Introduction**

The heritage of ADSF for Antenna Pointing Mechanisms is more than twenty years, with a series of different pointing mechanisms. Those mechanisms were designed to deploy and point large dish antennas as well as small antenna horns for the X- and Ka-Band.

Generally the requirements of such mechanisms include the velocity ( $<10$  deg/sec), the lifetime (of more than 5 years), and the accuracy ( $<0.2$  deg). These requirements are not too demanding, as the Antenna points towards the ground station and the satellite is in a low-Earth orbit.

For the current constellation, these requirements are more demanding. As the Intersatellite Link shall establish the RF communication between two MEO satellites, a very fast pointing velocity is needed ( $> 60$  deg/sec). A higher precision of  $<0.125$  deg and an overall lifetime of 12 years are also required. These changes had a significant impact on the heritage design. The actuation chain had to be modified with larger motors and bearings. This led to an intensive redesign process with an increased mass. The impacts of these modifications have been verified within the qualification program, which will be presented, including results, within this paper.

## **Intersatellite Link Antenna Pointing Mechanism Background**

For a constellation program, RF Intersatellite Links between single satellites can support ranging and communication for uploading mission data or tele commands. These data shall be uploaded from one single ground station to the next reachable satellite and transmitted by the Intersatellite Link (see Figure 1) to further dedicated satellites. For this function each satellite has to be equipped with two Antenna Pointing Mechanisms for data transfer in the K-Band.

To establish such a constant network, the APM has to be able to point in each vector direction of the hemisphere. Additionally the movement towards a new pointing destination has to be very quick in order to enlarge the time for the data link communication. ADSF has a substantial heritage in building APMs for communication to ground applications. ADSF follows the approach of elevation over azimuth axis pointing systems. These systems have proven their high reliability and robustness over a multitude of different missions and accumulated a time in orbit of more than 35 years.

---

\* Airbus Defence and Space, Friedrichshafen, Germany

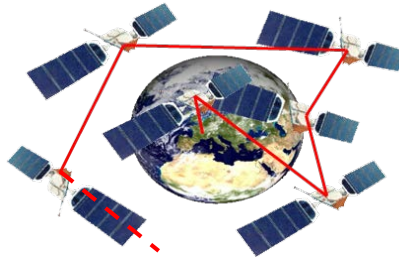


**Figure 1. Intersatellite Link – Principle**

For constellation programs, the components' cost have a higher impact than in nominal single satellite missions. A consequent design-to-cost approach was followed using open-loop stepper motors and as many standard off-the shelf elements as possible. In Figure 2 the different elements can be seen.

An elevation over azimuth axes approach was used for the APM design. An indirect (using gear wheels) actuation principle was chosen to ameliorate the power (holding current reduction) and pointing (gear ratio) budget. The Azimuth axis is supported by a bearing in O-configuration. In the azimuth axis there is a slip ring installed, transferring the power and signals to the elevation stage. The RF signal is transferred using a waveguide and two rotary joints (one to the spacecraft and one to the elevation stage). On top of the azimuth stage a stiff supporting structure (Yoke) is installed, providing the interfaces for the Elevation Axis with its Antenna Supporting Bracket, the elevation actuation chain (comparable to Azimuth actuation chain), and the interface for the HRM. The HRM is locking all relative movements of the Azimuth and Elevation Stage by transferring the loads into the spacecraft structure.

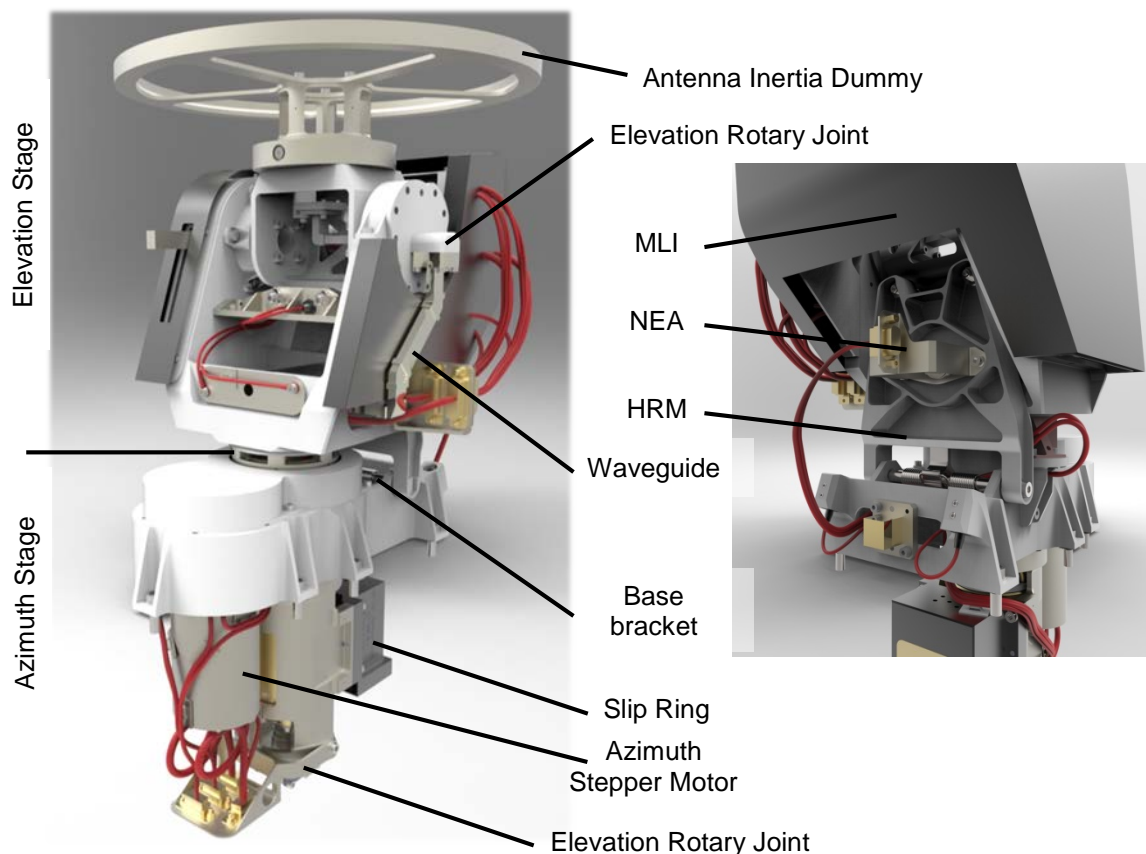


**Figure 2. Intersatellite Link Mechanism**

Compared to the heritage projects, the motor size had to be significantly increased in order to achieve the demanding velocities and motor torque margins according to ECSS. Besides this, the reference sensor of the azimuth axis had to be changed (2.7 million activations) from a mechanical precision switch to a Hall sensor switch. A demanding change was also the adaptation of the thermal management. As a constellation by nature has an orbit with a very high sun illumination and an orbit with almost no sun illumination; the variety of the thermal environment is more complex than for a sun-synchronous orbit.

All described changes led to increased masses and therefore higher vibration loads. The Hold Down and Release Mechanism and the bearings had to be adapted in order to handle these increased vibration loads.

### Qualification Approach

An Engineering Model (EM) philosophy was decided. The EM qualification approach is shown in Figure 3. The qualification test program was accompanied by a bearing breadboard test and a life test with a simplified life test model. This life test was started in an early project phase. The life test verifies the demanding life time requirement of 12 years active in-orbit time with 2.6 million revolutions.

As a cost saving action for the life test, it was decided that the life test model will be driven by Commercial Off-the-Shelf (COTS) electronics.

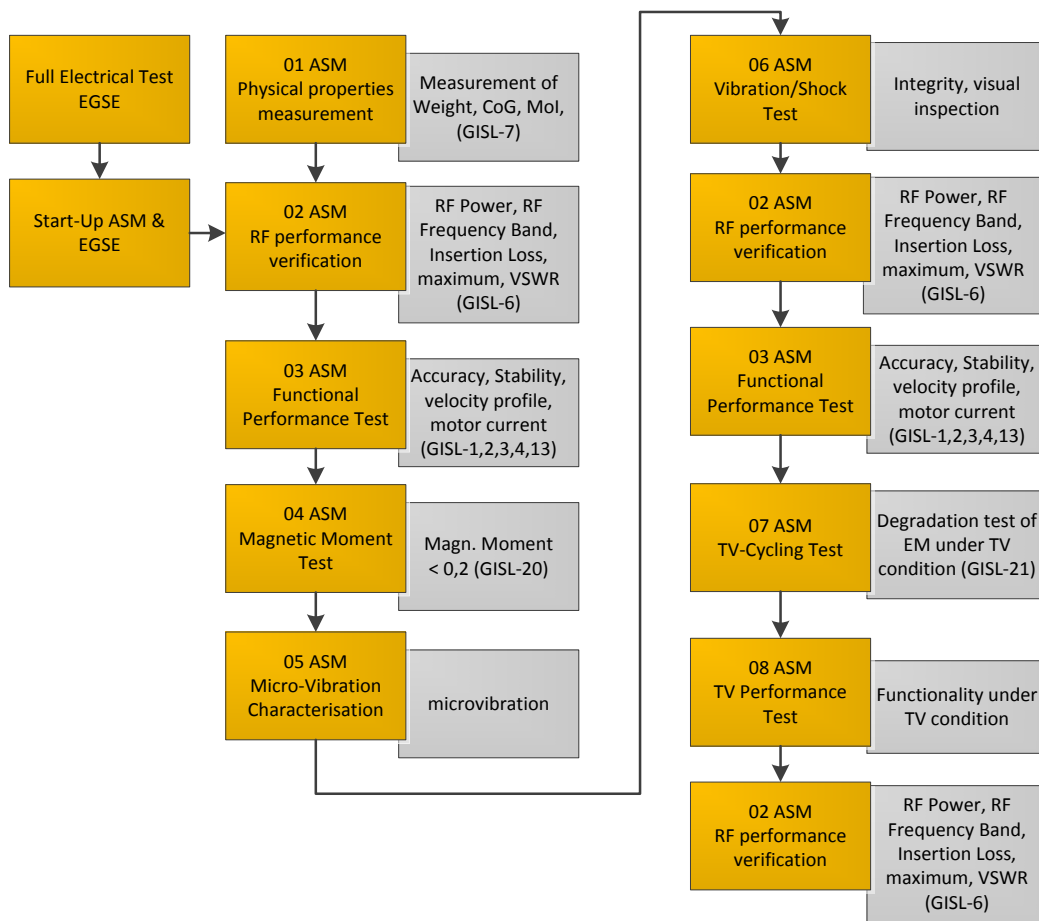


Figure 3. Qualification Test Sequence

During the start-up of the APM with COTS electronics no significant anomalies (e.g., wrong cabling or communication error) were found. An overall mass of 10.8 kg (as designed) was verified during the physical measurements.

## Testing

All testing was to be performed in the Friedrichshafen testing facility. Due to availability at the vibration test facility, it was decided to perform the vibration test at Airbus DS Ottobrunn. After a non-conformance report, the test was continued in Friedrichshafen.

### Bearing Characterization Breadboard Test

As the chosen bearings were increased in diameter compared to the heritage design, a breadboard test was performed to measure the impact on torque with the required velocity and temperature inputs. A customizable (all different types bearings used for the APM can be installed) bearing breadboard test setup was developed and manufactured. The test setup provides the ability to compare the influence of different bearing types, lubrication, materials and combinations. Performing the bearing characterization test as a breadboard test supports monitoring the quality of the procured components and provides the input data for the torque margin and the bearing analysis.

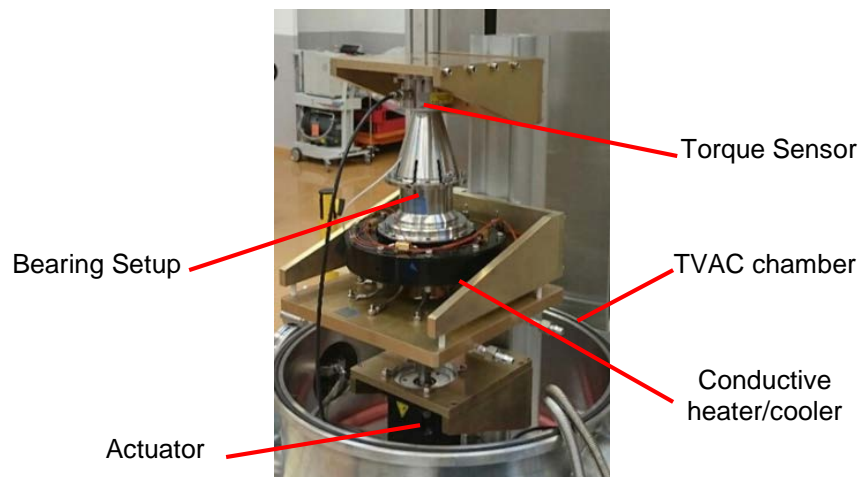


**Figure 4. Bearing Characterization Test Set-up in a TV chamber**

ISL bearing characterization was performed at seven different velocity levels (1 rpm, 3 rpm, 17 rpm, 25 rpm, 35 rpm, 45 rpm and 100 rpm) and four different temperature levels (-40°C, 0°C, 25°C and 65°C). Each characterization was started with a run-in test, turning the bearing clockwise and counter-clockwise for several minutes. After the run-in, the different velocity levels were repeated multiple times, deriving multiple resistive torque measurements.

Comparing the results of the measurements (see Figure 5), it can be concluded that the bearing performance was as expected in the torque margin analysis. The worst case torque assumed in the analysis was 75 N-mm and verified by a measurement of 72 N-mm (-40°C measurement). At a lower velocity level a higher, but still acceptable, deviation of 6 N-mm between analysis and measurement was found.

An interesting phenomenon was the higher rate increase of the resistive torque for hot and fast conditions. This was not investigated further, but viscous effects could be a possible source of such a behavior.

Breadboard testing gives Airbus DS GmbH the confidence of having a sufficient torque margin and that the friction behavior of the preloaded bearing configuration is modelled correctly.

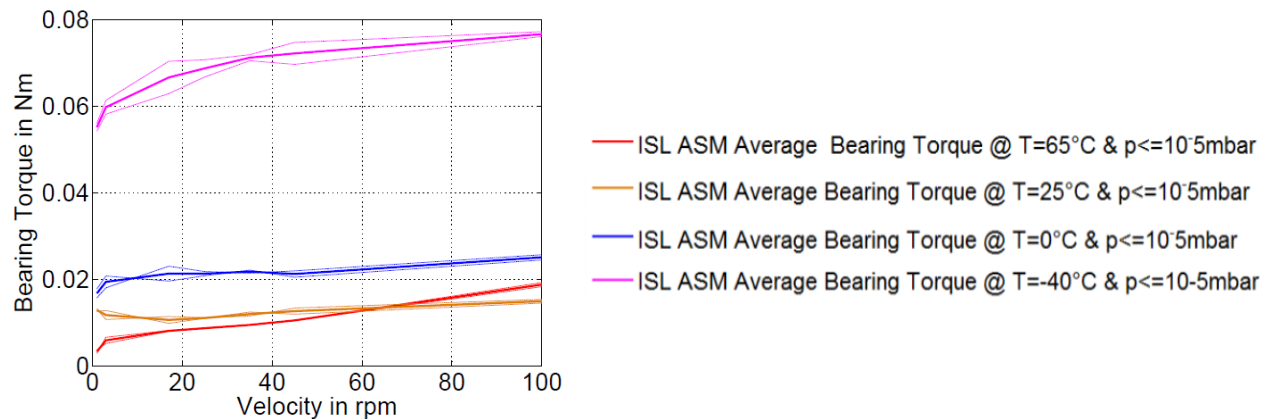


**Figure 5. Results of the Bearing Characterization measurements**

### Life Test

The initially planned life testing at the end of the qualification campaign was skipped in favor of a separate life test program with a simplified model running in parallel to the EM test campaign. The aim was to provide a life-tested mechanism at the end of the 1.5-year EM design and qualification phase.

Cost savings for the life test were realized by performing the test with the azimuth stage only. This solution was selected as the loads for the azimuth bearings (environmentally and in-orbit) were considered to be the worst case. The azimuth motor and both gears have the higher number of revolution during in-orbit life.

Prior to life testing, a proper environmental conditioning was essential for the credibility of the life test. This environmental conditioning consists of a vibration test and a thermal settling. The thermal settling in general is not a problem, and was performed directly before the start of the life test under the specified acceptance temperature level in a thermal vacuum chamber.

A higher effort was the task to set up the proper vibration level of the Life Test Model. The applied load levels for the life test model vibration test were not known or they had a low confidence level. This was the case due to the reconfiguration of the elevation axis and due to the early stage of the development phase. This conflict leads to a very high effort in the estimation of the vibration test levels for the life test model. The goal was to load the single components as high as possible (identical to the EM), but not to damage the bearings.

The decision was made to estimate the test levels for the center of gravity. With those test levels it was possible to predict the loading of the bearings and the actuator during the vibration test.

Bearing loads were applied with an elevation stage dummy mass implemented in the test setup. Initial approach to leave the dummy mass unsupported at the Hold-Down and Release Mechanism (HRM) led to unacceptable high bearing loads. An additional support structure became necessary and was implemented in the test setup. Designing and implementing a support structure, different from the EM launch lock design, required much more effort than expected. The additional change of the initial motor location induced further changes of the life test set-up. Those changes consumed the schedule margin for life testing.

During the performance of the accelerated life test, the time span of no motion (27 sec), due to communication, was removed. This was necessary to perform the 12-year in-orbit operation within about



7 months. Active cooling of the motor was necessary as the motor was continuously operating during the life time test without any interruption. Without cooling the motor would heat up too much.

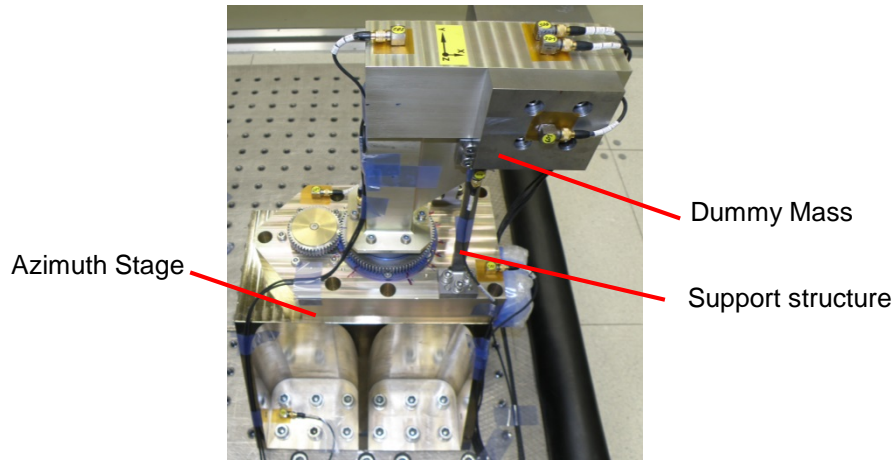


**Figure 6. ISL Life Test Model Vibration Test Setup**

The life test motion set was derived from the current link budget analysis. The motion set of 25 positioning commands was to be repeated during the whole life time test while the environmental condition was changed. The life test also verifies the rotation capability of the motor bearings, the correct function of the planetary gear stage and the spur gear. According to ESSS no significant degradation during the required lifetime was allowed.

Four main parameters were measured (Figure 7). The starting current with (blue) and without (green) detent torque, the resistance of all main and redundant windings (just one shown in red) and the slip ring resistance (yellow).

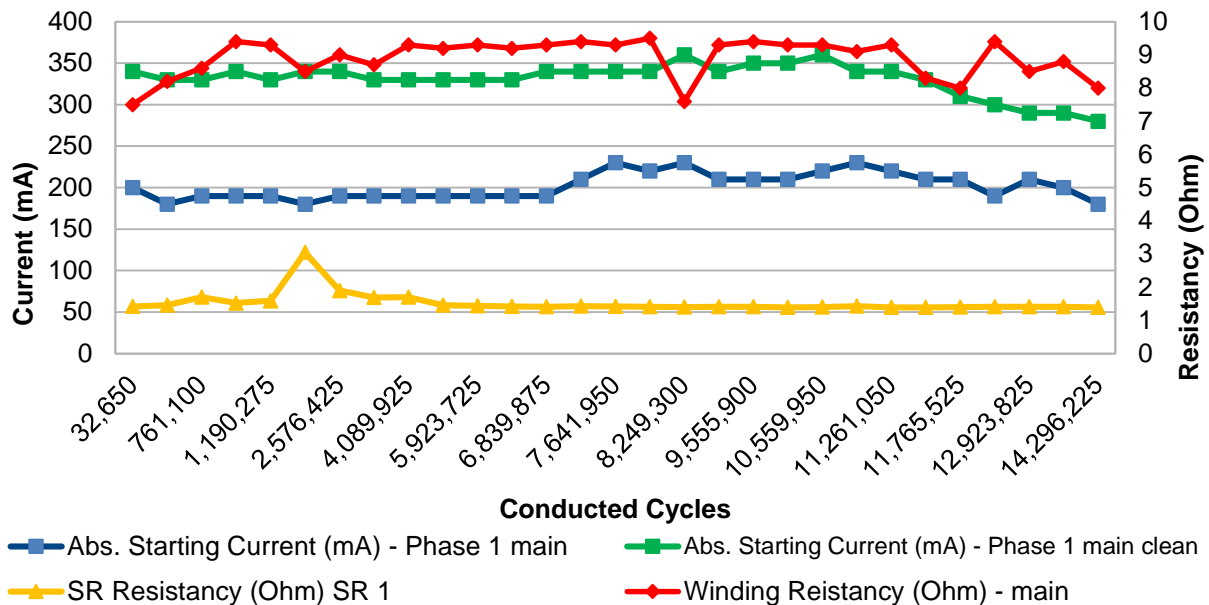


**Figure 7. ISL Life Test Model Intermediate results for starting current, motor coil and slip-ring resistance**



Having tested about 90% of the total life time (January 2016), it can be stated that all measured values indicate a full success of the life test. The starting motor current, slip ring resistance and motor coil resistance did not show any non-tolerable performance change.

### Performance Test

Test setup for performance testing (see Figure 8) allows a stiff installation of two high-resolution absolute encoders to avoid additional measurement errors. The performance tests include measuring:

- pointing accuracy and stability
- starting current measurements (with/without detent torque)
- reference switch characteristic
- power consumption of the motors under ambient conditions

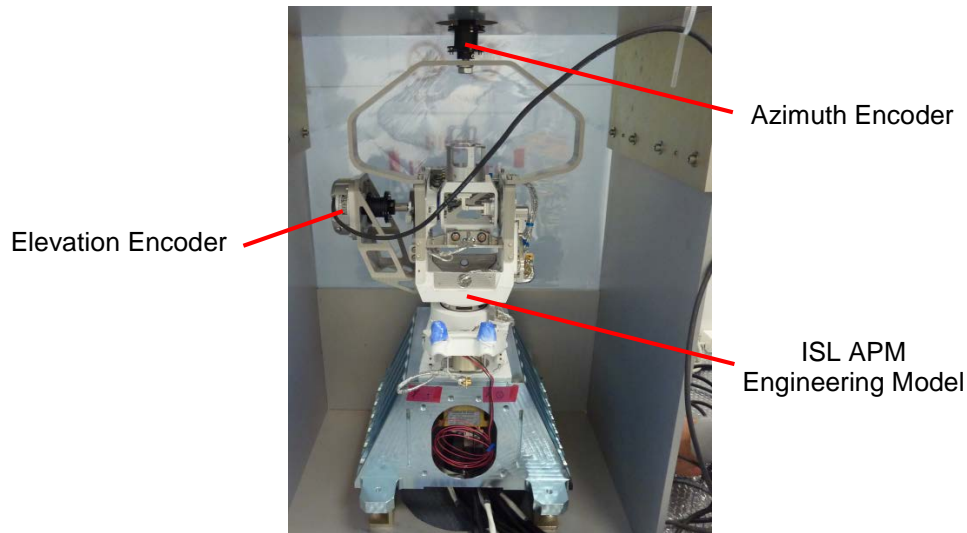


**Figure 8. ISL APM EM Performance Test Setup**

Evaluation of the results showed that the test can be concluded successfully even under worst case ambient conditions with a maximum pointing error of about 0.08 deg. The maximum pointing error is shown in Figure 9 – left side (25 nominal positioning commands in a time span of 100 sec are plotted). The power consumption of a single motor is about 14 W per motor. Power consumption for one APM with two axes is estimated to be 28 W. Due to the long transmitting time in relation to the motion time an average power consumption of about 6 W is estimated.

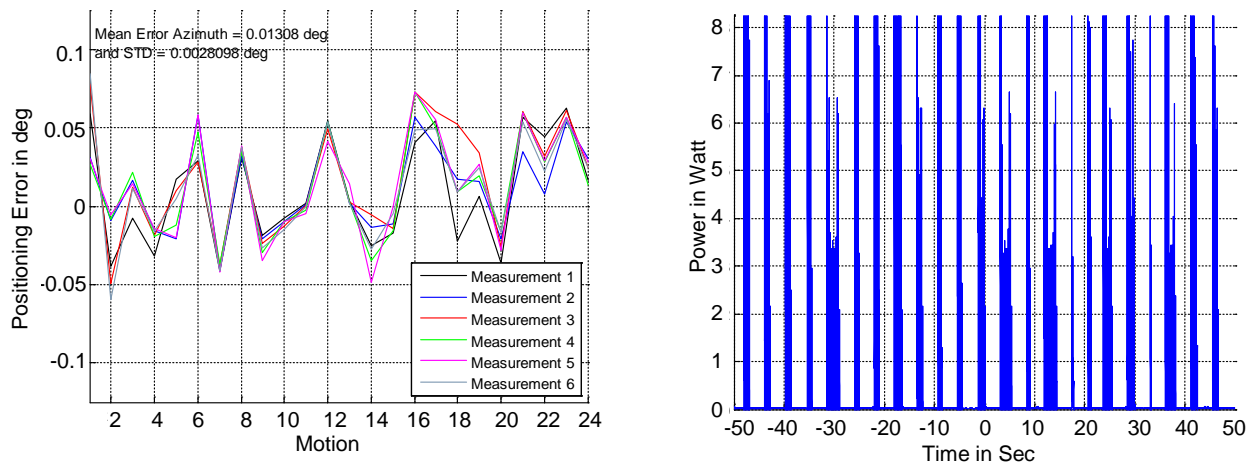


**Figure 9. ISL APM EM Performance exemplary Pointing & Power Test Results**

### RF Test

The RF Link (Wave Guide with Rotary Joints) was a new development subsystem from MIRAD AG Switzerland. RF-performance measurement was done by a set of 24 static two-port measurements (changing azimuth and elevation pointing angle). An intermediate measurement can be seen in Figure 10.

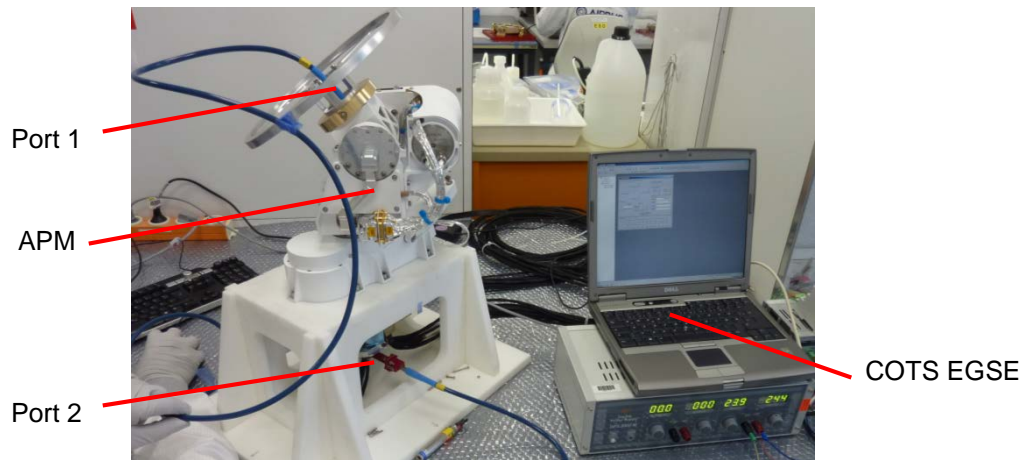


**Figure 10. ISL APM EM RF Test Setup**

Evaluating the Return Loss (Figure 11 – left) and Insertion Loss (Figure 11 – right) over the full motion spectrum showed successful performance results. The return loss was below 1.2 dB and the insertion loss was below 0.8 dB. The angular variation of the Return Loss was slightly above the expected 0.1 dB.

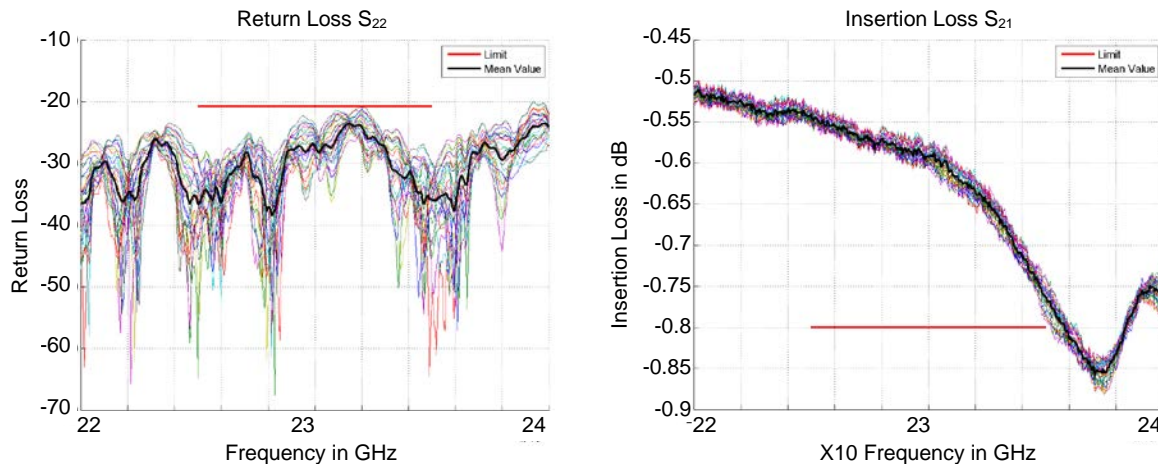


**Figure 11. ISL APM EM Return Loss (left) & insertion Loss (right) Test Results over the complete motion range**

All in all the performed work from MIRAD AG was fully in line with the required RF performance of the subsystem.

### Vibration Test

The specification for the launch loads was given as 20G from 5 to 60 Hz and 6G from 60 to 100 Hz for the Sine Vibration and  $0.12 \text{ g}^2/\text{Hz} \times (M+20 \text{ kg})/(M + 1 \text{ kg})$  for Random Vibration. The Vibration Test was performed at Airbus DS in Ottobrunn and Friedrichshafen. The vibration was controlled via base force notching. The base force was directly measured by four force sensors installed underneath the mounting interface (see Figure 12). The base force limits are defined via the quasi static design loads. In order to protect the Azimuth main bearings and the Actuator from over testing, secondary notches were used. The

bearings were limited to a peak Hertzian stress of 3360 MPa (including all ECSS ratings) and the Actuators were limited to 40 G acceleration at the center of gravity.

The X and Z axes could be qualified successfully with just minor usage of secondary notches. The Y axis was qualified to an input level of 5G. A load dependent behavior was found in intermediate testing (1/4 level limited to 10g response of the motor). The load dependent effect was investigated (see Figure 13). The ISL heritage design had to be adapted due to the more demanding requirements. The heritage HRM system did perfectly work for X and Z axis of the ISL, while enabling a frictionless release. In the Y axis, due to the design changes, too much load was transferred over the HRM Base interface. The enhancement of this interface, combined with some minor structural strengthening, will enable a qualification up to 20G load input.

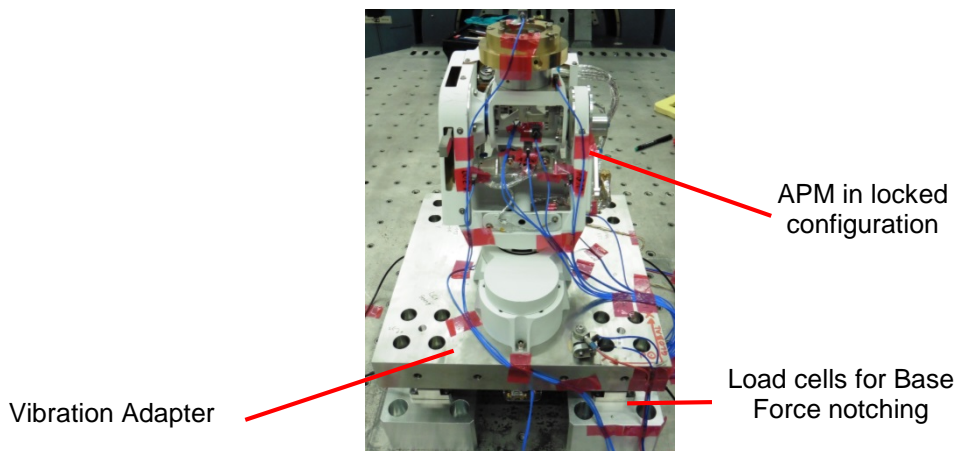


**Figure 12. ISL APM EM Vibration Test Setup**

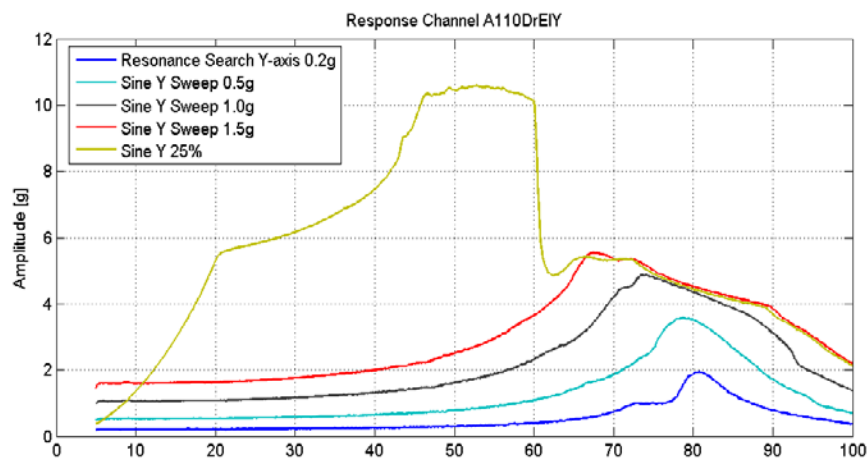


**Figure 13. ISL APM EM Y- Axis Vibration Test (Acceleration on Elevation Motor)**

As a series of subsequent qualification tests had to be done, the rework will be realized after the completion of the qualification test campaign. The residual risk for this rework and the final vibration qualification of the Y axis up to 20 G load input is limited. In summary, the EM vibration testing has proven its importance by identifying the need for the rework, while the equipment has nevertheless proven its viability for the usage in the constellation program.

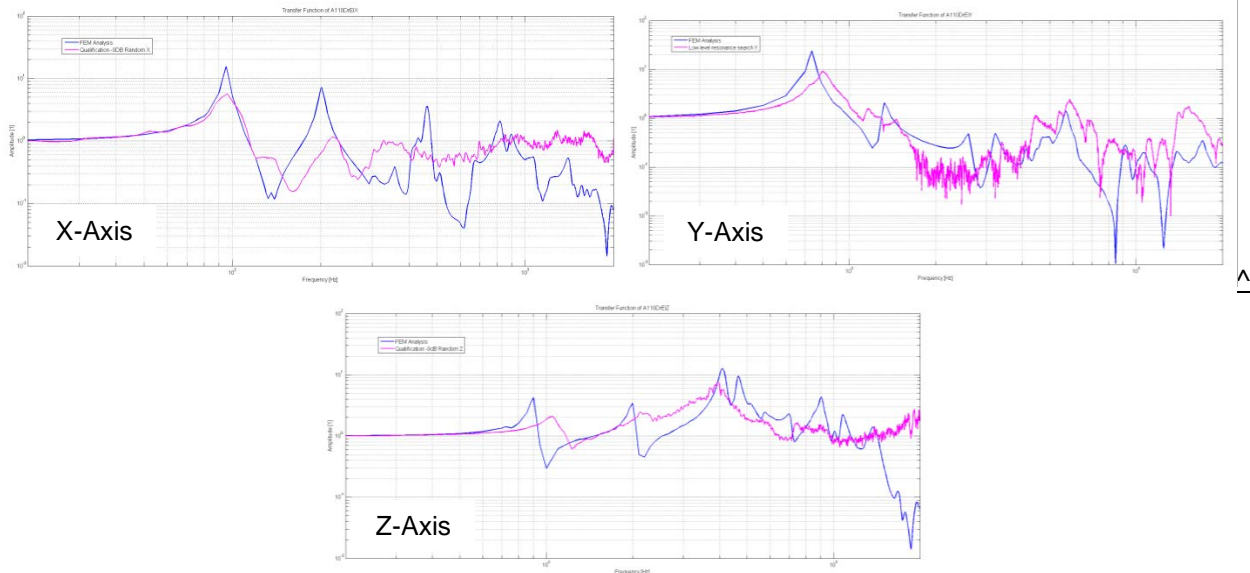


**Figure 14. ISL APM EM final Vibration Test Results – Transfer Function (analysis in blue vs. test in pink)**

### Thermal Vacuum Test

The described non conformance for the vibration test delayed the Thermal Vacuum (TVAC) test. TVAC test is about to be started, results will be part of the AMS presentation. During the TVAC test, a non-operational cycle will be performed, followed by a set of seven operational cycles. During the seven operational cycles the EM will be driven with a standard pointing profile extracted from the global pointing budget. As the ISL will also be activated during transient phases in space, this test is of major importance to guarantee the functionality under extreme thermal conditions. At dedicated inspection points the starting current and the power consumption will be measured in hot and cold conditions. These measurements will also verify the bearing characterization breadboard tests.

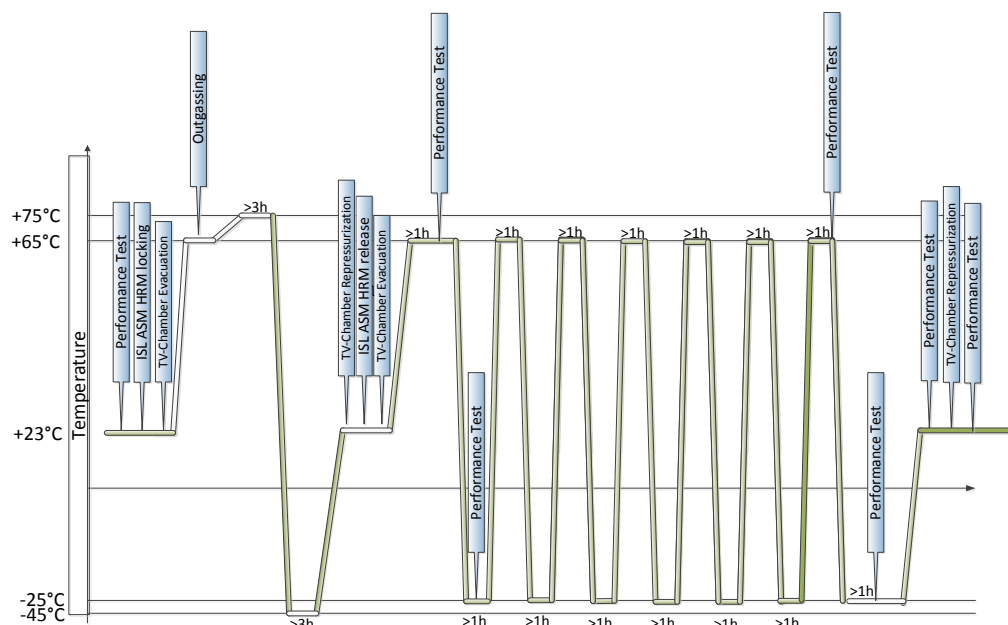


**Figure 15. ISL APM EM TVAC cycles**

### Microvibration Test

The micro vibration test was successfully performed in the mechanisms group test facility. The test setup was developed and continuously improved during the last years (principle shown in Figure 16). The micro vibration test sensors logs the forces acting over a time period. This data is subsequently analyzed using a Fast Fourier Transformation algorithm to identify the frequencies and amplitudes of the emitted vibrations. Details regarding the analysis method can be found in [2].

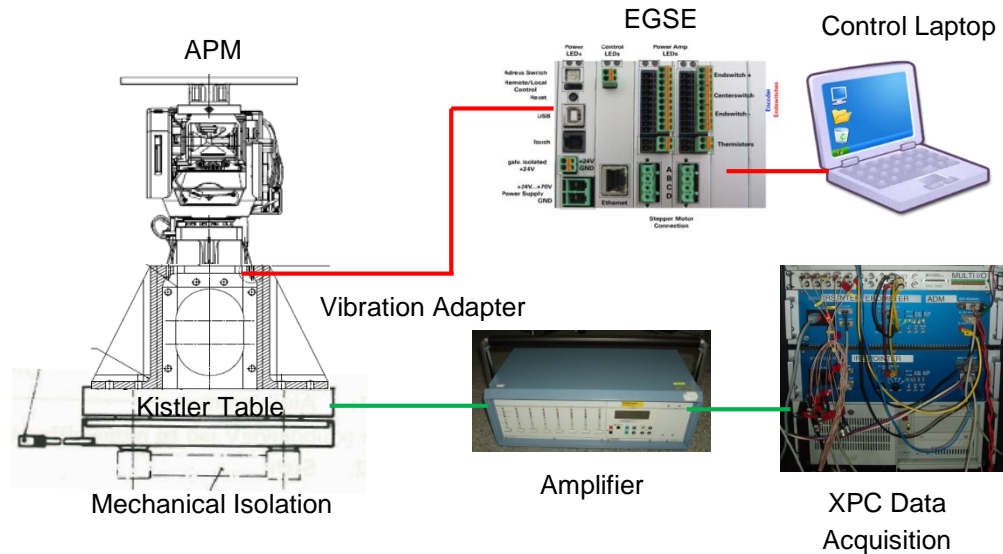


**Figure 16. ISL APM EM Microvibration Test Setup**

Both axes were tested separately with different velocities from 10 deg/sec to 90 deg/sec. The test results for the rotation of the azimuth axis at 70 deg/sec can be seen in Figure 17. A second test method was to perform a motion profile with both axes operating in parallel.

Test results evaluation showed that the required microvibration levels below 0.1 N and 0.1 N-m from 0-2000 Hz could not be met with the current stepper motors and motion profiles.

Additionally, an impact from the COTS electronics was seen. Tests comparing a COTS electronics and the flight electronics showed an improvement by a factor of 2 for the flight electronics. Dedicated micro vibration reduction designs were developed at Airbus DS [3] in the past. Those design improvements can significantly reduce the microvibration. Further technical optimizations to reduce microvibration at spacecraft level are ongoing at Airbus DS GmbH.

### Magnetic Moment Test

The Magnetic Moment Test is used to identify the influence of the magnetic components installed within the ISL APM EM on the satellite. Results of the EM can also be used to optimize the position of the APMs at spacecraft level. The two major sources of magnetic field emission are the stepper motors.

In order to identify the field emission the ISL APM EM was installed in a Helmholtz Facility. Firstly, the remanent (non-powered) magnetic field emission was measured (360 measurements around the ISL APM EM). Secondly, the field was measured in powered condition (standard motion profile).



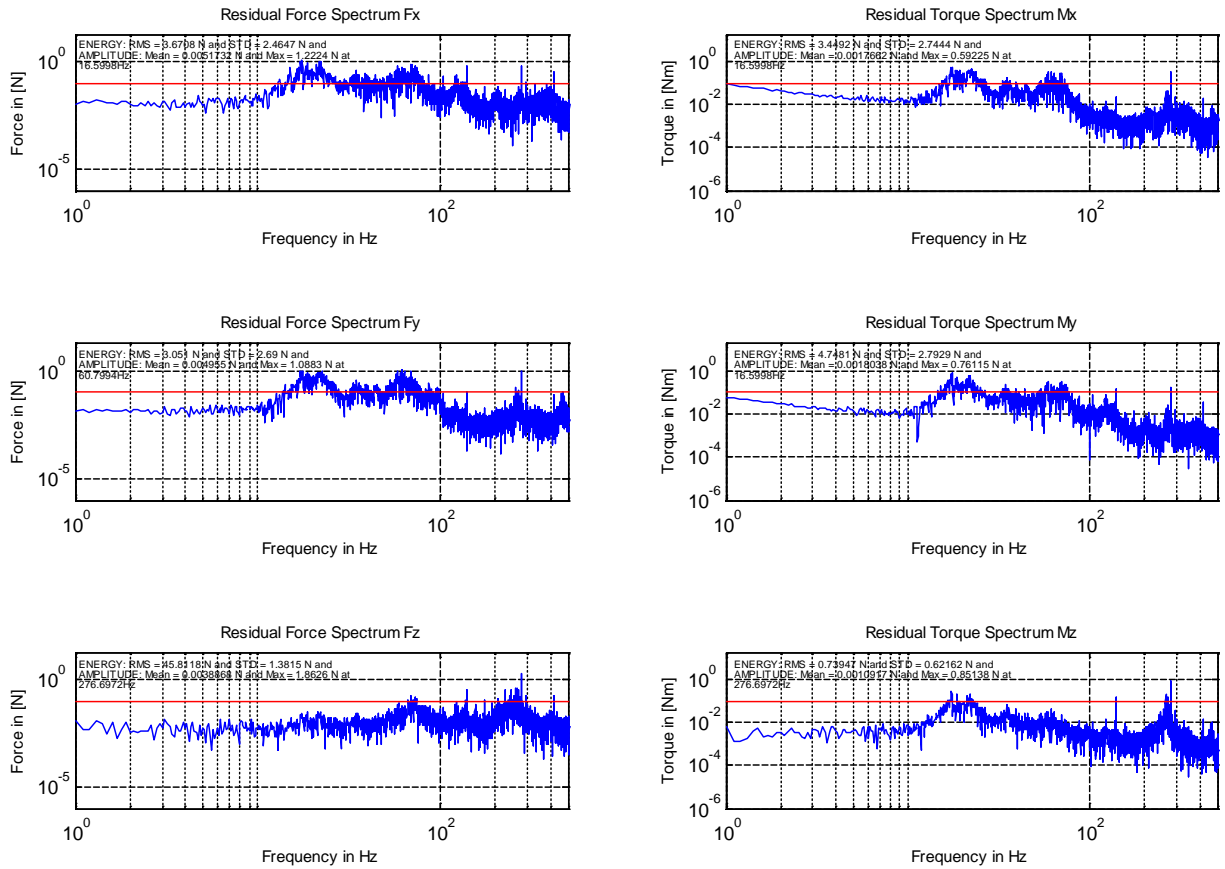


**Figure 17. ISL APM EM Microvibration Test Results for Azimuth Stage rotating at 70 deg/sec**

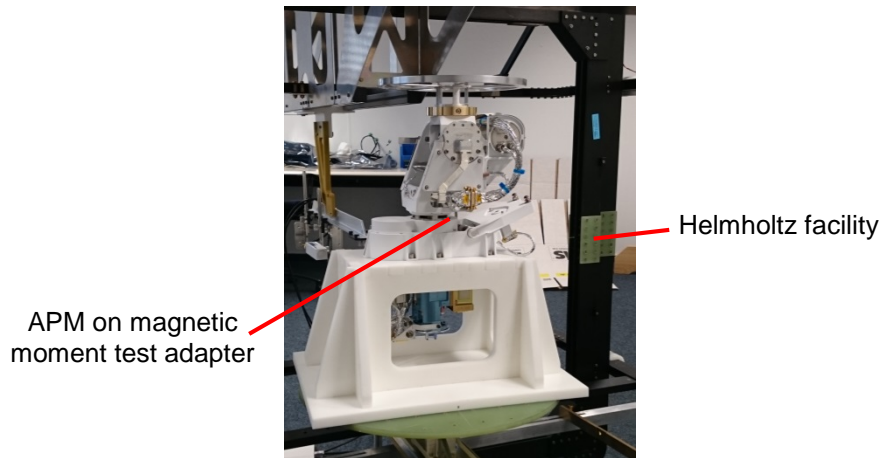


**Figure 18. ISL APM EM mounted in the Helmholtz facility**

In Figure 19 an exemplary AC field measurement of the powered status is shown. It can be seen that the actual change of position of the motors towards each other has a more important effect on the AC field, than the actual powered coils. The motor current shows just a minor effect on the AC field (see e.g., marked peak), while changed motor orientations lead to significant changes of the AC field of up to 280 nT.

To calculate the Magnetic Moment, the actual field measurements will be used to calculate ideal dipoles at the position of the motors. Using this approximation enables the calculation of the Magnetic Moment of these dipoles.

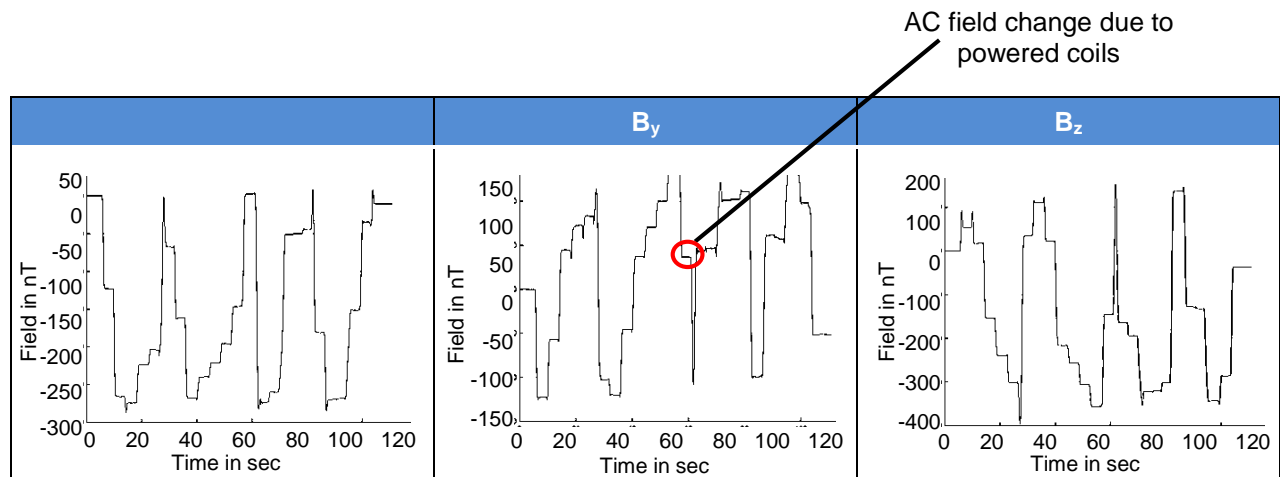


**Figure 19. ISL APM EM exemplary AC field measurement results**

Evaluating the results of the measurements, show that a non-powered Magnetic Momentum of  $2.2 \text{ Am}^2$  can be calculated. Variation of the magnetic moment is given over the motion of the motors towards each other. The maximum calculated Magnetic Moment is at  $4.2 \text{ Am}^2$  and the lowest calculated Magnetic Moment is at  $2 \text{ Am}^2$ .

Measurement and calculation does not meet the required values of  $0.2 \text{ Am}^2$ . The high Magnetic Moment is caused by the motor size and the mass and force of the magnetic material used in the motor. The current situation could be improve by changing the motor size or materials as well as shielding. But further discussions with the contractor showed that the stated non-conformance report can be accepted.

## Conclusions

### General

It can be stated that the chosen technical solution fulfills all major requirements. The required orbit lifetime of 12 years could be proven by an accelerated life test. The pointing performance is well within the needed requirement and the RF performance allows a successful communication. In order to fulfil the torque budget a powerful stepper motor was chosen. This stepper motor leads to certain violations of requirements like the magnetic moment and the microvibration.

Conclusion after all tests is that the ISL APM EM is successfully qualified (status after vibration test). All non-conformance reports for the current Engineering Model phase have been closed successfully and some further improvements for the APM have been identified to increase the performance and to gain some mass reductions.

Airbus DS Friedrichshafen delivers the ISL APM EM to Airbus DS Portsmouth after just 18 months of design, manufacturing and assembly/integration/test activities including a dedicated life test.

### Lessons Learned

For each qualification test the major lessons learned are:

The **Bearing Characterization Breadboard Test** provided at an early project state a series of very important results (lubrication verification, correct torque budget inputs, possible bearing working profile). As a lesson learned, this test will be standardized within the mechanism department to be used for all upcoming projects, in order to improve the internal bearing lubrication and torque database.

The adequate **Life Test** conditioning proved to be challenging when using a simplified Life Test Model. Therefore for further projects, if possible, the EM will be used instead of a simplified model. A lot of effort in the extra assessment and testing can be saved.

The **Performance Test** showed that the chosen technical solution (stepper motor, backlash-free gear with a low medium gear ratio and a bearing in O-configuration) can provide the needed accuracy of 0.1 deg without any challenges.

The **RF Test** demonstrated the possibility to reduce cost and time to integration by selecting a novel supplier. The RF performance was outstanding. This shall support an open supplier selection for the future.

The **Vibration Test** qualified the X and Z axes for a load input of 20G. Y-axis was qualified up to for 5G load input, as the load dependent effects had to be investigated in detail. The vibration test also showed the high value of such EM testing in order to reveal design challenges, occurring due to changes from heritage design solution. Functional analysis within the mechanism development process, connecting function to design elements could also help for future projects. With the proposed and investigated minor structural improvements the APM has proven its viability for the usage in the constellation program.

The lessons learned of the **TVAC Test** will be presented at the AMS conference.

The **Microvibration Test** and the **Magnetic Moment Test** are demonstrating a conflict of requirements. On the one hand side a certain velocity and accuracy is demanded. On the other side the motor sizing leads to the violation of the microvibration and magnetic moment requirements. This conflict of goals has to be assessed with the contractor. If the violation of the two named requirements cannot be accepted a more complex motorization concept has to be chosen (e.g., closed-loop Brushless DC Motor).

### **Acknowledgment**

The author thanks the co-authors and the whole Intersatellite Link Study team for the support and the shared effort. Special thanks to ESA for the funding of the Intersatellite Link Study.

### **References**

1. Danilidis, C., Eben, K., Lindemann, U. "A functional analysis approach for product reengineering", *Procedia Engineering* 9 (2011), 270-280.
2. M. Vitelli, B. Specht, F. Boquet, A process to verify the microvibration and pointing stability requirements for the Bepi Colombo mission, *ESA International Workshop on Instrumentation for Planetary Mission*. (2012)
3. Kozilek, H., Specht, B., Soon Yong, S., Gyu Lee, S. "Micro Vibration Improvement of a stepper actuated mechanism", *ESMATS 2013*, September 2013



## Design Development of a Combined Deployment and Pointing System for the International Space Station Neutron Star Interior Composition Explorer Telescope

Jason Budinoff\*, Keith Gendreau\*, Zaven Arzoumanian\*, Charles Baker\*, Robert Berning\*\*, Todd Colangelo\*, John Holzinger\*\*, Jesse Lewis\*, Alice Liu\*, Alissa Mitchell\*, Chuck Monroe\*, Richard Pugh\*\* and Roger Willey\*\*

### Abstract

This paper describes the design of a unique suite of mechanisms that make up the Deployment and Pointing System (DAPS) for the Neutron Star Interior Composition Explorer (NICER/SEXTANT) instrument, an X-Ray telescope, which will be mounted on the International Space Station (ISS). The DAPS system uses four stepper motor actuators to deploy the telescope box, latch it in the deployed position, and allow it to track sky targets. The DAPS gimbal architecture provides full-hemisphere coverage, and is fully re-stowable. The compact design of the mechanism allowed the majority of total instrument volume to be used for science. Override features allow DAPS to be stowed by ISS robotics.

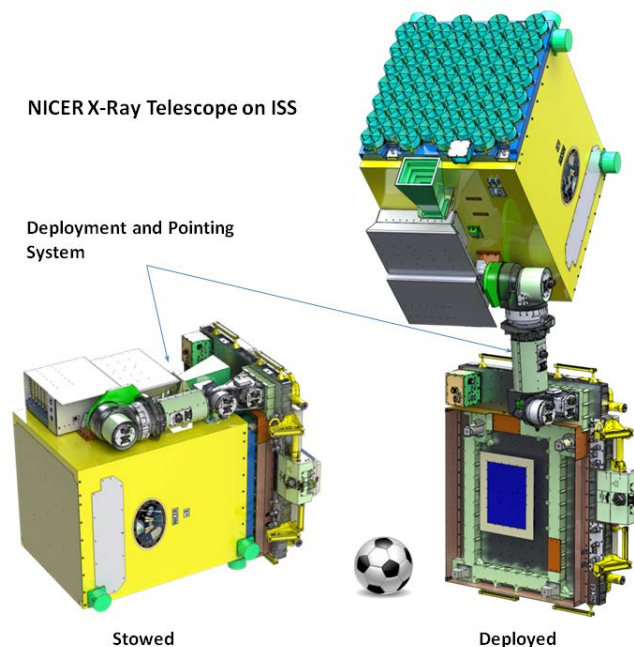


**Figure 1. NICER/SEXTANT in the stowed and deployed configurations**

### NICER/SEXTANT Instrument

The Neutron Star Interior Composition Explorer (NICER) / Station Explorer for X-Ray Timing and Navigation (SEXTANT) is a deployable, clustered array of 56 soft X-ray telescopes that will be installed on the International Space Station. The telescope cluster will track astronomical targets with a  $3\sigma$  error of  $<0.6$  milliradian (2 arcminute) of pointing error. NICER/SEXTANT will also demonstrate pulsar-based celestial navigation, and will be used as a receiver for experimental X-ray communications.

\* NASA Goddard Space Flight Center, Greenbelt, MD

\*\* Moog, Inc., Chatsworth, CA

## ISS Mission Implementation

NICER/SEXTANT will be delivered to ISS via the SpaceX Dragon vehicle in 2016, and has a mission lifetime of at least 2 years. During that time, the instrument will require 2-axis, full hemisphere pointing at >95% duty cycle, and many stow/deploy cycles. The instrument utilizes the Active Flight Releasable Attachment Mechanism (AFRAM) interface and will be robotically installed at Express Logistics Carrier #2 (ELC2), Site 7, shown in Figure 2.

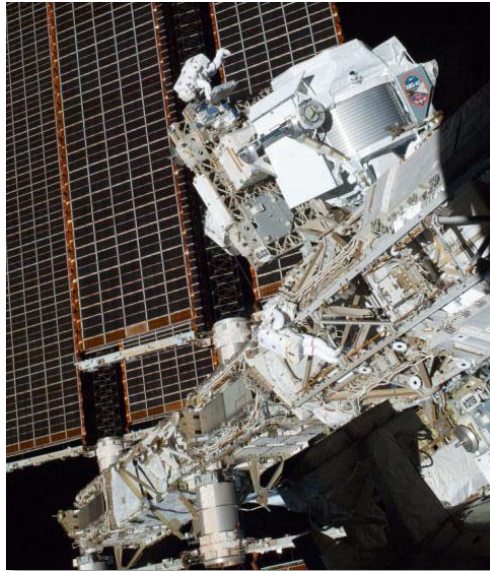


**Figure 2. NICER/SEXTANT will be mounted to ELC2, approximately where the EVA crew member is shown.**

### Deployment and Pointing System (DAPS) Mechanism

As an AFRAM-based payload, the NICER/SEXTANT instrument was subject to a limited launch envelope. It was important for the mechanism architecture to be compact, which allowed the majority of volume to be dedicated to science. An optimal architecture utilizing four actuators was devised that combined the deployment and pointing functions; this suite of mechanisms is called the Deployment and Pointing System (DAPS). It is similar to the architecture used to deploy and point the communications antenna on the Japanese Experiment Module [1].

### Architecture

The DAPS system is comprised of a deployment actuator, a deployment latch actuator, with an azimuth actuator and elevation actuator arranged in a biaxial gimbal. The gimbal actuators are oriented in an elevation over azimuth configuration. The gimbal actuators and deployment actuators are separated by a 275-mm boom. The deployment actuators, at the base of the boom, are mounted to the AFRAM plate. The gimbal actuators are connected to the large X-Ray Timing Instrument (XTI) Box, which houses the X-Ray telescope array. The XTI has a mass of 172 kg, and DAPS must point it at rates of approximately 1 degree/sec during slew and less than 0.4 deg/sec during science target tracking. Four frangible bolt launch locks constrain the XTI box directly to the AFRAM/Instrument Plate, which greatly reduces the launch loads that the DAPS will be subjected to.

### Deployment

After the NICER/SEXTANT instrument is installed on the ELC, the launch locks are released and the DAPS deploys NICER/SEXTANT from the stowed configuration into the operational configuration. The deploy actuator rotates the DAPS boom, pointing actuators, and XTI 84 degrees, clearing the launch lock towers and placing the XTI box above the ELC2 structure. The deploy latch actuator then inserts a pawl

into the rotor of the deploy actuator, mechanically latching it in place. The azimuth actuator then slightly rotates the XTI box to clear a hardstop feature, called the elevation hook. The hook is a simple linear bar connected to the boom. When the XTI is stowed, the hook is within a small ring on the XTI. This mechanically constrains the elevation from inadvertently shifting while the deploy actuator rotates due to the large center of gravity offset of the XTI relative to the elevation axis. While the elevation actuator detent has positive margin to resist this inertial torque, the hook was implemented to provide positive mechanical constraint resulting in an additional layer of safety. It ensures that the XTI box cannot swing out during deployment and potentially contact the ISS solar arrays, less than 0.5 m away.

With the hardstop feature cleared, the elevation actuator rotates the XTI box up in elevation, resulting in NICER/SEXTANT fully deployed and ready to begin science operations. The azimuth and elevation actuators in the pointing gimbal then slew to and track various astronomical targets, typically observing 2 to 3 different targets per orbit. Continuous tracking of targets through zenith is interrupted through the 10-degree keyhole; relatively rapid azimuth slewing enables these targets to be immediately re-acquired as they cross out of the keyhole. The volume swept out by all degrees of freedom is shown in Fig. 3.

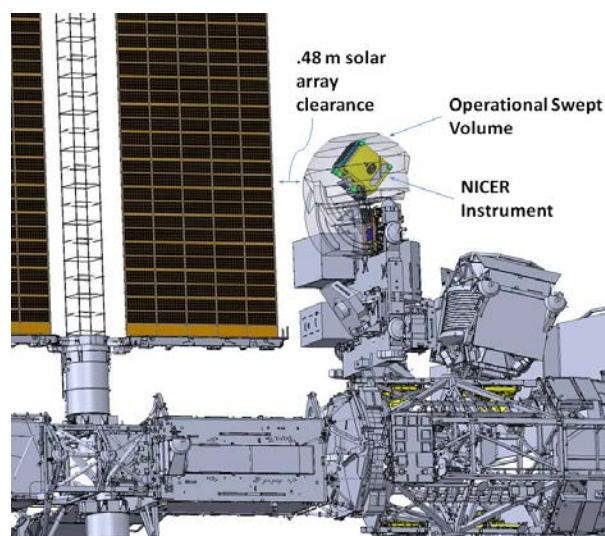


**Figure 3. The operational swept volume NICER/SEXTANT is shown. The clearance between the swept volume the starboard solar array is also illustrated.**

#### Re-Stowage

The NICER/SEXTANT instrument must occasionally return to the stowed configuration for ISS maneuvers, crew Extra-Vehicular Activity (EVA), local Extra-Vehicular Robotic (EVR) operations, and visiting vehicle proximity operations. The instrument also must be stowed prior to robotic removal and disposal. The DAPS stow process is the exact reverse of the deployment process. To increase the stowed stiffness after the initial (and permanent) release of the XTI launch locks, shear-bearing indexing conical surfaces on the AFRAM plate must engage their corresponding cups on the XTI. The alignment of these mating surfaces is critical to NICER/SEXTANT meeting its stowed stiffness requirement. The DAPS ensures that these surfaces align correctly prior to mating by using a precision guide channel which forces the relatively coarse positioning ability of the actuators into a repeatable precision trajectory which guarantees proper alignment upon contact. A guide pin on the XTI engages a precision slot on the DAPS bracket near the deploy actuator as the DAPS deploy actuator rotates through TBD degrees, nearing the final stowed hardstop. Azimuth position errors are corrected by the stow alignment slot. The torque resulting from engagement of the guide slot will backdrive the azimuth actuator into the correct orientation for engagement. The elevation axis is limited by hardstops within the actuator at 0 (stowed, end of travel) and 172 (maximum elevation, end of travel) degrees.

### External Hardstops

At some low intermediate elevations, and certain azimuth angles ranges, the XTI box could contact the ELC2. To prevent this from occurring, an external hardstop was incorporated into DAPS called the guardrail. The guardrail hardstop prevents any contact between the XTI and ELC2, while allowing elevations as low as 63 deg (~ 30 deg below the ISS local horizontal). The guardrail hardstop is a circular rail which collars the azimuth actuator and is fixed to the end of the boom. A limit bar protrudes from the elevation actuator output, and physically contacts the guardrail surface to constrain elevation motion. The guardrail has various flat profiles to allow the limit bar to clear it in the stow azimuth range. This hardstop architecture limits the minimum elevation of the XTI box to between 63 and 70 degrees in the ram azimuth quadrant, 80 degrees for most other azimuths, and allows elevations down to zero degrees only for engagement/disengagement of the elevation hook and stowing.

### **Mechanism Description**

The DAPS biaxial gimbal actuators must meet instrument pointing performance requirements, despite the small amount of torque noise, and resulting pointing error they inherently produce.

### Pointing Performance

The  $3\sigma$  pointing performance allocation for the DAPS is 0.32 milliradian (66 arcsecond), and is summarized in Table 1.

**Table 1. Pointing Budget**

<b>NICER/SEXTANT Pointing Budget</b>	<b>Estimated arcsec</b>	<b>Requirement arcsec</b>
Overall Instrument Pointing	87.2	120
ISS Low Frequency	$\pm 40$	$\pm 53$
star tracker calibration & structural/optical analysis	$\pm 9$	11.5
<b>DAPS System</b>	<b>46.3</b>	<b>66</b>

Early analysis showed that the actuators induced pointing error is much greater than the requirement. As expected, the largest error occurs when the actuator step rate coincides with structural resonant frequencies.

The NICER/SEXTANT payload has resonant structural frequencies <10 Hz which are excited by the pointing actuators. Since the operational actuator step rates will always pass through this frequency range, there are no feasible workarounds to avoid exciting these low frequency structural modes.

In order to reduce the excited pointing errors and meet the requirement, several mitigation methods have been implemented, including microstepping, actuator detent torque reduction, and the use of dampers.

### Microstepping

Implementation of microstepping in the actuator drive electronics was the first measure taken to reduce the stepper motor induced pointing error. Microstepping breaks a single cardinal step into smaller ones and softens the impacts on the output load, instead of moving through a single motor step quickly and generating a larger impulsive torque on the system. While microstepping did reduce the stepper induced pointing error, it was not sufficient to meet the pointing requirements. The issue resides in the motor detent torque. The motor powered torque must overcome the detent torque before it can move the motor from one step to the next step, even when microstepping. Overcoming the detent torque essentially generates torque impulses that exceed the detent torque. While these torque impulses are smaller than the cardinal step torque levels, they generate disturbances on the instrument and limit the benefits gained by microstepping.

### Detent Torque

The DAPS vendor recommended a reduction in the detent torque in order to further reduce the pointing errors. The detent torque was reduced by increasing the air gap between the rotor and stator. This also reduced the motor constant, and more power would be required to maintain torque output, but this was acceptable. This was tested on a development motor, which was used to determine the air gap size which balanced detent torque and motor constant. The same air gap modification procedures demonstrated on the test motor were used to manufacture the NICER/SEXTANT engineering test unit and flight actuators. The NICER/SEXTANT pointing actuator detent torque levels were lowered to less than 0.03 N-m at the output. The detent torque reduction had reduced the overall stepper-induced pointing error. Unfortunately, when the stepper actuator rates crossed the low frequency structural modes, the pointing error level still exceeded the requirement.

### Tuned Mass Dampers

One of the techniques for reducing vibratory motion is the tuned mass damper (TMD). The TMD is a resonant device designed to dissipate vibrational energy from the structure. They are passive mechanical devices that do not require power or electronics. The TMDs are particularly effective for NICER/SEXTANT, as they suppress low-frequency vibration excited by both stepper and ISS-induced disturbances. The NICER/SEXTANT TMDs were designed to provide 1-3% damping ratio for the first three flexible-body modes. They are oriented to reduce vibrations along the axes where the vibrational displacement occurs. The mounting locations of TMDs are shown in Figure 4. A sample of stepper-induced jitter results for the performance with and without TMDs are shown in Fig. 5.

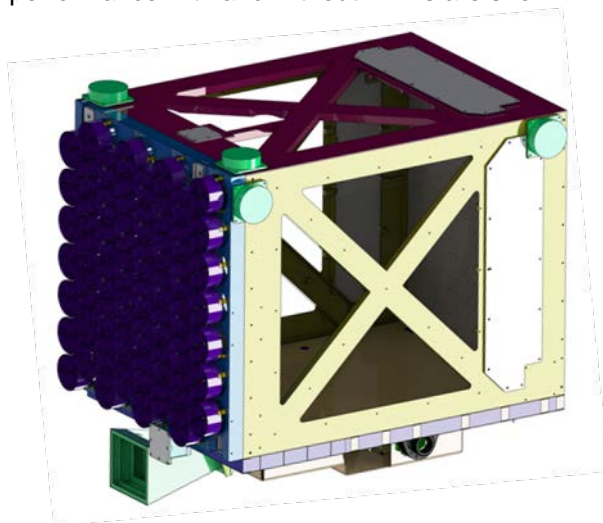


**Figure 4. Tuned Mass Dampers, shown in green, were added to the corners of the XTl box**

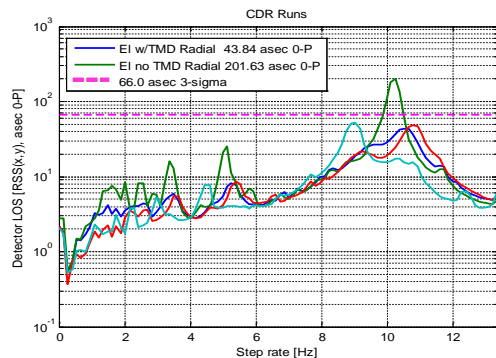


**Figure 5. The elevation actuator exceeds the 66 arcsecond requirement when step rates are near 10 Hz**



As shown in Figure 5, The TMDs were critical in meeting the pointing performance requirement. They greatly reduced the structural vibrations when the step rates pass through the structural mode frequencies. Similar results are shown in Figure. 6 for the ISS-induced jitter, where the TMDs not only reduced the peak jitter, but also stabilize the pointing performance due to ISS disturbance frequency variations.

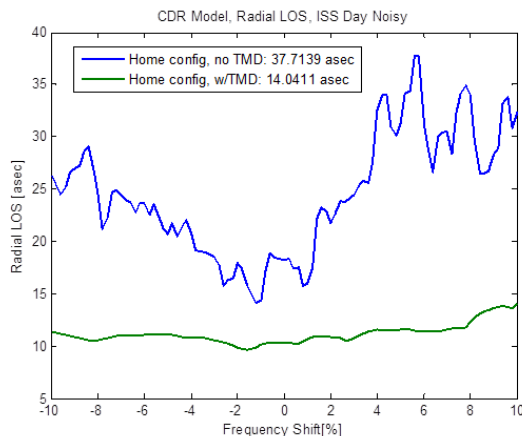


**Figure 6. Addition of the TMDs reduced the overall predicted pointing error (Radial LOS in the graph) by a factor of 2.7**

A combination of relatively low-cost techniques that included microstepping, low-detent torque, and TMDs were used to improve the NICER/SEXTANT pointing performance and meet the NICER/SEXTANT pointing requirement with adequate margin. Several tests (see Fig. 10) are currently underway to validate the pointing performance on the ground prior to launch.

### ISS Requirements Effects

The DAPS had to meet additional requirements from the space station program. Contingency considerations required that the NICER/SEXTANT instrument have interfaces to the ISS Special Purpose Dexterous Manipulator (SPDM) teleoperated robot. These interfaces would allow the SPDM to return the instrument to the stowed configuration if DAPS failed. This is necessary as the payload must be in the stowed configuration to fit within the disposal vehicle.

#### Robotic Interfaces

Each of the four actuators has a standard 7/16-inch (1.1-cm) EVR torque bolt coupled to the motor shaft. These bolts serve as an interface through which torque can be applied to drive the motor shaft, which is amplified by the harmonic drive gearing and rotates the actuator output. The torque bolts reside within Micro-Conical Fixture (MCF) Standard Dexterous Grapple Fixtures with their associated Modified Truncated Cone (MTC) visual alignment targets. These EVR interfaces are shown on the engineering test unit (ETU) actuator in Figure 7.

These bolts and EVR interfaces are on the motor faces of all DAPS actuators except the Azimuth pointing actuator. This actuator has the motor face buried within the boom and required a 90 degree gear box extension to allow the EVR bolt, MCF, and MCT to be accessible by SPDM. These interfaces are shown in Figure 8.

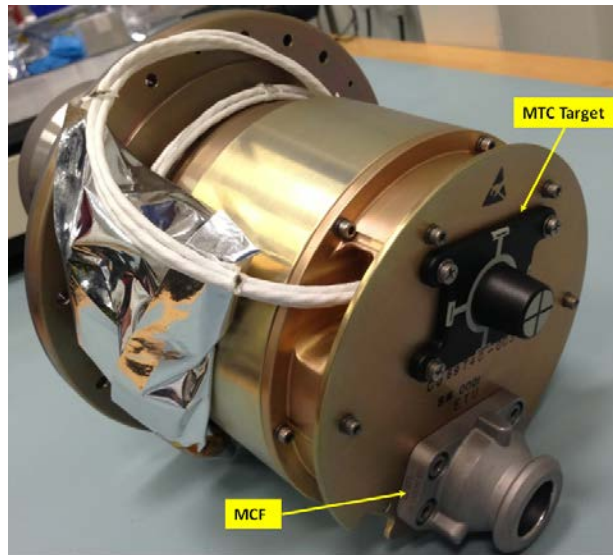


**Figure 7. Robotic interfaces are shown on the DAPS ETU actuator. The black MTC target sits above the MCF grapple fixture on the actuator face. The EVR bolt is buried within the MCF.**

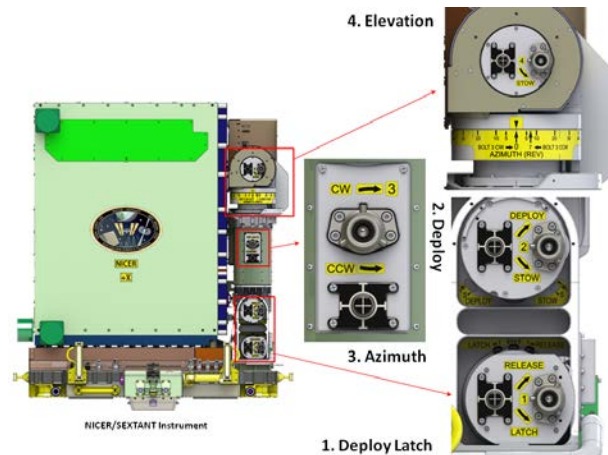


**Figure 8. DAPS ISS Robotic Interfaces. Each actuator has a MCT grapple fixture, a MTC visual target, and external labels.**

To accommodate an accidental runaway impact of the SPDM robot, DAPS had to demonstrate fracture margin against an impact of 556 N (125 lbf), and an EVA kick load of 556 N (125 lbf).

#### Torque Limiting

The minimum input from the SPDM torque driver is 6.7 N-m (5 ft-lbf). Should this amount of torque drive a DAPS actuator into a hardstop, internal damage may occur. A torque-limiter was built into the EVR interface to prevent accidental damage. Torque levels of 0.73 N-m (~6.5 in-lbf) are transmitted through the torque limiter.

#### External Markings

To facilitate the contingency robotic restow operation and meet Design for Minimum Risk requirements, external status markings and indicators (arrows on moving tabs) were implemented which indicated the displacement position of each axis. Each actuator had gradations labelled with return to stow position

EVR turn counts, and arrows indicated the direction to rotate the EVR bolt to return each axis to the stowed position. The location of these gradations and markings were unique for each axis. To meet EVA legibility requirements, the text was ~6.7 mm (18 pt.) or larger.

### Verification

The DAPS is being developed as a protoflight unit, with a single ETU actuator to validate low detent modifications and EVR interfaces. The ETU actuator is shown in Fig. 7.

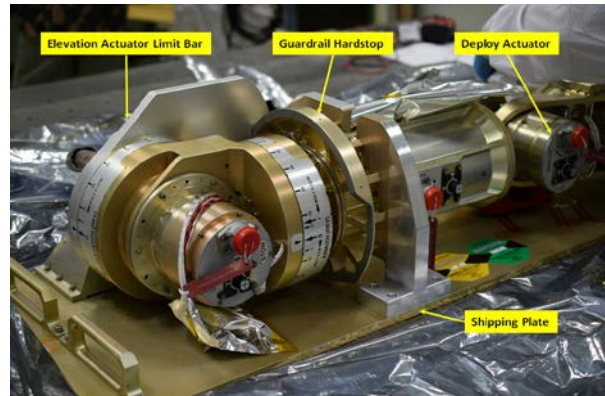


**Figure 9. DAPS flight unit as delivered to the NICER/SEXTANT instrument.**

As of this writing the DAPS has been delivered to GSFC and is undergoing performance testing as shown in Fig. 10. This is to be followed by integration into the NICER/SEXTANT instrument and environmental testing at the instrument level.

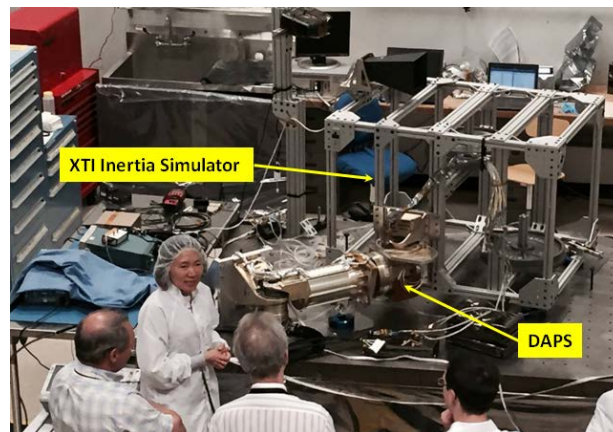


**Figure 10. DAPS flight unit during performance testing with an XTI inertia simulator floating on air bearings.**

### References

1. Stevenson, J., Katsuyama, Y., Fukatsu, A., Kurihara, K., Saito, T., Zoren, M., Mallonee, S., (1999). Development of the JEM ICS Antenna Pointing System In Space Mechanisms and Tribology, Proceedings of the 8th European Symposium (Ed. D. Danesy), ESA SP-438, European Space Agency, Noordwijk, The Netherlands



# Development of Compact Mechanically Driven Systems for High Strain Composite Slit-Tubes

Bruce L. Davis\* and Mark Lake\*

## Abstract

Since the pioneering days of space exploration, large deployable structures have played an important role in expanding satellite capability and performance. Perhaps one of the more prominent and simplistic building blocks of deployable structures is the rollable slit-tube boom, or a “Storable Tubular Extendible Member” [1,2]. This device functions in a mechanically similar fashion to a tape measure where a long metallic cross-section is rolled into a coil, providing a high packaging efficiency and the ability to deploy to various lengths. This technology has been commonly employed in space for 50+ years due to the simple nature of the design and the limited number of mechanical components required to deploy in orbit. Moreover, the industry has long known and applied a wealth of lessons learned from early flights of these simple devices [2]. Examples include using the slit-tube as a standalone structure to offset sensors or cameras from a spacecraft body to more fully integrated systems such as the primary drive mechanisms for telescoping booms used to deploy the sunshade on the James Webb Space Telescope. Despite the extensive use, this technology is limited when the deployable structure requires high precision or is subjected to large structural loads. For these cases a complex set of mechanisms consisting of rollers, guides, and bearings to unravel the metallic slit-tube becomes necessary in order to contain its considerable stored strain energy in the coil and properly manage its deployment. Conversely, the use of High Strain Composite (HSC) slit-tubes [3,4,5] can allow greatly increased boom strength and stability.

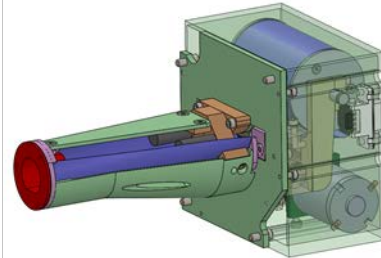
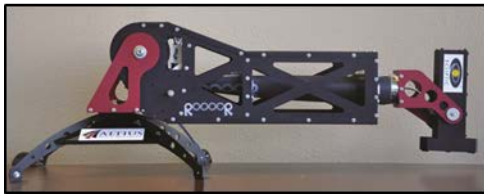
Roccor LLC, based in Louisville, Colorado is currently developing a series of HSC slit-tube deployers that take advantage of the non-isotropic material properties HSC materials to reduce their stored energy. Specifically, Roccor is developing HSC slit-tube laminates composed of traditional space-qualified materials, which are highly structural in the extended configuration but also have a relatively low stored strain energy in the stowed configuration. As a result, the need for a complex set of rollers and constraints on the coil are eliminated and the deployment device volume is reduced. In addition, these laminates provide near zero coefficient of thermal expansion (CTE) and/or the opportunity to embed internal conductors, which can act as an RF element or to transfer power/data without a standalone harness. The Roccor team has developed a series of integrated HSC slit-tube boom deployer systems that vary in size, performance and application. In this paper, a design review of four selected systems is outlined with a focus on the mechanical components enabling deployment/retraction while also ensuring structural rigidity. In addition, the best practices for ensuring adequate boundary conditions are also identified.

## Roccor’s High Strain Composite Boom Deployer Family

The four unique deployer systems discussed in this paper are identified in Figure 1. Each of these systems was designed for a specific application with a series of performance and operational requirements. A brief description of design considerations for each system follows below:

---

\* Roccor, Louisville, CO



<b>'DARPA Phoenix Camera Boom'</b> <ul style="list-style-type: none"> <li>• 2.5" (6.35-cm) diameter, circular cross section</li> <li>• 60" (1.5-m) deployed length</li> <li>• Embedded wires allowing power and data transmissions for distal camera</li> <li>• External motor</li> </ul>	<b>'NASA CubeSat Magnetometer Boom'</b> <ul style="list-style-type: none"> <li>• 0.75" (1.9-cm) diameter, circular cross section</li> <li>• 50 inch (1.3-m) deployed length</li> <li>• Near-zero CTE design, high precision distal end knowledge</li> <li>• CubeSat form factor</li> <li>• Magnetically clean</li> </ul>
<b>'DARPA Phoenix HIMast Boom'</b> <ul style="list-style-type: none"> <li>• 1" (2.5-cm) diameter with extended cross section</li> <li>• 180" (4.6-m) deployed length</li> <li>• Low CTE design, high precision distal location</li> <li>• Embedded high current power supply wires</li> <li>• Fits the NovaWurks 'HISat' envelope with an external drive motor</li> </ul>	<b>'NASA Asteroid Redirect Mission' (ARM)</b> <ul style="list-style-type: none"> <li>• 1.4" (3.6-cm) diameter, circular cross section with overlap</li> <li>• 80 inch (2-m) deployed length</li> <li>• Low CTE design</li> <li>• Internal motor</li> </ul>

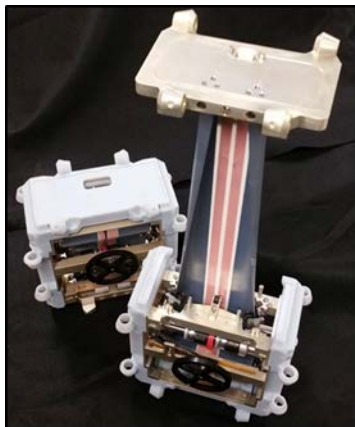


**Figure 1. The Rocco High Strain Composite Slit-Tube Deployer Family.**

#### DARPA Phoenix Camera Boom

This boom was designed to deploy and retract a camera (hundreds of cycles) in support of the DARPA Phoenix program. This boom utilizes a thin carbon fiber HSC laminate and was designed to be neutrally stable (same strain energy in deployed and stowed configurations) upon rolling. As a result, during operations the spool passively rolls / coils without requiring additional constraints. The boom geometry is circular with a 2.5" (6.35-cm) diameter with roughly a 300° included angle. The deployer volume is set so that the boom geometry is near fully recovered prior to exiting the front of the box to maximize structural efficiency. This system also utilizes a preloaded friction drive-wheel to deploy and retract the boom as well as radial roller supports to enable rigid boundary conditions of the deployed boom. Finally, thin copper wires are embedded into the composite material to allow for power and data transmission to a camera located at the distal end. A slip-ring is implemented into the spool to electrically connect the boom wires with the deployer. This feature eliminated the need for a separate, pull-out wiring harness.

#### DARPA Phoenix *HIMast* Boom

This boom was designed as a deployable building block element for re-configurable satellites, and provides improved structural performance, power transmission and deployed stability/precision as compared with the 'DARPA Phoenix Camera Boom'. In addition, this system was designed to fit within the mechanical envelope of the '*HISat*', a low-cost, modular satellite architecture that allows for rapid reconfiguration and on-orbit assembly under development by *NovaWurks* of Los Alamitos, California. The options for reconfigurability and potential to use multiple '*HIMast*' deployers in tandem led to the development of a unique, non-circular cross sectional shape shown in Figure 2. This shape is also convenient as it enables a flat surface to embed large copper wire traces to supply power at the distal end. This boom is composed of a combination of carbon and glass fiber materials to enable high strength, precision and thermal stability.

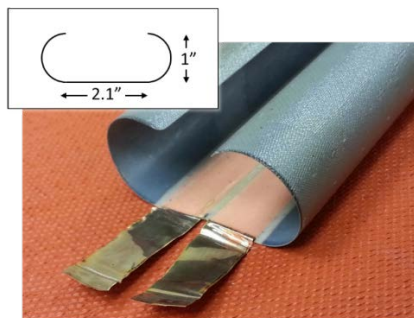


**Figure 2. '*HIMast*' Slit-Tube Cross-section**

Perhaps one of the most challenging aspects of the '*HIMast*' design was the 20x20x10 cm mechanical envelope available for the deployer mechanism. This coupled with the required structural performance of the deployed boom forced this design to have component-level proportions not typically seen in slit-tube systems. For example, a large spool was required that occupied roughly 1/3<sup>rd</sup> of the available volume which was not fully compatible with the natural spooling diameter of the composite. As a result, a preload on spool was required during retraction to ensure proper coiling. In addition, in order to ensure that the boom deployed perpendicular to the box, the composite had to be back-bent as it came off of the large spool. This required additional focus on the laminate design to ensure high strain levels and robustness. Another example of the high compactness of the system relates to the drivetrain design. Here the '*HISat*' architecture enabled external motor driving which eliminated the need for a dedicated motor. However this created several subsequent requirements such as the need to pass this mechanical power to adjacent '*HISat*' / '*HIMast*' boxes as well as the need to mechanically sequencing the systems. This led to a drivetrain design consisting of multiple gears, chains and slip-clutches shown in Figure 3. Here the mechanical input/output is shown as black wheels on the top and bottom while the elastic wheels interfacing the composite are shown in orange. Further details on this system designed are available within the literature [8,9].

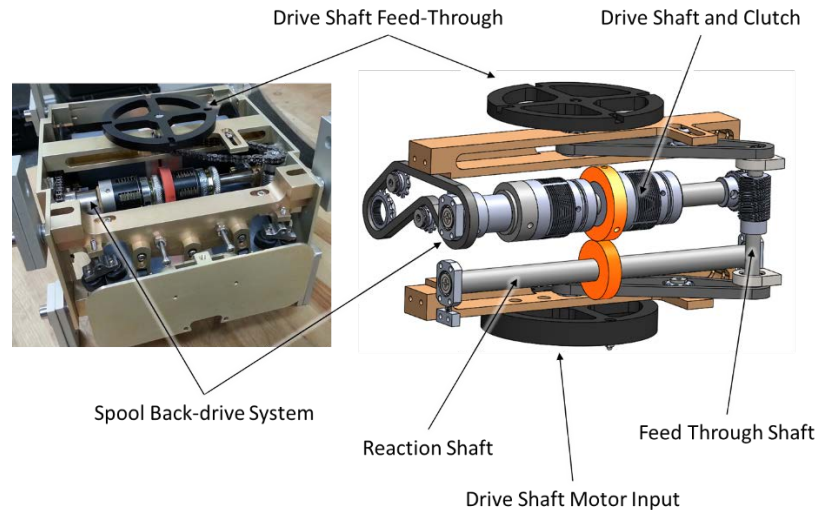


**Figure 3. 'HIMast' Drivetrain Design**

#### NASA CubeSat Magnetometer

This effort is currently under development with the NASA Goddard Space Flight Center in Greenbelt, Maryland. This project builds upon Roccor's previous experiences in fabricating high precision, thermally stable booms with a new focus of miniaturization into the CubeSat form factor, use of magnetically clean materials and need for low-cost hardware. This boom is 0.75" (1.9 cm) in diameter, has an included angle of 350° and a deployed length of 50" (1.3 m). This boom utilizes a thermally stable laminate design consisting of both carbon and glass fibers. Unique to this design are a series of roller-free boom support boundary conditions to reduce the number of moving parts and to maximize the available volume. In addition to meet precision, this system contains a highly geared-up drive train to ensure fine deployment resolution as well as a pin-latch mechanism and a composite insert to lock the boom at the desired deployed length. This boom also contains a hybrid elastic friction wheel and mechanical toothed interface to improve deployment length knowledge.

#### NASA Asteroid Redirect Mission

This boom system was developed in conjunction with a commercial group working to fabricate ground demonstration hardware in support of NASA's Asteroid Redirect Mission. This system closely resembles the 'DARPA Phoenix Camera Boom' deployer design outlined above however utilizes a higher fidelity laminate design, contains an internal motor and utilizes a new edge roller constraint scheme. The laminate design consists of a 1.4" (3.6-cm) diameter boom with a 400° overlap and a deployed length of 80" (2 m). The overlap strengthens the boom along the generally weaker bending direction where the open portion of the slit-tube is in compression. The internal motor is directly connected to the boom shaft and is capable of supplying an axial deployment force in excess of 20 lbf (89 N). The edge supports depart from earlier approaches where a wheeled interface is replaced with a hard metallic interface. Here the composite rubs against the surface enabling a stout boundary condition while eliminating additional moving components.

### **Lessons Learned in High Strain Composite Boom Deployer Design**

During the development of the four boom systems outlined above, several best practices and lessons learned were established by the Roccor team. In this section several of these details are outlined and design features that incorporate these best practices are discussed.

#### Designing HSC Slit-Tubes to be Neutrally Stable

The utilization of neutrally stable HSC materials offers an opportunity to fabricate unique structures with a wide range of performance properties. The design space ranges from one extreme where the neutrally

stable laminate slit-tube architecture passively deploys into an extended beam when unrestrained to the other extreme where the boom passively retracts into a compact coil. With proper tuning, a hybrid laminate design can be implemented that is *neutrally stable* – possessing equal strain energies in the stowed and deployed configurations. This attribute allows for the slit-tube to be manipulated between its stowed and deployed configurations without managing a significant change in strain energy and thus enabling a simplistic deployer system. The concept was first analyzed by Murphey and Pellegrino [10] and later by Shultz, Hulse, and Keller [11]. Figure 4 shows an example of a fiberglass composite slit-tube that is neutrally stable and remains partially coiled without external constraints.

Although it may seem ideal to tune the laminate design to be neutrally stable, often this can be challenging to achieve practically while balancing with other competing laminate requirements such as thermal stability or structural performance. For the case of the ‘*DARPA Phoenix Camera Boom*’ and ‘*NASA ARM Boom*’ deployers, these two designs had the flexibility to enable a neutrally stable boom. This resulted in deployer systems that contained fewer mechanisms and an overall lower unit cost. In the ‘*DARPA Phoenix HiMast Boom*’ and ‘*NASA CubeSat Magnetometer Boom*’ cases, this was not possible whereas the laminate design required added features to ensure tight packaging on the spool. Without this assistance, the coil diameter naturally grew to be ~50% larger than what was ultimately desired. For both of these cases, this was relatively easy to overcome by either adding a small retraction spring inside the spool or in the case of the ‘*DARPA Phoenix HiMast Boom*’ system, a chain and slip-clutch coupling to apply a desired and constant spool preload during retraction.



**Figure 4. Example of a Neutrally Stable Boom (Glass Fibers)**

#### Boom Formation Region

As the HSC material is rolled off of the spool, there is a ‘formation’ region where the boom transitions from a flattened geometry on the spool, to a fully formed cross section that is capable of supporting loads. It is the responsibility of the deployer to guide the boom through this transition and when enough depth has been established, create a stout boundary support to enable a rigid deployed structure. In practice, it has been found that the length of this formation region for a neutrally stable boom is approximately 9x the diameter of the coiled boom or the *envelope form factor*. Note that this length is substantially shorter than the factor  $8\pi$  analytically predicted 50 years ago by Rimrott for isotropic slit-tube booms, which illustrates a further advantage of neutrally stable laminate designs [12].

In ideal systems, the deployer envelope would fully encompass this *envelope form factor* to ensure that the boom exits the box with its fully formed cross section established and to provide adequate structural support to the base of the boom once deployed. However it has been Roccor’s experience that most practical spacecraft envelope constraints do not allow for this “luxury.” For the Roccor deployer family, the portion of the boom formation region covered by the deployer varies widely from the ‘*DARPA Phoenix HiMast Boom*’ system of 2x to the ‘*DARPA Phoenix Camera Boom*’ system of 6x. The optimized deployer length depends upon the design loads. High axial loads can be sustained with a relatively short deployer length while bending loads necessitate a relatively long deployer length. In the case of ‘*DARPA Phoenix HiMast Boom*’ the system design and requirements were able to close with the *envelope form factor* of x2 due to the mission architecture where multiple units would be used in tandem to form a hierarchal structure. For the cases where the boom deployers are less than x4 in length, additional considerations such as the distal end attachment method (see the *Distal End* section below) and the boom structural knockdowns must be considered.



### Distal End

The distal end, (i.e. the boom end fitting) is a complex component of any deployer system as its attachment method plays a large role in ensuring boom rigidity. Perhaps the most challenging aspect to this component is an attachment method that ensures boom torsional rigidity. Additional complexities arise for deployer systems that do not exit the box with a fully formed cross section. For these cases, the distal end must accommodate changes in the cross section geometry and lock into place once the boom reaches beyond the 9x *envelope form factor*. An example of this case is illustrated in Figure 5 and shows the closeout feature utilized for the '*DARPA Phoenix HIMast Boom*' system. Here as the numbers in the figure ascend, the boom is deployed out and the cross sectional geometry wraps and closes around the distal plate.

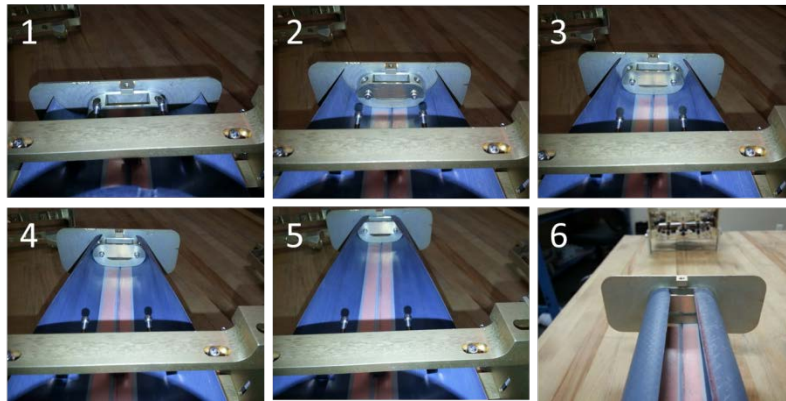


**Figure 5. Distal End Closeout, Roccor '*DARPA Phoenix HIMast Boom*' System**

For this case, it was found that the best distal closeout method was to use a series of kinematic mount interfaces that preloaded boom front edge against the distal plate to enable torsional rigidity. Other practices were trialed for additional improvement including the use of magnets, springs, etc., however with the large closeout length for this architecture, significant benefits for these added features were not realized. For Roccor's other deployers, the '*NASA ARM Boom*' system (with an envelope form factor of 4x), a distal plate was adhered and fastened to the end of the boom, as shown in Figure 6, and worked very well however minor, non-destructive edge buckling was noticed upon full retraction. Further design changes to the front roller supports relieved this effect. For the '*DARPA Phoenix Camera Boom*' deployer (envelope length of x6), a system utilizing a long, thin sheet metal plate adhered to the composite surface was incorporated without any observed issues.

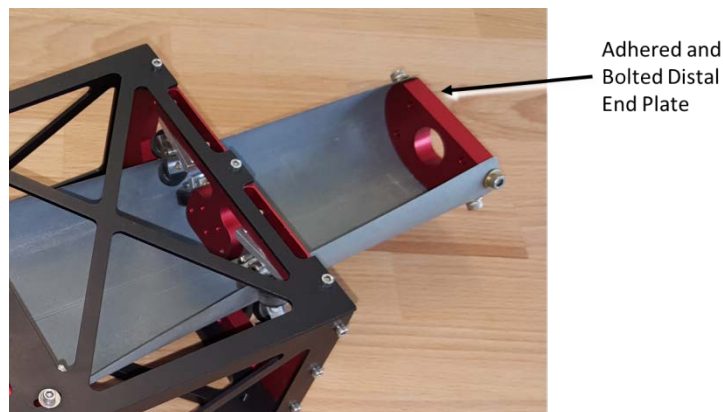


**Figure 6. '*NASA ARM Boom*' Deployer, Distal End**

Boundary Conditions: The root boundary conditions, along with the distal end, define the structural performance of the entire system. Within the Roccor boom deployer family, a myriad of boundary constraints mechanisms have been incorporated in an attempt to maximize rigidity while minimizing cost

and complexity. To date, all of Roccor's deployers contain at least two roller support planes, an aft set near the root end of the formation region and a forward end where the boom exits the box. The roller supports for each plane come in two types, a 'surface' roller that contacts the composite radially around the cross section and 'edge' rollers that guide and preload the open/exposed section of the slit-tube. In Figure 7, two 'DARPA Phoenix HIMast Boom' units are stacked in tandem with the distal end partially deployed. Here the difference between surface and edge rollers can be clearly seen. Each boom contains a maximum of two edge rollers, while a variable number of surface rollers are placed where the support is needed on both the inside and outside of the open cross section. For all of Roccor's boom deployers, the surface rollers are simplistic Delrin wheels that passively roll against the composite surface to provide support and low parasitic drag. In the case of the 'NASA CubeSat Magnetometer Boom' the small envelope does not allow volume for these rollers so the composite runs along a smooth, low-friction contoured material interface.

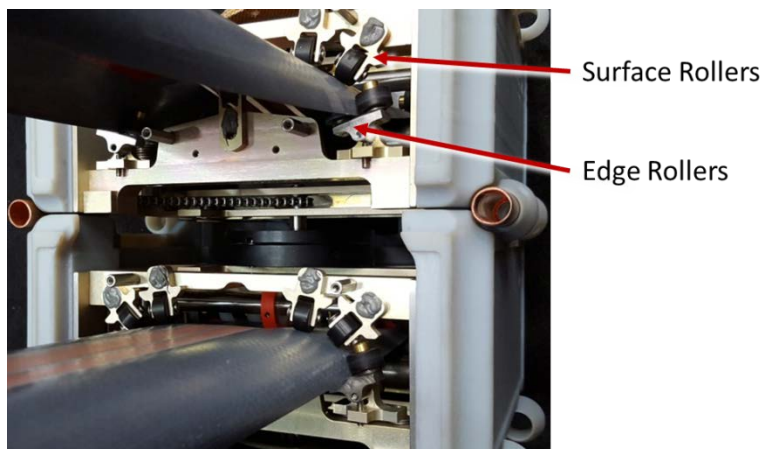


**Figure 7. 'DARPA Phoenix HIMast Boom' Boundary Condition Restraints**

The edge rollers within the Roccor family have evolved significantly as a need for deployers with high precision and robustness has been realized. The early design implemented for the 'DARPA Phoenix Camera Boom' deployer is shown on the left side of Figure 8. Here a ball-bearing pulley was used and preloaded against the composite edge with a spring-plunger system. This design concept worked well however it was challenging to tune the pitch of the wheel in order to align it to the composite edge. Slight misalignments caused the side of the pulley to rub against the composite causing damage and unpredictable performance. Furthermore, during the course of the deployment, slight changes in this angle occurred as the distal end moved away from the deployer box leading to degradation to the composite edge. The magnitude of the edge preload was also very limited in order to prevent composite edge degradation due to the small contact area between the circular edge pulley and the linear laminate edge. In addition, when the boom was subjected to lateral loads, the spring-plunger was in this load path which was often times too compliant and reduced the overall deployed performance.

The most current edge roller design is shown on the right side of Figure 8. This image is from the 'NASA ARM Boom' deployer system however this concept has been implemented into the 'DARPA Phoenix HIMast Boom' and the 'NASA CubeSat Magnetometer Boom' deployers. Here the composite slides directly against a flat, hardened steel block enabling a rigid line-contact interface along a defined length of laminate edge. In addition, two surface rollers are immediately adjacent to align and hold the edge in place. This system is designed to maintain the contact position even as the boom edge angle changes during the boom deployment. In addition, there is no compliance within this system other than a set screw to establish the initial edge preload during tuning (in higher TRL versions, any set-screw adjusters have been replaced with shim adjustment). Instead, the compliance within this interface is transferred into the composite laminate itself and the surface rollers locations are strategically placed to prevent undesired strains and binding. It is important to ensure that the boom edges are properly trimmed to ensure minimal variance – and hence change in edge preload - during the deployment of the slit-tube. In addition, proper edge treatments to

ensure smoothness and robustness are paramount when utilizing this method. One consequence of this design is added parasitic drag however the graphite to hardened steel interface is inherently low-friction. It has also been found that this system is robust and that the component receiving the most wear is the hardened steel in which minor  $<0.001$ -inch (25- $\mu$ m) grooves are present after extended use.

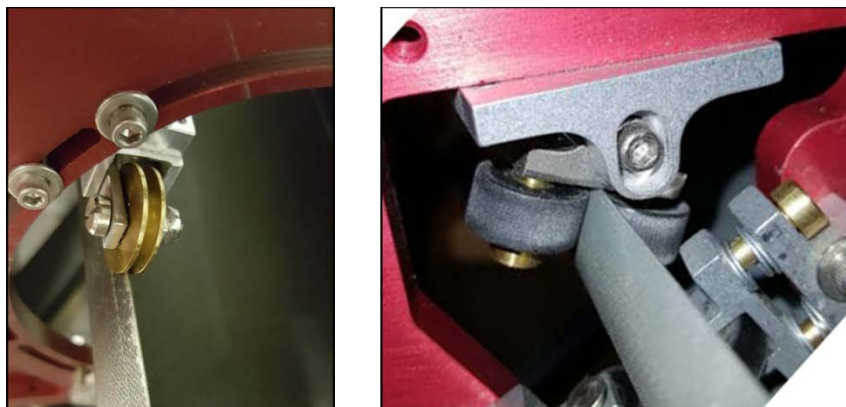


**Figure 8. Edge Roller Design: Pulley Wheel (left), Hard Metallic Stop (right)**

As a few final notes regarding the boundary condition restraints, the inclusion of adjustability to add preload to the edges and select surface rollers is a helpful feature. The variability in the composite fabrication process during a system development and the need for tuning can cause tedious tuning where ease of adjustability will help quicken this effort.

In addition, in some cases one can artificially decrease the need for the x4 or greater envelope factor (discussed above) by pinching the boom at the forward roller plane to more closely resemble the fully formed geometric cross section. This can be done within reason however does add additional strain to the composite, handling challenges during integration and increased parasitic drag. Rocco has successfully implemented this practice on the 'NASA CubeSat Magnetometer Boom' deployer.

### Drivetrain

Within the Rocco deployer family, the drivetrain design widely varies due to the requirements imparted for each application. The inclusion of internal motors vs external drives, the need for slip clutches to enable boom synchronization and the ability for mechanical pass-through to adjacent boxes are some examples the Rocco team has incorporated when considering drivetrain designs. A detailed discussion of this area is beyond the scope of this paper however the topic of the drive wheel design and placement is an important area to review. Within the Rocco family of boom deployers, it was found that the best method of driving the boom for deployment and retraction is via a friction wheel interface placed outside of the spool. Many existing systems for metallic slit-tubes incorporate a motorized spool inside the rolled boom as the primary drive mechanism. In conjunction with this, numerous rollers and pins need to be placed around the spool and boom exit point to 1) control the strain energy of the coil prior to applying drive forces, 2) counteract very high forces associated with radial expansion of the rolled boom imparted from the motorized spool and 3) ensure that the flattened boom does not buckle due to the spool drive forces as it exits the spool. When upgrading the system to include HSC booms, the need to constrain the spool is no longer present and hence placing the drive wheel outside of the spool reduces significant complexity and cost. For all four deployers outlined in this paper, a simplistic drive wheel with high durometer elastic material has been used with success as shown in Figure 9. For the case of the 'NASA ARM Boom' deployer, an axial preload of  $>20$  lbf (89 N) has been successfully demonstrated with this system.





**Figure 9. ‘NASA ARM Boom’ Deployer Drive Wheel**

#### Modeling the Formation Region

The geometry of the laminate formation region is a function of the material properties, laminate design, thickness, cross-sectional geometry and fabrication processes. These interconnected design features ultimately leads to a cross section that is hard to predict without empirical measurements. As such, it is important to fabricate a fully functional boom prior to initiating detailed deployer design. In addition, the formation region can change over time due to boom degradation, creep and thermal effects and should be fully understood prior to fabrication.

#### **Conclusion**

In this paper, the design traits of four unique deployer systems developed by Roccoor was presented with the goal to inform the reader of the wide range of design features and applications for High Strain Composite slit-tube deployable booms. In addition, common design practices were presented to provide a flavor for how the designs converged when developing these boom deployers as well as to provide lessons learned and future recommendations for new systems. The use of High Strain Composite structures in spacecraft deployables is an emerging field that offers the opportunity to develop simplistic, low cost systems that can supplant and reduce complexities of established deployable systems.

## References

1. Storable Tubular Extensional Member Device, US Patent # 3434674 A, 1969
2. Annon, "Tubular Spacecraft Booms (Extendible, Reel Stored)," Tech. Rep. SP-8065, NASA, Feb 1971
3. Wikipedia page on "High Strain Composite Structure", authored by Davis, B.  
[https://en.wikipedia.org/wiki/High\\_strain\\_composite\\_structure](https://en.wikipedia.org/wiki/High_strain_composite_structure)
4. Murphey, T., Francis, W., Davis B., Mejia-Ariza, J., Santer, M., Footdale, J., Schmid, K., Soykasap, O., Guidanean, K., Warren, P., "High Strain Composites", *Proceedings of the 2015 AIAA SciTech Conference, 2nd AIAA Spacecraft Structures Conference*, AIAA-2015-0942, [Pg 1-53], Kissimmee, Florida, 5-9 January 2015.
5. Francis, W. H., & Hulse, M. (2015). High Strain Composite Slit Tubes for Roll-Out Structures. In 2nd AIAA Spacecraft Structures Conference (pp. 1–12). Kissimmee, FL.
6. NASA Website on the International Space Station Solar Arrays:  
[https://www.nasa.gov/mission\\_pages/station/structure/elements/solar\\_arrays.html](https://www.nasa.gov/mission_pages/station/structure/elements/solar_arrays.html)
7. Im, E., Thompson, M., Fang, H., Pearson, J., Moore, J., Lin, J., "Prospects of Large Deployable Reflector Antennas for a New Generation of Geostationary Doppler Weather Radar Satellites", *Proceedings of the 2007 AIAA Space Conference & Exposition*, AIAA 2007-9917, Long Beach, California, 18-20 September 2007
8. Davis, B., Francis, W., Goff, J., Cross, M., Copel, D., "Big Deployables in Small Satellites" *28th Annual AIAA/USU Conference on Small Satellites*, [SSC14-VII-4, pp. 1-8], Logan, Utah, 2014.
9. Davis, B., Francis W., "High Performance Electrical Conductors in Composite Slit-Tube Booms", *Proceedings of the 2015 AIAA SciTech Conference, 2nd AIAA Spacecraft Structures Conference*, AIAA-2015-0226, [Pg 1-9], Kissimmee, Florida, 5-9 January 2015.
10. Murphey, T.W. and Pelligrino, S., "A Novel Actuated Composite Tape-Spring for Deployable Structures," *Proceedings of the 45th AIAA/ASME/ASCE/AHS/ASC Structures, Structural Dynamics, and Materials Conference*, April 2004, AIAA-2004-1528.
11. Shultz, M., Hulse, M., and Keller, P., "Neutrally Stable Composite Tape Springs," *Proceedings of the 47th AIAA/ASME/ASCE/AHS/ASC Structures, Structural Dynamics, and Materials Conference*, April 2006, AIAA-2006-1810.
12. Rimrott, F.P.J, "Storable Tubular Extendible Member – A Unique Machine Element," *Machine Design*, December 9, 1965.

# James Webb Space Telescope Deployment Brushless DC Motor Characteristics Analysis

Anh N. Tran\*

## Abstract

A DC motor's performance is usually characterized by a series of tests, which are conducted by pass/fail criteria. In most cases, these tests are adequate to address the performance characteristics under environmental and loading effects with some uncertainties and decent power/torque margins. However, if the motor performance requirement is very stringent, a better understanding of the motor characteristics is required.

The purpose of this paper is to establish a standard way to extract the torque components of the brushless motor and gear box characteristics of a high gear ratio geared motor from the composite geared motor testing and motor parameter measurement. These torque components include motor magnetic detent torque, Coulomb torque, viscous torque, windage torque, and gear tooth sliding torque.

The Aerospace Corp bearing torque model [1] and MPB torque models [2] are used to predict the Coulomb torque of the motor rotor bearings and to model the viscous components. Gear tooth sliding friction torque is derived from the dynamo geared motor test data. With these torque data, the geared motor mechanical efficiency can be estimated and provide the overall performance of the geared motor versus several motor operating parameters such as speed, temperature, applied current, and transmitted power.

## JWST Deployment Mechanism General Description

There are fourteen brushless DC motors that are used for the James Webb Space Telescope deployment mechanisms. Three of these motors are used in the Optical Telescope Elements deployment, which is the study of this paper. Most of these motors demonstrate excellent performance during flight tests. In order to assess the deploying margin on these systems, the geared motor performance characteristics, particularly the power losses, need to be estimated. Unfortunately, most of the tests for these motors are performed at the geared motor level. Therefore, the losses at the motor and the gearbox levels are not available. In order to extract these individual components, a geared motor model is developed. The model, then, is matched with the composite measured data to derive the individual torque components. The overview of the geared motor is shown in Figure 1.

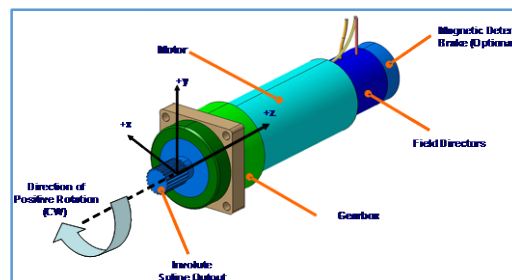


Figure 1. JWST Deployment Brushless DC Geared Motor Overview

---

\* Northrop Grumman Aerospace Systems, Redondo Beach, CA

### JWST Deployment Brushless DC Motor Parameters

The geared motor consists of a 3-phase, 4-pole, permanent-magnet brushless DC motor with an add-on resolver for position, and a 4608:1 planetary gearbox (4-stage). The detailed geared motor parameters are shown in Figure 2.

Number of Poles	4
Number of Phases	3
Motor Rotor Inertia	1.E-4 oz-in-s <sup>2</sup> (0.77 μN-m-s <sup>2</sup> )
Back EMF Constant (ambient), kb	2.11 mV/rpm
Winding Resistance (leg-to-leg) (ambient)	1.64 ohm
Winding Inductance (leg-to-leg) (ambient)	605 μhenry
Motor Torque Constant, kb	2.85 in-oz/A (0.020 N-m/A)
Operating Gearbox Shaft Speed	0.1 rpm
Gearbox Speed Reduction Ratio	4608
Maximum Applied Current	2 A

**Figure 2. PMSA Geared Motor Parameters**

### Brushless DC Motor General Equations

The simplified brushless DC motor torque governing equations are expressed as follows:

$$V = L \frac{dI}{dt} + RI + k_b \dot{\theta} \quad (1)$$

$$M\ddot{\theta} = (k_T I - k_{vm} \dot{\theta}^{.667} - k_{vg} \dot{\theta}^{.667} - k_w \dot{\theta}^2 - T_{cm} - T_{cg} - T_d) * (1 - k_{sg}) - \frac{T_l * 16}{GR} \quad (2)$$

where

V = voltage applied to the motor, volt

L = motor inductance, henry

I = net current through the motor windings, ampere

k<sub>T</sub> = motor torque constant, in-oz/A

k<sub>b</sub> = motor back emf constant, V/(rpm)

k<sub>vm</sub> = motor rotor bearing viscous torque constant, in-oz/(rpm)<sup>(2/3)</sup>

k<sub>w</sub> = motor rotor windage torque constant, in-oz/(rpm)<sup>2</sup>

k<sub>vg</sub> = gearbox viscous torque constant, in-oz/(rpm)<sup>(2/3)</sup>

T<sub>l</sub> = geared motor output torque, in-lb

T<sub>cm</sub> = motor rotor bearing Coulomb torque, in-oz

T<sub>cg</sub> = gearbox Coulomb torque, in-oz

k<sub>sg</sub> = gear tooth sliding coefficient

M = motor rotor moment of inertia, oz-in-sec<sup>2</sup>

T<sub>d</sub> = motor magnetic cogging or detent torque, in-oz

GR = gearbox gear ratio

In this equation, the motor and the gear box viscous torques are modelled using the MPB ball bearing viscous torque equation. This non-linear viscous torque model showed a remarkable comparison with the measurement data on geared motor spin-down tests reported by Tran and Halpin [3].

There are seven unknowns in the geared motor torque equations, which are listed as follows:

$k_{vm}$  = motor rotor bearing viscous torque constant, in-oz/(rpm)<sup>(2/3)</sup>

$k_w$  = motor rotor windage torque constant, in-oz/(rpm)<sup>2</sup>

$k_{vg}$  = gearbox viscous torque constant, in-oz/(rpm)<sup>(2/3)</sup>

$T_{cm}$  = motor rotor bearing Coulomb torque, in-oz

$T_{cg}$  = gearbox Coulomb torque, in-oz

$k_{sg}$  = gear tooth sliding coefficient

$T_d$  = motor magnetic cogging or detent torque, in-oz

There are only five usable sets of motor torque test data available. Two unknowns need to be estimated. Among these unknowns, for this particular application, the motor windage torque appears to be small and is predicted using the model developed by James E. Vukobratovic [4] as shown Equation 3.

$$T_w = \pi C_d \rho R^4 \omega^2 L \quad (3)$$

where

$C_d$  = skin friction coefficient. It can be determined by solving the below equation with a known Reynolds number

$$\frac{1}{\sqrt{C_d}} = 2.04 + 1.768 \ln(Re \sqrt{C_d})$$

$$Re = \text{Reynolds number} = \frac{Rt\omega}{\nu}$$

$\omega$  = rotor speed, rad/sec

$\nu$  = kinematic viscosity of air = 1.36e-4 ft<sup>2</sup>/s (12.6 mm<sup>2</sup>/s)

$\rho$  = air density = 0.0765 lbm/ft<sup>3</sup> (1.225 kg/m<sup>3</sup>)

$t$  = rotor/stator radial gap thickness = 0.002 in (0.05 mm)

$R$  = rotor radius = 0.5 in (13 mm)

$L$  = rotor length = 1 in (25 mm)

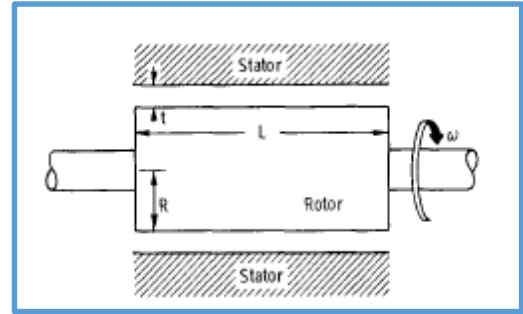


**Figure 3. Motor Rotor Parameters**

The skin friction coefficient and the windage torque versus rotor speed in air at room temperature and 70% relative humidity are plotted in Figure 4. From Figure 4, it is observed that the windage torque for this particular motor application is very small and can be ignored in the subsequent calculation.

The other unknown,  $k_{sg}$ , gear tooth sliding coefficient is derived from the geared motor stalled torque vs. current test and the geared motor dynamo test, which are shown later.

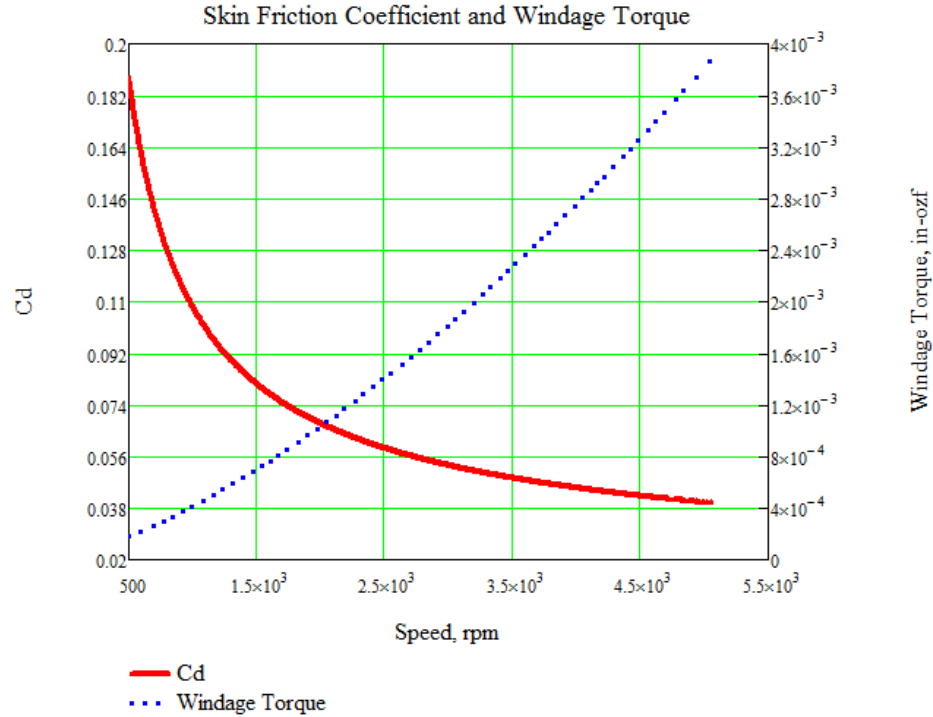


**Figure 4. Motor Skin Friction Coefficient and Windage Torque as a Function of Rotor Speed**

The rest of the five unknowns are extracted from the series of motor and geared motor tested conducted at the motor vendors and NGC listed as follows:

1. Motor No-Load Synchronous Test

Parameters:

Speed = 1800 rpm; no load; motor only; applied voltage, V: 3.0 volts; motor inductance, L=605  $\mu$ Henry; commutation frequency, f = 1000 Hz; motor winding resistance, R = 1.64  $\Omega$ ; kt = 2.85 in-oz/A (2.01 N-cm/A); kb=0.0021 V/rpm

Torque governing equation:

$$(k_T I - T_{cm} - T_d - k_{vm} \dot{\theta}^{.667}) = (k_T \frac{V - k_b \dot{\theta}}{\sqrt{R^2 + (L * f * 2 * \pi)^2}} - T_{cm} - T_d - k_{vm} \dot{\theta}^{.667}) = 0 \quad (4)$$

2. Motor Dynamo Test

Parameters:

Speed = 461 rpm; motor load torque, T<sub>ml</sub> = 3.0 in-oz (2.1 N-cm); applied current, I = 1.2 A

Torque governing equation:

$$(k_T I - T_{cm} - T_d - k_{vm} \dot{\theta}^{.667}) = T_{ml} \quad (5)$$

3. Geared Motor No-Load Synchronous Test

Parameters:

Speed = 1797 rpm; no load; geared motor; applied voltage, V: 3.58 volts; motor inductance, L=605  $\mu$ Henry; commutation frequency, f = 1000 Hz; motor winding resistance, R = 1.64  $\Omega$ ; kt = 2.85 in-ozf/A (2.01 N-cm/A); kb=0.0021 V/rpm

Torque governing equation:

$$(k_T I - T_{cm} - T_{cg} - T_d - k_{vm} \dot{\theta}^{.667} - k_w \dot{\theta}^2 - k_{vg} \dot{\theta}^{.667}) = (k_T \frac{V - k_b \dot{\theta}}{\sqrt{R^2 + (L * f * 2 * \pi)^2}} - T_{cm} - T_{cg} - T_d - k_{vm} \dot{\theta}^{.667} - k_{vg} \dot{\theta}^{.667}) = 0 \quad (6)$$

4. Geared Motor Stalled Torque from the Stalled Torque vs Current Test in Figure 8
- Parameters:  
Speed = 0 rpm; free current,  $I = 0.161$  A; motor winding resistance,  $R = 1.64 \Omega$ ;  $k_t = 2.85$  in-oz/A (2.01 N-cm/A)
- Torque governing equation:  
 $(k_t I - T_{cm} - T_{cg} - T_d) = 0$  (7)
5. The motor bearing Coulomb torque is predicted based on the Aerospace Corporation BRGS10C with the friction coefficient selected to be 0.15 for this bearing size and precision class with the measured preload of 2.5 lb (11 N). The bearing parameters and the output are shown in Figure 5. The predicted motor bearing Coulomb torque of 0.028 in-oz (0.20 mN-m) is comparable with the reported range of this motor Coulomb torque of 0.02 to 0.05 in-oz (0.14 to 0.35 mN-m) by the motor vendor [5]

The number of rows is 2				----- PROBLEM 1 RESULTS -----			
----- ROW 1 INPUT -----				UNMOUNTED	MOUNTED	MOUNTED AT	
						68 DEG. F	
						II= 68, IO= 68,	
FREE CONTACT ANGLE	11.20	BALL DEN LBS/IN <sup>3</sup>	0.2830	FREE DIAMETRAL PLAY	0.000464	0.000464	0.000464
NO OF BALLS	8.	IR PRESS FIT	-0.000200	FREE END PLAY	0.004734	0.004734	0.004734
BALL DIAMETER	0.093750	OR PRESS FIT	-0.000300	FREE CONTACT ANGLE	11.200	11.200	11.200
PITCH DIAMETER	0.437500	SHAFT ID	0.000000	IR PRESS FIT		-0.000200	-0.000200
IR CURVATURE	.5650	BEARING BORE	0.250000	OR PRESS FIT		-0.000300	-0.000300
OR CURVATURE	.5650	INNER RING OD (calculated)	0.381250	PRELOAD	2.60	2.60	2.60
IR H/D (49.8 degree)	.2000	OUTER RING ID (calculated)	0.493750	AXIAL DEFLECTION	0.000316	0.000316	0.000316
IR DM H/D (49.8 degree)	.2000	BEARING OD	0.625000	SOL AXIAL DEF.	0.000316	0.000316	0.000316
OR H/D (49.8 degree)	.2000	ROUSING OD	1.000000	CONTRACTION OF IR DIAM.	.000002	.000002	.000002
OR DM H/D (49.8 degree)	.2000	INNER RING WIDTH	0.196000	EXPANSION OF OR DIAM.	.000003	.000003	.000003
		OUTER RING WIDTH	0.196000	IR MEAN CONTACT STRESS	127296.	127296.	127296.
MODULUS OF ELASTICITY				OR MEAN CONTACT STRESS	105916.	105916.	105916.
SHAFT	0.30E+08	PRELOAD =	2.60	CONTACT ANGLE AT PRLD	12.654	12.654	12.654
BEARING RINGS	0.28E+08	1=UMI 2=MID AT 68f 3=MID AT TEMP		REQUIRED IR H/D AT PRLD	0.025	0.025	0.025
BALLS	0.28E+08	STRADDLE	0.156000	REQUIRED OR H/D AT PRLD	0.025	0.025	0.025
ROUSING	0.30E+08	AXIAL SPRING RATE	0.10E+21	--- THE TORQUE AND SPRING RATES BELOW ARE FOR BRG PAIR ---			
POISSON RATIO		AXIAL SPRING GAP	0.000000	----- BRG PAIR LOAD TORQUES IN-OZ -----			
SHAFT	.3000	TYPE OF DOUBLE ROW = 1.	-1=DF 0=DT	TORQUES BASED ON A FRIC. COEF. = 0.150			
BEARING RINGS	.2850	FACE FLUSH ERROR	0.000000	1. BALL TO RACE SPIN	0.01887	0.01887	0.01887
BALLS	.2850	FRICITION COEF AT SLOW SPEED	.150	2. BALL TO RACE ROLL	0.00733	0.00733	0.00733
ROUSING	.3000			3. MATERIAL HYSTER.	0.00150	0.00150	0.00150
COEF LINEAR EXPAN				TOTAL 1+2+3	0.02771	0.02771	0.02771
SHAFT	0.60E-05	IR CLAMPING FORCE(LBS)	0.	----- BRG PAIR SPRING RATES LBS/IN -----			
BEARING RINGS	0.56E-05	IR CLAMPING FRICITION COEF	.000	CAUTION! ASSUMES A RIGID PRELOAD SPRING			
BALLS	0.56E-05	OR CLAMPING FORCE(LBS)	0.	AXIAL	27511.	27511.	27511.
ROUSING	0.60E-05	OR CLAMPING FRICITION COEF	.000	RADIAL	269203.	269203.	269203.
OPERATING TEMPS-F							
SHAFT	68.0	FRICITION COEFFICIENTS					
INNER RING	68.0	CAGE TO LAND	.150				
OUTER RING	68.0	CAGE TO BALL	.150				
BALLS	68.0	BALL TO RACE	.150				
ROUSING	68.0	BALL POCKET DIAMETRAL CLR	0.0000				
LUBE VISCOSITY	0.	RADIAL DEF. VECTOR (DELR)	0.000000				
LUBE QUANTITY FACTOR	.000	AXIAL DEF. VECTOR (DELR)	0.000000				
----- LOAD AND SPEED INPUTS -----							
THRUST + --- ON SHAFT	0.	FILM PER SURFACE (FILM)	0.000000				
RADIAL + ^ UP ON SHAFT	0.						
MOMENT + CW @ ROW 1	0.						
ALPHA + CW	0.000200						
SPEED IR RPM	1.						
SPEED OR RPM	0.						

Figure 5. Motor Rotor Bearing Analysis Using the Aerospace Corporation BRGS10C

With five equations and five unknowns, the system of linear equations can be solved as shown in Figure 6. The result is summarized in Figure 7.

It is important to note that under high speed running conditions, this cogging or detent torque,  $T_d$ , has a mean value of zero and, therefore, does not constitute a loss of torque. The variation in the instantaneous value can, however, cause an unacceptable increase in the percentage ripple torque.

**Solve a linear system**  $Mx = v$

$$MX := \begin{bmatrix} 1 & 0 & 0 & 1800^{.667} & 0 \\ 1 & 0 & 1 & 461^{.667} & 0 \\ 1 & 1 & 0 & 1800^{.667} & 1800^{.667} \\ 1 & 1 & 1 & 0 & 0 \\ 1 & 0 & 0 & 0 & 0 \end{bmatrix} \quad x := \begin{bmatrix} T_{cm} \\ T_{cg} \\ T_d \\ K_{vm} \\ K_{vg} \end{bmatrix} \quad v := \begin{bmatrix} .3115 \\ .42 \\ .8794 \\ .4617 \\ .028 \end{bmatrix} \quad x := \text{lsolve}(MX, v) = \begin{bmatrix} 0.028 \\ 0.156 \\ 0.278 \\ 1.911 \times 10^{-3} \\ 2.777 \times 10^{-3} \end{bmatrix}$$

Figure 6. System of Linear Equations for Motor Torque Test Data

Torque Component or Constant	Value	
T <sub>cm</sub>	2.800E-2 in-oz	197.7 μN-m
T <sub>cg</sub>	1.560E-1 in-oz	1.102 mN-m
T <sub>d</sub>	2.780E-1 in-oz	1.963 mN-m
K <sub>vm</sub>	1.911E-3 in-oz/rpm <sup>0.667</sup>	13.49 μN-m/rpm <sup>0.667</sup>
K <sub>vg</sub>	2.777E-3 in-oz/rpm <sup>0.667</sup>	19.61 μN-m/rpm <sup>0.667</sup>
K <sub>w</sub>	1.600E-10 in-oz/rpm <sup>2</sup>	1.130 pN-m/rpm <sup>2</sup>

**Figure 7: Geared Motor Derived Torque Components**

The derived motor viscous torque of 0.001911 in-oz/rpm<sup>0.667</sup> (13.49 μN-m/ rpm<sup>0.667</sup>) is also comparable with this motor viscous torque constant, B<sub>v</sub>, of 1.33E-4 in-oz/rpm or 0.00162 in-oz/rpm<sup>0.667</sup> reported by the motor vendor [6].

The static gear tooth sliding coefficient is derived based on the geared motor stalled torque versus applied current test data. The geared motor stalled torque versus applied current condition can be modelled as follows:

$$V = L \frac{dI}{dt} + RI \quad (8)$$

$$T_s = (k_T I - T_{cm} - T_{cg} - T_d)(1 - k_{sg}) \quad (9)$$

where  $k_{sg}$  is the static gear tooth contact frictional torque loss coefficient, which is the only loss component depending on the transmitted torque.

By applying a linear regression to the stalled torque versus applied current data as shown in Figure 8, the slope and the x-intercept are expressed as follows:

$$k_{sg} = 1 - \text{slope}/k_t = 1 - 1.773/2.85 = 1 - 0.622 = 0.38 \text{ or } 38\% \text{ gear tooth loss at static loaded condition.}$$

$$T_{cm} + T_{cg} + T_d = 2.85 * 0.162 = 0.462 \text{ in-oz (3.26 mN-m)}$$

The dynamic gear tooth sliding coefficient is derived from the geared motor dynamo test, which has the operating parameters listed as follows:

Speed = 4608 rpm; load torque, T<sub>l</sub> = 375 in-lb (42.4 N-m) at gear shaft; applied current, I = 1.2 A  
Torque governing equation:

$$(k_T I - T_{cm} - T_d - k_{vm} \dot{\theta}^{0.667} - T_{cg} - k_{vg} \dot{\theta}^{0.667})(1 - k_{sg}) = \frac{T_l * 16}{GR} \quad (10)$$

From the data in Figure 7, the dynamic gear tooth sliding friction coefficient is derived to be 0.33, which is consistent with the static sliding friction coefficient of 0.38 extracted from the stalled torque vs current curve shown in Figure 8. The static and the dynamic gear tooth sliding coefficients are very close. To be conservative, the static gear tooth sliding friction coefficient will be used for the subsequent analysis.

The motor bearing viscous torque model is well described analytically by the MPB torque equation [2]. It's assumed that the gearbox viscous torque is also modelled using the MPB torque equation (Equation 11).

$$T_{visc} = a * 2.4 * 10^{-5} RPM^{0.67} (10^{10^{4.354 - 1.612 * \log_{10}(T)}} - 0.6)^{0.67} \quad (11)$$

where T is oil temperature in degree Kelvin, RPM is rotor speed in rev per minute, and a is a scaling factor to match with the measured data, which is derived to be 5.045 to match the derived composite geared motor torque constant. Figure 9 shows the geared motor viscous torque for different speeds and oil temperatures. This model uses the Brayco 815Z oil for both motor bearings and gearbox components.



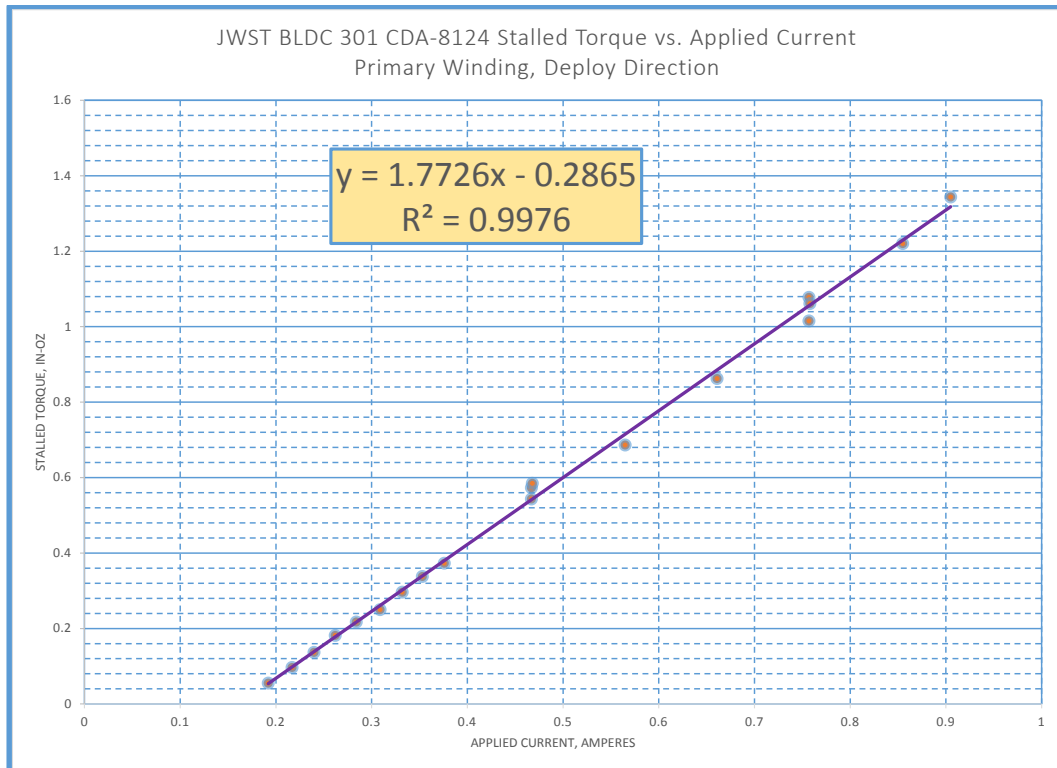


**Figure 8. Geared Motor Stalled Torque vs Applied Current Curve**

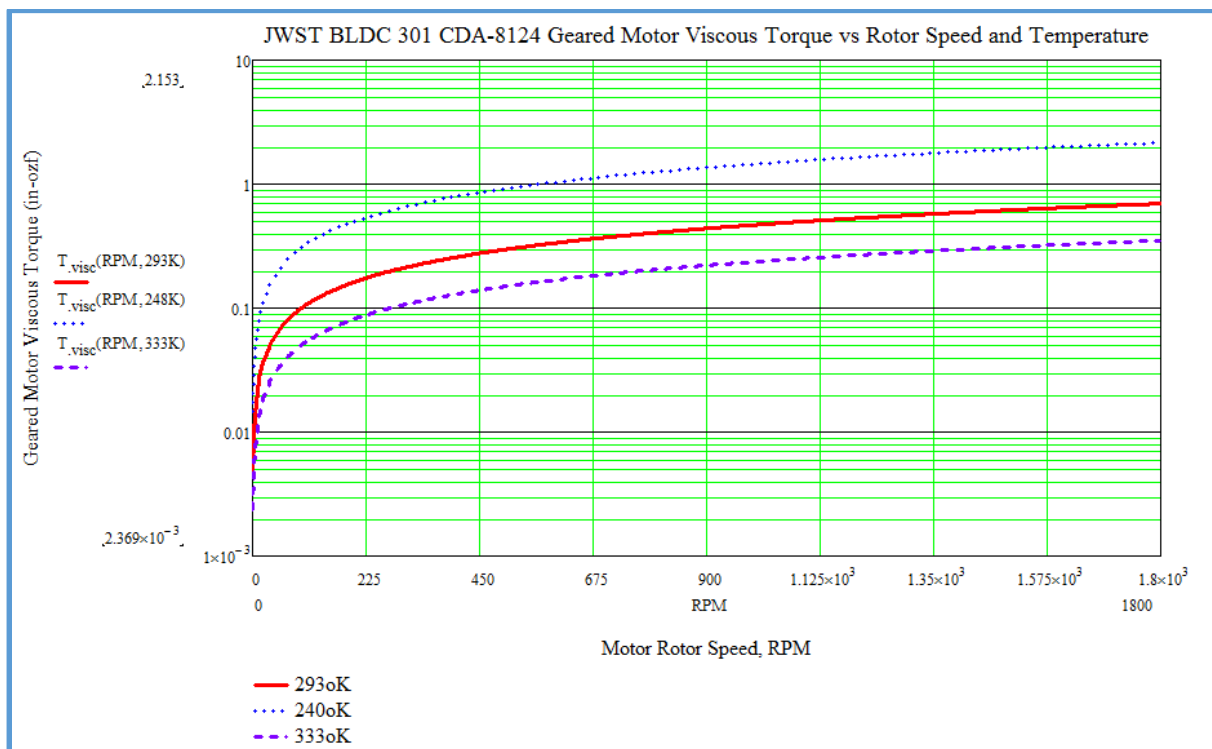


**Figure 9. JWST Motor Viscous Torque versus Operating Temperature and Rotor Speed**

To increase the fidelity of the geared motor model and its prediction, the model prediction is compared with the no-load current versus motor rotor speed test data. The governing torque model equation is expressed as follows:

$$V = RI + k_b \dot{\theta} \quad (12)$$

$$k_T I = T_{cm} + T_{cg} + T_d + k_{vm} \dot{\theta}^{.667} + k_w \dot{\theta}^2 + k_{vg} \dot{\theta}^{.667} \quad (13)$$

By applying the linear regression analysis from Equation 13 on the measured no-load current versus motor rotor speed as shown in Figure 10, the results from both the regression analysis and the model prediction using system of equations are plotted in Figure 10. From Figure 10, these two curves show a remarkable match.

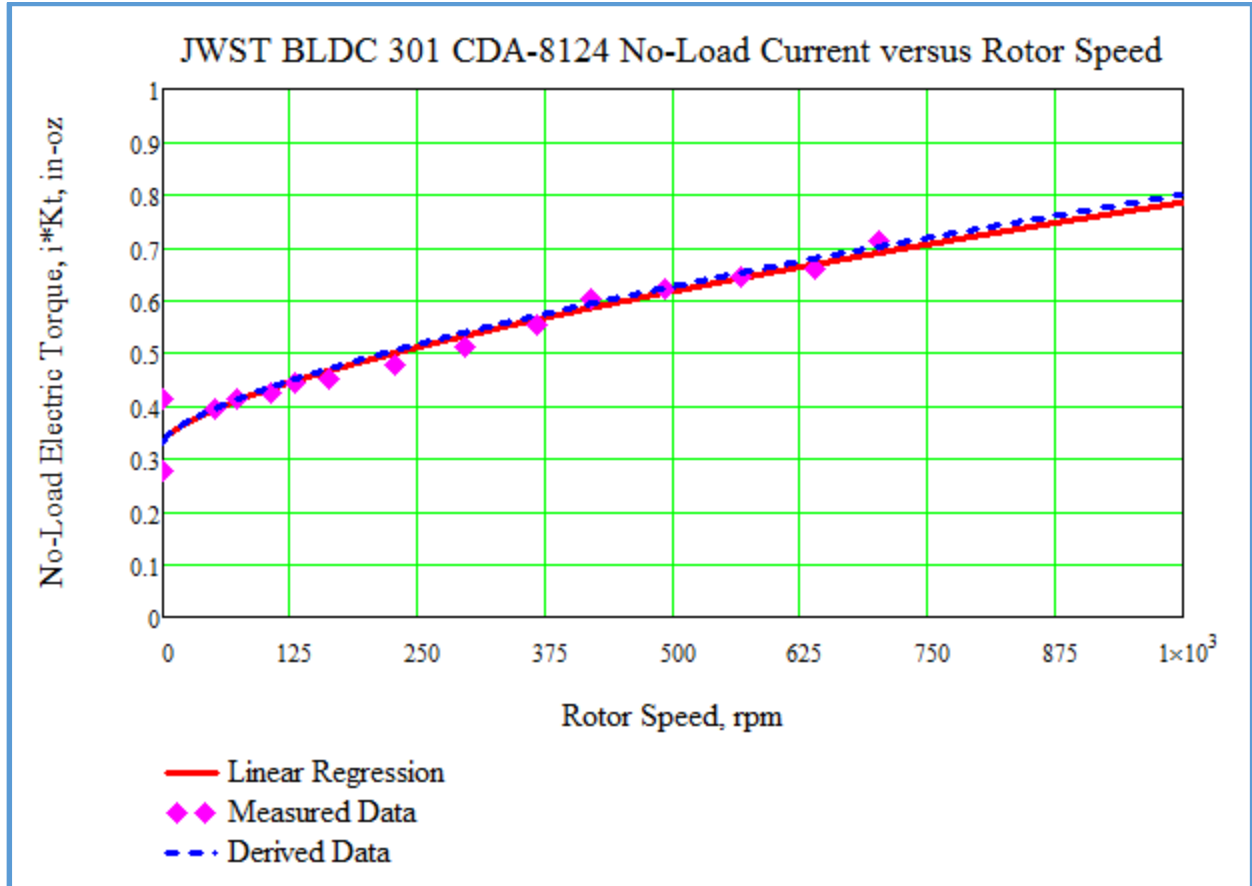


**Figure 10. No-Load Applied Current versus Rotor Speed for the Measured and Derived Data**

For the deployment, the applied current and the motor rotor speed are controlled with a forward control fashion. There is no force/torque feedback control. The gearbox output torque is expected to responded accordingly to the controlled input within a certain level of uncertainty under the imposed environmental conditions such as operating temperature, vibration induced load, humidity, etc. If the gear output torque exceeds a certain limit, deployment mechanical failure will occur. On the other hand, the gear output torque may not be sufficient to deploy the system. The limit between these values sometime is small.

The effect of motor parameter variation and environmental conditions on the geared motor output torque is evaluated as follows.

### Variation of Output Torque from a Given Applied Current

The geared motor output torque equation is expressed as follows:

$$T_{g\_load\_output}(i, \omega, T) := (1 - k_{sg}) \cdot k_t i - T_{cm} - T_{cg} - T_d - (k_{vg} + k_{vm}) \cdot \omega^{.667} \cdot \left[ \frac{10^{10^{4.354 - 1.612 \cdot \log\left[\frac{T}{(1K)}\right]}}}{10^{10^{(4.354 - 1.612 \cdot \log(293))}}} - 0.6 \right]^{\left(\frac{2}{3}\right)} \cdot \frac{GR}{16} \quad (14)$$

Applying the above procedure to the rest of the motors, all motor parameters, test data, and the torque components are calculated and shown in Figure 11. The geared motor output torque versus speed at room temperature and applied current of 1 ampere for three geared motors are plotted in Figure 12.

From Figure 12, at the nominal operating motor rotor speed of 461 rpm, the gear motor output torque can vary as much as 7%. The variation can be higher if the sample size becomes larger or both the primary and the redundant winding data are evaluated.

			Brushless DC Motor ID			Unit
			CDA-8124	CDA-8125	CDA-8126	
Measured Motor Parameters	Kt		2.85	2.9	2.85	in-oz/A
	R		1.64	1.63	1.63	Ohm
	L		605	595	614	mHenry
	Kb		0.00211	0.00214	0.00211	V/rpm
	f		1000	1000	1000	Hz
Test Measured Data	Motor No-Load	Vrms	3.6	3.6	3.6	Volts
		V[1]	0.3115	0.2715	0.3080	in-oz
	Motor Dynamo	Tml	3	3	3	in-oz
		I	1.2	1.2	1.2	Amperes
		V[2]	0.4259	0.4860	0.4259	in-oz
	Geared Motor No-Load	Vrms	4.3	4.3	4.3	Volts
		V[3]	0.8794	0.8581	0.8693	in-oz
	Geared Motor Stalled	X-intercept	0.4617	0.55825	0.5358	in-oz
		V[4]	0.4617	0.55825	0.5358	in-oz
	Motor Coulomb Torque	V[5]	0.028	0.028	0.028	in-oz
Motor Torque/Friction Components	Tcm		0.0280	0.0280	0.0280	in-oz
	Tgm		0.1560	0.1700	0.2230	in-oz
	Td		0.2780	0.3600	0.2850	in-oz
	Kvm		0.0019	0.0016	0.0019	in-oz/rpm <sup>.67</sup>
	Kvg		0.0028	0.0028	0.0023	in-oz/rpm <sup>.67</sup>
	ksg		0.3780	0.3050	0.3407	unitless

Figure 11. Geared Motor Parameters, Test Data, and Torque Component Values and Constants

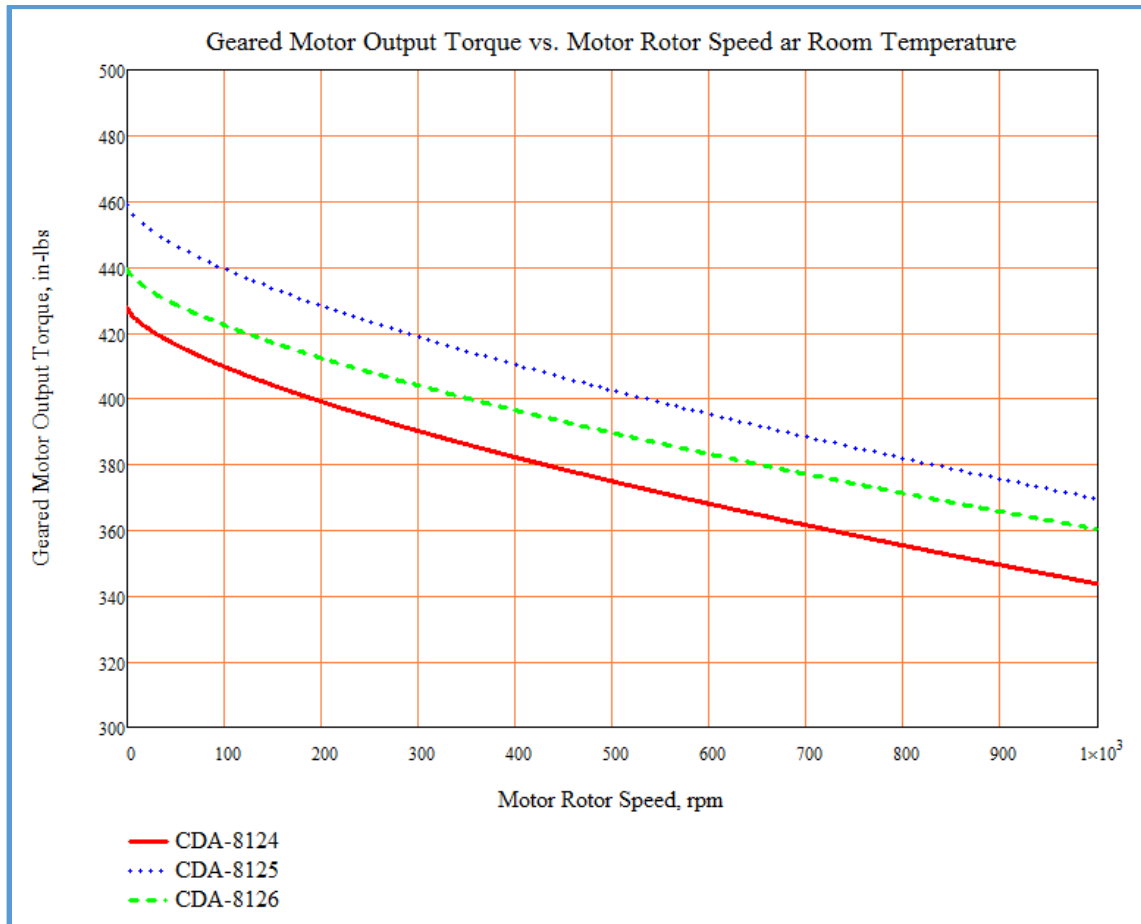


**Figure 12. Geared Motor Output Torque vs Speed for Three Motors**

### Environmental Induced Effects on Gear Output Torque

The environmental effects on the geared motor output torque are numerous. In the scope of this paper, only the temperature effect is evaluated. Applying Equation 14, the geared motor output torque versus operating speed at three operating temperatures: 243°K (cold), 293°K (RT), and 348°K (hot) and the given applied current of 1 ampere is plotted in Figure 13. From Figure 13, at the nominal operating speed of 461 rpm, the output torque variation can be as high as 75%.

It is observed that the combined effect of the motor parameter variation and the temperature can cause the output torque variation to be as much as 82%. This is a conservative prediction due to the small motor sample size (i.e., 3) and the motor parameters are evaluated for the primary winding and the deployment direction only.

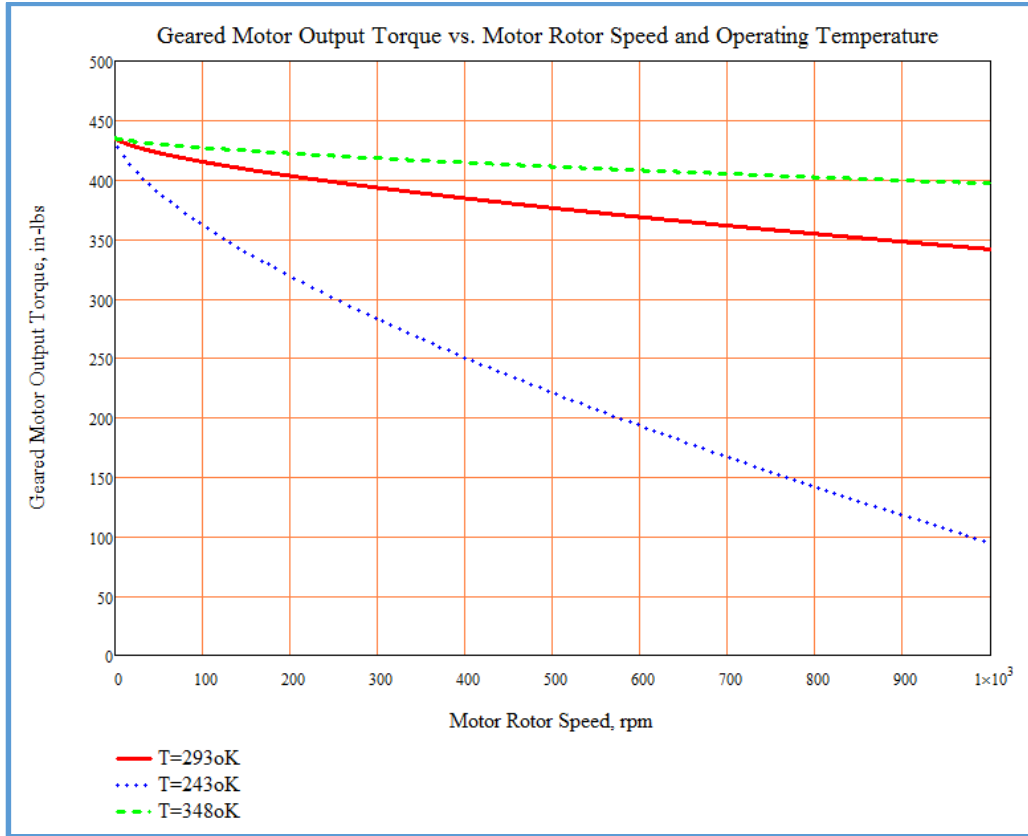


**Figure 13. Geared Motor Output Torque vs Speed for CDA-8124 at Different Operating Temperature**

### Geared Motor and Gearbox Torque Efficiency Calculation

For the motor evaluation, it's useful to show the geared motor and the gearbox torque efficiency. In general, the torque efficiency  $\eta$  of a motor is defined as the ratio between the input electrical power, i.e., the product of voltage times current, and the output mechanical power minus the power loss due to mechanical means, which is expressed as follows:

$$\eta_{motor} = \frac{(k_T i - T_{loss})(1 - k_{sg})}{k_T i} \quad (15)$$

where  $T_{loss}$  is the net projected torque loss of the motor and the gearbox to the motor rotor location due to speed, temperature, and windage, and  $n_{gslide}$  is the gearbox tooth power efficiency due to applied torque.

Using Equation 2 with motor parameters from Figure 11, the geared motor torque efficiency can be calculated as follows:

$$\text{geared\_motor\_}\eta(i, x, T) := \frac{k_T i - T_{cg} - T_{cm} - T_d - (K_{vg} + K_{vm}) \cdot \left[ \frac{10^{10^{4.354 - 1.612 \cdot \log\left[\frac{T}{(1K)}\right]} - 0.6}{10^{10^{(4.354 - 1.612 \cdot \log(293))}} - 0.6} \right]^{\left(\frac{2}{3}\right)} \cdot x^{.67} \cdot (1 - 0.378)}{k_T i} \quad (16)$$

Figure 14 shows the geared motor torque efficiency as a function of applied current and geared motor output torque at room temperature. From Equation 16, it is clear that the mechanical efficiency for the geared motor is a strong function of several motor operating parameters such as motor transmitted torque, operating speed, operating temperature, humidity, atmospheric pressure, etc. Therefore, it is not very specific and should be used as a guideline to motor selection or design/configuration comparison.

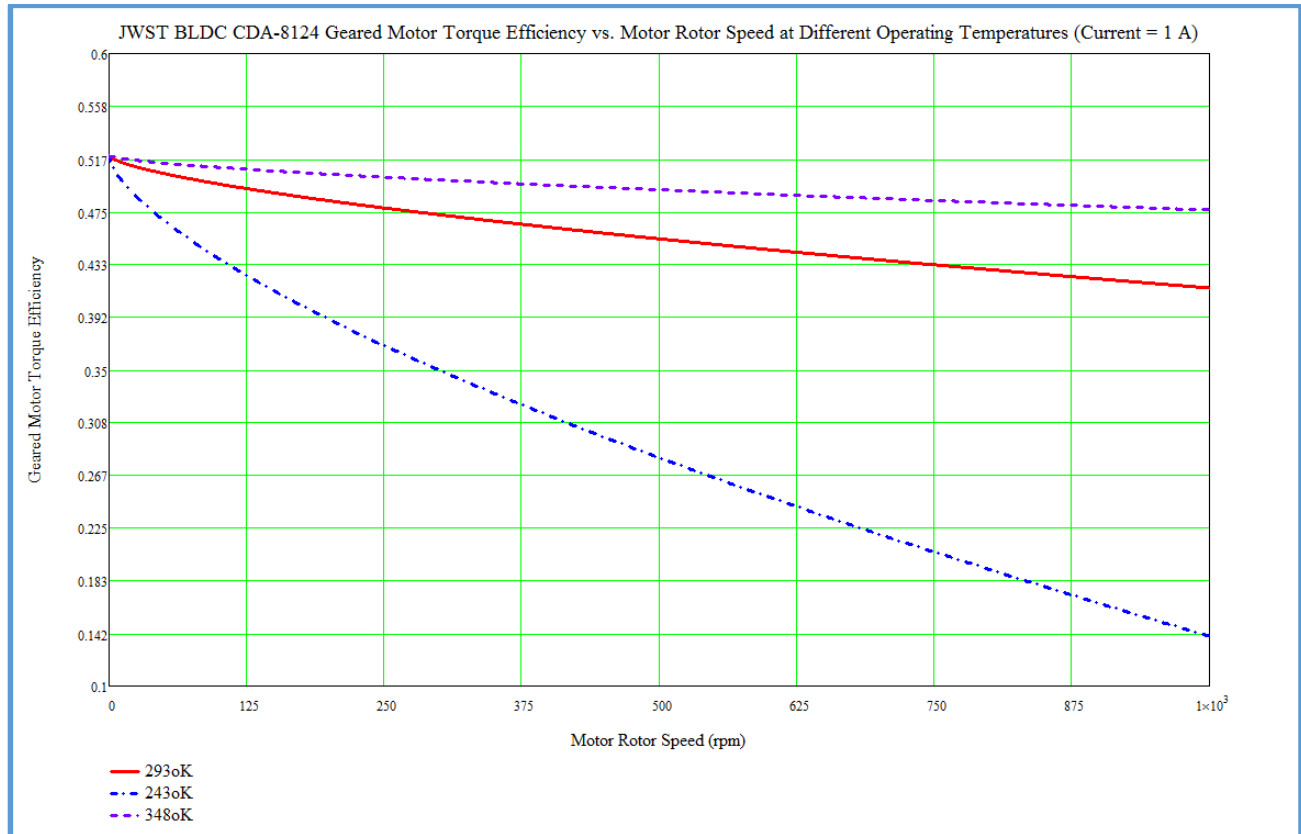


**Figure 14. Geared Motor Torque Efficiency vs Motor Rotor Speed at Different Temperatures**

The gearbox torque efficiency can be calculated as follows:

$$\text{gearbox\_}\eta(\text{torque}, x, T) := \frac{\text{torque} - T_{cg} - K_{vg} \cdot \left[ \frac{10^{10 \left[ \frac{4.354 - 1.612 \cdot \log \left[ \frac{T}{(1K)} \right]}{10^{(4.354 - 1.612 \cdot \log(293))}} - 0.6 \right]}{10^{(4.354 - 1.612 \cdot \log(293))} - 0.6} \right]^{\left(\frac{2}{3}\right)} \cdot x^{.67} \cdot (1 - 0.378)}{\text{torque}} \quad (17)$$

Where the values for each parameters for each motor are defined and can be found in Figure 11.

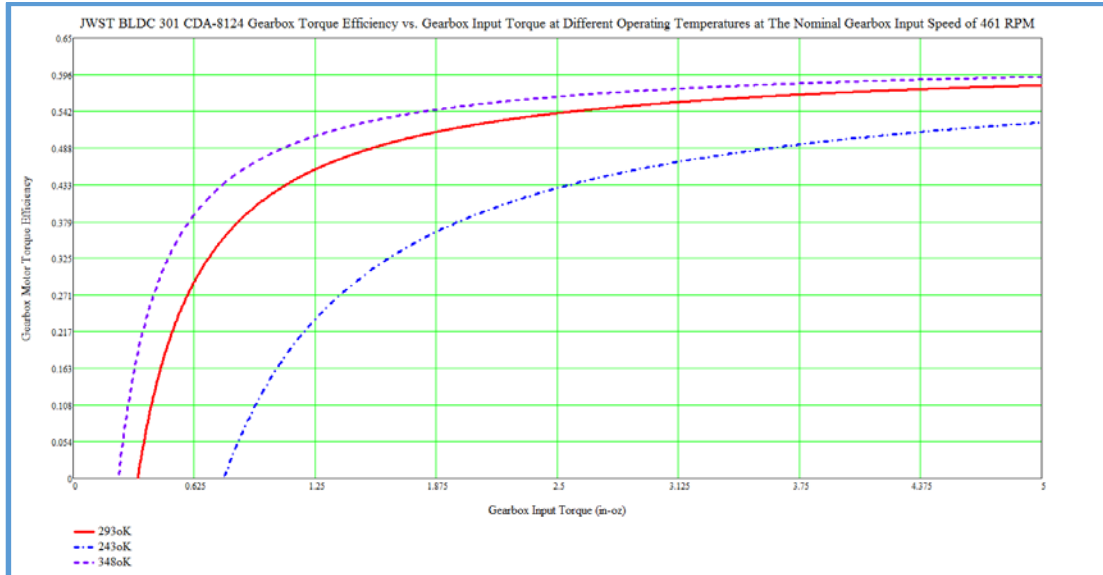


**Figure 15. Simulated Power Efficiency vs. Motor Rotor Speed and Operating Temperature at 1-A Applied Current**

It is observed that at low input torque, the gearbox torque efficiency is dominated by the Coulomb, viscous, and detent torques. However, at close to full load, the gearbox efficiency is controlled by gear tooth sliding friction coefficient.

### Conclusion

A brushless DC motor torque model has been developed in order to extract the geared motor torque component loss for the gearbox and the motor using data from motor measurements and the geared motor testing. The geared motor output torque and mechanical efficiency vary from motor to motor and are a strong function of the transmitted torque, rotor speed, and operating temperature.

If the geared output torque requirement is stringent, the motor characterisation process and the selected operating condition as shown above are a must in order to reduce the uncertainty.

### Lessons Learned

1. The geared motor output torque significantly varies from motor to motor and with operating conditions. The output torque variation has been shown to be 82%. If additional factors are accounted for, it can be 100% or higher. By characterizing each motor and selecting optimal operating conditions, the output variation can be significantly reduced.
2. The geared motor tests at the motor vendor should be well defined and the results should be verified at each step to assure that the physics can be understood or explained.
3. The MPB viscous torque model shows a good correlation with the geared motor test data and is proportional to the speed to the power of 0.667. The motor bearing Coulomb torque can be reasonably predicted using the ball bearing torque model in BRGS10C with a friction coefficient of 0.15 to 0.20 for small bearings (OD < 1 in (2.5 cm))
4. The gearbox efficiency is not a constant and a non-linear function throughout operating conditions.

## **References**

1. Ward, Peter, "Effects of Bearing Cleaning and Lube Environment on Bearing Performance", 29<sup>th</sup> Aerospace Mechanisms Symposium Proceeding, Houston, TX, 1995.
2. Leveille, A., The Aerospace Corporation Bearing Analysis Program, BRGS10C version 10C, 2005
3. Tran, A.N., Halpin, J.D., "JAMES WEBB SPACE TELESCOPE DEPLOYMENT TOWER ASSEMBLY DEPLOYING ANOMALY AND LESSONS LEARNED", 16th European Space Mechanisms and Tribology Symposium 2015, Bilbao, Spain - 23rd to 25th September 2015
4. Vrancik, J.E., "Prediction of Windage Power Loss In Alternators", NASA TN D-4849, Lewis Research Center, Cleveland, Ohio, 1968
5. Personal communication with staff at CDA InterCorp, Florida, USA Dec 23, 2015
6. Brushless Permanent Magnet Motor Engineering Reference Data, CDA InterCorp Catalog

## **Acknowledgement**

The author would like to thank Paul Reynolds, Optical Telescope Elements Mechanisms IPT leader, Dr. Scott Texter, NGC JWST Optical Telescope Elements program manager for their guidance, and my NGC colleagues Shaun O'Neill and Stan Klyza for technical discussion. The technical discussion with CDA InterCorp is also appreciated.



# Development of a Deployment and Latching Mechanism for a Pointing System on the Neutron Star Interior Composition Explorer (NICER) for Goddard Space Flight Center

Robert H. Berning\* and John J. Holzinger\*

## Abstract

Many space applications require high stiffness and stable latching systems. The Deployment and Latching Mechanism design for the Neutron Star Interior Composition Explorer (NICER), provides a stable, high-stiffness structure ( $> 1,500,000$  in-lb/rad ( $169$  MN-m/rad)) in the deployed and stowed positions. The Deployment and Latching Mechanism consists of a rotary deployment actuator, rotary latching actuator and an over-center slider crank mechanism latch. This design allows the NICER system to be repetitively latched in both stowed and deployed positions, providing locking (high stiffness) in both rotational directions. This paper describes the development, design, incorporation of lessons learned and testing of the Deployment and Latching Mechanism.

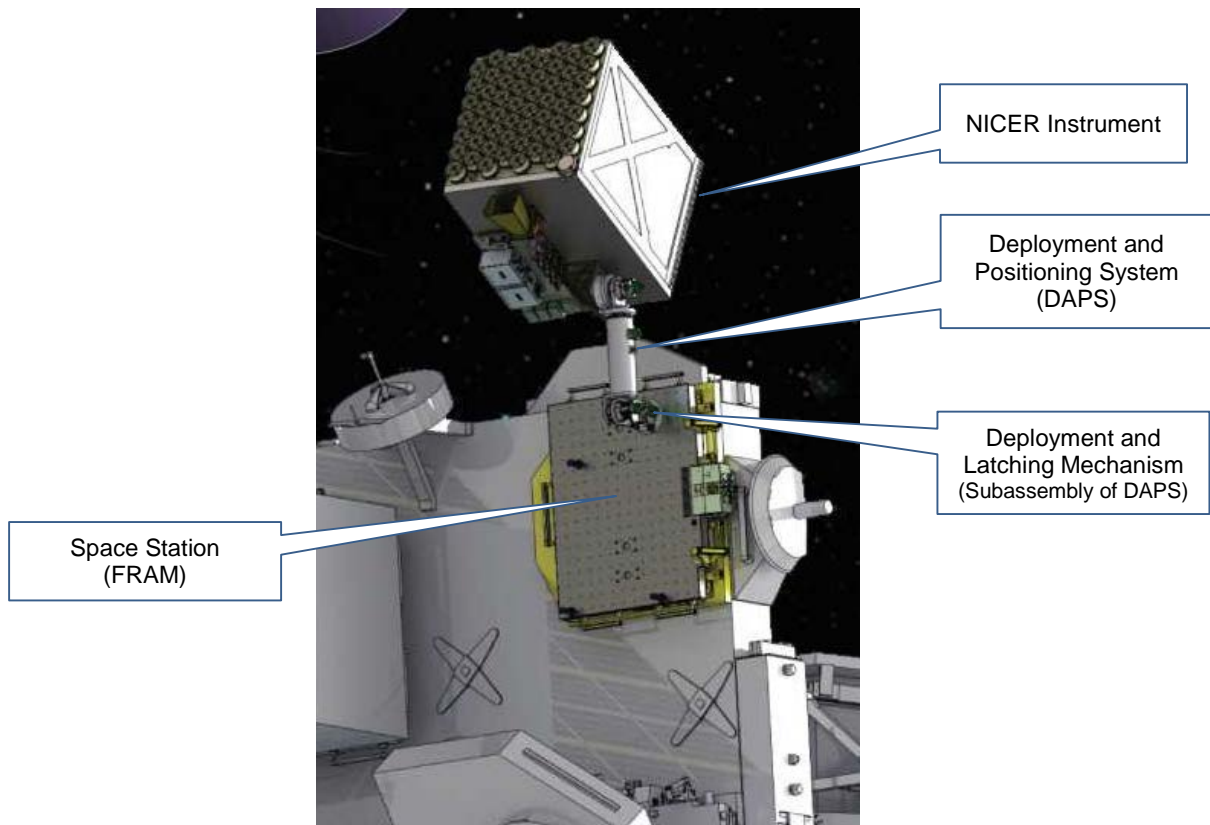


**Figure 1. Neutron Star Interior Composition Explorer (NICER)**  
(shown in Deployed and Latched Position)

---

\* Moog Inc. Chatsworth, CA

## Introduction

The deployment and latching mechanism is part of the Deployment and Positioning System (DAPS). The DAPS is an articulating mechanism for the NICER program consisting of a deployment and latching mechanism, a pointing mechanism, and an interconnecting boom structure. The DAPS provides a stable, high-stiffness structure in the deployed and latched positions for a star-tracker system that “enables (together with NICER’s GPS-based absolute timing) high-precision pulsar light-curve measurements through ultra-deep exposures spanning the 18-month mission lifetime.”<sup>1</sup> It has a deployment articulating arm that needs to be deployed 84° from the vertically stowed position and latched prior to pointing mechanism activation. The arm and the full instrument is required to be stowed and latched multiple times on board the International Space Station (ISS). A final stow and latch cycle is required for safe removal from the Space Station. DAPS has specially designed interfaces at the ISS interface and at the payload. The latch can provide locking for the ride to the ISS, multiple latched stow and deploy cycles on the ISS, and if required, it will perform a final stow and latch for removal from the ISS if necessary.

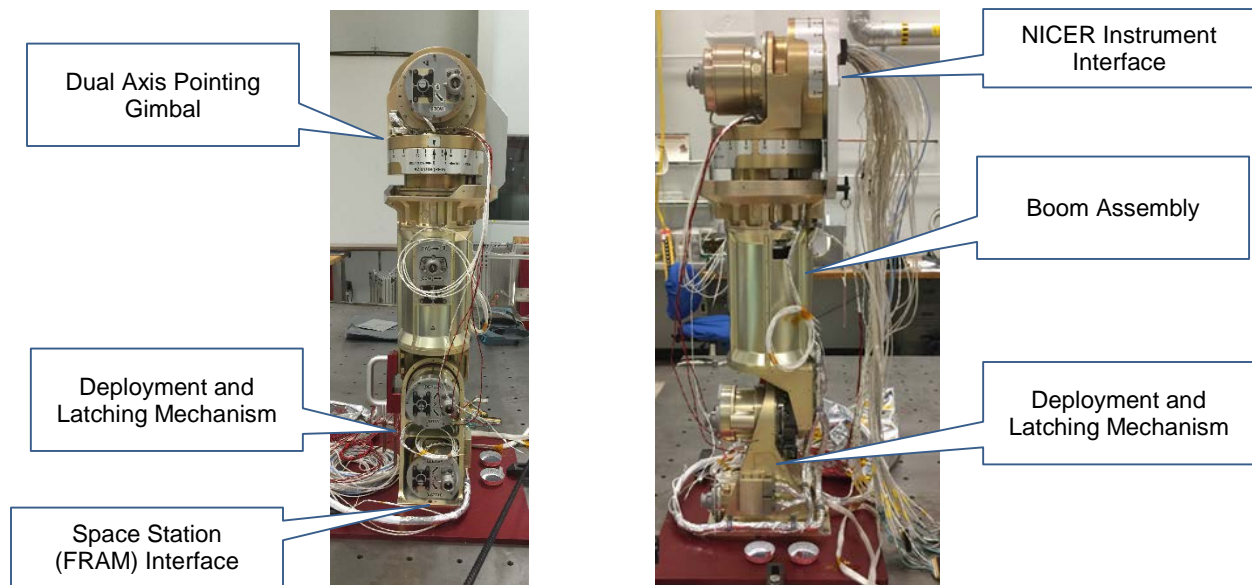


**Figure 2. Deployment and Positioning System (DAPS)**  
(shown in Stowed and Latched Position)

## Deployment and Latching Mechanism Development

The deployment and latching mechanism is a subassembly of the NICER DAPS located between the Space Station Flight Releasable Attachment Mechanism (FRAM) interface and the boom arm with a dual axis pointing gimbal attached at the boom end that is the x-ray instrument attach point. The deployment and latch mechanism enables positioning and latching of the NICER instrument in both stowed and deployed positions. It consists of a bracket that is mounted onto the FRAM and employs a Moog deployment actuator, a Moog latching actuator, and the latching mechanism. The deployment mechanism is operated by these two electro-mechanical actuators, each having a stepper motor coupled to a zero-backlash gear transmission. The boom is attached to the deployment actuator. This type of actuator configuration is a very common approach for many space-related deployment applications, thus, there is extensive heritage justifying the use of these actuation mechanisms.

The deployment actuator travel from stop to stop is 84°. At both the deployment actuator’s stowed and deployed positions, the latching actuator engages the latch to hold the deployment actuator position. Prior to deployment actuator operation, the latch actuator releases the latch to allow the deployment actuator to stow or deploy. This is accomplished using an over-center slider crank mechanism that prevents the

deployment actuator from rotating in the stowed and deployed positions. In one direction, the deployment actuator hardstop prevents movement and in the other direction, movement is prevented by the over-center slider crank latch mechanism contacting the latching actuator hardstop.

The initial idea was to develop a latch that utilized physical hardstops for stowed and deployed positions without using motor power to hold position. The NICER program required two position high stiffness latch locations capable of reacting to loads in both CW and CCW directions. Heritage designs utilized either motor holding capabilities, additional latch actuators for each position, or an over-center device that held one position but was not a high-stiffness mechanism. Based on program requirements, a new latch mechanism would be needed to do the job.

Moog quickly ascertained that the demanding stiffness requirements of this application would not be achieved with a simple dual-sided wedge design, and instead focused our design concept around an efficient single-sided wedge that could take advantage of the integrated hardstop. The latching concept was completed with an over-center crank, resulting in a two-direction latch with physical stops in both directions. The latching actuator provides the crank portion of the slider crank mechanism, positioning the plunger wedge in the latched or released position, while a bolt with integral wedge works as the slider. An integral travel stop was added to the bolt assembly to limit deployment actuator travel when non-operation loads are applied. Mechanism design locks latch in place by establishing a ridged structure between the deployment actuator and the latching actuator hardstop. Under high torque loading, the latch design will not open, which prevents gapping or unlatching of the mechanism.

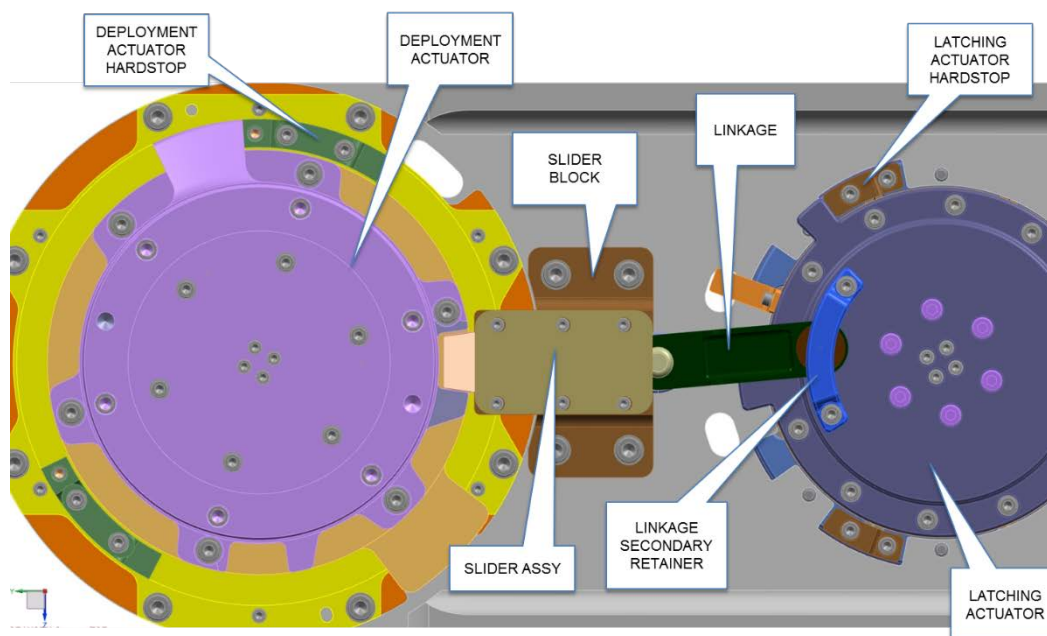


**Figure 3. Latch System Concept**

Though Moog heritage designs included Extra-Vehicular Activity (EVA) bolts, a unique addition to the NICER DAPS actuator mechanisms is the integration of the Extra Vehicular Activity (EVA) with the Extra-Vehicular Robot (EVR) attachment that is designed to provide the manual override of the actuator in case of loss of power. This EVA/EVR interface is designed to be operated by the astronauts or by the ISS robotic manipulator arm in a zero-gravity environment using a standard electrical powered driver. A magnetic clutch is provided to protect the zero-backlash gear transmission from being over-stressed. Also, the operating nomenclature on the actuator provides clear instruction and ease of viewing to reduce the potential for misuse. Each actuator's output position is indicated by a non-redundant potentiometer. NASA was planning to use cameras located on the robotic arm and possibly an astronaut's eyes to indicate revolutions of the

EVA/EVR bolt from hardstops or home positions to “ease” into the hardstops by counting revolutions and starting and stopping when hardstops were about to be engaged.

The latch design must prevent movement of the deployment actuator during NICER operation. Knowing this, a detailed free body diagram was created and used to create a mathematical model of the latch mechanism. The model optimizes the latch mechanism, by balancing input load with latch component loads and latching actuator performance. It also calculates all loads within the latch mechanism, torsional loading of the deployment actuator, latch component loads, friction, etc. The model can resize the latch mechanism for alternate load environments.

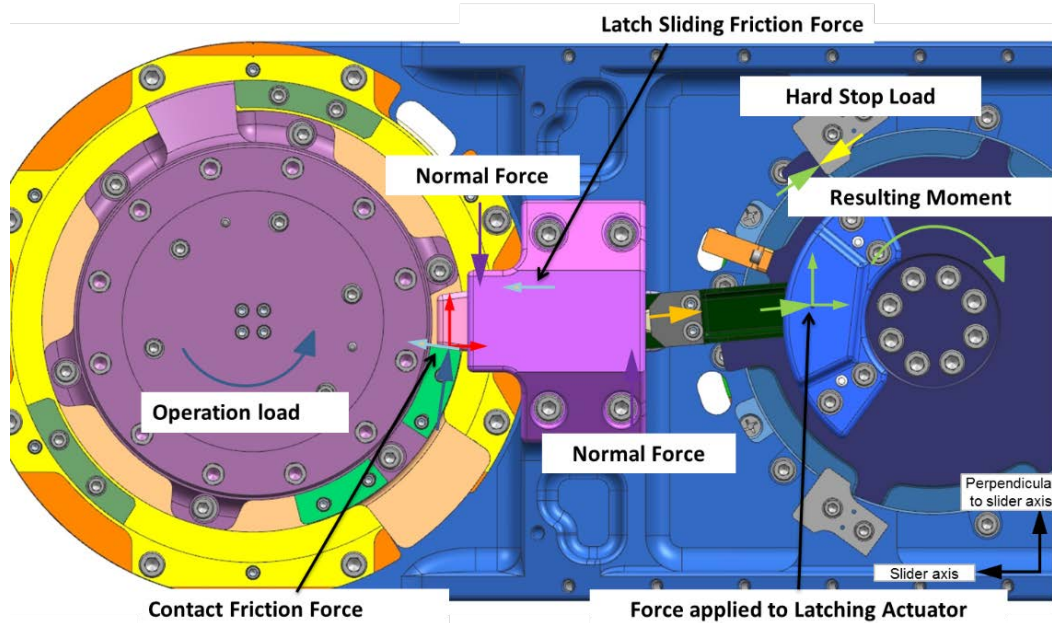


**Figure 4. Latch System Free Body Diagram**

Stiffness of the overall deployment system when latched was a critical design criteria. Each component was designed to maximize its individual stiffness to assure the latching mechanisms combined stiffness is as high as possible. A detailed tolerance stack was used to assure no misalignments or binding were possible.

Once the design was complete, a high-fidelity proof of concept tool was fabricated. The proof of concept tool was used to develop the assembly process and verify performance. Math model calculations were confirmed with the proof of concept tool, which correctly calculates the latch force and latch actuator torque.

To address life for the deployment and latching mechanism, the possibility of galling, seizing, friction and wear was reduced or eliminated. Life of the deployment and latching mechanism is accomplished with a four-fold approach.

1. All sliding surfaces, including shims, bolt components, slider block, link and link pins are made from non-galling stainless steel or a super alloy that is not galling coupled with the non-galling steel.
2. All sliding surfaces in the latching mechanism are diffusion layer hardened. Internally these parts retain the toughness of the original material and hardens only a thin outer layer. This hardening further protects the sliding surfaces from galling.
3. To help minimize friction of the sliding surfaces, protect these surfaces from galling and seizing, and reduce wear, a dry film lubricant is applied. This low temperature impingement-applied lubricant also is enhanced with the application of other lubricants (co-lubrication).
4. To further minimize the effects of friction, chance of galling and seizing, and wearing, a secondary grease lubrication was applied to all sliding surfaces of the deployment and latching mechanism.





**Figure 5. Proof of concept tooling**

The proof of concept tool utilized flight latching mechanism parts but used representative output flanges for both actuators and a plate instead of the flight mounting bracket. Duplex pair bearings were also mounted under each of the output flanges to simulate the flight configuration. The goal was to check the mechanism's tolerances, required torques and the torsional stiffness of the mechanism's deployment actuator at the stowed and deployed positions. The proof of concept tool also enabled assembly, shimming, and load setting operations to be finalized prior to the flight unit build.

Proof of concept testing was very successful, the latching mechanism exceeded all program requirements. Flight latch assembly began after completion of latch tool proof of concept testing. In-process stiffness testing reconfirmed math model results and verified flight latch stiffness.

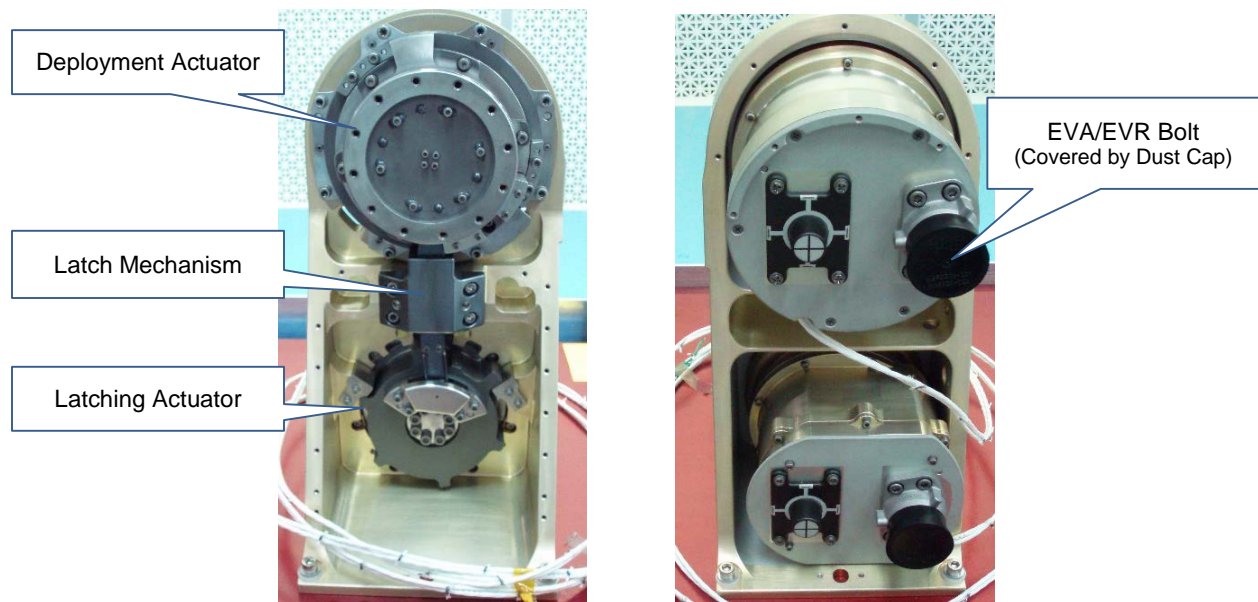
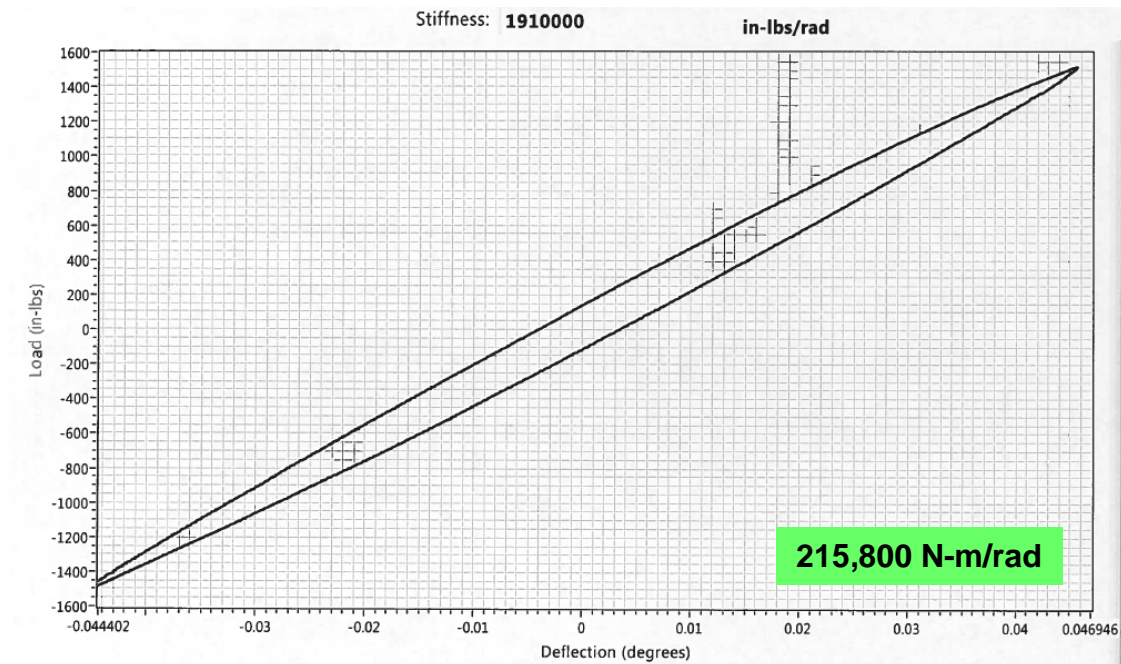
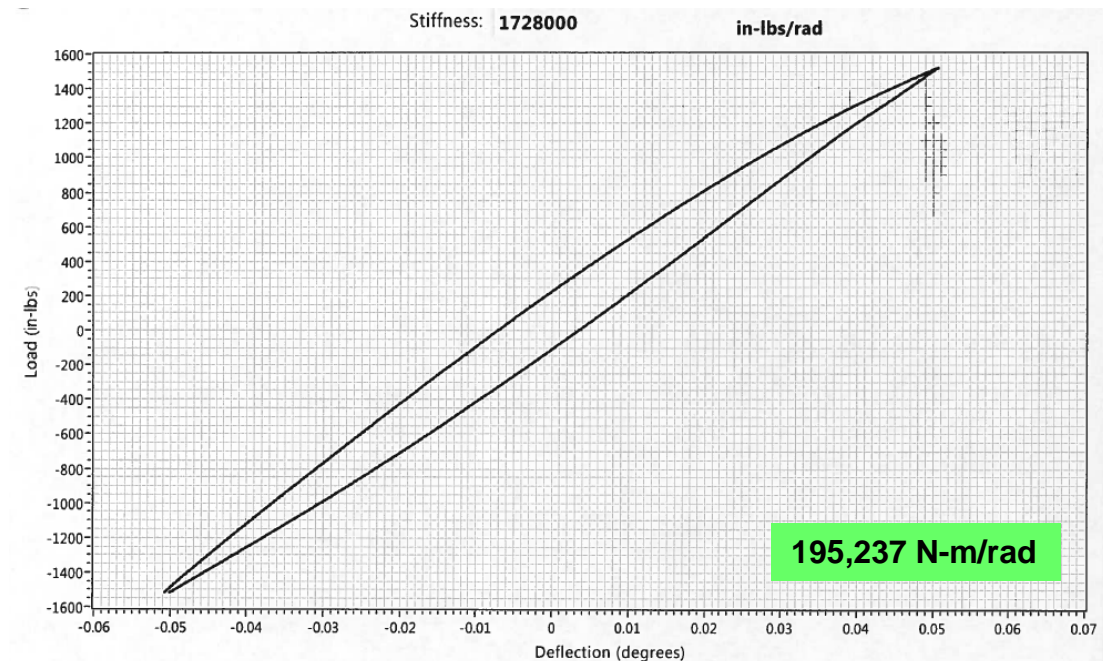


**Figure 6. Flight Latching Mechanism**

The Flight unit successfully completed in-process stiffness testing, with only a slight reduction of overall stiffness. Deployment and latch assembly was then completed with no issues. The deployment and latch mechanism successfully completed protoqual testing with no issues. Latch performance did not change after exposure to vibration and thermal vacuum.

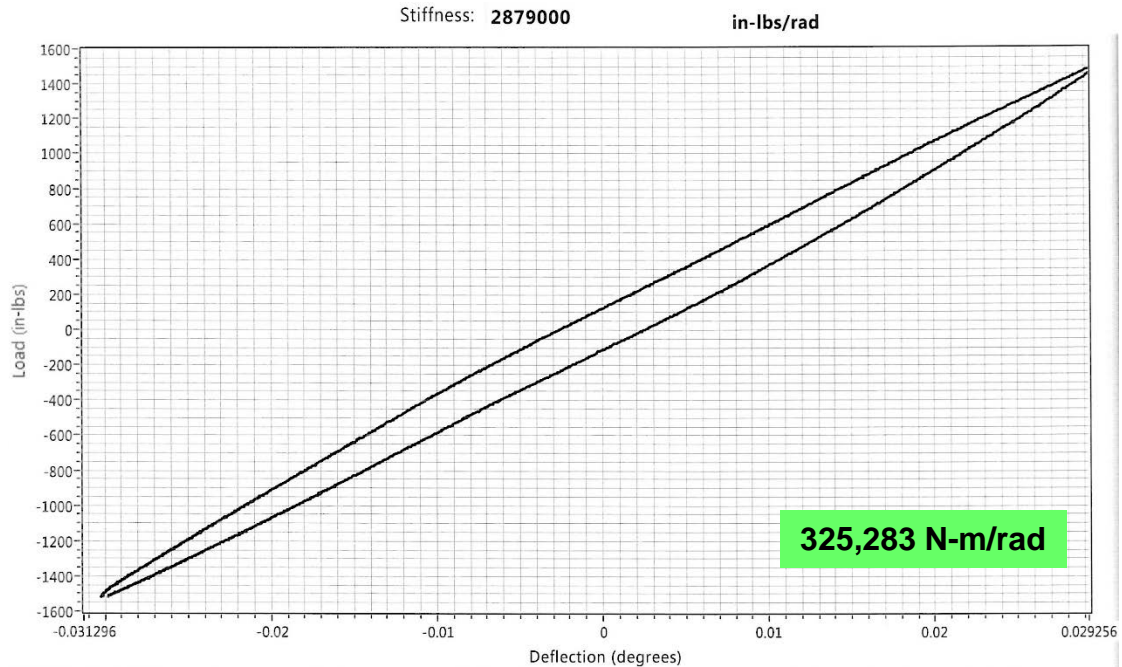


**Proof-Of-Concept Model Stiffness**

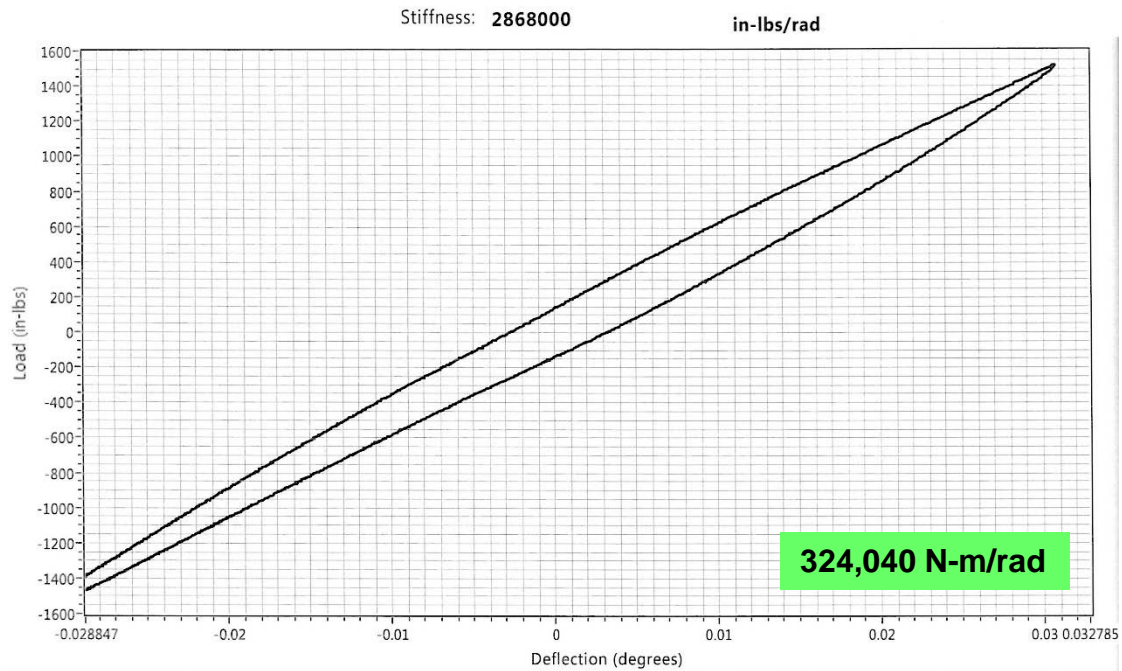


**NICER Deployment and Latching Mechanism Stiffness**

**Figure 7. Stiffness results**



**Life Test Unit Initial Stiffness**



**Life Test Unit Final Stiffness**

**Figure 8. Life stiffness results**

Life testing was completed using the proof of concept tooling. All non-flight latch components were replaced with flight versions and the latch was cycled 3000 cycles (latch then unlatch), 3000 in both deployed and stowed position. No wear or damage was observed, and latch performance was unchanged. Life testing demonstrated the effectiveness of the design and processes to greater than 2X the NICER life requirement. Extended life testing is currently in process.

## Lessons

During development of the deployment and latch mechanism, many key challenges were solved. The following is a list of useful lessons.

### Don't forget about spring hysteresis

Spring hysteresis is always a concern. Spring manufacturers typically only provide maximum force and spring rate. They are unable to provide accurate hysteresis values, since hysteresis is highly dependent on design and resultant friction. Development testing confirmed spring force dropped 10% - 20% after cycling. Moog planned for spring force hysteresis losses and performed cyclic spring force testing. Moog's new latch system compensates for all environmental conditions providing repeatable performance.

Initial design development needs to include spring force hysteresis losses in the design. All springs have hysteresis, so quantification of the hysteresis should be completed before finalization of fabrication of parts. Early development testing should be performed in flight configuration to determine actual force at final position.

### Iterate until optimal design is reached

Complex systems like the deployment and latch mechanism need to balance all the requirements. It would be easy to design a latch with 4 times the force required. There would be no concern of the latch moving when loaded, but torque margin requirements could not be met without increasing all other components. Problems arise from increased loads, friction (requires higher motor torque), and weight. Since this is a space mechanism, the latch is required to have a safety factor greater than three. To address this problem, the most critical requirement was determined to be the resultant force on the latch. The latch force was sized to be only slightly higher than the worst case resultant force on the latch. This established the baseline concept that was then optimized with the mathematical model. Through the optimization process, we balanced the latch capabilities to the motor capabilities, creating a more robust design while still maintaining a safety factor in excess of three. Moog's optimization of the deployment and latching system resulted in a system that exceeded program requirements.

Determine key requirements and balance the design around these requirements. Iterate until an optimal design solution is found.

### Design improvements could change operating scenarios

The NICER mechanism requires each actuator to have provisions to be overridden by a robot or astronaut's tool to return it to a stowed position in case of loss of power, motor failure, etc. Additional requirements were flowed down after completion of initial design requiring incorporation of range limiting features to prevent impact with space station structures. A limit bar and guardrail were incorporated into the design, this caused an issue with the EVA/EVR implementation. Moog designed a completely new compact clutch designed to slip before the actuator limits were reached, utilizing Moog extensive space heritage technology. This also protected the deployment and latch mechanism if the latching actuator was mistakenly left in the latched position and the deployment actuator EVA/EVR was engaged or the latch actuator was attempting to latch without the deployment actuator in either the stowed or latched position.

Laying out of all possible scenarios beyond the typical operating envelope can directly influence the design requirements. These can include the addition of safety features not only to limit unanticipated problems but also add to the robustness of the design.

### Manage your requirements

Torque margin is always the basis of design for electromechanical space mechanisms. Inertias, harness losses, internal losses of the mechanisms, etc. as well as the temperature extremes that these mechanisms must perform in, all have an effect on torque margins. In the case of the NICER program, factors of safety requirements were higher at the beginning of the program and dropped at different milestones as the design moved to finalization. During the Preliminary Design Review, the factors were greater than used during the



Critical Design Review and were further reduced for Acceptance/Qualification Testing. This progression almost insures acceptable margins for the mechanism if all loads and frictions are accurately determined or are conservatively estimated at the beginning of the design phase. At delivery, because the initial design will be driven by these higher factors of safety, the unit will assuredly have a higher torque margin than required. The proof of concept tool provided the design team friction and load values.

Torque margin requirements can be managed effectively if unknown variables like friction and losses can be anticipated or tested in a proof of concept model early during the program progression.

#### Proof of concept testing is invaluable

The bolt design utilizes a shoulder bolt to limit the travel of the bolt. Standard military part number shoulder bolts are made of 300 series stainless steel. 300 series stainless steel bolts have relatively low strength, low hardness, and are prone to gall. A shoulder bolt was manufactured from high-strength stainless steel to prevent galling. Initial development testing was performed used a 300 series shoulder bolt, before a high-strength shoulder bolt could be manufactured. The 300 series shoulder bolt galled as predicted and drag increased over time.

Proof of concept testing is invaluable to confirm design assumptions and identify possible issues. Testing should be performed as early as possible to limit schedule impacts.

#### Systematic analysis reduces system risks

High latch stiffness is critical to the NICER system. Stiffness of a system is a combination of its components and joints. Slippage between mating surfaces reduces overall stiffness. The deployment and latch mechanism uses many different methods to assure high latch stiffness. The latch design has no play between parts when latched, and all joints are sufficiently loaded to prevent slippage. The deployment latching system exceeded program expectations as analyzed.

When high stiffness is required, all play should be eliminated. A systematic tolerance analysis should be performed to minimize joint mismatch and slippage.

### **Summary and Discussion**

The Deployment and Latching Mechanism for NICER, utilizes an innovative new latching system. Providing a stable, high-stiffness structure in the two positions. The mechanism consists of two rotary actuators and an over-center slider crank mechanism latch. The system has successfully completed development, protoqual and life testing. Moog delivered the Deployment and Positioning System containing the deployment and latching mechanism on July 2015.

The deployment and latching mechanism solves many space systems problems:

#### High stiffness deployable platform

The design utilizes Moog's high reliable space heritage actuators providing robust repeatable positioning. The new latching system locks the platform firmly in place with very high stiffness, with no power applied.

#### High stiffness in multiple positions with repetitive latching

Design enables repetitive latching in multiple positions without any loss of stiffness in both rotational directions.

#### NASA robotic interfaces

Design incorporates NASA's new Standard Dexterous Grapple Fixtures, enabling robotic manipulation of all actuators by NASA's Dextre, also known as the Special Purpose Dexterous Manipulator.

#### High stiffness to weight ratio

In comparison, an extremely large actuator would be required to be powered on to meet equivalent stiffness.

The following is a quick summary of the system capabilities:

Torque: 56.5 – 113 N-m (500 – 1000 in-lb)

Unlatched Unpowered Holding Torque: 9 – 33.9 N-m (80 – 300 in-lb)

Latch Unpowered Holding torque: 171.2 N-m (1515 in-lb) [no movement]

Latch Unpowered Holding torque: >384.1 N-m (>3400 in-lb) [slight movement, no damage]

Stiffness: 169,477 N-m/rad min (1,500,000 in-lb/rad min) [at 384.1 N-m (1515 in-lb)]

The Deployment and Positioning System containing the Deployment and Latching Mechanism has completed protoqual testing and is in final integration, scheduled for launch in fall 2016.

Although the deployment and latching mechanism used a deployment actuator and a latching actuator, the mechanism is scalable. The NICER requirements dictated the sizes of the actuators used. Depending on the stiffness required and the torque required at the deployment actuator, the deployment actuator can be scaled up or down. The latching actuator is sized based on the load required in the bolt, the over-center load that is reacted by the actuator and the load the slider crank has to react to. The NICER deployment and latching mechanism is arranged in a vertical configuration with the latching actuator on the bottom. Depending on the available envelope, the latching actuator can be positioned anywhere radially around the deployment actuator. If envelope is available, a horizontal configuration would allow for a lower vertical profile and increased stiffness.

### **Future Work / Optional Designs**

#### Add intermediate latching positions with some loss of stiffness

Intermediate positions can be added. Hysteresis caused by change in torque direction would result in a loss of stiffness between the initial torque direction and the second torque direction.

#### Develop a two-slider design for intermediate positions with no loss of stiffness

The addition of a second slider independent of the first, contained in the same slider block, can be used to latch the deployment actuator at intermediate positions. The second independent slider will resist loading in the opposite direction. Clearance on the back side of each slider and shimming on the deployment actuator, will ensure loading in both directions. The loading in both directions will result in the elimination of system hysteresis and result in similar torsional stiffness in both directions.

#### Develop a two-slider design to enable $\geq 360^\circ$ output rotation (no hardstops needed)

The addition of the second slider, as described above, can also allow the deployment actuator to rotate more than  $360^\circ$  or if continuous rotation is required and to be latched in multiple predetermined positions.

### **Acknowledgments**

With the NICER DAPS program being a “collaborative effort between NASA’s Goddard Space Flight Center (GSFC) and Moog Inc.”<sup>2</sup>, the authors of this paper would like to extend a special thank you to Keith Gendreau, Zaven Arzoumanian, Charles Baker, Kuo-Chiu (Alice) Liu, and Alissa Mitchell and all of the NICER team at the NASA Goddard Space Flight Center for the opportunity to participate in this challenging and exciting program. Additionally, the authors of this paper would like to extend a special thanks to the entire Moog NICER program team, without them this system could not have been built.

### **References**

---

<sup>1</sup> NASA Website, <https://heasarc.gsfc.nasa.gov/docs/nicer/>

<sup>2</sup> Paraphrased from NASA GSFC Pointing, Deployment, and Latching Mechanism Hardware Assembly Performance Requirements Specification EXP-NICER-MECHM-SPEC-0016

# **Tape Hinge/Lenticular Strut Hinge Qualification and Evolution**

Donald Gibbons\*

## **Abstract**

A lenticular strut/carpenter's tape hinge was developed, qualified, and flown, with successful operation on orbit on several vehicles. The lessons from this effort were incorporated into a second-generation design. This design is suitable for large lightweight structures such as thermal shields and solar sails. While the initial design relied on the actual gossamer structure for the hinge functional testing, the evolved design can be tested in component-size facilities without loss of test fidelity, and integrated into various assemblies at vehicle integration resulting in a more affordable hinge, suitable for lightweight mechanisms.

## **Introduction**

The hinges have been built and were qualified and acceptance tested to a typical set of spacecraft mechanisms test requirements: torque output, vibration testing, thermal vacuum cycling and operation, and for the prototype or qualification unit, life testing. This hinge is not intended for high torque applications, but is suitable for lightweight deployable structures such as thermal shields or baffles, or for solar sail applications.

The hinge is shown in Figure 1. This simple design contains few moving parts. Functioning as a hinge, the basic mechanism is a flexure. This makes it ideal for lightweight applications because of the inherent insensitivity to temperature extremes during operation. The iterations on this design from qualification to flight hardware to re-use have improved the processes and decreased the costs associated with the build and test of the hinge.



**Figure 1. Stowed Installed Hinge**

---

\* Lockheed Martin Space Systems Company, Sunnyvale, CA

## History

### Original design

The hinge design was originally built to deploy a large membrane supported by a lightweight frame. This hinge was developed using engineering units to understand the operation of the hinge, and after development, the prototype or qualification unit was built to demonstrate design margin. The qualification test program included Torque Output testing, Thermal Vacuum testing, Thermal Cycle testing, Vibration testing, Acoustic testing, as well as Life Cycle testing. The lessons learned from the qualification unit were used to improve the processing of the flight units, which resulted in significant savings because multiple units were built for each shipset. Several shipsets have been flown and successfully deployed on-orbit.

### Second-Generation Design

When a new application was identified on a different spacecraft, the hinges were redesigned to deploy a panel-mounted membrane rather than the frame-mounted membrane. The hinge design was revised to be more modular and the test program was designed to minimize the manufacturing and test costs while maintaining the technical integrity of the hinge. While this iteration on the design was later determined to not be required for the mission, the proposed design changes are discussed, based on the lessons learned and the proposed benefits.

## Design

### Original design

The hinge design is a carpenter's tape or lenticular strut hinge. To increase the torque output without increasing the maximum strain there are a total of four tape spring elements, two in each orientation. The orientation of the tape springs was chosen to be in the convex orientation. The convex configuration allows for good control when flattening the hinge during stowing, as shown in Figure 2, as the two edges can easily be pinched during the stow operation. The material selected was chosen for the stiffness and strain rate. The hinges shown are painted black for thermal control.

The radius of the spring cross section in the free state is  $R_1$ . The stowed radius  $R_2$  is 80% of  $R_1$  on the inside of hinge. Our investigation into the design suggests that these two radii should be the same, however the installation required a smaller stowed radius than the spring cross section radius.

One effect this has is that the hinge, with a stowed radius smaller than the cross section radius, will not just rotate when released. When released, the hinge will rotate, but the stowed radius will expand until it is approximately the cross section radius. This effectively causes some unintended translation motion at the release point.

Sliding interfaces were examined at the attachment of the tape spring to the fitting, but the final design clamps all four tape spring elements and prevents any sliding at the ends of tape springs. While sliding interfaces were examined, these tended to move around more than desirable. Additionally, keeping the ends clamped means the ends are electrically bonded, which is ideal for ESD and other electrical grounding requirements. Structurally joining all four spring ends does create some non-linearity in the deployment torque as the outside tape spring constrains the interior elements and causes a secondary buckle shown in Figure 3. The secondary buckle wasn't detrimental to the hinge torque output, but is probably the source of some small nonlinearities in the torque output, discussed later and shown in Figure 10.

The stowed radius,  $R_2$ , is formed by the placement of the hinge support and the end fittings in the assembly. The support controls the stowed radius of the hinge and also prevents "rolling" of the stowed hinge. This "rolling" is where the center of the radius moves without any rotation, and because there is no net change in the total curvature of the spring elements, there is almost no resistance to this motion without the support. Without this support, the stowed hinge would have almost no structural stability. The hinge support and rolling direction are shown in Figure 3.

The stowed radius,  $R_2$ , has a natural curvature as shown in Figure 4. For this installation, the hinge support and frame control the stowed radius to a smaller radius than the natural curvature due to the interface constraints. The smaller stowed radius naturally results in higher stresses, but the compliance of the frame allowed some movement of the ends of the hinge, resulting in a larger radius and lower stresses in the hinges than a rigid structure would allow. An interesting result of this stowed configuration is that the hinge will move laterally as well in rotation to due to this tighter curvature and additional strain energy. This effect is shown in Figure 6. While this doesn't impact the operation of the hinge, the additional movement of the mechanism should be considered in the deployment dynamics and clearances during the release of the mechanism.



**Figure 2. Folding Hinge**

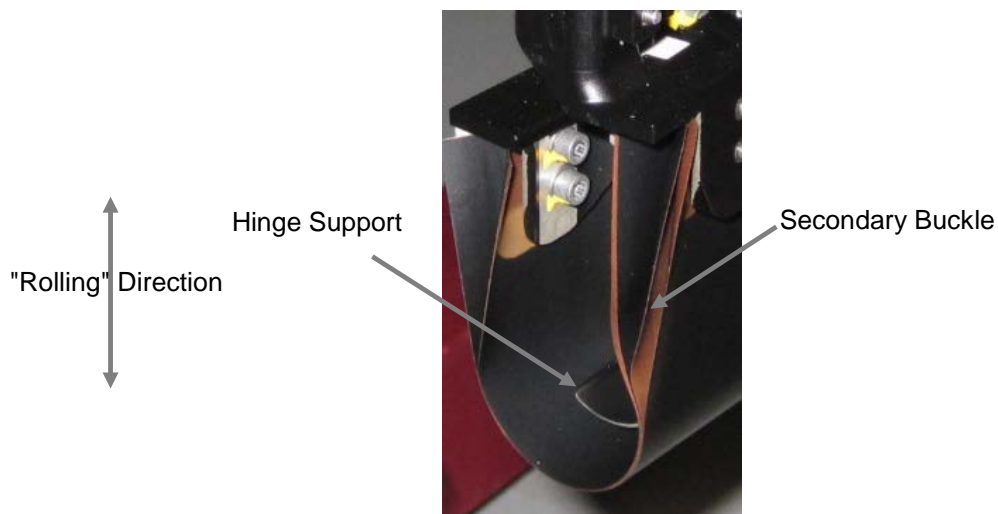


**Figure 3. Detail of Secondary Buckle and Hinge Support**

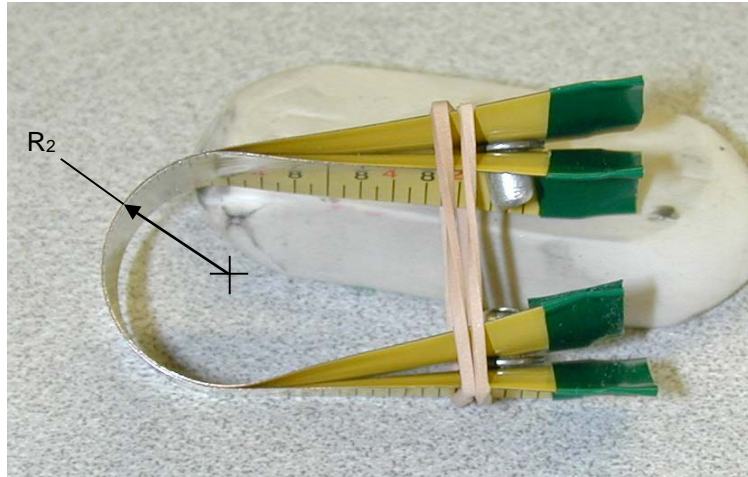


**Figure 4. Early Development Unit Showing Natural Curvature,  $R_2$ , of a Tape Spring**

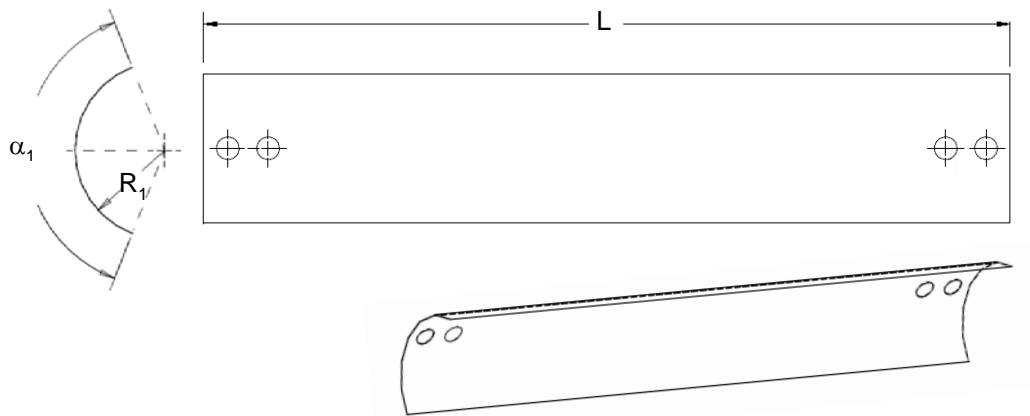


**Figure 5. Tape Spring Element Geometry**

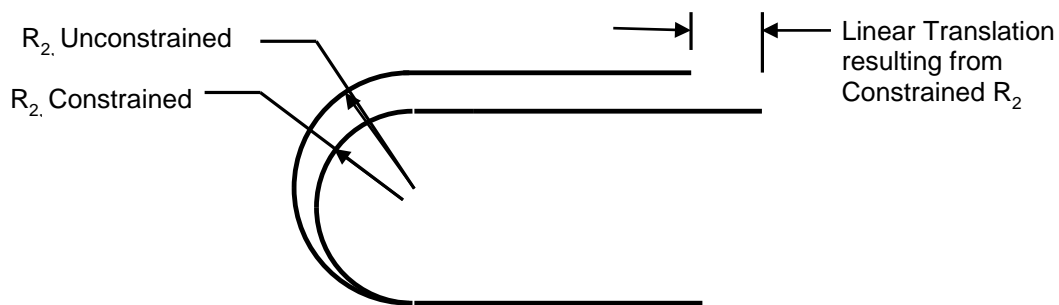


**Figure 6. Linear Shift Due to Hinge Stowed Radius Constraint**

#### Second Generation Design

With a goal of creating a more universal design, the hinge was redesigned to simplify the interfaces. The redesigned hinge is shown deployed in Figure 7 and stowed in Figure 8. The fittings were redesigned to mount to a flat panel rather than the tube frame. Because the hinge is open section, the torsional stiffness of the hinges is low and there is no need to have more than the two mounting screws since the hinge cannot transfer any significant load in torsion.



The redesign better established and maintained the hinge curvature, mitigating the lateral motion and simplifying the release dynamics. Increasing the stowed radius also allows use of a stiffer structure for the mechanism without the risk of overstress in the hinge springs. A tighter radius with stiff hinge fitting constraints could result in unacceptably high stresses or reduced life. Increasing the stowed radius does require more volume for the stowed hinge, but allows the use of the hinge with a structure of any stiffness without the risk of overstressing the tape spring.

The redesigned hinge incorporates shims between the hinge springs. This separates the leaves of the hinge to allow more room for the internal springs and eliminates the secondary buckle seen in Figure 3. The direct electrical bond between adjacent leaves is maintained with conduction through the shims, while providing clearance to eliminate the secondary buckling.

The acceptance test program was designed to allow substitution of a small test structure for the large flight structure, allowing for a cost-effective test program using smaller facilities and increasing the available facilities which can be used.

The resulting test program can be easily adapted to a variety of applications increasing the utility of the design for reuse on future missions. With the experience gained from these projects, it is possible to build and test affordable non-traditional mechanisms while maintaining traditional performance requirements.

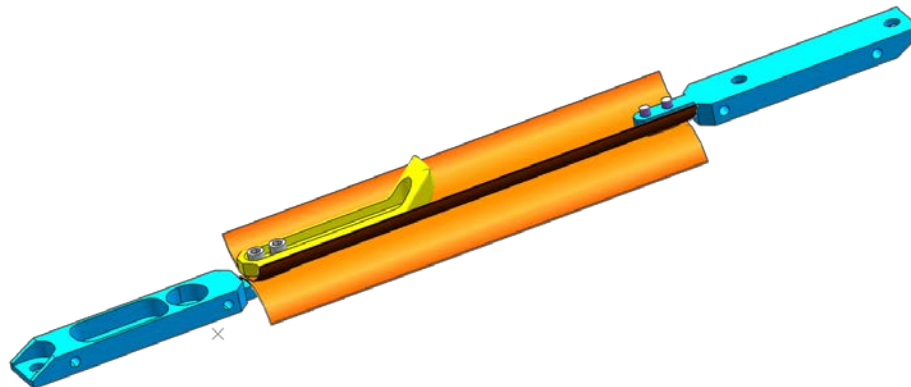


**Figure 7. Deployed Redesigned Hinge**

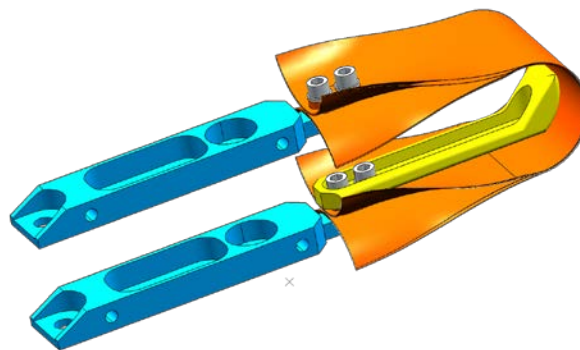


**Figure 8. Stowed Redesigned Hinge**

### **Original Design Testing**

#### Original Design

To verify the performance of each hinge, output torque testing was performed. The hinge fixture is shown in Figure 9. The torque output is measured without constraining the translation of the rotating end of the hinge. This is necessary because of two effects: the center of rotation of the hinge changes as the end of

travel is approached with the hinge radius essentially going to infinity when fully deployed, and the linear translation from the constrained radius needs to be free to move. The testing results in a torque versus angle plot for each hinge similar to the one shown in Figure 10. The output is characteristic of a tape spring hinge, with a relatively flat output while the hinge unbends and a peak as the transverse radius,  $R_1$ , unflattens. The initial torque is actually not zero, but this is a test effect due to the backlash in the test equipment. The final torque is actually zero, because the hinge springs are fully released, however because the hinge springs are unbuckled, there is significant resistance to stowing which is used to resist the on-orbit disturbance torques. The fully deployed hinge with unbuckled tape springs is a structure with the stiffness of the tape springs to react the external loads.

#### Second-Generation Design

No significant changes are planned for the new design. The fixture requires redesign for the new hinge interfaces but not for the test methodology which was successful and cost effective.

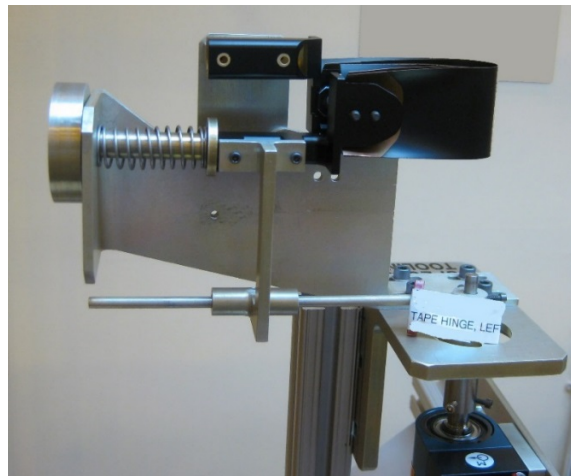


**Figure 9. Hinge Torque Output Test**

#### **Deployment Test**

##### The Original Design

The hinges installed into the mechanism are about 1750 mm by 1500 mm as seen in a deployed mechanism in Figure 11. This resulted in a relatively large deployment fixture.



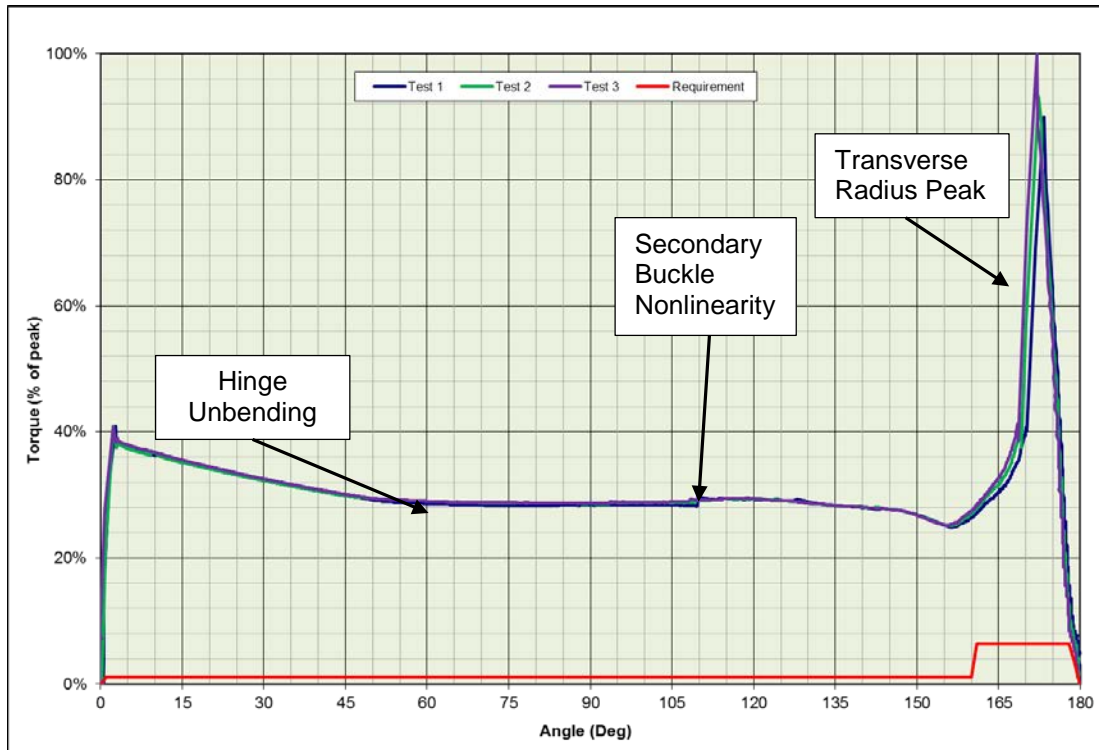


**Figure 10. Torque versus Angle**

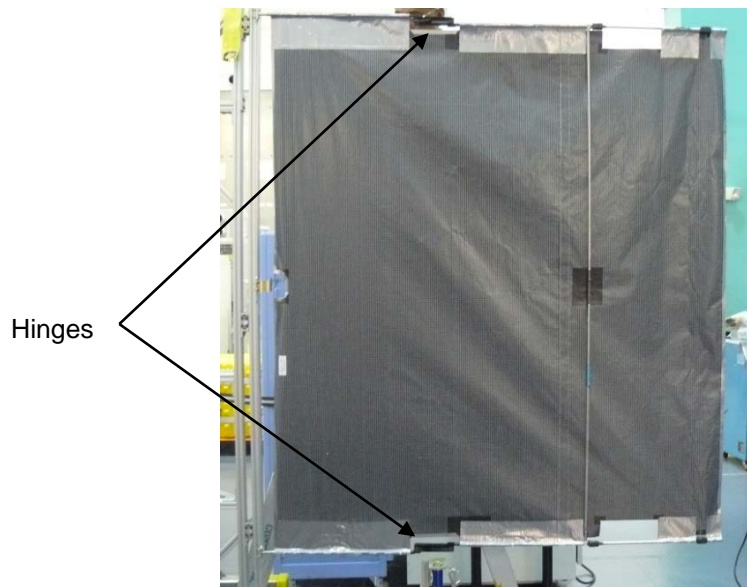


**Figure 11. Hinge Installed on Mechanism**

The first deployment fixture used during qualification is shown in Figure 12. This deployment fixture performance was good and with the base, was mobile and adjustable. The size of the fixture was limiting however. When testing one qualification or prototype unit, the size of the deployment fixture wasn't a significant issue. When testing multiple units per shipset, the size of the fixture quickly dominated the volume of the Ambient and Thermal Vacuum deployment floor space.



**Figure 12. Original Deployment Fixture**

Based on the original deployment fixture, a redesigned fixture was built. This fixture was designed to nest and minimize the required floor space when using multiple fixtures. The redesign did achieve the goal of being able to test an entire shipset of the mechanism in the Thermal Vacuum chamber at one time, allowing one chamber run for each shipset build, resulting in a significant cost savings. The redesigned fixture is shown in the vacuum chamber with the door open in Figure 13. Multiple fixtures can be seen behind the first fixture and mechanism.

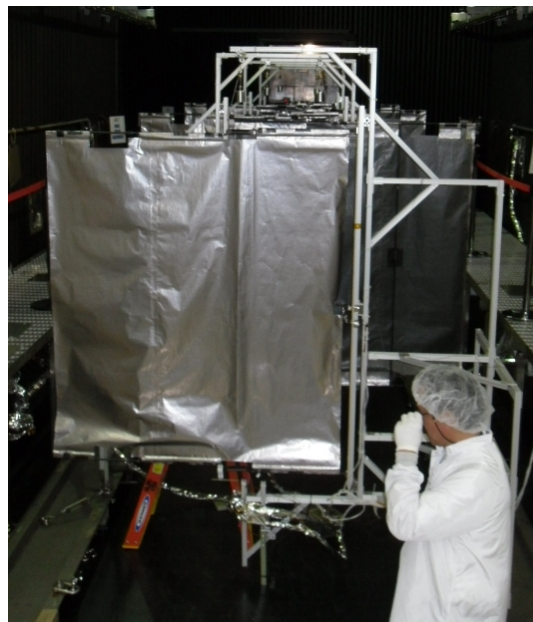


**Figure 13. Deployed Hinges in Large Thermal Vacuum Chamber**

Additionally, changes were made to the test telemetry collection. Support equipment fittings were made to simplify the installation of the hardware on the deployment fixture which reduced the installation and checkout time. The coupling to the telemetry was initially an issue due to the translation and center of rotation issues previously discussed. The redesign resulted in a tab which was fixed to the flight hardware,

so once the coupling was set up and initially adjusted, there was often no further adjustment required for each installation of flight hardware. This greatly reduced the time during setup during testing and resulted in consistent test results. Test results from one unit are shown in Figure 15. Note that the shorter times are in vacuum and are insensitive to temperature. The longer times are in air due to the damping of the air resistance during deployment.

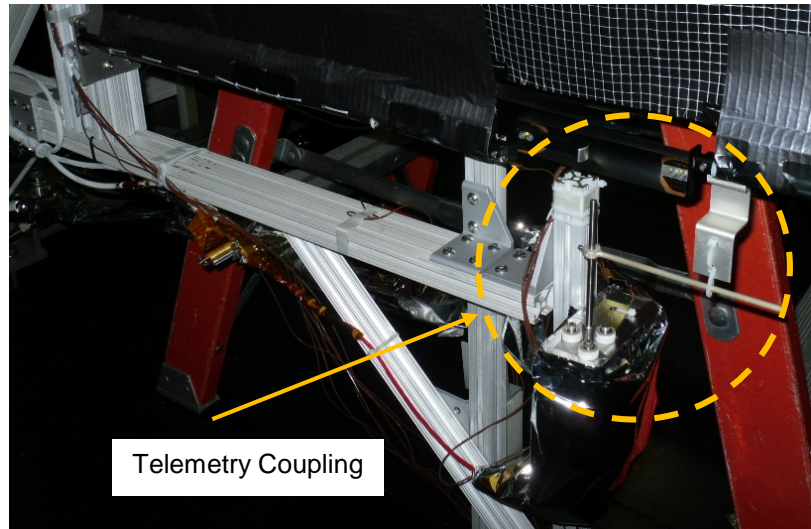


**Figure 14. Deployment Test and Deployment Test Telemetry**

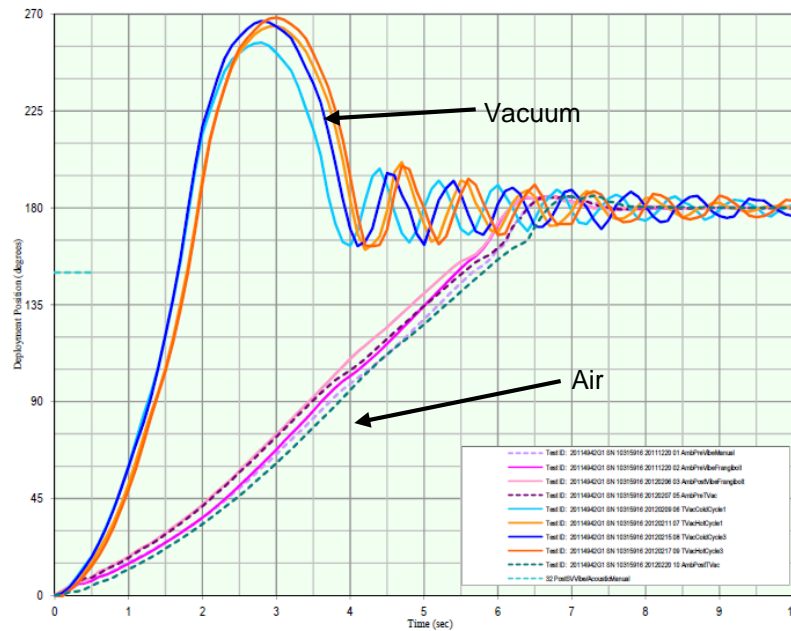


**Figure 15. Mechanism Deployment in Vacuum and Air**

Some additional deployment testing was performed during qualification. To investigate the impact of the alignment during installation, testing was performed on the qualification unit with off nominal rotations and translations in the hinges. Testing was performed with an induced twist or rotation in the hinge including the configuration shown in Figure 16. Deployment tests in this and similar off-nominal configurations demonstrated that there was no significant difference in the deployment of the mechanism with the twist when compared to the baseline. While every effort was made to properly align the hinges during installation, this testing was able to determine the sensitivity to alignment, and allow credible engineering assessment of the installation process.

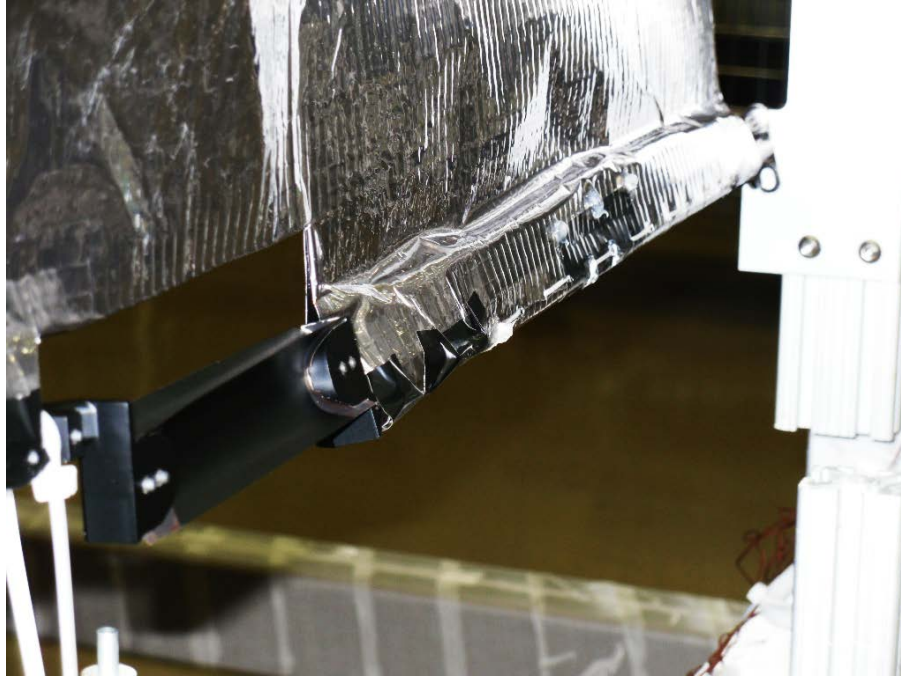


**Figure 16. Hinge Performance Verified with Induced Twist**

#### Second-Generation Design

The redesigned hinge was for a deployable shield, approximately 2000 mm by 500 mm, stowed in a height of approximately 50 mm. The mechanism is shown in Figure 17, with the stowed mechanism shown in Figure 18.

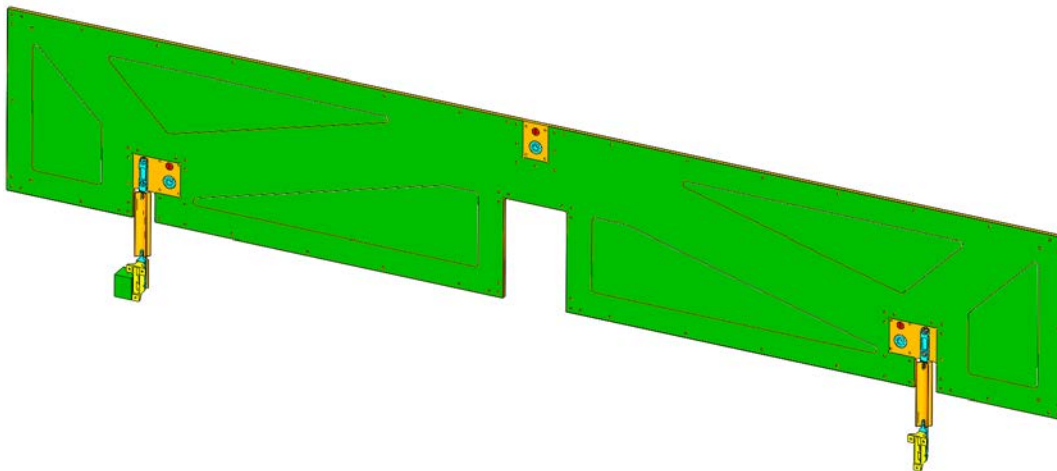


**Figure 17. Deployed Redesigned Hinge, Installed on Proposed Shield**

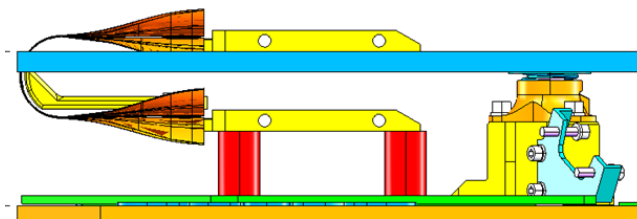


**Figure 18. Installed Redesigned Hinge**



In the original design, the size of the hardware drove the logistics and test costs and the test configuration was a driver in the hardware design. Based on this knowledge, the 2000-mm dimension of the flight panel was shortened to approximately 500 mm. The other dimensions were left unchanged, allowing a simple change to reduce the size of the test article. By maintaining the weight of the test panel equal to the flight panel, the moment of inertia about the deployment axis was left effectively unchanged. This resulted in the test article shown in Figure 19. This resized test article could be tested in component-sized facilities, and moved without large transportation equipment.

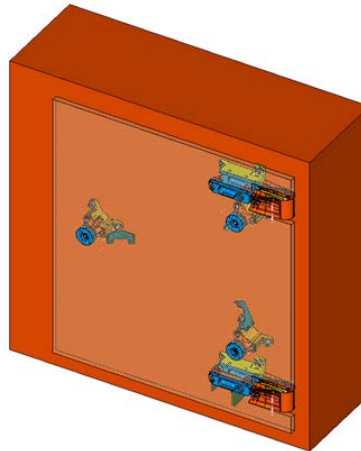


**Figure 19. Redesigned Hinge, Installed in Proposed Test Article on Notional Fixture**

Ultimately as the vehicle design matured, this panel was not needed to meet the mission requirements, and this deployable was removed from the baseline design. Conceptually, this test method is sound, and as other missions require shields, baffles, or sails, this method can be utilized to provide lightweight deployable mechanisms at a reasonable cost.

### **Lessons Learned**

These hinges are not traditional hinges. The tape spring hinges are undamped, have relatively low torque output, and do not have a fixed center of rotation. This can be further complicated if the curvature of the stowed hinge is not controlled as this can introduce additional “off-nominal” lateral translation, complicating the release and deployment. The relatively low torque output, the moving center of rotation and the possibility of lateral motion increases the difficulty of deployment testing by increasing the possibility of inadvertently constraining the mechanism during deployment testing.

The initial design of mechanism required the entire structure for testing the hinges. With an undamped hinge, testing with a representative inertia is needed to achieve flight-like deployment dynamics during test. The resulting large lightweight structures presented a number of logistical challenges.

The large size of the mechanism required significant floor space for manufacturing.

The large size of the structure required large and more expensive environmental test facilities. The test facilities used are typically used for vehicle-sized equipment, rather than component-sized hardware. The large size introduced significant air damping during ambient deployments and required large test fixtures. Large test fixtures require more space for storage and operation.

While the large lightweight flight hardware was easy enough to handle, transportation was difficult due to the size of the shipping containers. The containers were large and heavy, due to the container material needed to package the hardware.

Reducing the size of the test article for manufacturing and acceptance testing, reduces the cost and schedule of the build and test, and makes smaller test facilities feasible for use in testing. The support equipment for smaller hardware is easier to handle and store.

When a similar design was proposed, the lessons learned from the first program were incorporated into the new design to reduce the size of the test article. By maintaining the flight-like inertia, the testing maintains flight-like dynamics. The integrated deployable is tested for assembly, integration, and normal operation on the vehicle. Because the flight installation will be tested on the vehicle anyway, there are no additional hidden costs as a result of this approach, resulting in successful acceptance testing with all performance verified at a lower cost.

# Design and Development of NEA Scout Solar Sail Deployer Mechanism

Alexander R. Sobey\* and Tiffany Russell Lockett\*

## Abstract

The 6U (~10 cm x 20 cm x 30 cm) cubesat Near Earth Asteroid (NEA) Scout<sup>1</sup>, projected for launch in September 2018 aboard the maiden voyage of the Space Launch System, will utilize a solar sail as its main method of propulsion throughout its ~3-year mission to a Near Earth Asteroid. Due to the extreme volume constraints levied onto the mission, an acutely compact solar sail deployment mechanism has been designed to meet the volume and mass constraints, as well as provide enough propulsive solar sail area and quality in order to achieve mission success. The design of such a compact system required the development of approximately half a dozen prototypes in order to identify unforeseen problems, advance solutions, and build confidence in the final design product. This paper focuses on the obstacles of developing a solar sail deployment mechanism for such an application and the lessons learned from a thorough development process. The lessons presented will have significant applications beyond the NEA Scout mission, such as the development of other deployable boom mechanisms and uses for gossamer-thin films in space.

## Introduction

The NEA Scout solar sail design comes as a successor to two 3U (~10 cm x 10 cm x 30 cm) cubesats: the NASA Marshall Space Flight Center developed solar sail NanoSail-D<sup>2</sup> and the Planetary Society solar sail LightSail-A<sup>3</sup> (LightSail-B to be launched in 2016). Both spacecraft flew as technology demonstration missions in Low Earth Orbit: NanoSail-D in 2010 (Figure 1, left) and LightSail-A in 2015 (Figure 1, right). These two cubesats represent pathfinders on the way to utilizing solar sail propulsion in order to achieve science missions, such as the primary science objective for NEA Scout: image and characterize a Near Earth Asteroid. This mission would not ordinarily be possible with a 6U cubesat, however, NASA has taken an interest in applying cubesat form factors, methodologies, and risk to perform cost effective interplanetary science missions. Solar sail technology is a key to enabling that capability<sup>4</sup>. While it is conceivable for a 6U cubesat mission to reach a NEA with conventional chemical propulsion, both the number of targets and the launch window would be tightly constrained. By utilizing solar sail propulsion, intercepting a large number of targets in virtually any launch window is made possible. Cubesats are typically deployed as a secondary payload, and therefore have little to no control over changes in launch schedule and must remain flexible.

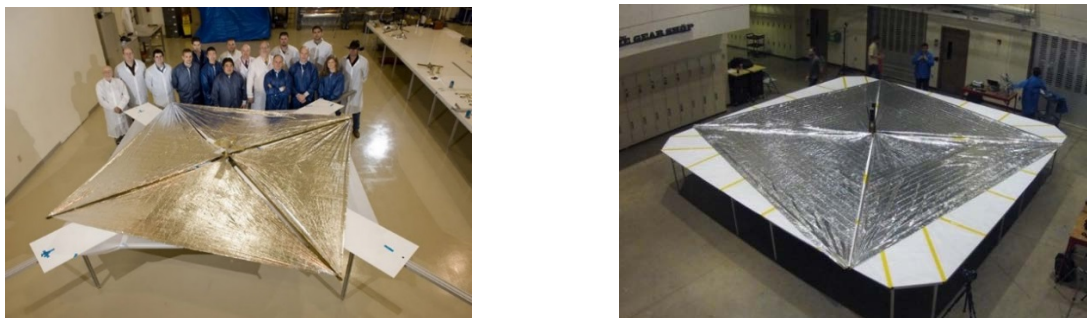


Figure 1. NanoSail-D 10-m<sup>2</sup> Sail (left) and LightSail-A 32-m<sup>2</sup> Sail (right)

---

\* NASA Marshall Space Flight Center, Huntsville AL



### NEA Scout Configuration

As a 6U, interplanetary cubesat, NEA Scout will address strategic knowledge gaps of near earth asteroids. The spacecraft accommodates an imager, star tracker, reaction wheels, avionics, power system, communications, and a reaction control system in addition to the solar sail subsystem (Figure 2). Volume is a premium within the fixed constraints of the 6U cubesat form factor (~10 cm x 20 cm x 30 cm). Mass, 14 kg total, is a demanding constraint as well. Solar sail acceleration is a function of sail area and spacecraft mass. To reach a target asteroid within 2.5 years and meet the 14-kg mass restrictions of the Space Launch System cubesat deployer, the total sail area needed to produce enough propulsion was calculated to be 86 m<sup>2</sup>, deployed with four booms at 6.8 m of length each.

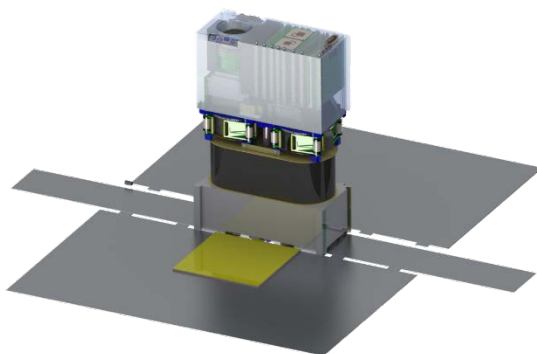


**Figure 2. NEA Scout Flight Configuration as of September 2015**

The solar sail subsystem (Figure 3) consists of a single 86-m<sup>2</sup> colorless polymer (CP1), 2.5-micron thick aluminized sail, sail spool assembly, four Elgiloy (stainless steel alloy variant) Triangular Rollable and Collapsible (TRAC)<sup>5</sup> booms at 6.8 m each, a gear-driven boom deployer assembly, a stepper motor, a motor controller board, and a sensor suite. The deployer design is based on the successful Nanosail-D deployer system with exception to the addition of a stepper motor which provides a slower, controlled deployment, two boom deployers instead of one, sensor feedback, and a single sail design on an oblong spool. The sail spool assembly mounts atop of the boom deployer assembly. The sail spool is allowed to freely rotate about a center post as the sail deploys. The center post doubles as a channel for the wire harness and cabling from the reaction control thrusters at the forward (sun facing) portion of the spacecraft to the avionics box in the aft as well as providing structural support between the two halves.

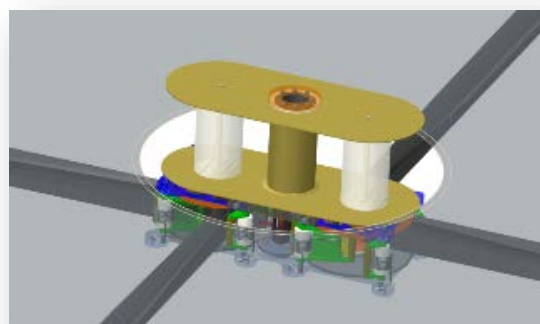
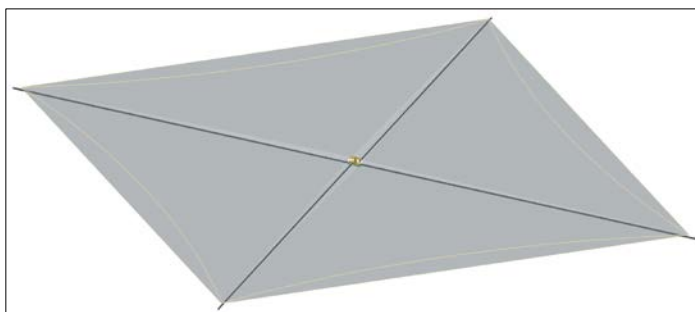


**Figure 3. NEA Scout 86-m<sup>2</sup> deployed solar sail (left) and sail spool and boom deployer assembly (right)**

The boom deployers displayed in Figure 4 consist of two boom spools, each with two booms per spool. Separating the booms into two spools is necessary due to the boom length requirement and the stowed volume constraint. The four booms each exit the deployer every 90 degrees. Each boom spool consists of a center hub, which the booms mount to, a thin top flange (shown in orange), and a geared bottom flange (shown in gray). The top flange primarily provides contact friction from the spool to the boom during deployment; therefore, only needs to be thick enough to avoid deflections into the top plate (shown in blue).

Due to packaging requirements, part thickness are kept minimal, specifically in long axis (3U direction) of the cubesat. The bottom geared flange remains thick to provide adequate gear contact with the center pinion gear, which is directly connected to the motor/gearbox.

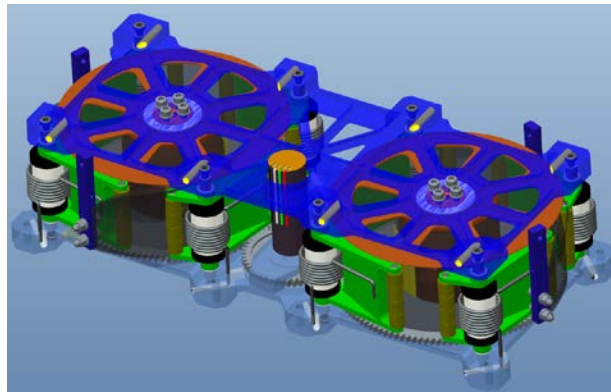


**Figure 4. NEA Scout Boom Deployer Model Stowed**

An earlier concept of the boom deployer consisted of two modular deployers which mounted onto the bus and connected through a center module containing the motor. One of the early concept deployer modules can be seen in Figure 5 both in Computer Animated Design and as a physical prototype. The benefits included ease of manufacturing and assembly. The concept was abandoned for the single base plate design primarily due to alignment concerns. With a single plate, it became significantly simpler to mount the three gears with minimal backlash while at the same time guaranteeing teeth would not bind during the large temperature fluctuations experienced during the early phases of the mission. Furthermore, a single base plate allowed for easier installation of the booms and greater alignment precision.

The 6.8-m-long TRAC booms typically have a slight bend upwards toward the weld side. This misalignment along the spine of the boom must be accounted for during installation of the boom. Each boom is to be installed in an orientation that minimized gravity effects (hanging downward). During installation, the tip of the boom is to be located at the desired plane perpendicular to the long axis (3U direction) before the boom is bolted/clamped at the root. By doing this for all 4 booms, the final plane of the sail can be controlled within acceptable angular limits. Finally, a single base plate allowed for load to be carried primarily through the plate itself instead of through the bus interface. This allows a mass reduction of the interface. Due to this design, the primary load path of the spacecraft is through the baseplate, which considers a single structure appealing.



**Figure 5. Early Concept: Modular Design of Deployers**

From the cross-section view in Figure 6, the inside of the deployer can be viewed. In this view, the booms spools are shown as translucent in order for the boom clamps (shown in yellow) can be seen. The clamps attach each boom to the center hub (shown in brown) with two 100-degree countersunk screws. Also in Figure 6 on the right, both the clamp and the hub themselves are rounded near the top to allow for the

boom to flare out at the base and add stiffness to the boom section nearest the deployer. Both analysis and testing have shown this flare necessary to achieve the highest boom buckling performance.

The spring-loaded boom arms, shown in green in Figure 6, are used to contain the boom spool during pre-deployment as well as deployment. Torsion springs are located at each arm and place pressure onto the boom spool at the Rulon J PTFE rollers. The necessity of these arms and their function is discussed in greater detail under the 'Design Challenges' section. Rollers on the backside of the arms serve to help guide the booms out during deployment and reduce friction. The backside rollers do not place pressure onto the boom spool directly.

The boom tip standoff allows for the sail to be attached to the boom slightly above the boom. This standoff is able to tuck in closely to the deployer in order to maintain the tight volume requirement. The boom tip standoff also serves as a hard stop, not allowing the boom tip to retract further into the deployer. It was noted during the vibration testing of LightSail-A, that the boom tips would retract into the deployer slightly. The retraction was not a great amount, but enough to possibly cause a failure. It was suggested by the LightSail-A team to add a hard stop at the boom tips. The boom tip standoff serves this function.

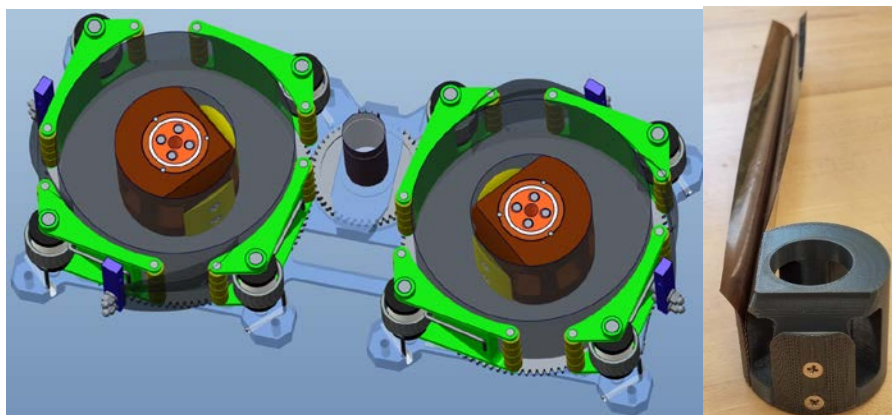


**Figure 6. Cross-Section NEA Scout Boom Deployer Model Stowed (left) and Boom Attachment to Hub (right)**

In order to minimize volume, Rulon J PTFE flanged sleeve bushings are used in place of bearings for the boom-spool interface. Two bushings contact both the top and bottom of the boom spool at center race. An example of this bushing can be viewed in Figure 7 shown in black (note the specific bushing in Figure 7 is standard PTFE and not the Rulon J variant). Both bushings sit on the top and bottom of the post. Only the bottom bushing is present in Figure 7. These bushings both significantly reduce friction and allow for tight alignment of the spools. As with several aspects of this design, volume constraints and form factor are the design drivers. Similar, but larger bushings are used for the sail spool.

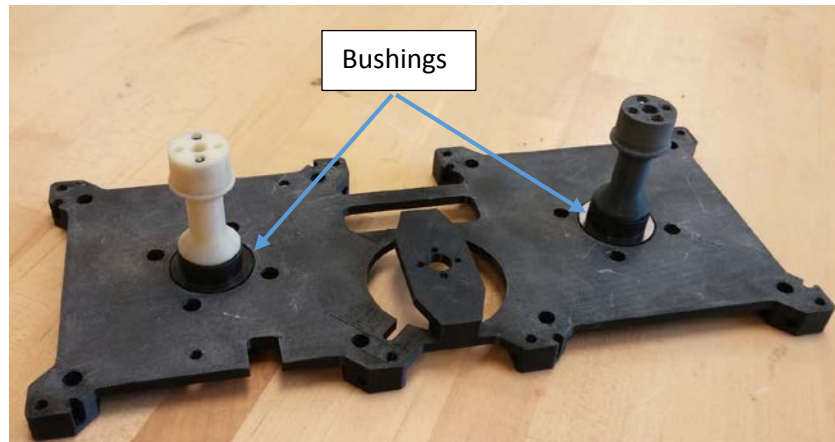


**Figure 7. Baseplate with Posts and Bottom Bushing Mounted**

The burn wire mechanism, shown in Figure 8, allows for the boom deployers to be locked down during launch and up until deployment of the sail. The mechanism itself is only a slight modification on the NanoSail-D burn wire mechanism that served the same purpose. The mechanism locks down one of the two spool geared flanges. By locking down one of the flanges, the entire geared system is unable to rotate.

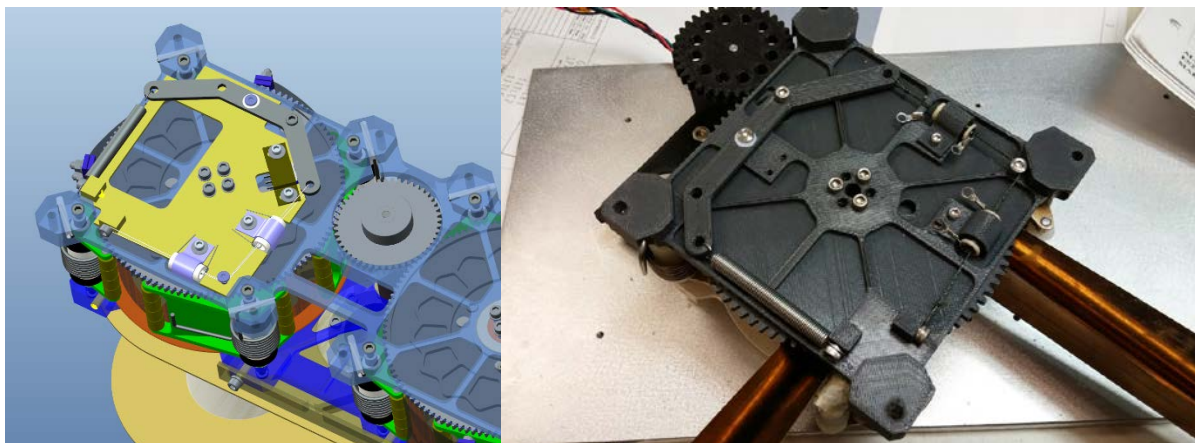


**Figure 8. Burn Wire Mechanism (left) and Early Prototype Burn Wire Mechanism (right)**

The geared flange (shown in Figure 9) is machined with a spoke pattern with sixteen recesses. These recesses allow the gear to be locked down at 22.5-degree intervals. The spring loaded lever (shown as gray in Figure 8) has a cylinder mounted to it (not shown). This cylinder fits into any one of the sixteen recesses of the spoke pattern when the gear is to be locked down. When locked down, a monofilament wire of 50-lb-test (220-N) Honeywell Spectraline is tied off to the spring-loaded lever in order to keep the cylinder tightly pressed into the recess. Once the Spectraline is cut, the spring-loaded lever swings open pulling the cylinder out of the recess into the gear's channel, allowing the spool to spin freely. In order to cut the Spectraline, two Nickel-Chromium wire heaters are added in series to the Spectraline (one being the primary heater and the other functioning as a redundant heater). The heater is a coiled Nickel-Chromium wire mounted into a ceramic sleeve. When enough current is run through the heater, in a matter of seconds, the Spectraline is effectively cut allowing the spring-loaded lever to fall into the open position. Ignoring minor dimensional adjustments, the burn wire mechanism remains similar to the NanoSail-D mechanism with the addition of a microswitch on the lever to provide feedback when the lever has opened.



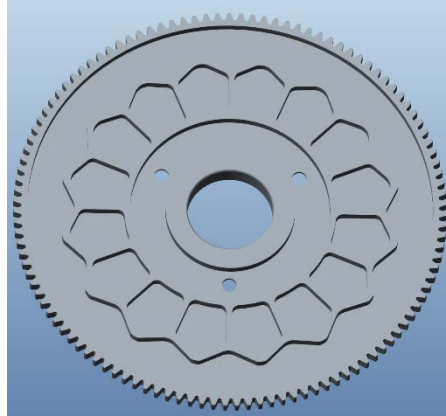


**Figure 9. Spool Gear Machined with Spoke Pattern for Launch Lock**

### **Design Challenges**

#### **Blooming**

NanoSail-D, LightSail, and NEA Scout utilize Triangular Rollable and Collapsible (TRAC) booms originally developed and patented by the Air Force Research Laboratory (AFRL). NeXolve (Huntsville, AL) currently has the design license for manufacturing and is on contract to produce the engineering development unit booms for NEA Scout (Figure 10). As the sail for each mission grew 10 m<sup>2</sup>, 32 m<sup>2</sup>, and 86 m<sup>2</sup> respectively, the boom length also grew: 2.2 m, 4 m, and 6.8 m respectively. At larger lengths, new complications arose during deployment. For example, due to the strain energy developed while spooling, TRAC booms slip past one another during deployment, causing the boom wraps to expand radially and create a gap between the central hub and the first boom wrap. This reaction is referred to as 'blooming' and leads to complications during deployment. If not controlled properly during deployment, 'blooming' can lead to suboptimal deployment and possible failure (Figure 11).



**Figure 10. Boom Deployer Prototype with flight-like TRAC booms**

Both NanoSail-D and LightSail-A addressed issues with 'blooming,' therefore the problem was identified early in the design. Early attempts at creating a MSC Adams multibody dynamic simulation solution proved futile as the forces inside of the deployer were difficult to quantify. These forces include: strain energy in the boom, torsion on the boom arms, contact friction of the arm rollers on the boom, friction between the boom spool flanges and boom wraps, and friction between subsequent boom wraps. It was evident early in the design phase that prototypes would need to be developed in order to understand and control 'blooming.' With the aid of fused deposition 3D printing and machined parts, several prototypes were built, tested, and iterated upon.

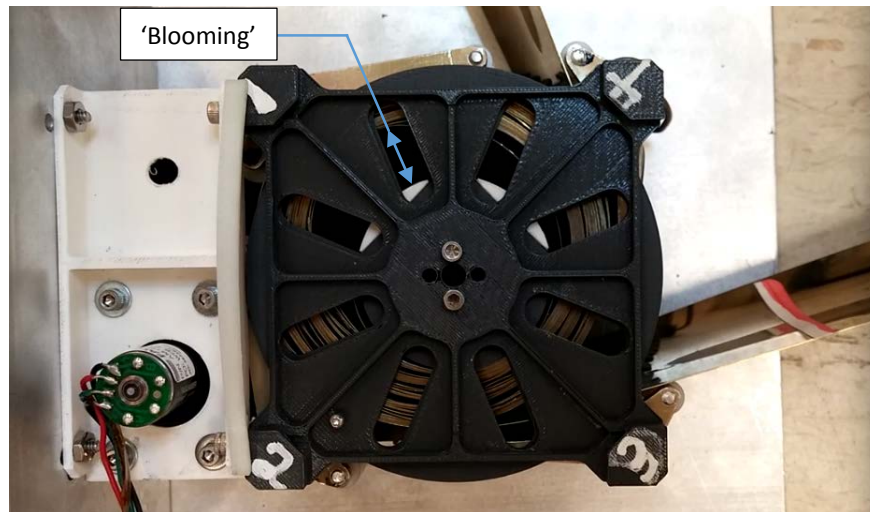


**Figure 11. Point of deployment where 'blooming' causes failure**

As seen in an early prototype in Figure 11, 'blooming' can cause a failure in primarily two modes: 1) the boom wraps expand radially into an oblong shape; eventually this shape can become large enough to bind up between boom arms 2) near to the end of deployment the gap at the center can become large enough that the boom root can possibly yield and bend backwards at the clamp. This second method of failure did not occur during lab tests as the deployment was halted before the root could yield, but if allowed to continue would have certainly occurred.

Several approaches have been developed in order to either eliminate or mitigate 'blooming' during deployment:

- 1) Adjustment of boom arm force on the boom wrap. By changing torsion springs, the contact force of the boom arms on the wrap can be adjusted to fit the necessary force. It was noted that as the boom length in the deployer increased, the required force also increased. A spring arm contact simulator was developed with compression springs and can be viewed in Figure 12. The compression springs allowed nearly instantaneous adjustment of the boom arm contact force. Once a force was found which eliminated blooming using the simulator, the compression spring force was then exchanged for a properly sized torsion spring creating the same force at the point of contact. It is to be noted that the greater the amount of force placed upon the boom wraps the more friction is introduced into the system and the greater the chance of locally yielding the boom. The contact force on the boom wraps should not be needlessly oversized.

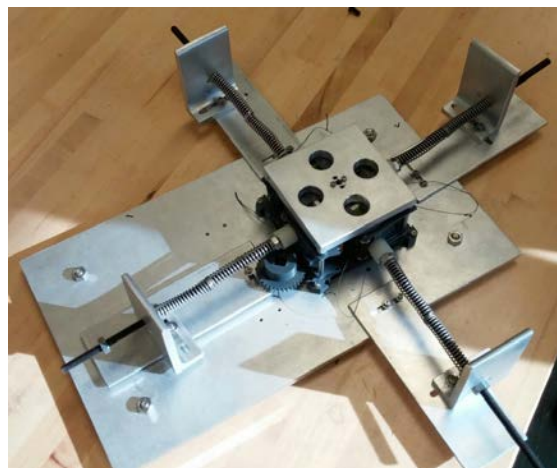


**Figure 12. Compression Spring Arm Contact Simulator**

- 2) At the point of contact between the boom arms and the boom wraps, friction needs to be minimized to allow the booms to glide past each roller. Excess friction will exacerbate 'blooming.' Early on in the design cycle, the rollers were exchanged from nylon, as was heritage with NanoSail-D, to Rulon J PTFE.
- 3) Adding friction between boom wraps decreased the ability for the booms to expand radially. This method was first noted by the LightSail-A design team. In order for the boom wraps to expand radially and cause 'blooming' they must slide past one another. By increasing the friction between the boom wraps this sliding is made more difficult, helping to alleviate blooming. This was shown to work with TRAC booms by scratching the surface with medium-grit sand paper.
- 4) Increasing contact and friction between the spool flanges and boom wrap aids deployment. By having one or both flanges directly contacting the boom wraps 'blooming' can be impeded to a small degree. It is desirable to minimize any extra height between the flanges.
- 5) Increasing the packaging efficiency of the rolled boom pair will also aid in a successful deployment. Tighter packing can be achieved by pulling the booms outward as they are being spooled inward.
- 6) Reversing deployment at intervals can assist in deployment when 'blooming' does occur (e.g., for every 1 m deployed, reverse 10 cm and repeat). If the boom begins to expand radially, reversing direction will tighten up the spool eliminating momentary blooming. It was shown during prototype testing that the boom wraps will constrict inward before retracting the boom back into the deployer.
- 7) Adding points of contact at the boom arm significantly alleviate 'blooming.' As pictured in Figure 13, by adding a rocker-bogie to the boom arms, we can double the points of contact from four to eight and decrease the contact at each point by half. This method has been shown through testing to be one of the most effective techniques in reducing 'blooming.' Furthermore, if 'blooming' does occur, the rocker-bogie motion has proven to handle the oblong rotation of the boom spool without binding. The rocker-bogie simply rotates back-and-forth around the bulged section of the boom wrap, where the single roller would come into contact with the bulged section creating a large tangential force. This tangential force would cause a spike in the required motor torque, which causes failure. Unfortunately this rocker-bogie design is unable to fit in the NEA Scout design volume.

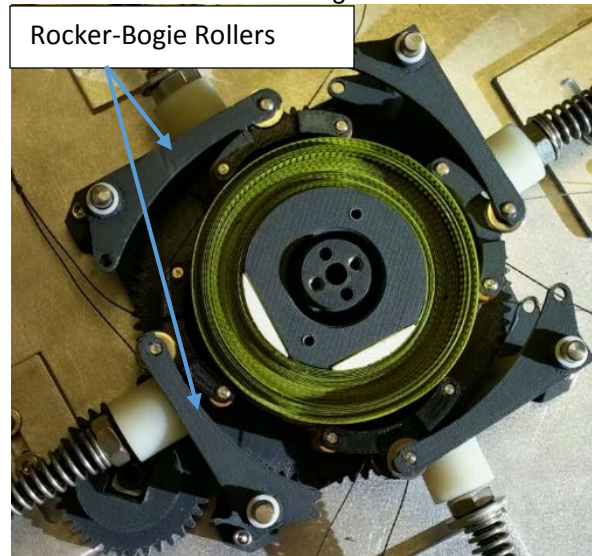


**Figure 13. Deployer Prototype with Added Rocker-Bogie Rollers**

These approaches are also applicable to other boom systems. In fact, during the development of the NEA Scout boom deployer, very slight modifications were made to allow for a split tape composite boom (Figure 14). The split tape composite boom spooled tighter and deployed with greater ease than the metallic TRAC boom. The improved deployment of the split tape composite boom when compared to the metallic TRAC boom can be attributed to 1) significant decrease in strain energy (comparable to force required to flatten the boom, 2) friction between boom wraps, and 3) ability to package into a tighter roll.



Despite the advantages of a split tape composite boom, including a large weight savings, its significantly greater height made it unable to package within the allotted volume. The composite boom required a height of 6.5 cm compared to 3.5 cm for the TRAC boom.



**Figure 14. Split Tape Composite Boom Deployer**

#### Stepper Motor

A stepper motor with a planetary gearhead is used to rotate the boom spools. It is important to note that given a well-balanced system the strain energy in the four booms will act to self-deploy the booms; therefore, ideally the stepper motor is used solely to hold back and step out the booms slowly. In practice, the motor is needed both to hold the booms back as well as push them out. NanoSail-D chose not to utilize a motor, and simply allowed the booms to self-deploy after activating the burn wire mechanism. This boom deployment took only a few seconds and could be considered too violent for a larger sail. Furthermore as the boom length increases, the necessity for a motor becomes more evident. LightSail-A chose to implement a DC motor with an encoder and a worm gear transmission into their single spool.

The limitation of the NEA Scout volume led to the use of a stepper motor with a planetary gearhead. The detent torque of a non-energized stepper motor is also seen as a benefit of a stepper motor and has proven to be enough force when combined with the gearhead to hold the boom in place. In place of an encoder, two infrared sensors are used to monitor deployment and provide feedback (shown in Figure 15; the brackets for each sensor are goldenrod). The first is an infrared gate sensor measuring a hole pattern machined into one boom spool's top flange (Figure 15, shown in orange, circled). This sensor provides 1.8-degree resolution at the boom spool. The second infrared sensor is attached to one of the boom arms and watches the boom as it exits the deployer. The sensor is positioned to read marks along the boom's welded edge. By measuring both the rotation of the spool and the deployment of the boom directly, it can be determined in real-time if and when 'blooming' occurs. The ability to measure possible 'blooming' allows for it to be mitigated by reversing the deployment as discussed earlier.

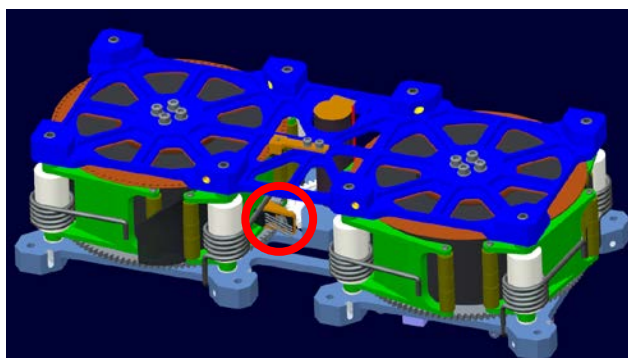


**Figure 15. Boom Deployer with Two Infrared Sensors Visible**

### TRAC Boom Thermal Deflection

The solar sail design for NEA Scout produced many design challenges. The original baseline for NEA Scout was a four quadrant sail in order to benefit from the heritage designs of NanoSail-D and LightSail-A. However, after examining the thermal environment experienced by the TRAC booms, it became evident that thermal deformation would prove too great for an effective, quadrant designed solar sail. Initial results for an unloaded 7.3-m TRAC boom at a 30° angle of incidence to the sun indicated 1.48 m of tip displacement (Figure 16). This result is one to one orders of magnitude greater than what would be considered acceptable from Guidance, Navigation, & Control. This is caused by the low thermal conductivity along the thin profile of the boom, the self-shading one half of the boom's profile by the sunward half, and the suboptimal optical properties of the uncoated TRAC boom (solar absorptivity and infrared emissivity).

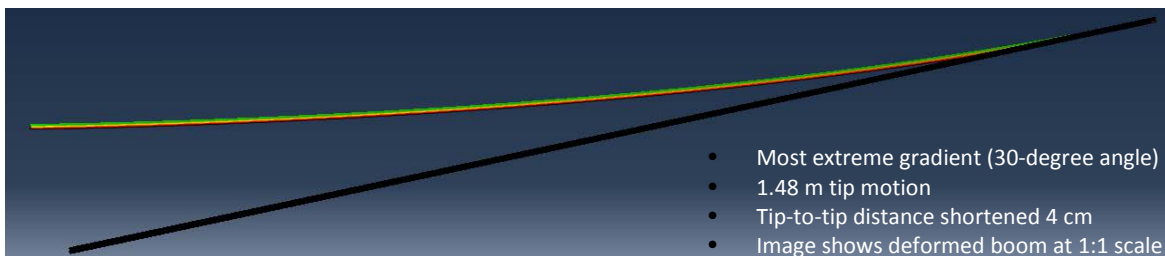


**Figure 16. 7.3-m Uncoated, unshaded, unloaded TRAC Boom during thermal analysis simulations**

Extensive analysis and testing were performed to determine the best method for mitigating boom thermal deflection, including an aluminum coating for the TRAC boom and the use of a 'sock' to keep the boom from direct sunlight. The final determination was to change the configuration to a single sail design, which would inherently shade that majority of the boom from the root to ~16 cm from the tip. An integrated model analysis shows that max out-of-plane boom tip displacement reduced from ~100 cm in the four quadrant case to ~4 cm in the shaded boom case (Figure 17). Figure 17 also shows a large amount of in-plane displacement that further convinced designers to move to a single sail. Additionally, the single sail increases the flatness of the sail, reducing the sail connection points from 12 to 4 interfaces.

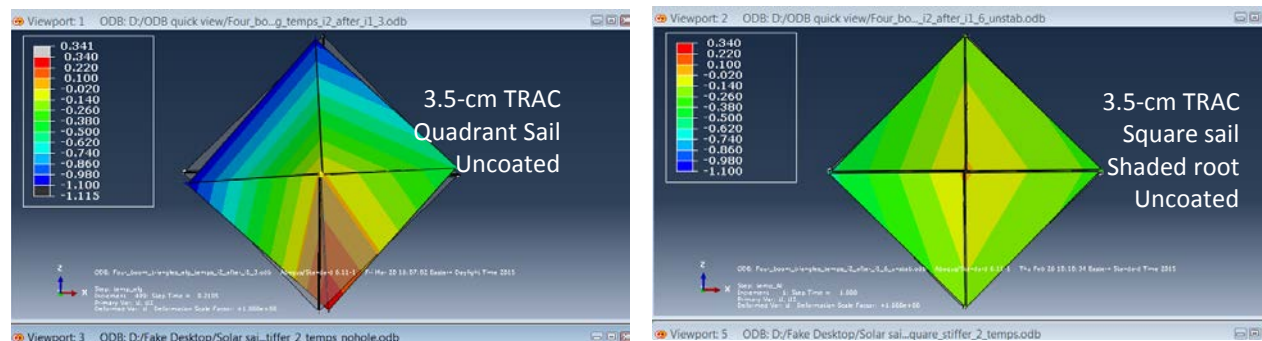


**Figure 17. Thermal deformation results for the four quadrant and single quadrant sail**

### Sail Spool Design

Designing a deployment scheme for a single sail entailed further complexities for the solar sail deployment mechanism. Due to the placement of the solar sail deployment mechanism in the center of the spacecraft bus, the single square sail is packaged onto a single oblong spool (Figure 18) in order to maximize the available volume. When spooled, the sail fits onto the spool in the shape of a racetrack. To protect the sail from pinch points during deployment, foam will pad the structure supports within the sail spool.



**Figure 18. Sail Spool Generation 1**

The sail spool assembly mounts directly to the boom deployer at four points. A center post is utilized to connect the two halves of the spacecraft structurally and pass-through a relatively large cable bundle. Due to the single sail design and the location of the solar sail module within the spacecraft, both cable harnessing and the primary load path must go through the center of the spool. The center post acts both as a systems tunnel and as the primary load path from the avionics portion of the spacecraft to the cold gas portion. The spool rotates independently from the rest of the system around the center post with the aid of two flanged sleeve PTFE bushings located on the top and bottom of the spool-to-post interface. These two bushings can be viewed in Figure 19. Only a small force from the booms are required to unspool the sail from the spool. This has been demonstrated in half-scale testing.

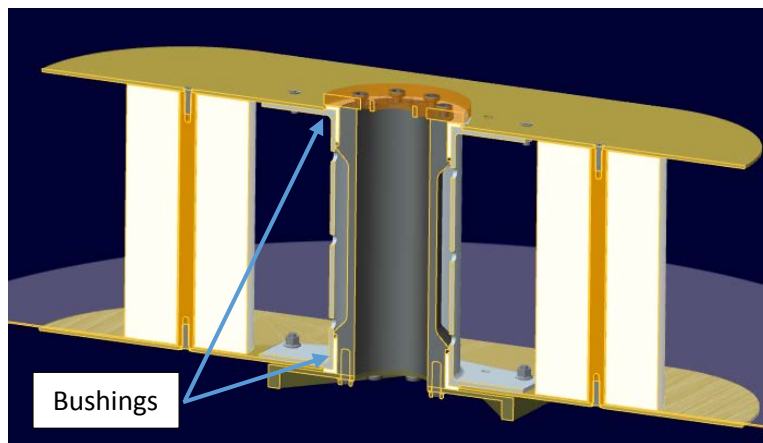


**Figure 19. Sail Spool Cross-Section Engineering Development Unit**

The center post (grey) remains hollow to allow for the bus cable harness to pass through.

#### Sail Connection to Booms

In order to optimize the load going into the sail, the connection of the boom tip to the sail corner will advance from a linear tension spring, as used by NanoSail-D and LightSail-A, to a constant force spring. The sail membrane is expected to thermally expand by ~2.9 cm more than the booms at each corner. In order to account for this, a long linear spring was designed with a low spring coefficient. Otherwise, a large force range would have to be accepted in the sail membrane and boom. By using a constant force spring, the force range should be constrained within a range of  $\pm 5\%$  and the size of the spring can be reduced, thus reducing the total boom length. For half-scale testing, 3 tension springs in series were used, similar to what is shown in Figure 20.

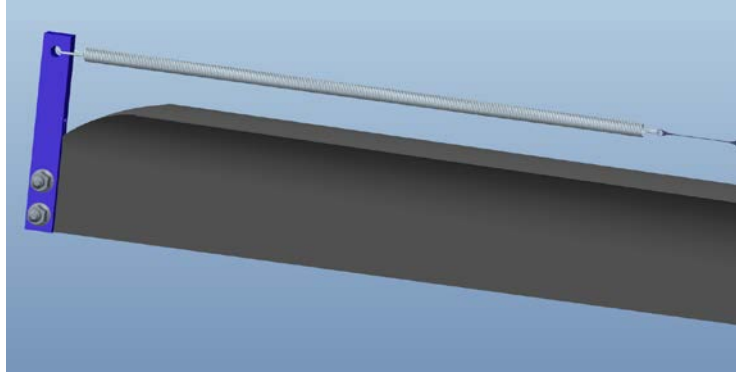


**Figure 20. Boom Tip to Sail Connection: Linear Tension Spring**

### **Sail Deployment Tests**

In preparation for the full-scale deployment tests to be conducted during the spring of 2016, scaled deployment tests were planned to gain better understanding of the fully integrated system and test functionality. Evaluating ground support equipment, optional test locations, and observations of rips and potential dynamic behaviors caused by the deployment were primary goals of the half-scale deployment tests. Previous analysis and component tests that focused on blooming, thermal deformation, and boom buckling fed into the test results.

The scaled deployment test utilized a 36-m<sup>2</sup>, 2.5-micron-thick Mylar material as a representative sail and four 4-m Elgiloy TRAC booms. For the first deployment (Figure 21), the team used two booms from AFRL and two produced by NeXolve. The second deployment utilized four 4-m TRAC booms manufactured by NeXolve. The sail spool and most of the deployer mechanism were fabricated from ABS material via a fuse deposition 3D printer. Metal fasteners, steel springs, ceramic rollers, and a stepper motor completed the deployer assembly.

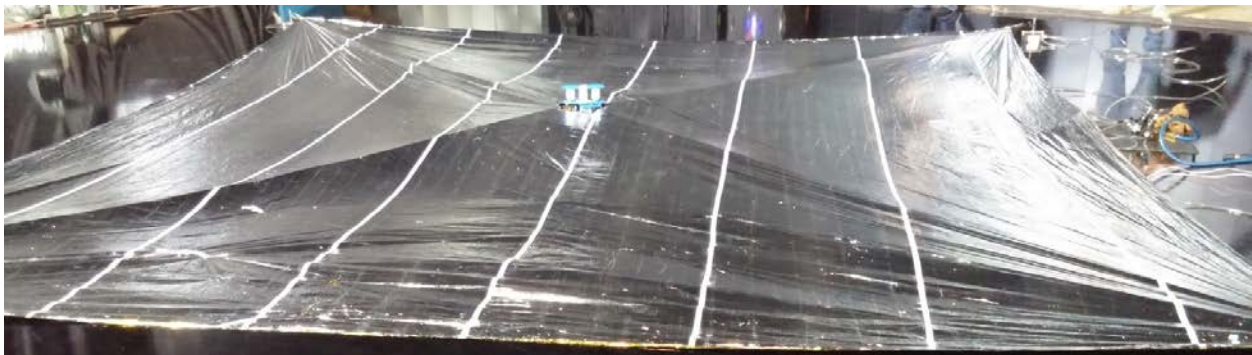


**Figure 21. First Deployed Half Scale Sail**

### Anomalies

To fold the sail, the team performed a z-fold pattern from one end of the sail to the center and z-fold pattern from the other end of the sail to the center. With both sides of the sail meeting in the center, the sail is then manually spooled onto the sail spool assembly. The sail folding is performed with minimal damage to the sail. All holes and rips caused by handling were patched with Kapton tape. After both deployments, approximately 30 holes and rips were accounted for throughout the acreage of the sail with the largest rip being the diameter of a nickel (21 mm).



The first deployment utilized four TRAC booms available at the time: two manufactured by AFRL and two manufactured by NeXolve. The AFRL booms had been through numerous component testing in development of the boom deployer assembly. Therefore, the AFRL booms incurred various cracks, weld delaminations, and deformations along the length of the booms. These defects prevented the booms from tightly spooling within the boom assembly (Fig. 22). Upon visual inspection prior to the first deployment, the NeXolve booms spooled noticeably tighter than the AFRL booms, improving the assumed packing efficiency calculated from previous components tests with the AFRL booms.

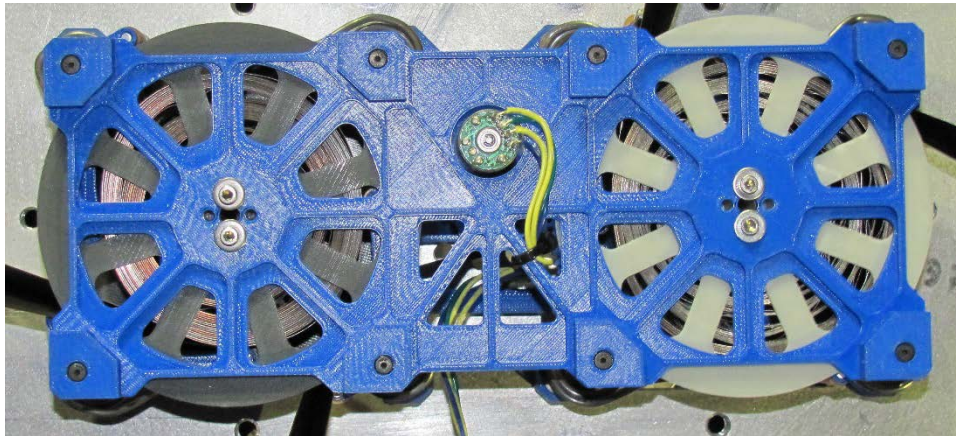


**Figure 22. NeXolve (left) and AFRL (right) 4m TRAC booms spooled prior to first deployment**

To overcome blooming, the team decided to deploy the sail in increments. The first 5 minutes of deployment extended the booms outward. Next, the deployer would be commanded to stop and reverse for 20 seconds. The reverse motion pulled the booms back into the deployer constricting the boom wraps around the center hub. This motion reduced the impact of ‘blooming’ while the booms continued to deploy. However, after the booms deployed approximately 3.5 m, the stepper motor stalled. The first deployment ended with the team manually deploying the final meter of boom and sail area.

The second deployment implemented lessons learned from the first deployment. The AFRL booms were replaced with newly manufactured booms provided by NeXolve. The sail material was refolded and spooled with Kapton patches for small knicks and rips. The stepper motor was replaced with a higher continuous torque output. Even though the 3D printed plastic gears were beginning to show wear, it was decided not to replace them at the time. This decision did not impact the second deployment. The full deployment went successfully with minimum blooming observed and without the need to mitigate ‘blooming’ by reversing the motor. The total deployment lasted 16 minutes for 36 m<sup>2</sup> of sail. The anticipated deployment time for the full sail is estimated to be approximately 30 minutes.



**Figure 23. Deployed Solar Sail After Second Deployment**

### **Conclusion**

The challenges inherent in development of such technology with the unusually rigorous constraints of a 6U cubesat require a thorough development program. The resulting lessons are enlightening to the complexities of a successful solar sail mission. As the project continues towards the manufacturing and test of the 86-m<sup>2</sup> sail with 6.8-m Elgiloy TRAC booms, these lessons will prove instrumental in advancing solar sail capability and expanding the use of the technology. Solar sails will continue to advance and enable future missions similar to NEA Scout to perform science objectives, which would not have been possible give similar design and launch constraints.

### **References**

1. McNutt, L.; Johnson, L.; Clardy, D.; Castillo-Rogez, J.; Frick, A.; and L. Jones. "Near-Earth Asteroid Scout." AIAA Space 2014 Conference; 4-7 Aug 2014; San Diego, CA; United States.
2. Whorton, M.; Heaton, A.; Pinson, R.; Laue, G.; and C. Adams. "NanoSail-D: The First Flight Demonstration of Solar Sails for Nanosatellites." Proceedings of the 22nd Annual AIAA/USU Conference on Small Satellites, Logan, Utah, USA, August 11-14, 2007.
3. Bidy, C.; and T. Svitek. "LightSail-1 Solar Sail Design and Qualification." Proceedings of the 41st Aerospace Mechanism Symposium, Jet Propulsion Laboratory, May 16-18, 2012.
4. Johnson, L.; Sobey, A.; Sykes, K.; "Solar Sail Propulsion for Interplanetary Cubesats." AIAA Propulsion and Energy 2015; 27-29 Jul 2015; Orlando, FL; United States.
5. Murphey, T. W.; and J. Banik. "Triangular Rollable and Collapsible Boom." The United States of America as Represented by The Secretary of The Air Force, assignee. Patent US 7895795 B1. 22 Oct 2007.

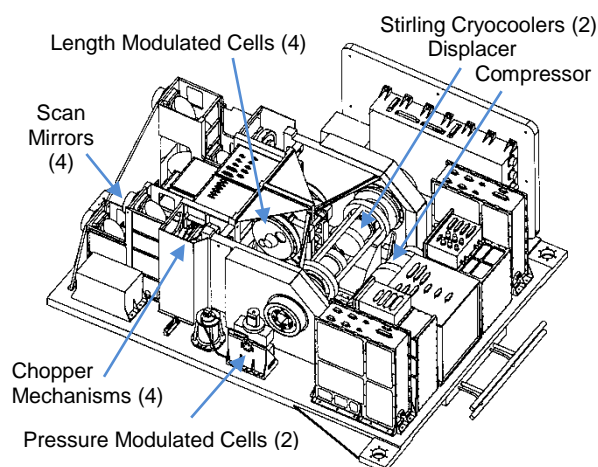
# MOPITT Mechanisms: 16 Years In-Orbit Operation on Terra

Andrew S. Gibson<sup>1</sup>, Florian Nichitiu<sup>2</sup>, Dwight Caldwell<sup>3</sup>, John Hackett<sup>4</sup>,  
Robert Deschambault<sup>5</sup> and James R. Drummond<sup>6</sup>

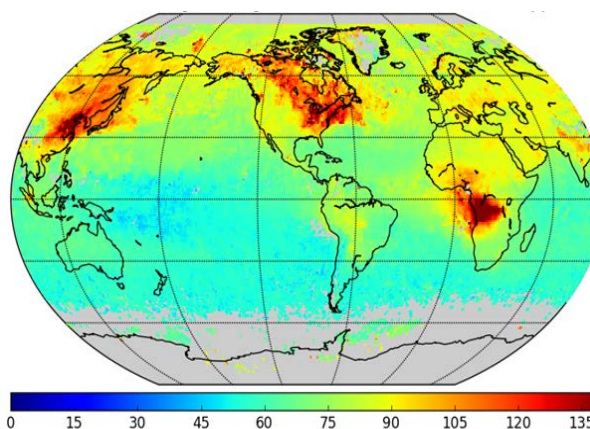
## Abstract

The 16<sup>th</sup> anniversary of the launch of NASA's Terra Spacecraft was marked on December 18, 2015, with the Measurements of Pollution in the Troposphere (MOPITT) instrument being a successful contributor to the NASA EOS flagship. MOPITT has been enabled by a large suite of mechanisms, allowing the instrument to perform long-duration monitoring of atmospheric carbon monoxide, providing global measurements of this important greenhouse gas for 16 years. Mechanisms have been successfully employed for scanning, cooling of detectors, and to optically modulate the gas path length within the instrument by means of pressure and gas cell length variation. The instrument utilizes these devices to perform correlation spectroscopy, enabling measurements with vertical resolution from the nadir view, and has thereby furthered understanding of source and global transport effects of carbon monoxide. Given the design requirement for a 5.25-year lifetime, the stability and performance of the majority of mechanisms have far surpassed design goals.

With 16 continuously operating mechanisms in service on MOPITT, including 12 rotating mechanisms and 4 with linear drive elements, the instrument was an ambitious undertaking. The long life requirements combined with demands for cleanliness and optical stability made for difficult design choices including that of the selection of new lubrication processes. Observations and lessons learned with regards to many aspects of the mechanisms and associated monitoring devices are discussed here. Mechanism behaviors are described, including anomalies, long-term drive current/power, fill pressure, vibration and cold-tip temperature trends. The effectiveness of particular lubrication formulations and the screening method implemented is discussed in relation to continuous rotating mechanisms and stepper motors, which have exceeded 15 billion rotations and 2.5 billion steps respectively. Aspects of gas cell hermeticity, optical cleanliness, heater problems and SEU effects on accelerometers are also discussed.



**MOPITT Instrument Layout**  
(showing mechanism locations)



**Carbon Monoxide Average Mixing Ratio (in ppbv)**  
(measured June-July 2015)

<sup>1</sup> Canadian Space Agency, St-Hubert, QC, Canada

<sup>2</sup> University of Toronto, Department of Physics, ON, Canada

<sup>3</sup> COM DEV International Ltd., Cambridge, ON, Canada

<sup>4</sup> Canadensys Aerospace Corp., Bolton, ON, Canada

<sup>5</sup> Christie Digital Systems, Kitchener, ON, Canada

<sup>6</sup> Dalhousie University, Halifax, NS, Canada

Copyright © 2015 Government of Canada. NASA has been granted permission to publish and disseminate this work as part of the Proceedings of the 43<sup>rd</sup> Aerospace Mechanisms Symposium, NASA Ames Research Center, May 4-6, 2016. All other rights are retained by the copyright owner.



## Introduction

The MOPITT instrument is a multi-channel thermal infrared (TIR) and near infrared (NIR) instrument that continuously measures the concentration of carbon monoxide (CO) on a global scale. The instrument was funded by the Canadian Space Agency and built by the prime contractor COM DEV International. Prior to the launch of MOPITT on the NASA Terra platform, the only global data available was for four short periods of measurements by the MAPS instrument on the Space Shuttle. Instrument retrievals have helped to understand the relationship of CO to ozone, which is linked to climate change. With MOPITT's high sensitivity to surface CO from simultaneous NIR and TIR signals, this has also been useful to support estimation of CO<sub>2</sub> sources. Data have also been used in combination with that of other instruments to produce improved data products as described by Gille [1]. The current baseline, given existing fuel, is to continue operation of Terra until the early 2020s.

The Terra platform is in a sun-synchronous polar orbit at an altitude of 705 km. From Terra, MOPITT has a horizontal spatial resolution of around 22 km x 22 km and a swath width of ~640 km, which allows global coverage every 3 days. MOPITT uses gas-cell correlation radiometry to detect atmospheric CO absorption at 4.6  $\mu\text{m}$  (TIR channels) and 2.3  $\mu\text{m}$  (NIR channels), [2]. The instrument contains a set of long life mechanisms shown in Figure 1, which provide critical functionality in the collection of CO data.

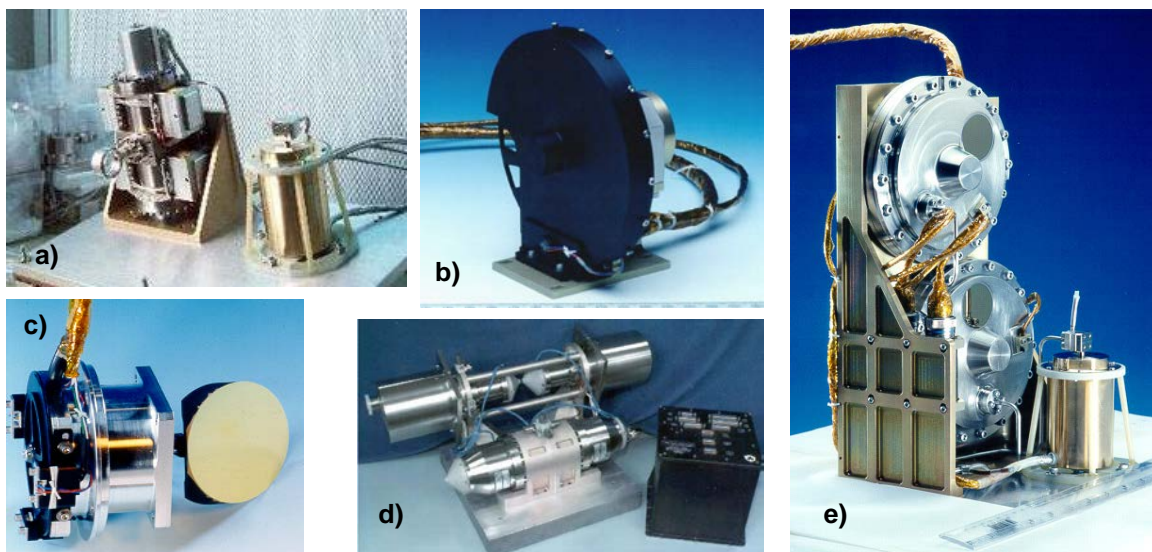


**Figure 1. MOPITT's Continuously Operating Mechanisms: a) Pressure Modulator Cell & Molecular Sieve, b) Rotating Vane Chopper, c) Scan Mirror Mechanism, d) Airbus Stirling Cooler & Lockheed Cooler Drive Electronics, e) Length Modulation Cells & Sieve**

MOPITT contains four optical chains which are each split into two independent channels (total of 8 channels). A summary of the optical channels and the mechanisms involved in each channel is given in Table 1. The optical signals are acquired via four stepper motor driven scan mirrors, each initiating an optical chain at the front end. The hybrid stepper motors for the scan mirrors were manufactured by Tecstar (now MOOG) and have achieved long lifetimes on the order of  $2.5 \cdot 10^9$  steps ( $1.8^\circ$ ) or travel equivalent to 12 million rotations, with bearings lubricated with MAC grease (Rheolube 2000).

The optical input signal is routed from the scan mirrors to four optical choppers, which turn continuously at fixed speeds of 1500 and 1800 RPM, with 16 vanes per rotation. Designed and built by COM DEV, three of the four chopper mechanisms have each achieved over 15 billion revolutions. Long life achievements have been facilitated by the use of MAC (multiply-alkylated cyclopentane) oil lubricated bearings (Nye 2001T with 1.0% tricresyl phosphate and 0.3% phenolic anti-oxidant). The formulation is

only slightly different from the more common additive formulation for Nye 2001, but was based on Draper Lab's long life heritage with PAO oils.

**Table 1. MOPITT Optical Channels and Mechanism Configuration/Timings**

Optical Channel Number	Channel 1	Channel 2	Channel 3	Channel 4	Channel 5	Channel 6	Channel 7	Channel 8
Chopping & Scanning Mechanism Numbers	Chopper & Scan Motor 1		Chopper & Scan Motor 2		Chopper & Scan Motor 3		Chopper & Scan Motor 4	
Modulating Mechanism	LMC 1		PMC 1	LMC 2	LMC 3		PMC 2	LMC 4
Gas Species in Modulating Mechanism	CO		CO	CH <sub>4</sub>	CO		CO	CH <sub>4</sub>
Pressure of Modulating Mechanism [kPa nominal]	20		7.5	80	80		3.8	80
Wavenumber Range [cm <sup>-1</sup> ]	52	40	52	139	52	40	52	139
Mid-Wavelength [μm]	4.617	2.334	4.617	2.258	4.617	2.334	4.617	2.258
Wavelength Range [μm]	0.111	0.022	0.111	0.071	0.111	0.022	0.111	0.071
Modulator Frequency (LMC or PMC Rate) [Hz nominal]	11.2		48.6	13.5	11.2		43.3	12
Nominal Chopper Frequency [Hz]	401		486		401		433	
LMC Angular Encoder Pulses [pulses per rotation]	72		N/A	72	72		N/A	72
Pressure Control Device Number	Sieve 1		Sieve 2	N/A	Sieve 3		Sieve 4	N/A
Stirling Cryocooler System	Compressor & Displacer 1 (Side B)				Compressor & Displacer 2 (Side A)			

**Side B** = indicates Side-B (partially redundant channels)

The input signals are optically chopped/filtered in various ways using gas samples via two types of specialized mechanisms: the Length Modulated Gas Cells (LMC) (1 per optical chain), and the Pressure Modulated Cells (PMC) – in 2 of 4 chains.

As described previously [4], each of the four LMC mechanisms contain a pair of optical rotors spinning inside separate cells at fixed speeds between 672 and 810 RPM. A brushless DC motor directly drives the rotor in the evacuated cell ('compensator cell'), which in turn drives a co-linear rotor located in the second sealed gas cell ('modulator cell') charged with CO or CH<sub>4</sub> via a magnetic coupling. The LMC motor and bearing configuration (including lubrication) is identical to that of the choppers, except for the housing material and bearing preload. All of the LMCs have achieved ~6 billion revolutions to date.

The two PMC mechanisms provided by Oxford University have continued to operate reliably, representing the longest running in-orbit heritage for PMCs to date, exceeding 2·10<sup>10</sup> cycles of linear motion. The MOPITT version was specially characterized to run at higher fill pressures (≤10 kPa). These devices are lubricant-free, utilizing diaphragm springs and clearance seals, with direct heritage from the Pressure Modulated Radiometer flown on the ISAMS instrument on UARS [5]. As they are the predecessors that enabled the current generation of long-life space cryocooler technology, lifetime results are not surprising.

To maximize signal-to-noise ratio and achieve optimal performance, indium antimonide infrared detectors were designed to be cooled to <90K using a pair of 50–80K Airbus Stirling Cycle Coolers (formerly BAe/Matra Marconi/Astrum) [3,9]. The coolers are driven by Cooler Drive Electronics manufactured by Lockheed Martin. The cryogenic cooling system for the detectors represents a duality of results in terms of life, having demonstrated one of the shortest and longest life-times in-orbit for Stirling devices to date. The failure of one displacer drive system after just over a year in orbit led to adjustments which allowed the 2<sup>nd</sup> cooler to continue running, with nominal vibration compensation provided by the opposing compressor. Partial redundancy of the optical channels reduced the impact of the failure on science return. Alongside the TIR ASTER cooler also on Terra, the prevailing MOPITT cooler system represents

the longest in-orbit Stirling cooler heritage point to date, surpassing those on the ERS satellites and leading slightly ahead of another Airbus cooler (from the same batch) flying on ODIN. Specific device behaviors, including updates on cooler vibration compensation, decontamination cycles, and accelerometer response to radiation environment are discussed later in the paper.

A summary of the mechanism life record is shown in Table 2, with some key tribological parameters and notes included for reference. The instrument is taken offline once per year for decontamination (approximately one week duration, usually in March), hot calibrations, and a PMC characterization sweep.

Two additional mechanisms on board MOPITT, the Earth and Space Port Covers, deployed successfully on 28 Feb 2000, retaining the ability to be re-closed if necessary. The port covers, as well as the other mechanisms, have been described previously [3,4]. Refer to these references for details of the mechanism designs and operation in the MOPITT instrument, and for a previous review of in-orbit mechanism performance after 5 years in orbit. The following section provides an update to that review, with further discussion of observations and status for the continuously operating mechanisms.

### In-Orbit Performance of Continuously Operating Mechanisms

#### Scan Mirror Mechanism Performance

The scan mirror sequence was described by Caldwell [3], covering a  $\pm 25.2^\circ$  swath with periodic swings to a space view and to an internal blackbody calibration. Figure 2 shows that the drive currents have been extremely stable over the mission duration. The current itself proves that the device was commanded reliably, while the response of the unit has been confirmed through consistency of data and encoder readings. The customized IR encoder readings, which provide 3 bits of information to indicate the center and edges of the swath, as well as calibration positions, have not generated any significant errors over the mission lifetime. An anomaly occurred with Scan mirror 1 on 06 Apr 2002, with current rising rapidly and oscillating for about 90 seconds before the voltage dropped to zero (see Figure 4a). The voltage drop is consistent with either a blown fuse or power supply failure. The current increase which preceded the failure was brief, with no obvious warning signs noted previously, so it is thought that the failure is more likely to be an electrical fault than a mechanism failure. Because this side of the instrument was already non-operational due to the cooler failure, no further in-depth investigation was pursued.

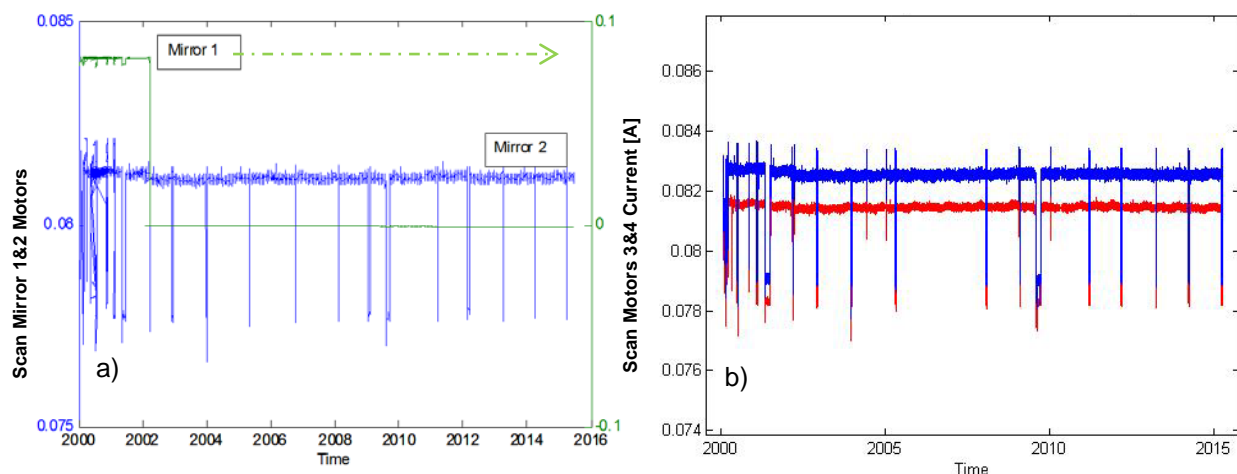


**Figure 2. Stepper Motor Current vs Time for a) Scan Motors 1 and 2, b) Scan Motors 3 and 4**

**Table 2. Mechanism Usage Summary Over 16 Years in Orbit (to 17 Jan 2016)**

Mechanism	Gas Fill	Freq/ Rate	Key Unit Parameters	Years Nominal Running	Cycles/ Rotations / Steps*	Mechanism Status	Specific Notes
Cooler 1 (B) – Compressor	He	44/43 Hz	13 bar fill pressure (abs)	15.5	2.1E+10 cycles	Continues to operate nominally. ~3 months for investigations.	Current compressor Stroke (A,B)=(6.24,5.00 mm <sub>p-p</sub> ). Displacer strokes (A,B)= (2.99,3.69 mm <sub>p-p</sub> )
Cooler 1 (B) - Displacer	He	44/43 Hz	90 K cold-tip (transitioning to ~310 K, 326 K)	1.2	1.6E+09 cycles	Displacer ceased nominal operation in 07 May 2001	Displacer B continues to move freely, driven by pressure wave as per Figure 9.
Cooler 2 (A) Compressor & Displacer	He	44/43 Hz	84 K±0.3 K over life	15.5	2.1E+10 cycles	Continues to operate nominally	14 decontamination cycles completed
PMC 1	CO 7.5kPa	48.6 Hz	Q factor of ~3, drive current of X	15.7	2.4E+10 cycles	Continues to operate nominally	Characterisations performed during decontamination cycles, used to monitor resonance/fill pressure.
PMC 2	CO 3.8kPa	43.3 Hz	Q factor of ~7 (at lower pressure), Drive current of 0.2A	15.7	2.1E+10 cycles	Continues to operate nominally	PMC 2 losing ~1% of pressure per year, current temp of 297-300 K. PMC amplitudes (1,2)=(4.84, 6.41mm)
Chopper 1		25.1 Hz 1505 rpm	Nye 2001T (130mg), TCP soaked 440C R6 duplex bearings	15.7	1.2E+10 rotations	Continues to operate nominally	All choppers have 16 vane openings. Duplex bearings operate in vacuum.
Chopper 2		30.4 Hz 1822 rpm	preload of 12.6±4.4N, Meldin 9000 retainers.	15.7	1.5E+10 rotations	Continues to operate nominally	
Chopper 3		25.1 Hz 1505 rpm	Lubricant Screening by Draper Labs (up to 5 cycles).	1.3	1.0E+09 rotations	Stopped in open vane position 04-Aug-2001	Chopper 3 failure had no impact to science, due to stability of signal/background
Chopper 4		27.1 Hz 1624 rpm	Optical encoder 16 pulses/rotation.	15.7	1.3E+10 rotations	Continues to operate nominally	
LMC 1	CO 20kPa	11.2 Hz 672 rpm	Nye 2001T (130mg), TCP soaked 440C R6 duplex bearings	15.7	5.5E+09 rotations	Continues to operate nominally	Modulator duplex bearing run in gas. Compensator duplex bearings run in vacuum (vented). Bearing assembly bake-out post screening performed to reduce optical contaminants from lubricant additives.
LMC 2	CH <sub>4</sub> 80kPa	13.5 Hz 810 rpm	preload of 22±4.4N, Meldin 9000 retainers.	15.7	6.7E+09 rotations	Continues to operate nominally. Lost 70kPa fill in 5 yr	
LMC 3	CO 80kPa	11.2 Hz 672 rpm	Lubricant screening by Draper Labs. Optical encoder with 72 pulses/rotation.	15.7	5.5E+09 rotations	Continues to operate nominally	
LMC 4	CH <sub>4</sub> 80kPa	12.0 Hz 720 rpm		15.7	5.9E+09 rotations	Continues to operate nominally	
Scan Mirror 1				1.9	3.0E+08 steps	Unit Stopped 13-Dec-2002	Failure not believed to be mechanism related
Scan Mirror 2		Rheolube 2000, 440C bearings with TiC-coated balls, Nylasint lubricant reservoir		15.7	2.5E+09 steps	Continues to operate nominally	Mirrors settle in <50 ms, stares for 400 ms per step over ±25.2° swath + deep space & blackbody calibration views ±90°
Scan Mirror 3				15.7	2.5E+09 steps	Continues to operate nominally	
Scan Mirror 4				15.7	2.5E+09 steps	Continues to operate nominally	
				15.7	2.5E+09 steps	Continues to operate nominally	

### Rotating Vane Chopper Performance

The rotating vane choppers 1, 2 and 4 were shown to have stabilized after 5 years, as reported previously [3]. The stable performance has continued over the subsequent 11 years. This slow stabilizing behavior and periodic trends are believed to represent effects of the porous polyimide retainers, with small changes in wear and related coupling to the bearing races (refer to Figure 3). Differences in the average current levels are partly driven by the relatively large preload tolerances, speed of operation, and manufacturing and assembly tolerances (described in Table 2).

Chopper 3 stopped working in 2001 after 1.3 years of operation. Current at the drive amplifier was observed to increase over about 45 seconds before going to zero (refer to Figure 4), which could be consistent with a short in the harness or some other electrical component failure (not consistent with an open circuit). The chopper failure was attributed to a previous issue with a blown fuse, while a NASA report cites the most likely cause of the blown fuse was related to a Transistor Drive Circuit [10]. Fortunately, the chopper stopped at a completely open position, which allowed for the reconfiguration of data processing without the chopper. The failure actually had no impact on scientific data due to the thermal stability of the instrument.

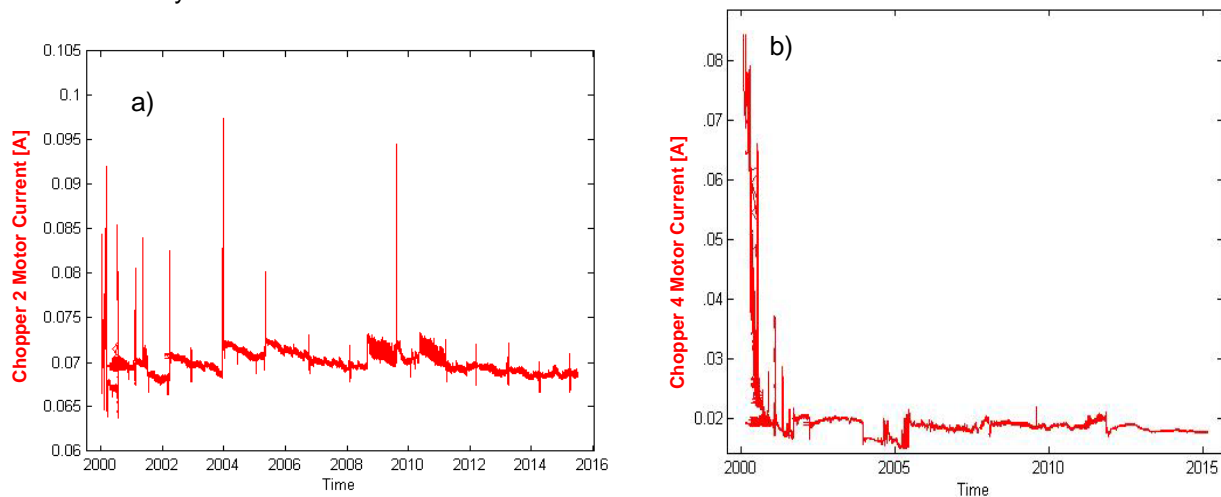


Figure 3. Chopper Brushless-DC Motor Currents of a) Chopper 2, b) Chopper 4

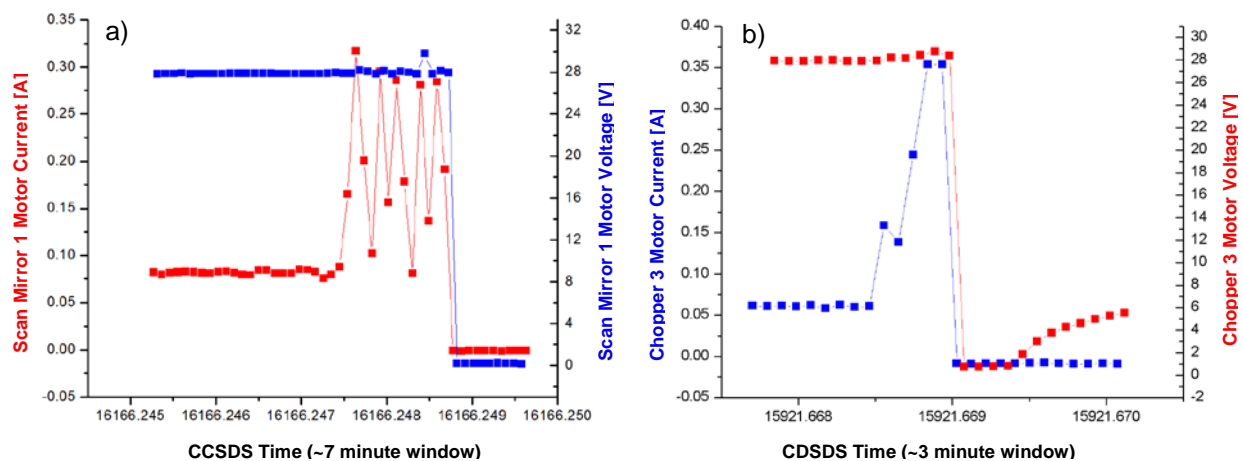
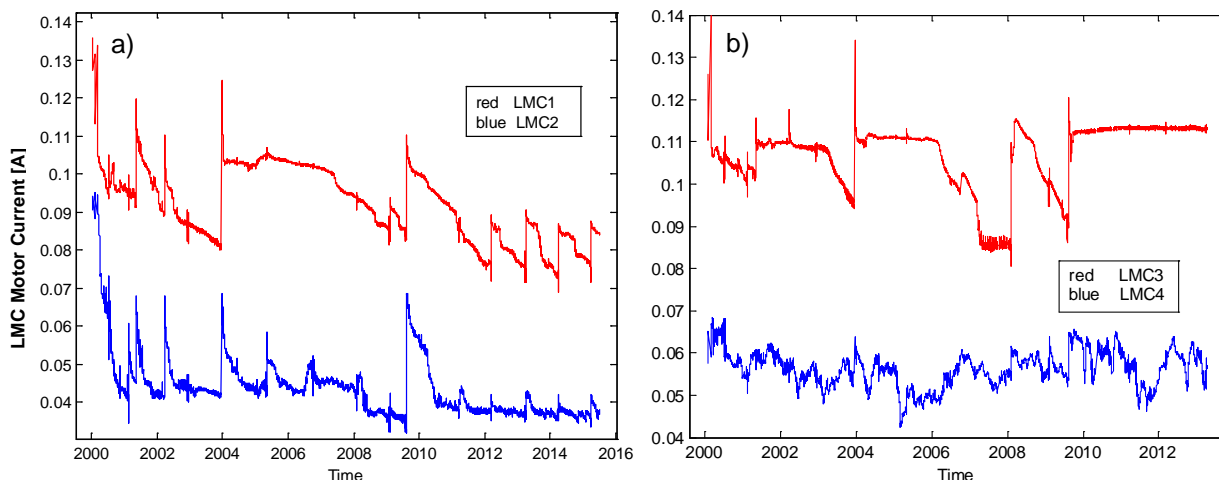


Figure 4. Motor Current and Voltage at Failure for a) Scan Mirror 1 and b) Chopper 3



### Length Modulated Cell (LMC) Performance

The LMC devices all show similar current excursions to the choppers, with subsequent recoveries to nominal levels, as shown in Figure 5. The current generally dropped over a period of 1-2 years before rising sharply back to the original current levels for a brief period. This trend repeated in a slightly different manner each time without any overall rise in current, so it can be considered to be stable overall. Choppers 1, 2 and 4 show some similar features (Figure 3). With the commonality of the LMC and chopper designs, the settling behavior is likely resulting from a change in friction of the retainer coupling to the balls and races (the choppers and LMC have the same bearing size and retainer, manufactured by Draper Laboratories). As the retainer wears or accumulates lubricant film, thresholds are reached where the active site shifts to another ball location and proceeds to settle again.



**Figure 5. LMC Brushless-DC Motor Drive Currents for a) LMCs 1&2, b) LMCs 3&4**

Optical cleanliness was one of the biggest design drivers for the LMC devices. In-orbit results demonstrate that contamination control was successfully managed as the long term radiometric gain measurements showed no significant build-up of contamination on optical surfaces over the mission, with the overall shift in gain being less than 1% in 16 years.

Each of the Length Modulated Cells were fitted with a pressure transducer, using high stability silicon-on-sapphire sensors (Sensotron). Pressure readings for these cells were expected to drop gradually due to gas leaks in the capillary bonded IR window seals (described previously in [4]), while the gold and indium plated Inconel seals around the largest perimeter of the gas cells could also contribute. The long-term trend for the pressure of LMC 3 and 4 showing the expected pressure drop is presented in Figure 6.

LMC 3 uses a molecular sieve to control the pressure and is showing a rate of pressure drop of about 1 kPa per year over the past few years. LMC 4 is a fixed pressure unit (no sieve), showing a slightly more rapid pressure decline since 2010 (~2.5 kPa per year), most likely due to leakage via the aging epoxy in the capillary bonds. LMC 1 lost about 10% of its pressure in the first 5 years. The LMC 2 pressure was stable at about 75 kPa for one year and then showed the most dramatic loss with pressure reduced to 5 kPa by 2005. The capillary bond for the optical windows was a newly developed process for this application, for which He leak testing, thermal cycling and ultrasonic inspection were performed to validate the engineering model hardware. The in-orbit results for two LMCs confirm that the bonding method is capable of lasting for a long-duration mission, but that screening methods and aging factors should be further considered (i.e., radiation testing and life-testing of the process is recommended prior to reuse). Alternatively, a diffusion bonding process could be evaluated as an option.

An anomaly was observed with Sieve 3 on 03 Oct 2009 (unrelated to the cooler anomaly) due to the heater for Sieve 3 turning off unexpectedly or failing. The heater can be activated to stabilize the pressure

in LMC 3, but it had not been used for this purpose prior to this point in the mission. The effect was for the LMC 3 pressure to drop from ~68.5 kPa to ~65.3 kPa over 10 hours. The pressure then remained stable around 65.25 kPa. One attempt to reactivate the heater of Sieve 3 was unsuccessful. The resulting action was to modify the MOPITT forward model (for LMC new cell pressure) used for science data. This recalculation was performed by the NCAR team with a good result, and deemed to have zero impact on the quality of science data retrieved by MOPITT.

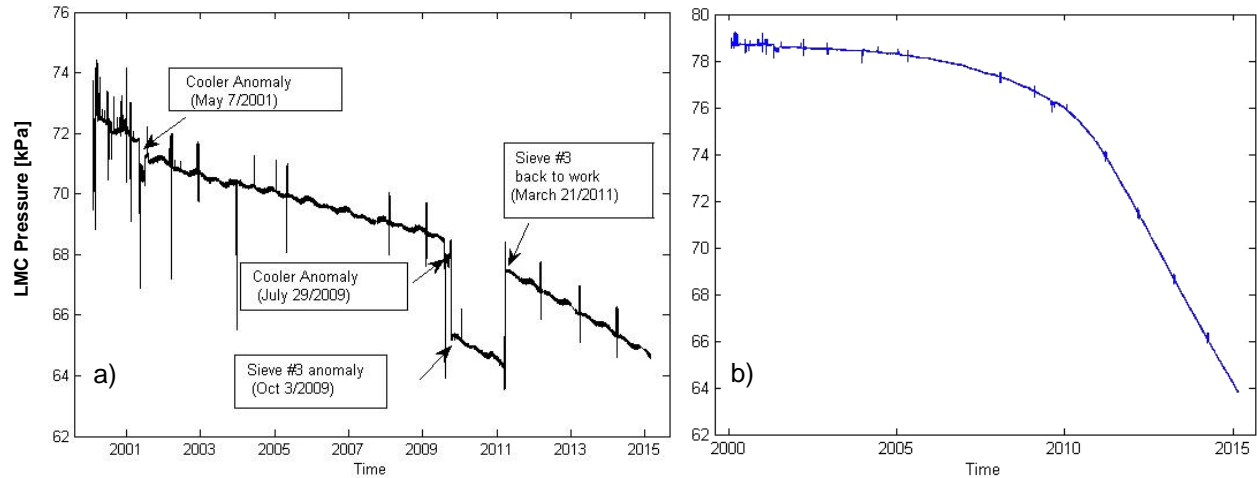


**Figure 6. Length Modulated Cells - Pressure Sensor Signals Over Life for a) LMC 3, b) LMC 4**

In 2011 the sieve was reactivated after an instrument reset during a calibration procedure, suggesting that the previous anomaly may have been due to an SEU effect. A later anomaly with Sieve 1 was thought to be similar to the Sieve 3 anomaly, occurring about a year later (02 Dec 2010) and resetting under similar circumstances.

#### Pressure Modulated Cell (PMC) Performance

The PMC devices have continued to operate as expected. Spikes in the data are believed to be due to effects related to decontamination cycles of the coolers. Referring to Figure 7b, the gradual drop in drive current for PMC 2 is consistent with a slow leak of gas approximately 1% per year, which affects the resonance of the mechanism. The step change in settings in 2001 is related to a change of setting after the cooler anomaly.

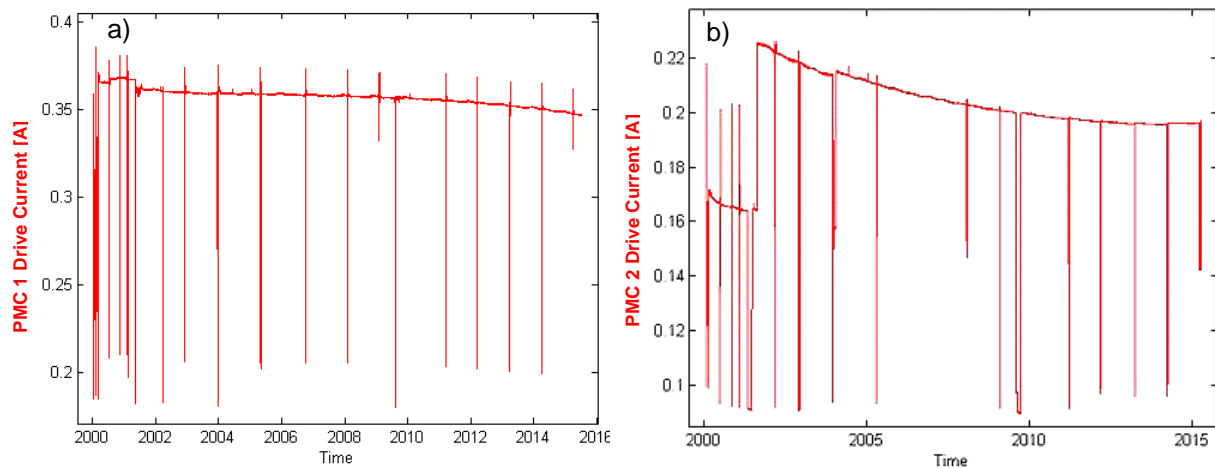


**Figure 7. Pressure Modulator Cell Drive Currents for: a) PMC 1, b) PMC 2**



In order to determine the mean operating pressure in the PMCs, it was necessary to make two sets of frequency scans with a change of sieve temperature between the two. The measurements of PMC motor current versus frequency were used to determine the resonant frequency of the PMC and using calibration runs obtained before and during spacecraft thermal-vacuum tests, a mean operating pressure could be determined. From the analysis done in March 2015, the PMC 2 pressure was  $3.505 \pm 0.015$  kPa. The rate of PMC2 pressure decrease is constant and is  $\sim 0.03$  kPa/year. The resonance shift of PMC 2 is estimated to be  $\sim 1$  Hz, having minimal effect on operation or efficiency. The ability to perform such in-orbit diagnostics is essential as the knowledge is needed for computations of optical filtering provided by the cell. This slow change in pressure has been accommodated through normal calibrations, allowing for updates to the optical filter models of this channel with little impact to data retrievals.

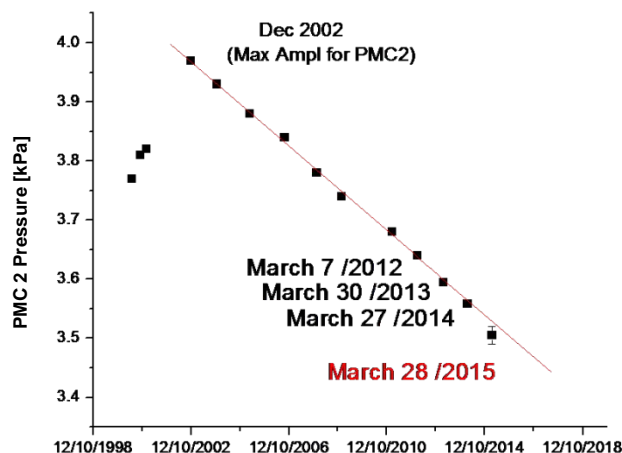


**Figure 8. Pressure Modulator Cells Mean Pressure Drop Over Lifetime for PMC 2**

#### Stirling Cycle Cryocooler Performance

On 07 May 2001 the cooler on side B of the instrument failed suddenly, without warning, as previously described [3]. One of the coolers had an out-of-limit condition for approximately 10 minutes before the instrument was put into Safe Mode, turning the coolers off. Observations [11] included a heating effect (2 K) at the displacer cold-tip B just before being turned off. Current telemetry indicated little change during the anomaly, which conflicted with possible explanations for the failure. It was learned from the vendor that the current telemetry for the displacer was not functional, which clarified the situation. The instrument was then power cycled, followed by a series of diagnostic tests which were run between 18 May and 26 Jun 2001, including the mapping of compressor to displacer stroke shown in Figure 9.

Phenomena consistent with pressure wave driving were observed in tests over varying amplitudes, explaining a different coupling between compressor B and its displacer. All tests showed that displacer B was not being driven electrically, but was coupled with the pressure wave from the compressor (phase control lost). Since that time, scientific data have been delivered by partially redundant channels 5-8 on side A, with the coolers working in an unbalanced mode to avoid end-stop collisions in the displacer. The cooler operating frequency was adjusted down slightly from 43.96 Hz to 43.0 Hz to reduce the cold-tip heating effect. This mode had cooler B operating at 82.5% of the amplitude of cooler A and produced some residual vibration, with the cooler working in the 'heating regime', warming the detector due to the lack of phase control (displacer B running free). The compressor B amplitude was fixed at  $5.0 \text{ mm}_{p-p}$ , while the amplitude of displacer B was held in the range of  $3.65 \pm 0.07 \text{ mm}_{p-p}$ .

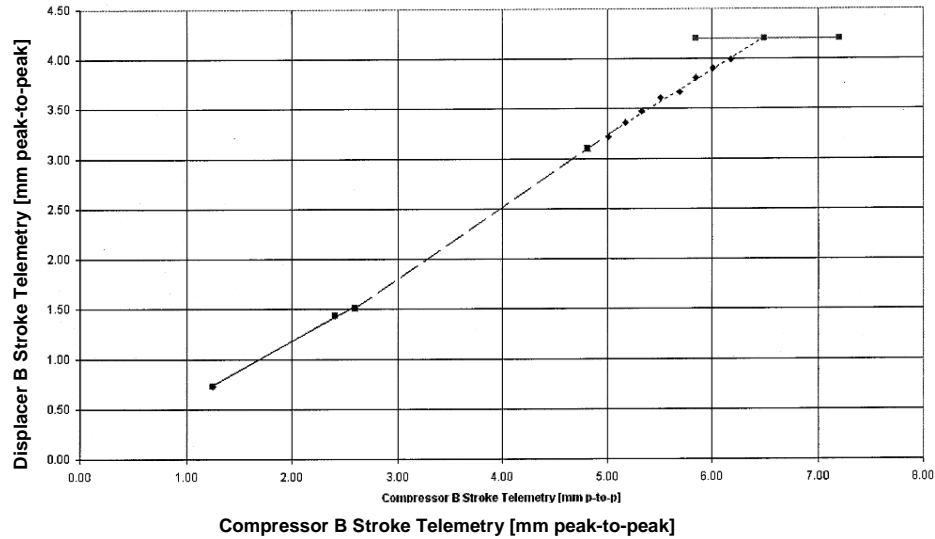


**Figure 9. In-orbit Displacer Stroke vs Compressor Stroke for Cooler (B) After Anomaly**

It has not been determined whether the displacer drive problem was related to the electronics, the harness or the displacer mechanism, just that an open circuit was experienced. From the behavior reported previously [6] and subsequent compressor operation, there was clearly no failure of gas seals, with no indication of pressure drop. The pistons were free to move so there was no obvious failure of a displacer coil bond to the coil former (a problem experienced due to silicone contamination affecting the bond of the motor coil, which was corrected in the subsequent batch of compressors built for the INTEGRAL mission [6]). It is notable that a lead-in spring failure was not completely ruled out and that the MOPITT cooler application is a rare case of a launch in the passive ‘unshorted’ condition (not actively controlled). Shorting had been reviewed as an option, but was not readily supported by the Lockheed Martin electronics. Displacers have inherently low damping compared to that of a compressor, so there was an acceptance of residual risk, with mitigation provided by testing to acceptance levels in this configuration. To preclude any residual risk of this nature in the future, it is recommended that coolers always be clamped by adequate shorting or active control during launch.

The long-term cooler displacer / compressor displacement data is shown in Figure 10. This shows the slow increase in ‘stroke’ needed to maintain the temperature control compensation for contamination build-up. The rate of increase reduces gradually with time and further decontamination cycles.

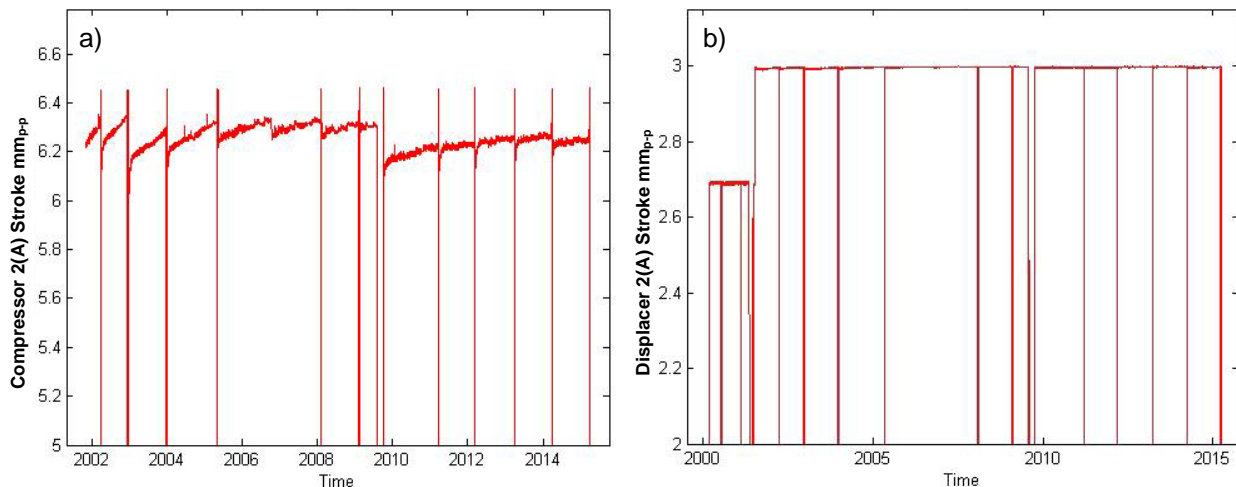


**Figure 10. Cryocooler Displacer and Compressor Displacement Over Lifetime**

The detector temperatures as maintained by the coolers are shown in Figure 11. Normally, the detector temperature on the non-cooling side B is stable around a warm temperature of 326 K and not varying more than 0.2 K (occasionally  $\sim 0.5$  K). The detector temperature on side A (coolers working with nominal amplitudes) is stable at  $\sim 84.0$  K. It continues to demonstrate a lessening of the rates of change of temperature after each decontamination cycle, as the cold-enclosure continues to be freed of moisture. However, the presence of contamination build-up (condensation) on the cold-tips is still noticeable, even after 16 years in orbit and many decontamination cycles.

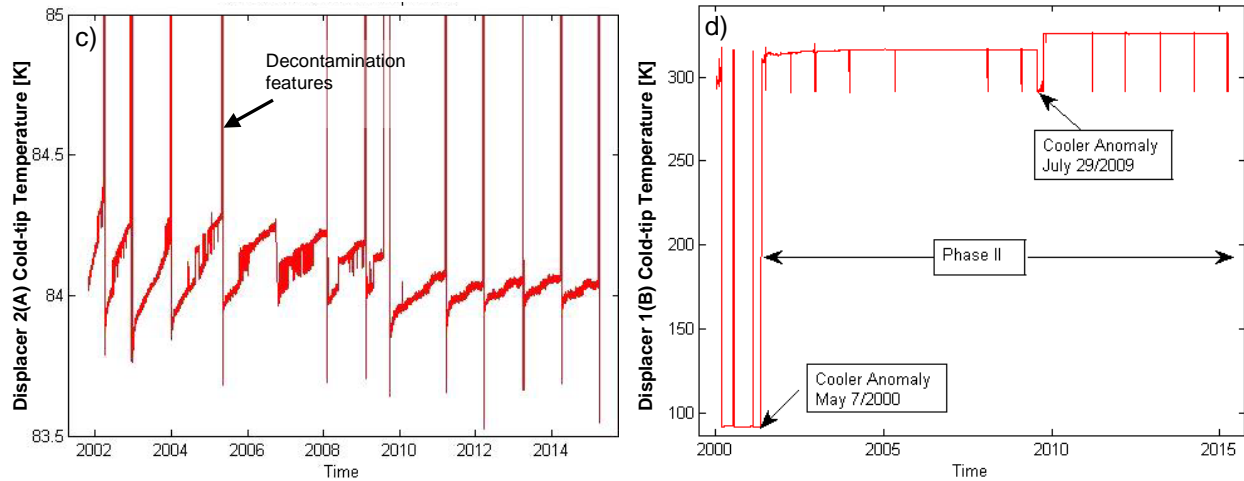


**Figure 11. Detector Temperatures Over Lifetime**

The ‘PDECs’ (position control) mode had been preferred prior to the failure as this mode was less sensitive to drifting than the ‘ADECS’ (accelerometer feedback) mode. Axial vibration levels were reduced to below  $0.12 N_{rms}$  in PDECs prior to the failure [9]. After the anomaly, the compressors were intentionally run at imbalanced strokes to allow the active detectors to cool, while keeping the failed displacer from being driven into its end stops. As a result, the unit has operated in this manual mode with temperature control on the active side for most of the mission. Variations of the axial induced vibration (Z) are driven primarily by seasonal parameters, but overall they are very stable. Increasing displacement (Figure 10) has little impact on residual axial vibration, as seen in Figure 12. Considering the overall situation, the vibration cancellation of the system is considered to be exceptional for the improvised balancing situation which needed to be adopted.

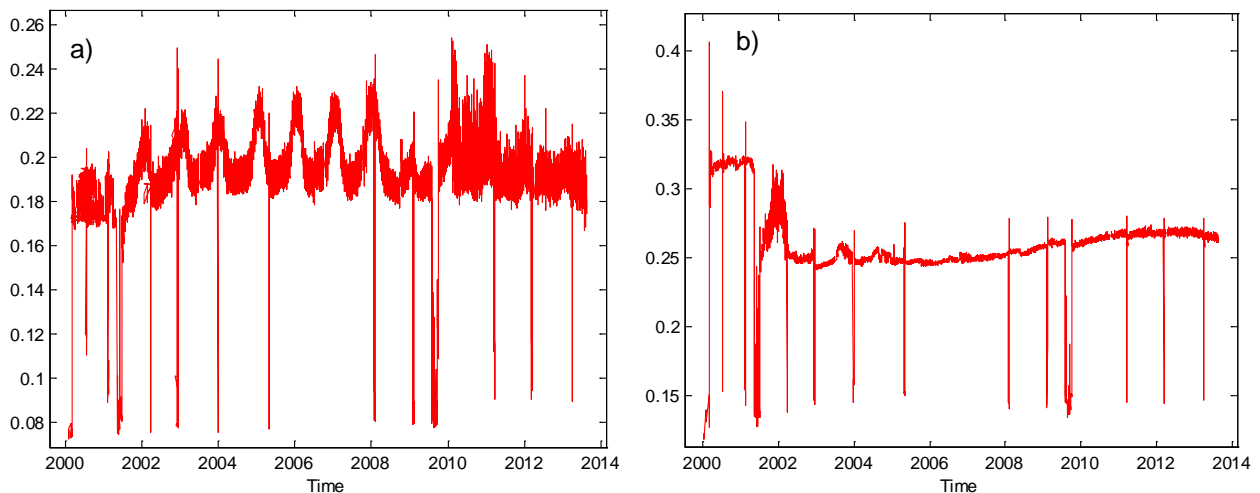


**Figure 12. Cooler Accelerometer Readings [ $N_{rms}$ ] a) Axial – Z axis, b) Lateral – X axis (Lateral Y-axis is very similar to X axis)**

Two further minor anomalies were recorded for the cooler system. On December 13, 2002 there appeared to be a transient transition to the 'door-bell' mode of the cooler (when the displacer B piston repeatedly strikes the end-stop of the body). The displacer being driven by the pressure wave was very near to full stroke and a small change in the amplitude resulted in this behavior. This could have been initiated by ambient temperature changes or small changes in fill pressure, etc. Telemetry was triggered by the displacer B amplitude which automatically turned off the coolers. The cooler was restarted after some testing and has continued to operate successfully.

A third cooler anomaly was similar to the previous one, having occurred on July 28, 2009. In this case, it was not possible to reactivate the cooler at the same unbalanced pre-anomaly setting (amplitude ratio of 82.5%). A slight modification was made to allow the cooler to continue to run with the B side compressor at 77.5% of normal amplitude; avoiding end-stop contacts (with ~0.5-mm margin) with the side B detectors heating at a slightly higher rate. The cooling rate on the working side (A) was unchanged. This mode of cooler operation induces a little more vibration but with a negligible impact on the spacecraft. Only the MISR instrument has reported a vibration induced effect and this was at a very low level.

Over the past 16 years, the Kistler AG piezoelectric accelerometers have recorded vibration outliers as short, high intensity signals, strongly correlated with the high energy radiation environment. Previously noted by Nichitiu [8], the accelerometers integrated into the cooler system have been demonstrated to provide a bonus measurement of space radiation. As a multi-component force transducer, the tri-axial accelerometers consist of a stack of quartz discs or plates and electrodes, with quartz discs cut in an appropriate axis. The orientation of the sensitive axes coincides with the axes of force components to be measured. An internal charge-to-voltage converter provides a low impedance output. During normal operation, there are short fluctuations (spikes lasting for only one telemetry sample), which appear as an increase in the level of vibration exceeding 4 sigma [8]. The sensor typically records a normal level within 8 seconds afterwards, the time between two consecutive telemetry samples. These spikes, or accelerator outliers, occur most often for the z-direction compressor vibrations. Outliers occur for other directions and for the displacer accelerometer, but their rate is very low.

The occurrence of the z-direction compressor transducer outliers is well described by a decreasing power-law as a function of magnitude. The spatial distribution of these observations is provided in Figure 13, showing accelerometer readings correlating significantly with the South Atlantic Anomaly (SAA) [8]. The high energy particles - the source of anomalous accelerometer signals - are localized mainly in the SAA region, while the polar regions, particularly the southern pole, are associated with a higher risk for satellites during intense solar proton events.

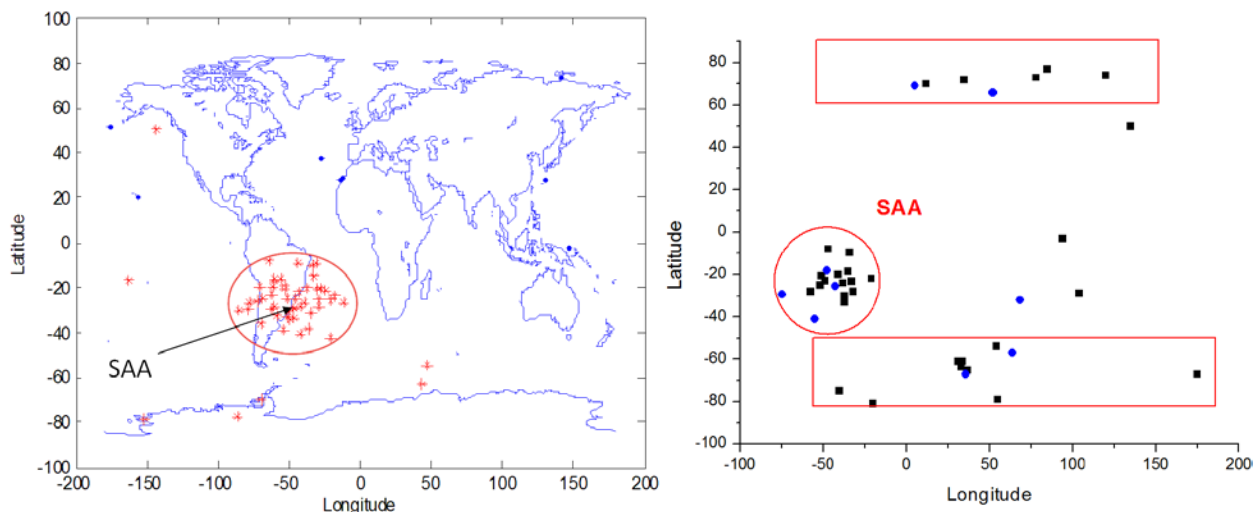


**Figure 13. Accelerometers Anomalies Due to Space Radiation (Incl. SAA)**

(a) Location during period of December 2014 to February 2015

(b) Locations of accelerator anomalies (4 day periods): Black = Cooler Off 2002/084, 2003/359, 4 days each; Blue= Cooler ON 2004/024 (indicated as year/day of year)

### **Lessons Learned & Conclusions**

The billions of rotations achieved for 7 rotating mechanisms demonstrates that the lubricant screening methods based on heritage with polyalphaolefin (PAO) oils were effectively transferred to the Nye 2001T oil. In the case of the LMC, there was a heightened concern for the presence of these additives, which exhibit much higher outgassing than the base oil. It was thought that the additive could provide benefits during the run-in process, so the screenings were all done similarly, but with the LMC bearing sub-assemblies baked prior to final installation in the housings. This approach did not appear to have any detrimental effects in terms of optics or lifetime for these units. Optical cleanliness continues to meet specification after 16 years in-orbit, where the gain of the system has remained very stable. Despite one cell having been gas-filled and the compensating cell being evacuated, there has been no significant difference between the paired rotors.

By current space mechanism standards, it may be viewed as fortunate that so much success has been achieved for such customized rotating mechanisms without pre-launch life testing. The schedule had precluded life testing at representative speeds, and accelerated life tests would have misrepresented the situation with an increased film thickness of lubricant. Without the desired life testing option, alternative measures were taken to increase the probability of long-life being achieved. The risk management strategy included:

- Sourcing the experience of Draper Laboratories involving design consultation, lubricant formulation, and implementing a screening process for the duplex bearings (resulting in as many as 5 iterations of run-in, cleaning and re-lubrication)
- TiC coatings implemented for scan mirror motor bearings
- Screening tests performed on the new lubricant formulation (Nye 2001T) for LMCs and choppers, which was a worthwhile quality measure. (4-ball tribometer screening test successfully identified a degraded batch of tricresyl phosphate additive prior to the new formulation being applied in the flight mechanisms, saving a great deal of cost, time and potential investigation efforts)
- Provision of power during launch, so as to run choppers and length modulators at 100 rpm during launch, as well as the associated drive system provisions to accommodate this mode

Films were observed during screening of LMC and chopper bearings, representing a suspected 'polymerization' of the lubricant running in or near the elastohydrodynamic regime [4]. It is believed that the TiC coating employed for the scan mirror motor bearings likely limited such phenomena, given that the overall travel of three of the scan motors is equivalent to  $>10^7$  rotations. The scan motors clearly operate in the boundary lubrication regime.

Significant achievements were made for both types of linear drive mechanisms, with both pressure modulated cells having performed flawlessly. A small leak in the PMC 2 system was managed using standard in-orbit calibration so as to have minimal science impact.

The cooler failure, which was abrupt in nature, may have been due to electronics, harness or the mechanism. Loss of science return was minimized for the cooler system failure case due to the partial redundancy of the optical channels of the instrument. The compressor from the impaired functional cooler has been used to compensate the vibration of the active cooler for the majority of the mission, with a high degree of success. Some adjustments in compressor settings were required to deal with minor drifts in the amplitude of the impaired (free-piston) displacer to avoid end-stop contact.

The launch configuration of the Stirling displacer without shorting (or active control), is thought to have incurred some residual risk despite having been tested at acceptance vibration levels. Where feasible, it is recommended to review such configurations closely and to ensure clamping by adequate shorting or active control to limit stroke variations during launch.

Decontamination heaters and the venting design have been vital to the ongoing reliable performance of the instrument, even after 16 years in orbit. It is emphasized that even with tight contamination controls, the system design must have adequate heater capacity to remove water vapor and other contaminants and adequate venting to ensure long life functionality. The venting design, material selection, and ground purging with dry gas were key to ensuring that the required frequency of decontamination cycles was not too high.

A capillary bonding method for sealing of germanium infra-red windows into the titanium housings showed the capability for use in a long duration mission, while the depressurization witnessed for two of the units may indicate that the related process controls could be improved.

Accelerometer anomalies continue to be caused by interaction of trapped particles from the sun with the neutral atmosphere. Other cooler applications with similar accelerometer arrangements should take note of the accelerometer phenomena cited herein for both the cooler control integrity and scientific value.

### **Acknowledgements**

The authors are grateful for the past contributions of the lead electrical designer, the late Dennis Henry, and the lead software engineer Ron Irvine, who helped ensure success of the MOPITT mechanisms via their dedication and expertise. Furthermore, many experts were consulted during the development and test phase of the mechanisms, including Casey de Kramer and Ed Devine (representing NASA), Richard Coco and Richard Walker (Draper Labs), Steve Gill and Rob Rowntree (ESTL), Guy Peskett (Oxford), Brian Jones (BAe), Ray von Savoye (Lockheed Martin), the late Derek Binge (Tecstar), George Bailak, Gurpreet Mand and Boyd Tolton (University of Toronto). The MOPITT instrument team is thankful for their guidance and sharing of expertise.

## References

1. Gille, J., Drummond, J.R., Edwards, D.P., Deeter, M.N., Masters, N.S., Emmons, L.K., Pfister, G., Yudin, V.A. "What 10 Years of MOPITT Data Have Taught Us About Tropospheric Chemistry", American Geophysical Union, 2009 Fall Meeting, abstract #U32A-03
2. Drummond, J.R., Zou, J., Nichitiu, F., Kar, J., Deschambault, R., Hackett, J. "A review of 9-year performance and operation of the MOPITT instrument", J. Adv. Space Res. (2010), doi:10.1016/j.asr.2009.11.019
3. Caldwell, D., Hackett, J., Gibson, A.S., Drummond, J.R., Nichitiu, F. "The design and flight performance of the MOPITT instrument mechanisms", Proceedings of 11th European Space Mechanism & Tribology Symposium, (2005), Proceedings 591: 99-106
4. Gibson, A.S., Hackett, J., Bailak, G. "Design of a Length Modulated Cell for Remote Sounding of Greenhouse Gases", NASA 33<sup>rd</sup> AMS, CP-1999-209259, (May 1999), pp309-324
5. Taylor, F.W., "Forty years of satellite meteorology at Oxford", Quarterly Journal of the Royal Meteorological Soc., Vol137 Pt B, Issue 655, pp277–285 (January 2011)
6. Venters, P. "The Pressure Modulation System in the Improved Stratospheric and Mesospheric Sounder", D.Phil.Thesis, University of Oxford (1991)
7. Gibson, A.S., Reed, J., Bradshaw, T.W.; Linder, M. "Heritage Overview: 20 Years of Commercial Production of Cryocoolers for Space", Transactions of the Cryogenic Engineering Conference - CEC, Vol. 52. AIP Conference Proceedings, (2008) Volume 985, pp. 493-505
8. Nichitiu, F., Drummond, J.R., Zou, J., Deschambault, R. "Solar particle events seen by the MOPITT instrument", Journal of Atmospheric and Solar-Terrestrial Physics 66 (2004) pp 1797–1803
9. Mand, G.S., Drummond, J.R., Henry, D., Hackett, J. "MOPITT On-Orbit Stirling Cycle Cooler Performance", Cryocoolers 11, Kluwer Academic/Plenum, New York (2001)
10. NASA-Terra Status as per webpage report, [http://terra.nasa.gov/wp-content/uploads/2014/03/ESMO\\_TerraWebStatus\\_June2014.pdf](http://terra.nasa.gov/wp-content/uploads/2014/03/ESMO_TerraWebStatus_June2014.pdf)
11. MOPITT On-Orbit Cooler Anomaly Interim Report, COM DEV RPT/MOP/50008/001-P0, 23-Jul-2001





# Electrical Noise Performance of Gold-on-Gold Slip Rings

Ron Hayes\*, Erik Mumm\* and Kyle Gotthelf\*

## Abstract

During development of a new slip ring design, our panel of subject matter experts was unable to find examples of how slip rings perform at very low current levels. This paper discusses the performance of Gold-on-Gold Slip Rings for micro-amp scale signals. We offer a concise overview of slip ring technologies and common applications and discuss the challenges associated with low current transfers in slip rings. We discuss the testing that Honeybee Robotics has completed, including a description of the test hardware, the test conditions (electrical signals, rotation rate, and lubrication scheme) and the resulting performance under flight-like conditions.

## Introduction

Slip rings are devices that make use of sliding electrical contacts to transmit power and signals across a rotating interface. In spacecraft mechanism applications these are commonly used in Solar Array Drive Assemblies, Bearing and Power Transfer Assemblies, and other applications requiring continuous rotation. These devices consist of a rotor (or slip rings) and brushes. Common material combinations used for slip ring assemblies (SRAs) are silver-alloy rings with self-lubricating sintered silver brushes, gold alloy plated rings with monofilament gold alloy brushes, and gold alloy plated rings with gold alloy fiber brushes. Of these basic types, perhaps the most common employed in flight applications over the last few decades has been the gold alloy rings with monofilament gold brushes, commonly referred to simply as “gold-on-gold”.

These gold-on-gold systems are most typically wet lubricated with either Brayco or Pennzane®-based oils depending on the temperature requirements. Of these lubricant types Pennzane® is the more common choice. Several formulations of Pennzane® (formulated and sold by Wm. F. Nye of New Bedford, MA) have been used successfully in flight SRA applications. These formulations include NYE 2001A (“neat Pennzane®”, i.e., without additives), NYE 2001 (with anti-wear and anti-oxidant additives), and NYE 2001-XPbNp (with anti-wear, antioxidant, and lead naphthenate additives, where the X is the mass percent of the latter, typically around 3% which is used in this testing).

Noise, or variations in the contact resistance between the rotating ring and the stationary brush as a function of rotation is an unavoidable characteristic of all slip ring designs. The number of brushes is usually chosen for current-carrying ability. Typically low-current circuits are designed to have only a few brushes in order to minimize the overall size, mass, and parasitic torque of a given SRA. This approach is contrary to reducing noise in those circuits because the more contacts a given circuit possesses, the lower the effective noise becomes as there are more parallel current paths involved. This limited contact scheme is by far the most common approach for signal-level circuits. While the parallel contact approach can reduce noise on a typical circuit; for circuits carrying very low currents this may be counter-productive. Since a substantial contribution to the electrical contact at the sliding interface is due to quantum mechanical tunneling (with the primary path being metal to metal contact) the voltage drop at the contact interface plays a role in contact quality and noise [6] (Holm). With high enough voltage, insulating films at the interface can be broken down or tunneled through. For very low current signals, such as those investigated as part of this study, the question arises: does sufficient voltage drop exist at the contact for these mechanisms to contribute to conduction? This was addressed in this study.

---

\* Honeybee Robotics Spacecraft Mechanisms Corporation, Longmont, CO

Noise characterization is an important test for any slip ring, as it can be the best indicator of the health of the contact system. For circuits carrying power, those that are heavily averaged, and other robust signals are generally insensitive to noise on the slip ring. However, some signals can be very sensitive. Stick-slip behavior is evident in torque traces which results in noise peaks associated with these events (as shown in Figure 2 for a typical slip ring assembly). The noise spikes in this figure correspond to the leading brush sliding forward on the ring while the trailing brush remains in contact; the leading brush is momentarily open for this brief period of time. Low current analog signal circuits, for example, pose a particular challenge. Other researchers have proposed slip ring noise has contributed to anomalous encoder readings and resulted in control problems on orbit [1] (Koss and Woolaway). Though the Windsat SRA discussed by Koss and Woolaway was of a unique configuration in terms of the materials used, rotational speed, and total number of revolutions (life), their findings warrant further investigation into the integrity of low-current signals on slip rings.

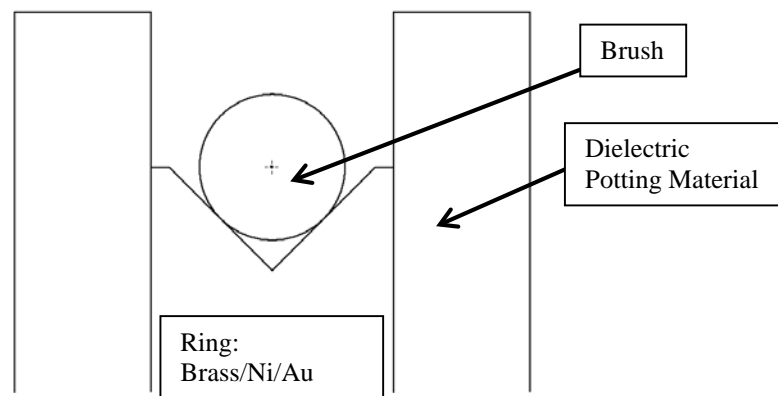


**Figure 1. Cross-section of brush ring interface.**

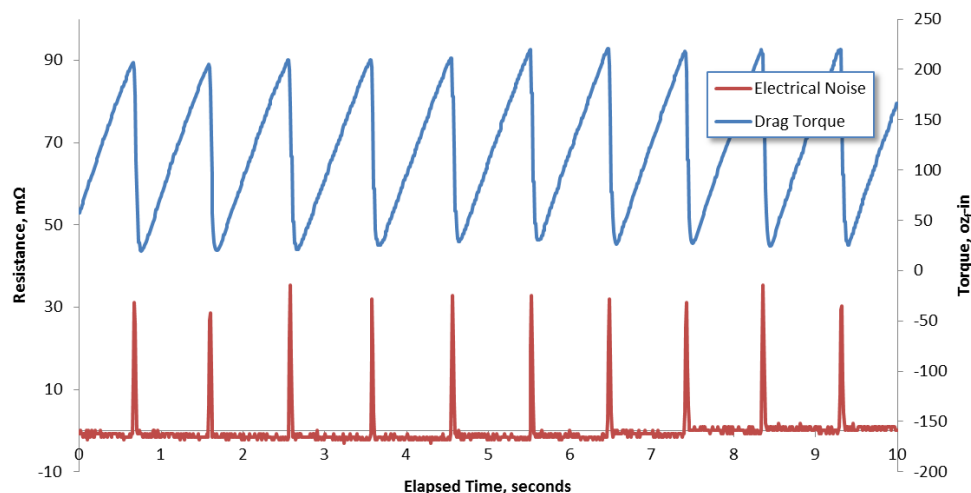


**Figure 2. Typical signal (2-brush) gold-on-gold slip ring resistance and drag torque as a function of time. The behavior seen here is common at low rotation rates where stick-slip behavior is prevalent. At higher speeds, those commonly used for noise testing, stick-slip is virtually non-existent. Brush design, lubricant selection and drive configuration can drastically affect this behavior. One of the products of this study will be noise level comparisons over a range of rotation rates.**

## Experiment Design

To characterize performance of a gold-on-gold slip ring we designed and fabricated a two-channel slip ring assembly using flight-like materials and processes. This SRA makes use of brass rings, cut with a 90-degree v-groove (Figure 1) then nickel and hard-gold plated. The rings are integrated onto an insulating shaft and mounted to an aluminum housing on a pair of preloaded radial contact bearings. The brushes are Neyoro 28A, a Au-Ag-Ni alloy commonly used in space flight slip ring applications [5] (Pitney). The brushes are monofilament (homogeneous). They are mounted on a PWB brush block which is then assembled to the housing. The brushes are adjusted for appropriate contact force with the rings and aligned with the center of the v-groove.

The 2-channel SRA was lubricated with NYE 2001A and run-in in both directions under laboratory conditions. After cleaning and inspection the SRA was re-lubricated with NYE 2001A and tested in air and under vacuum conditions with the signals and speeds outlined in Table 3. Cleaning was performed using a hexane rinse with the brush block and brush in-place so as not to disturb the contact system alignment. After cleaning the unit was re-lubricated with NYE 2001 in the same quantities as before and the tests re-run. In a similar manner the rings are cleaned and re-lubed for NYE 2001-3PbNp and tested.

The results presented herein will summarize the effect of rotational rate and lubricant selection on slip ring resistance and noise as a function of rotation rate.

## Experiment Configuration

Testing was conducted on a two-channel slip ring. The slip ring itself was procured per a source control drawing from Electro-Miniatures Corporation of Moonachie, NJ. The slip ring was machined from brass tube with 90-degree v-grooves which were nickel then hard gold plated per the vendor's standard processes. Brushes were procured from the same source and were produced by Deringer Ney of Vernon Hills, IL.

**Table 1. Ring and brush details.**

	<i><b>Material/Dimension</b></i>	<i><b>Specification/Units</b></i>
Ring Substrate	Red Brass	ASTM B36
Ring Diffusion Barrier	Electrolytic Nickle	Technic WS
Ring Wear Surface	Hard Gold	MIL-G-45204 Type I, II
Ring Pitch Diameter	70.61±0.051 (2.780±0.002)	mm (inches)
Ring V-Groove Angle	90	Degrees
Brush Material	Neyoro 28A	ASTM B477
Brush Composition	Au/Ag/Ni	75%/22%/3% by weight
Brush Format	Circular Cross-Section, Monofilament	
Brush Diameter	0.406 (0.016)	mm (inches)
Brush Force	6.0 gram-force	nominal

Testing was done in a thermal vacuum chamber under ambient temperature conditions (20-24°C) at  $10^{-4}$  to  $10^{-5}$  torr pressure. The Unit Under Test (UUT) was driven from outside the thermal vacuum chamber through a ferrofluidic feedthrough by a 1.8-degree commercial hybrid stepper motor using 256:1 microstepping and a 100:1 planetary gearhead. This yields a step size at the slip ring of 1.23  $\mu$ rad. The test slip ring in the chamber is shown in Figure 3.

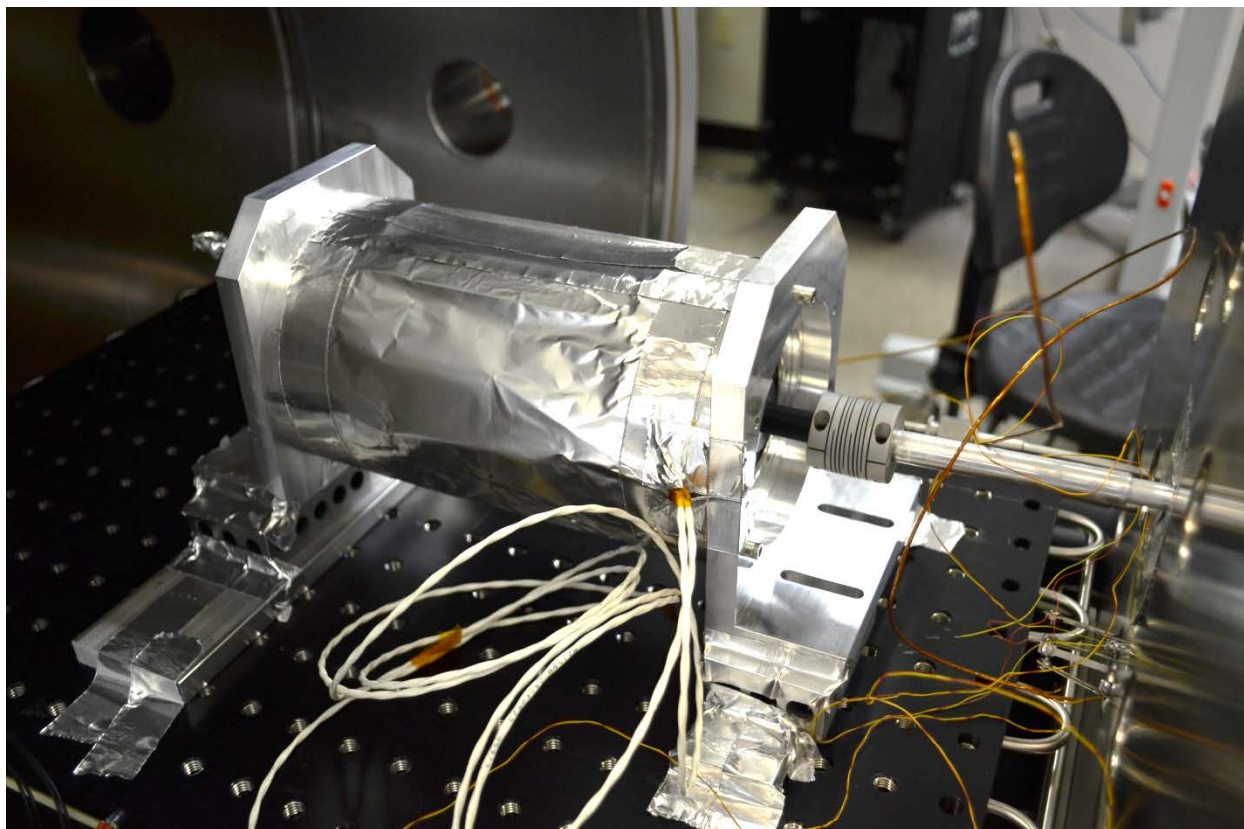


**Figure 3. UUT in chamber before door closure. Slip ring assembly is shielded using aluminum foil and aluminum tape. Drive shaft exits to the right of the photo to chamber feed through.**

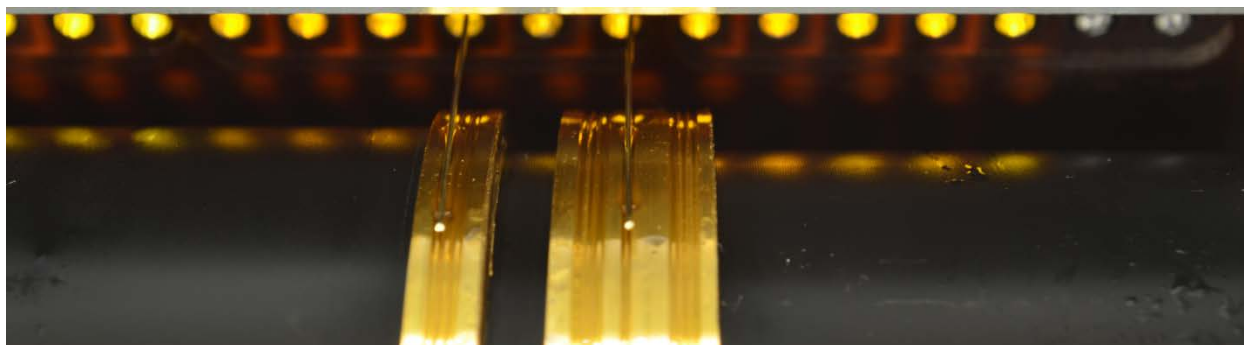


**Figure 4. Slip ring brushes in v-grooves. Heavier than typical lubricant application is present in this photo taken during run-in.**

### **Procedure**

The slip ring was assembled and the brush blocks aligned with corresponding rings. Figure 4 shows the brushes in the slip rings used in this test.

The rings were lubricated with neat Pennzane® (NYE 2001A) and run-in under standard laboratory conditions (atmospheric pressure and room temperature) for 2000 revolutions minimum in each direction. After run-in the system was tested under lab conditions to verify performance and ensure test protocols were appropriate. Lubricant quantity was judged visually by evaluating the meniscus at the brush/ring interface. Material and configuration information for the slip ring is given in Table 1.

Power was applied to the slip rings using a battery and voltage splitter arrangement. Figure 5 shows the electrical schematic for this setup. A series of resistors was used to set the current applied to the slip ring pair. This battery arrangement was used because commercial power supplies proved to be too noisy for these tests as the noise levels resulted in unacceptable signal-to-noise ratio.

Using the battery pack approach we were able to effectively eliminate power supply noise and deal primarily with environmental and A/D noise in the DAQ. Our background noise level was on the order of  $80\text{--}100\text{ }\mu\text{V}_{\text{pk-pk}}$ . This background noise level dictates the peak-to-peak noise that can be resolved in the test and therefore our effective signal-to-noise ratio.

Typical noise levels in this type of slip ring are on the order of tens of milliohms per circuit, meaning that for a circuit pair in series that value is multiplied by  $\sqrt{2}$ . Therefore, we expected approximately 30 milliohms of noise. Table 2 shows the voltage level of the expected noise as a function of applied current via resistor value in the power supply circuit (Figure 5).

**Table 2. Power supply and slip ring test electrical parameters, including environmental (background) noise levels and calculated signal to noise (S/N) ratios and resolvable noise levels.**

Resistor Value	Battery Voltage	Sense Resistor	Nominal UUT Resistance	Actual Current	Nominal Current	Background Noise Level	Slip Ring Pair Resistance	Noise Spec Limit	SR Voltage Drop	S/N Ratio	Unfiltered Resolvable Noise
100 $\Omega$	12.3V	10 $\Omega$	0.35 $\Omega$	110mA	100mA	100 $\mu\text{V}$	131m $\Omega$	30m $\Omega$	14.6mV	146	900 $\mu\Omega$
1k $\Omega$	12.3V	10 $\Omega$	0.35 $\Omega$	12mA	10mA	100 $\mu\text{V}$	131m $\Omega$	30m $\Omega$	1.6mV	15.9	8m $\Omega$
10k $\Omega$	12.3V	100 $\Omega$	0.35 $\Omega$	1.2mA	1mA	100 $\mu\text{V}$	131m $\Omega$	30m $\Omega$	160 $\mu\text{V}$	1.6	82m $\Omega$
100k $\Omega$	12.3V	100 $\Omega$	0.35 $\Omega$	120 $\mu\text{A}$	100 $\mu\text{A}$	100 $\mu\text{V}$	131m $\Omega$	30m $\Omega$	16 $\mu\text{V}$	0.16	0.88 $\Omega$
1M $\Omega$	12.3V	100 $\Omega$	0.35 $\Omega$	12 $\mu\text{A}$	10 $\mu\text{A}$	100 $\mu\text{V}$	131m $\Omega$	30m $\Omega$	1.6 $\mu\text{V}$	0.016	8 $\Omega$

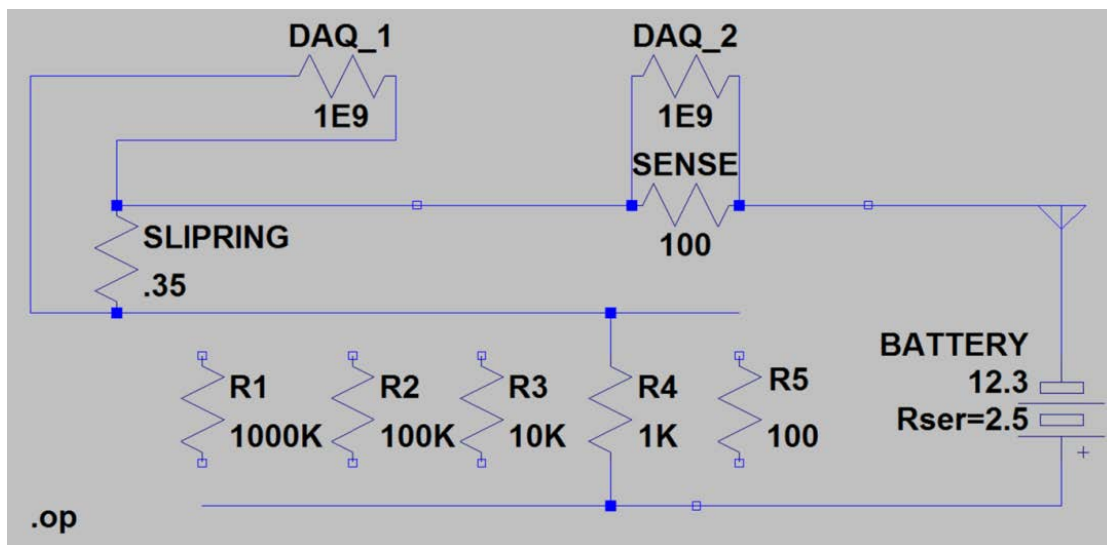


**Figure 5. Power supply circuit used to control current to the slip rings under test.**

Current was measured and recorded continuously by measuring the voltage drop across a high-power resistor for each measurement. In this way, the current across the slip rings was directly measured, variations of which was accounted for in our resistance measurements. Two sense resistors were used depending on the current applied and tailored to the test case. A 10- $\Omega$  resistor was used for high current cases (120 mA and 12 mA) and a 100- $\Omega$  resistor was used for all other cases. In this paper, we will refer to these current levels by their nominal values (e.g., 100 mA instead of 110 mA) for convenience and

simplicity. Our DAQ was set up with two A/D channels, one for the voltage drop across the slip ring and one for the sense resistor. Resistance was calculated in real time for each test as opposed to a nominal current used and voltage being recorded. A sample resistance data set is given in Figure 11. Data were acquired at 100 kHz on both channels, a 100-Hz second-order low-pass filter was used on the current channel while the noise channel was recorded at 100 kHz broken into three levels, each defined by a second order low pass digital filter. One was set at 10 kHz, another at 1 kHz and the last at 100 Hz. Filtering the raw noise data was also beneficial in reducing the resolvable noise and effectively increasing the signal-to-noise ratio, allowing us to decrease the resolvable noise levels from approximately 8  $\Omega$  for the unfiltered signal to approximately 1.25  $\Omega$  using the 1-kHz filter.

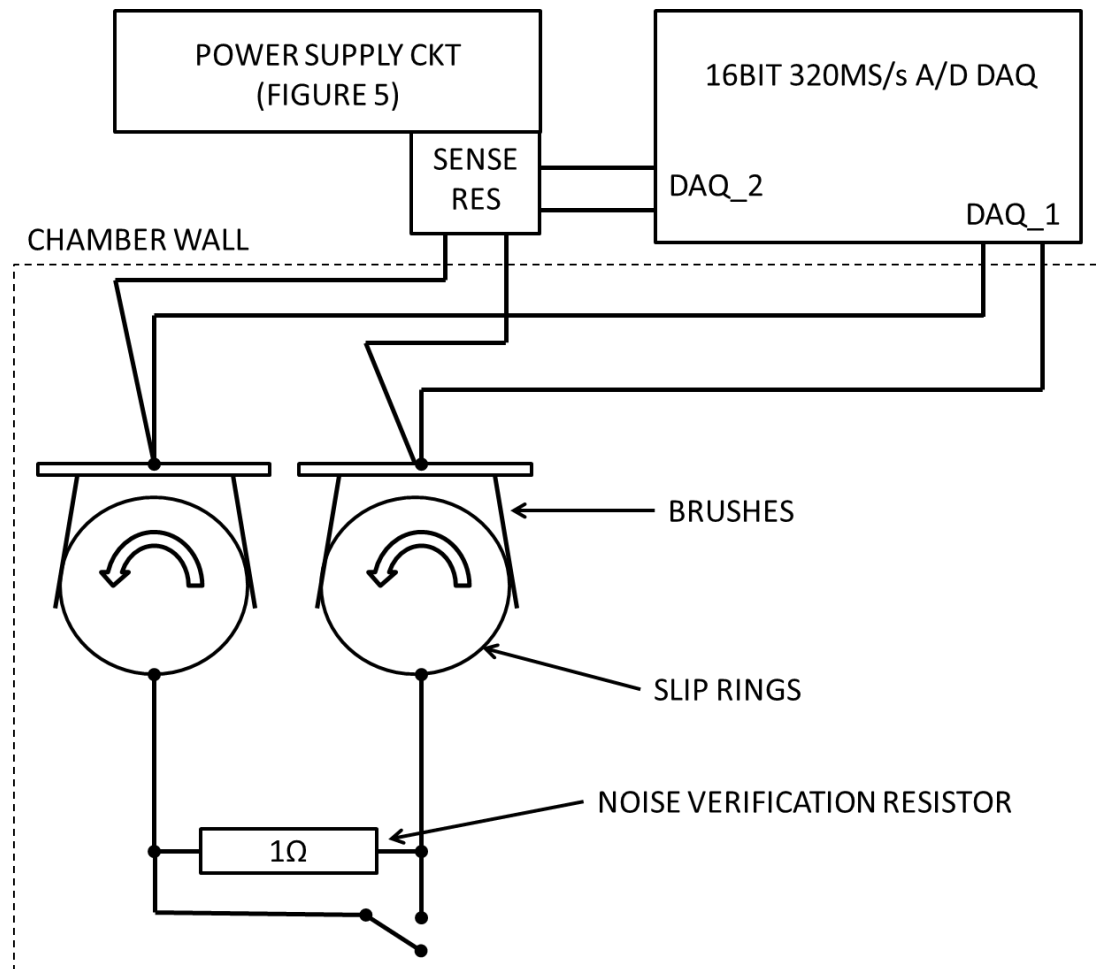


**Figure 6. Schematic representation of test setup. Switch at resistor is normally closed, it is only open for transient detection tests described herein.**



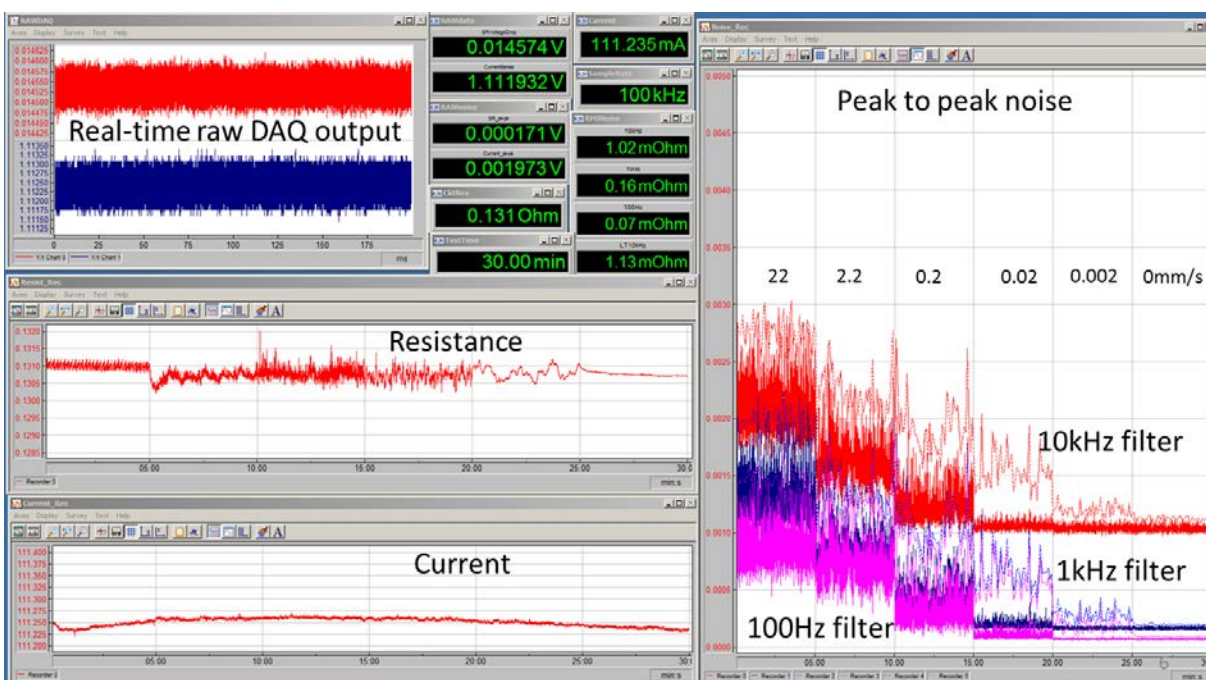


**Figure 7. Annotated sample of DAQ test interface showing ongoing test.**

Because the background noise levels in our production environment and test setup could not be reduced below approximately 100  $\mu\text{V}$ , we were unable to measure true slip ring contact noise directly at current levels below around 1 mA. Although our threshold noise levels effectively raise our measurement noise floor and reduce our signal to noise ratio, we can still resolve noise events of a certain magnitude. Filtering the raw noise data helps to improve our signal-to-noise ratio and allows us to easily see a 1-ohm change in the slip ring resistance as witnessed by our test for sensitivity on the UUT in-situ at ambient pressure. To do this, we connected a 1-ohm resistor as shown in Figure 8 and ran our data acquisition program to collect resistance and noise data (Figure 9) while our lowest ( $\sim 10 \mu\text{A}$ ) current level was applied. The resistor was attached as shown in Figure 8; connections were sprung against one another so that short duration transitions in resistance could be induced. The oscilloscope trace in Figure 8 captures one of these transitions at 32  $\mu\text{s}$ . The screen shot in Figure 9 shows the impact of this test on the captured data. Despite the short duration of the resistance transition induced by the test, all filtered groups recorded the event; also of note is that the resistance trace also recorded the corresponding increase in measured circuit resistance. This gives confidence that transient open circuit events are captured in the test data for very low current levels.

## Results

### Lubricant and Rotation Rate Trials

Our results indicate that in our ambient temperature, high vacuum test environment the NYE 2001A and 2001 lubricant formulations behaved similarly at all tested rotation rates, with the formulated version (2001) providing slightly better performance across most rates and currents (see Figure 10 for a subset of these results). Neither of these lubricants exhibited measureable performance differences between operation in air at standard pressure and hard vacuum.

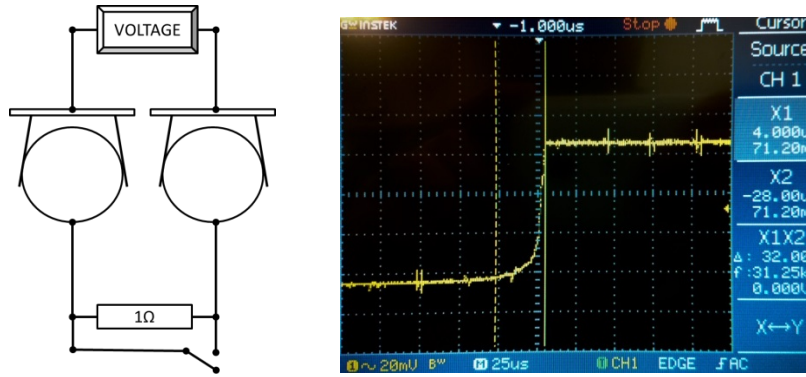


**Figure 8. Oscilloscope trace from noise sensitivity test using 1Ω resistor (schematic on left)**

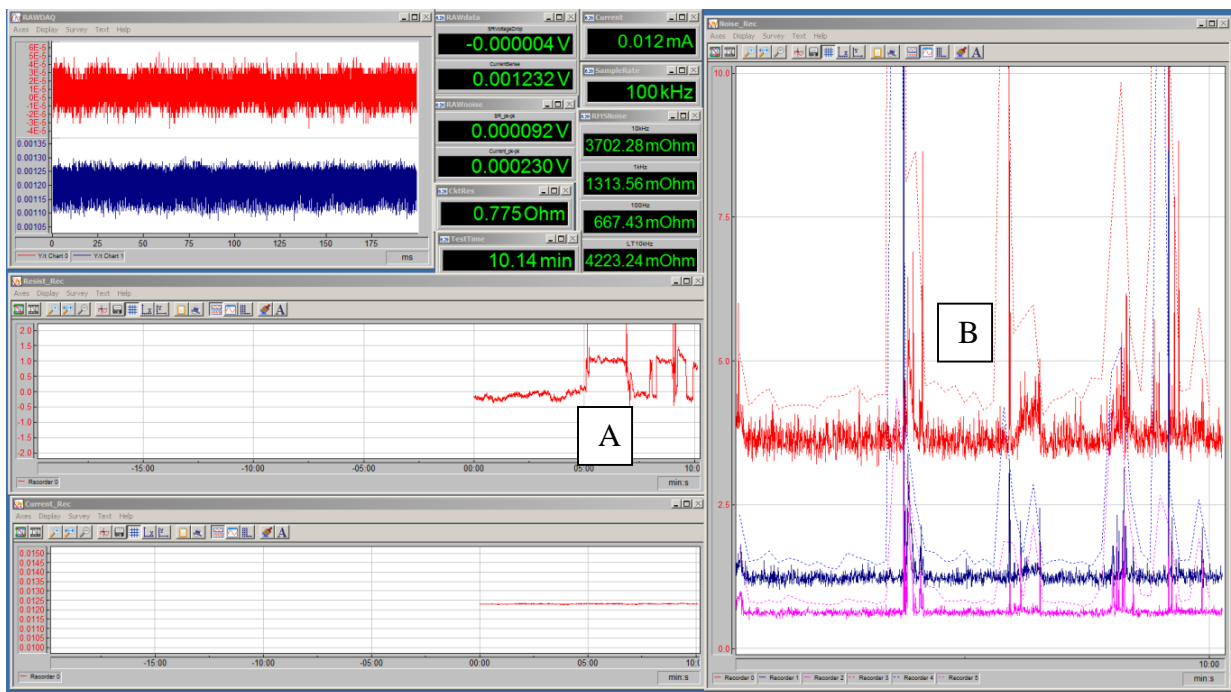


**Figure 9. Test interface screen capture of resistor sensitivity test. Baseline shift in resistance is evident at (A), and peaks associated with transitions in (B) with all variously filtered noise traces responding. In the resistance trace (A) the baseline resistance shift is 1 ohm, in the noise trace (B) the peaks are several ohms.**

### Current Level Effects

We found no effect of current on noise in our testing. At the low current levels tested here, it was not possible to fully characterize noise at our mid and low range currents. We did show that we were able to resolve noise levels over threshold levels that are a function of the applied current itself (Table 3). We did not find any instance of noise levels above these thresholds for any lubricant, environment, or rotational speed tested. While we do see an apparent increase in noise levels for lower currents, as in, we cannot confirm these are real as the background noise levels are of the same magnitude as the measured noise.

### Role of Environment Pressure

While the neat oil (2001A) and formulated oil (2001) results did not indicate differences between operation in air and vacuum, the 2001-3PbNp formulation did. Figure 12 is a graph of the extended 1-kHz filtered noise measurement for the UUT in both air and vacuum with 100-mA DC current applied. We found that the lead naphthenate produced higher noise levels in vacuum at our highest speed levels but performed better than the other formulations at lower speeds (Figure 13). The cause of these differences in noise performance is not investigated as part of this study.

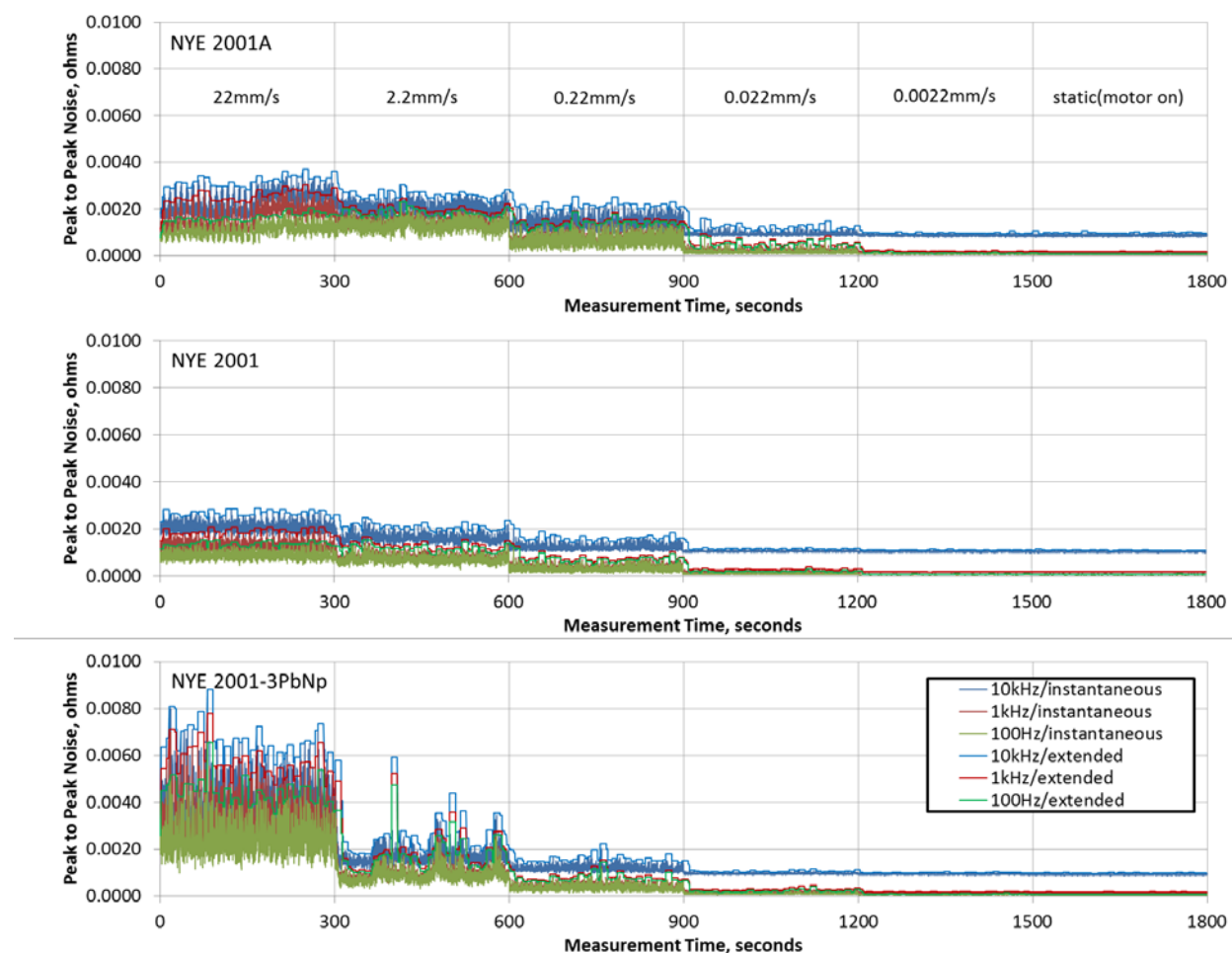


**Figure 10. Peak-to-peak noise as a function of time for various surface speeds (rotation rates) and ring lubricant. These graphs show the instantaneous peak to peak noise (over 0.2 s, solid lines) and the extended peak to peak noise (over 10 s, bars). Data are presented filtered using a low pass 10-kHz filter, 1-kHz filter, and 100-Hz filter.**

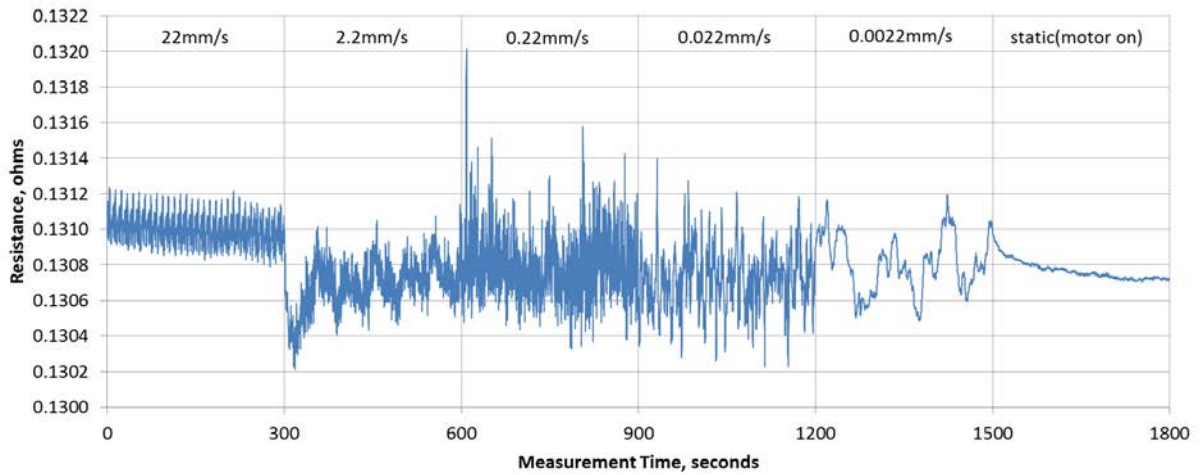


**Figure 11. Slip ring resistance history corresponding to NYE 2001 100-mA test. This is the primary measurement from which noise performance is derived.**

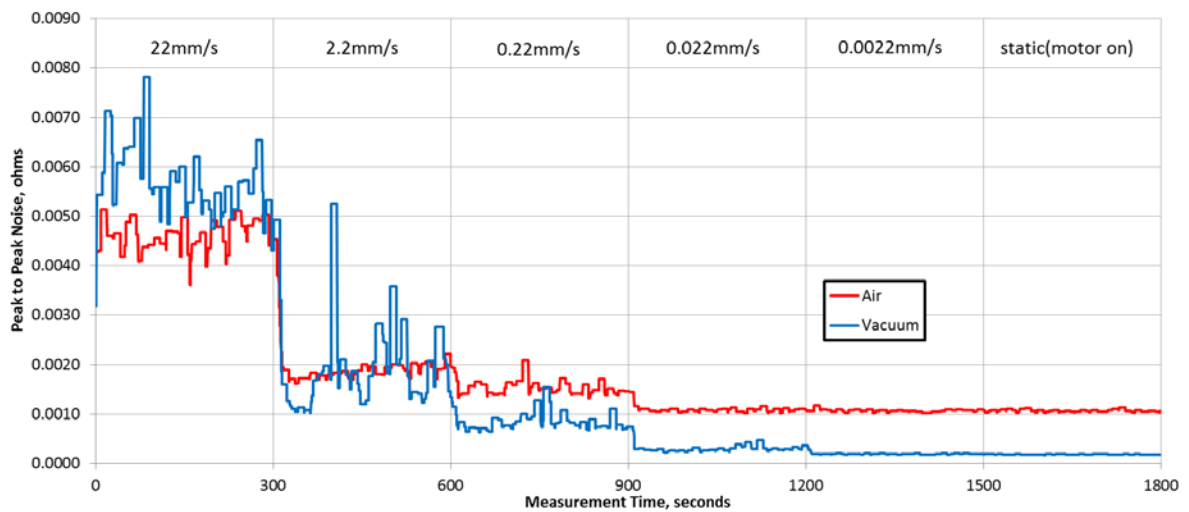


**Figure 12. Extended (10 second) noise results at tested surface speeds with 100 mA applied for 2001-3PbNp in air and in hard vacuum filtered using 1-kHz low-pass digital filter.**

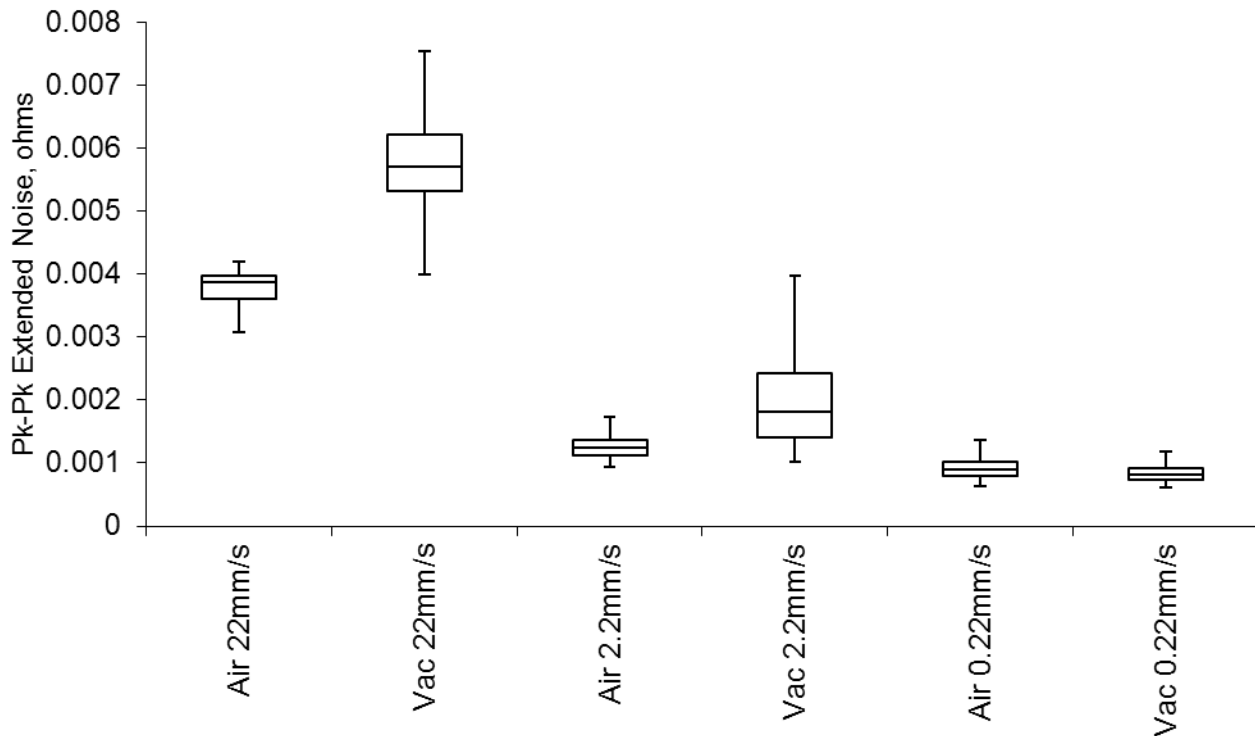


**Figure 13. Box and whisker plot of air and vacuum extended noise results for NYE 2001-3PbNp 100-mA tests at 22, 2.2, and 0.22 mm/s. In the 22 and 2.2-mm/s cases the vacuum noise was higher than the noise in air, in the 0.22-mm/s case the opposite is true, the vacuum result has lower noise than the air result. All statistical tests to a 95% confidence level via analysis using Student's t-test.**

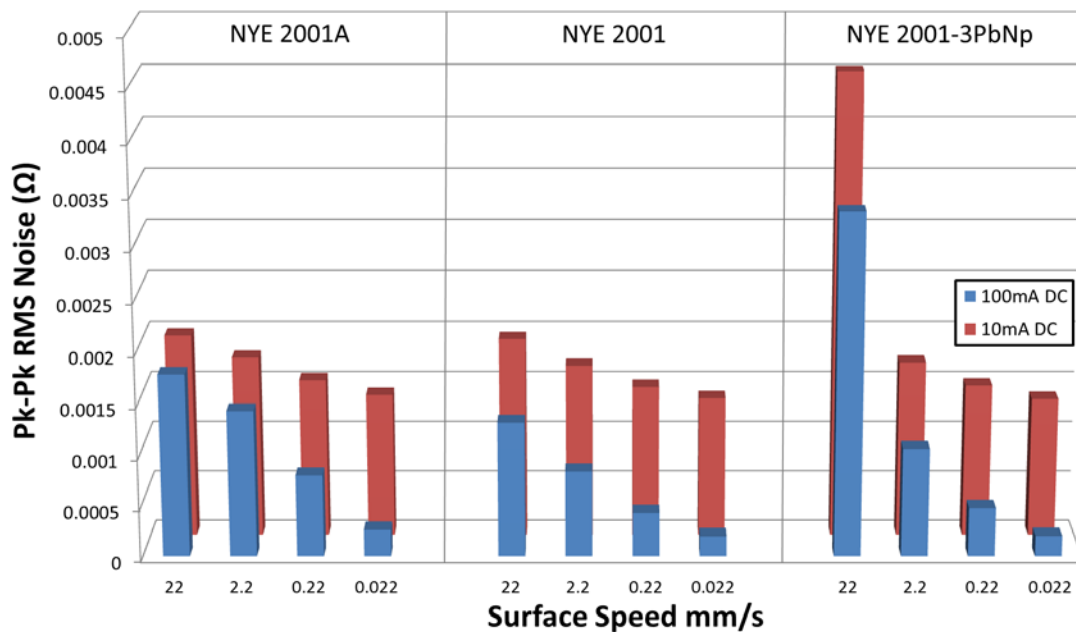


**Figure 14. Peak-to-peak RMS noise through 1-kHz low pass filter for both 100 mA and 10 mA**

**Table 3. Peak to peak RMS noise result for each lubricant/current/rate configuration. It should be noted that at current levels below approximately 1-mA background (environmental) noise dominates the slip ring noise signal. The values presented in this table for the lower currents tested are below the unfiltered threshold noise levels in Table 2, this was achievable by incorporating low pass filters, in the case of the results in this table the filter used was 1 kHz.**

Lube Formulation	Nominal Current	Measured Slip Ring RMS noise (1kHz low pass filter)			
		Rot.Rate (mrad/s)/rpm/Surf.Speed (mm/s)			
		630/6.0/22	63/0.6/2.2	6.3/0.06/0.22	0.63/0.006/0.022
NYE 2001A	100mA DC	0.00178	0.00143	0.00080	0.00026
NYE 2001A	10mA DC	0.00198	0.00176	0.00154	0.00139
NYE 2001A	1mA DC	0.0127	0.0127	0.0126	0.0126
NYE 2001A	100µA DC	<u>0.120</u>	<u>0.122</u>	<u>0.123</u>	<u>0.120</u>
NYE 2001A	10µA DC	<u>1.25</u>	<u>1.29</u>	<u>1.28</u>	<u>1.26</u>
NYE 2001	100mA DC	0.00131	0.00084	0.00043	0.00020
NYE 2001	10mA DC	0.00195	0.00168	0.00147	0.00136
NYE 2001	1mA DC	0.0122	0.0124	0.0123	0.0122
NYE 2001	100µA DC	<u>0.118</u>	<u>0.120</u>	<u>0.119</u>	<u>0.118</u>
NYE 2001	10µA DC	<u>1.22</u>	<u>1.24</u>	<u>1.24</u>	<u>1.23</u>
NYE 2001-3PbNp	100mA DC	0.00334	0.00106	0.00048	0.00020
NYE 2001-3PbNp	10mA DC	0.00453	0.00171	0.00149	0.00136
NYE 2001-3PbNp	1mA DC	0.0132	0.0124	0.0123	0.0122
NYE 2001-3PbNp	100µA DC	<u>0.119</u>	<u>0.119</u>	<u>0.119</u>	<u>0.119</u>
NYE 2001-3PbNp	10µA DC	<u>1.24</u>	<u>1.25</u>	<u>1.25</u>	<u>1.24</u>

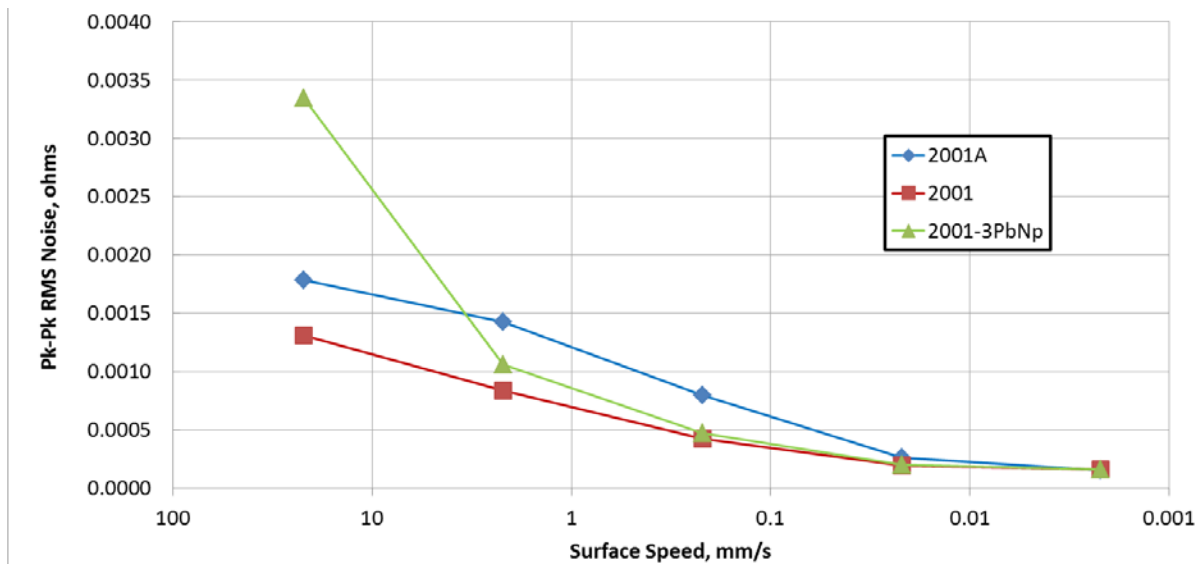


**Figure 15. Peak-to-peak RMS noise (from Table 3) for the three lubes studied. Noise was measured in hard vacuum with 100-mA nominal current applied.**

## Conclusions

We found that of the three lubricant formulations tested, NYE 2001 performed the best in terms of noise. NYE 2001A (neat Pennzane) was a close second at our highest surface speed (22 mm/s), while the formulation of 2001 containing lead naphthalate was the worst in terms of noise at that speed. At our intermediate surface speeds, the 2001-3PbNp was better or the same as 2001A and at our slowest test speeds it was nearly identical (Figure 15). We also found that while 2001A and 2001 noise performance did not change to a measureable degree between ambient conditions and hard vacuum, the 3PbNp formulation did, with noise increasing in vacuum by a small but significant amount at our higher two test speeds (Figure 12) but better at speeds 0.22 mm/s and lower.

No measurable slip ring noise was found at currents less than 1 mA for any configuration tested. Put another way, RMS 1-kHz low-pass slip ring noise was less than 0.125 ohm at 100- $\mu$ A levels and less than 1.3 ohms at 10- $\mu$ A levels.

All tests conducted in this study followed the trend of noise levels reducing with decreasing surface speed (rotation rate). In most cases tested the peak-to-peak noise levels at our lowest surface speed (0.0022 mm/s) were indistinguishable from a static slip ring.

## References

1. Koss, Steve and Woolaway, Scott, "Lessons Learned From the Windsat BAPTA Design and On-Orbit Anomalies", 38<sup>th</sup> Aerospace Mechanisms Symposium, (2006), pp 209-222.
2. Courtois, C., Miller, M. et al. "Advanced Slip Ring Solutions (ASR)", 14<sup>th</sup> European Space Mechanisms & Tribology Symposium – ESMATS, (2011), pp. 313-317.
3. Mondier, J.B., Sirou, F., and Mäusli, P.A., "Life Test of the Scarab Instrument Slipring Units", 9<sup>th</sup> European Space Mechanisms & Tribology Symposium – ESMATS, (2001), pp. 99-106.
4. Feusier, G., Mäusli, P.A., and Gass, V., "Improved Characteristics of Slipring Assemblies Making use of Gold on Gold Metallic Contacts", 10<sup>th</sup> European Space Mechanisms & Tribology Symposium – ESMATS, (2003), pp. 169-175.
5. Pitney, Kenneth E., Ney Contact Manual: Electrical Contacts for Low Energy Uses, J.M. Ney Company, 1973.
6. Holm, Ragnar, Electric Contacts: Theory and Applications, Springer, Berlin, 3<sup>rd</sup> printing, 2000.





# Slip Ring Electrical Anomalies Found After Protoflight Vibration Testing

Troy Nilson\*, Scott Christiansen\* and Chad Hebert\*

## Abstract

Following protoflight component testing of a Solar Array Drive Assembly (SADA), post-test electrical measurements revealed shorted circuits caused by slip ring brush displacement. Initial investigation, disassembly and analysis suggested the root cause was related to insufficient preload in an axial bias spring constraining the slip ring rotor. Successful rework and re-test supported this conclusion. However, later tests of similar hardware for a subsequent program resulted in a comparable electrical anomaly. Original investigation results were reviewed and found to still be valid. However, additional contributing factors were identified that led to the reoccurrence of the anomaly. This paper explores the discovery, investigation, analytical approach, and ultimate resolution of a SADA slip ring anomaly.

## Introduction

Over the past ten years, Sierra Nevada Corporation's (SNC) Space Systems group has designed, built and successfully flown a highly reliable and robust SADA (Figure 1) capable of transferring several kilowatts across a structurally integrated rotating interface connecting large solar arrays to spacecraft.

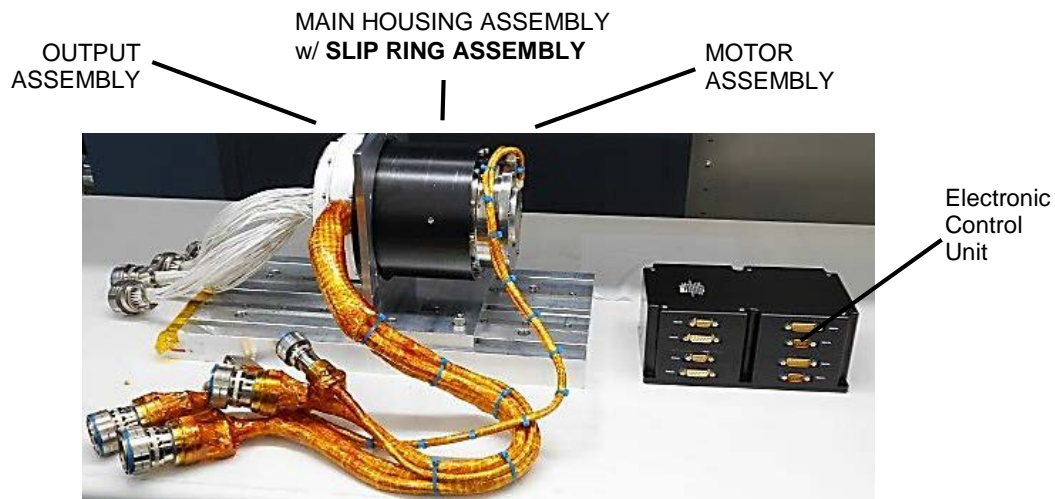


**Figure 1. SADA System w/ Electronic Control Unit**

Commonly experienced with high-reliability, low-volume production, the path to accomplishing this success has been achieved through desire for quality and focused efforts while working through design and test challenges. These challenges guided SNC through a series of events that allowed the engineering team to develop a highly refined SADA design and design process that optimizes the use of analysis tools such as high-fidelity Finite Element Modeling (FEM) to ensure design success. This paper explores the discovery, investigation, analytical approach and ultimate resolution of a SADA slip ring anomaly.

---

\* Sierra Nevada Corporation, Louisville, CO

## Environments and Hardware Description

To help understand the nature and subtle nuances of the SADA slip ring anomaly, it is necessary to understand required operational and test environments as well as discuss the various SADA subcomponents and related design goals. SNC was contracted to develop an electromechanical rotary device (and related Electronic Control Unit) designed to structurally support and rotate a greater than 20 kg-m<sup>2</sup> inertia payload (i.e., large solar array panel). The design was required to survive a 7-year mission in a high-vacuum space environment with thermal extremes ranging from -30°C to +70°C. Of particular interest to this discussion, the SADA was also required to withstand structural loading associated with random vibration testing and endure a thermal vacuum life cycle test of more than eighty thousand rotational cycles without slip ring electrical degradation or other electromechanical failure. Examples of the test setup, configuration, and levels are shown in Figure 2 and Figure 3,

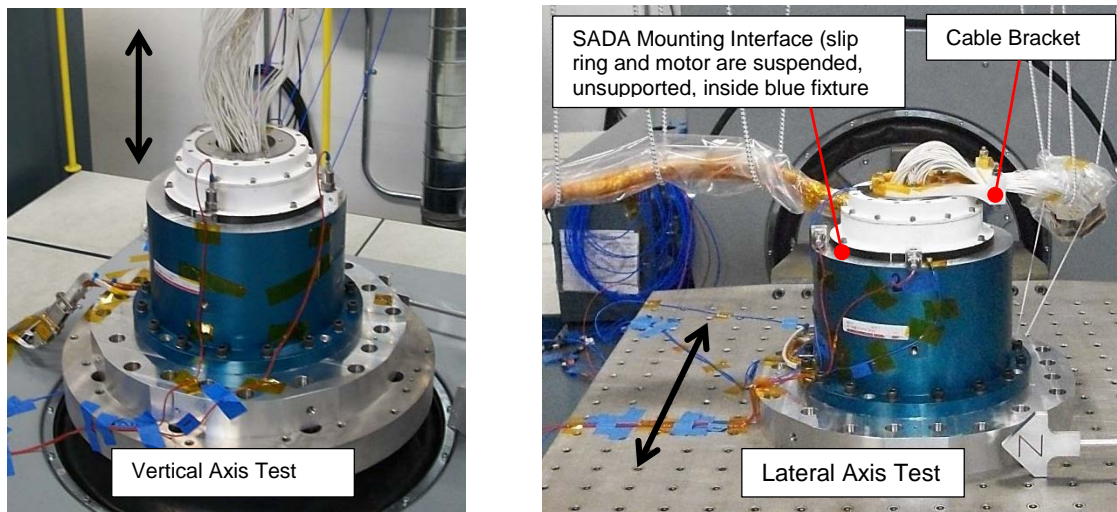


Figure 2. Photos of SADA Hardware Setup for Vibration Testing

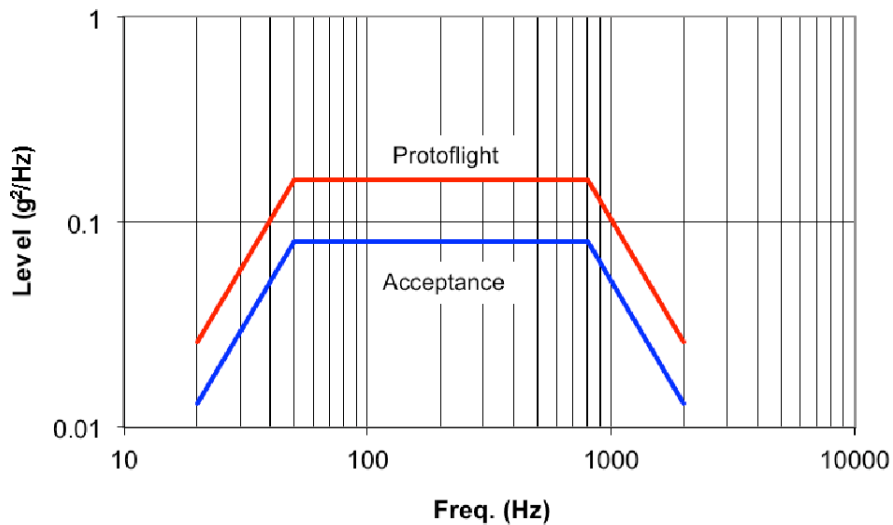
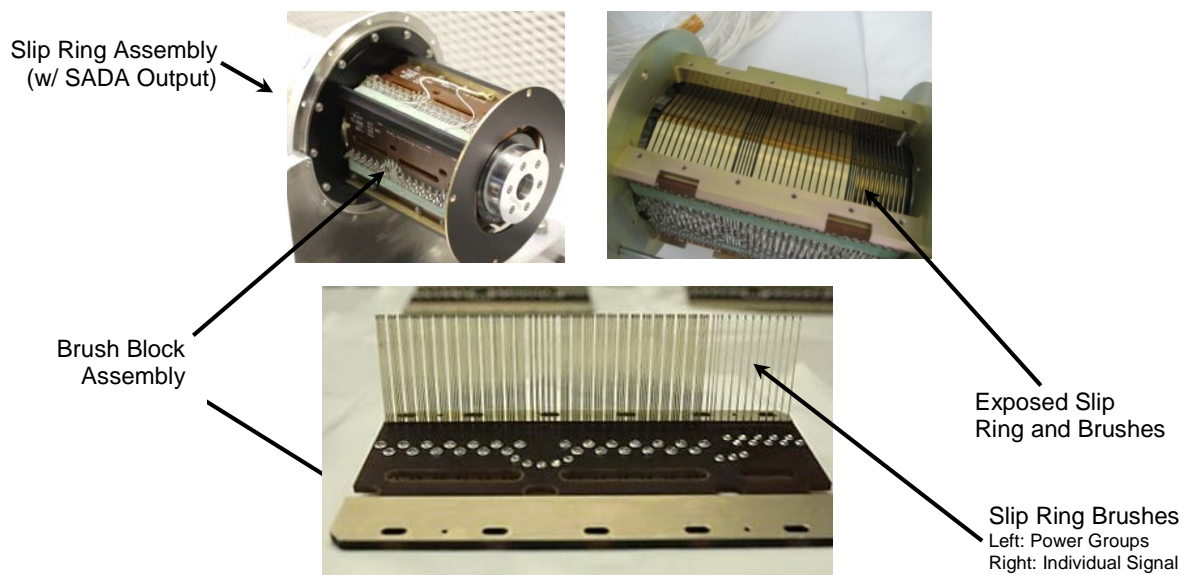


Figure 3. Specified Vibration Test Spectrum

At first glance, the noted g-levels do not appear to be unusual or exceedingly difficult design requirements. Standard design practices pre-anomaly were to ensure design integrity with positive margins up to 3-sigma peak acceleration loads. However, later evidence demonstrated this protoflight test profile, when applied to the SADA mounted in a very stiff test fixture, combined to produce SADA resonant modes that resulted in unexpectedly high (i.e., statistically low probability) input loads. In fact, resonant modes were later discovered to excite SADA components to as high as 2 to 3 times the control Grms input level. Additionally, these high responses contained greater than 6-sigma peaks during component vibration tests.

The SADA, illustrated in Figure 1, consists of four main subassemblies including the output, main housing, slip ring, and motor. The output assembly has a payload attachment interface that incorporates a set of duplex bearings designed to carry radial, axial and moment loads of the attached payload. The slip ring assembly shown in Figure 4 and Figure 5 consists of four brush block assemblies each with a series of gold alloy wires (i.e., brushes) supported and attached to printed circuit boards. Each brush rides in individual v-grooves machined into the slip ring rotor and each circuit/set of ring grooves (1 to 5 grooves per group) is physically and electrically insulated from each other with a raised insulation barrier as shown in Figure 5. This slip ring assembly is supported between the output assembly and another set of trailing bearings within the main housing assembly. At the opposite end of the SADA, away from the output assembly, the geared stepper motor is mechanically grounded to the main housing assembly and coupled to the output assembly torque transfer shaft passing through a clearance hole in the slip ring rotor. The completed assembly weighs approximately 12 kg and measures approximately 20-cm outer diameter by 23-cm long.



**Figure 4. Slip Ring Assembly w/ Exposed Rotor and Brushes**

This configuration incorporates several competing design objectives including meeting requirements to support very high moment and axial loads between the SADA mounting flange and the solar array attachment point while outputting very high stiffness as well as minimizing output drag to address a low disturbance torque performance requirement. The solution was to incorporate a high-precision, moderately-preloaded duplex bearing mounted as close to the payload as possible. These trades lead to a cantilevered design optimized for launch and on-orbit mission requirements but less desirable for component-level vibration tests and related SADA test boundary conditions.

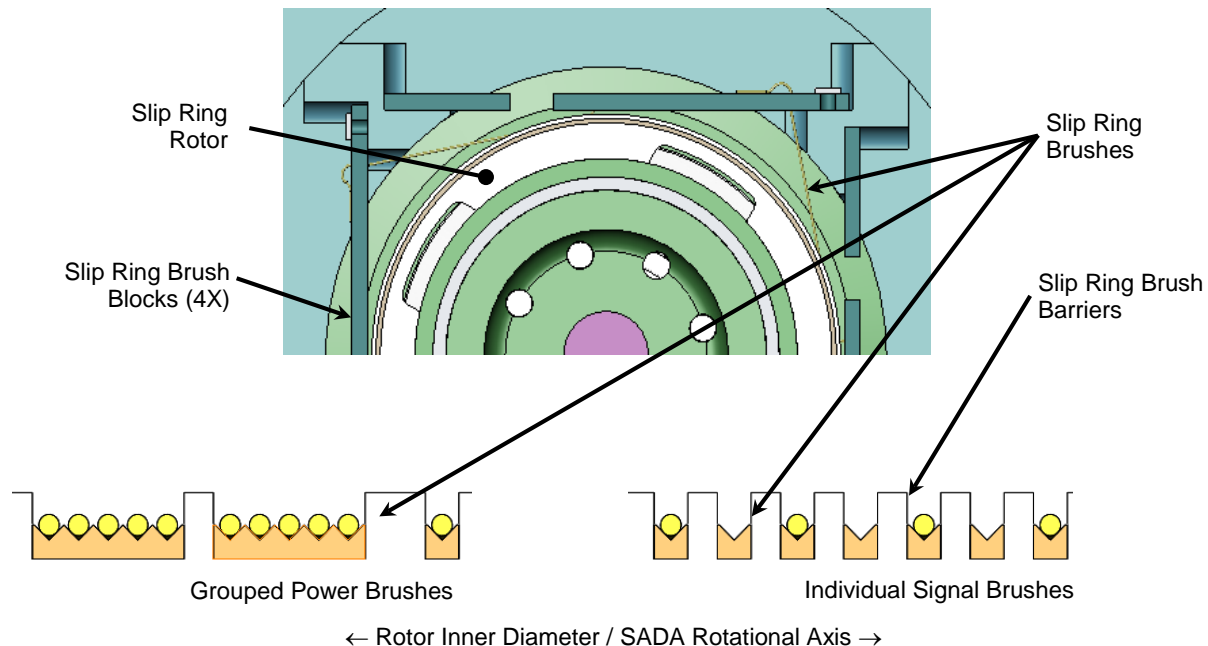


**Figure 5. Illustration Slip Ring Rotor Ring Grooves and Brush Orientation**

Other competing design goals central to the SADA slip ring design are related to brush preload. The relatively high cycle life requirement was best achieved through lightly preloaded brushes where lower forces would result in less drag and less wear at the contact point between the slip ring brushes and the rotor. Reduced brush drag and wear increases drive torque margins and decreases debris generation within the mechanism. Efforts to limit debris generation over time minimized contamination risk to other mechanical components within the SADA (such as bearings) and helped lower brush electrical stick/slip noise by allowing the brushes to remain solidly in contact with and electrically bonded to the slip ring rotor.

In contrast, the requirement to sustain random vibration loads was better addressed through higher brush preload. Higher preload provided increased margin against brush/rotor gapping during vibration testing and increased chances that the brushes would remain in assigned grooves, keeping them isolated from neighboring rings to prevent unacceptable short circuits. Increased brush preload also minimized brush contact resistance and sliding contact noise.

While these competing design goals were challenging, SNC optimized the design, balanced these competing requirements and ultimately developed and manufactured a highly reliable and viable mechanism. The design has been integrated into several spacecraft and has several years of on-orbit mission success despite various challenges related to a short circuit anomaly that occurred during component-level testing.

### **Anomaly Discovery**

During a standard post-test electrical check after a typical random vibration protoflight test of a newly developed and built SADA, SNC encountered the first of two key events associated with the slip ring short circuit anomaly. An electrical circuit isolation test confirmed several slip ring circuits had shorted together. Following this discovery, various other post-test functional checks were performed. The successful completion of these performance tests confirmed the SADA had no physical damage to any other components and, aside from the electrical anomaly, was operating as expected.



Through extensive design and data review, analysis, and disassembly of the SADA, SNC confirmed a random selection of slip ring brushes had ‘jumped’ across the rotor electrical insulation barrier and moved from assigned rotor grooves to neighboring grooves. The result was an anomalous ring-ring short circuit that caused the isolation test fault. Figure 6 shows a 3D radiographic image of displaced and shorted signal brushes.

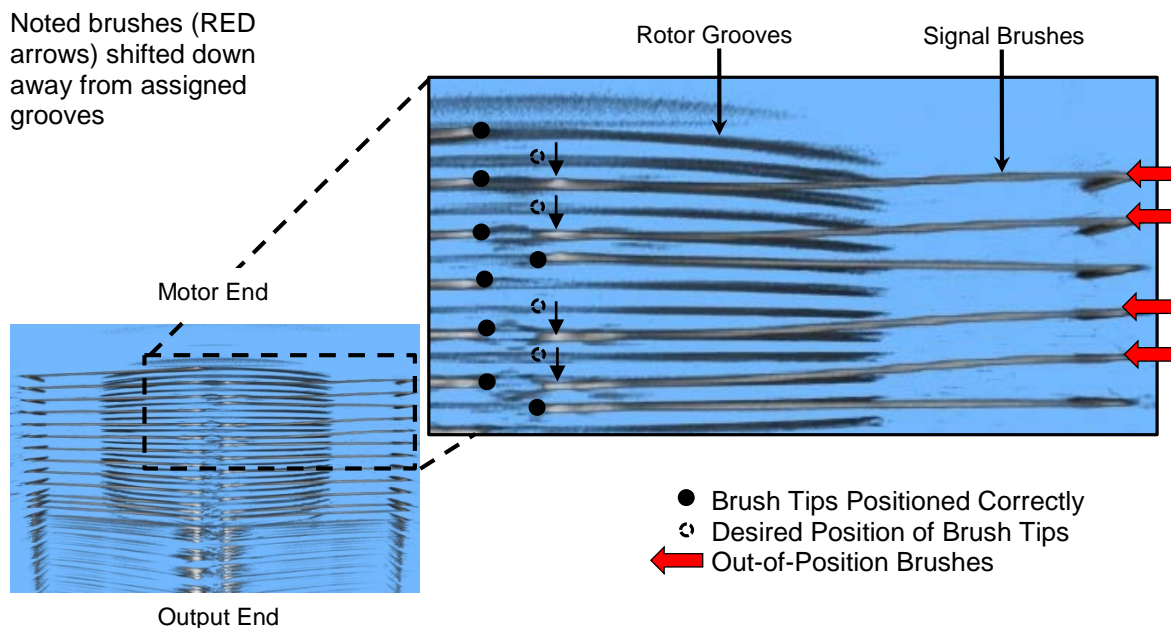


**Figure 6. Radiographic Image of SADA Slip Ring with 4 Shorted Signal Brushes**

This image was derived from 3D X-ray imaging processes and techniques not commonly available at the time of the initial investigation. However, the image is presented here because it clearly illustrates the condition of the brushes in a similar short circuit condition. Signal brushes are shown misaligned with the slip ring rotor grooves as they appear axially along the slip ring rotor. The right side bottom view of Figure 5 is a sketch of the desired alternating pattern for signal brush position. Four signal brushes shown in Figure 6 do not follow this pattern, (RED arrows) indicating movement away from their assigned grooves and causing a short circuit between adjacent rings.

Due to the enclosed configuration of the SADA, visual confirmation of the slip ring rotor and brush condition was not feasible. Prior to the application of this 3D X-ray imaging technology, other methods such as standard electrical isolation tests and resistance measurements were used to confirm the initial slip ring fault. Electrical isolation test results allowed the team to adequately identify the precise circuits involved but they did not provide enough data to confirm which brush moved to which ring. To collect the additional data required, the team utilized high-fidelity resistance measurements of each identified anomalous slip ring circuit pair. By comparing measured parallel resistance to historical values, the circuit with the displaced brush(es) could be identified by higher than expected resistance readings.

After testing was conducted to identify the presence of the displaced brushes, it was found through further data review and analysis that the slip ring rotor preload spring force was not providing enough holding force to axially stabilize the rotor during random vibration testing. The investigation team believed this insufficient rotor preload allowed the rotor to “gap” and axially oscillate during test. These oscillations resulted in very high undamped impact loads each time the rotor re-seated against internal axial hardstops. This rotor impact imparted forces into brushes beyond established preload that, when combined with resulting complex nonlinear brush dynamics, caused the brushes to break contact with the

slip ring rotor and move onto adjacent circuits. This hypothesis was confirmed with a successful random vibration re-test following SADA rework by repositioning the brushes to their assigned grooves and increasing the rotor axial preload to withstand higher-than-expected rotor acceleration responses.

Several years later, after two successful SADA on-orbit missions, protoflight vibration testing once again resulted in shorted slip ring circuits. Because of historical issues with slip ring rotor preload, initial discovery efforts focused on the as-built condition of new hardware and found rotor preload to be slightly underrated. However, subsequent rework to correct rotor preload did not prevent brush movement during vibration re-tests. It became evident that underrated rotor preload was not the only physical cause for the anomaly and SNC began a rigorous in-depth investigation to reevaluate other underlying causes.

### **Anomaly Investigation**

Dealing with problems associated with the structural response of complex mechanical systems can be extremely challenging, especially when investigation and discovery must be conducted on fully assembled flight hardware with limited visibility or access to key components. This 'black box' scenario once again became the backdrop for another rigorous investigation into the root cause analysis of the shorted brushes.

The investigation centered on three key areas including review of design/analysis/build documentation, assessment of dynamic responses on various SADA components, and development of test correlated predictive analytical tools. First, an extensive review of build documentation found the SADA parts to be correctly manufactured and assembled to print. Review of various structural analysis reports confirmed positive load margins. All evidence, additionally supported by rigorous visual inspections during hardware disassembly, convinced the engineering team that the anomaly did not occur as a result of a failed or incorrectly assembled component. No obvious root cause explanation was found, so the team focused on the second area of interest, dynamic response, which quickly became the primary focus of the investigation.

The team shifted the investigation focus to data mining, including exhaustive efforts to collect, evaluate, and categorize prior SADA acceptance test data. The effort began with a rigorous study of accelerometer output time history in an attempt to further quantify the frequency and nature of peak input loads. Data consisted of several vibration tests and re-tests of similar SADA hardware, test setup, and vibration input profiles conducted throughout a ten-year period.

Time history vibration data revealed that unexpected intermittent responses greater than 6 sigma were present during test, including tests that resulted in shorted slip ring circuits. Figure 7 illustrates an example of a time history plot recorded during a prior SADA vibration test. This finding was crucial to the investigation because it confirmed that the typical 3-sigma threshold used for design and analysis was inadequate for the design of this particular component as tested under the specified vibration spectrum and related test boundary conditions. Review of this data provided a comprehensive understanding of vibration test effects on and interaction with the SADA that contributed to the team's ability to develop a viable method of predicting dynamic response during future tests.

Discovery of these random peak loads was a critical breakthrough in the investigation. It became immediately clear that prior design efforts did not account for these significantly higher dynamic events. The persistence of these higher events in historical data highlighted a need to increase the previous minimum design standard from 3 to 6 sigma or greater for this particular component and to begin work on the development of higher fidelity predictive modeling techniques.

As the effort to develop predictive modeling techniques began, it became apparent that trying to quantify and predict the dynamic behavior and movement of hundreds of independent brushes reacting against the slip ring rotor would be very challenging. However, the team realized that it was not necessary to fully understand or predict the complex nonlinear behavior of brush dynamics. Instead, the engineering team



developed an analytical method to predict the load at which a brush would gap ('lift-off') away from the rotor. The underlying theory was that a brush that does not gap cannot inadvertently displace to adjacent slip ring circuits. The plan was to compare the recovered brush tip reaction loads to the as-built brush preload and establish margins against gapping. With this approach in mind, efforts shifted to predicting gapping events rather than trying to understand complexities of brush dynamics once gapped. Finite element analyses became the focus in this next phase of the investigation with the primary goal to refine and test-correlate an existing SADA finite element model (FEM) and develop a high-fidelity predictive tool.

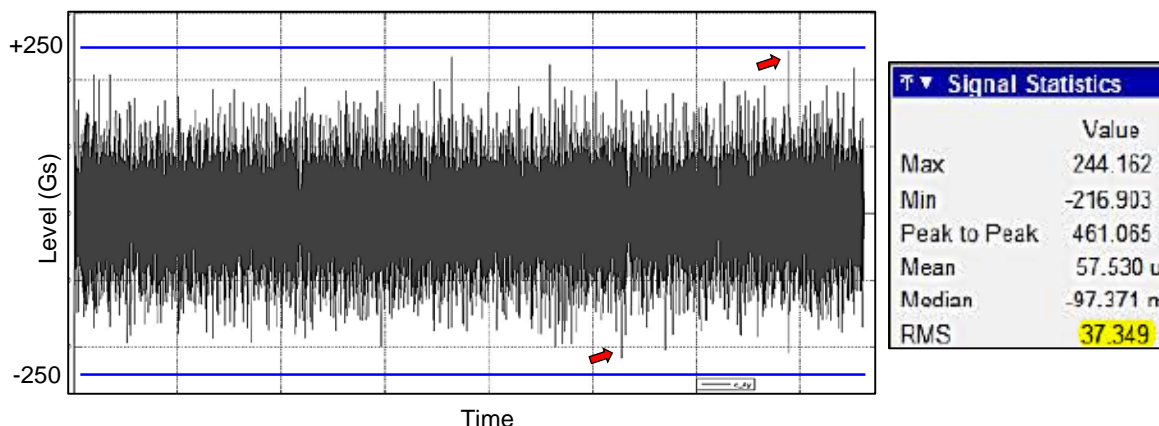


**Figure 7. Accelerometer Response Data - Time History Recorded During Vibration Testing**

This process to refine the existing SADA FEM started with a fundamental update to incorporate individual brushes around and along the slip ring rotor. Several power ring brush groups as well as a series of single signal brushes were placed in strategic locations including areas where known short circuit events had occurred. Each brush was modeled to closely match the shape, cross-sectional geometry, and mechanical properties of the brushes used. Most importantly, these brushes were restrained at the contact points between the brush tip and rotor. The purpose of these FEM updates was to devise a method of recovering brush/rotor reaction loads that could be then be compared to as-built brush preload. This comparison could then be used to establish gapping margin estimates for SADA exposure to various input spectrum and random vibration test conditions. With this goal to accurately predict the 'lift-off' threshold, further FEM development and refinements continued.

The next phase of this FEM development involved test-correlating the analytical model to the as-built hardware. The process began with comparison of FEM results to prior test data. Comparison confirmed that the refined model was closely predicting the SADA response, but two issues surfaced and complicated the task of further FEM refinement. First, prior data review and data mining efforts found minor variations in test setup, SADA design, and boundary constraints associated with the various tests. These minor test and hardware configuration differences were not unexpected given the progressive development of the SADA spanning several years and following many different test programs, each with its unique assembly and test history. Variables included minor differences in cable bundle boundary constraints, rotational alignment, rotor axial preload, brush contact preload, accelerometer placement, and vibration test equipment/facilities. Table 1 summarizes some of these configuration differences. Because the historical data sets were complicated by these differences, precise tailored FEM correlation was extremely challenging and it became clear that additional test data would be required to continue the FEM model-correlation and refinement effort.

**Table 1. Example of Various Hardware Test Configurations**

Output Fiducial Alignment	Diving board orientation RE: Table X axis	Diving board orientation RE: Table Y axis	Diving board orientation RE: Table Z axis	Diving board orientation RE: Case Fiducial	Should be: Diving board orientation RE: Case Fiducial	Bus wire exit X axis	Bus wire exit Y Axis	Bus wire exit Z axis
-60°	N/A	N/A	N/A	N/A	-105°	Back Left	Back Left	Front Left
-60° to -120°	Right	Right	Back	-105°	-105°	Back Left	Back Left	Front Left
+86°	Back	Back	Left	+165°	+75°	Back Left	Back Left	Front Left
Aligned	Left	N/A	Front	+75°	+75°	Back Left	N/A	Front Left

Note: Use of the term 'diving board' is synonymous with output cable bundle and clamp

The second issue with the historical data involved accelerometer placement and related availability of response data. Standard vibration tests include application of strategically placed accelerometers on the exterior SADA surfaces and surrounding test fixtures to recover selected mechanism dynamic responses during test; this placement on the exterior is typical. Other more sensitive components are housed within an enclosed structure to protect them from contamination and handling prior to launch. These sensitive components are very seldom accessible, making instrumentation and recovery of dynamic response difficult. Because this short circuit anomaly involved dynamics of sensitive internal SADA components, the lack of sensors and response data nearer to the brushes raised concerns regarding FEM correlation accuracy.

To address these two challenges, a tailored low-level vibration test (-6 dB) was conducted on flight hardware reworked to as-designed configuration (i.e., verified slip ring rotor preload and properly repositioned and aligned brushes). The test article was instrumented with strategically placed accelerometers consistent with the orientation and position defined in protoflight test setup documentation and found during data review of historical tests with one exception. One additional accelerometer was temporarily installed deep inside the SADA on the slip ring rotor shaft. This additional sensor was critical to SNC's understanding of the SADA response within the mechanism nearer to the brushes. Test results were then used to further refine the FEM and complete the development of this test-correlated predictive tool to within 1% of measured values.

Figure 8 illustrates an example of results from a lateral (z-axis) low-level random vibration test compared to simulated output of the refined FEM. As shown, the peak level and resonant frequency of the rotor shaft for both the test and predictive model align very closely around 650 Hz, which indicates a highly refined FEM model. All remaining axes were test correlated in a similar manner to complete the effort. Armed with a newly-developed, high-fidelity test correlated FEM, SNC was able to analyze earlier anomalous tests and confirm low brush force margins when tested to the specified levels. FEM model predictions using baseline protoflight test levels shown in Figure 3 confirmed that the slip ring rotor shaft modes closely aligned with the SADA primary structural modes. Resonance at this aligned frequency significantly increased the likelihood of very high peaks (6 sigma and greater) and explained higher-than-expected brush contact point response loads. Figure 9 illustrates the first mode of the SADA structure at the far end of the cantilevered assembly (i.e., motor end) aligned with data collected on the interior of the SADA at the end of the slip ring rotor shaft nearest the brushes that shorted. Analysis results confirm that when tested to the required protoflight vibration levels while constrained in test fixtures as defined in related protoflight test procedures, brushes would exceed preload and gap with as little as 3.8-sigma events. And as discussed earlier, greater than 6-sigma events were not uncommon. This finding clearly supports the statement of cause noted below.

Primary Physical Cause: *Protoflight testing to specified vibration levels induced loads into SADA and related slip ring brushes sufficient to overcome brush preload and force brushes to adjacent slip ring circuits. This condition resulted in ring-ring short circuit.*

*Root Cause: Required protoflight random vibration test levels and associated test boundary conditions uncharacteristic of flight environments created response loads that exceeded the design capability of the SADA brush configuration.*

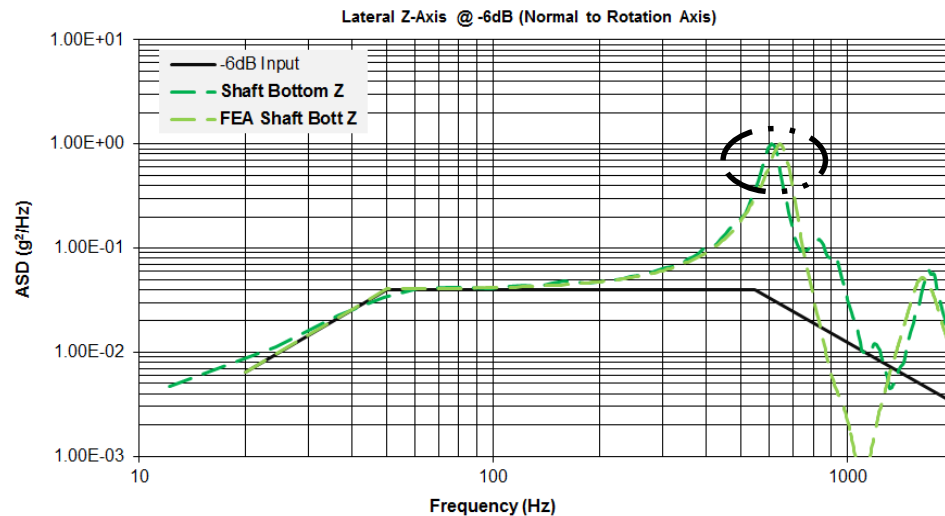


**Figure 8. Data plot of test correlated FEM for lateral Z-axis response**

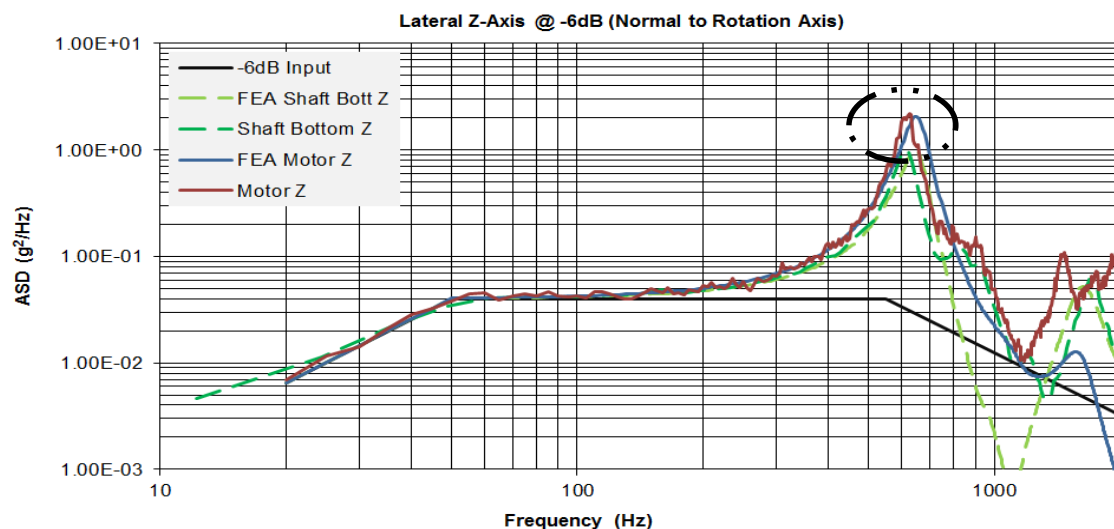


**Figure 9. Data illustrating SADA Primary Structural Modes Aligned with Rotor Shaft Modes**

### Anomaly Resolution

The engineering team initially considered various options to physically modify the SADA design and address the likely recurrence of shorted brushes. Analysis efforts began to assess whether-or-not modifications to stiffen primary structural parts of the SADA (i.e., housings, supports, etc.) would help shift and separate the SADA primary structural mode from the peak brush mode. Without significant impacts to the SADA envelope and mass, FEM analysis results confirmed this was not a viable option. The team

also considered improvements to mechanically constrain brushes to keep them within assigned rings and below insulation barriers. This modification could either be implemented with a deployable launch lock configuration or by snubbing brushes to limit stroke once installed and assembled in their assigned grooves. However, associated design changes would have required significant development effort and included an array of additional technical risks. Cost and schedule constraints combined with related technical risks ultimately made the feasibility of fundamental design changes to fully assembled and qualified hardware in the middle of final acceptance testing very undesirable.

Without making physical changes to the SADA, the only other viable options were to either re-evaluate and modify test boundary conditions to more accurately represent spacecraft test and launch environments or tailor the random vibration test profile (via force limiting, notching, and/or other profile changes) to limit input loads to reasonably margined levels. To address the first potential solution, the team further reviewed spacecraft test and launch data and confirmed that the required component test levels combined with the rigid SADA/fixture boundary conditions resulted in very different SADA input loads. Review found SADA component level test loads were significantly higher than any loads measured at the SADA when integrated with the payload and mounted to the spacecraft. In addition, data also revealed that the majority of energy input into the SADA during launch and spacecraft level tests occurred well below the SADA resonant frequency of 650 Hz. These findings confirmed beliefs that component tests resulted in SADA loads far above of levels needed to demonstrate compliance with launch and spacecraft test environments.

It is well known that accurate physical simulation of launch/interface boundary conditions at the component level is extremely difficult and complex and the team believed that attempts to lower SADA input loads by changing test boundary conditions would be very risky. Any change would significantly lower the team's understanding and certainty related to SADA response during test and the value of a known response far outweighed the risks of uncertainty. Major design changes to the SADA test boundary conditions were not implemented. However, one minor change was feasible.

To more accurately match cable bundle loads and related SADA rotor shaft dynamic response during test, a minor change to the SADA test boundary conditions was implemented. This involved modifications to the output cable bundle support and clamping method. Brackets were manufactured and installed on the SADA to more accurately represent the as-integrated SADA/spacecraft configuration. FEM analysis confirmed the change would improve margins, and any easily-implemented change for the better with relatively low impact to program cost and schedule made sense. This configuration difference can be seen in Figure 2 where the installation of a cable clamp is shown in the image on the right.

Because major changes to boundary conditions were not feasible, the team changed focus to solutions that involved vibration test profile modifications. Because early test instrumentation did not include an accelerometer at the cantilevered end (i.e., motor end) of the SADA, review of available test data identified the SADA primary structural mode related to brush movement to be an axial mode near 800 Hz. The protoflight profile (Figure 3) coincidentally included a plateau out to 800 Hz. The team believed excessive loads on the rotor high enough to cause brush movement could be minimized by decreasing the test profile roll-off point from 800 Hz to 550 Hz. Re-tests to this modified profile did not solve the problem and related slip ring short circuit conditions persisted. This indicated that the initial understanding of the brush movement was incomplete.

It is important to note that at the time of this 550-Hz modified profile testing, development of a high-fidelity FEM model was incomplete. In fact, it was the recurrence of the short circuit anomaly following the 550-Hz test that caused an aggressive shift in the investigation and ultimately lead to the discovery of the 650-Hz lateral mode discussed earlier.

Rather than continuing to resolve the problem by marginally changing test spectrum profiles, output from the new high-fidelity FEM model was used to justify the application of more rigorous test techniques and manage excessive SADA responses. Vibration test profile-notching and force-limiting were two

techniques considered. Ultimately, a plan was developed to utilize force-limiting to reduce peak loads at mechanism resonant frequencies. The Semi-Empirical method from NASA-HDBK\_7004C ("*Force Limited Vibration Testing*") was the approach implemented. This test method uses load response data from force gauges placed at the component/fixture mounting interface for closed-loop feedback to the shaker control system. The goal was to modulate shaker input into the test article and reduce the overall PSD at select frequencies while maintaining a pre-determined force level at the input.

As discussed earlier, FEM simulation results from the refined model highlighted the SADA first lateral mode around 650 Hz. The refined model was used to run force-limited simulations to predict the effects of a deep notch in the shaker input around the SADA resonant frequency shown in Figure 10. Simulation results match data recovered from successful SADA re-tests. For reference, this result is compared to GEVS minimum workmanship levels.

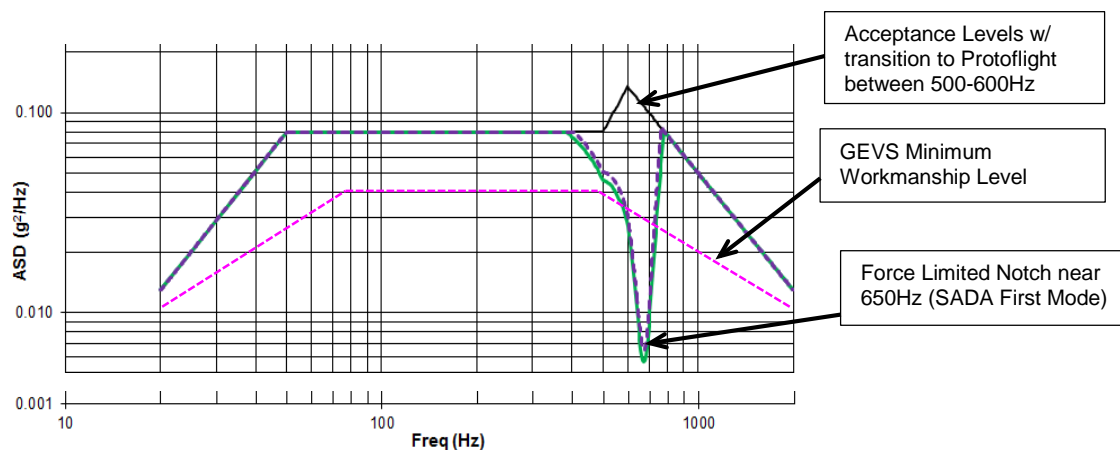


**Figure 10. Profile Comparisons - Force Limiting FEM Predictions (Lateral Axis)**

While this force-limited test method worked to address the immediate concerns of the ongoing program (i.e., the re-tested SADA did successfully survive the force-limited tests), the method is not preferred. The modified process and resulting profile did not adequately address the high brush loads at the second mode where as little as 3.2-sigma events could cause slip ring brushes to gap. Additionally, this type of testing is extremely time consuming and resource intensive. High-level engineering oversight by skilled dynamists prior to and during each run is required to ensure the control system and feedback process yield precisely correct test article input loads. Numerous low-level tests are required and run prior to each full-level test for each axis. With each run, response data must be scrutinized to verify that control set points are properly configured to achieve desired input response at full level. This intensive oversight and test complexity combined with the inherent risk and increased costs motivated the team to find a different approach to address the over-test problem for subsequent SADA tests.

Figure 11 is an example of key output from the improved test-correlated FEM and related analytical process. It shows the FEM prediction for brush force during the force-limited test shown in Figure 10 and clearly identifies both the first and second modes of the SADA that were believed to be responsible for the brush excitation during test. These results depict a peak brush/rotor contact load of 1.25 grams with contributions of 0.5 gram at SADA resonant frequencies up to 650 Hz and the remaining 0.75 gram at frequencies from 650 Hz up to the second mode near 1600 Hz. Results from simulations like these helped the team realize the importance of secondary resonant effects in any planned solution intended to mitigate brush movement during test. As the plot illustrates, energy in the brushes was significantly larger due to the second higher frequency peak. This was a very important finding that highlighted a need to seriously consider the impact of higher as well as lower frequency content when defining future test profiles.

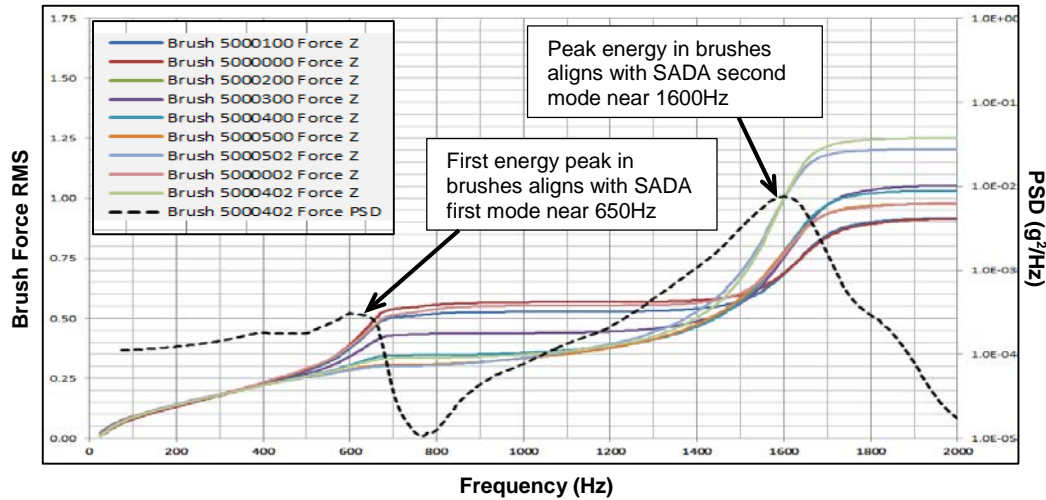


**Figure 11. Cumulative Brush Force (RMS) – Force Limiting FEM Predictions (Lateral Axis)**

The engineering team now had a nicely correlated FEM, a strong understanding of slip ring brush behavior, and recent experience with force-limited vibration test challenges. The desire for a new follow-on program was to utilize the FEM to analytically justify modification to existing vibration test requirements and ensure input levels remained well below brush gapping threshold of the exiting design. Several scenarios were evaluated during prior investigations while others were run to help assess new options and find a preferable compromise. Table 2 summarizes results from a few scenarios along with brush preload predictions. While analytical values do not quite achieve the gapping factor design goal of 6 sigma or greater, significant improvement can be seen in the gapping factor column.

This improvement was possible because brush gapping problems were well understood from prior investigations. This knowledge led to a slight but crucial change to the as-built brush preload that simply involved narrowing the preload tolerance window. Confidence that the as-built SADA included these higher preloads was gained by measuring brush preload at both the slip ring subassembly level and after integration with the SADA. This tolerance change resulted in a 25% increase over the minimum allowable brush preload previously specified, minimized the extent of random vibration profile tailoring required, and preserved the validity of the qualified SADA design. Implementation of this change left the remaining task of defining and justifying an acceptable random vibration test profile modification.

**Table 2. Examples of FEM Brush Gapping Results with Margin Estimates**

Random Vibe Environment	FEM Brush Preload Prediction (grams)			Minimum Allowable Brush Preload (grams)	Gapping Factor ( $\sigma$ )
	Z Axis (lateral)	X Axis (lateral)	Y Axis (axial)		Z Axis (lateral)
550 Hz roll-off, Protoflight (brushes shorted during test)	1.6	1.1	1.2	4.0 5.1*	2.5 3.2
550 Hz roll-off, Force Limit 30G (not tested)	1.2	1.0	0.9	4.0	3.3
350 Hz roll-off, Protoflight/GEVS (passed tests)	1.0	1.1	1.0	5.0 5.5*	5.0 5.5

\*Measured sample average brush force

The prevailing opinion of design reviewers was that any modified profile needed to closely match the required protoflight level and deviations from these levels had to remain above component minimum workmanship standards to comply with accepted industry standards defined in NASA technical standard



GSFC-STD-7000 (General Environmental Verification Standard (GEVS)). Figure 12 compares the proposed test levels (i.e., Final Modified Profile, plot 4) with GEVS and other historical profiles. These comparisons highlight the strategic reduction in test input levels at frequencies greater than 350 Hz and contrasts the proposed profile to those associated with unsuccessful SADA tests.

The proposed test profile met most criteria and was ultimately approved by the review community. The 350-Hz roll-off was selected because it was safely under the approximate 650-Hz natural frequency of the SADA but well above (and inclusive of) significant response expected at the SADA during launch and spacecraft level tests. The profile also included a transition at 600 Hz from a straight to a kneed ramp. This transition kept the test levels above GEVS minimum workmanship requirements and mitigated concerns voiced during force-limiting tests when input significantly dropped below GEVS at the notched frequency (Figure 10).

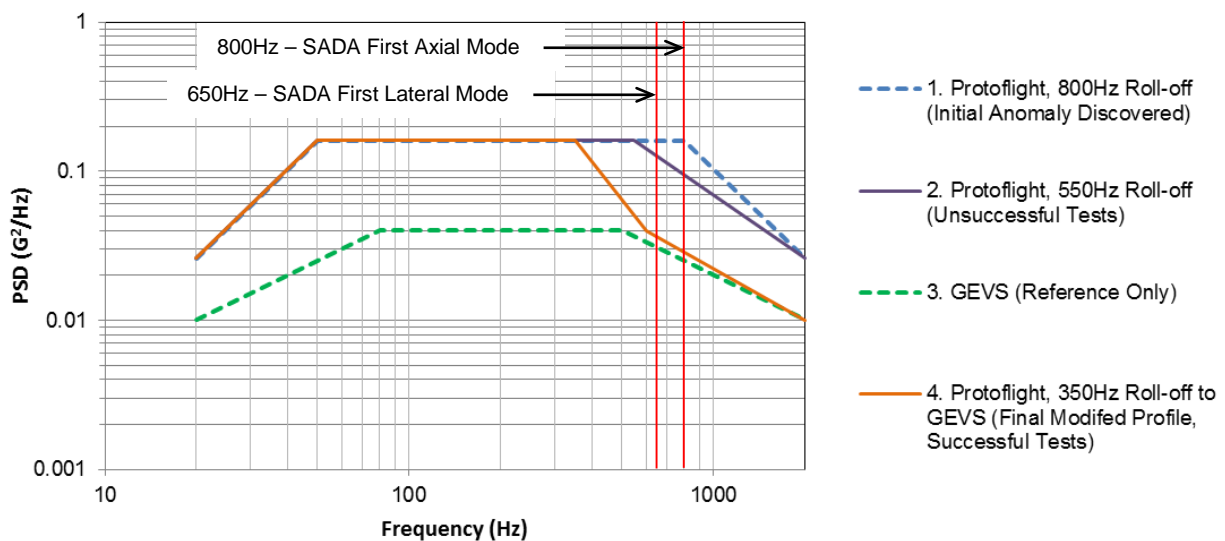


**Figure 12. Final Tailored Vibration Profile Comparison**

The final modified profile did fall slightly short of the design goal to demonstrate analytical margin against 6-sigma dynamic load events but the team felt the risk of gapping remained very low. Brush force margin against an estimated 5.5-sigma load event still represented a very low likelihood of occurrence and the design included additional inherent force margin against brush movement out and away from an assigned groove if brush gapping did occur. This modified profile was validated when SADAs built for the follow-on program passed all required protoflight testing, including slip ring electrical isolation and resistance checks, without issues. Review of post-test 3D radiographic brush block and rotor images similar to Figure 6 confirmed all brushes were properly aligned and positioned within assigned rotor grooves after exposure to the modified test profile.

### Summary

The combination of increased minimum brush preload and testing to a modified random vibration test profile ultimately resulted in the successful completion of the SADA protoflight test program. This final success was a result of efforts from analysts, designers, and the entire review community starting with the discovery of the initial fault through to the successful delivery of several sets of hardware. During this process, significant insights were gained that will help mitigate the recurrence of similar problems in future designs.



Complex mechanical systems require a significant amount of scrutiny to ensure all fundamental frequencies are characterized and understood. This is especially true for systems that contain compliant structure housed in a very rigid primary structure. In the case of this SADA, the design guideline to evaluate dynamic loads against 3-sigma events for certain components seemed appropriate during the design and development phase. However, the investigation that followed the slip ring short circuit anomaly clearly identified a need to look beyond this 3-sigma guideline and apply a much higher standard, closer to 6 sigma. This need to increase load margins must be balanced with associated increased costs as well as other technical trades that may drive design complexity and technical risk.

During any design evaluation phase to consider whether-or-not increased load margins are required, test boundary conditions deserve a very critical review. Test boundary conditions can significantly impact technical trades and design decisions. Often, as seen in this case, component boundary conditions during protoflight or acceptance vibration testing rarely represent the as-integrated final flight configuration with the spacecraft. Understanding these differences and working to tailor test requirements prior to test to match component input levels (often at test specific resonant frequencies) can save countless investigation hours and wasted costs.

Familiarization with all forms of test and hardware evaluation technology is also beneficial. During this investigation, the team utilized complex force-limiting vibration test methods, high-fidelity test correlated FEMs, and advanced technology 3D radiographic imaging to resolve a very difficult technical challenge. However, the selection of applicable technology (new or old) is a far more important consideration than the use of new high-tech methods and equipment in general. For example, this investigation warranted the use of 3D imaging because the problem confirmation and re-test validation would have been significantly more difficult without it. This may not be true for future programs when reviewing new designs where alternatives to this technology, such as design modification to include view ports, may be more appropriate.

As with any complex problem, it is important to exhaustively consider alternatives, utilize technology appropriately, and support highly collative design experiences. In this case, SNC successfully did this to link high brush loads encountered during protoflight vibration testing to high SADA resonant peaks atypical of flight-like conditions. Findings from extensive data review, analysis, and design assessments highlight the need to thoroughly understand the impact of test boundary conditions and related mechanism resonant modes when designing complex mechanisms. Brush preload, beam shape and cross section, rotor support structure, and fundamental mechanism frequencies all interplay to present significant design and test challenges.

Despite the challenges faced during component level testing, SNC remains convinced that the SADA design is well suited to meet all mission requirements. To date, seven of these SADAs are successfully performing all required on-orbit operations and have accumulated more than 35 years of total operating time.

# High-Performance Reaction Wheel Optimization for Fine-Pointing Space Platforms: Minimizing Induced Vibration Effects on Jitter Performance plus Lessons Learned from Hubble Space Telescope for Current and Future Spacecraft Applications

Martin D. Hasha\*

## Abstract

The Hubble Space Telescope (HST) applies large-diameter optics (2.5-m primary mirror) for diffraction-limited resolution spanning an extended wavelength range (~100-2500 nm). Its Pointing Control System (PCS) Reaction Wheel Assemblies (RWAs), in the Support Systems Module (SSM), acquired an unprecedented set of high-sensitivity Induced Vibration (IV) data for 5 flight-certified RWAs: dwelling at set rotation rates. Focused on 4 key ratios, force and moment harmonic values (in 3 local principal directions) are extracted in the RWA operating range (0-3000 RPM). The IV test data, obtained under ambient lab conditions, are investigated in detail, evaluated, compiled, and curve-fitted; variational trends, core causes, and unforeseen anomalies are addressed. In aggregate, these values constitute a statistically-valid basis to quantify ground test-to-test variations and facilitate extrapolations to on-orbit conditions. Accumulated knowledge of bearing-rotor vibrational sources, corresponding harmonic contributions, and salient elements of IV key variability factors are discussed. An evolved methodology is presented for absolute assessments and relative comparisons of macro-level IV signal magnitude due to micro-level construction-assembly geometric details/imperfections stemming from both electrical drive and primary bearing design parameters. Based upon studies of same-size/similar-design momentum wheels' IV changes, upper estimates due to transitions from ground tests to orbital conditions are derived. Recommended HST RWA choices are discussed relative to system optimization/tradeoffs of Line-Of-Sight (LOS) vector-pointing focal-plane error driven by higher IV transmissibilities through low-damped structural dynamics that stimulate optical elements. Unique analytical disturbance results for orbital HST accelerations are described applicable to microgravity efforts. Conclusions, lessons learned, historical context/insights, and perspectives on future applications are given; these previously unpublished data and findings represents a valuable resource for fine-pointing spacecraft or space-based platforms using RWAs, Control Moment Gyros (CMGs), Momentum Wheels, or other ball-bearing-based rotational units.

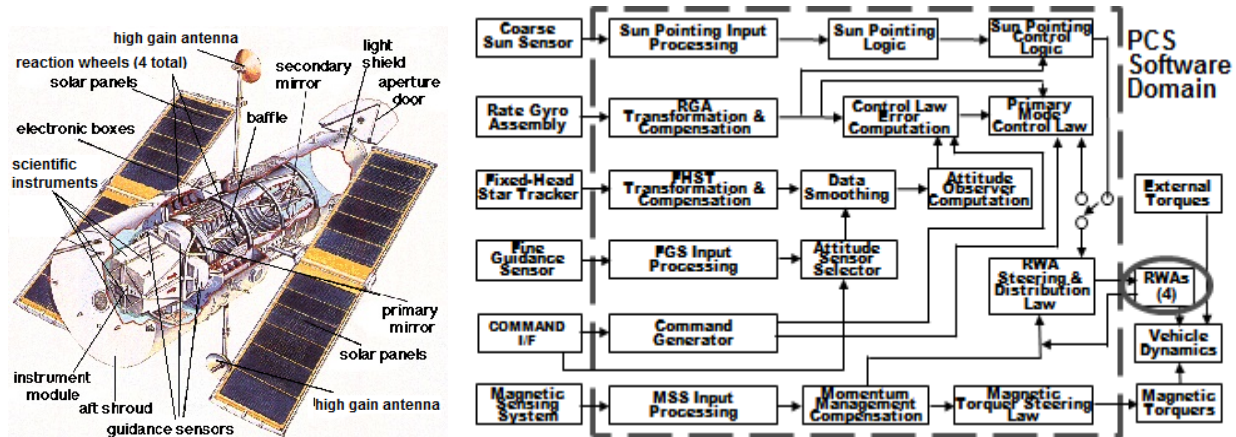


Figure 1. HST Deployed Configuration Cutaway & PCS Block Diagram Highlighting RWAs<sup>1,2</sup>

\* Lockheed Martin Space Systems Company, Sunnyvale, CA

## Introduction/Background: HST Pointing Accuracy using High-Performance/Low IV RWAs

Spacecraft Attitude Control Systems (ACSs) use Inertial Measurement Units, along with other sensor data inputs (Star Tracker, Sun Sensor, Fine Guidance Sensor (FGS), etc.) to Command and Data Handling or Line-Of-Sight Computer control algorithms to command inertia wheel counter-torque outputs in a traditional 3-axis momentum-management scheme (Fig. 1)<sup>1,2</sup>. HST's PCS uses 4 RWAs (i.e., variable-rate, fixed-spin-axis units) in an overall canted-pyramidal arrangement to generate torques for large target-to-target maneuvers/attitude changes ( $\sim 6^\circ/\text{min}$ ) as well as for highest-precision fine-pointing operation.

## HST LOS Critical Performance System Jitter Dependence due to RWA Induced Vibrations

HST achieves stringent LOS pointing stability (top-level specified at  $<7$  milli-arcseconds over 24 hours) on celestial objects for long exposures using a structured flow-down budgeting methodology<sup>3</sup>. Analogous means have been refined and applied to other space platforms (e.g., International Space Station microgravity<sup>4</sup>). Imaging can take hundreds of hours via 20-minute exposures; typically 2 per orbit. Repeatable LOS pointing accuracy is  $<0.01$  arcsec (over 100 hours). FGSs detect angular deviations due to on-orbit disturbances (see Table 1 sources<sup>5</sup>) to generate countering minute RWA rotation speed changes to maintain PCA LOS/attitude control; down to  $<\sim 2$  milli-arcseconds as sub-allocated. Other fine-pointing satellites obtain LOS levels via alternate ACS architectures/units (see Table 2<sup>5</sup>). Note that there is a fundamental ACS/PCS tradeoff (in normal attitude hold mode) between smaller RWAs (correspondingly small rotor mass and potentially less stringent residual unbalance) operating at higher maximum rotation rates (much higher IV); or using a larger RWA, that, if driven to tight residual unbalance limits, spins significantly slower (typically much lower IV). It may be more upfront affordable to impose tighter tolerances/balancing in smaller RWA rotor-bearing assemblies, but, as discussed below, may not be overall optimal. RWA IV limits get significant attention due to several inherent aspects: 1) rotation rate can assume any value in a wide spin-rate range, and 2) commanded rates reached and held (i.e., steady-state) dwell sufficiently long for fully-saturated resonance excitation at structural dynamic mode frequencies.

**Table 1. Fine-Pointing Satellite Disturbance Examples with Reaction Wheels Highlighted<sup>5</sup>**

Source	On-Orbit Satellite Disturbance Type	Mitigation Approaches
Orbital Torques	Atmospheric Drag, Gravity Gradient, Solar Pressure/Impingement, Residual Magnetic Momentum, Thermal-Radiant Field Changes	Orbit Choice, Minimizing Drag Area, Align Center-of-Pressure/Center-of-Mass
Operations	Commanded Maneuvers/Slews Stimulating Low-Damped Structures	Profiling, Ops Constraints/Stay-Outs
Mechanical	Gimballed Antennas, Solar Array Drives, Thermal Electric Coolers, Cryocoolers, Maneuver-Induced Excitations, Thermal Creak/Snap	Body-Fixed Antennas/Solar Arrays, Stiff Structures, Isolation, Profiled Maneuvers
Sensor	Star Tracker Errors – Noise Equivalent Angle, Spatial/Centroiding Errors, Star Catalog Errors, Velocity Aberration, Alignment Variations/Errors Gyro Errors - White Noise, Random Walk, Bias, Scale Factor, Alignment	Higher Quality/Performing Sensors, Better Filters/Estimators
Actuator	<u>Reaction Wheels</u> Command Noise, Command Quantization, Residual Static Imbalance, Dynamic Imbalance, Bearing/Drive Harmonics	Higher Quality/Perf. Wheels, Higher Control Bandwidth, Isolation Approaches

## RWA Concept-of-Operations (CONOPS) and Basic Induced-Vibration Test Data Considerations

Most HST disturbers (Fig. 3), if threatening jitter limits, can typically adjust their operations, i.e., selectively power off, switch operating modes/profiles, modify duty cycles, and/or transition to alternate capabilities. However, using RWAs creates a unique situation due to operating constantly to maintain HST stability<sup>6</sup>. Also, since constantly commanded torques react to small always-changing external torque effects/phenomenon, RWA rotational rates do not have a priori predictability during each orbit's phases. As a result, there arose a focused demand for IV analytical investigations along with other disturbance source

characterizations; subsequently prompting additional analytical studies to minimize HST LOS jitter impacts as described herein.

PCS analyses originally showed RWA orbital rotation rate predictions of up to 5 Hz (4 RWAs operating); with a potential reach to 10 Hz (600 RPM) under rare unfavorable pointing attitudes. However, estimates later climbed to ~20 Hz (1200 RPM) considering the additive effects of: 1) higher-than-normal solar-cycle activity (where Earth's ionosphere expands causing higher atmospheric drag torque), 2) lowest-possible orbit altitude forecasts (from later-than-expected Space Shuttle service mission/boosts originally planned to occur ~5 years), and 3) assuring mission capabilities in the unlikely event of an RWA or magnetic torquer failure. Note that, due to RWA criticality, HST studies have been undertaken to find approaches to maintain stability if up to 2 RWAs fail<sup>7</sup>. Above worst-case rates and margins set upper bounds for LOS jitter studies.

**Table 2. Spacecraft LOS Error Control Methods, Pointing Accuracies/Stabilities, & Examples<sup>5</sup>**

Spacecraft Pointing Accuracy Approximations Obtained via Various System Approaches/Architecture Implementations		Spacecraft Relative Approximate Pointing Accuracy Requirement Level
Pointing/Stability Performance Sensors (each step down includes data/improvement from above)	Pointing Accuracy (arcsec, $3\sigma$ )	Typical Commercial Stabilized Satellite Geoeye2 & SIM Widefield Infrared Survey Explorer (WISE) Reference Spacecraft & A2100 Variants SIRTF & Deep Impact Spacecraft Flyby Kepler
Two Star Trackers	60-100	
Adding Gyros	30-60	
Co-locate attitude sensors with instrument	3-30	
Improving Star Catalog	1-3	
Using Instrument to Sense Orientation or Using Fine Guidance Sensors	0.1-1.0	Extrasolar Planetary Imaging Coronagraph (EPIC)
Fast-Steering Mirrors/Advanced Isolation Systems	0.003-0.1	
Systematic Managing/Reduction of all Pointing Error Sources + Interferometric Star Sensor in Optical Path + Source-Structural Mode Separation/Decoupling	Sub-milli-arcsec	Hubble Space Telescope

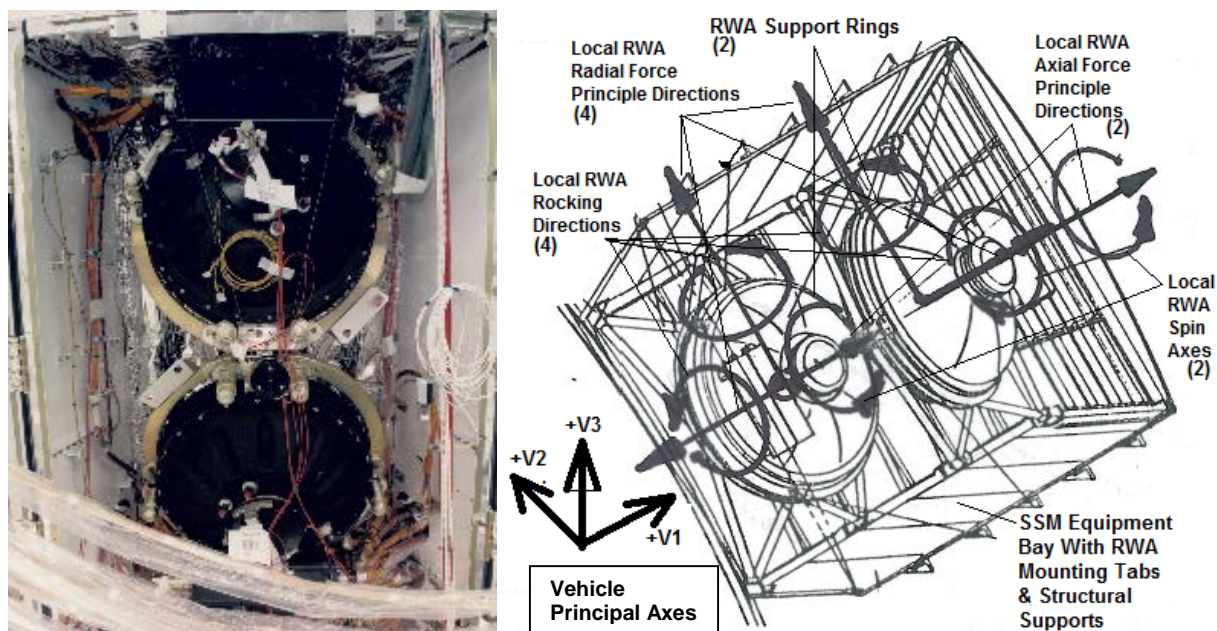


**Figure 2. RWAs (2 of 4) in HST SSM Locations & Diagram of Local Principal Directions/Orientations**

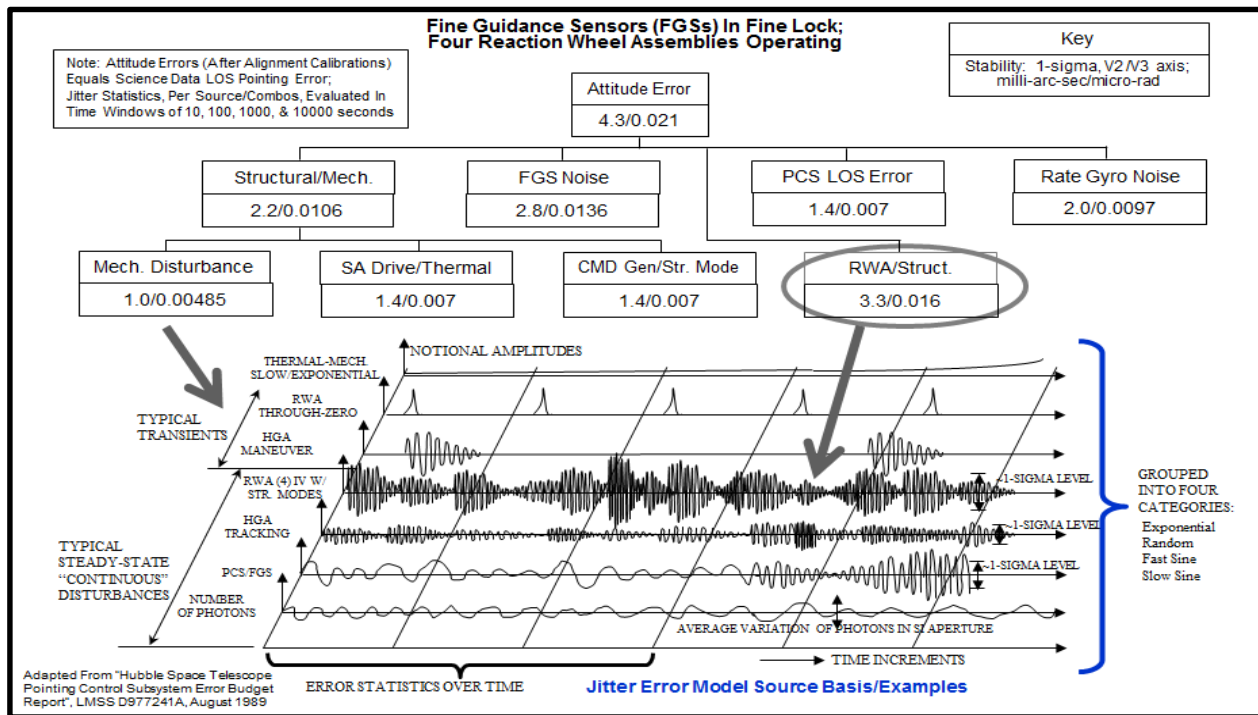


**Figure 3. HST SSM PCS Pointing Error Budget & LOS Notional Disturbance-Managed Elements<sup>3,8</sup>**

### RWA Fundamental Mechanical Noise Vibrational Disturbances Relevant to HST Induced Jitter

RWA IV noise characteristics fundamentally emanate from intrinsic core/assembly imperfections, but can change due to micro-effect combinations; e.g., bearing surface lubricant re-distribution over time can create small non-deterministic detectable deviations. Dynamic fine-balancing is a proven approach to minimize IV; specifically at basic rotation rates (i.e., 1.0 harmonic ratio). IV macro-characterization is not normally of much concern except for predicting end-of-life issues in many rotating assembly applications; but much more critical when applied to highly sensitive transducer/sensor platforms. Although judicious drive motor current monitoring can track long-term bearing friction changes/instabilities, it cannot reliably detect nor correlate well to small IV changes along RWA force/moment axes. Detailed, in-situ, and statistically-valid data are needed to quantitatively ascertain maximum expected IV levels and bound variations/uncertainties; more specifically, design-specific root sources, secondary empirical manifestations, trends/correlation, and externally-imposed conditions that can directly impact jitter limits, system allocations, and margins. The effort documented here was first driven solely to enable HST jitter verification efforts for comparison versus specified top-level limits and sub-level budgets, since acquired IV data are simply input sources for jitter modeling/analysis forcing-functions. However, due to discovery of jitter's hyper-sensitivity to IV, it became clear after gaining significantly more detailed analytical data (discussed below) that contributions from harmonics and ground-to-orbital transitions must also be known/bounded for credible on-orbit predictions. Prior to data compilation, wide speculative ranges (i.e., orders-of-magnitude) existed regarding possible worst-case changes due to relatively modest effects. Alternately, if variability found can challenge IV measured under highly benign lab and handling situations, what unforeseen excessive IV might result from much more severe disturbing effects (e.g., temperature/pressure changes, or launch-ascent vibrations).



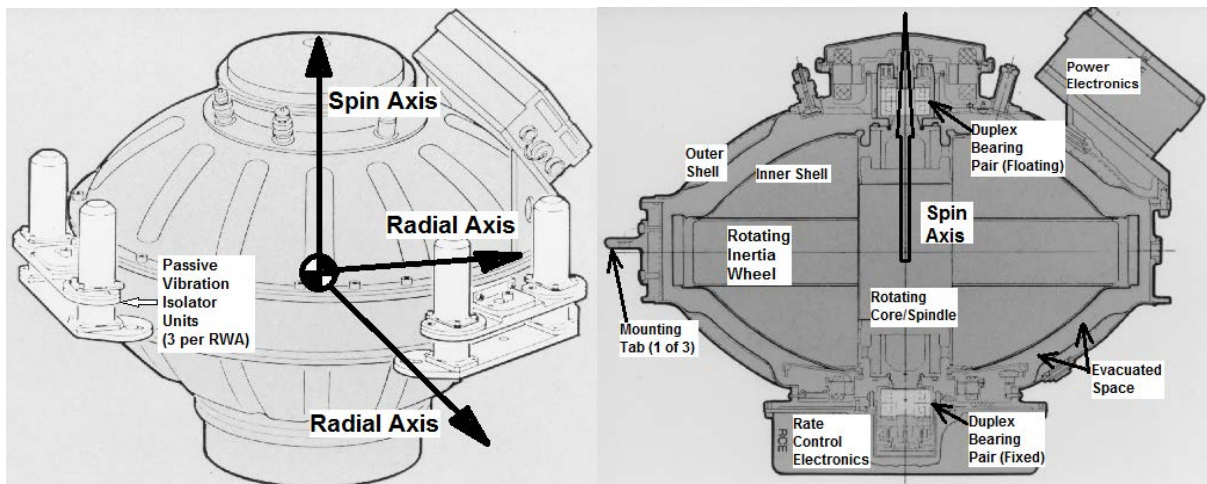


**Figure 4. RWA Local Principal IV Directions (Shown on Isolators) & Cutaway Mechanical Features<sup>9</sup>**

### **Fundamental RWA IV Disturbance Characterization: Accompanied by Higher Harmonics**

Prior program experience clearly demonstrated that RWA fine-balancing methods – along with significant margins (vs. required limits), performed at minimum-detection levels on high-stiffness test fixtures at rated design speed (e.g., 3000 RPM) with repeated trial-and-error reductions, were successful. At first, because HST RWA imbalance/IV is specified across a range of predicted on-orbit operating speeds, basic 3-axis IV force amplitude data was measured and reported at agreed-to increments of 500 RPM. As RWA IV verification occurred (circa 1984) flight unit acceptance test data were requested. Additionally, to compare value trending versus precursor Engineering Evaluation Unit that supported HST proposal efforts' fundamental performance analyses, spectral plots (force-amplitude-vs-frequency) at selected 200 RPM increments were obtained. It was noted that, while attaining required fine-balance levels with significant margins (i.e., 1.0 radial force harmonic), additional RWA high-amplitude IV peaks (Fig. 5) became prominent (not suppressed by fine-balancing), the first indicator of prominent harmonic content amplitudes that tower over primary IV (~10 times balanced 1.0 harmonic level). At the time, high-frequency harmonics/ratios were seen as an interesting curiosity and not explicitly addressed or enveloped in jitter analytical assessments. PCS experts were not concerned because this IV content was so far beyond practical active control limits.

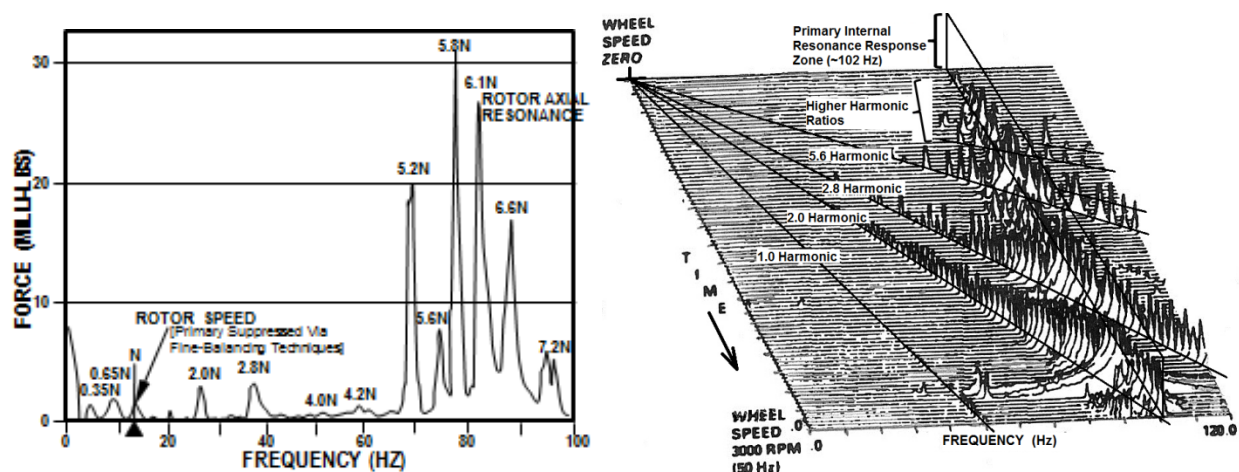


**Figure 5. Typical RWA IV (800 RPM/13.33 Hz) & Waterfall-Style (Slowly Increasing Speed) Plots<sup>9</sup>**

## Early HST RWA-Induced Jitter Tenets/Insights Driven by First Principles and Simplified Analyses

Early HST studies, founded in approaches used on classified satellites, were solely devoted to predicting disturbance effects on an LOS central pointing vector along with minimizing other known image-distorting effects (e.g., tight thermal control, PCS-specific sources) along with large separation of primary structural mode frequencies from the maximum active control bandwidth frequency (target of 5-to-10x). To support this, Lockheed's proposal efforts built a representative full-scale Structural Dynamics Test Vehicle, a medium-fidelity prototype/demonstrator with flight-like structural components' design, analysis, materials, fabrication, and test approaches. It was also sufficiently versatile to support ongoing development efforts. This Structural Dynamics Test Vehicle formed a core structural building block subsequently detailed and outfitted (circa 1987) as the Smithsonian's National Air and Space Museum HST exhibit article<sup>10</sup>. Although RWA IV forces are small (conveniently measured in milli-lb/milli-newtons) inputs to a mammoth 11500-kg (~25000-lb) spacecraft, HSTs milli-arcsecond-level LOS resolution/stability jitter requirements (~100X below prior satellite limits) posed a substantial analytical and testing challenge. RWA's required fine-balance limits (see below) relate directly to primary (1.0 harmonic) IV amplitudes at rotation speed(s). Engineering tasks focused on 4 areas perceived as the most-difficult for achieving stringent jitter levels:

- 1) High "Scissors Mode" (Fig. 6) frequency, wherein the inner Optical Telescope Assembly and outer Support Systems Module (SSM) structures pseudo-kinematically pivot in opposite directions (pitch & yaw axes), is highly dominant jitter contributor; driven as high as practicable (target >15 Hz).
- 2) RWA rotor size to be relatively large and kept at low operating speeds (nominally <5 Hz) to minimize primary unbalance radial forces (believed highly dominant) to avoid stimulating Scissors Mode jitter.
- 3) RWA radial force driven to minimum attainable levels for state-of-the-practice-unbalance/IV-setup detection levels (<milli-newton) by applying challenging unbalance/tolerance minimizing approaches.
- 4) RWA bearings were specified to be of proven tightest tolerances, acquired in same-production lots, and then checked by fine balancing for *acceptable* primary balance disturbances. In principle, it was thought that higher-frequency vibrations were insignificant (and not specified) compared to the paradigm on runout/unbalance threats: more extended efforts not considered needed nor practicable.

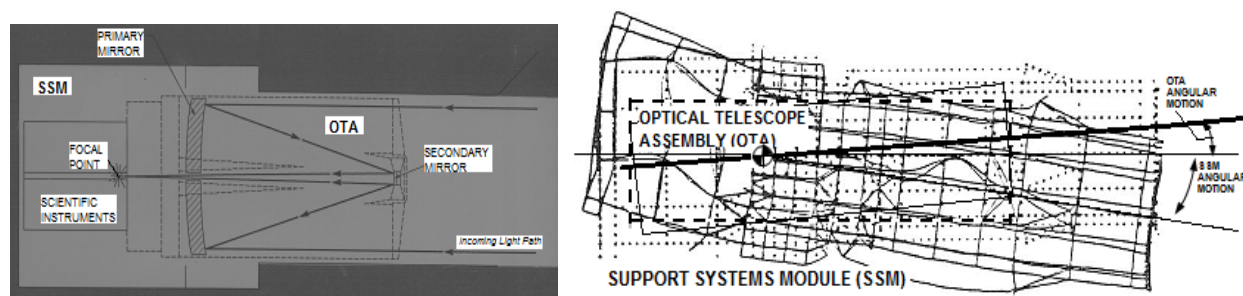


Figure 6. LOS Reflective Optical Path Diagram & Scissors Mode Dynamic FEM Plot (Pitch Direction)<sup>9,11</sup>

### Lessons Learned: Historical Background and Perspectives on Unforeseen HST Jitter Problems

Early HST efforts (rudimentary computing technology) predicted structural dynamic disturbances by use of laborious hand calculations and relatively simplistic calculator/computer analysis. Finite Element Model (FEM) static stress analysis was barely more advanced and transitioning simultaneously alongside classic hand calculations/checks; as an example, stress analysis result uncertainties still necessitated classic full-scale extensively-instrumented Proof Load tests. Maturing during HST Preliminary/Critical Design Review efforts (circa 1978) were sufficiently capable, more readily available, and reasonably reliable Structural Dynamic modeling-analyses tools to begin to compute end-to-end disturbance/jitter characteristics with improved details including, for the first time, more refined secondary effects. Around 1982, emergent ray-trace modeling tools (e.g., employing Zernike polynomials) provided actual magnification-derived LOS values for individual optical elements moving/distorting relative to each other and a centralized reference



LOS path. Dynamic FEMs<sup>11</sup>, due to computationally intensive eigenvalue calculations, were judiciously reduced (limited to ~900 dynamic Degrees-of-Freedom (DOFs) and 412 nodes-gridpoints) as compared to much larger DOFs (>10 times) in structures-stress static models. This helped offset conflicting needs of having adequate analysis fidelity yet computer runs (via the most capable computers available) that could complete within practical timeframes. These were typically a cluster of all-night runs (~15 hour run-time if not encountering convergence problems) taking several days to compile 157 modes (0-to-75 Hz). Many cross-checks/iterations occurred on the reduced dynamic FEM to prove stiffness properties replicated more refined stress FEMs plus mechanical assembly prototype test results. High criticality was placed on meeting regular re-analysis deadlines, so a significant amount of pre-computation efforts were expended on sparse-matrix sequencing methods and trial-and-error connectivity-optimization schemes to compress run-times lower within an assortment of additional competing constraints, e.g., most capable computer available (Sperry Univac 1100/92; 36-bit, 133MFLOPS) vying with top-priority classified programs' runs.

During a typical LOS jitter evaluation (re-assessed often due to evolving mass properties data, structural refinements, and updates of stiffness values), that involved checking all mechanical disturbers (e.g., tape recorders, high-gain antenna gimbals, RWAs), an unexpected RWA jitter impact was unexpectedly discovered coming from a very subtle model input coding error. Upon reviewing a typical RWA overnight run's graphical jitter results, a high-amplitude (i.e., ~5 times normal; significantly exceeding specification) spike of jitter appeared at a previously unseen higher frequency (~30 Hz) that had no analog in any prior results. This highly anomalous result prompted an intensive and focused effort of input data review and re-checks/cross-checks. Using some model insights (e.g., what compound dynamic modes were showing high generalized responses near that frequency) and localization (e.g., what input-output response combinations are proximate to responsive LOS optical elements) plus multiple trial-and-error eliminations, appearance (and disappearance) of the large jitter value was related to a single RWA mass property input line of code. Although continuation of data values on a line was allowed by the modeling-analysis program (with no error indications), data extensions were truncated/ignored at 80 characters due to prior program limits of punched card inputs not noted in computer code documents. Subsequently, this got corrected to allow *unlimited* input strings via continuation symbols. However, this investigation created a totally new serendipitous insight beyond just a trivial code error. This tiny error caused a specific RWA mass property (local "rocking" rotor inertia) to be reduced, but valid within the code's execution/error detection abilities. Thereby, on the given base stiffness (a validated value), driving RWA local IV disturbance moments to more effectively stimulate a very-high-frequency complex mode (~90 Hz) previously not believed to be a jitter issue. Amplified by the local RWA mode, IV inputs were injecting much larger generalized modal moments directly into the rigid SSM core/base structure; in turn, efficiently driving a previously unrelated angular coupled modal displacement at a higher and complex-system-mode frequency involving a smaller relay Optical Telescope Assembly optical element, namely secondary mirror motion. This created the very first analytical awareness that, after significant mitigation of the 4 main RWA-scissors-mode/fine-balancing concerns discussed above, a "new" system issue suddenly developed into a formidable jitter threat from RWA high-frequency inputs (not amenable to simple unbalance corrections) stimulating local IV-input modes that could then couple with higher frequency resonant modes locally dithering optical components. Such high-frequency modal response, combining with test-derived low structural damping (~0.005) at small forcing amplitudes, needed much less (~25 times) input forces/moments than previous IV/unbalance disturbance values. HST's secondary mirror's suspended mass is ~5% of the primary mirror's mass; minute angular movements through a very high effective optical magnification displaced it sufficiently to impact LOS jitter.

This near-overnight revelation radically transformed previous jitter-problem paradigms. Engineering pursuits immediately shifted to ferret out high-frequency disturber characteristics, along with much more attention to accurately model refinements of input disturbers' mounts and regions near optics, especially proximate support structure stiffness elements. All this while still adhering to severely limited FEM DOF detailing/frequency-range constraints. This also led directly to assuring highly optimized (i.e., high local stiffness still within tight mass limitations/budgets) RWA support-mount structural element representations to drive local response modes up in frequency (target >60 Hz, based on the next higher local compliance being RWA mounting-tab-to-outer ring stiffness that was difficult to redesign), without creating new side

effects, e.g., more optical-mode complex cross-couplings. A highly-iterative effort, involving stress, design, and manufacturing engineers, eventually found a viable design approach meeting strict mass limits.

As a related aspect, significantly stiffer base/mount (in local DOFs) and improved knowledge of RWA high-frequency outputs initiated a quick-response RWA vibration isolation feasibility assessment. Those results led directly to developing a unique fluid-damped passive vibration isolation system (e.g., Fig. 4), applying a pseudo-kinematic interface approach while retaining HST Orbital Replaceable Unit capabilities via astronauts using standard tools<sup>8,9</sup>. Findings and techniques were later applied to large aeronautical and aerospace systems<sup>12,13</sup>. Insights also directly caused investigation of IV high-frequency harmonics, how IV is modeled/bounded, sources for IV variation amount evidence, and data regarding IV measurements of ground-vs-orbit uncertainties/variations<sup>14</sup>. Concerns also emerged about the potential for a dense field of IV harmonics (see Fig. 5 rightmost resonance zone) to converge via a non-obvious combination of input forces-moments to create a “perfect resonance storm”, collectively stimulating a reactive high-frequency complex mode involving several smaller optical components. Data on realistic damping values were also investigated due to emerging evidence that classic high-amplitude damping approaches (i.e., elastomerics) tend to substantially diminish at low force levels; prior analyses used damping derived from high-amplitude forces (~3%; i.e., launch-level vibrations). Fortunately, due to efforts attacking 4 jitter priorities (above), IV test setup detection capabilities could effectively collect sufficiently sensitive amplitude-spectral data with minimal modifications thereby avoiding yet another added development-improvement effort. The author had sole responsibility for dynamic modeling, model validity, substantiating damping data, RWA isolation system requirement development, and jitter result accuracy verification during this time. Regularly, separate high-detail dynamic models were rapidly created for a key subassembly or unit to then integrate a simplified version into the full HST model that closely replicated local mode frequencies/shapes. Efforts included successful conduct of a thorough model audit/review with NASA Subject Matter Experts. Due to such attention/refinements, subsequent HST modal tests concluded that analysis results compared very well with the pre-test structural dynamic model<sup>2</sup>. For a period, circa 1985, this Level 1 RWA-IV-based LOS jitter requirement threat was the foremost program technical concern, receiving considerable attention and visibility at quarterly reviews. Although not a heroic save of HST performance, its importance is notable.

### **RWA IV Disturbance Source Considerations Relative to Classic Wheel Bearing Imperfections**

HST RWAs are deemed state-of-the-art (for their size) due to several unique aspects: 1) strict screening of matched duplex bearing sets via preliminary runout measurements and added data checks acquired in pre-acceptance runs on a fine-balanced EDU rotor (e.g., <50% yield for flight-qualified ABEC 9 production lots), 2) unusually high number of fine-balance iterations, 3) attention to spectral signature/trends in fine-balance iterations, and 4) lubricant (derived Andok C) tailoring for robust stability in HST operating conditions. The RWA vendor was highly motivated by a potential to advance existing knowledge of low-noise wheels. IV arises from 3 primary imperfect root causes: 1) rotor-bearing assembly mass unbalance/asymmetries, 2) minute bearing/race/retainer imperfections, and/or 3) drive configuration/physical forces. These can be separately differentiated, but, as combined, create the total disturbance output spectral signal. In theory, using first-principle fundamental physics, precise definition of bearing parameters/geometry, tolerance build-up, and misalignments would allow near-perfect knowledge of all detected IV ratios and provide some indication of relative intensities. However, in practice, spurious microscopic-level effects (e.g., lubricant/tribological interactions, surface conditions/finish, temperatures, minute ball bearing preload fluctuations, etc.) manifest as deviations in internal contact-surface placements and amplitude excursions which exponentially grow with rotation speed, but are not possible to consistently predict or practicably ascertain in use. If a candidate geometric-based imperfection(s) is below a readily measurable threshold (or is excessively difficult/costly to investigate or measure further), a deeper quantitative root is not tractable; e.g., ball bearing/cage localized out-of-roundness or duplex-pair-to-duplex-pair eccentricities.

### **Primary Static-Dynamic Unbalance on Rigidly Mounted Rotating Masses as Applied to RWAs**

Rotor balance and related bearing stability/dynamics is well studied and analyzed<sup>15,16</sup> and summarized here for high-precision RWAs. Figure 7 shows key parameters and balance quality grades. Once specifying a

grade/limit, a maximum allowable residual unbalance (e.g., in g-mm/kg) is determined for the rotor mass and prescribed service/reference speed. Note that maximum allowable residual unbalance calculations assume that rotor mass is evenly distributed about the center-of-gravity and along the shaft between bearings. For reference, a typical (~10 lb<sub>(mass)</sub>) spacecraft RWA static balance limit is 0.007 oz<sub>(mass)</sub>-in; equating to 44 μ-inch (1.1 μ-m) unbalance offset. HST's large RWA (44 lb<sub>(mass)</sub>) rotor) spec limit is 13.4 μ-inch (0.34 μ-m). One RWA's post-environment IV test resulted in 2.5 μ-inch (0.063 μ-m), an 80% margin.

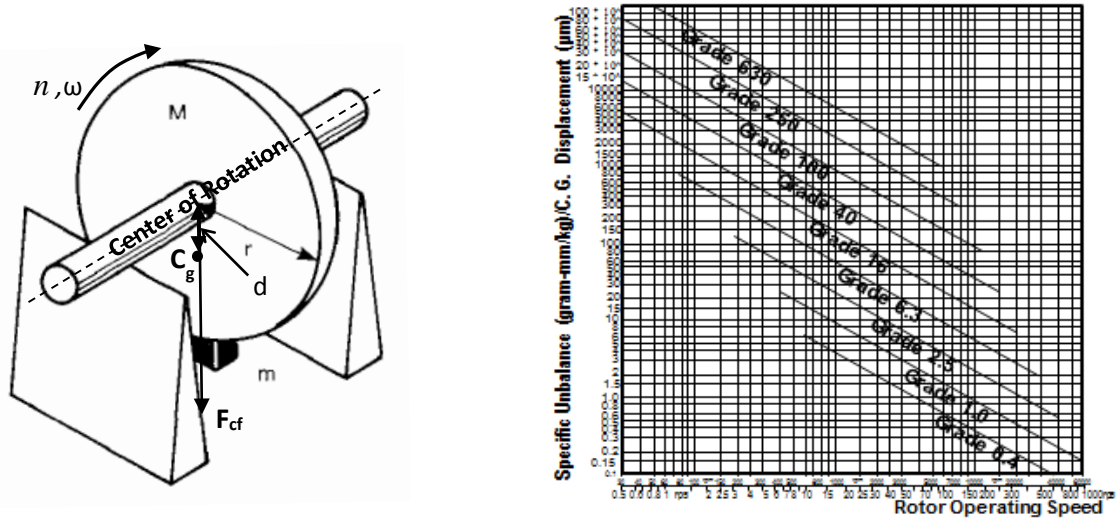


**Figure 7. Rotating Mass Unbalance Parameters & ISO Standard 1940 Balance Quality Grades<sup>15</sup>**

Output sinusoidal centrifugal force amplitude ( $F_{cf}$ ) is related to rotor unbalance parameters by the following:

$$F_{cf} = M * d * \omega^2 = M * d * (2\pi f)^2 = M * d * \left(2\pi \frac{n}{60}\right)^2$$

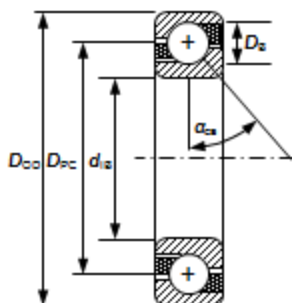
Where M is rotor mass, d is effective distance between rotor center-of-rotation and center-of-gravity/mass, ( $C_g$ ), and operating rotation rate is given by n (RPM), f (Hz), or ω (angular velocity in radians/second). For a designated ISO Standard 1940 Balance Quality Grade, the fundamental relationships are:

$$e = \frac{v}{1000 * \omega} = \frac{v}{1000 * 2\pi f} = \frac{v}{1000 * 2\pi * \frac{n}{60}}$$

Where e is specific residual unbalance (gm-mm/kg)/displacement (μm), v is balance grade (based on angular rate and relatable to effective radius d via rotor mass); rate parameters are as above. Resulting RWA unbalance (1.0-ratio) IV propagates at a frequency matching the commanded rotation frequency.

#### IV-Related Empirical Findings Relative to Bearing Geometries and Geometric Imperfections

Since IV characterization stems from fundamental bearing design aspects, geometric parameters lead to IV ratios/relationships. For example, HST RWA bearings (a tailored variant of commercially available 304H-type angular contact ball bearings) have design dimensions shown in Table 3 relative to Figure 8.



BEARING PARAMETER	304H NOM. VALUES	101-TYPE NOM. VALUES
Inner Bore ( $d_{IB}$ )	20mm (0.7874 inch)	12mm (0.4723 inch)
Outer Diameter ( $D_{OD}$ )	52mm (2.0472 inch)	28mm (1.024 inch)
Pitch Circle Diam. ( $D_{PC}$ )	35.6mm (1.402 inch)	20.2mm (0.796 inch)
Ball Diameter ( $D_B$ )	11.1mm (0.438 inch)	4.7mm (0.1875 inch)
Number of Balls (N)	8	10
Contact Angle ( $\alpha_{CA}$ )	18.6 degrees	15.0 degrees
Material	52100 CEVM	52100 CEVM
Tolerance Class	ABEC 9	ABEC 9
Max. Runout Allowed	.0012 mm (.000047")	.0012 mm (.000047")
Bearing Configuration	2 DF Duplex Pairs	2 DF Duplex Pairs

**Figure 8 and Table 3. 304H & Comparable 101H-Series Bearing Basic Design Parameter Values [9]**

### Bearing Retainer Vibration Harmonic Ratio Calculations for a Forced Rotation Situation

Based on classic bearing theory, with an analog to planetary gear systems with a static outer ring gear and driving-torquing sun gear, the two fundamental relationships between vibrations caused by inner/outer ring raceway ball-contact imperfections are related via the cage/raceway rotational speed. The ratio of bearing cage-retainer speed/frequency to inner rotor shaft speed/frequency is given by the equation:

$$\frac{f_c}{f_r} = \frac{1}{2} \left( 1 - \frac{D_b}{D_{pc}} * \cos \alpha_{CA} \right)$$

Where  $f_c$  is cage/retainer rotation speed/frequency,  $f_r$  is inner ring/shaft rotation speed/frequency,  $D_b$  is nominal ball diameter,  $D_{pc}$  is the pitch circle diameter, and  $\alpha_{CA}$  is the nominal contact angle. This leads to a key ratio value (for 304H) of 0.35. Similarly, the ratio relative to outer ring speed/frequency is given by:

$$\frac{F_c}{F_r} = \frac{1}{2} \left( 1 + \frac{D_b}{D_{pc}} * \cos \alpha_0 \right)$$

Where  $F_c$  is cage/retainer rotation speed/frequency,  $F_r$  is effective outer ring passage speed/frequency, and other parameters are the same as above. This leads to a second key ratio value (for 304H) of ~0.65.

Non-spin-axis ratios for a 304H duplex bearing pair would all have a theoretical basis origin due to one of the following ratios: 0.35, 0.65, 1.0, 8.0 (same-ball inner return ratio), or 0.0588 (1/17; same-ball-retainer geometric alignment return ratio). Other ratios are known to exist (i.e., Fig. 5), however, were of significantly lower intensity or are difficult to identify at RWA dwell speeds prescribed in test procedures. For HST RWAs, IV tested/tracked/reported ratios (set of 8 neglecting 0.65 detection issue) are in Table 9.

**Table 9. HST RWA Bearing Set Basic IV Tested/Tracked/Reported Harmonic Ratios**

Theory-Based Ratio	Empirically-Established Ratio	Description of Root Source/Cause	Sig. Figures Known
0.3521	0.35	RATIO OF BEARING CAGE/RETAINER SPEED TO ROTOR SPEED	2
0.6479	Detection Difficult	RATIO OF BEARING CAGE/RETAINER SPEED TO OUTER RING PASSAGE	2
1.0000	1.00	MISALIGNMENT OF ROTOR CENTER-OF-MASS & SHAFT ROTATION POINT	AS PRECISE AS RWA
2.0000	2.00	SECOND HARMONIC OF 1.0 (RACE-TO-RACE MISALIGNMENT/WHIRL)	AS PRECISE AS RWA
2.8168	2.82		3
5.1832	5.18	N (# OF BALLS - 8) TIMES 0.65 (BALL PASSAGE ON INNER RACE)	3
5.6336	5.60	SECOND HARMONIC OF 2.8 (BALL PASSAGE ON OUTER RACE)	3
--	7.50	CAUSE NOT KNOWN WITH CERTAINTY; ONLY EMPIRICALLY DERIVED	~2
--	8.50	CAUSE NOT KNOWN WITH CERTAINTY; ONLY EMPIRICALLY DERIVED	~2

At first RWA IV data assessments, there was no analytical-empirical basis correlating a harmonic's amplitude to another harmonic's amplitude thus all harmonics (and their amplitude variations) were perceived as individual and independent uncorrelated entities. See discussion below concerning the validity of this viewpoint. For 101-type bearing RWA assemblies, key ratios are somewhat different, as delineated in Table 10.

Prompted by pure-analysis deficiencies, empirical IV data have dominated quantifying RWA disturbance macro characteristics, harmonic ratios, IV levels, variations, and relative trends. Extractions from refined IV data studies led to a need for a comprehensive common basis to compare resultant IV macro-effects. Per classic intrinsic physical principles, some element of bearing Geometric Runout (expressed via a geometry-related value that generally rises and falls in league with overall IV amplitudes) is presumed fundamentally responsible for non-spin-axis harmonic vibrations. Since dominant effects (e.g., primary unbalance) are

directly relatable to classic parameters of imbalance coupled with bearing “goodness” (similar to long-standing static/dynamic rotating assembly methods), and since larger unbalance (very generally) causes a 2<sup>nd</sup>-order growth of all noise components as rotation rate builds, an alternate means of absolute/relative “geometric” error was sought. Setting aside design-specific harmonic ratios, an equation form is desired that can be reverted to classic unbalance-runout types of values/assessments. Also, unlike primary unbalance, its value is to enable directly relating bearings independent of rotor mass. A summary treatise, reference perspective, derived relationship, and example values for this methodology/criteria follows below.

**Table 10. 101-Type Bearing Set Basic IV Tested/Tracked/Reported Harmonic Ratios**

Theory-Based Ratio	Empirically-Established Ratio	Description of Root Source/Cause	Sig. Figures Known
0.3862	0.385	RATIO OF BEARING CAGE/RETAINER SPEED TO ROTOR SPEED	2
0.6138	Detection	RATIO OF BEARING CAGE/RETAINER SPEED TO OUTER RING PASSAGE	2
1.0000	1.00	MISALIGNMENT OF ROTOR CENTER-OF-MASS & SHAFT ROTATION POINT	AS PRECISE AS RWA
2.0000	2.00	SECOND HARMONIC OF 1.0 (RACE-TO-RACE MISALIGNMENT/WHIRL)	AS PRECISE AS RWA
3.8623	3.88	10 (# OF BALLS) TIMES 0.39 (BALL PASSAGE ON OUTER RACE)	3
4.0000	4.00	THIRD HARMONIC OF 1.0 (RACE MISALIGNMENTS/COMPOUND WHIRL)	AS PRECISE AS RWA
6.1376	6.14	10 (# OF BALLS) TIMES 0.61 (BALL PASSAGE ON INNER RACE)	3
--	7.17	CAUSE NOT KNOWN WITH CERTAINTY; ONLY EMPIRICALLY DERIVED	~2
7.7246	7.72	SECOND HARMONIC OF 3.85 (BALL PASSAGE ON OUTER RACE)	3
8.0000	8.00	FOURTH HARMONIC OF 1.0 (RACE MISALIGNMENTS/COMPOUND WHIRL)	AS PRECISE AS RWA

### Geometric-Based-Error Method Allowing Direct Comparison of Harmonic Disturbance Magnitudes

Based on empirical HST RWA IV datasets plus a quest for comparing similar configuration bearings with other sizes (i.e., varied harmonic ratios) and local directions, a quantity termed “Equivalent Geometry Error” ( $E_{GE}$ ) was established as a straightforward approach for analytical evaluation based on a least-squares best-fit-curve methodology imposed on IV second-order equations, facilitating direct comparisons related to amplitudes present in compound harmonic IV signals' data. It was intended to apply to any RWA data acquired by similar test criteria and number of data points (i.e., via computing curve-fit second-order coefficients). Fundamental  $E_{GE}$  is computed for a chosen harmonic ratio via the following formula:

$$E_{GE\ n} = C_n \frac{\sum (F_{ni} * \omega_{ni}^2)}{\sum (\omega_{ni}^4)}$$

Where  $C_n$  is a varying constant for a particular harmonic ( $n$ ) and, for HST RWAs, is equal to the following 4 key values when wheel speed ( $\omega_{ni}$ ) is expressed in revolutions-per-minute (RPM), output sinusoidal force peak amplitude ( $F_{ni}$ ) is expressed in pounds (lb), and  $E_{GE}$  ( $E_{GE\ n}$ ) is expressed in inches (in).

$$C_{1.0} = 821.5 ; C_{2.0} = 205.3 ; C_{2.8} = 103.3 ; \text{ and } C_{5.2} = 30.6$$

When derived in stated parameter units, resulting units are in/lb-min<sup>2</sup>. Note these are also relatable independent of DOF. As derived from IV datasets, the number of points used needs to be enough for reasonably consistent computation stability (varies by frequency range), yet not so many to interpose distorting effects of RWA/fixture resonances; points typically range 4-20. This may require insightful judgment/iterations for the optimum number of points for calculations while rejecting data outliers.

### Induced Vibration Harmonic Ratios Basis in RWA Spin-Axis Torque/Moment Primary Direction

Spin-axis harmonic ratios are governed by an entirely separate set of physical effects compared to other IV DOFs. Design-specific drive motor physics/construction creates minute fluctuations (termed torque

ripple) in otherwise steady torques imparted to the RWA ring-tab-base-mount rigid structural interface at ratios differing from non-spin-axis forces/moments. HST's RWA motor is a 2-phase, 8-pole, brushless direct-current design with resolver, a configuration resulting in torque ripple harmonic ratios summarized in Table 11. Internal control/filtering features are utilized to minimize all except the 16.0 and 32.0 harmonics. RWA torque ripple limits are standardly specified (with margins), and precisely measured in acceptance tests. Note that, as verified for HST, torque ripple IV dynamics are a negligible (i.e., nearly undetectable analytically or in system tests) contributor to overall optical system LOS jitter for all but the very lowest frequency modes and under assumed worst-case maximum levels. The low torque ripple DOF result is due to convergence of several favorable jitter factors: 1) electro-magnetic origins lead to readily-applied circuit/processing minimization techniques, 2) IV amplitudes are extremely low compared to other local moment DOFs in primary RWA operational speed ranges, 3) high relative rotor inertia, 4) much higher relative rotor structure effective stiffness (i.e., much higher internal rotor torsional mode frequencies), 5) much higher HST structural ring effective stiffness, and 6) intrinsic HST structural dynamic mode impediments to enable stimulating complex-compound optical paths/components to cause LOS jitter. Also favorable is that torque ripple levels are reliably less than required limits, highly stable over time (i.e., no significant wear source), and not measurably affected by operating conditions or environmental changes.

**Table 11. HST RWA Spin-Axis Motor-Design-Driven Harmonic Ratios**

<b>Theory-Based Ratio</b>	<b>Empirically-Established Ratio</b>	<b>Description of Root Source/Cause</b>	<b>Sig. Figures Known</b>
4.0000	4.00	COMBINED RESOLVER & ELECTRONIC DEMODULATION OFFSET WITH OTHER EFFECTS; DC BIAS OF EITHER SINE OR COSINE WINDING	AS PRECISE AS RWA
8.0000	8.00	ELECTRONIC GAIN MISMATCH; MISMATCH OF SINE/COSINE WINDING CURRENT AMPLITUDE FOR GIVEN COMMAND	AS PRECISE AS RWA
12.0000	12.00	ELECTRONIC NONLINEARITIES	AS PRECISE AS RWA
16.0000	16.00	MOTOR-RESOLVER RIPPLE; RELATED TO WINDING TYPE/CONSTRUCTION	AS PRECISE AS RWA
32.0000	32.00	MOTOR-RESOLVER RIPPLE; RELATED TO WINDING TYPE/CONSTRUCTION	AS PRECISE AS RWA
48.0000	48.00	COMBINED ROTOR-RESOLVER RIPPLE & MOTOR COGGING, DUE PRIMARILY TO MAGNET ATTRACTION NEAR LAMINATION SLOTS	AS PRECISE AS RWA
96.0000	96.00	MOTOR-RESOLVER RIPPLE; RELATED TO WINDING TYPE/CONSTRUCTION	AS PRECISE AS RWA

#### **Feasibility Investigations Validating a Chosen 4-Harmonic Subset for Adequate LOS Jitter Assessment**

Upon thorough study of this abundance of potential jitter error contributors and harmonic ratios, there quickly arose a huge obstacle: managing such a tremendous amount of data inputs and output assessment summaries. It seemed a potentially impossible task due to so many separate data/combinational elements:

- Virtually unlimited number of individual RWA IV frequencies to dwell at within predicted range limits
- 157 dynamic modes (to 75Hz) in jitter evaluations; at practical model/analysis computational limits
- 3 LOS jitter axes; vertical, lateral, spin about image plane centerline (HST pitch, yaw, roll)
- 5 RWAs (one spare – but any 4 could be potentially used); each with its own unique IV signature
- 20 possible RWA-location permutations 5 flight-certified RWAs could be in any of 4 flight positions
- 6 local DOF IV input force/moment signals for each RWA; with further breakdown as follows
  - 20 detectable axial-force harmonic ratios applicable to 1 principal local DOF on each RWA
  - 28 detectable radial-force harmonic ratios applicable to 2 principal local DOFs on each RWA

- 7 known axial-moment harmonic ratios applicable to 1 principal local DOF on each RWA
- 8 (at least) known radial-moment harmonic ratios applicable to 2 principal local DOF per RWA
- 20 viable flight-unit sets of IV datasets; a mix of partial (i.e., due to penalty re-tests) and full
- 30 axial-DOF isolation system stiffness-damping combinations to evaluate; with and without isolators
- 34 radial-DOF isolation system stiffness-damping combinations to evaluate; with and without isolators

Changing any single one of these elements/parameters results in a different jitter pass-fail value compared to specified limits. Based on prior results, none of these individual aspects could be readily dismissed as insignificant in ferreting out a previously undiscovered but potentially crucial LOS impacting combination. For one specific example, most results (but not all) showed jitter-budget peaks/threats (within operational frequencies) dominated by axial forces, where fine-balancing has no mitigating effect; a counterintuitive outcome compared to conventional wisdom that radial force unbalance is most likely to threaten jitter. The potential permutations seemed endless, most formidable being so many harmonics present in the 5 RWA DOFs. One fortunate aspect was, due to such low damping (i.e., 0.005), the computed damped frequency of a potential high-jitter-response mode is essentially equal to its computed undamped frequency (within ~2-3%), therefore, jitter analyses were constructed to evaluate response at each specific computed mode frequency (i.e., eigenvalues; 157 for full HST orbital model), with inserts of intermediate-increment values smoothly bridging the region between a computed mode peak and the overtaking rising portion of the next-higher-frequency jitter spike (again, due to low damping's very sharp peak). Once these means were accomplished (in conjunction with a separate jitter assessment determining solid baselines for 4 most-likely flight RWAs with adequate data choosing a representative and full dataset for each), studies shifted to compare jitter results using a robust subset containing the 4 most prominent IV harmonic ratios (i.e., 1.0, 2.0, 2.8, and 5.6 in 2 radial and 1 axial DOFs) versus an entire set of detected harmonic ratios (30 axial; 34 radial). By comparatively using all harmonic ratios from a representative high-amplitude dataset for each RWA DOF, results showed conclusively that 4 key harmonic ratios (e.g., Fig. 9) are excellent indicators for RWA jitter predictions and establishing a jitter baseline for further isolation and placement optimization studies; while maintaining timely and efficient computational processing and reporting<sup>14</sup>.

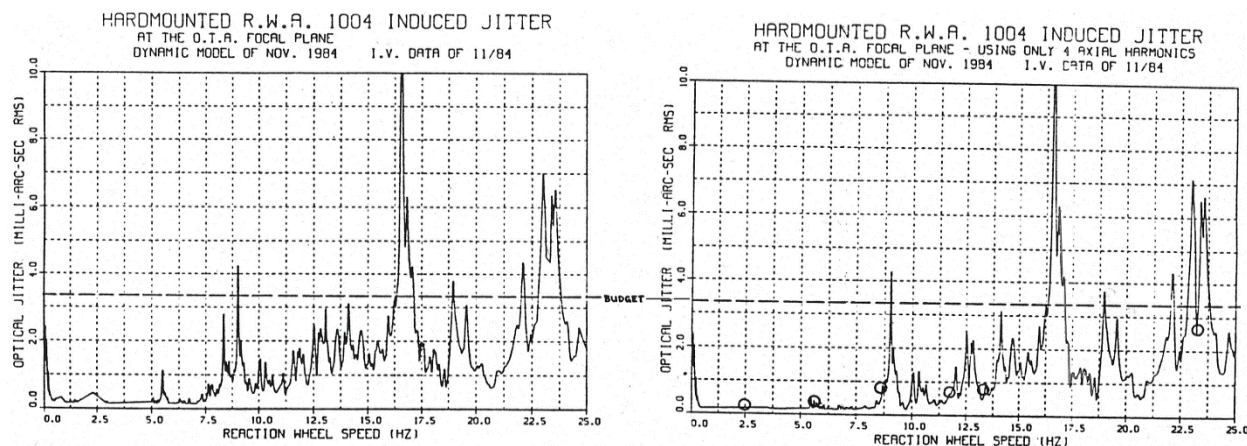


**Figure 9. LOS Jitter Results using All RWA IV Harmonic Ratios versus Subset of 4 Key Ratios<sup>14</sup>**  
**[Circles are limited spots where 4 key ratios under-predict jitter spikes compared to full-set results]**

#### **Lessons Learned: Newly-Refined Correlative Analytical Investigation for RWA IV Key Harmonics**

Fundamental conjecture, based on first principles, initially supposed that residual unbalance coupled with stringent bearing/retainer tolerances define the means to successfully ensure low-IV rotating assemblies. As this IV investigation demonstrated via statistically robust harmonic ratio data mining, there is much more to this basic characterization for a specialized fine-pointing application. Knowing what IV output frequencies,



as a function of realistic RWA operating speeds, are dominant can demand extensive test data and analytical exercises. However, if some ratios are found to be closely correlated, there is the potential to extrapolate or bound overall IV with substantially reduced testing/post-test analysis (i.e., early analyses results can support that a limited test data set affirms upper-level jitter requirement compliance thereby reducing test data collection). It is highly desirable that clear, robust trends emerge readily from straightforward examinations of the IV data collection; e.g., testing a hypothesis that radial force primary unbalance (1.0 harmonic) consistently tracks and predicts axial force 1.0 harmonic (or other ratios) IV data. This data set provides, for the first time, a viable opportunity to quantify potential correlations once any particular rotor-bearing physical properties / harmonic relationships are known within consistent bounds. This creates a practicable set (12) of candidate correlations (relying upon the 4 key harmonic ratios) within each DOF (3; axial force, radial force, radial moment) and dual ratios (4; 1.0-to-2.0, 1.0-to-2.8, 1.0-to-5.2, and 2.8-to-5.2). Extending further, 12 DOF cross-axis pairings are correlated (12; same-ratio pairs). If no strong correlations exist within these 24 IV pairings (some are, in first-order theory, tied to the same root imperfection; while some are not), then reaching for even more obscure relationships would not likely be fruitful for the efforts expended (e.g., test data collection system noise dominates relationships). Until such analysis is conducted, there is no solid analytical basis for common relationships in data sets or root imperfections. The E<sub>GE</sub> methodology discussed above (via 2<sup>nd</sup>-order coefficients) serves as a common basis for cross-harmonic comparisons. IV harmonics with relatively poor and good correlations are in Figure 10: E<sub>GE</sub>s in units shown above. Summarizing, results are mixed yielding some but few strong correlations.

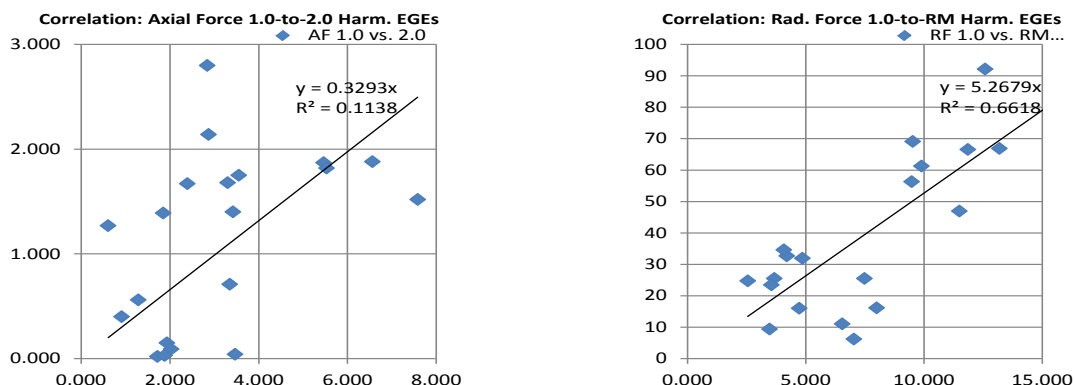


**Figure 10: Examples of Relatively Low (AF1.0-AF2.0) & High (RF1.0-RM1.0) IV Data Correlations**

### RWA IV Analytical Assessment Investigation Overview/Summary

Multiple flight IV datasets, addressing known/available RWA vibrational and variability data sources, are researched, analyzed, and compiled herein; a valuable reference for comprehensive RWA jitter analysis characterizations. Specifically, this treatise: 1) collects, compares, and statistically evaluates 4 dominant harmonics for 20 IV ground-based data sets in local principal RWA axes, 2) exposes rationale for the relative dominance of those 4 harmonics for jitter predictions, and 3) presents comparative data on 32 previously undetected/unknown less prominent harmonics. Values are presented via a combination of summary tables and graphs. This also provides fundamental insights for pre-determining rotor-bearing factors driving IV harmonic ratios, estimating same-size/design bearing characteristics, and solidifying the validity, applicability, and robustness of IV measurements when several factors are considered that may significantly skew actual LOS on-orbit jitter amounts away from test-based analytically-predicted values.

### Specific Basis, Background, and Objectives for Overall RWA IV Dataset Investigation Effort

Effects potentially impacting IV values (and are present in ground-to-orbit transitions) have been explored with the RWA supplier's SMEs and summarized below. Specific IV study super-objectives are:

- 1) determine values and ferret out attributable root causes of IV known variations that directly affect ground-ambient measured IV test data value differences, and

- 2) determine magnitude bounds for expected variability present in applying IV test data values acquired in ground test lab-ambient conditions to the on-orbit jitter performance analyses.

The two foremost bodies of data/knowledge available to address these study goals are, chronologically:

- 1) large body of test data accumulated on a comparably-sized CMG production program at the RWA supplier under independent engineering and Research & Development investigations, and
- 2) 20 IV data sets obtained on delivered RWA flight complement set (4 flight units, 1 spare).

This study combines applicable data available from these 2 key database sources. It also introduces heretofore unpublished additional relevant data and insights gained from:

- 1) early developmental tests performed on the Engineering Development Model RWA (primarily investigating the effect of different temperature extremes on RWA performance),
- 2) IV tests performed in support of RWA isolation system program development (primarily concerning newfound evidence that there seems to be more potentially significant RWA harmonics than previously investigated), and
- 3) numerous discussions conducted between LM and the supplier's technical personnel conducted over a two-year timespan (i.e., primarily concerning the predicted temperature variation effects which are perhaps the most difficult to quantify/bound).

### **Induced-Vibration Variation Based on RWA Acceptance Test Series Data**

Acceptance tests on four flight RWA units (designated 1001, 1002, 1004, and 1005) and one flight spare unit (1003) were completed by the supplier and resulting data packages were delivered to LMSSC and reviewed for completeness and correctness (Ref. 1 & 2). Portions of the full acceptance test results (IV test results) have been extracted and compiled. An investigation was initiated to study and analyze in detail the 20 full or partial applicable datasets (out of 24 total) produced during all flight unit acceptance testing; four early, partially unsuccessful IV tests on the first-produced unit (1001) used a different rotor-bearing assembly, so it was not deemed applicable due to its unique mechanical configuration. It was later restored to the same configuration as the other flight units after a rework/rebuild, so only those data sets were applicable. The investigations focused specifically on: 1) assessing general data trends and consistencies, 2) quantitatively evaluating variability characteristics and factors, and 3) extracting heretofore unknown comparative data on additional harmonics. This last effort was important to assess which harmonics had a significant system-level impact on LOS jitter since it was a challenge to determine the effect based on simple first principles. It should be noted that between each dataset all RWAs are exposed to varying environmental/test conditions (e.g., Random Vibration or Thermal-Vacuum Cycling), so results exhibit effects from both: 1) variations generated by adverse environmental exposures that may alter micro-structural conditions particularly in the bearings-lubrication (i.e., conditions simulating expected launch-to-orbit and/or simulated on-orbit operating conditions), and 2) variations due to low-intensity handling and inherent test-to-test random factors (presumed to be significantly smaller than extreme environment exposures). It is impossible to determine precisely how much IV dataset-to-dataset variation is due to which of these specific causes. However, attempts were made to limit/bound the changes<sup>14</sup>.

Investigations applied the following specific methodology sequence to study/filter the large amount of IV data from the 20 data sets comprising over 3700 individual speed-with-magnitude data points total:

- 1) Accumulate, basic sort, tabulate, and scrutinize all available-viable data; exclude or interpolate-adjust highly-anomalous or significantly out-of-family data measurements (i.e., clear outliers).
- 2) Evaluate then document preliminary conclusions; founded upon prior jitter analyses results.
- 3) Compute second-order best-fit-curve coefficients for the amount (sometimes variable) of dataset points and corresponding frequencies for each dataset.
- 4) Select overall compatible criteria for establishing the "final" curve more-direct comparisons.
- 5) Compute baseline second-order best-fit-curve coefficients and equivalent geometry error values based on above-chosen criteria/comparisons.
- 6) Tabulate and graph results; evaluate results and produce consolidated conclusions.

A top-level list of all RWA IV acceptance test datasets (24) and subsets (20) studied are in Table 12. Consolidated tables of detailed dataset values for local RWA directions and harmonics are in Appendix A. Computational results of second-order coefficients and root-mean-square (RMS) errors for best-fit-curves,

involving varying numbers of data points (rotation speeds) per curve, for key harmonics are in Tables A-1 to A-5. These tabulations established the foundation for final criteria to evaluate dataset curve differences. Rationale/justification for final selection of axial data points used for comparative evaluation of the four primary harmonics in local axial force, radial force (2), and radial moment (2) directions is in Appendix B. The four harmonics, as discussed above, are sufficient for HST LOS jitter analytical assessments<sup>14</sup>.

**Table 12. Master Tracking List for All HST RWA Acceptance Tests Containing IV Datasets<sup>14</sup>**

RWA No.	Func. Tests Completed	IV Tests Completed	Test Data Name/Designation	Start Date	Data Vol.	Comments
1001	9	8	1 – First Full Functional	11/26/84	IV	Full IV Set ← Rotor Rebalanced
			2 – First Full Func (Retest)	11/29/84	IV	Full IV Set
			3 – Post Vibe Abbr. Func.	12/04/84	V	Minimal IV ← Rotor Changed**
			4 – Final Full Functional	12/11/84	VI	Minimal IV
			5 – Abbreviated Functional	01/06/85	VII	Partial IV Set
			6 – Abbreviated Functional	01/16/85	VII	Partial IV Set
			--- Mini-Functional	01/18/85	VIII	No IV Data
			7 – Abbreviated Functional	01/21/85	VIII	Partial IV Set
			<b>8 – Final Functional Test</b>	<b>01/26/85</b>	<b>IX</b>	<b>Full IV Set [Jitter Baseline]</b>
1002	4	3	1 – Ambient Functional	12/04/84	IV	Partial IV Set
			2 – Post Vibe Abbr. Func.	12/07/84	V	Partial IV Set
			3 – Partial Abbr. Func.	02/8/85	V	No IV Data
			<b>4 – Final Functional Test</b>	<b>02/13/85</b>	<b>VI</b>	<b>Full IV Set [Jitter Baseline]</b>
1003*	4	3	1 – First Functional	01/17/85	Prel.*	Partial IV Set
			2 – Abbreviated Functional	01/19/85	Prel.*	Partial IV Set
			3 – Partial Abbrev. Func.	07/08/85	Prel.*	Partial IV Set
			4 – Final Full Functional	---	---*	---*
1004	8	6	1 – First Full Functional	09/15/84	IV	Full IV Set
			2 – Post Vibe Abbr. Func	09/21/84	V	Full IV Set
			3 – Abbreviated Functional	11/18/84	VI	Partial IV Set
			<b>4 – Final Full Functional</b>	<b>11/23/84</b>	<b>VII</b>	<b>Full IV Set [Jitter Baseline]</b>
			5 – Short Functional	01/05/85	VIII	No IV Data
			6 – Final Abbreviated Func.	01/08/85	VIII	Partial IV Set
			7 – Mini Functional Test	01/18/85	IX	No IV Data
			8 – Abbreviated Functional	01/21/85	IX	Partial IV Set
1005	6	4	1 – First Full functional Test	11/25/84	IV	Partial IV Set
			2 – Post Vibe Abbr. Func.	12/09/84	V	Partial IV Set
			3 – Short Functional Test	01/05/85	V	No IV Data
			<b>4 – Final Functional Test</b>	<b>01/13/85</b>	<b>VI</b>	<b>Full IV Set [Jitter Baseline]</b>
			5 – Short Functional Test	01/19/85	VII	No IV Data
			6 – Abbreviated Functional	01/23/85	VII	Partial IV Set

\* Data not yet completed and officially delivered by final compilation/reporting.

\*\* RWA 1001 prior IV data collected non-compliant and not consistent with final rotor flight configuration.

### General and Specific Findings Derived from Detailed Investigations of Compiled RWA IV Test Data

Evaluation of compiled IV data resulted in these findings (ordered roughly from general to more specific):

- 1) IV datasets generally show expected consistency, and reconfirms the fact that all flight-accepted RWAs met specification limits with no evidence of systematic test errors or glaring discrepancies.

- 2) Most variations in each RWA's data/test-to-test differences seem to be related to test apparatus/data-gathering/data-processing/handling variances/limitations versus definitive trends that clearly indicate a detectable physical change within the RWA unit.
- 3) Clearly notable anomalous data points are rare (<~1%), and appears that the supplier's computer processing program that selects peak values for harmonics is generally functioning as-expected.
- 4) Significant test data variances are observed in higher harmonics at RWA rotational speeds that place the harmonic in proximity to the known rotor-housing resonance passage frequency.
- 5) Four primary axial harmonics (1.0, 2.0, 2.8, and 5.2) generally provide sufficient data for valid set-to-set comparative evaluations: other axial harmonics were either unreliable criteria (e.g., 0.35), or provide too few data points in the range of interest for conclusive evaluation (5.6, 7.5, and 8.5).
- 6) There is no evidence of a strong correlation between overall noise data and stage-of-acceptance testing or retesting; however, the first set of data (obtained immediately after mechanical build-up, checks, and fine-rebalancing) tends to be one of the quieter sets for any individual RWA.
- 7) There is no evidence of strong correlation between final rotor unbalance level (indicated by radial force 1.0 harmonic) and overall RWA noise output/jitter (indicated by four key axial harmonics).
- 8) General correlation exists between radial force and radial moment IV for the 4 key harmonics.
- 9) Data obtained near any harmonic's passage of the RWA's internal natural resonance (~85-90 Hz) is commonly highly inconsistent from dataset to dataset; also, data for other harmonics not near the resonance range can regularly show abnormal variation due to the influence of the harmonic-passage phenomenon (another harmonic), so should always be checked for validity/outlier status.
- 10) The qualitatively noisiest overall dataset appears to be set #5 on RWA 1004; quietest overall dataset appears to be set #1 or #3 on RWA 1003.
- 11) The most "typical" dataset recommended for preliminary jitter assessment for RWA 1003 is #3.
- 12) The RWA 1004 2.0 harmonic data (all DOFs) is consistently abnormally low (no known reason); speculation is inordinately small values for imperfection in runout(s) and bearing cage roundness.
- 13) Overall qualitative noise rankings for HST RWAs (ordered noisiest to quietest) are:

Ranked by Force Unbalance  
[1.0 Radial Harmonic]

- 1) 1005
- 2) 1003
- 3) 1001
- 4) 1002
- 5) 1004

Ranked by Overall Noise Output  
[Using 4 Key Axial Harmonics]

- 1) Tie – 1001
- 1) Tie – 1005
- 3) 1002
- 4) Tie – 1004
- 4) Tie – 1003

- 14) Datasets chosen for most-representative-but-not-overly-quiet (therefore as-tested, but leaning to normal-to-high noise variance) baseline HST jitter predictions (e.g., investigations for isolation properties studies) are #4 (1001), #3 (1002), #4 (1004), and #3 (1005); all are full datasets from last full functional acceptance test runs, and have the following qualitative validity assessments:
  - 1001 – no clear trend; 1.0 and 2.8 harmonics tend low, while 2.0 and 5.2 tend high.
  - 1002 – tends to be somewhat higher values overall than average 1002 dataset
  - 1004 – typical dataset
  - 1005 – typical dataset

#### **Orbital IV Structural Dynamic Predictive Capability Evaluations and Results Confirmation**

As discussed above, HST ground modal test investigations, via a suspended (stowed configuration) with flight-like units plus mass simulators substituted for some equipment boxes/modules, confirmed excellent correlation between data and pretest analytical results for structural mode frequencies, mode shapes / transmissibilities, damping, and predicted known-source responses. Findings validated models required for dynamic load/clearance requirement verification (i.e., launch and ascent) and jitter evaluation (deployed configuration not practical to realistically ground test). Although a recommended Lockheed plan was put forth enabling on-orbit measurements (e.g., using a minimal set of accelerometers, largely based on already-installed ground test instrumentation) to verify HST dynamics and jitter performance, NASA chose to not fund such efforts. The decision was predicated upon a low and acceptable risk assessment; wherein existing evidence supports that all on-orbit disturbances are identified, accounted for, worst-case bounded,

and met system requirements (with margin). However, with the unexpected on-orbit discovery of a thermal-change-induced sudden energy release causing the PCS performance to fail requirements, alternate forensics were improvised to check suspected source(s) and the nature of the phenomenon<sup>17</sup>. The only onboard sensors deemed sensitive enough to obtain dynamic data were gyros, HST-designated Rate Sensor Units (RSUs). RSU telemetry, along with the correlated dynamics allowed the root cause to be well-correlated with other data (e.g., via event timing and which known mode frequencies are excited by the phenomenon plus what disturbance locations are likely to excite particular modal responses) and eventually traced to locations within the 2 solar arrays. Extremely flexible when deployed (due to weight-optimized design), solar arrays with extended bi-stem supports were expected to slowly deform when reacting to thermal changes transitioning through terminator crossings from orbital day to night. However, it was discovered instead that one solar array would “lock-up” for some time then abruptly snap into a different bowed position. This sudden impulse was sufficient to cause FGSs to lose interferometric lock on designated guide stars reverting to coarse-sensing mode and typically resulting in a loss of science. The ensuing investigation found a documented history of orbital disturbances occurring during transitions from orbital day-to-night (EOD) and night-to-day (EON), plus near-steady-state conditions during middle of orbit day (MIDD) and middle of orbit night (MIDN)<sup>17</sup>. RSU telemetry data sensing vehicle rotational rate changes were extensively measured under these conditions, and these data proved useful in computing linear accelerations experienced on the spacecraft at given distances from the HST center-of-gravity<sup>18</sup>.

These established capabilities allowed, for the first time, an opportunity to confirm other orbital dynamic jitter-related predictions thereby, also opening an applicability to other large space platform microgravity predictive approaches<sup>4,12</sup>. Subsequently, a unique analytical effort was initiated to compute HST structural dynamic responses (accelerations) due to prescribed input forces/moments substantiated with actual on-orbit telemetry measurements for a specific known input disturber propagating through proven HST dynamics to a sufficiently sensitive and known output receiver. Although RWA IV input levels were well-established due to earlier efforts described, viable direct orbital response results for RWAs was not practical due to several pragmatic issues: 1) as researched, ground-to-orbit RWA IV variability could be substantial and non-deterministic<sup>14</sup> (i.e., although it had been bounded, it could not be precisely known within that range what long-term IV level was present on any given RWA at a particular time), 2) telemetry acquisition data rates were not high enough to readily resolve key high-harmonic-ratio signal components (one of the factors supporting the earlier decision to not pursue on-orbit jitter verification), 3) on-orbit RWA rotational rates where telemetry was most available during HST science acquisition tended to be near the lowest values of pre-launch predictions (typically 0-3 Hz) which resulted in inherently very low RWA IV disturbance levels, 4) effective vibration isolation highly suppressed RWA IV<sup>9</sup>, and, lastly (due largely to such low IV levels from 3 and 4), 5) HST telemetry data had never detected nor distinctly identified a response clearly due to RWA IV frequency inputs above general on-orbit operational noise environments. However, upon further investigation, an alternative disturbance source was found allowing a highly reliable/consistent on-orbit basis for an analytical approach: Engineering/Science Tape Recorders (ESTRs). HST's ESTRs (2 onboard for redundancy) countered RWA impediments by having consistent IV-to-response knowledge: 1) highly repeatable ground test IV data showing no basis for significant variability transitioning to orbit or due to changing conditions (e.g., designed for similar performance independent of overall tape position/condition, i.e., start-of-reel/end-of-reel), 2) time-congruent telemetry available (at 2 different disturbance frequencies matching 2 stable ESTR recording rates), 3) telemetry data uniformly exhibits a dominant and unambiguous signal presence when an ESTR is on, and 4) source and receiver have distinct local orthogonal principal directions (corresponding to the ESTR input IV known dataset directions and RSU output dynamic model along with sensed response directions (i.e., no need for a coupled coordinate transformation of amplitude caused by difficulty in discerning which response directions' signal intensity was from which individual disturbance DOF). Specifically, the local primary spin axis of ESTR tape reels is coincident with the vehicle V1 axis which is also accurately aligned with one of the principal RSU sensing axes - a favorable situation.

As measured, RSU angular acceleration telemetry signals encompassed all operating onboard sources up to 20 Hz, including solar array residual motions, ESTRs, High Gain Antenna Gimbals, etc. To isolate ESTR-only contributions, a filter was applied since the effective frequency bandwidth is reliably known (quite

narrow for ESTR). An ESTR has a precise frequency output during slow-speed recording at 1.375 Hz; repeatedly reconfirmed in on-orbit tests<sup>18,19</sup>. Telemetry data are bandpass filtered (1.1-1.5 Hz) via a Blackman window for each principal HST axis (V1, V2, and V3). Bandpass rates are then differentiated for each Solar Array orbital event type, producing RSU angular accelerations. Results are multiplied by the distance to the HST C.G. to obtain an equivalent local linear acceleration at 3 specific locations. Root-mean-squared (RMS) values (over time) are then computed for each orbital disturbance period. As a specific reference, worst-case-maximum computed acceleration for the known ESTR input primary frequency (i.e., 41 inches-per-second recording rate) is 0.75  $\mu\text{g}$  (axially) and 0.49  $\mu\text{g}$  (radially).

Once the on-orbit model is correlated for the ESTR known reference source, RWA inputs are applied. Since ground-to-orbit additive RWA IV variability cannot be known with certainty, worst-case as-tested IV forces and moments (with 4 key harmonic ratios; 1.0, 2.0, 2.8, and 5.6) define input amplitudes; derived from computed coefficients<sup>14</sup>. Periodic (i.e., pure sinusoidal) time histories are created for each RWA harmonic for 2 different rotation rates: 3 Hz (nominal on-orbit maximum) and 10 Hz (typical-4-wheel case/condition upper bound). Individual time histories for the 4 key harmonics are combined by direct addition, no time-phasing nor dithering is done to simulate random phasing. Time histories are combined simultaneously at an RWA rotor source (for all local DOFs) in the HST on-orbit dynamic FEM. Resulting frequency-domain response, i.e., Fast-Fourier Transforms (FFTs), are developed; 2 typical input-output examples (10 Hz RWA) of response at the SSM Equipment Bay (EB) (V2 direction) and RSU (V1 direction) are shown in Figure 11<sup>20</sup>. Note dominant modal (i.e., non-optical here) transmissibilities at 10, 20, 28, and 52 Hz: isolation system damped resonances are present. Also note that, summed results are primarily dominated by rigid body responses to the set force/moment RWA inputs, with the additive structural response being minimal (further confirmation that the RWA isolation system is performing as intended). Summary HST results are listed in Tables 13 and 14. Note that this was a first on-orbit reference confirmation leading to the level of challenge presented in attaining low microgravity limits for the International Space Station<sup>12</sup>.

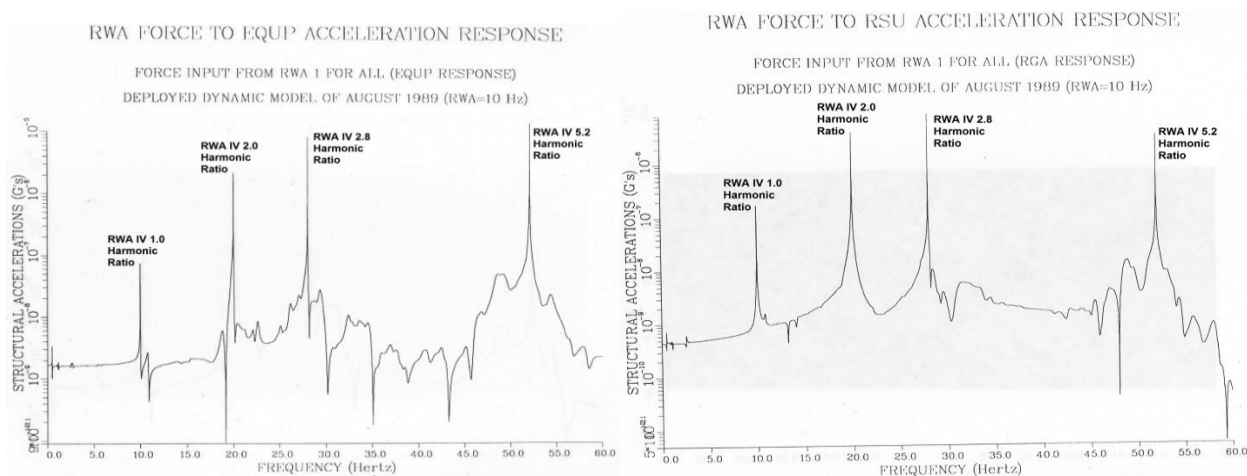


**Figure 11. HST Microgravity-Related Acceleration Response - Examples at EB (V2) & RSU (V1)<sup>20</sup>**

**Table 13. HST On-Orbit Acceleration Results; ESTR 1.375 Hz Input during Solar Array Transitions (4)<sup>20</sup>**

HST Prin. Direction	EON Event	MIDN Settling	EOD Event	MIDD Settling
V1 <sub>RMS</sub>	0.49 $\mu\text{g}$	0.49 $\mu\text{g}$	0.66 $\mu\text{g}$	0.65 $\mu\text{g}$
V2 <sub>RMS</sub>	0.03 $\mu\text{g}$	0.02 $\mu\text{g}$	0.04 $\mu\text{g}$	0.02 $\mu\text{g}$
V3 <sub>RMS</sub>	0.09 $\mu\text{g}$	0.05 $\mu\text{g}$	0.12 $\mu\text{g}$	0.05 $\mu\text{g}$

**Table 14. HST On-Orbit Acceleration Results; RWA Primary Harmonic (4) Inputs-to-HST Locations (3)<sup>20</sup>**

HST Prin. Direction	Forward	Equip.	RSU Near
Distance from HST C.G. →	194 inches	57.2 inches	81.3 inches
RWA Speed = 3 Hz (180 RPM)	-	-	-
V1 <sub>RMS</sub>	0.08 µg	0.18 µg	0.10 µg
V2 <sub>RMS</sub>	0.33 µg	0.30 µg	0.11 µg
V3 <sub>RMS</sub>	0.05 µg	0.49 µg	0.08 µg
RWA Speed = 10 Hz (600 RPM)	-	-	-
V1 <sub>RMS</sub>	4.45 µg	8.17 µg	7.76 µg
V2 <sub>RMS</sub>	8.62 µg	13.23 µg	5.63 µg
V3 <sub>RMS</sub>	5.44 µg	3.41 µg	7.24 µg

### Systems Engineering (SE) Introduction/Overview for Basic RWA Sizing and Affordability for Jitter

Looking ahead to future uses and affordability issues, spacecraft SE RWA choices for jitter-performance-versus-cost prompts many considerations. Because 1) costs are critical overall program drivers, 2), ACS/GN&C subsystems are a notable contributor to satellite costs, 3) RWAs are an essential stabilized spacecraft need, 4) RWAs are, on a mass-sizing basis, one of the more costly single components, 5) supplier alternatives are a relatively small set of options to push for competitively lower pricing, and 6) cost-performance trades are a basic system engineering tool to determine component selection, there is a need for quantitative cost evaluations. To a first order, RWAs are chosen (allowing for adequate margins in power, mass, angular momentum, etc.) as small as possible via two key values: 1) spacecraft size (i.e., maximum spin-axis-control inertia), and 2) maximum required slew rate. However, considering stringent jitter limits, RWA tradeoffs become more complex. Smaller RWAs otherwise capable of the basic station-keeping/pointing mission commonly have several inherent deleterious impacts: 1) smaller RWA designs have smaller parts (i.e., bearing components and reduced dimensions) that impact efforts to keep tolerances low (without other compensating efforts) and raise harmonic ratios' frequencies (i.e., see prior 304H-vs-101H), 2) smaller RWA mass lowers local reaction mass for mitigating prime IV disturbance energies originating at bearing imperfections, 3) higher spin speeds for a target angular momentum value forces IV amplitudes (i.e., non-spin-axis harmonics) to increase significantly (i.e., by speed squared) that also drives more responsive transmissibilities, and 4) smaller rotor fine-balance adjustments are often more challenging. A seemingly straightforward more-affordable choice for minimal-size RWAs, with upfront acquisition cost savings, can actually translate to *higher* final cost to attain and successfully verify IV limits. Figure 12 shows NASA-mission subsystem percentage costs and similar relationships for other large satellites<sup>21,22</sup>. Note that, very generally, atypical elements of NASA's widely-varied missions (planetary landings/fly-bys, manned space, solar monitoring, etc.) can drive more complex orbital mechanics/GN&C rather than RWA costs compared to GEO satellite platforms driven by station-keeping commonalities, e.g., normal transfer-to-orbit plus pointing stability. Although a complex military satellite program can drive costs from roughly three to eight times higher than basic commercial/NASA missions due to demanding requirements (reliability, threat hardening, etc.), proportions shown in Figure 12 are roughly scalable and percentages are representative. Note that ACS is non-trivial: typically of the order of 5-8% of mission costs<sup>21,22</sup>.



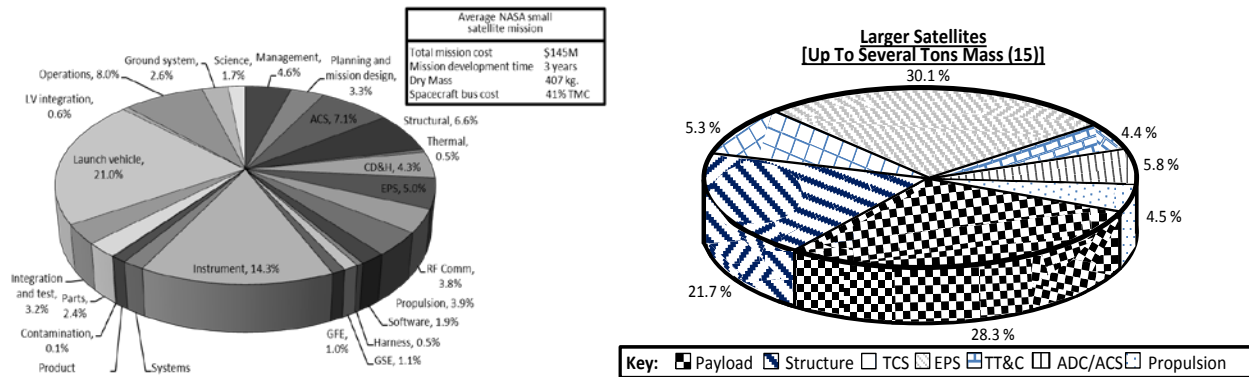


**Figure 12: General (Scalable) Cost Proportions for Typical NASA Spacecraft and Large Satellite System-Missions<sup>21,22</sup>**

Estimated ACS-related costs have limited utility unless the scope (i.e., actual size) of a particular RWA unit is better quantified. An established tool for SE parametric cost analysis applies multiple-program data to create Cost Estimating Relationships (CERs) for the size/performance needed and historical known-costs (adding development-related factors). RWA CER equations have been determined, however, they depend on unit mass, whereas per-axis maximum angular momentum capability drives basic tradeoffs. Therefore, as a bridge, a relationship between mass and angular momentum is established (with good overall correlation)<sup>22,23</sup>. Note that this relationship encompasses RWAs from ~3-300 kg, so is relevant for medium-to-large satellites, but needs revision for micro/small-sat applications<sup>24</sup>. To assess future capabilities, the connection from RWA angular momentum to mass to CER (Figure 13) was validated by comparisons with recent (circa 2014) known inertia wheel procurement costs to substantiate lower and high bounds; cost analysis sources show an RWA range of roughly 1.5-5.0% of satellite procurement costs<sup>25</sup>, a typical range for RWA per-set costs are approximately 3-4% of overall satellite procurement costs<sup>26</sup>.

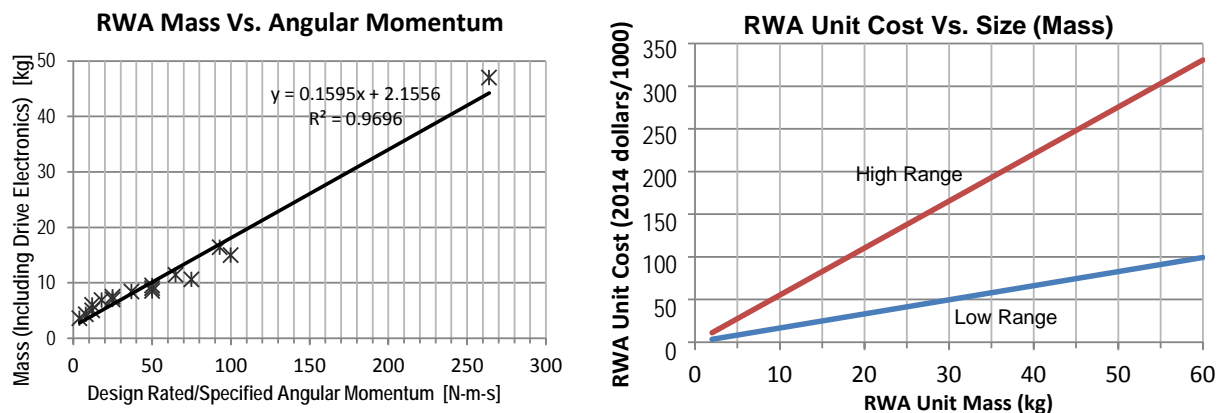


**Figure 13. RWA Angular Momentum Sizing & Cost-Estimating-Relationship Projection<sup>22,23,24,25</sup>**

Note that a wide variety of programmatic factors (e.g., small or singular procurements, design qualification for a particular mission-environments, quality control-related requirements, special testing, added documentation and particular added program requirements, etc.) raises costs: higher range/limit of values. Alternately, larger contract buys (often an impediment with high-performance spacecraft), minimal testing, minimal documentation, and low procurement overhead can drive costs towards lower bounds.

## RWA IV Data Study Conclusions

### Executive-Level RWA IV Study Conclusions:

Based on these overall assessments, summary conclusions for state-of-the-art RWA IV values are (note that, although not rigorously quantified, the values given are intended to represent ~2-sigma variation):

- Test-to-test amplitude is generally within  $\sim\pm 35\%$  of the average dataset value for a specific RWA.
- There is no evidence of large (e.g.,  $\sim 3$ -sigma) RWA-to-RWA mechanical noise/jitter variations if all are otherwise flight-acceptable/spec-compliant, no out-of-family/trending/anomalous RWA quality issues.
- IV LOS jitter analytical result variation for ambient-test-to-nominal-orbit-condition transitions is approximately  $\pm 25\%$  for average RMS values and  $\pm 50\%$  for peak RMS values.
- IV LOS jitter analytical result variation factor for ambient-test-to-worst-orbit-condition-transitions is approximately  $\pm 50\%$  for average RMS values and  $\pm 100\%$  for peak RMS values.

### Specific RWA IV Study Insights/Conclusions:

Based on the foregoing evaluations and detailed investigations, the following detailed conclusions result:

- Qualitative analysis and review of IV datasets substantiate their validity and confirmed in this study effort basic tenets of RWA bearing-rotor construction, imperfections, and first-order physics.
- IV testing dataset variations, including both test-to-test and environmental-exposure variations, for key (linked) 2.8 and 5.2 axial-direction harmonics show 1-sigma variances of approximately  $\pm 0.6$  and  $\pm 0.3$   $\mu\text{inch}$  ( $\pm 0.015$  and  $\pm 0.007$   $\mu\text{m}$ ) equivalent geometry error respectively: equating to  $\sim\pm 35\%$  variance on the all-RWA average value(s). [Ref. Ap. A tabular data]
- IV testing data set variations, including both test-to-test and environmental-exposure variations, for key (linked) 1.0 and 2.0 radial-direction harmonics show 1-sigma variances of approximately  $\pm 2.0$  and  $\pm 0.4$   $\mu\text{inch}$  ( $\pm 0.50$  and  $\pm 0.10$   $\mu\text{m}$ ) equivalent geometry error respectively: equating to  $\sim\pm 35\%$  variance on the all-RWA average value(s). [Ref. Ap. A tabular data]
- Total combined (via RSS summing) expected variations due to transition from ground to nominal and extreme orbital environment conditions in axial and radial direction 1.0 harmonics have the largest test data basis; accounting for variations of roughly  $\pm 1.5$  and  $\pm 3.0$   $\mu\text{inch}$  ( $\pm 0.04$  and  $\pm 0.08$   $\mu\text{m}$ ) equivalent geometry error respectively: equating to  $\sim\pm 20\%$  and  $\sim\pm 40\%$  variance on the all-RWA average value(s). [Ref. Ap. A tabular data]
- Total combined (via RSS summing) expected variations due to transition from ground to nominal and extreme orbital environment conditions in other-direction higher key harmonics are not well known/characterized and speculative, but are estimated to account for variations of roughly  $\pm 0.8$  and  $\pm 1.5$   $\mu\text{inch}$  ( $\pm 0.02$  and  $\pm 0.04$   $\mu\text{m}$ ) equivalent geometry error respectively: equating to  $\sim\pm 25\%$  and  $\sim\pm 50\%$  variance on the all-RWA average value(s). [Ref. Ap. A tables]
- HST RWA LOS jitter analytical results variability estimate for ambient-to-nominal-orbit-condition transitions correspond to 0.74 to 1.16 milli-arcsecond average RMS values and 4.54 to 10.22 milli-arcsecond for peak RMS values for the overall noisiest-worst-case RWA dataset (1005).
- HST RWA LOS jitter analytical results variability estimate for ambient-to-extreme-limit-orbit-condition transitions correspond to 0.62 to 1.40 milli-arcsecond average RMS values and 3.41 to 13.63 milli-arcsecond for peak RMS values for the overall noisiest-worst-case RWA dataset (1005).
- Additional RWA harmonics should be evaluated in overall jitter analyses, depending upon general system fidelity required and engineering judgment on a potential for high frequency disturbances to affect optical train elements. [Ref. Ap. A tables for comparison of relative harmonic magnitudes]

## Summary

A RWA IV jitter optimization treatise, focused on an ultra-fine-pointing spacecraft utilizing state-of-the-art RWA IV balancing/measurements along with system engineering aggregated efforts, is documented. Key findings, methodologies, overviews, and intertwined details for lower-level elements within HST's design-test-analysis evolution, commonly with nuanced discoveries and counter-intuitive paradigm shifts in approaches and resolution path, are summarily discussed often within a background/historical context. However, a clear focus is also maintained on how these multiple dependencies contribute to present and

future LOS-pointing satellite developments, as well as how they translate to other spacecraft units with a potentially deleterious IV signature, e.g., rotating or dithering components, etc. From a global viewpoint, it can seem difficult to see how a few-ounce miniscule part's (i.e., RWA bearing raceway/retainer) barely measurable imperfections can amplify into a formidable challenge for a ~12-ton spacecraft's primary LOS jitter allocations under unfavorable conditions. Although not common for most satellites to engage all of these approach details, attainment and prudent management of lower-level IV data is essential for fine-pointing space platform's success. This paper's predominant value is in exposing both applicability guidance plus revealing insights/means to pursue in-depth key details to attain fine-pointing requirements.

## References

1. Dougherty, H. J., Rodoni, C., Rodden, J., Tompetrini, K., "Space Telescope Pointing Control", AAS/AIAA Paper 83-365, Astrodynamics, Vol 54 1 & 11, Advances In The Aeronautical Sciences, 1983.
2. Beals, G. A., Crum, R. C., Dougherty, Hegal, D. K., Kelley, J. K., Rodden, J. J., "Space Telescope Precision Pointing Control System", AIAA Technical Paper 86-1981, AIAA Guidance, Navigation, and Control Conference Proceedings, 1986.
3. Beals, G. A., "Hubble Space Telescope Pointing Control Subsystem Error Budget Report," LMSS Report D977241A, Lockheed Martin Space Systems Company, Sunnyvale, California, August 1989.
4. Hasha, M., A. Blackwell, L. Chang, G. Sarver, "Facility Vibration Limits in Micro-gravity and Low-gravity Environments: An Allocation Methodology", AIAA 35th Aerospace Science Sciences Meeting, Accelerations and Countermeasures in the Reduced Gravity Environment Session, Reno, NV, 1997.
5. Kendrick, S. E., Stober, J., Gravseth, I., "Pointing and Image Stability for Spaceborne Sensors – from comet impactors to observations of extrasolar planets" SPIE Journal Vol 6265, 62652V-1, 2006.
6. Dougherty, H. J., Rossini, R., Simcox, D., Bennett, N., "Space Telescope Control System Science User Operations", AAS/AIAA Astrodynamics Specialist Conference, Lake Placid, NY, August 1983.
7. Hur-Diaz, S., Wirzburger, J., Smith D., "Three Axis Control of the Hubble Space Telescope Using Two Reaction Wheels and Magnetic Torquer Bars For Science Observations", AAS 08-279, F. Landis Markley Astronautics Symposium, June 2008.
8. Rodden, J., H. Dougherty, F. Reshke, M. Hasha, and P. Davis, "Line of Sight Performance Improvement with Reaction Wheel Isolation", AAS Pub. 86-005 Guidance and Control Conference, Keystone, CO, Feb 1-5, 1986.
9. Hasha, M., "Passive Isolation/Damping System for the Hubble Space Telescope Reaction Wheels", NASA Conf. Pub. 2470 21st Aerospace Mechanisms Symposium, NASA-JPL-LMSC, Houston, TX, Apr 29-May 1, 1987 [Recipient of George Herzl Award for Best Technical Paper].
10. Launius, Roger D., DeVorkin, David, "Hubble's Legacy: Reflections by Those Who Dreamed It, Built It, and Observed the Universe with It", Smithsonian Proceedings and Other Publications, 2014.
11. Hasha, M. D. "SSM Stowed Dynamic Model of February 1983", Engineering Memorandum S&M 357, LMSC, June 1983.
12. Hasha, M., "Compatibility of the Space Station Freedom Life Sciences Research Centrifuge with Microgravity Requirements", ASME Conf. Pub. 90-WA/AERO-6 Winter Annual Meeting, Dallas, TX, Nov 25-30, 1990.
13. Hasha, M. and J. Hirata, "SOFIA Telescope Assembly Jitter Reduction Using Advanced Passive Isolators", AIAA 33rd Aerospace Sciences Meeting, Space Sciences and Astronomy Session, Reno, NV, Jan 9-12, 1995.
14. Hasha, M. D., "Reaction Wheel Mechanical Noise Variations," Engineering Memorandum SSS 218, LMSC, June 1986; which includes Ross, G., Hasha, M. D., plus "Applicability of Key Harmonics For Predicting Reaction Wheel Jitter Trends", Internal Communication Report, LMSC, 11 September 1985.
15. BRÜEL and KJAER, "Static and Dynamic Balancing of Rigid Rotors", Application Notes, Germany, Naerum Offset, 1989.
16. Mauriello, J. A., et al., "Rolling Element Bearing Retainer Analysis", Army Air Mobility Research and Development Laboratory Publication AD-774 264, November 1973.
17. Lallo, M. D., "Experience with the Hubble Space Telescope: Twenty Years of an Archetype", Cornell University Library/Space Telescope Science Institute Publication, 2012.

18. Camino, T. S., "HST Solar Array Feathering Test II Test Report", Engineering Memorandum SPS 648, LMSC, July 1991.
19. Camino, T. S., Hasha M. D., "Structural G Level Accelerations at 1.0 and 100.0 inches from CG of HST during Solar Array Feathering Test II to be used as a Demonstration for Space Station", Engineering Memo Communication, September 1991.
20. Sills, J. W., Hasha, M. D., "Derived Structural Accelerations for the HST Due to Reaction Wheel Harmonic Steady State Inputs and Engineering/Science Tape Recorders Telemetry Data, Interdepartmental Communication Report, LMSC, 16 September 1991.
21. Guerra, Lisa, "Cost Estimating Module – Space Systems Engineering Version 1.0", Course Materials Developed under NASA Exploration Systems Mission Directorate in association with the University of Texas at Austin, 2010.
22. Aas, C., Zandbergen, B.T.C. , Hamann, R.J., Gill, E.K.A., "SCALES – A System Level Tool for Conceptual Design of Nano- and Microsatellites", 7th IAA Symposium on Small Satellites for Earth Observation, Berlin, Germany, May 4-8, 2009.
23. Larson, W.J., Wertz, J.R., "Space Mission Analysis and Design" or "SMAD", 3rd Ed., Microcosm Press & Springer, 1999.
24. Aas, C. L. O., Zandbergen, B. T. C. , Hamann, R.J., Gill, E .K. A., "Development of a System Level Tool for Conceptual Design of Small Satellites", 7<sup>th</sup> Annual Conference on Systems Engineering research 2009 (CSER 2009), April 20-23, 2009.
25. Aerospace Corp. Small Satellite Cost Model Ver 7.4, CER via [www.coursehero.com/GeorgiaState/ASTR/ASTR 6300](http://www.coursehero.com/GeorgiaState/ASTR/ASTR 6300) [homework 7 - page 4 of 13].
26. Comparisons with Internal Engineering Assessments, Internal Guidelines Discussion between D. Anderson and M. Hasha, September 1, 2015.

## Appendix A: Consolidated Specific Details for RWA IV Dataset Values

**Table A-1. Computed Values for RWA Axial Force Principal Direction Key Harmonics (4)**

Data Set	1.0 Harmonic		2.0 Harmonic		2.8 Harmonic		5.2 Harmonic	
RWA S/N - Set	2 <sup>nd</sup> -O Coef (mlb/RPM <sup>2</sup> )*	Eq. GE (μin)	2 <sup>nd</sup> -O Coef (mlb/RPM <sup>2</sup> )*	Eq. GE (μin)	2 <sup>nd</sup> -O Coef (mlb/RPM <sup>2</sup> )*	Eq. GE (μin)	2 <sup>nd</sup> -O Coef (mlb/RPM <sup>2</sup> )*	Eq. GE (μin)
1001 – 1 (P)	9.22	7.58	7.40	1.52	19.53	2.02	28.80	0.88
1001 – 2 (P)	7.99	6.56	9.17	1.88	23.44	2.42	31.86	0.98
1001 – 3 (P)	6.65	5.46	9.13	1.87	16.83	1.74	35.68	1.09
1001 – 4 (F)	6.73	5.53	8.86	1.82	16.14	1.67	34.49	1.06
1001 – ave.	7.65	6.28	8.64	1.77	18.98	1.96	32.71	1.00
1002 – 1 (P)	1.11	0.91	1.97	0.40	15.33	1.58	26.71	0.82
1002 – 2 (P)	0.74	0.61	6.17	1.27	19.39	2.00	33.31	1.02
1002 – 3 (F)	2.26	1.85	6.78	1.39	18.18	1.88	37.68	1.15
1002 – ave.	1.37	1.12	4.97	1.02	17.64	1.82	32.57	1.00
1003 – 1 (P)	4.07	3.35	3.45	0.71	6.91	0.71	16.79	0.51
1003 – 2 (P)	3.50	2.87	10.40	2.14	24.16	2.50	18.92	0.58
1003 – 3 (P)	2.91	2.39	8.12	1.67	16.50	1.70	6.21	0.19
1003 – ave.	3.49	2.87	7.32	1.50	15.86	1.64	13.98	0.43
1004 – 1 (F)	1.57	1.29	2.73	0.56	17.60	1.82	17.77	0.54
1004 – 2 (F)	2.09	1.72	0.11	0.02	9.00	0.93	15.43	0.47
1004 – 3 (P)	2.35	1.93	0.74	0.15	16.36	1.69	19.92	0.61
1004 – 4 (F)	2.48	2.03	0.43	0.09	15.10	1.56	22.38	0.69
1004 – 5 (P)	4.22	3.47	0.21	0.04	26.38	2.73	37.47	1.15
1004 – 6 (P)	2.29	1.88	0.13	0.03	15.51	1.60	18.62	0.57
1004 – ave.	2.50	2.05	0.72	0.15	16.66	1.72	21.93	0.67
1005 – 1 (P)	3.46	2.84	13.65	2.80	21.13	2.18	19.29	0.59
1005 – 2 (P)	4.32	3.55	8.53	1.75	29.91	3.09	20.72	0.63
1005 – 3 (F)	4.02	3.30	8.17	1.68	30.92	3.19	19.69	0.60
1005 – 4 (P)	4.16	3.42	6.82	1.40	27.74	2.87	21.57	0.66
1005 – ave.	3.99	3.28	9.29	1.91	27.43	2.83	20.32	0.62
ALL – ave.	3.81	3.13	5.65	1.16	19.30	1.99	24.17	0.74

\* Note: all milli-pound/RPM<sup>2</sup> values shown are 10<sup>6</sup> times actual values for tabulation clarity.

**Table A-2: Computed Values for RWA Radial Force Principal Direction Key Harmonics (4)**

Data Set	1.0 Harmonic		2.0 Harmonic		2.8 Harmonic		5.2 Harmonic	
RWA S/N - Set	2 <sup>nd</sup> -O Coef (mlb/RPM <sup>2</sup> )*	Eq. GE (μin)	2 <sup>nd</sup> -O Coef (mlb/RPM <sup>2</sup> )*	Eq. GE (μin)	2 <sup>nd</sup> -O Coef (mlb/RPM <sup>2</sup> )*	Eq. GE (μin)	2 <sup>nd</sup> -O Coef (mlb/RPM <sup>2</sup> )*	Eq. GE (μin)
1001 – 1 (P)	8.56	7.04	7.67	1.57	13.89	1.43	7.90	0.24
1001 – 2 (P)	7.96	6.54	2.42	0.50	9.78	1.01	3.31	0.10
1001 – 3 (P)	9.73	8.00	5.65	1.16	12.41	1.28	10.07	0.31
1001 – 4 (F)	9.11	7.48	4.11	0.84	10.81	1.12	7.89	0.24
1001 – ave.	8.84	7.26	4.96	1.02	11.72	1.21	7.29	0.22
1002 – 1 (P)	4.23	3.47	3.69	0.76	7.52	0.78	6.76	0.21
1002 – 2 (P)	5.76	4.73	4.58	0.94	5.93	0.61	6.26	0.19
1002 – 3 (F)	11.59	9.52	3.94	0.81	6.28	0.65	6.40	0.20
1002 – ave.	7.19	5.91	4.07	0.84	6.58	0.68	6.48	0.20
1003 – 1 (P)	14.43	11.86	5.59	1.15	9.26	0.96	3.66	0.11

1003 – 2 (P)	12.05	9.90	7.85	1.61	9.05	0.93	3.13	0.10
1003 – 3 (P)	11.54	9.48	10.51	2.16	9.55	0.99	4.28	0.13
1003 – ave.	12.67	10.41	7.98	1.64	9.29	0.96	3.69	0.11
1004 – 1 (F)	4.47	3.67	2.74	0.56	7.25	0.75	2.03	0.06
1004 – 2 (F)	4.32	3.55	4.08	0.84	11.17	1.15	5.38	0.16
1004 – 3 (P)	3.11	2.55	4.29	0.88	9.67	1.00	4.25	0.13
1004 – 4 (F)	5.12	4.20	4.42	0.91	7.71	0.80	3.41	0.10
1004 – 5 (P)	4.97	4.08	4.13	0.85	12.25	1.27	4.79	0.15
1004 – 6 (P)	5.92	4.86	4.41	0.91	6.86	0.71	2.45	0.07
1004 – ave.	4.65	3.42	4.01	0.82	9.15	0.95	3.72	0.11
1005 – 1 (P)	14.00	11.50	6.29	1.29	10.52	1.09	3.72	0.11
1005 – 2 (P)	16.05	13.19	5.60	1.15	28.47	2.94	12.17	0.37
1005 – 3 (F)	19.26	15.82	3.49	0.72	12.07	1.25	2.59	0.08
1005 – 4 (P)	15.33	12.59	3.27	0.67	11.08	1.14	6.25	0.19
1005 – ave.	16.16	13.28	4.66	0.96	15.53	1.60	6.18	0.19
ALL – ave.	9.38	7.70	4.94	1.01	10.58	1.09	5.34	0.16

\* Note: all milli-pound/RPM<sup>2</sup> values shown are 10<sup>6</sup> times actual values for tabulation clarity.

**Table A-3. Computed Values for RWA Radial Moment Principal Direction Key Harmonics (4)**

Data Set	1.0 Harmonic		2.0 Harmonic		2.8 Harmonic		5.2 Harmonic	
RWA S/N - Set	2 <sup>nd</sup> -O Coef (mlb/RPM <sup>2</sup> )*	Eq. GE** (μin)	2 <sup>nd</sup> -O Coef (mlb/RPM <sup>2</sup> )*	Eq. GE** (μin)	2 <sup>nd</sup> -O Coef (mlb/RPM <sup>2</sup> )*	Eq. GE** (μin)	2 <sup>nd</sup> -O Coef (mlb/RPM <sup>2</sup> )*	Eq. GE** (μin)
1001 – 1 (P)	0.76	6.23	3.60	7.40	15.91	26.43	43.06	13.18
1001 – 2 (P)	1.34	11.01	3.83	7.86	21.92	22.65	36.61	11.21
1001 – 3 (P)	1.97	16.14	4.00	8.21	14.78	15.26	71.85	22.00
1001 – 4 (F)	3.10	25.51	2.49	5.11	20.08	20.74	104.23	31.91
1001 – ave.	1.79	14.72	3.48	7.15	18.17	18.77	63.94	19.58
1002 – 1 (P)	1.14	9.36	2.01	4.14	18.23	18.83	14.82	4.54
1002 – 2 (P)	1.95	16.02	2.13	4.37	14.61	15.10	35.26	10.79
1002 – 3 (F)	8.41	69.13	0.93	1.91	15.98	16.51	15.14	4.63
1002 – ave.	3.83	31.50	1.69	3.47	16.27	16.81	21.74	6.66
1003 – 1 (P)	8.10	66.54	5.23	10.74	18.91	19.53	31.67	9.70
1003 – 2 (P)	7.46	61.25	4.82	9.89	19.73	20.38	44.98	13.77
1003 – 3 (P)	6.85	56.30	24.45	50.21	23.46	24.23	18.16	5.56
1003 – ave.	7.47	61.36	11.50	23.62	20.70	21.38	31.60	9.68
1004 – 1 (F)	3.10	25.47	1.63	3.35	20.90	21.59	13.61	4.17
1004 – 2 (F)	2.85	23.45	0.77	1.58	18.77	19.39	81.01	24.80
1004 – 3 (P)	---***	---***	---***	---***	---***	---***	---***	---***
1004 – 4 (F)	3.98	32.71	2.59	5.31	15.11	15.61	17.47	5.35
1004 – 5 (P)	4.21	34.61	3.39	6.97	15.18	15.68	44.90	13.75
1004 – 6 (P)	3.89	31.95	1.82	3.74	16.31	16.85	60.08	18.39
1004 – ave.	3.01	24.70	1.70	3.49	14.38	14.86	36.18	11.08
1005 – 1 (P)	5.72	46.98	2.35	4.83	18.54	19.15	10.70	3.28
1005 – 2 (P)	8.14	66.90	3.85	7.90	25.98	26.84	17.20	5.27
1005 – 3 (F)	10.49	86.16	3.35	6.87	27.05	27.94	11.61	3.55
1005 – 4 (P)	11.22	92.15	0.86	1.78	31.35	32.38	44.94	13.76
1005 – ave.	8.89	73.05	2.60	5.35	25.73	26.58	21.11	6.46
ALL – ave.	4.73	38.89	3.70	7.61	18.64	19.26	35.86	10.98

\* Note: all milli-inch-pound/RPM<sup>2</sup> values shown are 10<sup>5</sup> times actual values for tabulation clarity.

\*\* Note: a physical interpretation/meaning of Equivalent Geometry Error (EGE) for radial moments is vague.

\*\*\* Note: abbreviated test series obtained only axial and radial force IV data; no radial moment data

**Table A-5: Computed EGE Coefficients for All Detected IV Radial Force Harmonic Ratios**

Harm. Ratio ↓ RWA →	<u>1001</u>	<u>1002</u>	<u>1003</u>	<u>1004</u>	<u>1005</u>	<u>Ave.</u>
<u>0.35</u>	1.67**	1.70**	1.83**	1.20**	1.63**	1.61
<b><u>1.00</u></b>	8.84**	7.19**	12.67**	4.65**	16.16**	9.38
<b><u>2.00</u></b>	4.96**	4.07**	7.98**	4.01**	4.66**	4.94
<b><u>2.82</u></b>	11.72**	6.58**	9.29**	9.15**	15.53**	10.58
3.00	1.16*	--	1.39	2.07	1.49	1.53
3.12	2.27*	--	2.23	1.31	1.70	1.88
3.25	3.84*	--	2.98	1.62	4.74	3.30
3.60	1.81*	--	1.95	0.59	1.49	1.46
3.84	4.47*	--	5.13	1.14	6.31	4.26
4.00	2.86*	--	1.77	2.69	2.95	2.57
4.14	8.33**	6.37**	8.10**	3.91**	5.64**	6.47
4.55	5.26*	--	3.54	1.05	3.07	3.03
4.74	3.61*	--	3.63	1.39	3.07	2.93
5.00	2.85*	--	1.95	0.93	1.75	1.87
<b><u>5.18</u></b>	7.29**	6.48**	3.69**	3.71**	6.18**	5.34
<u>5.60</u>	14.39**	8.46**	5.99**	7.49**	13.71**	10.00
5.76	3.16*	--	2.01	2.51	14.50	5.55
6.00	16.05*	--	13.50	12.20	13.80	13.89
<u>7.50</u>	10.37**	7.26**	7.67**	3.48**	3.27**	6.41
8.28	11.45*	--	5.32	11.90	7.72	9.10
<u>8.50</u>	12.04**	10.01**	11.96**	11.49**	8.00**	10.70
8.70	--	--	--	--	11.80	11.80
9.00	10.90*	--	1.04	4.00	14.00	7.49
10.20	--	--	--	6.59	10.50	8.54
10.44	8.13*	--	7.01	4.85	10.10	7.52
10.80	7.22*	--	8.07	3.34	17.10	8.93
11.22	18.25*	--	22.00	19.30	29.50	22.26
11.88	13.80*	--	18.10	11.70	27.70	17.83

Note: all values shown are  $10^6$  times actual computed values.

Note: underlined plus bold items are 4 key harmonic ratios; underlined-only are next 4 secondary ratios.

-- Harmonic ratio value is below reliable detectability for this RWA's IV data.

\* Average value for 2 data sets for this particular RWA.

\*\* Average value for all data sets for this particular RWA.



## Appendix B. Consolidated Validity Evaluations for RWA IV Datasets for Orbital IV Values

The CMG program data has several specific attributes as well as *deficiencies* listed below:

- 1) it measured effects (spin-axis reorientations) with established bases in HST RWA IV data,
  - 2) it is a large enough body of data to provide valid statistical insights (where available and relevant for the specific effect being addressed), and
  - 3) it is similar enough to the HST RWA design and contemporaneous configuration to provide applicable or extrapolate-able data and/or insights.
- 1) *it does not directly address all variation effects sought,*
  - 2) *it only measures effects on the radial direction 1.0 harmonic (i.e., unbalance/asymmetry) so inferences are needed for estimating effects on other harmonics and directions,*
  - 3) *CMG program is classified, so it limits access to analyze in a more detailed quantitative fashion data directly obtained; therefore, reliance turns towards supplier expertise and overall extrapolated guidelines from that database, and*
  - 4) CMG is not purely identical to the HST RWA design/configuration, creating some added uncertainty for full validity of applying extrapolations and engineering judgments.

The high value for accumulated CMG program data is to allow assessment of dataset variation due to:

- 1) change in spin-axis orientation in a 1-g gravitational field,
- 2) change from 1-g ambient to 0-g (or microgravity) orbital force field,
- 3) change from 1-atmosphere ambient to vacuum external-internal housing pressures, and
- 4) change from 70 deg F ambient to 50-90 degree F orbital operating temperatures.

Although the CMG data collected is the most relevant data available, it has noted constraints/caveats for directly-applicable data sought due to gaps in some key areas (i.e., no higher-ratio harmonics).

- A) HST RWA Acceptance Test Procedure (ATP) IV test dataset collection is most directly applicable to the issue (i.e., design similarity), possessing the following attributes to allow investigating variabilities/causes:
- 1) it is precisely measured data on flight configured and realistically-tested RWAs,
  - 2) it is a relatively large consistently-controlled sampling, implying decent statistical validity, and
  - 3) it manifests negligible influence from some effects which alter IV output (e.g., wide swings in temperature or stress distribution changes during the test intervals).

It also has the following specific *deficiencies*:

- 1) *each RWA is subjected to environmental exposures (random vibration or thermal-vacuum tests) between IV tests, so different dataset curve values solely due to fundamental IV test-to-test variations cannot be separately accounted for, and*
- 2) *amount of datasets for each RWA (3-4 typically, a lone exception being 6 on RWA 1004), is not sufficiently large for very high statistical significance if scatter is large (sometimes occurred).*

The predominant value for IV test data collected is to provide the assessment basis for variations due to:

- 1) inherent RWA-to-RWA unit variation (i.e., determining which RWA will generally produce more or less jitter relative to another or the average, and how different the jitter variation would be),
- 2) test-to-test variations caused by inherent randomness and/or test setup/method limitations, and
- 3) test-to-test variations caused by exposure to environmental test conditions (i.e., Random Vibration and Thermal-Vacuum) plus inter-test handling/transport (believed to be much less significant).

The major restriction to more effective use of this body of data for more precise evaluation is that there is no definitive method for separating the last two effects: no data has been taken on an RWA without having both effects present; data scatter from both effects is notable.

## Acknowledgements

The author gratefully acknowledges support and encouragement from SMEs and colleagues, specifically Gary Beals, Eugene Skelton, Stu Loewenthal, Larry McGovern, Gary Goble, Rob Peabody, Ed Boesiger, Jon Kirschenbaum, and Tara Somerday.

# Microspine Gripping Mechanism for Asteroid Capture

Ezekiel G. Merriam\*, Andrew B. Berg\*\*, Andrew Willig\*\*, Aaron Parness\*\*, Tim Frey+ and Larry L. Howell\*\*

## Abstract

This paper details the development and early testing of a compliant suspension for a microspine gripper device for asteroid capture or micro-gravity percussive drilling. The microspine gripper architecture is reviewed, and a proposed microspine suspension design is presented and discussed. Prototyping methods are discussed, as well as testing methods and results. A path forward is identified from the results of the testing completed thus far. Key findings include: the microspine concept has been established as a valid architecture and the compliant suspension exhibits the desired stiffness characteristics for good gripping behavior. These developments will aid in developing the capability to grasp irregularly shaped boulders in micro-gravity.

## Introduction

Recent exploration efforts have been focused on Mars and near-earth asteroids. However, current mobility technology (e.g., wheeled vehicles and touch-and-go probes) are inadequate for detailed exploration of sub-surface Martian caverns or the micro-gravity environment of asteroids [1]. Gravity-independent microspine grasping mechanisms have been demonstrated to have the necessary mobility to access these difficult terrains. Proof-of-concept robots such as SpinyBot and Lemur IIB have been shown to provide climbing capability and gripping force in the presence of gravity, and have additionally been demonstrated to function in inverted, harder-than-zero-g tests [2].

A central element of these systems is the mounting of spines to compliant suspensions that permits the system to conform to rough surfaces, placing a large fraction of many spines in contact with the surface [3]. Many microspine grippers thus far demonstrated have relied on polymer and elastomer flexure elements (the part of the suspension that deflects to achieve motion), which will not perform adequately in the space environment. To advance the technology and enable missions in space, the flexure components of the microspine must be converted to space-grade materials that will function robustly in the space environment.

This paper details the current state-of-the-art of microspine graspers, discusses the current proposed flexure system, and presents the testing methods used to validate the new flexure design. Results are discussed and design refinements are proposed.

## Background

Microspine grippers seek to imitate insects and arthropods that use the large numbers of small spines to climb surfaces [3]. These spines engage with asperities on rough, hard surfaces to provide grip. Because the number of spines is large, the load can be distributed among the spines so that the load on an individual spine can be quite small and still in aggregate react large forces normal to the surface. In robots, these spines can be mounted on an architecture of hierarchical compliance: robotic arms position the gripper over the surface to be grasped, a linkage arm positions cassettes along macro contours of that surface, and microspines opportunistically grasp local surface asperities to provide grip. The motion of an individual microspine allows it to conform to small-scale surface roughness, and is provided by a compliant suspension.

---

\* Brigham Young University, Provo UT

\*\* Jet Propulsion Laboratory, California Institute of Technology, Pasadena CA

+ Rochester Institute of Technology, Rochester NY

\*\* Brigham Young University, Provo UT

This concept was originally developed to provide the ability to climb porous and dusty vertical walls. It also has applications in exploring rocky or icy space environments. Since the microspine gripper does not rely on reaction forces from the surroundings to provide preload, it can be used in micro-gravity to provide reaction forces for other operations. For example, microspine grippers could be used in conjunction with a percussive impact drill, providing the necessary reaction force to hold the drill against a surface. Such a gripping mechanism could be used to retrieve a boulder from an asteroid.

#### Design Refinements

Development of this design is targeted on the objective of increasing the load capacity of the microspine gripping device. This follows two avenues: increase the number of microspines engaged in a given surface, and eliminate failure modes observed in the suspension. These failure modes include flexure pull-out and tangling. Subtle geometric changes in the suspension and gripper are being explored to increase the number of spines engaged with the surface. Alternative manufacturing methods may be able to mitigate the flexure pull-out, while more accurate manufacturing may reduce the tendency of the suspension to tangle with adjacent suspensions.

### **Gripper Design**

This section gives an overview of gripper concept of operations (CONOPS) and summarizes some historical variations.

#### Gripper CONOPS

The microspine grippers that have been constructed at the Jet Propulsion Laboratory include a variety of architectures, but share several essential features. They all are used to provide reaction forces based on a rough surface. Operations proceed along a similar outline (see Figure 1).

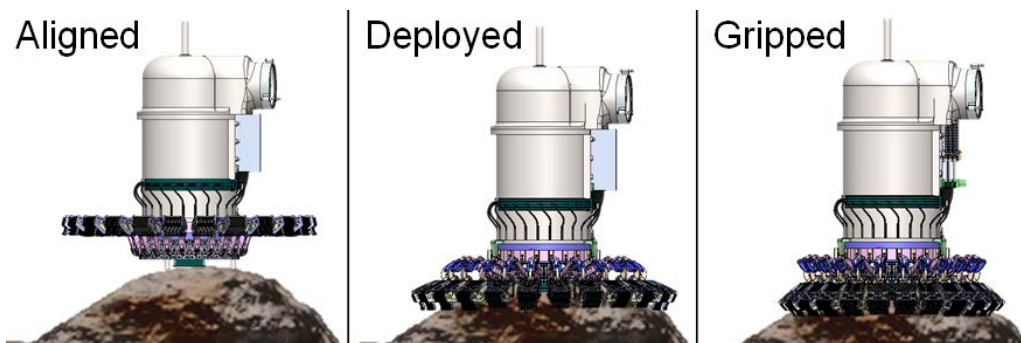


**Figure 1. Illustration of gripper function, broken into three steps: alignment with the surface, deploying the microspine carriages, and gripping of the surface.**

1. The gripper is placed in contact with a surface and aligned with the surface normal.
2. The microspines are dropped so that they make contact with the surface.
3. The mechanism applies tension to the microspines, so that all of the spines are dragged in towards a central axis.
4. The tool is now in the “gripped” state, and can be used to support various activities, including drilling, crew activity, towing or similar tasks.
5. Tension is unloaded in the system, bringing the tool to a “released” state.
6. The gripper tool can now be lifted away from the surface.

#### Historical Variations

This technology has been applied in many different configurations. Figure 2 shows a sampling of some of these designs.





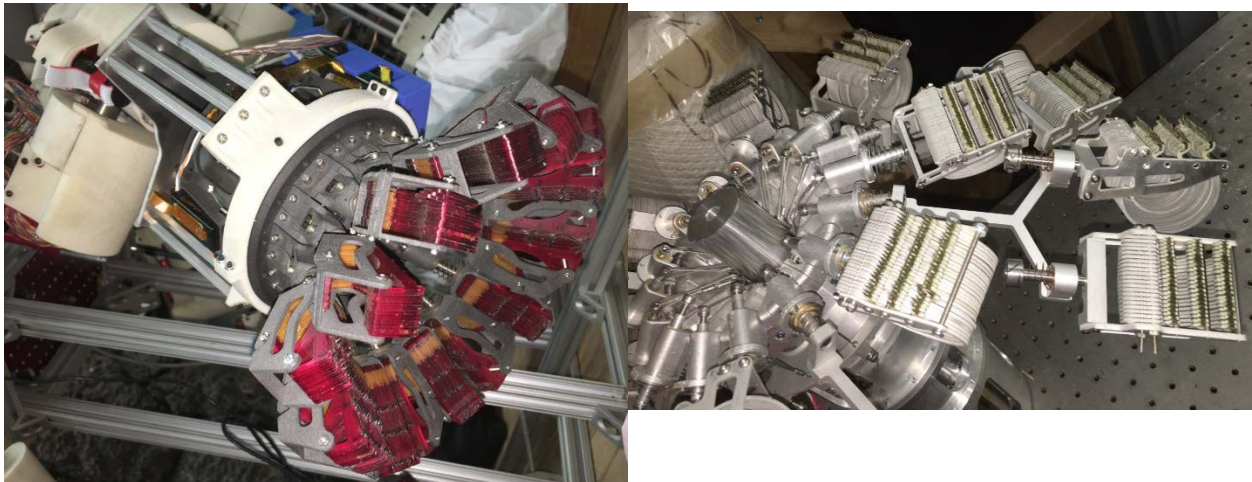
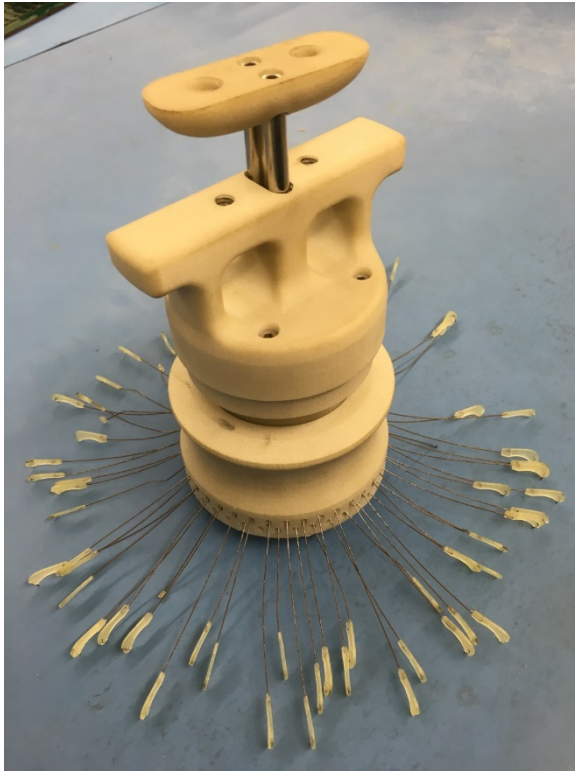


**Figure 2. Examples of previous incarnations of microspine grippers. Top: NEEMO anchors. Upper middle: Lemur IIB climbing robot. Lower middle: Hand-actuated climbing paddles. (Parness and Discovery Channel, 2009) Bottom: Test grippers with elastomer flexures (left) and aluminum hoop flexures (right).**

The following sub-sections describe functional elements common to all microspine gripper designs.

### Spines

The spines on each gripper provide the surface interface. A variety of sizes and profiles have been investigated, but most systems have used #6 fish hooks, cut off to an appropriate length. Sizes from #4 to #26 have been used in various configurations. These hooks get mounted in the next assembly by pressing into a cavity, then potting with epoxy. The primary selection criteria for a given application are strength to

support the estimated loads, and slenderness and sharpness appropriate to intrude into asperities expected to be present in the gripping surface. That is, smaller hooks can take advantage of finer asperities, larger ones can support more load on each hook.

#### Surface Conformance

The spines described above are mounted into a flexible element that provides a degree of conformance to the surface. This flexibility enables the hook to make contact with the surface while allowing other spines to continue moving towards the surface. The design goal is to maximize the number of hooks that make contact with the surface and establish a firm grip.

For cases where the microspines are grouped into “cassettes” or “carriages”, a roll degree of freedom was implemented to allow the group to conform to the bulk surface angle.

#### Load-Sharing

Similarly, as a groups of spines is dragged across the surface, some spines will catch in asperities before others. It is desirable that the spines that have not yet caught continue to move along the surface until they catch, or the mechanism end of travel is reached. However, compliance in this degree of freedom must produce high forces to provide grip.

#### Movement across surface/Application of Tension

Grippers have used a variety of sources for the primary tension that drags the spines across the surface. Some handheld units use the grip force of a hand to actuate. The ARM gripper will use a motorized tool drive on the spacecraft to drive a lead screw, producing motion across the surface.

This movement has also been transferred in a variety of ways among the historical examples shown in Figure 2. The Lemur and NEEMO grippers used a straight shaft pulled through a rotating barrel joint. The “Alien Wire Gripper” used compliant wires sliding through a 3D-printed channel.

#### Motion Takeup

The gripper is designed so that a single actuator applies the inward (x-direction) pulling force. However, the individual carriages may not all move inward the same amount. To absorb these differences in motion, the carriages are cable actuated with springs in series with the actuating cables. When a single carriage has a sufficient number of its microspines engaged with the rock surface, the cable spring will begin to deflect. This allows the actuator to continue to move or apply increasing force to the other carriages without over-actuating fully-engaged carriages.

Each stage of the system is designed to share load among an uncertain number of elements that are engaged with an unknown surface.

### **Microspine Suspension Design**

#### Design Requirements

Design requirements were derived from previous experience using microspines in climbing and grasping robots. Approximately optimal stiffness values were found from prototypes using elastomer flexure elements; one key challenge was designing a metal suspension system that could match the low stiffness of the elastomeric versions. These design requirements are listed in Table 1. Z is the direction orthogonal to the surface to be gripped, and x is the radial direction.

**Table 1. Key design requirements for stiffness and motion of the compliant suspension.**

Metric	Value
$k_z$	0.005 N/mm
$k_x$	0.5 N/mm
$\Delta z$	0.010 m
$\Delta x$	0.012 m
Maximum rotation	15°
Maximum envelope	0.075 m x 0.075 m x 0.002 m
Factor of safety on material failure	1.25

In addition to the quantifiable design requirements listed above, several requirements were proposed that cannot easily be reduced to a single number. These are listed here:

- The mechanism should be simple to build in desired quantities
- The mechanism's x-direction stiffness should sharply increase at the extreme limit of travel
- The mechanism should be capable of nesting with itself to enable greater density of microspine placement
- The mechanism should, as much as possible, isolate x and z displacements

#### Design Overview

The key feature of the proposed design (shown in Figure 3) is that it achieves the required low-stiffness performance by utilizing metal ribbon flexures arranged to form two orthogonal parallel-guiding mechanisms. This serves the function of isolating the x and z stiffness values, allowing them to be independently tailored. Additionally, displacement is partially decoupled. Finally, the rotation of the end stage is inherently small.

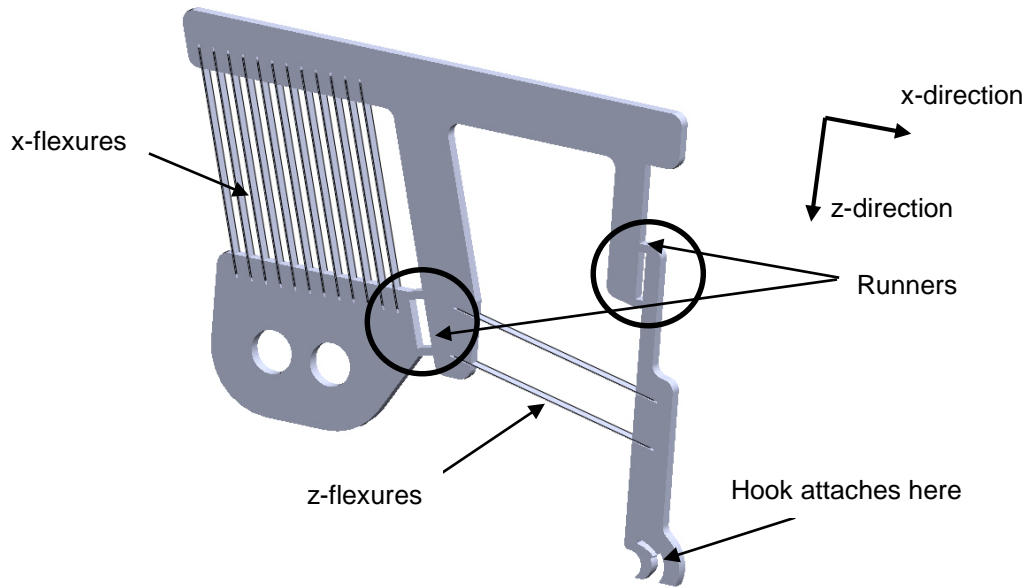


**Figure 3. Rendering of CAD assembly model of microspine suspension indicating key design elements.**

By mounting ribbons in a parent material instead of using the parent material itself, the combined mass is reduced and the target stiffness for each degree of freedom can be achieved more reliably. The slenderness of the metal ribbon provides the desired compliance while the parallel-guiding nature of the mechanism restricts its motion to the desired directions.



The x-flexures and z-flexures provide motion in the x- and z-direction, respectively. The stiffness of these two flexure systems must be dramatically different – by two orders of magnitude. This stiffness difference is accomplished using two strategies. First, the x-flexures are much thicker than the z-flexures. Second, as the upper limit of thickness was approached in the x-flexures, more flexures were added. This addition of flexures increased stiffness without increasing maximum stress.

The proposed parallel-guiding design was initially analyzed using the pseudo-rigid-body model approximation [4], and then the design was analyzed using finite element analysis in the commercial package ANSYS. The finite element model is shown in Figure 4. For simplicity, these models only analyze the flexures; the rigid sections are neglected.

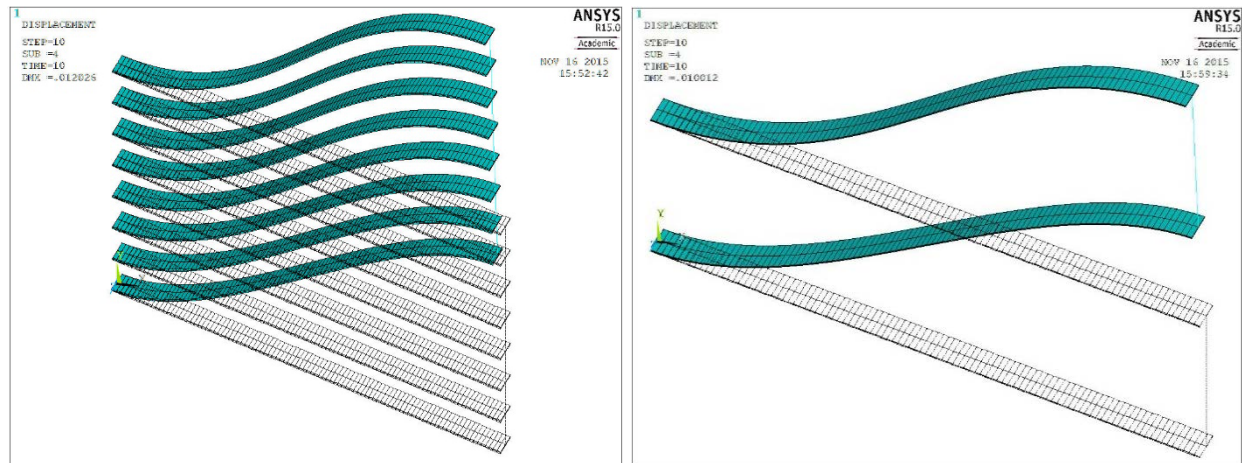


**Figure 4. Finite element models of the x-direction flexures (left) and z-direction flexures (right). Green elements are the displaced state; outlines show the initial state.**

It was found that neither wire electro-discharge machining (EDM) nor water-jet cutting would be able to fabricate extremely slender flexures. If these manufacturing methods were used, thicker flexures would have to be employed. With thicker flexures, the flexure would need to be unacceptably long to avoid material failure and would violate the envelope restrictions. Thus, the complexity of affixing metal ribbon flexures was deemed acceptable due to the significant performance advantage.

#### Design Details

Refer to Figure 3 during the following explanation of design features. Two candidate materials were considered for the flexures. 1095 spring steel at a full hard temper is available in a range of standard thicknesses and has a high yield strength. Alternatively, the class of alloys known as metallic glass offers high performance, but alloys available in ribbon or sheet form are limited, and low-quantity production of custom alloys is expensive. However, metallic glass is a superior choice for the flexure material because of its high  $S_y/E$  ratio. Finite element models and preliminary testing showed that the steel flexures would yield slightly if taken to the full displacements in the x- or z- directions. The low cost of steel made it acceptable for prototyping, but superior performance is predicted if the challenges of procuring metallic glass ribbon can be overcome.

To simplify fabrication, the rigid three sections are all cut from the parent material as one piece. Connected by runners, these sections are to remain together until the flexures are fixed in place. Then the runners can be severed, allowing the mechanism to move freely.

The hook attachment is accomplished first by harvesting the tips off of commercially fishhooks, then pressing the hook into the hook attachment geometry. The gaps are then filled with aerospace epoxy, which

is allowed to cure. When the design enters production, it is intended that hook tips can be specially ordered to eliminate the harvesting step.

#### Prototype Fabrication

While much information on the stiffness and displacement behavior of the compliant suspension can be discovered from finite element modeling, the gripping behavior and interactions with neighboring microspines is difficult to model. Therefore, several rounds of prototyping were employed to investigate the behavior of the suspension.

To lower costs and reduce lead time, initial prototypes were laser cut from 1.6-mm-thick acrylic sheets. They were built at 1:1 scale. Flexures were cut from steel shim stock of the appropriate thickness using hand shears. The shearing operation imparted significant curvature to the flexures, which was removed by plastically deforming the flexures to straighten them. The flexures were then cut to length and fixed to the acrylic cut-outs with cyanoacrylate. These prototypes are shown in Figure 5. In early versions, the fishhook was omitted to decrease prototyping time and improve safety.

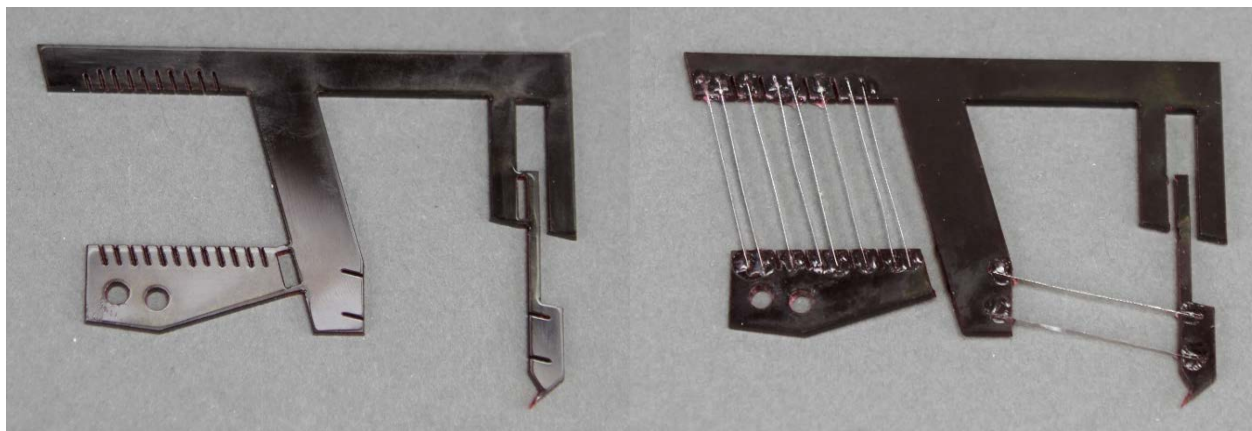


**Figure 5. Acrylic-steel prototypes in two stages of production. On the left is the acrylic suspension body before the addition of steel flexures. Note that the three independent sections are held together with runners. On the right is the completed prototype with steel flexures embedded and runners removed.**

These acrylic-steel prototypes were subjected to the stiffness testing described in the next section. Once the accuracy of the finite element model was established, additional prototypes were fabricated to observe their behavior as an array. In this iteration, steel hooks were included to facilitate initial tests of grasping ability.

The behavior of these acrylic-steel prototypes was sufficient to warrant further investigation and aluminum-steel prototypes were built. The aluminum was cut from 1.6-mm (1/16<sup>th</sup>-inch) 6061 aluminum sheet material on a waterjet cutter. Future versions could be cut using a wire EDM to improve machining precision, or using waterjet to do most of the cutting and then using EDM to cut the finer details such as the channels where the flexures attach. A waterjet-cut blank is shown in Figure 7.

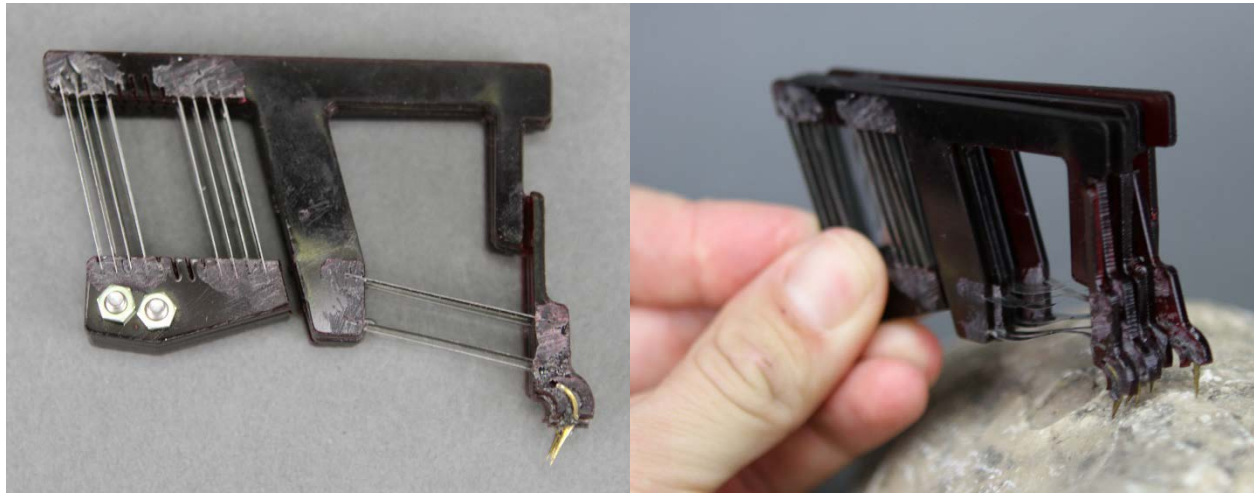


**Figure 6. An array of acrylic-steel prototypes.**

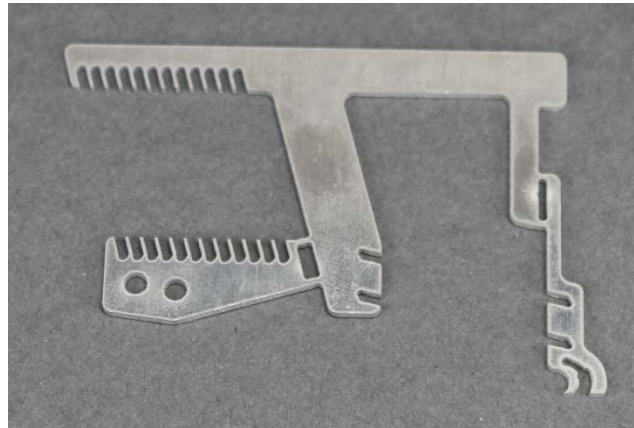


**Figure 7. An aluminum blank into which steel flexures will be bonded.**

After cutting on the water-jet, the blanks were de-burred. Because of the large kerf of the water-jet, the flexures were fixed in place with adhesive tape prior to bonding. The tape was arranged to form pockets into which epoxy was injected, bonding the flexure to the aluminum. This process was labor intensive; future iterations will be altered to avoid the painstaking application and removal of the tape. Alternatively, Teflon fixtures could be designed to contain the epoxy and hold the flexures during curing. In all, 24 aluminum-steel prototypes were built and tested. These were assembled into the test gripper and loaded. Testing is further described in the following section.

### **Testing**

At this point the design is currently undergoing testing and design refinement. Initial testing separately measured stiffness of the suspension along each desired motion direction. Then a sufficient number of prototypes were built to allow for a gripping capacity test to be conducted on natural rock surfaces using a test stand. The maximum load supported by eighteen microspine suspensions and spines in a test gripper was measured; results indicate that the design merits further testing and refinement.

### Stiffness Testing

To confirm that the new suspension design met stiffness targets, individual suspensions were tested in a force-displacement jig. A known displacement was applied and the resulting force was measured. This testing is shown in Figure 8.

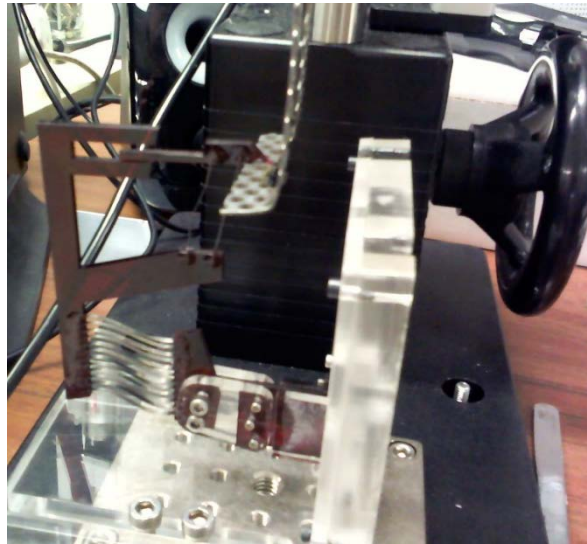


**Figure 8. Stiffness testing of the x-direction suspension. This prototype was constructed from laser-cut acrylic (1.6-mm thick), with steel shim stock for the flexures.**

### Grip testing

Figure 9 shows the test equipment used to obtain data on the gripping capabilities of the microspine flexures.

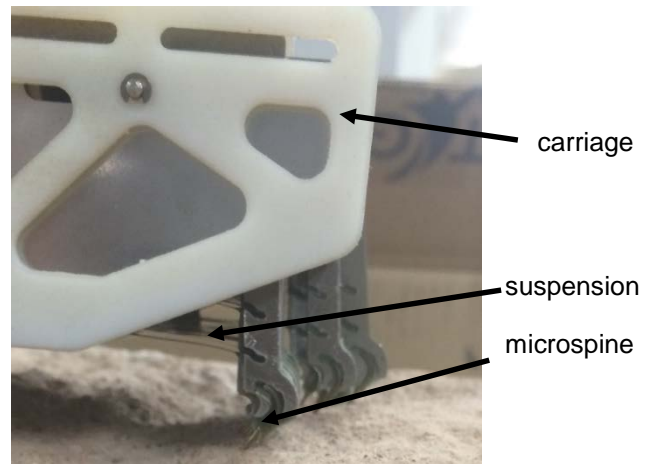
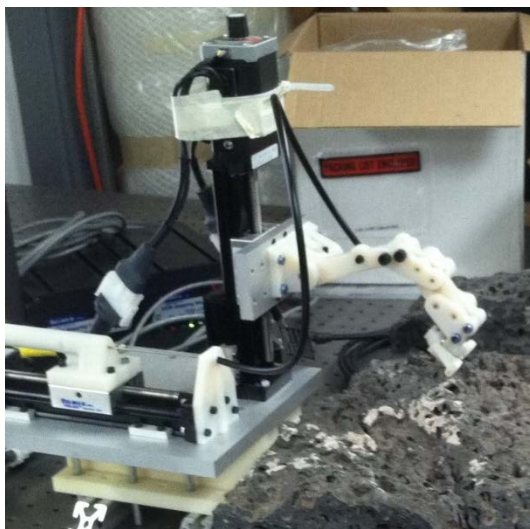


**Figure 9. Testing on the microspine gripper in a test fixture. Top: The entire test fixture, with independent x- and z- stages to test gripping force in each direction (the rock is scoria). Bottom: Close-up view of microspines during testing (the rock is rhyolite).**

The purpose of grip testing is to quantify the force a given microspine design can support. The rig shown in the top half of Figure 9 is able to measure the forces in the x- and z- directions independent of one another. Although the x-direction force may not seem to contribute to the vertical load capacity, there is a relationship between the load capacities in the x- and z- directions. This test setup gives more repeatable



results more rapidly and requires fewer microspine specimens than other testing techniques that consist of attempting to lift large rocks.

## Results

The most important design function is to provide a large reaction force. Therefore, the gripping force in the x and z directions was measured as the critical performance metric. Figure 10 shows a plot of force testing data with x-direction force plotted on the x-axis and z-direction force plotted on the y-axis. This single carriage of microspines is generating nearly twenty newtons of vertical reaction force. Used in an array, as is typical for this architecture, the total vertical reaction force could reach hundreds of newtons.

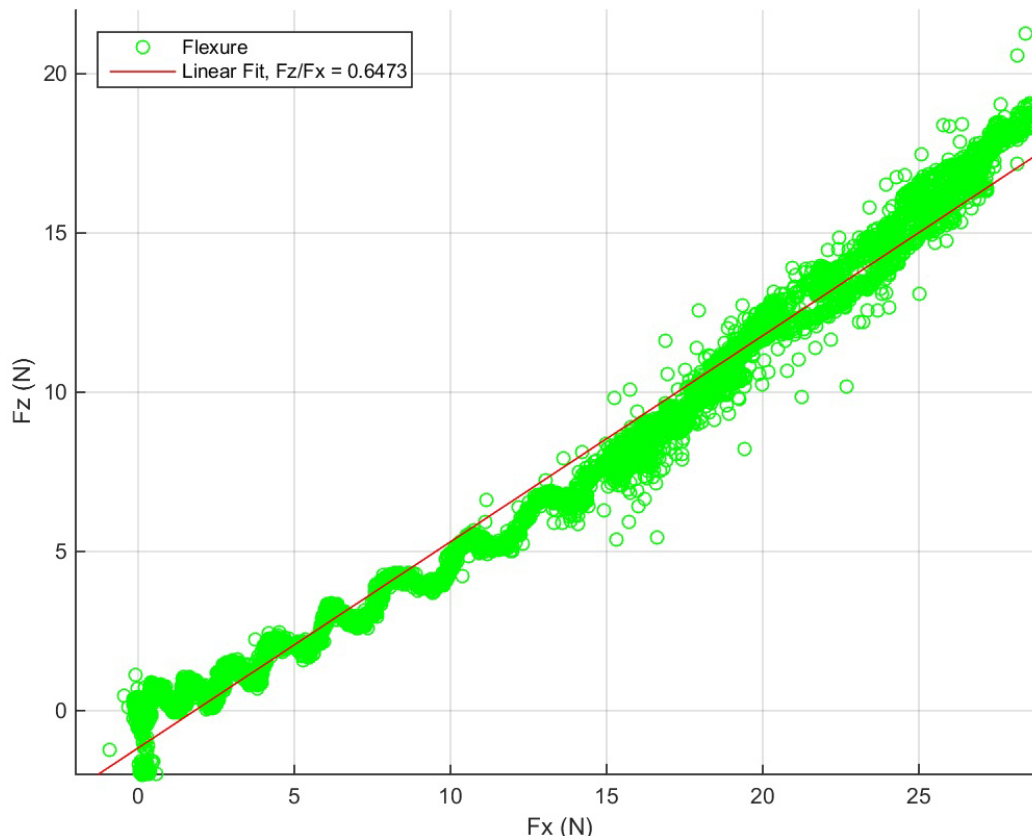


**Figure 10. Representative plot of x- and z- directional forces.**

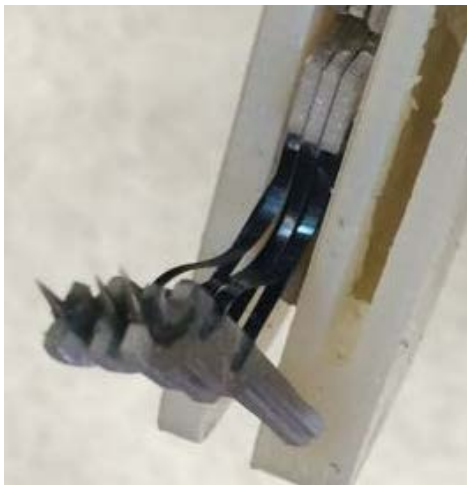
In these early stages of testing, we discovered many design issues that must be addressed. Figure 11 shows several of the most common or serious issues that arose.



The original test gripper experienced interference with the rock sample, necessitating a redesign that provided adequate clearance.



If an x-direction compression load is exerted on the z-direction flexures, this crimping failure can result, indicating the need to protect the flexures from compressive loads.



The flexure arrays being bolted too tightly into their carriages caused this binding/tangling failure. Here, the flexures are only undergoing elastic deformation and can be untangled without loss of performance.



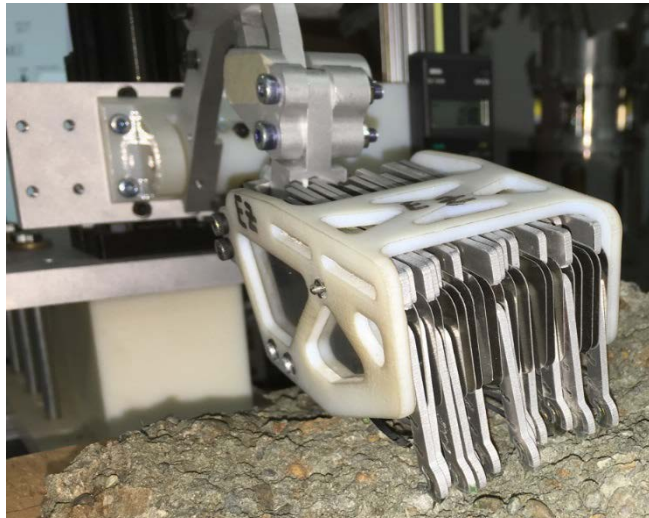
This photo shows a hook that has shifted in its mounting epoxy due to a high transverse load.



Another binding/tangling failure. Layering thin Teflon sheets between the microspines has been proposed as a solution to the tangling problem, and it may also alleviate the binding issue.



Pullout failure of the z-direction flexure due to overload in the x-direction. This failure must be guarded against with better surface preparation of the flexure material.



Test run incorporating divider sheets to reduce tangling.

Figure 11. Several design issues that came to our attention during testing.

#### Design Changes

One of the most important shortcomings in the suspension design was the susceptibility to tangling. To remedy this, divider sheets were included between neighboring microspines. Other problems revealed included susceptibility to binding, flexure pull-out, and flexure crimping. The binding and crimping problems



are being addressed through changes in the carriage design that prevent pinching and x-direction compressive loads. Flexure pull-out will be addressed by using better surface preparation and high-quality epoxy that is not past its shelf life.

## Conclusions

This work presents the development of a compliant suspension for a microspine gripper assembly suitable for use in space as a drill anchor or as part of an asteroid-capture mission. A brief overview of the microspine architecture has been presented, along with the design details for a compliant parallel-guiding suspension system. The testing method has been outlined and results summarized.

It has been shown that the proposed design has potential to provide adequate gripping force in asteroid-capture or micro-gravity drilling application. The critical issues of tangling, binding, and flexure pull-out appear solvable and are currently being addressed. With additional design, prototyping, and testing, the microspine architecture could provide a reliable, scalable, space-capable anchoring system.

## Lessons Learned

- The microspine architecture can be effectively translated into space-grade materials.
- The rock surface-microspine interaction is complex and stochastic, making modeling difficult. Therefore, extensive prototyping and testing is necessary to understand performance.
- Proper use of inexpensive prototypes can speed development compared to purely analytic or numeric models
- Proper consideration should be given to all stages of manufacturing and assembly to produce meaningful test specimens.

## Acknowledgements

The research was carried out at the Jet Propulsion Laboratory, California Institute of Technology, under a contract with the National Aeronautics and Space Administration. This work was supported in part by a NASA Office of the Chief Technologist's Space Technology Research Fellowship.

## References

- [1] A. Parness, M. Frost, N. Thatte and J. P. King, "Gravity-Independent Mobility and Drilling on Natural Rock Using Microspines," in *IEEE International Conference on Robotics and Automation*, Saint Paul, Minnesota, USA, 2012.
- [2] A. Parness, M. Frost, N. Thatte, J. P. King, K. Witkoe, M. Nevarez, M. Garrett, H. Aghazarian and B. Kennedy, "Gravity-independent Rock-climbing Robot and a Sample Acquisition Tool with Microspine Grippers," *Journal of Field Robotics*, vol. 30, no. 6, pp. 897-915, 2013.
- [3] A. T. Asbeck, S. Kim, M. R. Cutkosky, W. R. Provancher and M. Lanzetta, "Scaling Hard Vertical," *The International Journal of Robotics Research*, vol. 25, no. 12, pp. 1165-1179, 2006.
- [4] L. Howell, *Compliant Mechanisms*, John Wiley Sons, Inc, 2001.

# Hammering Mechanism for HP3 Experiment (InSight)

Jerzy Grygorczuk<sup>1,2</sup>, Łukasz Wiśniewski<sup>1,2</sup>, Bartosz Kędziora<sup>1,2</sup>, Maciej Borys<sup>1,2</sup>, Rafał Przybyła<sup>1,2</sup>,  
Tomasz Kuciński<sup>1,2</sup>, Maciej Ossowski<sup>3</sup>, Wojciech Konior<sup>1,2</sup>, Olaf Krömer<sup>4</sup>, Tilman Spohn<sup>5</sup>,  
Marta Tokarz<sup>2</sup> and Mateusz Białek<sup>1,2</sup>

## Abstract

This paper provides a description of the specific design features and nuances of the Hammering Mechanism, a drive unit for the HP3 mole-type penetrator for NASA's InSight mission. State of the art for this type of mechanism and an overall system overview are provided. Particular attention is focused on key components of the system that make it an effective mechanism. The main design changes introduced to the mechanism are related to three main domains: mechanism architecture and principles, increase of efficiency and simplification of the design, and functionality. A few critical lessons learnt are also described.

## Introduction

The following paper discusses the development of the Hammering Mechanism (HM) for the HP3 mole-type penetrator – the drive unit of DLR's heat probe instrument for NASA's InSight mission. The Hammering Mechanism is a drive system of the HP3 penetrator whose purpose is to transport thermal sensors more than the required three meters below Martian surface (5 meters being the desired depth) [4]. The original concept of the mole-type penetrator mechanism was provided by Gromov et al. in [1] and then evolved through the PLUTO instrument for the Beagle2 mission [2], the proposal for an ExoMars instrument [3], to implementation in the InSight mission [4]. The most recent development of the Hammering Mechanism was done by Astronika and the Space Research Centre of the Polish Academy of Sciences (CBK), under contract and in close cooperation with DLR. Even though the concept remains the same, the final design, as implemented by Astronika for the purpose of this mission, significantly improved the system's performance with respect to the previous ones.

The article begins with a general introduction of the penetrator's design and their known solutions (state of the art). The specific system architecture of the HP3 Hammering Mechanism is provided in the System Overview section. The core of the paper comprises particular design features that made the mechanism more effective and improved its performance. This includes spring distribution, cam optimization, bearing description, dedicated roller design, multiple locking/unlocking launch lock system, and the mechanism's lubrication and coatings principles that significantly simplified the mechanism and increased its performance with respect to previous versions. Provided at the end are three lessons learned, which concern problems with cracking of tungsten alloys, removal of a spring clutch and the improper harness tensioning that may lead to a decrease in the penetrator's performance if not properly done.

## State of the Art

The Hammering Mechanism (HM) mentioned in this text is part of a bigger system of a mole-type penetrator HP3 and its Support Structure onboard the InSight lander (Figure 1). A mole-type penetrator, in general, is an assembly that consists of three main assemblies: Hammer (HA), Suppressor Mass (SM), and Outer

---

<sup>1</sup> ASTRONIKA Sp. z o.o., Warsaw, Poland

<sup>2</sup> Space Research Centre of the Polish Academy of Sciences, Warsaw, Poland

<sup>3</sup> Warsaw University of Technology, Warsaw, Poland

<sup>4</sup> German Aerospace Center (DLR), Institute of Space Systems, Bremen, Germany

<sup>5</sup> German Aerospace Center (DLR), Institute of Planetary Research, Berlin, Germany

Casing with the Payload. The original idea of the system was provided in [1] and in principle, the Hammer is pulled up on its Cam by the rotational movement of a motor axis with a roller which periodically loads the Drive Springs located between the Hammer and the Suppressor Mass. After release from the Cam, the Hammer accelerates downwards eventually hitting the Outer Casing and causing its penetration, whereas the Suppressor Mass travels upwards and its movement is compensated by a Brake Spring and Wire Helix in its rear part.

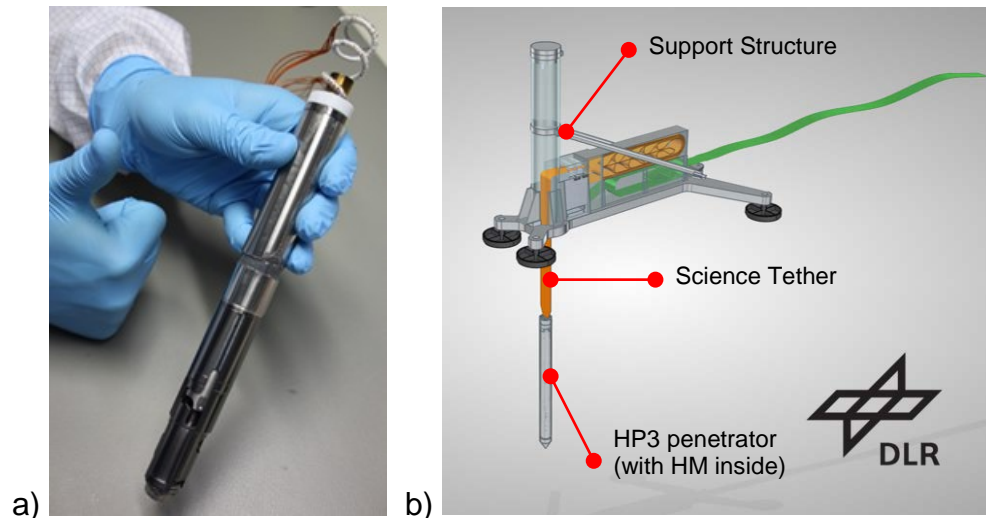


**Figure 1. a) HP3 Hammering Mechanism (FS), b) HP3 overall system (credits: DLR)**

The energy distributed between the Suppressor Mass and the Hammer depends on the mass ratio between those two assemblies. In some sense, the penetrator behaves like a mechanical diode, with high penetrating force provided by the Hammer's impact on the Outer Casing and a small pulling up reaction force. The Suppressor Mass travels up adequately and its kinetic energy is compensated by gravitational potential and compression of a Brake Spring located between the Suppressor Mass and the Outer Casing. The reaction force of the Brake Spring should be less than the holding forces of the Support Structure that guides the penetrator at the beginning of movement, and later the friction force between the Outer Casing and the regolith. The detailed sequence of operation was provided in [5] for HP3 and also in [6] and [7] for CBK's KRET developments.

The HP3 penetrator uses a cam mechanism to perform the strokes, which has clear advantages like: the simplicity of control (just powering the motor in one direction), straightforward locking and unlocking of the system using the rotating movement of the motor, and space heritage through the development of PLUTO for the Beagle 2 mission [1, 2, 3]. The disadvantage is a relatively short compression of the drive spring (and hence stroke energy), which is limited by the height of the cam. Inspired by PLUTO's design, NASA engineers also developed a spring-loaded mole-type penetrator [8].

Contrary to DLR's solution, CBK developed another mechanical penetrator – KRET, which also accumulates stroke energy in a spring, but this solution used a special latch grip which allowed the motor to perform multiple rotations before the hammer was latched. As a result higher compression values could be achieved as well as higher stroke energies (2.2 J in KRET 1 and 3.5 J in KRET 2), see [6]. In this solution the motor's current was monitored and the direction of movement of the motor interchanged accordingly.

Aside from the mechanical solutions, electromagnetic ones are known and utilized, for instance the space flown (TRL 9) MUPUS device for ESA's Rosetta mission [9]. This type of penetrator has the energy stored in a capacitor and released through an electromagnetic coil with a hammer accelerated as a moving core of the electromagnet. Based on this design further developments were provided, such as the CHOMIK device for the Phobos-Grunt mission [10], and the prototype of a High Energy and Efficiency Penetrator [11]. The disadvantage of such a solution is that it requires a capacitor that should be close to the drive coil

and as a consequence occupies a lot of volume, limiting the depth of penetration to the length of the penetrating rod (the drive unit is kept above the surface). The remaining qualities are just advantages like simplicity and reliability of the system as well as the possibility to apply different energy levels. There exists a prototype of an electromagnetic mole-type penetrator, where the capacitor was removed outside the outer casing and a stock of 5 electromagnets was used; it is the recently developed EMOLE within ESA PECS project [12].

### System Overview

The Hammering Mechanism, as specifically mentioned in this paper, is located inside the Outer Casing and consists of the Hammer and the Suppressor Mass assemblies, together with Drive Springs, a Brake Spring and a Wire Helix (see Figure 2). From the point of view of integration, the HM is divided into: Hammer Lock Assembly (HLA), Axis Bearing Assembly, and Motor Assembly (MA). HM is guided against Outer Casing with a so-called Tongue Assembly, which is also important for the launch lock feature of the device. The actual details and components of the design are shown in Figure 2.

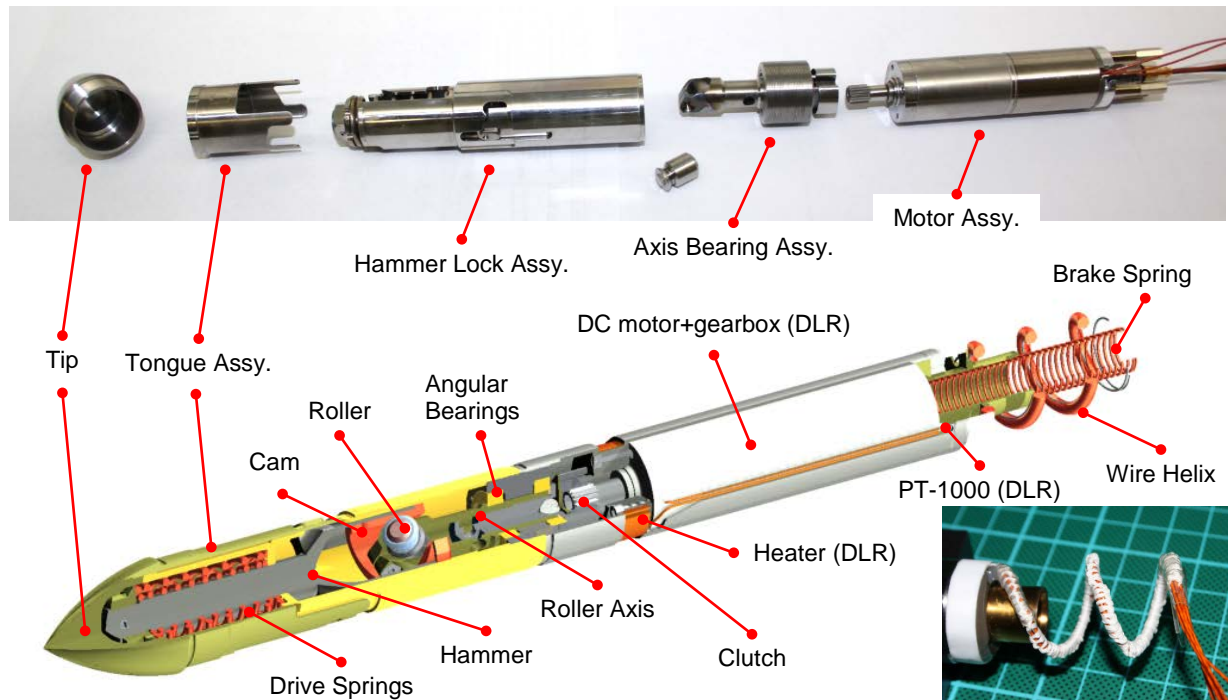


**Figure 2. Components of HM. top: pre-PFM parts, bottom right corner: Wire Helix**

The HLA consists specifically of the Hammer mounted with the Cam located inside the Hammer Housing. Two drive springs (inner and outer) are used with opposed coil turns and are located freely inside the Hammer Housing. They are protected against falling off by a Hammer Nut (screwed and pinned at the tip of the Hammer). The HLA is fixed with the MA through the Bearing Housing that is a part of the Axis Bearing Assembly. The HLA and the MA are counter torqued against each other on the Bearing Housing's thread. The pair of angular bearings located in the Bearing Housing provide axial rotation for the Roller Axis. The Axis is coupled with a gear shaft through a Clutch Element, which provides 40° of angular deadband in the movement of the axis. This angle is important for the phase of operation when the Roller (mounted at the end of the Roller Axis) falls off the Cam's edge and rotates freely the Axis with respect to the Cam to allow for the unconstrained movement of the Hammer.

As a drive unit, a customized Maxon DC Motor Unit DCX22 with Planetary Gearhead GP 22 HP is used, which was installed inside the Motor Housing by screws and using 3M Scotch Weld Epoxy Adhesive 2216 B/A Gray as a filler. Near the front part of the gear box and outside of the Motor Housing, a heater was

mounted to provide temperature control of the Motor Unit. A single PT-1000 sensor, used to monitor the temperature, was mounted in the back plate of the Motor Unit and covered with a Spring Support part. The DC motor, heater and PT-1000 were components for which DLR was responsible.

The MA is finished with the already mentioned Spring Support, which guides all 6 cables, protects their solder points (covered completely with 3M Scotch Weld Epoxy Adhesive 2216 B/A Gray), and provides space for beginning of a Wire Helix formation. The Wire Helix is a bundle of cables partially thermally formed and distributed along a Wire Guide (a gentle compressive spring) wrapped together into a continuous splice using lancing tape. The Brake Spring is a relatively narrow compression spring located inside the Spring Support (Wire Helix remains in parallel to it - outside the Spring Support). For this reason it is prone to buckle, but the Spring Support is long enough to provide constant guiding of the Brake Spring together with the corresponding Inner Guide on the side of the Payload Cage. The actual description of the rest of the HP3 mole penetrator system including Payload cage and Outer casing can be found in [5].

Worth mentioning is that in some sense each penetrator, including the HP3 instrument, may become a self-destructive device if is not designed correctly. Consequently, each joint and connection between parts have to be selected carefully, and, given the very limited volume for the mechanism, most of them have to be connected permanently. For instance, Araldite AV138/HV998 adhesive was used on threads to protect them from unscrewing, tight fit dowels used to connect Cam with the Hammer, press-fits and riveting of the Roller parts and welding in the Tongue Assembly elements. In most cases, disassembly of such connections is not possible without partial destruction of the mechanism.

### **Design Improvements and Significant Technological Features**

The actual cooperation with DLR in the field of the Hammering Mechanism redesign and development began in late 2013. As a result of this cooperation, the final hardware was significantly improved in comparison to the previous versions [1, 2, 3]. Having an easy access to the in-house workshop and vast heritage in penetrators' design, the Space Research Centre PAS and Astronika, in cooperation with Warsaw University of Technology that provided tribological surfaces, was capable of rapid changes in the design and actually developed a new Hammering Mechanism for the HP3 mole instrument. The actual concept change was provided in November 2013, design freeze in December 2013 and successfully working pre-PFM model operating in February 2014. Six models were developed in total in years 2013-2015: pre-PFM, HM-1, HM-2, HM-3 (Life Test Unit), HM-4 (FM) and HM-5 (FS). The final design consists of 38 individual parts and components (82 total parts). The main design changes are described below and are related to three main domains: mechanism architecture and principles (rearrangement of subassemblies' layout and order), increase of efficiency and simplification of the design (improvement of tribological properties and bearings implementation), and functionality (launch lock redesign).

#### **No preload on the drive springs**

In the previous design the drive spring was preloaded, which theoretically could result in better utilization of the spring's characteristics. In fact, it is particularly important to sustain a free movement of the Hammer and the Suppressor-Mass in this type of mechanism, even at the expense of preload benefits. For this reason the preload option was removed and replaced with a free movement of all assemblies. This simplifies the behavior of the mechanism and consequently travel phases of each assembly and its impact moments can be clearly distinguished. The preloaded spring constrained the previous design to have the drive spring located between the rear part of the Hammer and front of the Motor Assembly. This caused the improper load distribution on the Hammer; namely it was pushed from behind instead of being pulled from the front, as it eventually was solved. Application of the pulling force in front of the Hammer (precisely on the Hammer Nut) naturally stabilizes the Hammer movement in the Hammer Housing and cancel all clamping possibilities or friction losses. The actual loading sequence is shown in Figure 3.

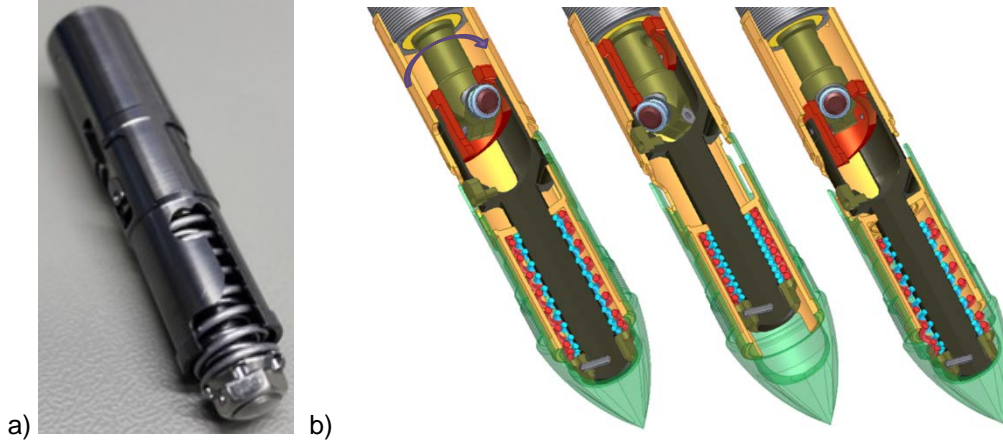


**Figure 3. a) Hammer Lock Assembly, b) Cam loading Drive Springs compression sequence inside the Hammer Housing (Cam-Roller engagement, disengagement, travel of Hammer)**

#### Cam optimization

Resignation from the spring preload, prompted the requirement to use higher cam inclination to provide higher spring compression and increase accumulated energy. A new approach to the cam design was undertaken with the following assumptions: the torque characteristics should be constant for most of the cycle time, the overall angular width of the cam is  $280^\circ$ , maximum reasonable angle at which the roller can roll in is  $30^\circ$  and allowable cam height is 15 mm (in contrast to the previous 7.8 mm). Eventually, the Cam starts with  $30^\circ$  angle inclination and continues until the plateau of constant torque is reached (which is at about  $78^\circ$  of Cam angle, this corresponds to 0.2 Nm of constant torque), then the inclination of the cam smoothly decreases to keep the resulting torque at the same level together with the increasing force of the drive springs. The actual cam profile and expected torque characteristics together with corresponding equations are shown in Figure 4 and Figure 5 (friction losses are assumed to be negligible). The symbols' meanings are:  $\varphi$  – angle of the Cam;  $\varphi_0$  – angle of the Cam at which the inclination starts to change from  $30^\circ$ ;  $h(\varphi)$  – height of the Cam;  $T(\varphi)$  – expected torque on the gear shaft;  $R$  – radius from the rotational axis to the working point of the Roller at the Cam;  $k$  – stiffness of the Drive Springs. Additional advantage of higher cam is that when Roller disengages from the Cam losses are expected, and partially the actual few millimeters of the height of the cam is not 100% effective. Hence, it is much better to have higher cam since this transition phase (between rolling and falling) has twice smaller relative contribution to the disturbance of the movement of the Hammer. It has also much more travel distance to accelerate and provide effective impact on the Outer Casing.

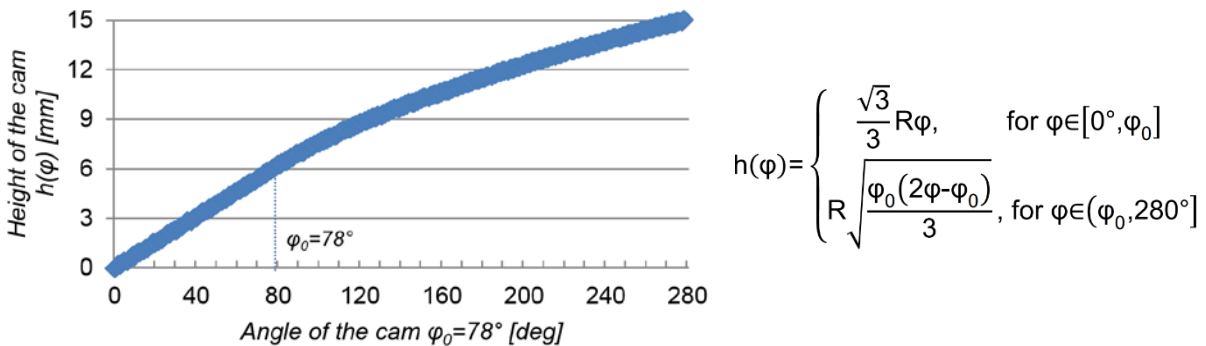


**Figure 4. Theoretical shape of the Cam (symbols for equation described in the text)**



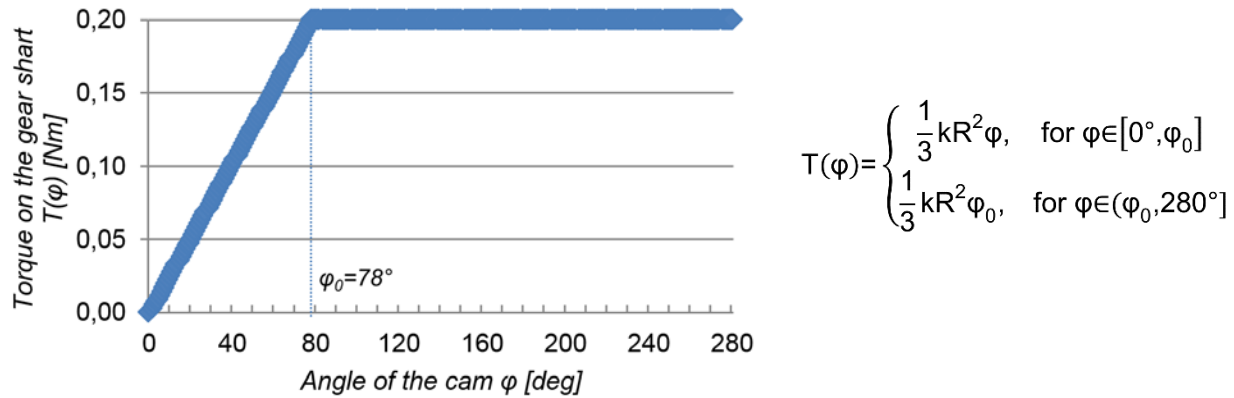


**Figure 5. Theoretical torque on the gear shaft and (symbols for equation described in the text)**

#### Mass distribution and energy optimization

The proper mass ratio of the Outer Casing, Hammer and Suppressor Mass plays an important role in the system's efficiency and performance. It is particularly important to have the highest possible mass of the Suppressor Mass assembly and the lowest mass of the Hammer Assembly. This will result in high energetic stroke of the Hammer and low kinetic energy of the SM assembly to be compensated by the Brake Spring and the Wire Helix. At the same time, the mass of the Hammer Assembly should be balanced with the mass of the Outer Casing to achieve the best possible energy transfer between those assemblies. High density materials were used to accomplish this in the limited volume of the mechanism; in particular tungsten alloys were used for the Hammer (Wolfmet HE3925 alloy) and the Motor Housing (Wolfmet HE395). HE3925 remains more ductile, which was particularly important for the Hammer – the part that experiences the highest loads (over 10000g). Incidents of cracking were encountered in the scope of the project (described in the lessons learnt section), nevertheless the Hammering Mechanism together with the selected materials proved its durability in thousands of strokes performed (qualification level was 45000 strokes). The achieved mass ratios also allowed for the use of more energetic drive springs (c.a. 0.7 J), which is an important factor to sustain effectiveness or even allow for penetration of the mole in the regolith. In the final design, the achieved masses of the Hammer and Suppressor Mass assemblies are 0.11 kg and 0.46 kg correspondingly, so the actual Hammer kinetic energy is about 0.57 J and for the Suppressor Mass is 0.14 J.

#### Lubrication plan

All of the sliding bushings were replaced either with ball bearings (for all rolling movements) or advanced tribological surfaces that were provided by Warsaw University of Technology and Lodz University of Technology. This led to the vast simplification of the mechanism's design and also increase in its efficiency. Different coatings and surface treatments were used wherever applicable: lead (PVD), MoS<sub>2</sub> (PVD), TiN. The general rules were to: 1) use MoS<sub>2</sub> on all sliding surfaces (it was also used on tungsten alloy for the first time), 2) lead on rolling or stroke surfaces and also springs, 3) and TiN on all titanium surfaces. All surfaces were hardened (nitrided) before the deposition of coatings, with the exception of Tungsten alloys, which reveal relatively larger hardness on their own (24-26 HRC). The actual main materials and tribological coatings are shown in Figure 6.

The applied surface modification processes increased wear resistance of the used steel, titanium and tungsten parts of the HP3 device. Applying MoS<sub>2</sub> magnetron sputtered coating significantly reduced wear rates and friction coefficient of these materials. In case of titanium alloy (Ti6Al4V), additional plasma nitriding process was necessary in order to improve the lifetime of MoS<sub>2</sub> coating. Additional tests using „ball on disc” tribometer with Al<sub>2</sub>O<sub>3</sub> ball were performed to prove the rightness of MoS<sub>2</sub> application on Tungsten (HE 395) and titanium alloy (tests in air). As it can be seen in Figure 7 the coefficient of friction for tungsten alloy has significantly reduced and stabilized after MoS<sub>2</sub> deposition (from 0.5-0.7 to below 0.1). For the case of titanium alloy, the tests revealed that the use of nitride titanium surface as a base surface for MoS<sub>2</sub> deposition can increase the wear resistance of the coating over two times (the test ended after 1100 m).



Additional tests for this type of tribological pair can be found in [13]. Figure 8 shows wear traces of the tested samples clearly showing higher wear resistance for nitrided titanium and tungsten with MoS<sub>2</sub> sputtered.

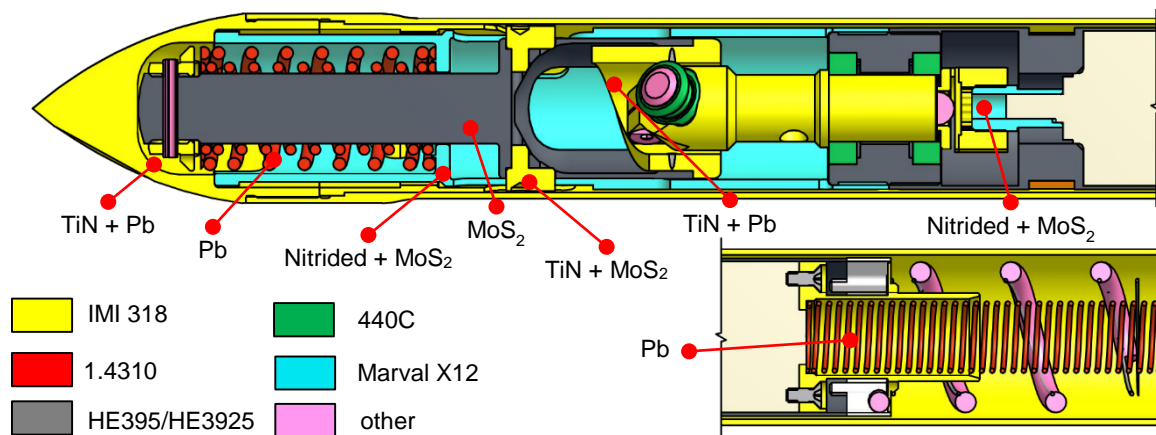


**Figure 6. Materials and coatings of the Hammering Mechanism**

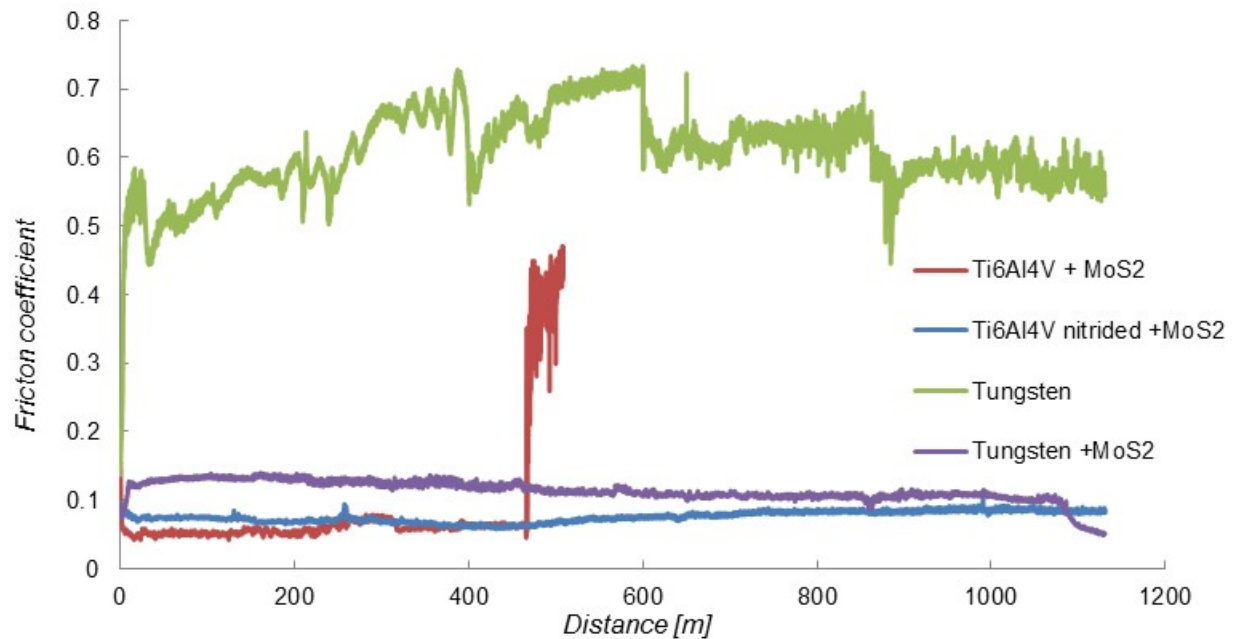


**Figure 7. Friction coefficient changes as a function of friction distance of used materials after different surface treatments (“ball on disc” test against Al<sub>2</sub>O<sub>3</sub> ball under 10-N load) in air**

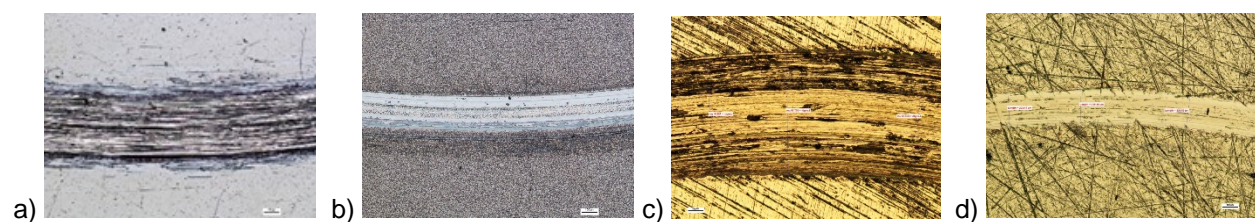


**Figure 8. Wear traces of Ti6Al4V (a), nitrided Ti6Al4V (b) and tungsten alloy (d) coated by MoS<sub>2</sub> in comparison to uncoated tungsten alloy (c); pictures are in the same scale**

Worth mentioning is that the mechanism was required to be tested also in air and room temperature and some wear of the coatings was expected. For this reason, all sliding and rolling surfaces (previously coated) were additionally lubricated with Braycote 601EF. The deposition of the Braycote was done by application of the excess of Braycote on the desired surfaces and its removal with a dust-free wipe until a film of it was left. The typical method of grease plating could not be used because of assembly complexity and multiple bonding steps interchanged with the lubrication process. Often masking had to be used, especially for deposition of the coatings ( $\text{MoS}_2$  and lead) as shown in Figure 9ab. Unfortunately,  $\text{MoS}_2$  did tend to wear from the Hammer Lock Pins ( $\text{Ti6Al4V}$  nitrided +  $\text{MoS}_2$ ) during mechanism inspection runs that were done yet before Braycote application, see Figure 9c.

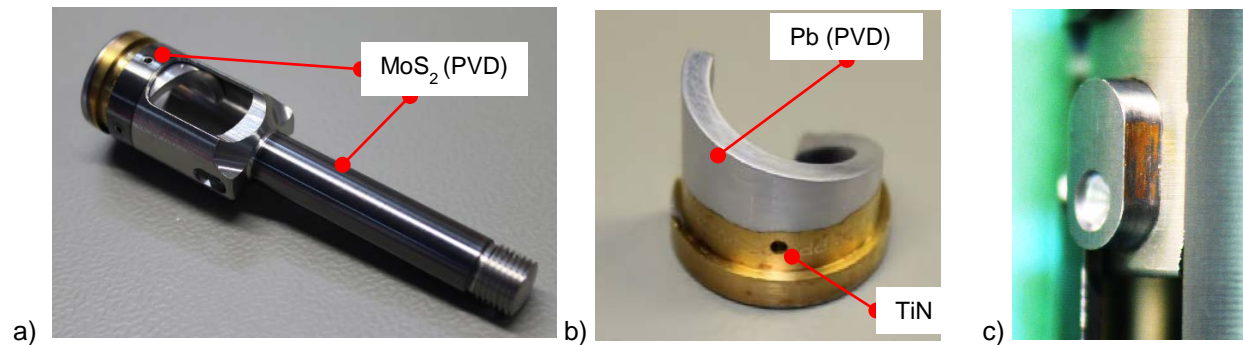


**Figure 9. Appearance of different coatings and surface treatments; a) Hammer ( $\text{MoS}_2$ ), b) Cam ( $\text{TiN} + \text{Pb}$ ), c) wear of  $\text{MoS}_2$  on Hammer Lock Pin ( $\text{TiN} + \text{MoS}_2$ )**

### Bearings

Together with tribological coatings the bearings were implemented to take over loads induced by drive spring tensioning and cam torqueing. Angular bearings (440C, PEEK cage, O-configuration) were implemented to support rotational movement of the Roller Axis. The actual design is shown in Figure 10. The bearings are inserted on the Roller Axis part with a slip fit, they are separated from each other by the mean of the Bearing Housing where slip fit is used as well. The bearings are loaded from the side of the Motor Clutch Element, through the Outer Clutch Element that is screwed into the Roller Axis and stops on a distance washer and inner ring of one of the bearings. The washer is adjusted to the height which provides cancellation of the clearances in the bearings and stops on it after the locking torque is applied. The Outer Clutch Element has a left hand thread which corresponds to the direction of rotation of the gear shaft. This is an additional means of locking the connection (besides glue and torque applied).

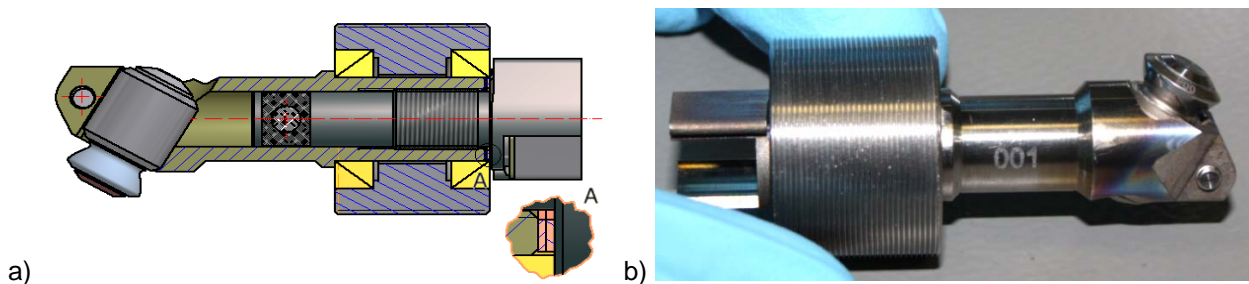


**Figure 10. a) Half-section of Axis Bearing Assembly, b) Picture of Axis Bearing Assembly**

The bearings are not sealed and external lubrication was applied. This is a low velocity application (15 rpm) and again the Braycote 601EF was used. As shown in Figure 11, six drops of Braycote were applied on the bearings balls with the total mass of about 0.03g (which is about 20% of the maximum volume of bearing that can be filled). Then the lubricant was spread around by rotating the bearing.

Additionally, an individual design of the bearings for the Roller Assembly was implemented (Figure 12) that significantly improved the Drive Springs loading process. To provide better load characteristics, it is

mounted on the Roller Axis at 60° angle to the main axis (see Figure 10a and Figure 12a), so not only radial but also axial forces are introduced to the assembly. As an assembly, it has 34 rotating parts (12 balls and 22 rollers), compacted into a Ø9.2x14.9 mm envelope and undergoes 87 N of radial and 50 N of axial periodic load from the Drive Springs. The design of the Roller is interesting itself and evolved a few times until it reached the presented design. It consists of the Roller Shaft which has to be a single part to ensure coaxial surface for the rotating parts. The Roller part has a press fit with Roller Shaft. The back of the Roller is closed with a Roller Washer, which does not take loads except for holding needles from escapement and it is joint to the assembly by a Roller Rivet made of 1H18N9T (EN 1.4541) stainless steel. The balls take over the axial loads. All parts, with the exception of the rivet, are 440C stainless steel hardened to 58 HRC. The interior of the Roller Assembly is lubricated with Braycote 601EF, which was applied by injection after the actual assembly – the lubricant was pressed into the Roller Assembly to fill 100% of the roller volume (which is about 0.15g). Then the Roller was rotated with 50-100 rpm for 60 seconds to remove the excess of lubricant. This resulted in 66% of lubricant remaining in the volume of the Roller (about 0.10g). The measured drag torque of the Roller with the Braycote in room temperature was c.a. 0.5 N-mm, which would have marginal influence on the gear shaft torque (close or less than 1%). One of the tests, with the pre-PFM model, revealed that even the blocked Roller can still be successfully elevated on the Cam with the provided motor, therefore increase of drag torque in lower temperatures is not critical for the mechanism. The large amount of Braycote plays an important role in sealing the Roller from unwanted debris.

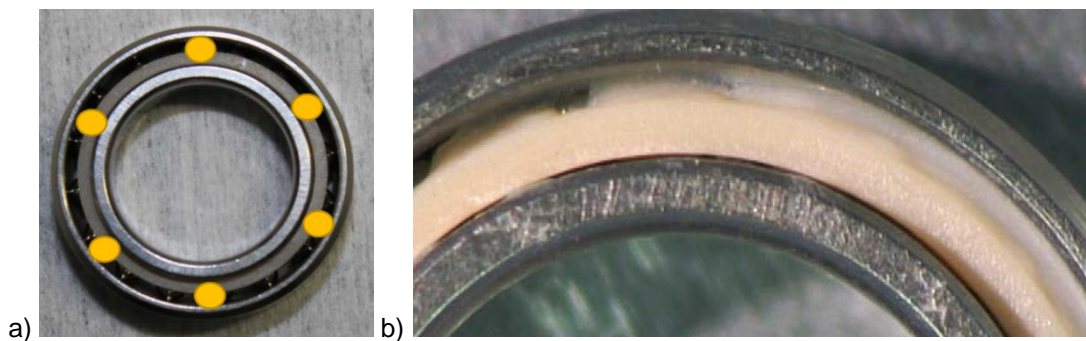


**Figure 11. Angular bearing lubrication: a) Braycote application area, b) close-up**

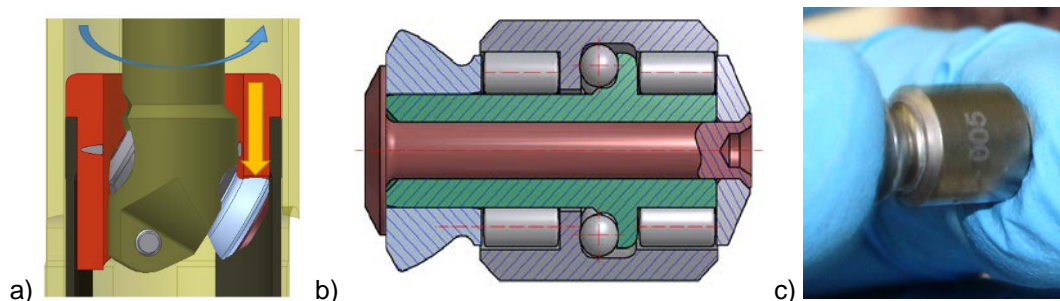


**Figure 12. a) Roller loading, b) Half-section of the Roller, c) Roller hold in fingers to show the scale**

#### Launch Lock system

Functionality of the launch lock system was improved in the scope of the project. The final design allows for multiple locking and unlocking of the Hammer against the Suppressor Mass and the Suppressor Mass against the Outer Casing (i.e., Tongue Assembly) without the necessity to disassemble the whole mole mechanism (particularly important for planetary protection procedures). The Hammer Housing possesses dedicated slots (axially symmetrical on both side of the Hammer Housing) in its walls to allow for proper guidance of Hammer Lock Pins and Tongue Assembly Lock Pins and constraints the vertical movement of the traveling masses in its normal operation mode. Besides the guidance slots, it also possesses the dedicated lock notches, that are used in the locking and releasing modes of operation, see Figure 13 and Figure 14 for details.



A reverse operation of the motor is used to lock the mechanism. The motor starts to turn counter-clockwise and eventually the Roller pushes the Cam and as a result the whole Hammer Assembly. While the Hammer rotates inside the Hammer Housing, the Hammer Lock Pins encounter slope of the lock notches and slide up about 1.5 mm upwards. Eventually, they cross maximum elevation of the notch and drop into the final position in the launch lock pocket slightly loaded in that position by the Drive Springs. The motor still continues to rotate and the Hammer Lock Pins stop on the Tongue assembly fork-shaped features, see Figure 13. As a result, it is now the Suppressor Mass to start rotating in the opposite direction with respect to the Tongue Assembly. While it rotates, the cut-outs on the bottom of the Suppressor Mass change their position until the Tongue Assembly Lock Pins are positioned in the launch lock pocket of the Suppressor Mass, see Figure 14. Both pairs of the Launch Lock Pins are located in little local pockets that keep the assemblies in place during vibrations. They are not likely to freely jump out of this position because the gear shaft would have to start rotating, which requires multiple rotations of DC motor, but this is not happening during the launch.

The unlocking is just a matter of powering the motor in the operational (hammering) mode. The Roller Axis would start then to rotate clockwise and eventually the Roller encounters the Cam. The Hammer Assembly now elevates and as a result the Hammer Lock Pins are released from the launch lock pockets in the Hammer Housing. Consequently the Hammer Assembly is turned with respect to the Suppressor Mass (in the Hammer Housing) towards the normal operation guidance slots. Eventually the Hammer Lock Pins reach the opposite fork-shaped feature of the Tongue Assembly and resist against it, which allows now the Suppressor Mass assembly to start rotating backwards with respect to the Tongue Lock Pins and eventually position all the assemblies and their lock pins in corresponding guidance slots of the Hammer Housing.

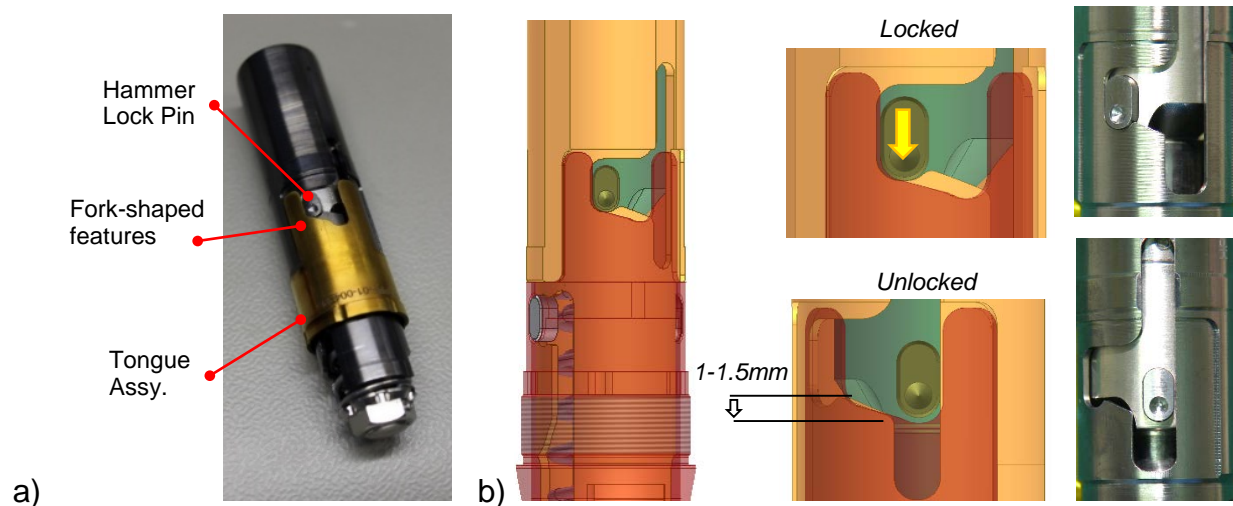


**Figure 13. Launch lock design details; a) Hammer Lock Assembly with Tongue Assembly in locked position, b) Hammer locking on Suppressor Mass (right pictures without Tongue Assy.)**

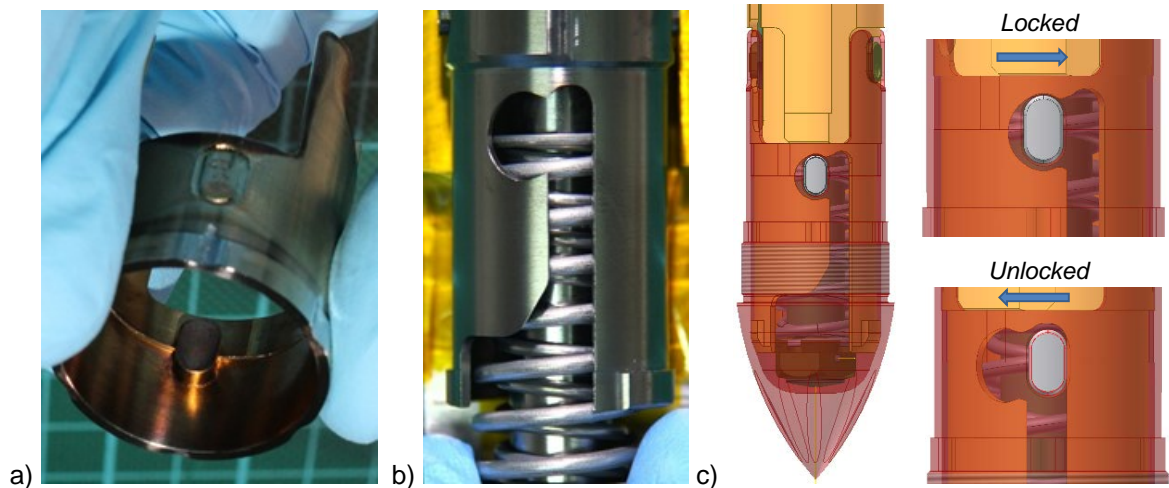


**Figure 14. Launch lock design details: a) Tongue Assembly with visible one of Lock Pins, b) Hammer Housing slot for SM guidance, c) Suppressor-Mass locking on Tongue Assembly**

### Lessons Learned

The implemented changes allowed to achieve relatively high energy penetration strokes as for the given constraints of mass and Cam height, with much improved efficiency. The resulting average power consumption was 0.6 W (0.33/0.72 W peak values). As a result, the overall efficiency of the system is 30%. The average work cycle of the Hammering Mechanism is about 4s. Figure 15 shows the motor's current record from the first two strokes of the HM-4 unit (FM). Spring loads and release phases can be seen on this plot. When compared to the previous Figure 5, it can be clearly seen that the cam profile optimization works as expected: the uniform increase of current represents the 30° inclination slope, then the current keeps constant value (and motor constant load) until the Roller reaches the edge of the Cam.

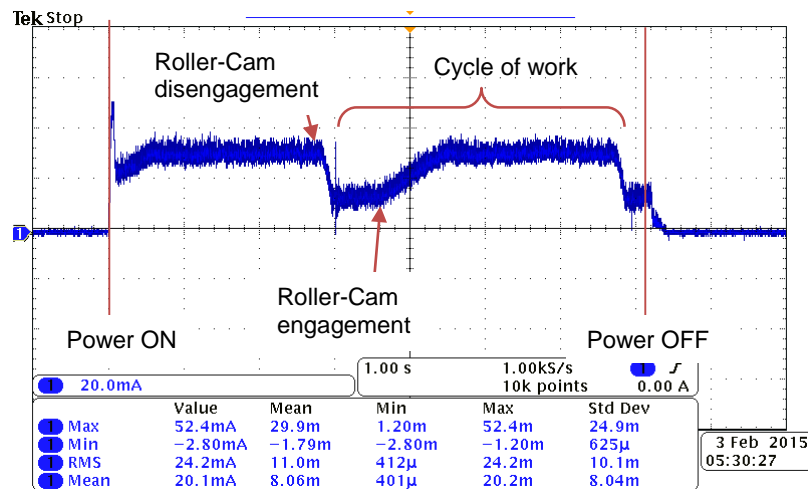


**Figure 15. Current record of first two strokes of HM-4 (FM)**

Besides satisfactory results that have been achieved, there were few sensitive issues encountered that are worth mentioning here.

One of such issues was connected with Tungsten alloy that was used for the Hammer and Motor Housing parts. Initially, only HE 395 alloy was used, with which CBK already had experience during development of KRET penetrator. Eventually a few cases in which this material revealed its brittle nature occurred. This happened in the Hammer parts in the area of Hammer Lock Pin location. The crack appeared in the notch

area as shown in Figure 16a and propagated. It could appear either at the moment of assembly or manufacturing. It was decided to change the material of the Hammer to HE 3925 alloy, which is more ductile. In fact the cracks in Tungsten alloy are hard to detect by direct visual inspection, also its surface features and specific reflection capabilities very often look like crack which appears not to be in the end (example shown in Figure 16b). Besides a very detailed visual inspection (microscopic with magnification over x20) of all tungsten parts, also a scanning electron microscope was used and in some cases even X-ray computer tomography (which was limited just to single millimeters of penetration due to high density of tungsten). Eddy current detection method was also investigated but due to complex shapes of the investigated parts the interpretations of measurements was not unequivocal. Starting from HM-3 model a new material was used and also all notch areas significantly modified to limit all the possible stress concentration areas. It is important to mention that no cracking was recorded for the Hammer parts during their operation and qualification tests, both for HE 395 (in HM-1 and HM-2) or HE 3925 material (for HM-3, HM-4 and HM-5).

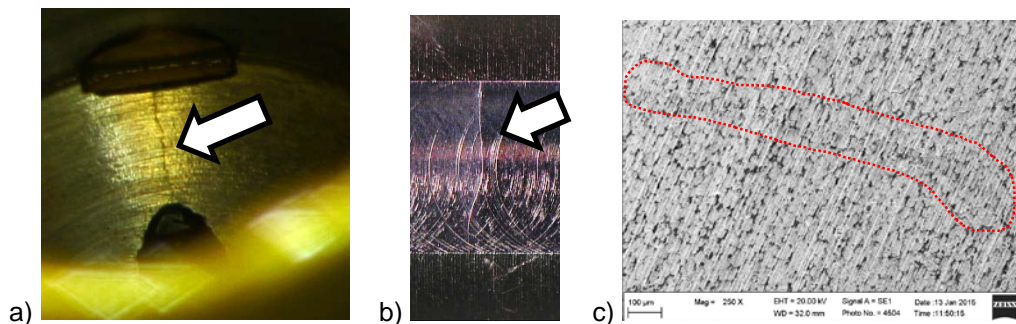


**Figure 16. a) Hammer crack in the Hammer Lock Pin area (view to the interior of Hammer part), b) Motor Housing Scratch (not a crack), c) magnification of Tungsten alloy HE 3925 inspected surface (SEM, x250, inspected scratch inside the contour)**

Besides tungsten alloy issues, a fatigue cracking was experienced. Models HM-1 and HM-2 have been implemented in a Clutch Spring in a form of two symmetrical 0.2-mm bands of 1.4310 steel that connected the Inner Clutch Element with the Outer Clutch Element. The purpose of the Clutch Spring was to provide the additional accumulation of energy which was used during Cam-Roller disengagement. The Clutch Spring was to kick off the Roller from the edge of the Cam and eventually reduce the losses of energy connected with rolling out. Due to the schedule constraints, the actual laboratory tests that were performed after the HM-1 and HM-2 development shown a fatigue failure of the spring after 15000 strokes (whereas qualification level was 45000 strokes). The actual effect of kicked-off rolling out can be noticed on the high-speed camera videos, but in the end the actual change of the mechanism's overall performance (stroke energy) was unnoticeable. In further models (HM-3, HM-4 and HM-5) the Clutch Spring was removed from the design. In other words, if properly designed the Clutch Spring could bring benefits to this type of the mechanism, but is not obligatory.

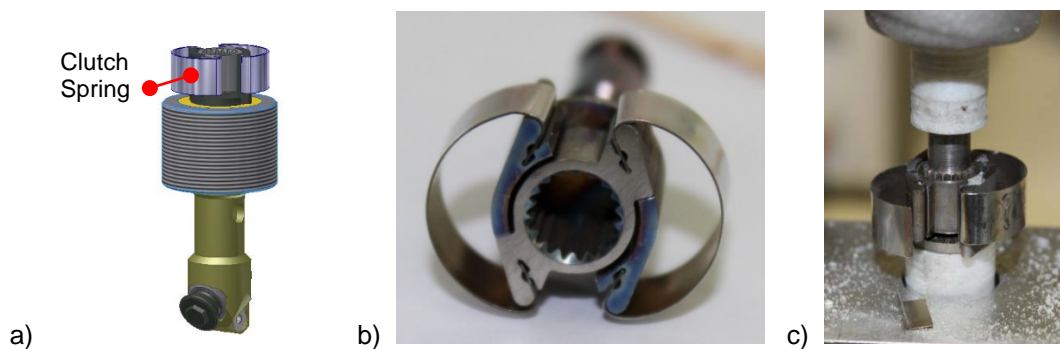


**Figure 17. a) Clutch Spring location in Axis Bearing Assembly, b) The actual appearance of Clutch Spring, c) Broken Clutch Spring during the tests**

The last issue worth mentioning, discovered during trial runs of the Hammering Mechanism after its integration, was its sensitivity to improper twisting of the Wire Helix with respect to the Payload Compartment and Outer Casing. The Wire Helix, which is a handcrafted component, is prone to be not fully repeatable and each mechanism required individual adjustment of the twisting angle inside the Outer Casing. The only way to do it is to properly tension it by twisting its fixation points - one with respect to the other. The direction of twisting is of a high importance and it cannot be too tight since it would interfere with Spring Support and Brake Spring and also not too wide, since it would start sliding on the Outer Casing or even block the movement of Suppressor Mass (while expanding too much while being compressed during hammering). The unpredicted influence of that tensioning was encountered during trial runs – Wire Helix when tensioned against its coil direction (in the direction that causes its diameter expanding) creates a twisting torque on the Suppressor Mass as well. This is not noticeable until the actual movement of masses begins and Suppressor Mass can undesirably slightly twist back, resulting in a situation where the fork-shaped features of the Tongue Assembly partially collide with the accelerating Hammer Assembly (namely Hammer Lock Pins). This was called a bottle-neck effect since Hammer Lock Pins for a very short time are pressed on one side by an edge of the Hammer Housing slot and corner of a fork-shaped feature in the Tongue Assembly. This cannot stop the Hammer, but can decelerate it and result in damped hammering action. The actual event sequence is shown in Figure 18a. The effect can be easily omitted when the Suppressor Mass will always be pulled by the Wire Helix in the direction indicated in Figure 18b.



**Figure 18. a) Sequence of Hammer Lock Pin movement including bottle-neck effect; b) Rear part of Suppressor Mass and Wire Helix. Arrow indicates in which direction SM should be properly pulled by Wire Helix to omit bottle-neck effect**

## Conclusions

The article presented the actual summary of main technological features of the Hammering Mechanism for the HP3 mole penetrator. Particularly, principle and justification for drive springs location was discussed, which should always provide stabilized pulling force on the Hammer. DC Motor operation characteristics were improved by Cam's profile optimization and confirmed with actual tests and current records. Also the principle for Cam profile design and optimization were provided with 30° initial slope inclination requirement. Significant attention was paid to the lubrication process, which was particularly important for the simplification of the design and increase of its reliability. Uncommon coatings were provided like sputtered MoS<sub>2</sub> on Tungsten alloy or on plasma nitrided Titanium alloy, supported by results of tribological tests. Some wear of MoS<sub>2</sub> on Hammer Lock Pins was experienced and additional Braycote 601EF lubrication was provided to improve the wear resistance and durability of the coatings. Besides lubrication, the bearing description was discussed including the especially interesting design of a very small Roller (Ø9.2x14.9 mm) with total of 34 rotating parts that can take over axial and radial loads. Last but not least, the novelty of the design was the Launch Lock system that allows for multiple locking and unlocking of the mechanism without necessity of penetrator's disassembly.

Problematic areas of the design were additionally highlighted. Tungsten alloy selection and its durability for high impact application was provided. Encountered problem with cracking of the material were indicated, which was solved by particularly intensive inspection process on each phase of parts development. Also



Clutch Spring design was discussed together with actual fatigue problems that led to the resignation of implementation of this mechanism's component. Eventually an assembly problem was described, connected with the bottle-neck effect on the Hammer Lock Pins movement, possible to omit by careful tensioning of the Wire Helix.

The Hammering Mechanism achieved successful performance results with power consumption kept at relatively low level, below 1 W, which proves the rightness of the implemented design.

### References

1. Gromov V.V. et al.: The mobile penetrometer, a "mole" for sub-surface soil investigation. In Proc. of 7<sup>th</sup> European Space Mechanisms and Tribology Symposium. 1997.
2. Richter L. et al.: Development of the "Planetary Underground Tool" subsurface soil sampler for the Mars Express "Beagle 2" Lander. Advanced Space Research, No. 8, pp. 1225-1230. 2001.
3. Richter L., Krömer O.: Application of a Remote Controlled Hammering Drill from Space to Deep Sea. Oceans 2009 – Europe, IEEE. doi: 10.1109/OCEANSE.2009.5278132.
4. Spohn T. et al.: InSight: Measuring the Martian heat flow using the Heat Flow and Physical Properties Package (HP3). In Proc. of International Workshop on Instrumentation for Planetary Missions. 2012.
5. Lichtenheldt R., Schäfer B., Krömer O.: Hammering beneath the surface of Mars-Modeling and simulation of the impact-driven locomotion of the HP3-Mole by coupling enhanced multi-body dynamics and discrete element method. 58th Ilmenau Scientific Colloquium (IWK), Ilmenau, Germany, 2014.
6. Grygorczuk J. et al.: Technological Features in the New Mole Penetrator "Kret". In Proc. of 13th European Space Mechanisms and Tribology Symposium ESMATS, Vienna, 2009.
7. Seweryn K. et al.: Low velocity penetrators (LVP) driven by hammering action—definition of the principle of operation based on numerical models and experimental tests. Acta Astr., vol 99, pp. 303-317.
8. Stoker C. R., Gonzales A., Zavaleta J. R.: Moon/Mars Underground Mole. NASA Tech. Conf., 2006.
9. Spohn T. et al.: MUPUS—A thermal and mechanical properties probe for the Rosetta lander Philae. Space Science Reviews, (2007) 128: pp. 339–362. DOI: 10.1007/s11214-006-9081-2
10. Grygorczuk J. et al.: Advanced Mechanisms and Tribological Tests of the Hammering Sampling Device CHOMIK. In Proc. of 14<sup>th</sup> European Space Mechanisms and Tribology Symposium ESMATS, Constance, 2011.
11. Grygorczuk J. et al.: High Energy and Efficiency Penetrator-HEEP. In Proc. of 15<sup>th</sup> European Space Mechanisms and Tribology Symposium ESMATS, Noordwijk, 2013.
12. Grygorczuk J. et al.: Mole Penetrator Driven by an Electromagnetic Direct Drive (EMOLE). In Proc. of 16<sup>th</sup> European Space Mechanisms and Tribology Symposium ESMATS, Bilbao, 2015.
13. Grygorczuk J. et al.: Specialized Hybrid Rolling Bearings for Space Use – Project ROLOKOS. In Proc. of 16<sup>th</sup> European Space Mechanisms and Tribology Symposium ESMATS, Bilbao, 2015.

# Testing and Measurement of Mechanism-Induced Disturbances

Laoucet Ayari\*, Michael Kubitschek\*, Gunnar Ashton\*, Eric Marquardt\* and Steve Johnston\*

## Abstract

Many space mechanisms with moving parts such as gimbals, cryocoolers, shutter mechanisms, filter wheels, fast steering mirrors, and reaction wheels produce dynamic forces and torques that have the potential to interfere with the function of other onboard instruments. Jitter sources include direct reaction forces and torques from linear and rotary actuators, inertial imbalances, misalignments and internal loads operating against asymmetric inertia and or stiffness to name a few. The drive to address disturbances from mechanisms in space hardware is prompted by the need to meet certain mission requirements, e.g., signal quality from a science-producing instrument, line of sight stability, or optical jitter. The minimization of jitter can be approached through integrated analytical procedures and experimental tests capable of identifying the source, nature and magnitude of the driving forces and torques. Even if a mechanism is designed to eliminate jitter, e.g., having reaction cancellation features, small loads are always present due to manufacturing tolerances, slight imbalances, and coupling between degrees of freedom. In this paper, we discuss advances made in the measurement verification process of jitter loads at Ball Aerospace & Technologies Corporation (BATC) over the past few years. In particular, the strategy used to deal with a wide range of loads and applications prompted the development of a capability to custom build measurement platforms with the needed performance using modular hardware. Examples of jitter mitigation and cancellations are discussed to illustrate some of the work carried over the past decade.

## Introduction

Force and moment platforms (FMPs), also known as dynamometers, are now commonly used to measure imparted loads in the six degrees of freedom from either operating mechanical systems with moving parts placed on top of the device or non-operating systems excited using shakers and stingers. Such devices can be used in many applications, including JPL's force limiting during vibration testing of space hardware [1], static and dynamic balancing of rotating systems [2], measurement of inertial properties, and hybrid testing where a subset of the unit under test is accounted for through the application of equivalent loads obtain from real-time simulations [4]. The other use of such devices is in jitter measurement [3] and is the subject of the current contribution.

FMPs use three or more judiciously encapsulated tri-axial force sensors between two sufficiently rigid plates. They are designed to be statically determinate, so that all torques are transmitted mainly as forces through the load cells. Loads from the tri-axial force sensors are related to the forces imparted on the top interface plate through a system of equilibrium equations. The unit is then calibrated as a system to measure resultant dynamic loads on top of its surface.

Depending on the geometry of the FMP, the number and type of force sensors and the characteristics of the unit under test, there are limitations on the capability of the FMP. These limitations are on the magnitude and accuracy of the imparted forces and torques, their frequency range and the sensitivity of the system as an instrument. In addition, depending on the test location and whether a low frequency table is used, there is a noise floor that needs to be characterized prior to each test.

Because of the wide range of requirements from one program to another, BATC elected to implement a strategy that builds custom FMPs tailored for each program using modular hardware. FMPs are built from

---

\* Ball Aerospace & Technologies Corp., Boulder, CO

a toolkit of hardware and flexible software to respond to the particular needs of the application producing jitter.

The paper addresses the experience and capabilities for jitter verification at BATC. In particular, the following topics are discussed:

- (a) The modal characteristics of measuring platforms and their dynamic coupling with the behavior of the instrument under test. Often, the potential for interaction between the instrument and the measurement platform prompts the identification of the frequency content of the setup in the frequency band of interest. In addition, the type, number and layout of the force sensors together with the choice of the encapsulating hardware are discussed in light of stiffness and measurement requirements.
- (b) The different methods used for dynamic calibration of a six-degree of freedom FMP in light of the test setup environment, and applicable requirements. These include harmonic stinger tests, frequency response function tests, speaker tests and independent measurement verification, e.g., through a Vibration Lab data acquisition system network or portable systems.
- (c) The handling of background noise to ensure adequate measurements. There are two sources of background noise: one from the measuring equipment used in the test setup and the other is of environmental origin, often induced by nearby operating machinery and/or human activities.

Finally, the paper gives examples of jitter measurement, mitigation and verification of mechanisms, including cryocoolers and momentum wheels.

### **Measurement Verification**

Fast steering mirrors, gimbals, reaction wheels, shutter mechanisms, cryocoolers and other instruments with moving components impart dynamic loads that require proper characterization to meet mission requirements such as those involving line of sight stability, optical jitter and image quality. These dynamic loads need to be measured and often mitigated using advanced design layouts. In certain mechanisms involving optical systems such as fast steering mirrors, gimbals, reaction wheels, shutter mechanisms, cryocoolers and other instruments with moving components, inertial load couplings and reactions from actuation need to be cancelled and therefore the verification of imparted loads becomes essential during the integration of the mechanisms. In many applications, jitter elimination is addressed through either active or passive isolation systems. The performance of such systems needs to be evaluated through measurements and FMPs are essential for such verifications.

Over the past twenty five years, BATC built and internally calibrated several multi-degree of freedom precision FMPs to measure jitter and reaction loads from space instruments. Some of the tables are static and others are dynamic, capable of simulating complex multi-axis external jitter input. These tables were used for multiple space programs and in multiple environments, including vacuum, cold temperature, simulated weightlessness (as low as a fraction of 1 Hz). In addition to simultaneously measuring three forces and three moments in the time and frequency domains, the tables were used for static and dynamic balancing, JPL's force limiting during environmental testing, and bearing contact angle verification. Depending on the application, FMPs were developed to meet a variety of requirements involving particular geometric configurations, weight, stiffness, and low jitter load amplitudes and frequencies. Some FMPs were built for applications where the frequency of interest is around 0.5 Hz. Other dynamometers were built to handle high frequency measurements where stiffness requirements are dictated by high bandwidth control loops (e.g., fast steering mirrors).

Because there is no dynamometer that can address all sorts of requirements from one program to another, BATC elected to acquire the capability to rapidly put together customized exported force and torque (EFT) test setups depending on the mechanism under test and what is being measured. To this

end, the EFT Facility at BATC acquired dozens of tri-axial sensors of varying capabilities, high quality in-line charge amplifiers, signal conditioners, and a large number of input/output multichannel, high resolution and high dynamic range analog DAQ cards. The hardware for developing FMPs is modular so that the right equipment is selected to support single or multiple setups at a time. The tool kit to allow quick FMP implementation and currently allows for measurement magnitudes ranging from  $3\text{E-}5\text{ N}$  to  $200\text{ N}$ , with higher/lower ranges possible. Multiple special EFT stiff tables (Figure 1) provide a low 5-Hz isolation system with a top plate providing a standard 2-inch (5.1-cm) grid mounting pattern. Clean tents with  $15^{\circ}\text{C}$  to  $25^{\circ}\text{C}$  temperature control provide enclosures when stringent cleanliness or environmental levels are required for flight hardware.



**Figure 1. EFT tables with clean tents: 30,000 lb (60" x 60") (left) and 4,400 lb (36" x 34") (right)  
133 kN (1.5 m x 1.5 m) (left) & 19.6 kN (.91 m x .86 m) (right)**

The extent of stiffness verification of FMPs is performed first through analysis using a finite element model representing the load cells and encapsulating plates with and without the mechanism under test and later, once assembled, using frequency response function testing. To ensure that the setup configuration does not contribute to the measured data at particular frequency ranges, frequency response functions are expected to have clean frequency responses. That is no gains (or tolerable gains) in the frequency range of interest must be shown, as illustrated in Figure 2, when the setup is excited in the three axes and at different locations of the top plate of the FMP.

For example, the first generation 1-kHz FMP is shown in Figure 3. The system uses three Kistler type 9067 tri-axial load cells, nine Kistler 5010B0 charge amplifiers, National Instruments type PCI-6033E data acquisition card, and utilizes LabVIEW's interface software to acquire data at 5000 samples/sec. The system resolves the three orthogonal forces from each of the three tri-axial load cells to the three resultant forces in the X, Y and Z axes and three moments  $M_x$ ,  $M_y$ , and  $M_z$ . Jitter forces and moments are measured from 1 Hz to 1 kHz with a resolution of 0.5 Hz. Upon acquisition, fast Fourier transforms are performed on the data to provide frequency domain equivalent data through a software interface.

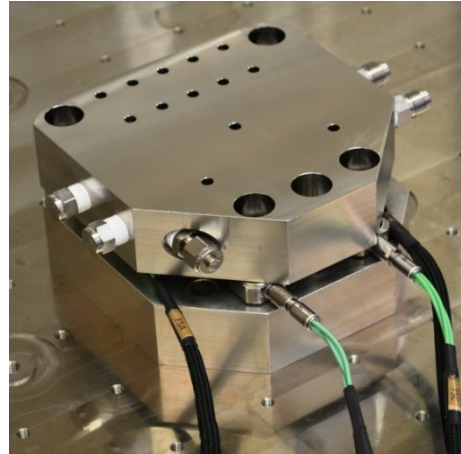
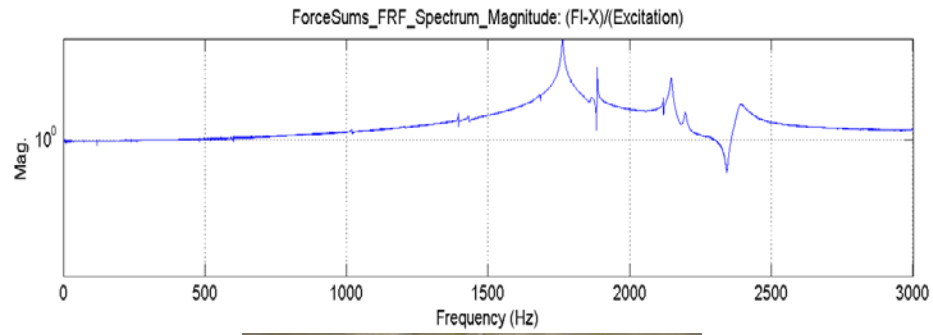


**Figure 2. Tap test showing clean response to high frequency with little gain (top) and partial FMP hardware during assembly (bottom)**

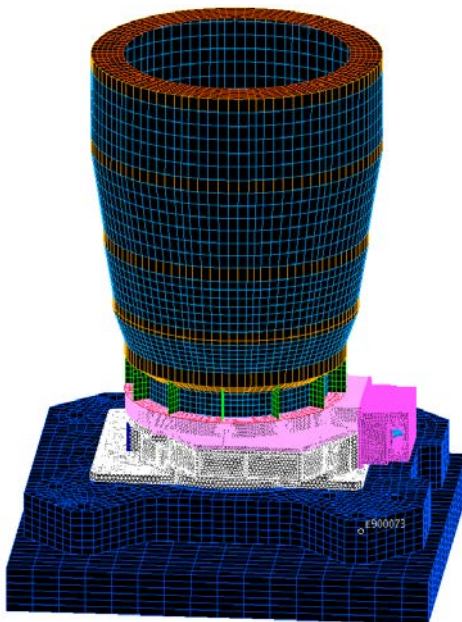


**Figure 3. An Integrated example of a model of a mechanism with a later generation of BATC FMP (left) and 1 KHz FMP, charge amplifiers and computer system for data acquisition (right)**



EFT testing generates large amount of data over short time spans. In addition to data acquisition and management, the Ball-developed Dynamic Measurement and Analysis software platform provides real-time fast Fourier transforms and power spectral densities, and sliding window analysis. Multiple dynamometers can be used within a single setup with real-time viewing of time-domain and limited frequency domain. A configuration file allows for quick addition of new dynamometers and sensors such as encoders and accelerometers. Finally, both real time and frequency data can be easily imported into Excel or MATLAB for processing with a suite of scripts, allowing analysis and automatic data plotting.

### Background Noise Measurement

When characterizing EFT from mechanisms, identification of the magnitude and spectral properties of the noise floor at different times of day (and sometimes at different physical locations) is performed. The noise floor is lower during the late evening/early morning time, and when testing is performed in the massive reinforced concrete test pit facility which is part of a large testing facility at BATC. The noise floor magnitude depends on the type of electronics used in the FMP design, its size, and whether an EFT table is used for support. Typical background noise is less than  $1\text{E-}4\text{ N}$  as illustrated in Figure 4. The bulk of the noise is of environmental nature. At times, shutting down equipment in the vicinity of the test may be required, and facilities in upper floors or nearby urban roads are usually noisier.

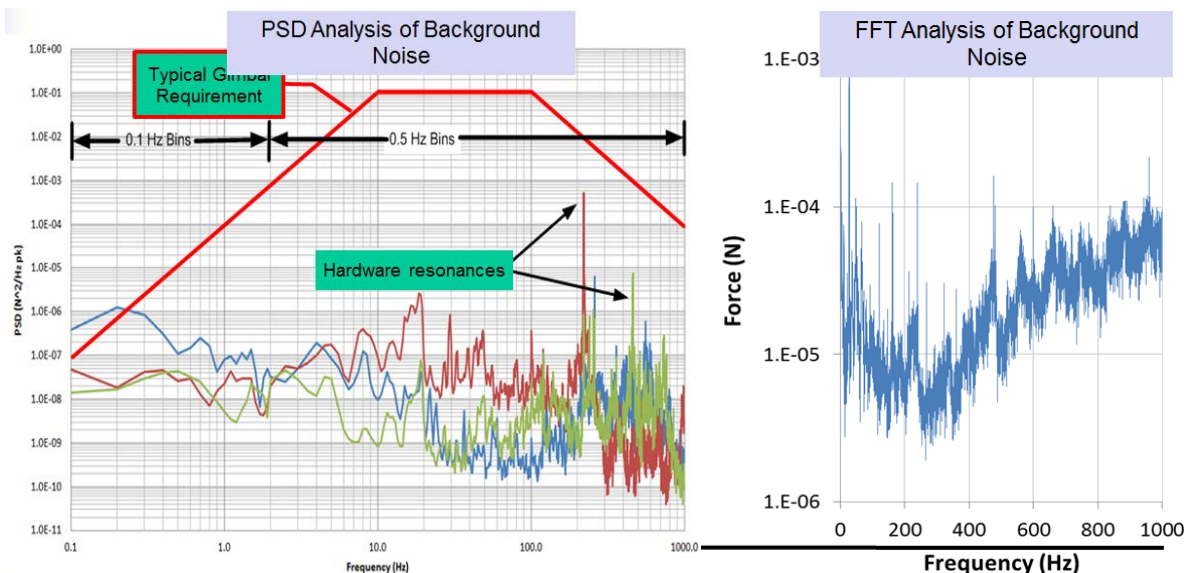


**Figure 4. Typical background noise characterization processed by a dynamometer**

When noise gets in the way of measurements at a particular frequency range, special filtering is used to extract the necessary signal of interest. Signal-to-noise ratio measurements significantly improved through a development program in which a new set of quality electronics are integrated. Reference [2] presents an example where filtering using a 10-Hz low bandpass was required to achieve balancing of a rotating mechanism. An example of dynamometer noise floor measurement for the Y-axis is shown in Figure 5. In this case, the maximum noise of 0.00175 lbf (7.8 mN) was measured and was less than the derived 0.004-lbf (17.8-mN) limit needed for accurate measurements of the static and dynamic imbalances of the GMI instrument.

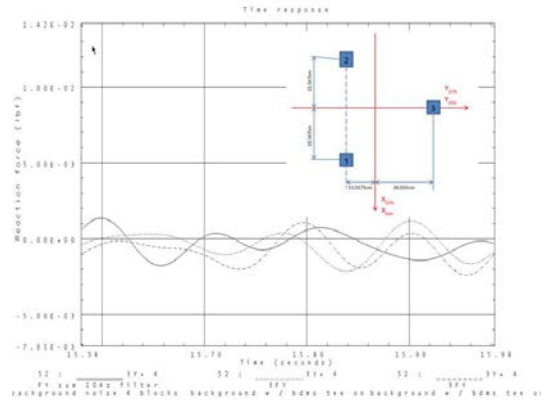


**Figure 5. Noise floor showing measurements filtered using low bandpass of 10 Hz**

### Calibration of EFT Setups

BATC developed several procedures to calibrate its EFT setups as a system. These include harmonic stinger tests, frequency response function tests, and speaker tests. EFT setups are first analyzed to identify their modal characteristics with and without the mechanism intended for measurement. To ensure a good correlation between analysis and tests, the spring rates of the load cells themselves are characterized and are accurately modeled. Once the model of the setup is properly correlated with test data, and its predicted response is validated through combinations of sine sweeps and tap testing, an integrated model of the correlated setup and the unit under test is evaluated to ensure adequate stiffness of the setup. Again, there should be no gains that would affect measurements in the expected jitter frequency range. At this stage, the FMP is ready to proceed for calibration as a unit.

The calibration of the FMP entails three parts. First, the setup is shown to have the necessary sensitivity to accurately make the necessary measurements. The noise floor is identified and compared to the program requirements which are either specified or derived from higher level requirements. At a minimum, the noise floor is required to be one order of magnitude below the minimum measured force/torque in the six degrees of freedom.

Second, the forces measured by the FMP are validated using two separate and independently calibrated data acquisition systems and three loading methods. This is performed to isolate and quantify the source and magnitude of potential random measurement errors and identify the load cells/channels that may be erroneous. Harmonic stinger tests are used to excite the setup at certain frequencies. A calibrated load cell is placed at the interface between the stinger and the EFT setup to measure the input force. The input force is also measured using the setup as the sum of the contributions of all load cells through its transformation matrix relating the individual loads to the resultant forces and moments of the FMP. The input load is applied separately along the different axes of the setup and is required to match the measured output load. The Spectral Dynamics data acquisition system at BATC's Vibration Lab is often used as the first independent mean for measurement. A second portable data acquisition system is used to ensure concordance with the reference input load. The fixity of the FMP setup is evaluated to ensure that the most adequate and practical configuration among clamped, simply supported and free-free that delivers the most separation between the modes of the setup and the jitter forces frequencies is used. Finally, Speaker tests are used as a source for input loads that can be placed at different locations of the setup and different heights above the interface plate of the FMP. The calibration consists in applying known forces using a speaker precisely located and oriented on the setup and measuring the reaction forces and moments imparted on the surface of the plate. The speaker is attached to a fixture through an encapsulated load cell. The speaker is actuated using a form generator to deliver loads of varying magnitudes at particular input frequencies. Tests are required to show that the input load from the



speaker force transducer and the measurement from the setup are the same in different orientations. In particular, this test is important in the calibration of the measured three moments.

Third, the calibration program evaluates data collected from auxiliary tests with rotating payloads with known, off-axis masses which are precisely located on a rotating disk mounted to the FMP.

These tests assess the performance of the setup in measuring certain loads that result from simultaneous measurements from all load cells, over a good range of amplitudes. Such tests can also be used for trouble shooting and mitigation prior to handling critical hardware.

When the unit under test has large moving surface areas, jitter measurements may require testing in near vacuum environment to ensure that air drag is not affecting the inherent jitter measurements. BATC has developed the necessary tooling to ensure that tests are conducted under such condition in vacuum chambers. Of course, such environments require a good portion of the setup to be vacuum compatible.

### **Examples of Jitter Mitigation and Isolation**

#### Mechanical Cryogenic Refrigeration

Traditionally, high-precision space infrared instruments have been cooled using expendable cryostats which are inconvenient in the sense that they are not only large and heavy; they are also short-lived, and only capable of cooling small detectors. Cryostats are however highly reliable, because they are passive and have no exported jitter to impact sensitive optics and detectors.

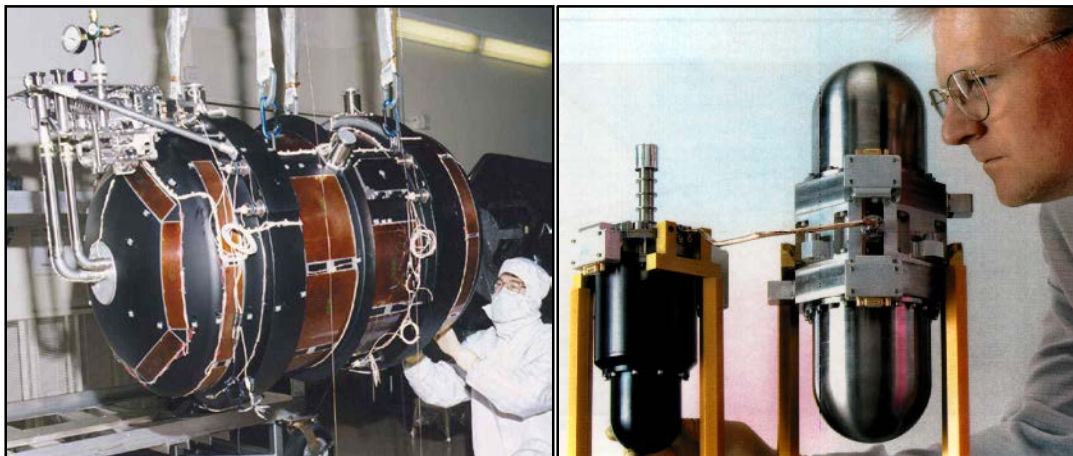


**Figure 6. Early expendable cryostats (left) and cryocoolers (right)**

In the past two decades, mechanical cryogenic refrigerators (cryocoolers), shown in Figures 6-7, saw their reliability improved dramatically. They can support much larger (10-100X) detectors and sustain missions of much longer durations (2-5X). But, cryocoolers have moving mechanisms that can produce significant jitter. Until recently, these levels of jitter have been unacceptable for the highest precision space instruments.

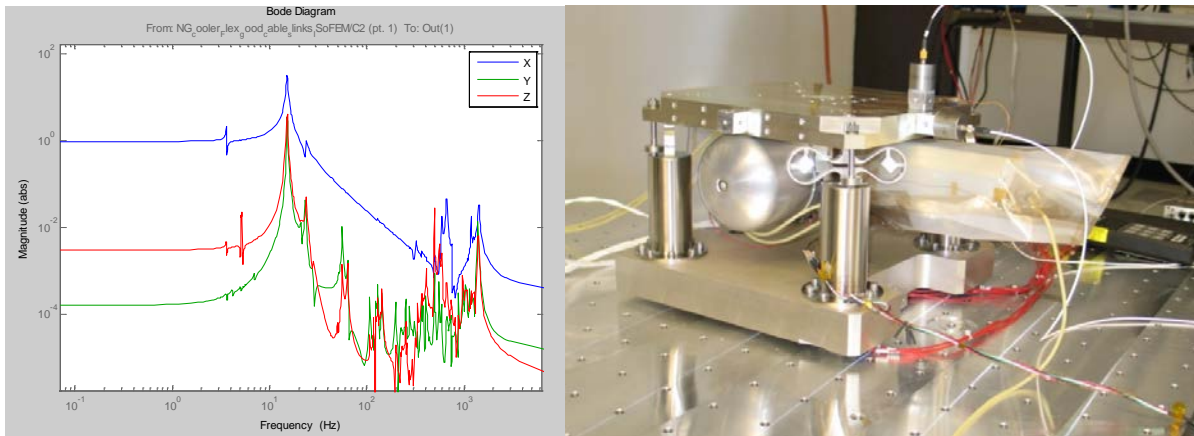


**Figure 7. Bode plots of the BATC cryocooler (left) and cryocooler with soft mount (right)**

BATC addressed exported force and torque (EFT) mitigation of cryocoolers on the basis of simple passive concepts using mature, flight-proven elements with performance verification using a high-fidelity EFT test bed. Effectively, low resonant soft mounts of about 10 Hz are introduced to (a) maximize attenuation at cooler operating frequencies greater than 67 Hz, and (b) minimize cross talk and moments (see Figure 2). As a result, the cooler EFT is attenuated by more than a factor of 40, from 400 mN to about 10 mN. The soft mount isolators use flight-proven heritage. The cooler itself has good flight heritage with internal vibration control already <400 mN. The EFT mitigation program improved the performance of BATC's line of cryocoolers dramatically as illustrated in Figure 8.

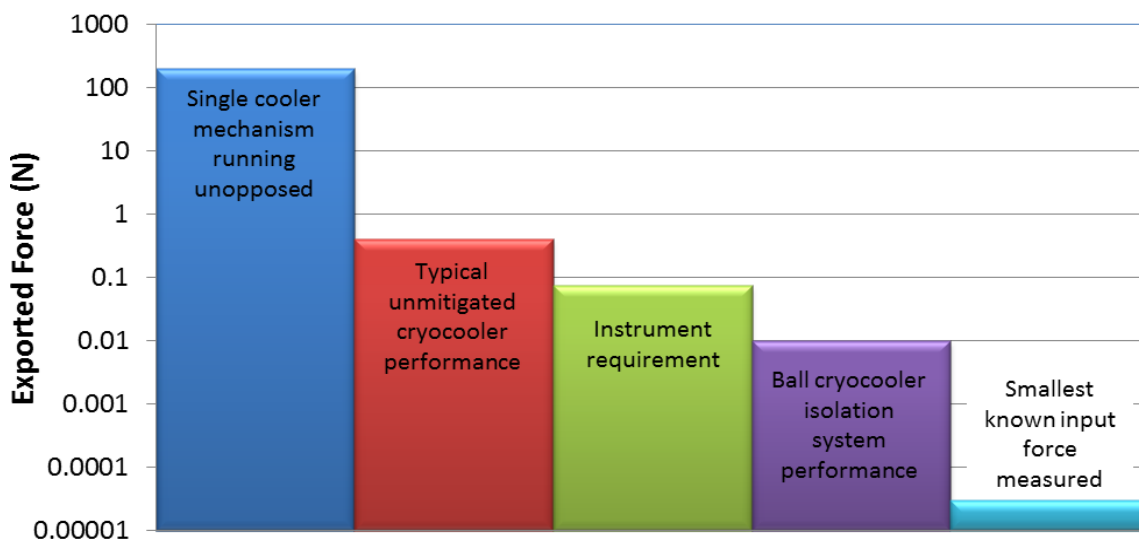


**Figure 8. Isolation performance of BATC's cryocoolers**

EFT control is achieved at several levels. First, at the system level BATC transitioned from a single cooler mechanism to a mechanism pair. This has brought down the imparted loads by allowing for the design of effective actuation control architecture with reaction cancellation over the frequency range of interest. In addition, the design of a soft mount system has provided additional reduction of the exported loads.

#### Isolation in Reaction wheels

Jitter due to reaction wheel vibration is isolated through constrained-layer flexures. The flexures were developed during a BATC R&D program in which three competing designs were proposed. The final

design retained for testing was produced in collaboration with CSA Engineering and was built to flight hardware standards using materials with proven flight heritage.

The jitter isolation mounts are an assembly of soft flexures that attach between a reaction wheel and the spacecraft interface, providing low frequency isolation in the six degrees of freedom, yet they deliver relatively high second order spring surge modes. Thus, by design, jitter isolation mounts have their first six modes below 10 Hz and all subsequent modes above 100 Hz.

The final jitter isolation mount design, shown in Figure 9, is a hexapod of six struts configured in a Stewart platform. Each strut is made of two centrally connected rings of 10-mil (.025-mm) thick 3M ISD142R viscoelastic layer constrained between two 9-mil (.23-mm) thick and 0.5-in (1.3-cm) wide 300-series stainless steel sheets.

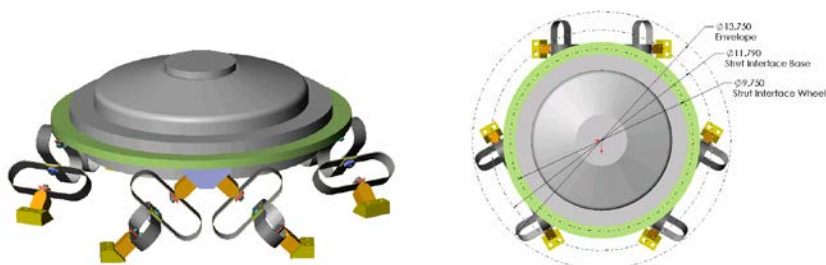


Figure 9. BATC Robi Wheel on jitter isolation mount

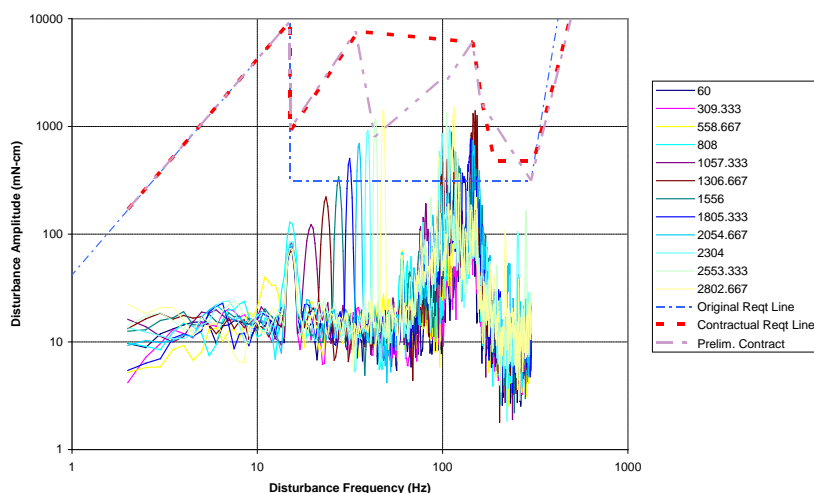


Figure 2.4: X-axis disturbance torques/wheel speeds in RPM.

Figure 10. BATC Robi Wheel on jitter isolation mount and zero-*g* air lift (left) and typical requirement program verification (right).

## Conclusion

Ball Aerospace & Technologies Corporation made substantial capital investment to develop good control of exported forces and torques from space mechanisms. And over the past decade, there has been a continuous improvement of the hardware and analysis tools used to develop advanced verification capabilities.

In order to meet a wide range of jitter requirements from multiple programs, BATC elected to have the capability to rapidly design custom FMPs for each application by combining modular hardware. This choice prompted the development of a facility with tool kits of multiple input channels, sensors of different capacity and sensitivity, high-performance filters, shakers of different sizes, and data acquisition systems. The EFT facility at BATC includes soft tables for the elimination of environmental disturbances. In the pursuit of quietness, testing has been carried in several environments, such as a massive reinforced concrete pit and vacuum chambers. Recently, the EFT facility has successfully characterized BATC's line of cryocoolers, shutter mechanisms and performed static and dynamic balancing of rotating instruments, to name a few.

FMPs have the advantage of providing resultant jitter forces and moments imparted by a mechanism either directly at its mounting interface or at a higher assembly interface, depending on what is tested. Other methods of jitter verification, such as those based on the recovery accelerations or motions, from accelerometers or transducers would have the disadvantage of being indirect methods and are therefore less reliable. The main disadvantage of FMPs is in the introduction of additional spectral content from the measuring device itself. However, such addition is monitored and separation from the frequency band of interest is one of the elements of the design process. FMPs may be considered complex to develop. However the return on investment is quite important, especially when high performance is required from precision mechanisms and instruments.

## References

1. Force Limited Vibration Testing, NASA-HDBK-7004C, 2012
2. Ayari, L., Kubitschek, M., Ashton, G., Johnston, S., Debevec, D., Newel, D. and Pellicciotti, J. "GMI Instrument Spin Balance Method, Optimization, Calibration, and Test", Proceedings of the 42<sup>nd</sup> Aerospace Mechanisms Symposium, NASA Goddard Space Flight Center, May 14-16.
3. Marquardt, E.D., Glaister, G., Marquardt, J.S., Raab, J. and Durand, D., "Testing Results for Low Exported Force and Torque Cryocooler Mounts," Cryocoolers 17, ICC Press, Boulder, CO (2013),
4. Ayari, L. "Hybrid Testing & Simulation- The Next Step in Verification of Mechanical Requirements in the Aerospace Industry," Hybrid Simulation Theory, Implementation and Applications, Victor Saouma, Mettupalayam Sivaselva Editors, 2008.

# Development and Testing of a High-Precision Position and Attitude Measuring System for a Space Mechanism

Nikolay Khanenya, Gabriel Paciotti\*, Eugenio Forzani\* and Luc Blecha\*

## Abstract

This paper describes a high-precision optical metrology system – a unique ground test equipment which was designed and implemented for simultaneous precise contactless measurements of 6 degrees-of-freedom (3 translational + 3 rotational) of a space mechanism end-effector [1] in a thermally controlled ISO 5 clean environment.

The developed contactless method reconstructs both position and attitude of the specimen from three cross-sections measured by 2D distance sensors [2]. The cleanliness is preserved by the hermetic test chamber filled with high purity nitrogen. The specimen's temperature is controlled by the thermostat [7]. The developed method excludes errors caused by the thermal deformations and manufacturing inaccuracies of the test jig.

Tests and simulations show that the measurement accuracy of an object absolute position is of 20 micron in in-plane measurement (XY) and about 50 micron out of plane (Z). The typical absolute attitude is determined with an accuracy better than 3 arcmin in rotation around X and Y and better than 10 arcmin in Z. The metrology system is able to determine relative position and movement with an accuracy one order of magnitude lower than the absolute accuracy. Typical relative displacement measurement accuracies are better than 1 micron in X and Y and about 2 micron in Z. Finally, the relative rotation can be measured with accuracy better than 20 arcsec in any direction.

## Introduction

The metrology system was developed by Almatech (Switzerland) within the framework of the Solar Orbiter project. The mission overall goal is to produce images of the Sun at an unprecedented resolution and perform closest ever in-situ measurements. The Slit Change Mechanism (SCM) is part of the SPICE (SPectral Imaging of the Coronal Environment) instrument which provides spectral imaging of the solar disk, corona and characterizes plasma properties of the Sun. The SCM itself was previously presented at the 42<sup>nd</sup> Aerospace Mechanisms Symposium [1]. The SCM prototype is shown in Figure 1, the metrology system is shown in Figure 2.

The SCM end effector shall move with a high accuracy and repeatability. These performances shall be verified by test during qualification campaign. No off-the-shelf measurement equipment could be found that fulfils all requirements such as geometrical limitations, measurement accuracy, cleanliness, specimen surface properties, gravity direction, test repeatability, temperature stability, and temperature range. During the early stage of the project, a wide range of measurement means were studied. All contact measurement devices were ruled out as the specimen surface is delicate and the displacement introduced by any mechanical contact would bias the measurement. Indeed, the SCM end effector is only supported by leaf spring elements with low stiffness and thus its position is very sensitive to any external forces. Laser 3D scanners (e.g., [3]) have insufficient accuracy. Confocal 3D microscopes (e.g., [4]) and digital holographic microscopes (e.g., [5]) have a too small observation distance and a small field of view, which makes them incompatible with the test setup. X-ray 3D scanners (e.g., [6]) cannot be combined with an environment control system. Therefore, a unique high-precision measurement system was

---

\* Almatech, Lausanne, Switzerland



developed. It combines Keyence sensors [2] and Huber thermostat [7] with Almatech software and hardware.

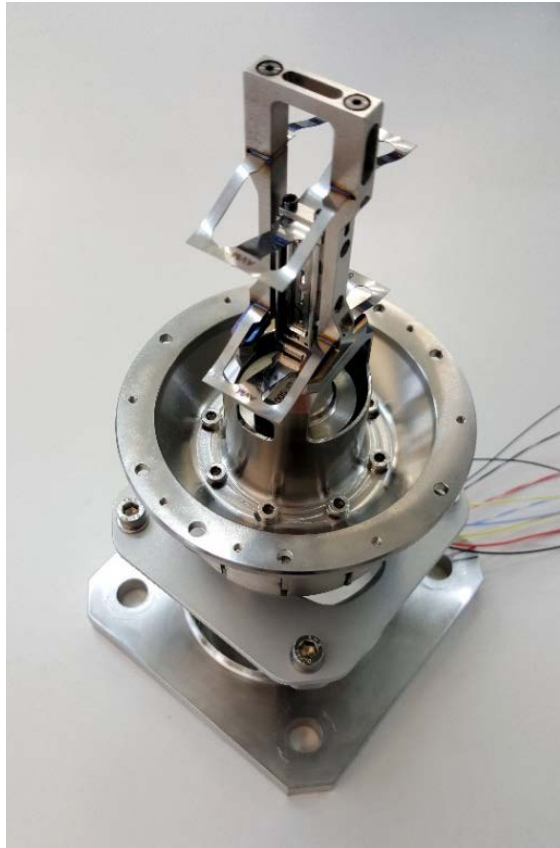


Figure 1. Slit Change Mechanism prototype

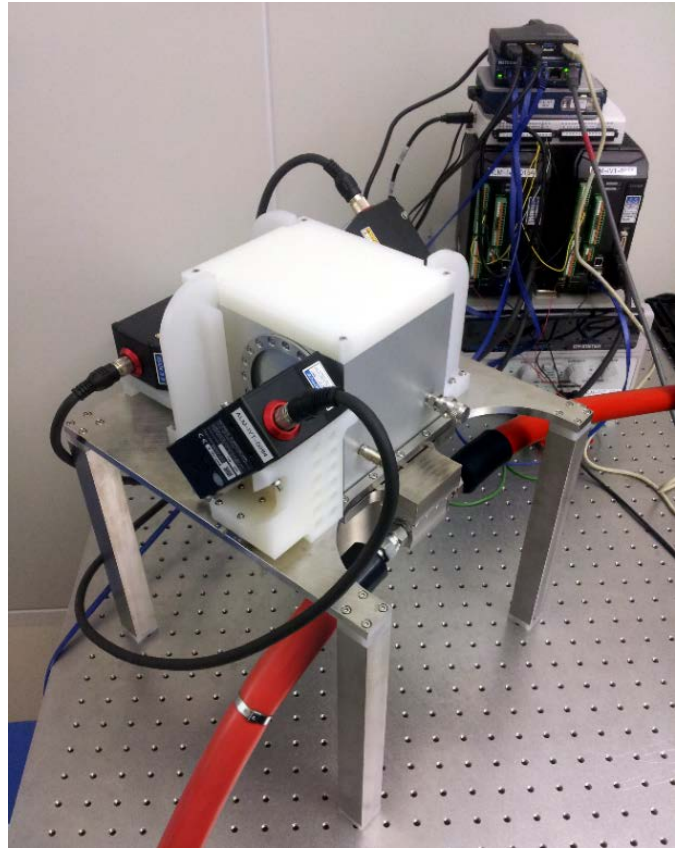


Figure 2. Metrology system

### Key features

The metrology system has the following key features.

- **6 degrees-of-freedom**  
Simultaneous measurement of specimen's absolute position and attitude in 3D.
- **Clean environment**  
The environment around the specimen is clean and hermetically sealed. It is purged with high purity nitrogen, providing an environment better than ISO 5 (class 100).
- **Temperature control**  
Mechanical interface temperature is controlled by external thermostat [7] within the range from  $-40^{\circ}\text{C}$  to  $+200^{\circ}\text{C}$  with stability of  $0.01^{\circ}\text{C}$ . Change of the temperature does not affect spatial measurement accuracy as the measurement devices are thermally isolated from the observed specimen.
- **Contactless measurement**  
The measurement is purely optical and will not damage the surface of the test subject. In addition, no measurement bias is introduced from any contact force.
- **System self-calibration**  
A self-calibration methodology was developed. The self-calibration enables the metrology system to deduce positions and attitudes of its own sensors without using any additional measuring equipment.

The self-calibration allows excluding errors caused by the assembly inaccuracies and the thermal deformations of the metrology system structure.

- **Sensor combination (fusion) method :**

Thanks to an advanced algorithm combining the information from individual sensors, the final accuracy of the system is higher than the accuracy of its components.

### Object under Observation

The specific object tracked by the metrology system is the SCM end effector which is called Carrier. It is a small titanium part ( $40 \times 11 \times 7$  mm; 2.4 g) which carries a cartridge with silicon slits. The Carrier moves to change the slit aligned with the sunlight beam. The Carrier is shown in Figure 3. The yellow-marked surfaces are used by the metrology system to track the position and the attitude of the Carrier. Carrier is coated with a black mat coating.

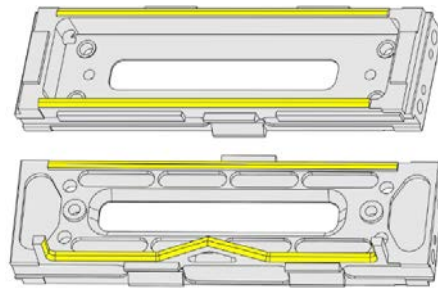


**Figure 3. SCM end-effector**

### Hardware layout

The metrology system hardware is shown in Figure 6, a cut view is shown in Figure 5, and the corresponding diagram is shown in Figure 4. As shown in Figure 4, the whole setup is located in a clean room ⑩. The test subject ⑨ is installed inside of the heat exchanger ⑧. The heat exchanger is a copper structure with observation openings and a channel for the heat transfer fluid. Fluid circulates between the heat exchanger and the external thermostat ⑦. The Heat exchanger is installed inside of the hermetic aluminium chamber ② with sealed glass windows. The chamber is purged through the dedicated valve with high purity nitrogen ⑤ to maintain a low humidity level as well as a cleanliness level better than ISO 5. 2D distance sensors ① are installed on micrometer positioning stages outside the chamber. They observe the test subject through glass windows. Sensor heads and the chamber are supported by the same structure ⑥ which is made of stainless steel and polyvinylidene difluoride (PVDF). Sensor heads are connected to the acquisition devices ③ which, in turn, are connected to the computer ④.

For the particular SCM that is sensitive to microvibration, the system was installed on the optical table with air pneumatic bearings to reduce microvibrations. Mechanical stops protect the test subject and sensors from unintentional contact with other parts of the system during the assembly.

Sensors have a limited operational temperature range, therefore sensor support structures are made of PVDF with multiple holes for a better thermal decoupling from the heat exchanger. The temperature at the interface of the test subject is monitored by thermocouples.



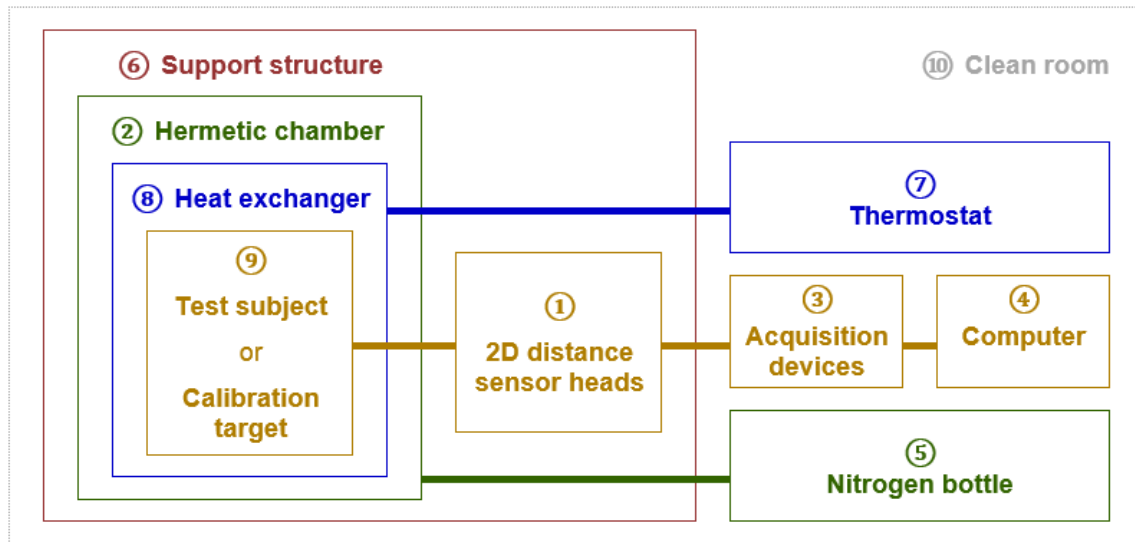


Figure 4. Metrology system diagram

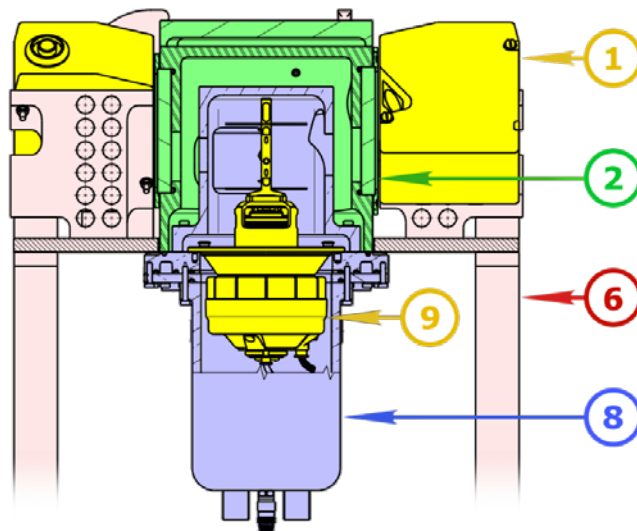
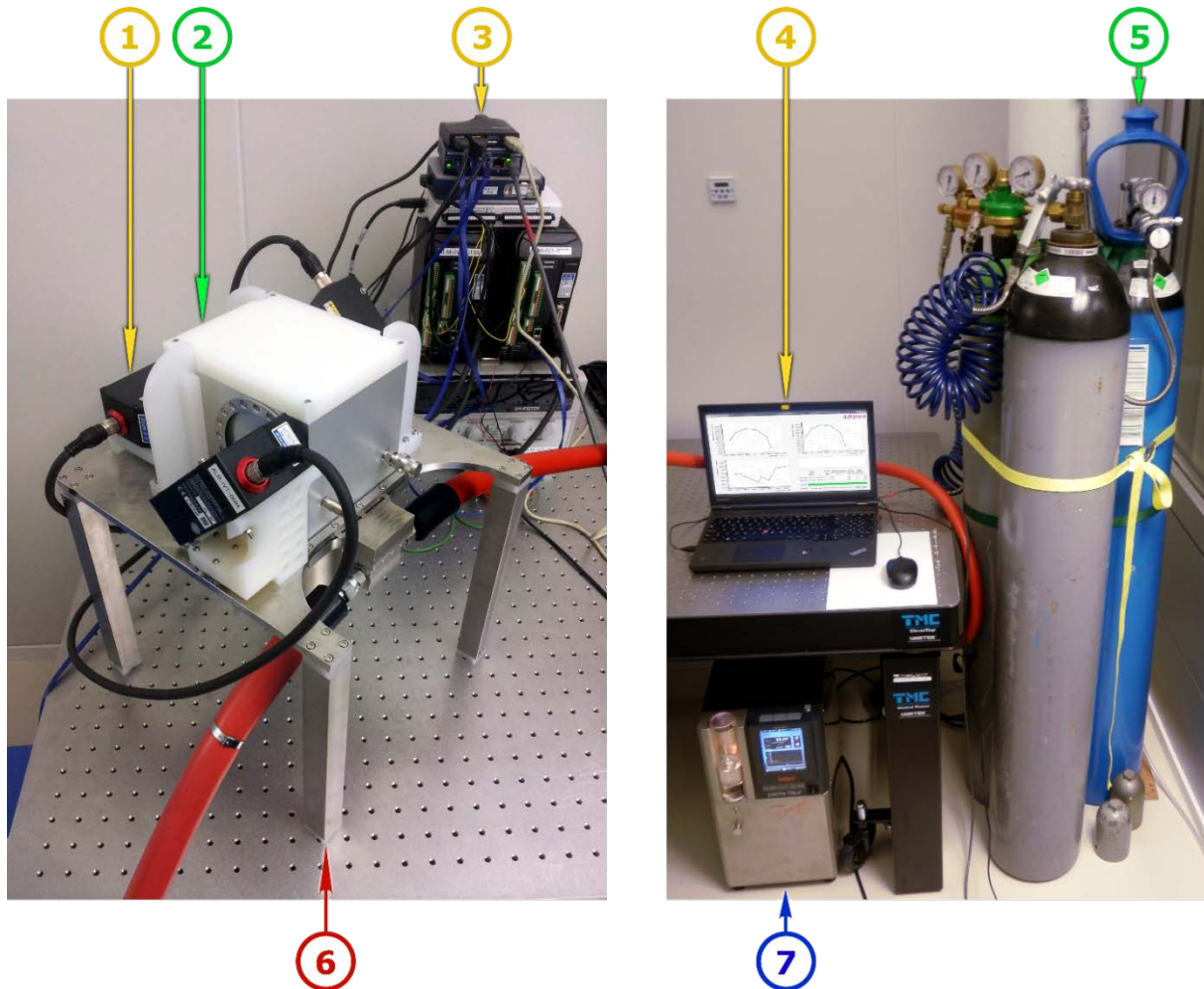


Figure 5. Metrology system cut view



**Figure 6. Metrology system hardware**

### **Measuring principle**

Specimen position and attitude in 3D are calculated from the raw data acquired by three 2D distance sensors [2] which are aligned as shown in Figure 7. Each 2D distance sensor captures a cross-section of the Carrier as shown in Figure 8. The combination of the 3 cross-sections is processed by a software developed by Almatech to provide an accurate position and attitude.

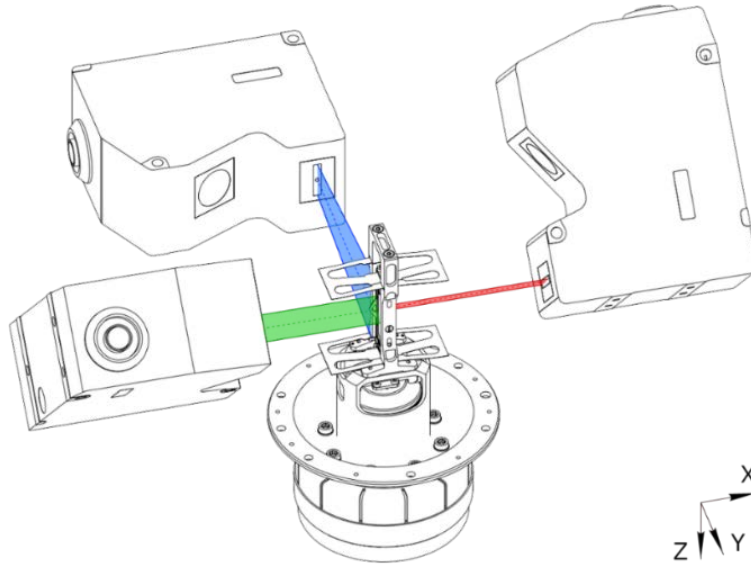


**Figure 7. Position and attitude of the sensors**

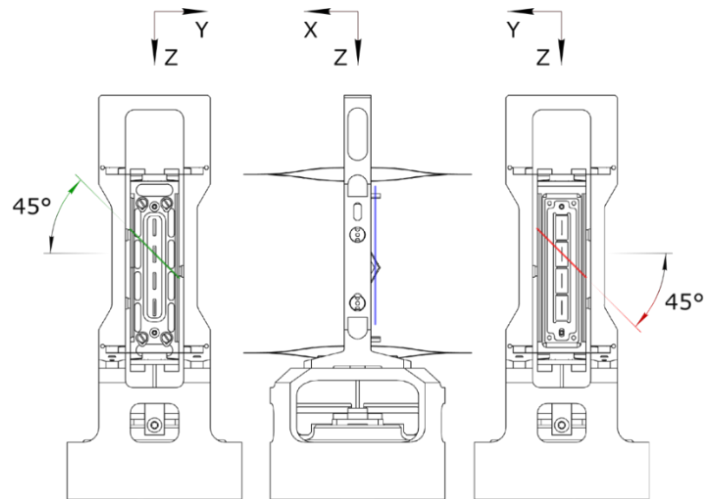


**Figure 8. Test subject sections observed by the sensors**

The algorithm contains the following major steps:

1. Acquisition of the specimen cross-sections (shown in Figure 8) from the 2D laser distance sensors. Cross-sections are represented by the arrays of points;
2. Fitting the polylines to the acquired points using linear segmented regression. Calculation of polyline vertices coordinates and evaluation and their uncertainties;
3. Calculation of specimen position and attitude by minimizing error between measured vortices and specimen model.

The 1<sup>st</sup> step (acquisition of raw measured points) is done using application programming interface provided by the sensor manufacturer. Raw measured points are shown in Figure 9 as the blue dots.

In step 2, the software calculates cross-sections vertices coordinates from the measured points coordinates. Cross-section best-fit profile is shown in Figure 9 as a blue polyline. Initial set of points is

split into subsets so that each subset contains points of a single line. The boundaries between subsets are found by minimization of the sum of quadratic mean errors of best-fit lines.

Vertices coordinates are not the only output of the 2<sup>nd</sup> step. Uncertainty is also automatically estimated for each vertex in order to reach a higher accuracy during sensor fusion. Sensor fusion is a process of combining sensor data such that resulting information has less uncertainty than would be possible when these sources were used individually.

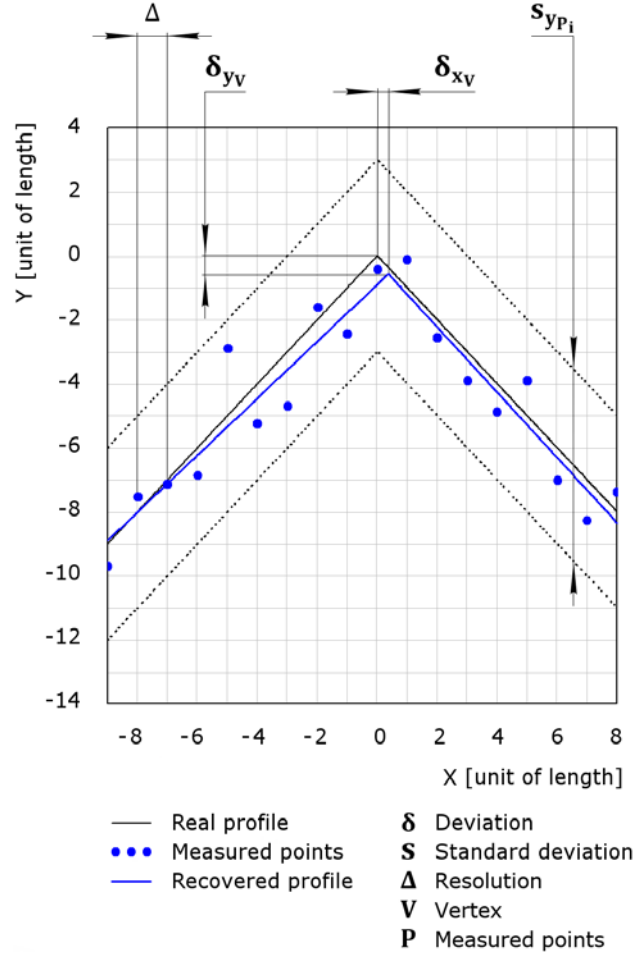


**Figure 9. Real and recovered profiles**

Uncertainty of each vertex coordinates depends on multiple parameters, such as size and arrangement of lines in the field of view. The equation to estimate the vertices coordinates uncertainty is derived from the following set of equations:

$$y_{L_i}(x) = k_i \cdot x + b_i \quad (1)$$

$$y_{L_1}(x_V) = y_{L_2}(x_V) = y_V \quad (2)$$

$$k_i = \frac{\text{cov}(x_{P_i}, y_{P_i})}{\text{var}(x_{P_i})} \quad (3)$$

$$b_i = \text{mean}(y_{P_i}) - k_L \cdot \text{mean}(x_{P_i}) \quad (4)$$

$$s_{y_{P_i}} = \sqrt{\frac{1}{n_i - 2} \cdot \sum_{j=1}^{n_i} (y_{P_{ij}} - y_{L_i}(x_{P_{ij}}))^2} \quad (5)$$

$$x_{P_{ij}} = \left(j - \frac{1}{2} + \Theta\right) \cdot \text{sign}(i) \cdot \Delta \quad (6)$$

$$S_{F(a_1, a_2, \dots)} = \sqrt{\left(s_{a_1} \cdot \frac{\partial F}{\partial a_1}\right)^2 + \left(s_{a_2} \cdot \frac{\partial F}{\partial a_2}\right)^2 + \dots} \quad (7)$$

where

- $x, y$  – Coordinates in the sensor frame
- $i$  – Index of the line. The vertex is formed by two lines (1 and 2).
- $j$  – Index of the measured point. Each line may contain different number of points.
- $y_{L_i}(x)$  – Best-fit function for the line  $i$ .
- $k_i$  – Estimator of the slope coefficient for the line  $i$ . It is a trigonometric tangent of the angle between the best-fit line  $i$  and the X axis.
- $b_i$  – Estimator of the intercept coefficient for the line  $i$ . It characterizes the shift of the best-fit line  $i$  along the Y axis.
- $x_V, y_V$  – Coordinates of the vertex which is formed by intersection of two lines.
- $\text{cov}(\dots)$  – Covariance.
- $\text{var}(\dots)$  – Variance.
- $\text{mean}(\dots)$  – Average.
- $x_P, y_P$  – Coordinates of measured points.
- $n_i$  – Quantity of measured points in the line  $i$ .
- $s_{y_{P_i}}$  – Estimate of quadratic mean distance (along Y axis) between measured points and the best-fit line  $i$ .
- $\Delta$  – Resolution of the sensor head. This value is the distance between neighbour measured points along X axis.
- $\Theta$  – Coefficient which characterizes the distance between the vertex and the nearest measured points. Its value lays in the range between -0.5 and +0.5.
- $S_{F(a_1, a_2, \dots)}$  – sample standard uncertainty of some function  $F$  with the arguments  $a_1, a_2, \dots$

Equations 1, 3, and 4 represent a linear regression as per [9]. Regression gives a better result than orthogonal Deming regression due to the specific internal architecture of the sensors. Equation 7 is a well-known variance formula for uncertainty propagation from [10]. Vertex coordinates are derived from equations 1 and 2 as:

$$x_V = \frac{b_2 - b_1}{k_1 - k_2} \quad ; \quad y_V = \frac{k_1 b_2 - k_2 b_1}{k_1 - k_2} \quad (8)$$

Equation 7 is applied to equations 3, 4 and 8 to calculate uncertainties of the vertex coordinates. For that, the coordinate system origin is aligned with the vertex. Coefficient  $\Theta$  of the equation 6 is assumed equal to 0.5 which is the worst case estimate. The standard uncertainty of the vertex coordinates is:

$$s_{xv} = 2 \cdot \sqrt{\frac{\left(\frac{s_{y_{P_1}}}{\eta_1}\right)^2 + \left(\frac{s_{y_{P_2}}}{\eta_2}\right)^2}{(k_1 - k_2)^2}} ; \quad s_{yv} = 2 \cdot \sqrt{\frac{\left(\frac{s_{y_{P_1}}}{\eta_1}\right)^2 \cdot k_2^2 + \left(\frac{s_{y_{P_2}}}{\eta_2}\right)^2 \cdot k_1^2}{(k_1 - k_2)^2}} \quad (9)$$

Where  $\eta$  are coefficients which characterize quantity of points in each line as:

$$\eta_1 = \frac{n_i \cdot (n_i - 1)}{n_i + \frac{1}{2}} \quad (10)$$

Once the positions of vertices are calculated, the metrology system software proceeds to the 3<sup>rd</sup> step which searches for the corresponding position and attitude of the Carrier. This is done by solving the following system of equations. The system is solved using a variation of Nelder–Mead method [11].

$$\left\{ \begin{array}{ll} \mathbf{p}_{v_{ijk}}^s = \mathbf{a}_{s_i}^{I-1} \cdot \left( \mathbf{a}_t^I \cdot \mathbf{p}_{v_{ijk}}^t \cdot \mathbf{a}_t^{I-1} + \mathbf{p}_t^I - \mathbf{p}_{s_i}^I \right) \cdot \mathbf{a}_{s_i}^I & (11) \quad \text{Conversion of vertices coordinates from Carrier frame to sensor frame. See Figure 11.} \\ \mathbf{p}_{e_{ij}}^s = \mathbf{p}_{v_{ij0}}^s + \left( \mathbf{p}_{v_{ij1}}^s - \mathbf{p}_{v_{ij0}}^s \right) \cdot \frac{\mathbf{p}_{v_{ij0}}^s \cdot \mathbf{z}}{(\mathbf{p}_{v_{ij0}}^s - \mathbf{p}_{v_{ij1}}^s) \cdot \mathbf{z}} & (12) \quad \text{Intersection point of the line (Carrier edge) and the xy-plane (laser beam of the sensor). See Figure 10.} \\ \sum_{i=0}^{n_s-1} \sum_{j=0}^{n_e^i-1} \left( \mathbf{m}_{e_{ij}} \cdot \left( \mathbf{p}_{e_{ij}}^s - \tilde{\mathbf{p}}_{e_{ij}}^s \right) \right)^2 = f \rightarrow 0 & (13) \quad \text{Sum of weighted distances between points (measured and assumed) of intersection.} \end{array} \right.$$

where ● — scalar values

● — 3D vectors

● — 3×3 matrixes

● — quaternions

$\mathbf{p}_{v_{ijk}}^s$  — assumed position of the Carrier vertex  $ijk$  in the coordinate system of the sensor  $i$

$\mathbf{p}_{v_{ijk}}^t$  — assumed position of the Carrier vertex  $ijk$  in the coordinate system of the Carrier

$\mathbf{a}_{s_i}^I$  — assumed attitude of the sensor  $i$  relative to the SCM interface

$\mathbf{p}_{s_i}^I$  — assumed position of the sensor  $i$  relative to the SCM interface

$\mathbf{a}_t^I$  — assumed attitude of the Carrier relative to the SCM interface

$\mathbf{p}_t^I$  — assumed position of the Carrier relative to the SCM interface

$\mathbf{p}_{e_{ij}}^s$  — assumed position of the point of intersection between flat laser beam of the sensor  $i$  and the Carrier edge  $ij$  which connects vertices  $ij0$  and  $ij1$  in the sensor  $i$  coordinate

system

- $\tilde{p}_{eij}^{s^i}$  — measured position of the intersection point  $ij$  defined above
- $z$  — binomial unit vector  $(0;0;1)^T$  of the sensor coordinate system basis
- $n_s$  — number of sensors in the metrology system
- $n_e^{s^i}$  — number of the Carrier edges observed by the sensor  $i$
- $M_{eij}$  — scale matrix which contains the uncertainty of measured intersection point  $ij$

$$M_{eij} = \begin{bmatrix} (s_{eij}^x)^{-1} & 0 & 0 \\ 0 & (s_{eij}^y)^{-1} & 0 \\ 0 & 0 & 0 \end{bmatrix}$$

- $s_{eij}^x$  — uncertainty of X-coordinate of the intersection point  $ij$
- $s_{eij}^y$  — uncertainty of Y-coordinate of the intersection point  $ij$

- $f$  — objective function which shall be minimized. It characterizes the deviation of the assumed intersection points from the measured intersection points

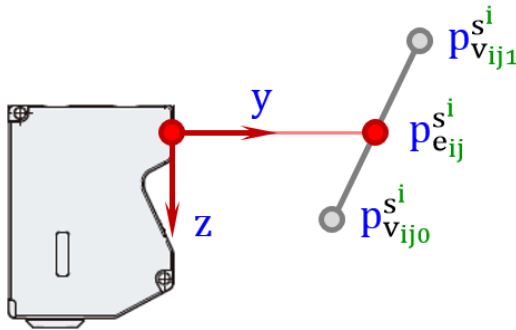


**Figure 10. Intersection point of the Carrier edge and the laser beam of the sensor**

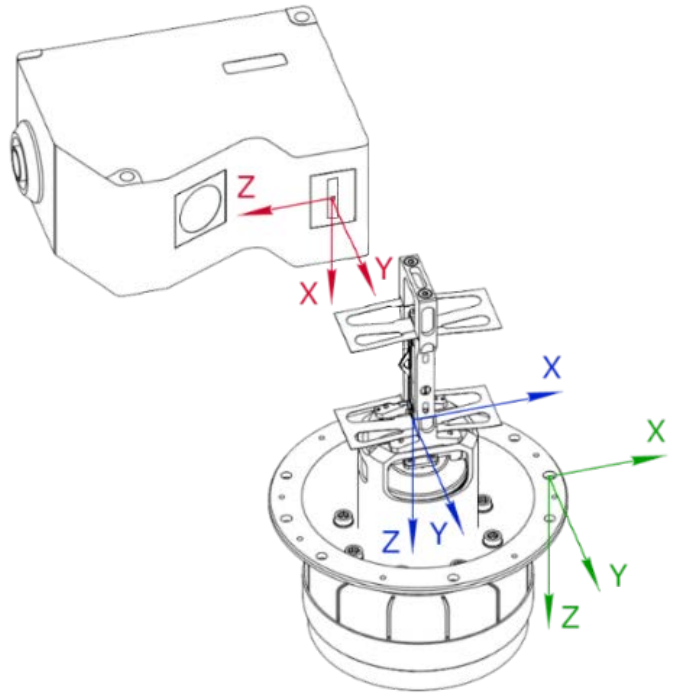


**Figure 11. Coordinate systems (frames). Red is a sensor frame. Blue is a Carrier frame. Green is a SCM interface frame.**

### Self-Calibration

To reach high accurate measurements, both Carrier's geometry and positions of the sensors shall be known. Carrier's geometry is measured before test using the coordinate measurement machine. Positions and attitudes of the sensors are calculated during a so-called self-calibration process. The sensors measure a calibration target (shown in Figure 12) which has known geometry and position in SCM interface frame. The geometry of the calibration target was optimized to determine the position and



attitude of each sensor using a single cross-section which is captured by the same sensor. Cross-sections observed by the three different sensors are shown in Figure 13.

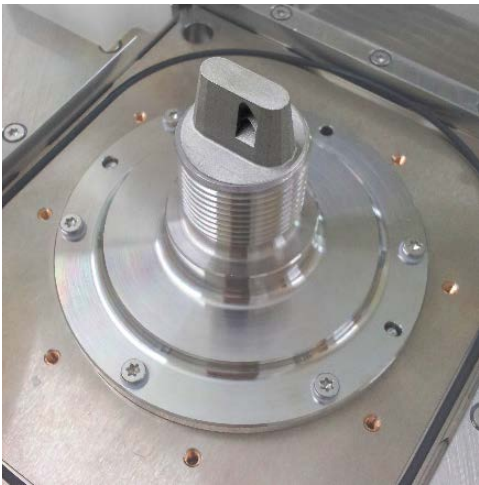


**Figure 12. Calibration target**

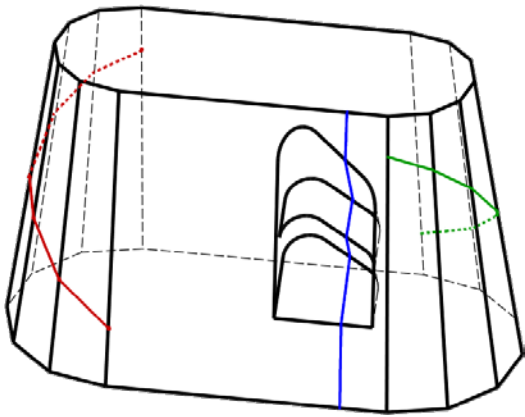


**Figure 13. Calibration target sections observed by sensors**

The calibration target is made out of Invar to minimize thermal expansion effects. This allows accurate measurement over a specific temperature range.

Position and attitude of each sensor is deduced several times for different temperature points. This approach allows minimizing the errors caused by the thermal deformation of the metrology system structure. Self-calibration also minimizes the bias caused by the deflection in the glass windows. Calibration target sections, as they appear in acquisition software interface written by Almatech, are shown in Figure 14 (refer to Figure 13 for sensor positions).

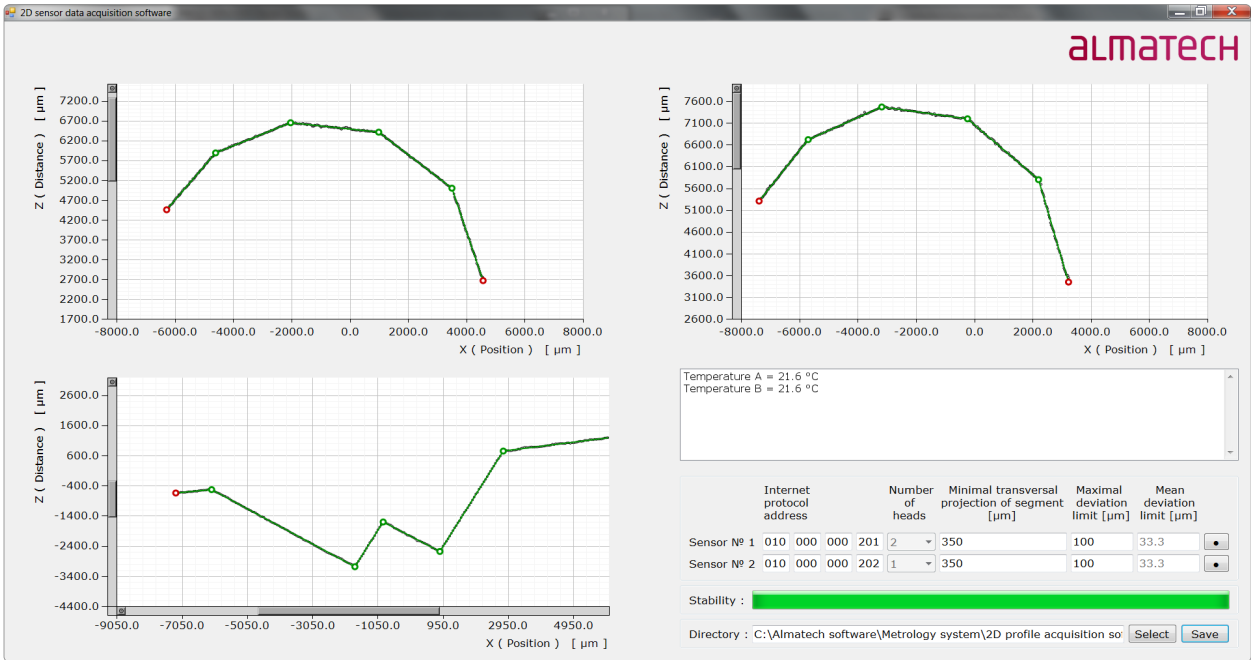


**Figure 14. Calibration target sections as they appear in the acquisition software interface**

## Results

Multiple real-life tests and software simulations were performed to determine the final accuracy of the metrology system with a high level of confidence. The tests were the following:

- Test of self-calibration accuracy (sensors positions self-determination accuracy);
- Test of inaccuracy caused by remounting of test subject and calibration target;
- Test of sensors accuracy with the representative surface optical properties;
- Test of sensors accuracy with the representative geometry.

The estimated result accuracy of the system is shown in Table 1.

**Table 1. Measurement uncertainty of the metrology system**

Parameter	Translation [ $\mu\text{m}$ ]			Rotation [arcsecond]		
	X	Y	Z	X	Y	Z
Repeatability	0.7	0.4	2.3	11	20	14
Absolute coordinates' accuracy	14.4	23.3	52.4	68	178	570

## Lessons learned

For accurate sensor fusion, it is important to take into account that the measurement uncertainty is different for each measurement. Measurement uncertainty of the vertex coordinates depends on multiple parameters, such as size and arrangement of lines in the field of view. The values specified in the sensor datasheet are deduced by the manufacturer for a very particular test case, therefore they cannot be considered as an accurate estimate. For proper evaluation of the vertices coordinates' uncertainty, Almatech derived the equation 9 and performed multiple tests.

It is also important to take into account that the accuracy and reliability of laser distance sensors depends strongly on the optical properties of observed surface. For better and consistent performance, the surface shall be mat (i.e., reflection shall be diffuse). Several surface treatments of nickel-iron alloy were tested (see Figure 16). Micro-ball shot-peening was selected because it showed the best combination of high performance and low impact on specimen's geometry.



From right to left :

1. M : Shot peening + Passivation
2. M+Nc : Shot peening + Chemical nickel plating
3. Nc : Chemical nickel plating
4. Ngm : Mat galvanic nickel plating
5. no label : Passivation only

**Figure 15. Surface treatment samples**

## **Outlook**

The metrology system will be used at each stage of Slit Change Mechanism test sequence to monitor possible changes of its accuracy. The accuracy checks will be performed after the SCM assembly, the vibration tests, the shock test, the thermal vacuum tests and the life-cycling. All tests which require actuation of SCM will also be performed in the chamber of the metrology system in order to prevent SCM bearings coating from oxidation.

## **Conclusion**

A unique metrology system (hardware and software) for simultaneous precise contactless measurements of 6 degrees-of-freedom of the Solar Orbiter Slit Change Mechanism Carrier is implemented. It features high accuracy, cleanliness, and temperature control. Tests and simulations show that the measurement accuracy of an object absolute position is of 20 micron in in-plane measurement (XY) and about 50 micron out of plane (Z). The typical absolute attitude is determined with an accuracy better than 3 arcmin in rotation around X and Y and better than 10 arcmin in Z. The metrology system is able to determine relative position and movement with an accuracy one order of magnitude lower than the absolute accuracy. Typical relative displacement measurement accuracies are better than 1 micron in X and Y and about 2 micron in Z. Finally, the relative rotation can be measured with accuracy better than 20 arcsec in any direction.

## **Acknowledgements**

To Keyence (Switzerland and Belgium) for support in accessing the available sensors compatible to our surface treatment requirements.

## References

1. Paciotti G., Humphries M., Rottmeier F. and Blecha L. "Development and preliminary testing of a high precision long stroke Slit Change Mechanism for the SPICE instrument." *Proceedings of the 42nd Aerospace Mechanisms Symposium, NASA Goddard Space Flight Center*, (May 2014), pp. 31-44.
2. Technical specification of Keyence 2D distance sensors « LJ-V »  
Access : <http://www.keyence.com/products/measure/laser-2d/lj-v/specs/index.jsp>  
[accessed 2015-09-27]
3. Technical specifications of Handyscan 3D handheld 3D Scanner [Online]  
Access : <http://www.creaform3d.com/en/metrology-solutions/products/portable-3d-scanner/technical-specifications-handyscan-3d>  
[accessed 2015-08-30]
4. Technical specification of Keyence 3D laser scanning confocal microscope VK-X [Online]  
Access : [http://www.keyence.com/products/microscope/laser-microscope/vk-x100\\_x200/specs/index.jsp](http://www.keyence.com/products/microscope/laser-microscope/vk-x100_x200/specs/index.jsp)  
[accessed 2015-08-30]
5. Description of Lyncée Tec reflection digital holographic microscope [Online]  
Access : <http://www.lynceetec.com/reflection-dhm/#1>  
[accessed 2015-09-27]
6. Technical specification of Nikon X-ray inspection system MCT225 [Online]  
Access : [http://www.nikonmetrology.com/en\\_EU/Products/X-ray-and-CT-Inspection/Metrology-CT/MCT225-for-Metrology-CT-Absolute-accuracy-for-inside-geometry/\(specifications\)](http://www.nikonmetrology.com/en_EU/Products/X-ray-and-CT-Inspection/Metrology-CT/MCT225-for-Metrology-CT-Absolute-accuracy-for-inside-geometry/(specifications))  
[accessed 2015-08-30]
7. Description of Huber temperature control system « Petite Fleur » [Online]  
Access : [http://www.huber-online.com/en/product\\_listing.aspx?group=1.01](http://www.huber-online.com/en/product_listing.aspx?group=1.01)  
[accessed 2016-01-20]
8. Description of Acktar coating « Fractal Black » [Online]  
Access : <http://www.acktar.com/category/FractalBlack>  
[accessed 2016-01-20]
9. Kenney J.F. and Keeping E.S. "Linear Regression and Correlation." *Ch. 15 in Mathematics of Statistics, Pt. 1, 3<sup>rd</sup> edition*, Princeton, New Jersey, (1962), pp. 252–285.
10. Ku H. H. "Notes on the use of propagation of error formulas". *Journal of Research of the National Bureau of Standards, Vol. 70C, No 4*, (October 1966), pp. 263-273.
11. Nelder J.A., Mead R. "A simplex method for function minimization." *Computer Journal* 7, (1965), pp. 308–313.

# Development and Testing of a Bi-Stable Actuator based on a High Transition Temperature Shape Memory Alloy

Gabriel Paciotti\*, Jacques-Eric Bidaux\*\*, Hervé Girard\*\*, Fabrice Rottmeier\* and Luc Blecha \*

## Abstract

Pyrovalves, i.e., valves actuated by a pyrotechnical device, are very often used in space propulsion systems for their fast response, high reliability, low mass and low cost. However, they are hazardous and single use items. Their operation induces shocks and can generate contaminants. If a slower actuation is required or possible, shape memory-based actuators avoid the generation of shocks and contaminants while being fully resettable and non-hazardous devices.

The goal of this project was to develop a bi-stable Shape Memory Alloy (SMA) actuator for a specific Slow Acting Latch Valve with long life capability. The benefits of this actuator makes it interesting not only for valve actuation but also for any device that has to be actuated in a smooth and reliable way.

This paper presents the development of a bi-stable actuator based on high temperature shape memory alloys.

## Introduction

Shape Memory Alloys undergo a phase transformation upon cooling from high temperature austenitic phase to a low temperature martensitic phase. This phase transformation is the basis for the unique properties of these alloys. At room temperature, the SMA can be readily deformed (low yield strength). When heated above the reverse transformation temperature  $A_f$ , the alloy reverts to austenite and recovers its previous shape. This property is known as the shape memory effect. With proper selection of SMA materials and production processes, the transition temperatures can be tailored to the engineering needs.

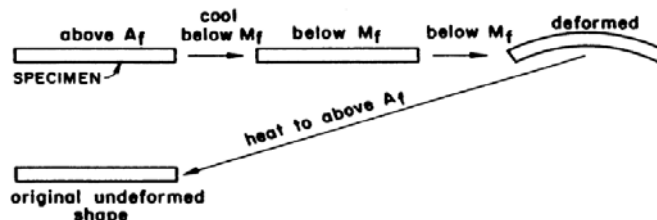


Figure 1. Shape memory effect principle

The team designed, manufactured and tested an actuator based on a high-temperature shape memory alloy. The SMA actuator main features are:

- High reliability
- Smooth-acting
- Resettable
- Light and compact
- High temperature SMA alloy (above 120°C)
- Withstands launch loads as high as 28.3 g<sub>RMS</sub>
- Made of space-compliant materials

\* Almatech, EPFL, Lausanne, Switzerland

\*\* University of Applied Sciences and Arts Western Switzerland, Sion, Switzerland

The SMA actuator developed by Almatech is based on the following operating principle: electric current is used to heat up multiple SMA wires (in a parallel configuration) changing their crystalline structure in such a way as to shorten them and actuate the integrated latching/de-latching mechanism. Thanks to this bi-stable custom-designed latching device, no power is needed to maintain the actuator in one or the other stable positions.

The overall dimensions of the developed actuator are shown in Figure 2.

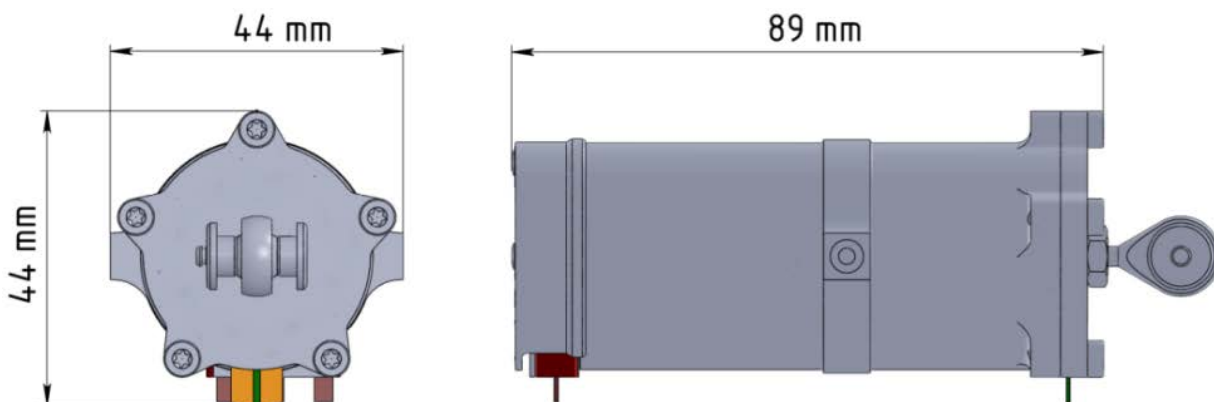


**Figure 2. Overall dimensions of the Actuator**

### Main Requirements

Table 1 presents the main requirements that drove the design of the actuator.

**Table 1. Main design requirements**

Characteristic	Value
Mass :	< 200g
Overall max dimensions :	100 x 60 x 60 mm <sup>3</sup>
Lifetime (with ECSS factors) :	≥1000 cycles
Power consumption (DC) :	<50 W (28V)
Output force:	165 N
Latching stroke:	< 1.7 mm
Total stroke	> 2.2 mm
Actuation time (slow actuation):	5s < t < 60s
Max non-operating temperature (Qual):	-10°C / 120°C
Max operating temperature (Qual):	-5°C / 100°C
Launch vibration load :	28.3 g <sub>RMS</sub>
Other feature	bi-stable (stable in both open and closed positions with no power supply)

### Main Challenges

Nickel-Titanium (NiTi) alloys are the most commonly used materials for their shape memory effect. They are off-the-shelf products and relatively low cost due to their extensive use in the biomedical and general industrial fields. While their maximum transition temperatures ( $M_s$ ,  $M_f$ ,  $A_s$  and  $A_f$ ) are well adapted to these applications, they are all under 100°C, which limits considerably their use in space mechanisms design. In order to widen the application range of SMAs in space mechanisms, Almatech has initiated, in collaboration with the University of Applied Sciences of Sion, Switzerland, a new development based on another shape memory alloy, CuAlX. CuAl-based material can feature, with the adequate composition and treatments,

transition temperatures higher than 120°C. In addition, shape-memory strains up to 8-10% can be observed with these SMA alloys representing a significant advantage over standard NiTi alloys limited to shape-memory strains up to 6-7%. On the other hand NiTi alloys are electrically resistive and can therefore be directly heated by Joule effect using through current as energizing source. Due to their high copper content, CuAl-based alloys have the main drawback of being electrically conductive such that CuAl-based actuators shall be equipped with a dedicated heating system that also needs to withstand deformations as large as 10% while keeping its full heating functionality. Higher transition temperatures and larger deformations make in general the CuAlX more suitable for space applications, however at the cost of a more complex SMA heating design.

Mechanically, the challenge was to establish a bi-stable design (no electrical current needed to maintain both end positions) that is highly reliable and able to sustain the launch loads without state change. Friction, wear, fretting and cold welding are issues that have been considered and worked around during the actuator development phase, but the true challenge turned out to be the mechanical stability of the bi-stable mechanism during launch, which required a particular effort.

### SMA Wire Actuator Main Features

SMA wires work in traction in their straight configuration to provide their full capability while being accommodated in parallel in the actuator to allow redundancy.

The main challenge in the heating system design was to sustain the large actuation deformation (8-10%) produced by the CuAlXx alloy. Indeed to take full advantage of the capabilities of the selected SMA material, the wire was equipped with the following elements:

- Wire Ends, providing the mechanical interface
- An electrical crimp for electrical back loop through the SMA
- A heating system to provide the necessary thermal power to the SMA

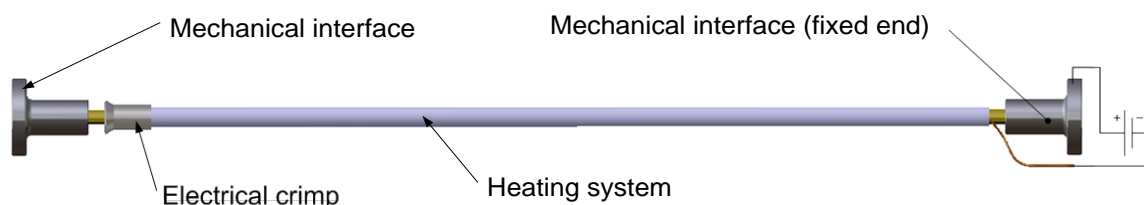


**Figure 3. Equipped SMA Wire**

A performance test highlighted the capacity of the naked wire (wire without heating system) to perform several thousands of cycles, making the required 1000 cycles life test easily achievable for the SMA itself.

The dimensional change leading to actuation is intrinsic to the microstructure of the material and therefore heavily dependent on the production processes. High reliability of the SMA wire can therefore be insured by a thorough control of the production processes and characterization of production batches. The heating system was identified as the main design challenge very early in the project and a particular effort was dedicated to improve its design and reliability. Therefore, each wire features a redundant heating system. In addition to this heating system redundancy, the device was designed to be fully operative and delivering the full nominal force with a single disabled SMA wire, providing a double redundancy in the system.

The SMA wire heating system is based on the use of a geometrically adaptive external heating element running along the full length of the actuating wires. The SMA wires being conductive, they are used as return lines to allow the electrical powering from a single side. This avoids the use of movable electrical connections following the extended and retracted states of the actuating wires on the opposite side.



On the moving end, an electrical crimp makes the electrical connection (see Figure 4) between the heating system lead and the SMA wire, while the opposite end (the fixed end) is directly connected to the electric power supply. The heating system lead located on the fixed end is connected to the other pole of the electrical supply.

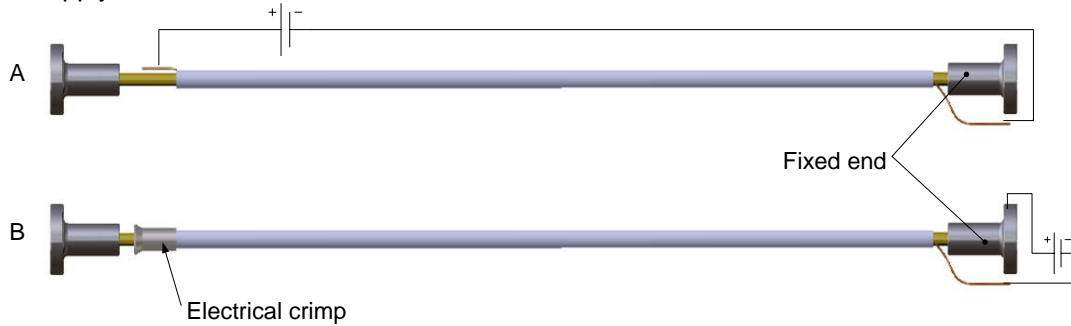


**Figure 4. Electrical interface: (A) Flying leads after heating system installation (B) Connection from the fixed side**

The thermal interfaces of the SMA wire system plays an important role in the performance of the full system. Although radiation is not negligible for space conditions, preliminary tests first focused on the conductive interface design. The initial SMA performance tests showed the strong impact of the conductive interfaces on the overall wire thermal behavior. It was observed that the conductive thermal flux significantly lowers the end of the wire temperature (see Figure 5). This gradient induced a significant loss of the net stroke of the sample by limiting the extent of the shape memory effect.

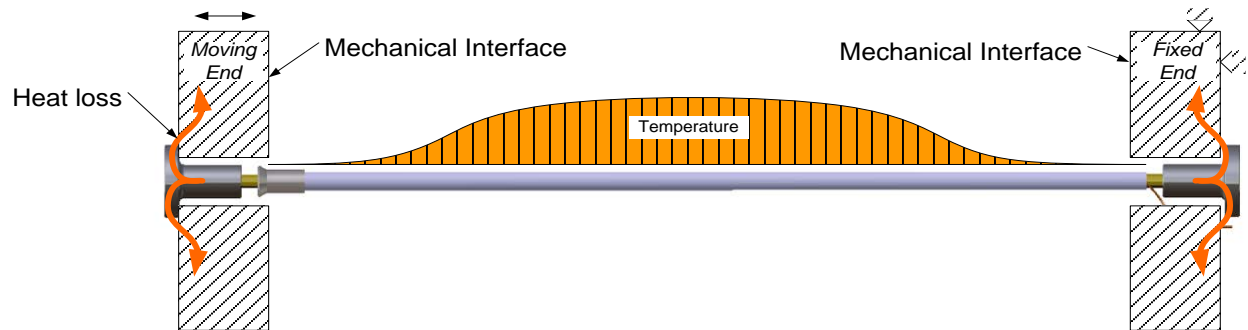


**Figure 5. Temperature losses in the mechanical fixation**

To enhance the thermal uniformity, the wire ends were thermally insulated from their supporting elements in a second setup. This led to the design shown in Figure 6 applied at each end of the SMA wire. While on one hand thermal insulation is desired to maximize the performance of the SMA wire by a uniform heating over its full length, heat rejection is required after SMA wire heating such that it can come back to its initial state and be actuated again with a new thermal cycle. Therefore, a compromise has to be found on the thermal insulation design that considers the trade-off between SMA wire heating efficiency and required actuation cycling times.

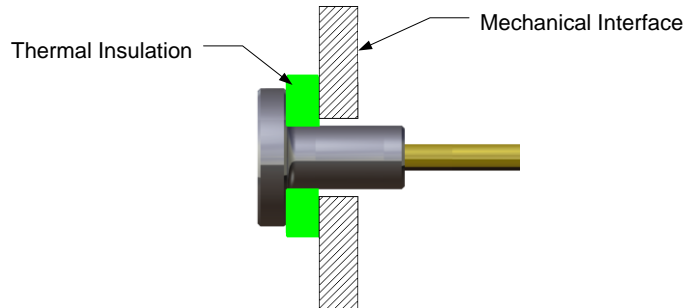


**Figure 6. Thermal insulation at mechanical interface**



**Figure 7. Wire End crimped to the SMA wire sample**

### **Stroke Control**

The lifetime performance of a SMA being limited by its exposure to over stroke, overstress and overheating conditions, the powering of the SMA wires needed to be controlled to meet the required lifetime performance of 1000 cycles. In order to do so, an electrical switch has been integrated in the design to cut-off the powering of the SMA wires as soon as the system is latched and a mechanical end-stop has been integrated to guaranty a repeatable rest position after cooling down of all SMA wires.

The switch is integrated on the backside of the actuator. A switch lever is pushed down by a Spring Blade as illustrated in Figure 8. The switch is released once the Pusher rod is in latched position.

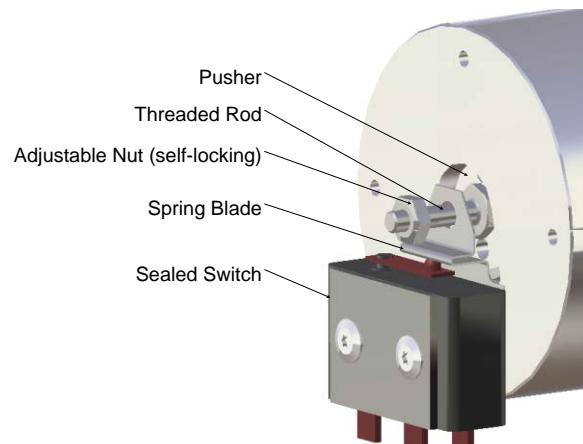


**Figure 8. Switch actuating system**

When the SMA Wires are activated, the Pusher rod travels forward. Once the adjustable nut supported by the threaded rod touches the Spring Blade, it shuts off the electrical supply and heating of the SMA wires.



**Figure 9. Fully assembled SMA Actuator**

### **SMA Actuator Test Sequence**

The test campaign consisted of the following test sequence:

- a. Cycling tests at SMA wire assembly level
- b. Cycling tests at mechanism level
- c. Mechanism vibration test

The first test aims to verify the correct actuation of a wire alone before integration into the actuator. It allows to ensure its capability to actuate under the required load and over the required number of cycles. Full performance test results of the developed Engineering Model were prioritized over the verification of its structural resistance to launch loads, such that these tests were performed at the end of the campaign and followed by final functional tests. The corresponding test results are presented hereafter.

### **SMA Wire Cycling Test Results**

The goal of the life test was to demonstrate the maximum number of actuation cycles that can be performed by an equipped SMA wire. The pass/fail criteria considered was the successful achievement of more than 1000 actuation cycles with 2.7-mm stroke under 70-MPa load.

The schematic drawing of the test jig is shown in Figure 10. The equipped wire samples were mounted to the fixtures of the test jig and a weight was attached to the lower fixture. The test setup is such that the initial position of the weight can be either in contact with the platform (load relief) or hanging on the SMA wire (free load). The SMA wire is actuated using the developed heating system using a constant current. The wire shrinks when actuated and lifts the weight in a loaded configuration. The displacement is measured using an LVDT transducer. As soon as the required displacement is achieved, the current is switched off. The weight then gradually returns to its initial position as the wire cools down and a new cycle is initiated. The test finishes when the predefined number of cycles are performed. The SMA wire temperature is monitored continuously using a type K thermocouple.

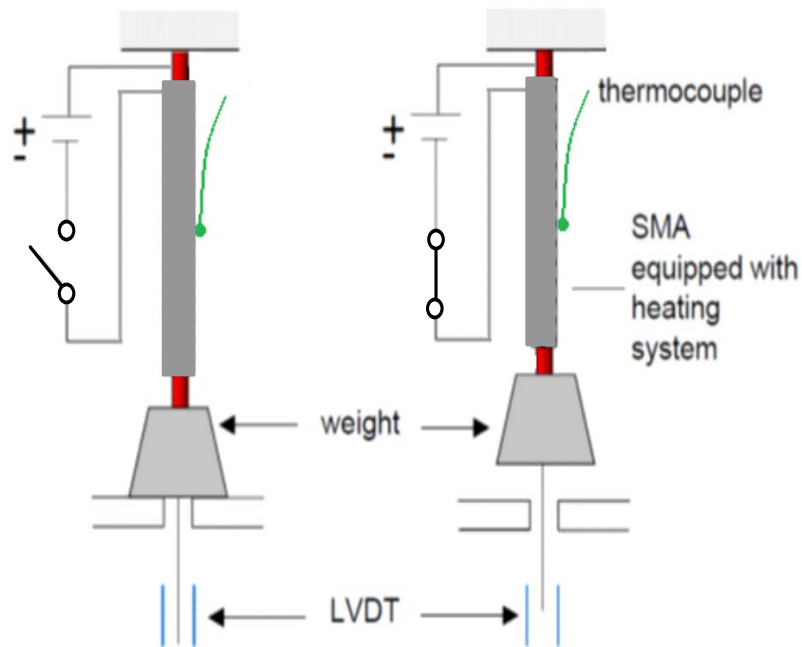


**Figure 10. Schematic drawing of the equipped SMA wire test jig**

The tests were performed starting from two initial positions: free load (weight hanging) and offloaded (weight in contact with the platform). The position of the upper fixture was adjusted using a micrometric screw.

Two tests were performed with the following load conditions:

- 40 MPa (30.62 N), to verify the ability of the SMA to reset (recover the original position)
- 70 MPa (51.12 N), the maximum determined stress for infinite cycling

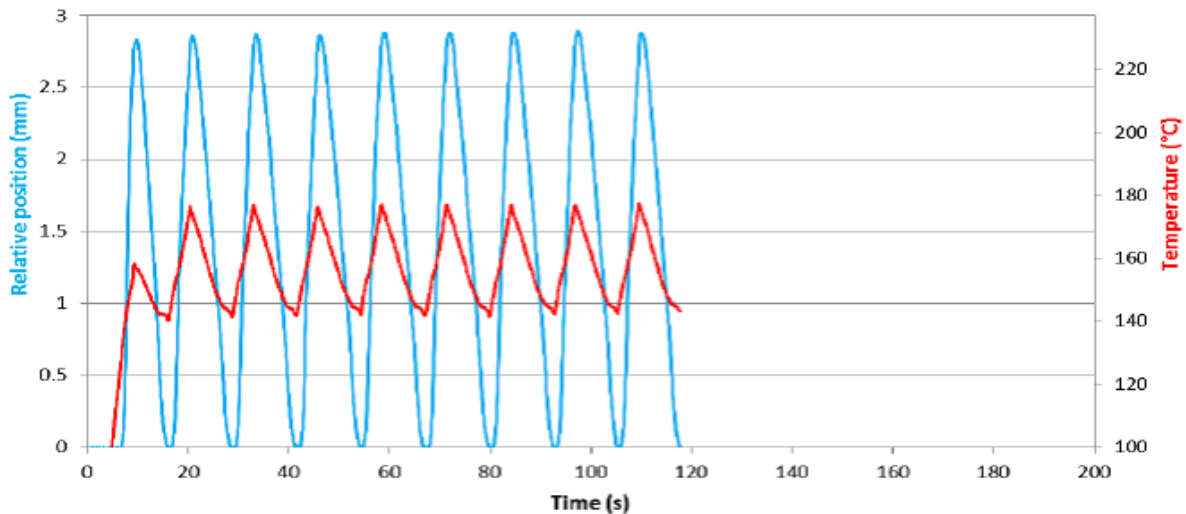


**Figure 11. Cycling under the load of 70 MPa**

Figure 11 shows a uniform cycling demonstrating the adequate behavior of the wire at 70 MPa. The same test was performed at 40 MPa demonstrating its ability to reset fully at this stress level.

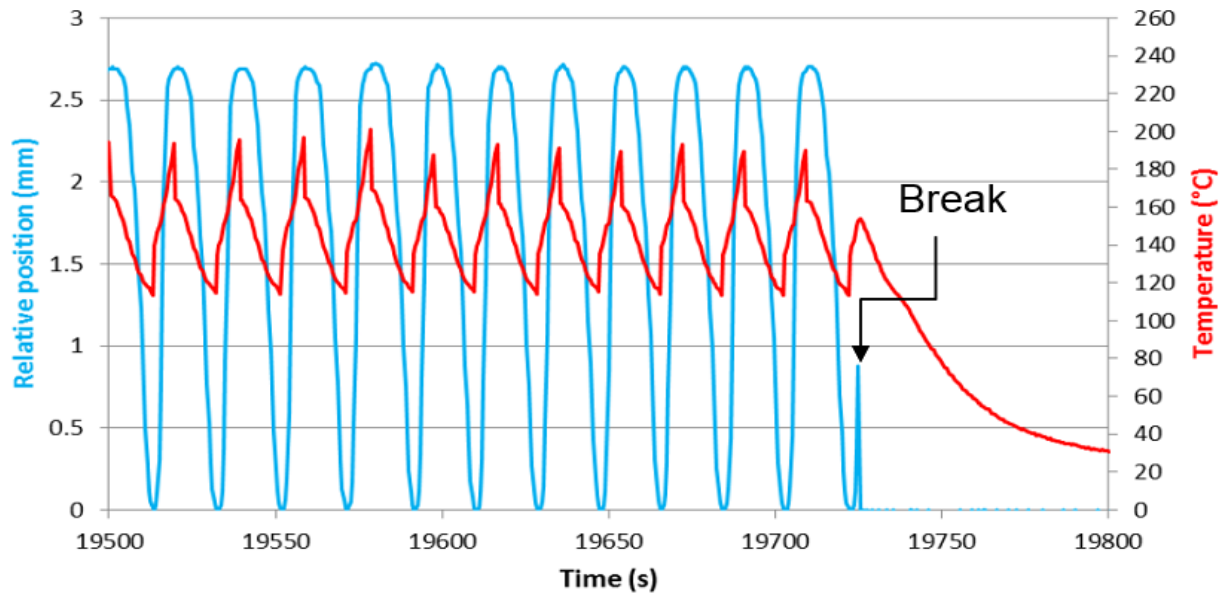


**Figure 12. Cycles 7646-7657, load 70 MPa, stroke 2.7 mm, current 1.94 A**

By the end of the test, 7657 cycles were successfully performed as illustrated Figure 12. During the cycle 7658, a fatigue failure occurred close to the middle of the wire as shown in Figure 13.



**Figure 13. Equipped wire after wire failure**

### **Actuator Cycling Test Results**

In order to study the cycling and time-dependent properties of the actuator, the following test was performed:

- Loading force = 96 N (reduced from the theoretical 175 N to ensure SMA cycling survival and verify the heating system over the full lifetime requirement)
- Power supply : 1.79 A, 27.8 VDC, 49.8 watts
- Cooling time between cycles = 15 seconds (to ensure that the actuation time at the next cycle will not be affected by an incomplete cooling at the previous cycle)
- Heating time limit = 15 seconds (overheating risk)
- Standard ambient temperature and pressure conditions

The actuator survived the required 1000 cycles and switched its state (latched or released) automatically at each cycle. The cycling test of the actuator was fully successful as illustrated in Figures 14 and 15 showing the four initial cycles and the last four cycles.

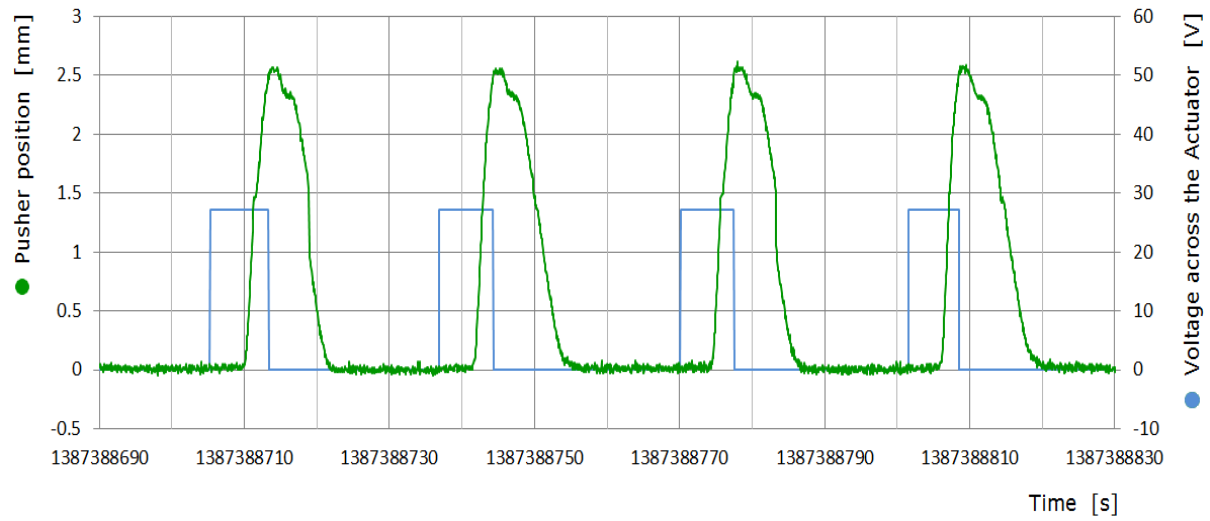


**Figure 14. Cycles 1-4**

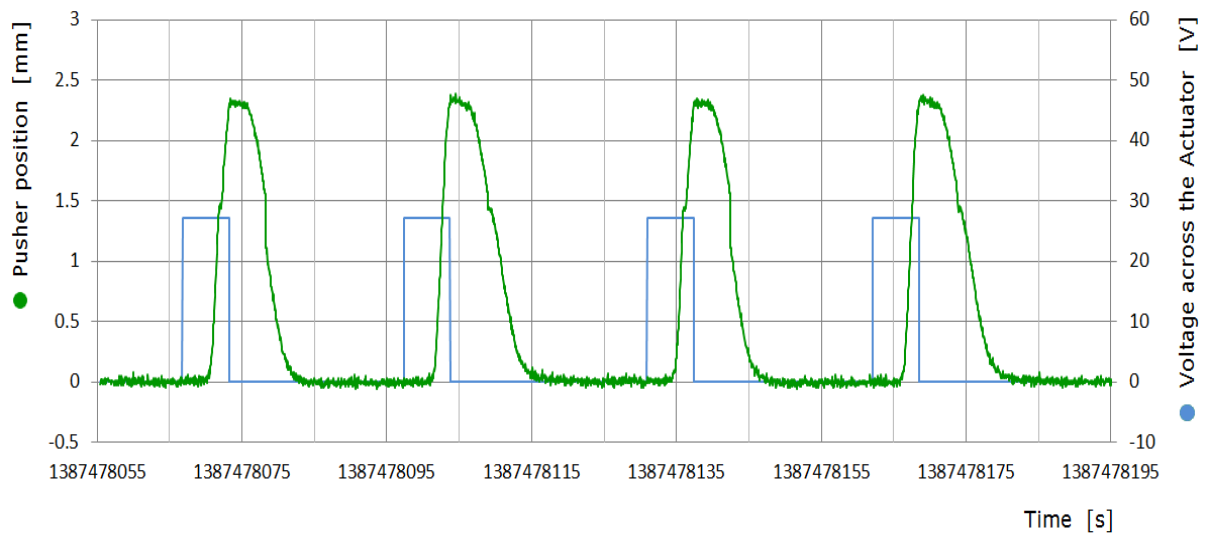


**Figure 15. Cycles 1054-1057**

### Actuator Vibration Test Result

Resonance search and random vibration tests were performed in order to ensure adequacy of the actuator design to the required launch loads. The tests were performed in axial and radial directions.

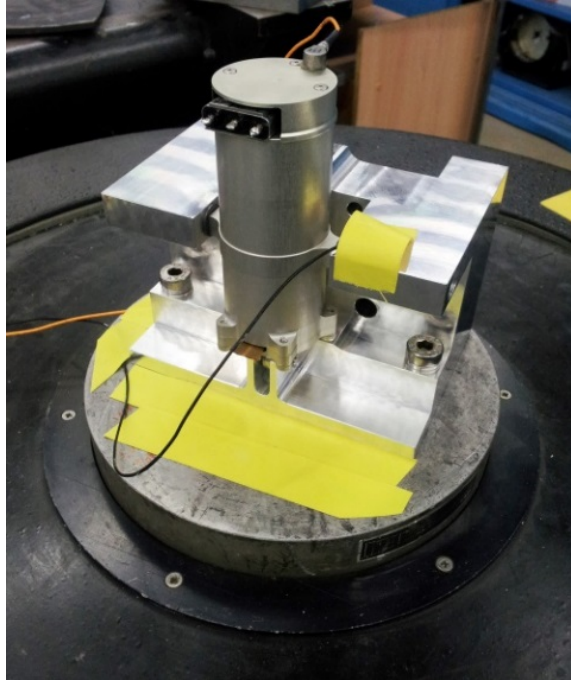


**Figure 16. Axial vibration of the Actuator**

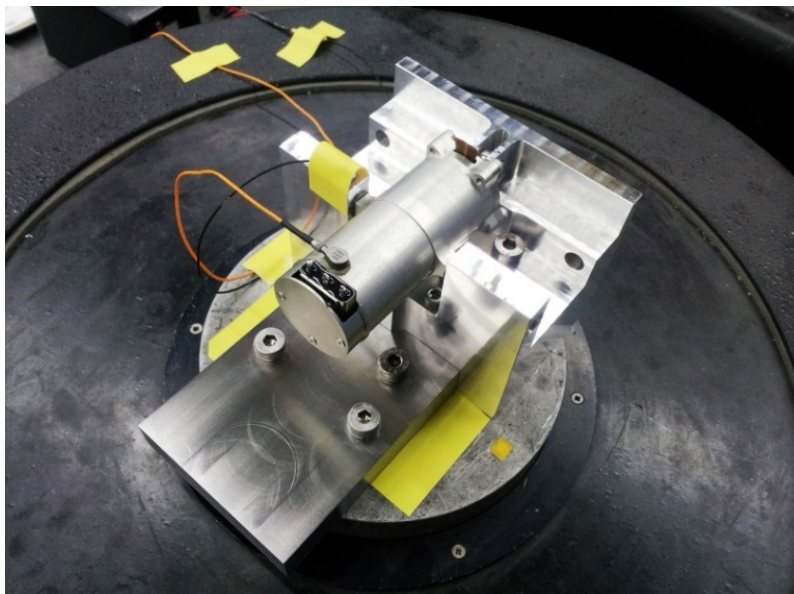


**Figure 17. Transverse vibration of the Actuator**

The overall acceleration of the applied random vibration profile was 28.3 g<sub>RMS</sub> and the total test duration was 3 minutes. The vibration spectra acquired during the tests are shown in Figure 18 and Figure 19.



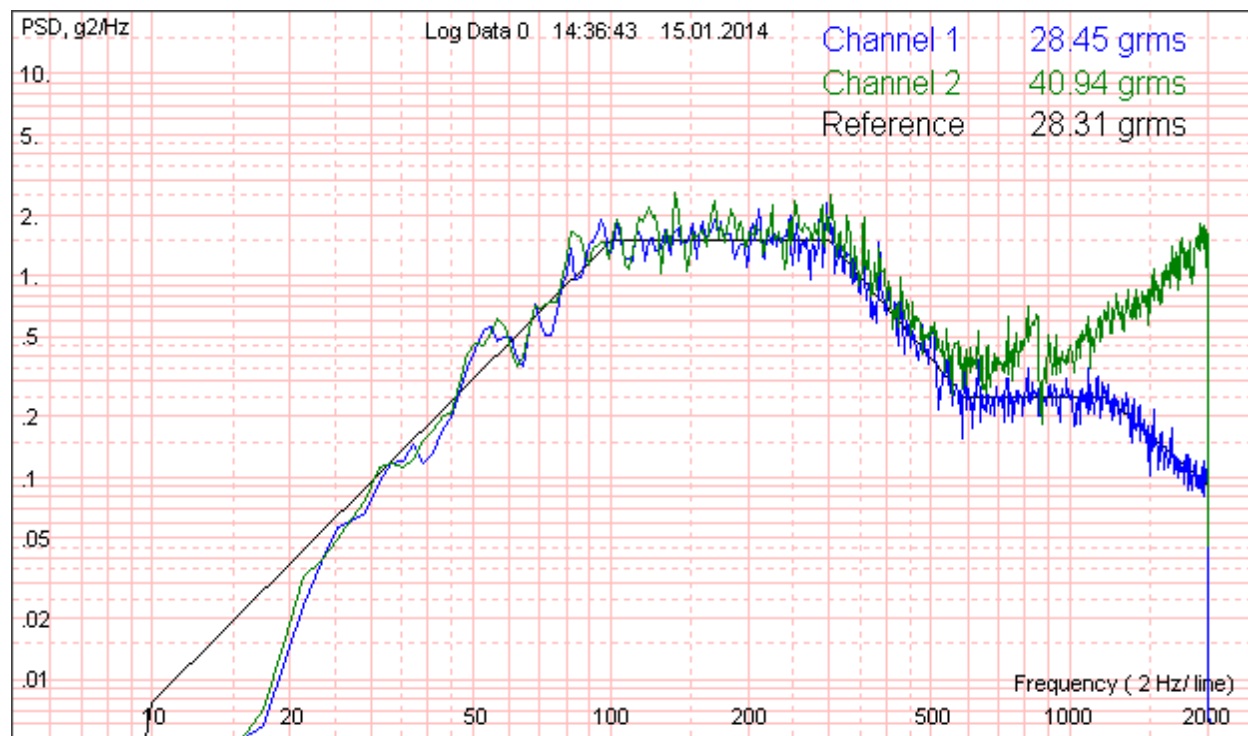


**Figure 18. Random vibration spectrum in the axial direction**

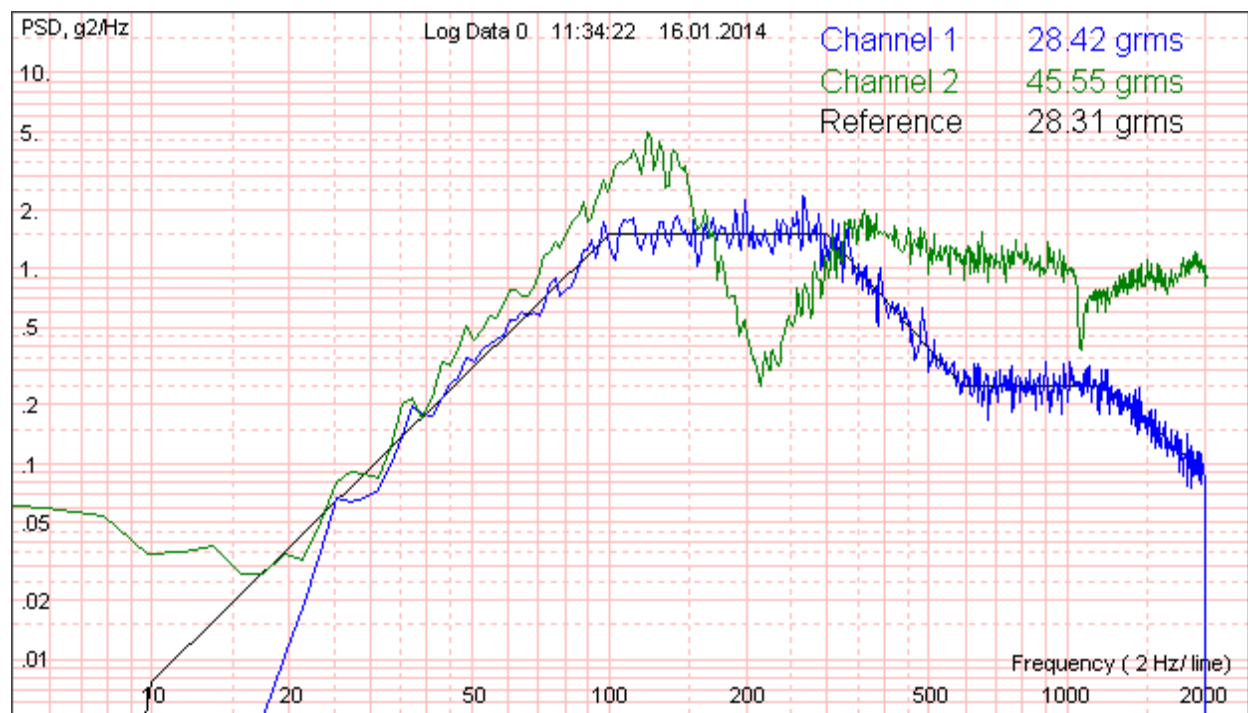


**Figure 19. Random vibration spectrum in the radial direction**

The SMA actuator successfully sustained both axial and transverse random vibrational loads with overall acceleration of 28.3 g RMS and duration of 3 minutes each. No changes in the resonance search results were observed before and after the random loads application showing that no structural failures have

occurred. A post-test functional verification showed that the actuator remained fully operational after the test. It proves that the design is able to survive the required launch vibration loads.

### Synthesis of Actuator Characteristics

**Table 2. Actuator main characteristics**

Characteristic	Value	Requirements
Mass :	118 g	< 200g
Overall dimensions :	89 x 44 x 44 mm <sup>3</sup>	100 x 60 x 60 mm <sup>3</sup>
Lifetime:	1055 (stopped, no damage)	> 1000 cycles
SMA wire lifetime:	> 7657 cycles	--
Verified output force:	49.8 W (27.8V, 1.79A)	< 50W (28V)
Latching position:	96N*	165N
Maximal stroke:	1.5 mm	< 1.7mm
Push duration:	2.5 mm	> 2.2mm
Pull duration:	6.5± 0.4 s	5s < t < 60s
Max operating temperature:	11.9±5.4 s	5s < t < 60s
Launch vibration load:	120°C	> 70°C
	verified	28.3 g <sub>RMS</sub>

*\*The quality of the produced CuAlX monocrystalline wire samples was not sufficient to reach the cycling stability under the required force. It was therefore decided to reduce the test load at 96 N (from 165 N) for the test campaign. Recently, industrial quality level CuAlX wires are commercially available and should meet the design load of 175 N.*

### Conclusion

A bi-stable actuator based on a high transition temperatures Shape Memory Alloy has been successfully designed, manufactured and tested. This mechanism, able to provide slow-acting pushing and pulling forces, showed great repeatability over a high number of actuating cycles demonstrating high overall reliability of the selected design.

One major challenge was to design a SMA heating system compatible with the use of high transition temperature SMAs that are highly conductive and have shape-memory strains up to 10%. A novel heating system has been developed and successfully tested on single wire setups as well as on a fully integrated mechanism.

Through this project, the technology based on high transition temperatures SMA reached the readiness level TRL-4. Further material characterization tests on industrial quality CuAlX wire as well as additional environmental tests are to be performed to reach TRL-5.

# Holding brakes for Space Mechanisms with Minimum Power Requirement

Ted Hopper\*, Christoph Stuckmann\*, Scott Starin\*\* and Walter Whitehead\*\*

## Abstract

In space applications, the rotational axes of mechanisms that are driven with electric motors need to be secured, not only during launch but very often during most of their operational life or cycle. Holding brakes are therefore required, which are mostly engaged in the un-energized condition. Such brakes should, however, require a minimum of electrical power during release, as energy is at a premium in space. It is also important to avoid or to minimize thermal losses.

In this paper various alternative holding brake technologies are presented with their characteristic advantages and disadvantages.

## Introduction

One preferred motor type for space use is the hybrid stepper as this electric motor type has good torque density. It can further operate without angular position feedback and exhibits a high intrinsic detent torque at many holding positions per revolution (typically 200). However, there are also many applications that require servo or torque motors that do not or should not exhibit any natural salient holding-torque positions. In this case or when a stepper motor is used for the design of a specific mechanism but its detent torque is insufficient, a brake must be implemented, which must also fulfil a major secondary requirement – low or better zero power consumption in the holding condition. We consider four interesting brake implementations that can meet this requirement:

- Locking and release mechanisms
- Friction holding brakes
- Reluctance brakes, passive
- Reluctance brakes, active

Locking and release mechanisms - electromagnetic, pyrotechnic (when only one-time operation is required) etc. – are common in space applications but are not described here further.

Friction holding brakes, usually with spring operation and electromagnetic release, are frequently used in industry. Two suitable configurations for space use are presented below. This type of brake has the advantage of allowing the motor shaft to be held in any position but it has the significant disadvantages of mechanical interference and wear; it also requires a mechanical separation movement of two brake plates. It is often a major challenge to ensure safe movement of the brake plates over the wide and demanding environmental conditions of space application.

The passive reluctance brake is also employed in space. It has a symmetrical geometry using highly salient poles on stator and rotor, which cause the brake to relax automatically to preferred positions with a high detent torque, thereby holding the shaft in one of these positions.

The fourth option, the “active reluctance brake”, we believe to be unique. This has been developed to meet the requirement of zero or minimum torque or damping when excited. Like the passive reluctance brake, it also has no wearing or mechanically interfering parts and consumes no power when active.

---

\* MACCON GmbH, Munich, Germany

\*\* Avior Control Technologies, Inc., Longmont, CO

## Friction Holding Brakes

We have developed a disk type of friction brake for a rotating antenna drive application on a drone, not directly for space but for stratospheric use. It has therefore been qualified to environmental conditions, very similar to space – low air pressure (100 mBar) and low temperatures ( $-60^{\circ}\text{C}$ ).

In order to achieve high torque, the design makes use of the large diameter of the torque motor, which is to be secured by the brake when the motor is stationary or inactive. A thin stainless steel ring is mounted around the rotational axis, attached to the rotor of the motor. This ring has high torsional stiffness but is flexible in the axial direction to allow for some freedom of motion of the mechanism in the shaft axis.

Two brake calipers with pinching brake pads are mounted around the disk. These calipers are operated by mechanical springs to apply braking friction force to the disk and thereby braking torque to the motor. Electric solenoid actuators release the pads and reduce the brake torque to zero.

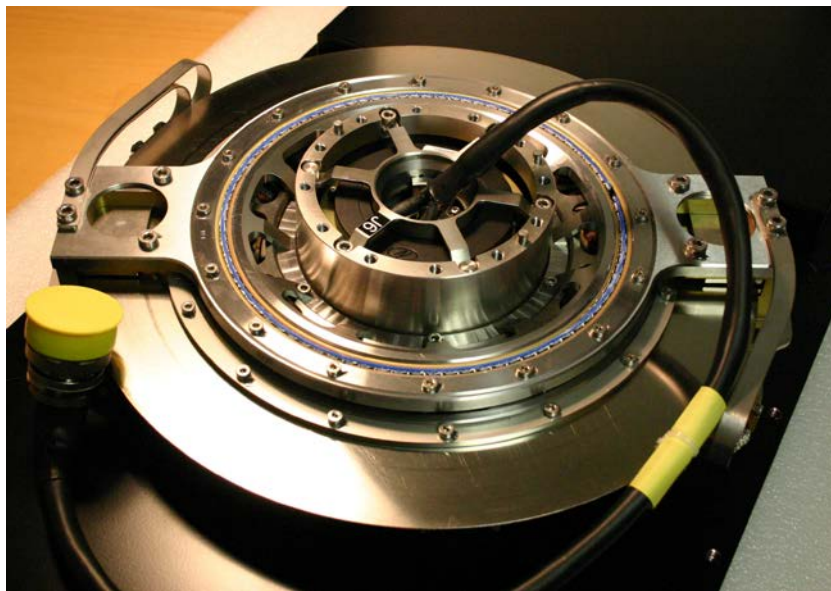


**Figure 1. 10-Nm Friction Disk Brake (MACCON)**

This brake also fulfills another demanding requirement. Due to the sensitivity of the application, it was specified that a specified maximum level of reaction torque on the supporting structure may not be exceeded if the brake is operated, while the motor is rotating. The brake described requires 36 W to release but only 7 W to maintain the released condition. Due to the springs incorporated in the calipers this brake is fail-safe.

Now we describe another type of friction brake, which can achieve high braking torque values in a much smaller diameter thanks to the large torque multiplication factor of a gearbox. Figure 2 shows a high torque brushless DC actuator with an integral gearbox and friction disk brake. This actuator is used in a robotic arm application where power-off holding of a large moment is required. While the peak torque of the brushless actuator is 22 Nm, the unpowered holding torque of the brake is 8 Nm reflected to the output shaft. With the mechanical advantage of the gearbox, a small friction disk brake provides significant power-off holding torque provision for a minimum of mass and volume.

A disadvantage of both friction disk brakes is the relative high power needed to pull-in or activate the free-running condition of the actuator. For instance, the brake design in the actuator in Figure 2 draws 7 W power at 28 volts DC, the rated voltage. The voltage and power to maintain free-running actuation is

however significantly lower, as it takes less than one watt holding power to maintain the brake in the disengaged condition.

There are several methods to minimize the sustained power draw of both friction brake designs described above. Since the “drop-out” or engagement voltage is significantly less than the pull-in voltage, the control system may simply reduce the excitation voltage after the free-running condition has occurred. The activation happens quickly, in about 10 ms. As it may not be desirable to regulate the voltage, it is simpler to have two separate coils in the brake bobbin assembly. This is also an option for redundancy. The second “low power” or “sustaining” winding may be used to allow deactivation of the first “high power” or “activation” winding after the free-running has been achieved. The “sustaining” coil winding may have significantly higher resistance to minimize power draw compared to the “activation” coil winding. This schematic is represented in Figure 3.

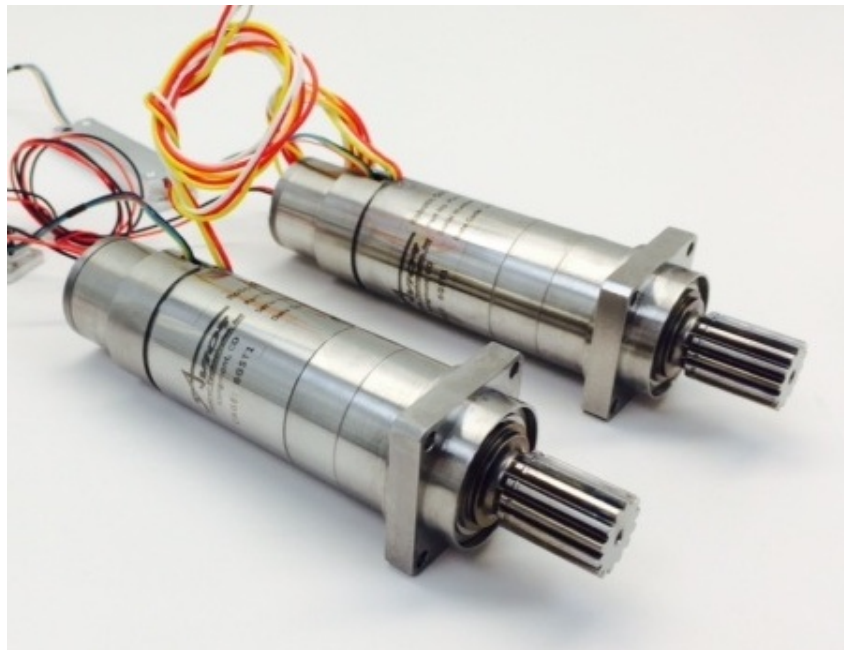


**Figure 2. 22-Nm Actuator with Integral Friction Disk Brake (Avior)**

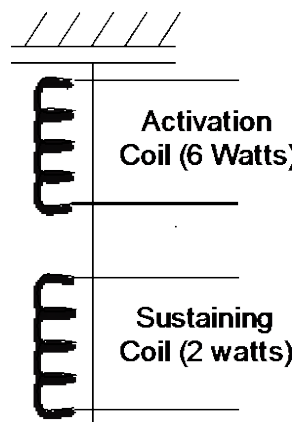


**Figure 3. Dual Coil Brake Schematic (Avior)**

A method to easily remove the power from the “activation” coil is to add a “blocking” capacitor in series with the winding. As the DC excitation is applied to the “activation” coil winding, the current flows through the winding, as the inductance allows. Once activated, the current levels off and the blocking capacitor drains the current down to zero. This is a simple method that does not require additional logic or switches to disable the “activation” coil.

### Passive Reluctance Brakes

Passive reluctance brakes (or detent brakes) are always active, which in turn means that the motor needs sufficient starting torque to overcome the brake detent torque in addition to any stall load torque. However, once the shaft is rotating, the additional power needed to run the motor drops, as the reluctance torque equally assists as well as resists motion; the effect of this pulsing load torque drops with increasing speed. Typically this type of brake only offers a limited number of holding positions per revolution (4,6,8,12 etc.).

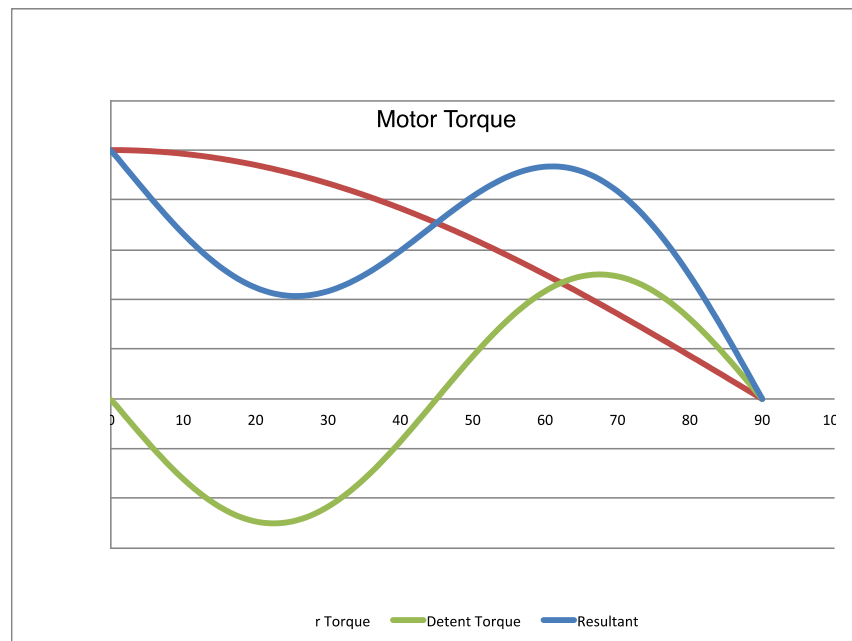


**Figure 4. Stepper Motor and Reluctance Brake Torque vs. Position Plot (Avior)**

Figure 4 shows a Motor Detent Brake Torque versus position (or Torque-Theta) plot of a stepper motor combined with a passive reluctance brake. In this configuration, the motor steps and stable brake detent positions coincide. At each step of the stepper motor, the torque drops off from the peak torque to zero in a cosine function (for sinusoidal back EMF). The detent brake repels against the motor torque for the first half of the step, and assists in the second half of the step. While the area under the curve integrates out, it is over-simplistic to state that the detent brake does not have an impact on dynamic performance. In fact, the detent brake may have a positive affect on performance. Since it can add torque as the stepper motor is approaching the stable step position, the rotor accelerates faster through zero and creates more overshoot at cardinal stepping frequencies.

As described in [1], overshoot in a stepper motor creates cardinal maxima and minima torque variations at various points along the torque-speed curve. The addition of the detent brake inherently attenuates the pull-in torque of stepper motor actuator at low pulse-rates. The actuator pull-in torque curve in Figure 5 shows performance with and without a 19-mm passive detent brake that produces 1.0-Nm torque at the output. As you see at low velocities, the whole torque of the detent brake reduces the available pull in torque. As the step rates increase, there are varying affects of the detent brake. The pull-in torque attenuates or

increases at varying step rates. At high velocities, above the mechanical time constant, the detent brake has virtually no effect on the actuator performance.

The advantages of the passive brake configuration are zero energizing power and no control circuit requirement.

Using this brake directly on the servomotor shaft before a high-ratio reduction gearbox allows its dimensions to remain small and minimizes servocontrol problems, which result from the motor having to operate against the high ripple torque of the reluctance brake. Positioning is intentionally limited to the preferential positions of low reluctance to which the brake is naturally biased. It is interesting to note that the pull-out torque is much less affected by the detent brake. In other words, the pull-out torque performance of an actuator with a detent brake closely matches the pull-out performance of the same actuator without a detent brake. We strongly recommend full characterization with simulated load inertia of actuators incorporating passive detent brakes.

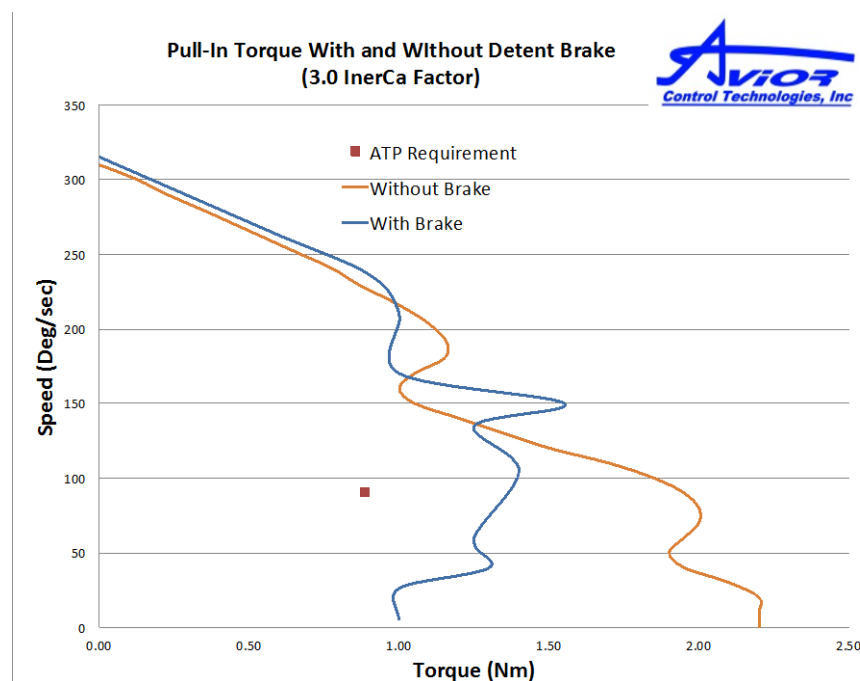


**Figure 5. Pull-In Torque Performance**

### Active Reluctance Brakes

This active reluctance type of brake will be used in a valve actuator of a space vehicle launcher. The solution chosen has a special stator/rotor geometry with many positions of minimum reluctance per revolution. Permanent magnets fitted in the stator cause this brake to have 200 preferred holding positions (of  $1.8^\circ$  pitch) with a closely defined holding torque value. The permanent magnet field can however be neutralized by passing current through a single winding in the stator, thus allowing the mechanism to rotate with minimum magnetic drag. Energizing the coils causes the flux coupling between stator and rotor to be shifted into the stator back iron resulting in a magnetic short-circuit for the permanent magnets.

The first application we have realized is illustrated in Figure 6. It has an outer diameter of 120 mm, a length of 30 mm, and a holding torque of 3.3 Nm. The torque characteristic of the active reluctance brake over one pitch is shown in Figure 7 and the flux distribution in both operating conditions in Figure 8.



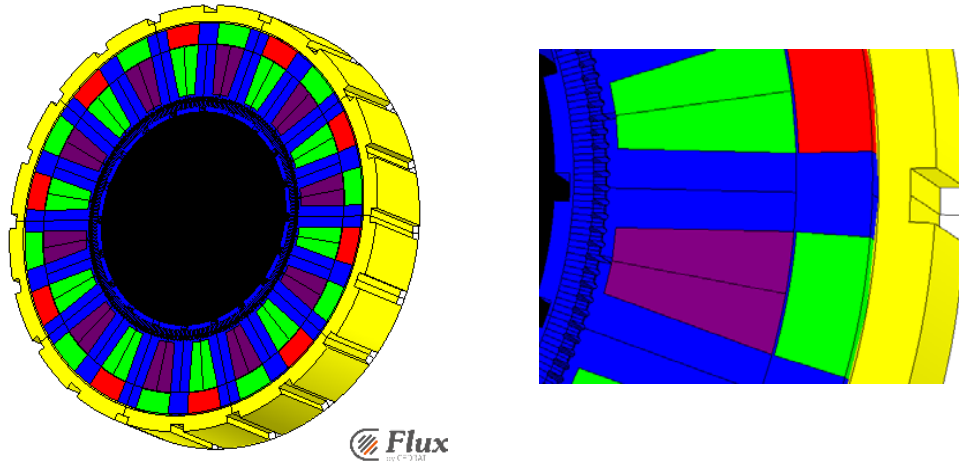


Figure 6. Active Reluctance Brake (MACCON)

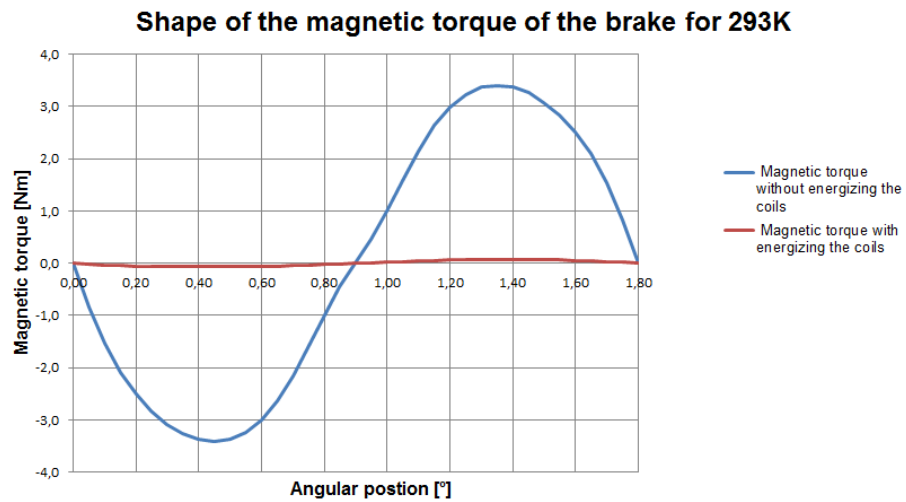


Figure 7. Holding torque of Active Reluctance Brake over 1.8° (MACCON)

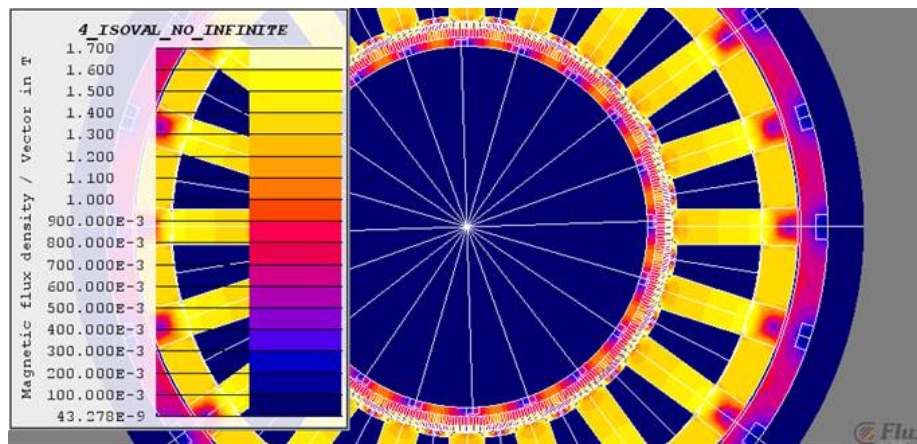
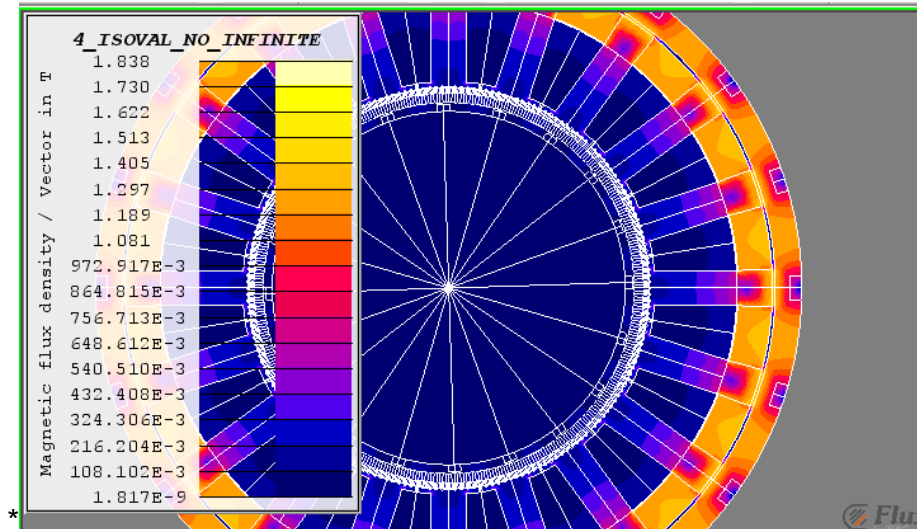


Figure 8A. Magnetic Flux distribution in active reluctance Brake with stator coils energized (MACCON)



**Figure 8B. Magnetic Flux distribution in active reluctance Brake with stator coils not energized (MACCON)**

The clear advantage of this brake design is the high number of preferred braking positions per revolution, 200, without the need to energize the brake. There is also a good geometrical match between the brake and its matching motor design dimensions. On the negative side it does require high excitation power (58 W) to release, i.e., for the neutralization of its holding torque. However in applications where release is only needed for a short periods, this energy dissipation can be accepted.

### Conclusions

The four holding brake configurations described in this paper have been especially designed for demanding high reliability and space applications. As they offer very differing mechanical configurations and braking characteristics, it is probable that one of these configurations will serve any new electro-mechanical drive or actuator application.

All brake designs discussed share the essential properties of requiring zero energy, when braking torque is required and of being fail-safe. If the energy supply fails, the holding condition is guaranteed. Passive-reluctance brakes offer the advantage of no power excitation whatsoever, but detailed characterization of performance with simulated load inertia is recommended, due to induced operational pull-in torque variations and thus an increased step-response overshoot. Additionally, passive reluctance brakes are not recommended for use with servo-systems, because brake torque may be a significant source of load disturbance for the servocontrol system.

Lastly, all the active brake configurations can be made electrically redundant, with the simple implementation of a second excitation or release coil [2]. Friction disk brakes designs may use an unbalanced power configuration with a two-coil option to minimize quiescent power draw by means of a higher resistance sustaining coil.

### References

1. Scott Starin, Cutter Shea, "Primer – Stepper Motor Nomenclature, Definition, Performance and Recommended Test Methods", Proceedings of the 42nd Aerospace Mechanism Symposium, NASA Goddard Space Flight Center, May 14-16, 2014
2. Ted Hopper, Dr. Markus Anders, Christoph Stuckmann, "Building electric motors for space, with redundancy and high reliability", Proceedings of the 14th European Space Mechanisms and Tribology Symposium 2011



# Lean Development of the Future Actuator

Mathias Burkhalter<sup>\*</sup>, Matthias Schulke<sup>\*\*</sup>, Beny Wüthrich<sup>\*</sup> and Oliver Kunz<sup>\*</sup>

## Abstract

The increasing commercial pressure on the market is something that is generally seen by companies whether in the space business or not. As a result of this, companies have to adapt their development strategies to remain competitive in the future. However, the space industry is bound to strict rules, regulations and requirements that do not just allow the deletion of processes and reducing product prices with the risk of reduced quality. Therefore, RUAG is exploring a new industrial approach for space mechanisms development. The approach has three cornerstones. One is the early and deep involvement of the suppliers in new developments, the second is the set-up of the development logic itself, and the third is to have an extensive concept phase. This paper describes the development and breadboard tests of the Future Actuator performed by RUAG Switzerland together with Harmonic Drive AG Germany.

## Introduction

RUAG Space in Zürich has an important footprint in the aerospace business and especially in the field of space mechanisms. RUAG's mechanisms portfolio covers a wide range from actuators, solar array drive mechanisms, antenna and thruster-pointing mechanisms up to multi-functional mechanisms for scientific instruments. RUAG has highly skilled employees and is known for its quality and schedule reliability. Still RUAG has to cope with the relatively high cost base in Switzerland and the currently unfavorable exchange rate of the Swiss Franc. In order to increase the competitiveness and secure the position in the market, RUAG Space has to be more efficient than other companies outside Switzerland. Therefore, RUAG is constantly working on improvements in all fields. One of the inputs leading to the idea for the development approach used for the Future Actuator evolved from a story about the development of the Pratt & Whitney PT6 propeller turbine [5] where a small team developed a revolutionary propeller turbine in a short time. One of the key elements for the success was the team consisting of young team members combined with experienced ones. In the end, the team built the turbine the "wrong way" around into the aircraft (inverse turbine airflow to flight direction) which is not the first and logical solution but has some significant advantages. Out of this story, the idea arose to set up a team that shall develop a new unconventional solution without being influenced and limited by existing rules. At the same time as this idea for the alternative development approach came up, RUAG started to think about a successor of the established SARA21 actuator, which is currently a very attractive product on the market. Consequently, the two objectives were combined and the "Future Actuator Project" was born.

Equipment development in the space business, in most cases, is done in collaboration with a customer. Both sides profit from this approach as the customer gets a product developed exactly to his needs and the supplier can reduce risks and expect some funding for the development. For very specific developments like instruments for scientific satellites, this is in most cases the best strategy. For products which after the development allow a wider customer base, the co-funding for developments has the risk that the launch customer may influence the development too strongly. In the past, customer expectations and interventions sometimes led to an increased effort, and caused schedule and cost impacts. Therefore, the lean development approach deployed for the Future Actuator is a viable alternative to co-developments with customers. For the Future Actuator RUAG decided to perform the entire development on an internal Research and Development budget and, even more, without the involvement of a specific customer. Except

---

<sup>\*</sup> RUAG Space, Zurich, Switzerland

<sup>\*\*</sup> Harmonic Drive AG, Limburg, Germany

## Project Definition

The project definition described here presents the approach implemented in the Future Actuator development program. The entire development program is divided in three phases:

- The project budget was small and therefore the program had to be planned carefully. For this reason, the Research & Development included only phase 1 and 2. The third phase was postponed until the test results were available. In the meantime the third phase –has been initiated and is running.

Before the requirements and concept definition phase, a market survey was performed. The market survey showed that there are a number of products on the market with very similar performance to the RUAG standard actuator SARA21. Additionally, there is a tendency towards actuators with higher gear ratios and smaller step sizes as well as extreme price pressures from the customer.

The requirements definition was split in two areas, the programmatic and the technical requirements. For the programmatic requirements, there was the question where the actuator should be positioned on the market. There were three possibilities:

- Based on the feedback from key customers, it was known that next to performance the price is the most important factor for the product. Therefore, RUAG decided to focus on a combination of performance improvement in parallel with a price reduction.



The technical requirements were derived from customer feedback and performance parameter evaluation. In brief, the main targeted improvements (compared with SARA21) were:

1. Higher torsional stiffness
2. Higher detent torque
3. Smaller step size
4. Same or smaller mass and dimensions

In the beginning, the requirements were limited to the top-level requirements and the first concept was based on these top-level requirements. Then key suppliers were selected and the concept was iteratively refined together with the key suppliers. This allowed the suppliers to offer, without interface limitations, the best possible product for the application. Based on this configuration the requirements were revised and further broken down. From this moment the requirements got a weighting factor which was used to give priorities in case of conflicts. This way of requirements definition supported with weighting factors allowed a straightforward optimization of the concept.

#### Demonstrator Definition

Soon it became clear that the project would result in an advanced product which has two main technological elements: a compact gear stage with a high gear ratio and a robust and contactless position sensor. Both technologies were new and their performance could not be defined and analyzed accurately enough. Therefore, the only possibility was to test the technologies in order to assess whether they comply with the requirements. For this, it was decided to build a breadboard model that would allow the determination of the performance parameters. This technology demonstrator was called the Future Actuator. The breadboard model, compared to a qualification model or other advanced models allowed a quick and simplified development and testing cycle. This was exactly what was needed to evaluate the compatibility of the selected technologies with the next generation of rotary actuators. It was decided to build the breadboard as close as possible to the anticipated final configuration to ensure a reliable performance data under all environmental conditions. The breadboard was split in two areas: the gearbox with the main bearing and position sensor and the motor. With this modular arrangement, the motor is independent from the gearbox. The modularity of the motor is a feature that has two main advantages: one is that the motor can be selected based on the tested performance; the second is that the motor could be easily exchanged, which allows the customer to exchange the motor with minimum impact to the overall product, if needed.

### **Development at RUAG**

The Future Actuator development was a kind of experiment to test some development aspects that were not used before at RUAG. One aspect of the development was the team size. The team was very small and having such a small team had the advantage of quick decisions and iterations. The disadvantage was the lack of collaborative inputs, which had to be compensated. In RUAG, all employees are located close to each other, which allows access to the needed know-how very easily. This circumstance was intensively used and all the experts were consulted constantly in order to ensure the maximum benefit from internal know-how. The decision process was very short which allowed a quick definition of the concept.

#### Design Thinking

The development approach used for the Future Actuator was very much in line with the design thinking approach. The design thinking approach aims at open-minded development of products with higher complexity. There are different interpretations of the design thinking.

At RUAG, the design thinking approach is understood as follows:

1. Identify and understand the need (requirements)
2. Create different solutions and select the best concept
3. Get inter-disciplinary inputs to refine the concept
4. Test early and be flexible in this phase
5. Improve the product based on test results and updated customer requirements

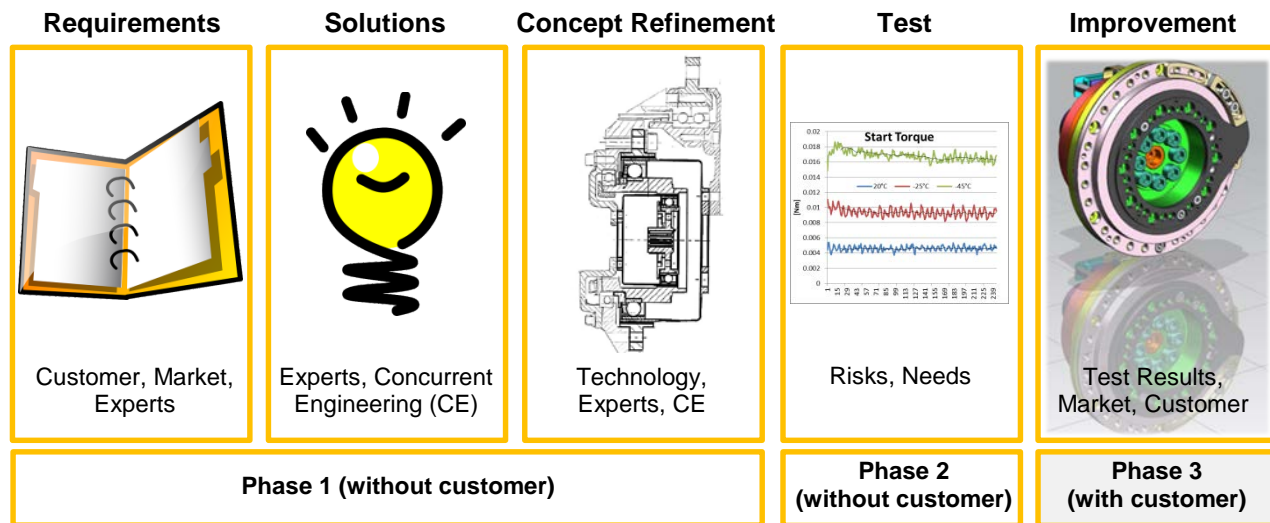


**Figure 2. RUAG Applied Design Thinking Flow**

From the five principles listed above often only the first four can be used in classical space product development. The reason is that in most cases a one-off product is being developed with fixed customer requirements. These boundary conditions do not allow the implementation of the lessons learned from testing, but with the Future Actuator breadboard model the test results can be implemented in the follow-on qualification model. The following is a short description of what is understood by the five principles.

The first point aims at the clear understanding of the requirements, which is often a key for the success of the project. If no specific requirements are available (like for the Future Actuator) the definition of a set of generic requirements is the first task. The requirements definition is then a combination of market research, customer wishes and technical capabilities. Out of them, the first set of requirements can be derived.

The second point aims at concept elaboration. Here an open mindset is required and this is the moment where unconventional solutions have to be addressed. At RUAG often brainstorming sessions in the Concurrent Engineering (CE) facility (see Figure 3) are used for this.

The third design thinking principle concerns the concept refinement. Also here the internal CE facility is used for the design and concept review sessions. Preferably they are held in various small steps where different design aspects are optimized instead of one big design review. It is recommended to stay long in the concept phase and to avoid going too early into the details and detailed models. This provides large flexibility, inclusion of innovative aspects and enables late changes with minimum impact.

The fourth principle is focusing on tests. The need for tests is always a trade-off between risks and programmatic constraints. However, it turned out to be very valuable to test certain aspects early. The problem is that often simple tests get overloaded with other constraints and “nice to have things” which then make the tests expensive and long. Therefore, it is very important to focus on the initial goals and to keep tests as simple as possible. In addition, it is important not to block flexibility during testing with too stringent procedures and plans. During the Future Actuator test campaign, tests were added and removed during the program as needed which proved very helpful.

The fifth point aims at the optimization and preparation for series-production readiness of the product based on available test results and updated customer requirements. For the Future Actuator, these improvement activities are currently ongoing. Based on the test results the customer revises his requirements and RUAG consolidated the concept accordingly.



### Concurrent Engineering

RUAG has its own Concurrent Engineering facility, which is frequently used in early developments and running projects.

The RUAG CE facility is small but it is a powerful tool established in 2013 for the specific needs of RUAG. It is derived from facilities at ESA/ESTEC and École Polytechnique Fédérale de Lausanne. Two main elements are taken from the existing CE facilities. The room itself and the CE process with the focus clearly being on the process. The RUAG specific process defines the rules and guidelines for the different CE sessions. The CE facility at RUAG is used for meetings such as brainstorming sessions, project initiation (project or proposal), design reviews, and project reviews. A CE session is conducted by a moderator and CE sessions are repeated in a rhythm of approx. 2 weeks. The number of CE sessions depends on the project complexity and varies between 2 and 4 sessions. The RUAG CE process is very flexible and can be quickly implemented. The additional advantage of the RUAG CE facility is that it is suitable for both large and small projects.



**Figure 3. RUAG's CE Facility**

For the Future Actuator, the CE facility was used for various reviews. This started with the overall concept review and then continued into more and more detailed topics down to the lubrication trade-off. With this approach the Future Actuator was in a constant review loop instead of one or two big reviews. Whenever there was an open point, the CE room was used until a clear way forward was agreed. Due to the number of reviews, a considerably large number of experts could be invited for the short CE sessions. By doing so, a wide range of valuable inputs was received in a very efficient way.

### Future Actuator Development

For the Future Actuator, the development activities started with concept elaboration. With the available requirements, it was evident that for a high precision mechanism a high precision gearbox was needed. All other components had to be built around the gearbox. One of the main findings was that the needed gear ratio required more than one gear stage. The gear technologies suitable for the application were planetary gears, spur gears or Harmonic Drive® gears. It was quickly clear that a combination with at least a strain wave gear was needed to achieve the performance requirements. RUAG already had a smaller actuator based a combination of a planetary gear and a strain wave gear under development. Therefore, RUAG already had a good understanding of the advantages and drawbacks of this concept.

RUAG contacted Harmonic Drive AG Germany and explained the mechanism's goals instead of delivering a detailed requirements specification. Based on this, the conceptual development started. Concepts were discussed and optimized in several loops between the two companies. Finally, a new concept, with a two-stage Harmonic Drive® gear was identified as the most interesting one for the Future Actuator. The concept had the advantage of being backlash free, which is a major asset for this overall gear ratio.

With the decision on the gear configuration made, the work started on the rest of the actuator. The design of the actuator followed a strict design to cost approach. Many concepts and design studies were prepared

but most of them were withdrawn in the frame of the design reviews. Part of the design to cost approach was evaluation of the anticipated product cost in series production.

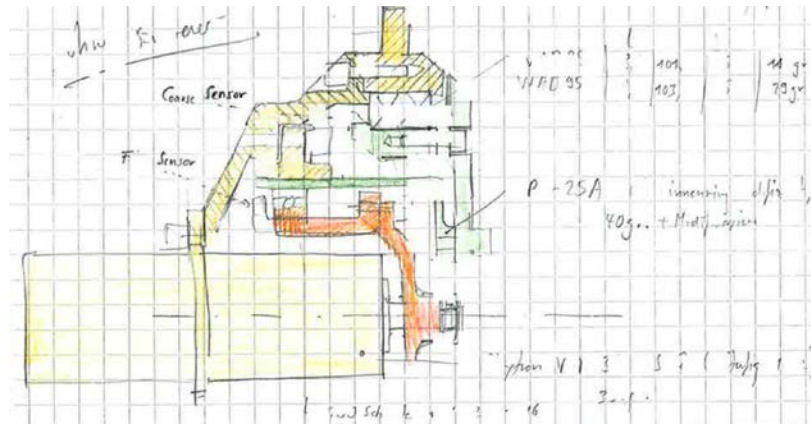


**Figure 4. Future Actuator concept drawing with planetary gear**

The design to cost was not only considered on mechanism level but also on system level where it was ensured that instead of a dedicated electronics for each actuator, a central electronics for all actuators was possible. At the end of the breadboard design loop, the cost for the series standard was available and could be compared with the programmatic requirements. It is important to mention that design to cost does not necessarily mean that the cost of all components has to be driven down as much as possible. It is more the correct balance between cheaper parts combined with high quality ones. Or, in other words, the design shall be optimized around performance and cost and not around requirements. With the selection of high quality parts where appropriate, savings in different areas can be achieved. Therefore, the design to cost approach is a weighing-up of the pros and cons of different parts always considering the top-level requirements.

Another aspect of the design to cost approach is a reduction of the number of parts. Therefore, specific attention was paid on the number of parts in the actuator. Specific attention was also paid on a compact design, short load path, robustness and small mass. The goal was to design the actuator that it fits into the volume and mass of the existing SARA21 but with improved internal load path and high robustness.

The high gear ratio caused an additional and new design constraint. For the actuator development, the goal was set to allow the actuator to run against the hard end stop. Therefore, the end stop was designed for an output torque of 300 Nm. Despite the high torque, the mechanical end stop had to be light and slim. Therefore, the end stop geometry was optimized to achieve the optimal contact geometry only under load in order to avoid a punctual contact surface under high load. In addition, the material coating was chosen to avoid cold welding under high contact stress. However, an end stop has its disadvantages and if possible should be avoided.

#### Sensor Selection

The position sensor is a specific element of the Future Actuator. The potentiometer used in the SARA21 is a well proven and low price solution but it cannot comply with the Future Actuator accuracy. Therefore, the goal was to replace the potentiometer with a contactless sensor which should be able to perform an absolute position measurement directly at the output shaft.

With the position sensor, basically the same approach was followed as for the gearbox. Based on a preliminary concept the supplier was contacted with goals instead of requirements. Together, the concept was elaborated, refined, developed and implemented. Many sensor technologies were considered in the trade-off and the decision was made to use a magneto resistive (MR) sensor which showed very promising results in another project at RUAG. During the sensor evaluation process different MR sensor solutions

were investigated. On the one side there were different means how the magnetic field can be generated and on the other side the sensor could be combined with other sensor types to achieve the required accuracy. Many solutions were withdrawn for cost, space or other reasons. The solution finally selected for the Future Actuator is simple and flexible. The sensor head itself is very compact and shows a high resistance against radiation and vacuum as well as a long lifetime.

The sensor offers its potential only in combination with the electronics. Different commercial sensors with integrated electronics are available. However, terrestrial electronics are in most cases not compatible with space requirements. A qualification of a commercial non-space electronics was not considered as the qualification risk of such a device is too high. In addition, it is preferable to integrate the electronics in one box instead of having each actuator equipped with its own radiation-hardened electronics. Therefore, the focus was on the sensor itself and the development of an algorithm to achieve the needed absolute position accuracy.

#### Breadboard Definition

The Future Actuator design phase was focused on the flight design but for the breadboard model compromises were needed to comply with the small budget and the schedule constraints. Therefore, the design was modified for the breadboard. With this approach a good mix between a cheap and fast breadboard model together with high representativeness was achieved.

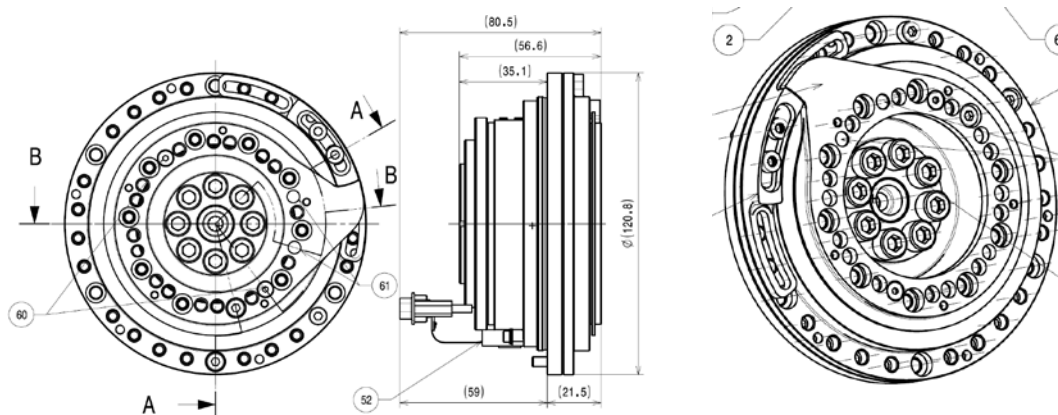


**Figure 5. Future Actuator Breadboard Model**

One important modification was the removal of some coatings. Based on RUAG experience, the removed coatings mainly had an influence on the lifetime and the lifetime was not tested on the breadboard. The other modification was the motor interface. As the final motor should be selected based on the test results the motor could not be selected at this stage. Therefore, the motor interface was kept modular to comply with the test environment.

#### **Collaboration with Harmonic Drive AG**

Gears based on the strain wave gear principle have a remarkable record in space applications [1]. They are backlash free and enable high ratios while being compact. This results in high torque density and low weight solutions. Furthermore, strain wave gears enable high accuracy and reversibility of motion. All these features/ characteristics were required. Harmonic Drive AG, Limburg, Germany, proved to be a capable, strong partner in previous application related activities and targeted development of space rated Harmonic Drive® gears based on the strain wave gear principle. Based on a basic set of technical requirements, collaboration with Harmonic Drive AG was initiated in an early project phase. There was no frozen specification which had to be fulfilled. On that basis a fruitful, open minded cooperative work environment was set. This was very appreciated by both parties, as it enabled elaboration of the best solutions using knowledge and resources from both sides, RUAG and Harmonic Drive AG.

Requirements and their respective impact on the design of the product were discussed. Capabilities of different Harmonic Drive® gear types and configurations could be involved due to the early project phase. In general, the primary basis for fulfillment of requirements is the suitable choice of an existing gear configuration. But with increased requirements and/ or contrary gear characteristics it may be necessary to introduce targeted modifications to existing Harmonic Drive® gear types or even to develop a new Harmonic Drive® gear type to fulfill the requirements. Early collaboration with Harmonic Drive AG enabled targeted introduction of modifications to strengthen the actuator performance/ features. Solutions prepared by Harmonic Drive AG were exchanged and discussed on a regular basis. During the concept definition the concept was sent back and forth between the companies and modifications were implemented from both companies. With this iterative approach, the concept improved quickly and at the end, a very unconventional, highly integrated solution was found.

The collaboration took place under a very open minded collaboration and both sides tried to maximize the product. This was only possible with due to a trustful environment between the two companies which is also a matter of the team setting and the personalities involved. In the end it resulted in a Harmonic Drive® gear concept that met the requirements and furthermore exceeded the expected actuator performance. The concepts, which were elaborated during joint discussions in early project phase, were designed in detail and assessed with respect to the operation scenario during design/ development phase by Harmonic Drive AG.

### **Development at Harmonic Drive AG**

Harsh environmental conditions in space present challenges to configurations, base materials and lubricants and cause the need for space-rated gears to differ from gears for industrial applications in items such as material and documentation. With a development team for gears related to non-industrial applications, Harmonic Drive AG is active on the field of space-related development and testing within several projects to support users and to strengthen space applications using strain wave gears [2, 3].

Strain wave gears with ratios up to 160 are common, but also higher ratios, such as 320, are possible and already realized by Harmonic Drive AG. For higher ratios, strain wave gears can be combined with a pre-stage. Configurations to combine a pre-stage gear with a Harmonic Drive® gear are conceivable for space applications especially as high integration is important. Thus one can benefit of the advantages of a gear based on strain wave gear principle while realizing higher ratios than one stage could provide.

The final concepts combined two strain wave gears resulting in a possible ratio range from 2500 up to approximately 18000. A gear ratio of approximately 5000 was selected for the Future Actuator. A rotatory input motion is transmitted by 2 stages to a rotatory output motion. Due to restrictions regarding installation space, weight and robustness the intention was to highly integrate the 1st stage in the 2nd stage. Designs were elaborated and evaluated regarding characteristics such as their assembly effort, compactness and operability. A full finite element model of the double-stage strain wave gear was created to assess the operability and to dimension the parts according the operation scenario. Several optimizing loops were performed during which the design was adapted to the operation scenario. This resulted in the design of a very compact, back-drivable component set with high accuracy and a high gear ratio.

### **Testing at Harmonic Drive AG**

To characterize the component set at Harmonic Drive AG, test equipment was designed, documented and manufactured. During an acceptance test, the no load starting torque, no load back driving starting torque, transmission accuracy and torsional stiffness were measured as reference. Furthermore, the parts were visually inspected before delivery. Three component sets were manufactured and characterized at Harmonic Drive AG. The results of the transmission accuracy and stiffness measurements are presented in the following.



**Figure 6. Double-Stage Gear after assembly at Harmonic Drive AG**

The trend of the transmission accuracy of one gearbox during operation is shown in Figure 7. The transmission accuracy of the gear represents a linearity error between input and output angle and is defined as the sum of the maximum positive and negative (see “min/max” in Figure 7) differences between theoretical and actual rotation angle. As expected, analyses showed that transmission accuracy of the 2nd stage is dominant. The transmission accuracy of the 1st stage has a minor influence. The measured values of the transmission accuracy of all manufactured component sets are shown in Table 1. All component sets showed good values which were within the specified range ( $<2.9 \times 10^{-4}$  rad). Beside the transmission accuracy, the torsional stiffness of each component set was measured. Torsional stiffness is calculated from the measured torsion angle when applying a load at the output shaft whilst mechanically locking the input shaft. The torsion curves are shown in Figure 8. Calculated stiffness values are presented in Table 2.

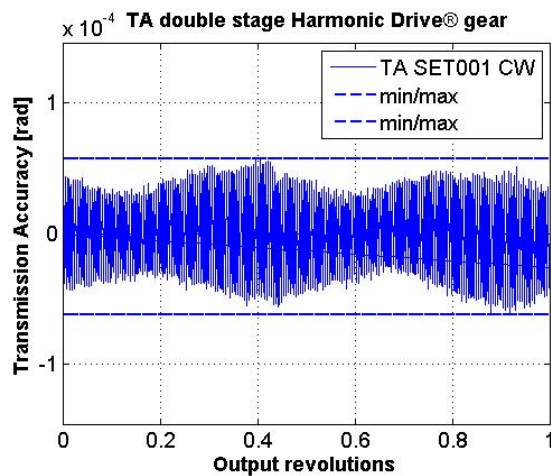


**Figure 7. Transmission Accuracy**

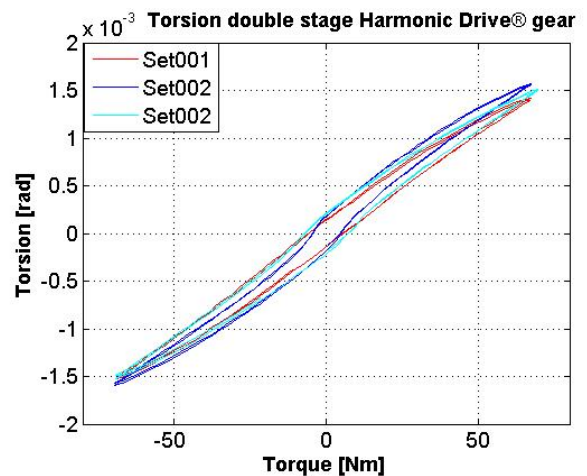


**Figure 8. Torque – Torsion curve**

**Table 1. Transmission accuracy**

Component Set – No.	Direction of rotation	Transmission Accuracy	
		$\times 10^{-4}$ [rad]	[arcsec]
001	cw	1.2120	25
	ccw	1.2605	26
002	cw	0.8727	18
	ccw	0.8242	17
003	cw	1.4060	29
	ccw	1.5514	32

**Table 2. Measured Torsional Stiffness**

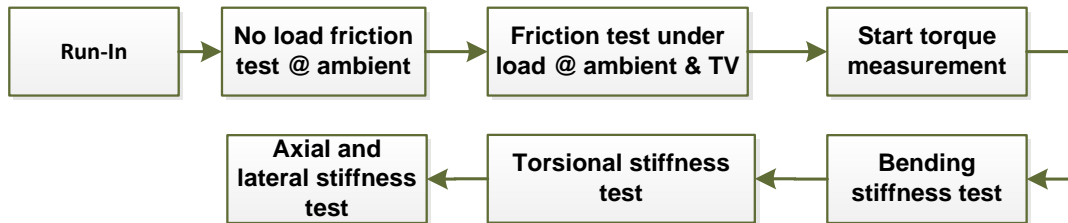
Component Set – No.	Stiffness K1 [Nm/rad]	Stiffness K2 [Nm/rad]	Stiffness K3 [Nm/rad]
	0...14 Nm	14...48 Nm	48...67 Nm
001	40500	42400	46300
002	28700	41000	45400
003	31500	42400	46200

**Testing at RUAG**

The Future Actuator test program had to mitigate all identified potential risks and to ensure the mechanism was properly understood before going into Phase 3 of the development. Therefore, the Future Actuator test program had two main objectives.

1. To characterize the performance of the actuator without the motor
2. To derive the needed inputs for the motor selection

Based on this, the test program was tailored to cover the above defined needs and a comprehensive test program was defined in order to properly characterize the Future Actuator breadboard model. The following breadboard tests were performed:

**Figure 9. Future Actuator breadboard test program**

A life test was not included in the breadboard test program as the lifetime requirements for the actuator are not very demanding. For the motor, the lifetime will be more challenging due to the high gear ratio but the motor will be subject of Phase 3. The fact that the Future Actuator has exactly the same interface to the spacecraft and the similar overall dimensions to the SARA21 allowed to use existing test infrastructure. This circumstance saved the project a lot of time and effort. Therefore the preparation time for the tests was considerably small.

**Run In Test and No Load Friction Test**

It is known that the strain wave gears have a run in effect [1] and therefore it was important to understand this effect with a double-stage strain wave gear. For this test the no load test setup was used (see Figure 10). As the first gear stage is the dominant one for the friction torque, also the first stage was dominant for the run-in effect.

The Future Actuator run-in test results showed that the torque reduction and behavior during the run-in of the double-stage Harmonic Drive® gear was very similar to a normal single-stage Harmonic Drive® gear. The torque reduction is in the range of 15%.

In the middle of the run-in the rotational direction was changed which can be seen in Figure 10 as a torque increase for a short sequence in the middle of the test sequence. This behavior is in-line with standard strain wave gears. After the run-in, the no load running input torque was in the range of 6 to 10 N-mm depending on speed and start condition.



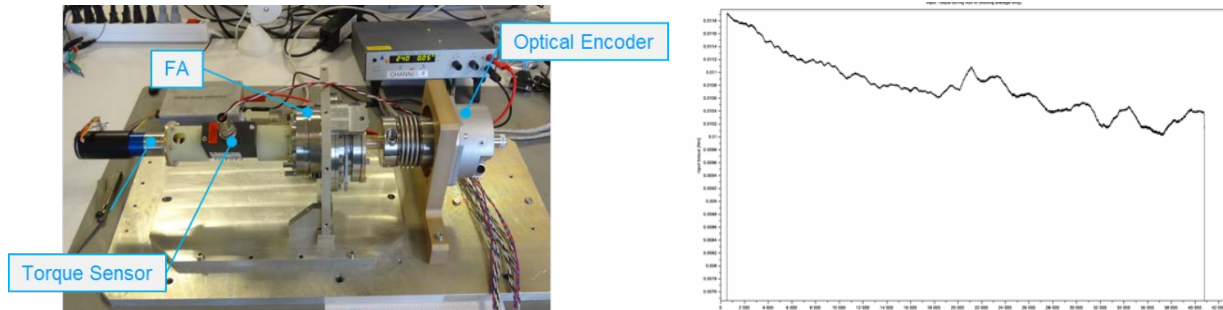


**Figure 10. No-Load Test Setup and Run In Test Results**

#### Friction Test under Load

The goal of the second test was determination of the input torque under different loads in ambient and vacuum conditions.

At ambient temperature the mechanism was tested to an output torque of up to 200 N-m (limit of the test setup) without any problems. As such high torque levels are not the target application, the high test was only performed once. The nominal test was performed up to 70 N-m output load, which covers the nominal applications. For the torque test at ambient condition, the actuator was integrated in the torque test setup (Figure 11) where the load was generated by a SARA21 model connected with a gear stage. The gear stage allows testing the unit without going to the limit of the SARA21. During the test, the test item was operated at different speeds and the resistive torque was continuously increased. This step was repeated several times for both rotational directions and at different speeds, as the resistive torque of the double-stage Harmonic Drive® gear at cold temperature is very important for the motor selection. The friction test was also performed in vacuum at cold and hot temperature. For this test, again the SARA21 test infrastructure was used (Figure 13). For the TV test, the Future Actuator test setup had to be adapted in order to keep the motor and torque sensor temperature in the specified range.

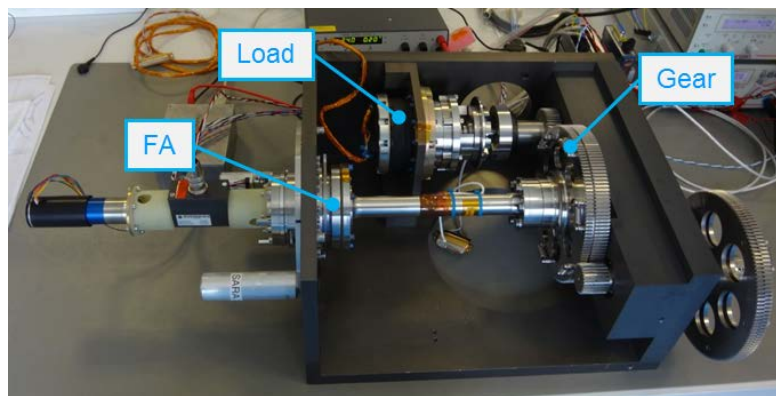


**Figure 11. Torque Test Setup**

The test results showed, as expected, a linear increase of the input torque vs. output torque (Figure 12). Over the temperature the input torque increases in a non-linear way.

#### Start Torque Test

The start torque also called break-out torque [4] is the torque at the beginning of a rotation which can be higher than the nominal running torque. The goal of the test was to measure the start torque behavior of the double-stage strain wave gear at different temperatures.

The tests, performed under TV, showed that the Future Actuator start torque behavior is very similar to a normal Harmonic Drive® gear and the start torque is temperature dependent. At hot temperature it is almost



not present and at cold temperature the effect was stronger. For the Future Actuator the start torque reached a maximum of 15% above the nominal running torque.

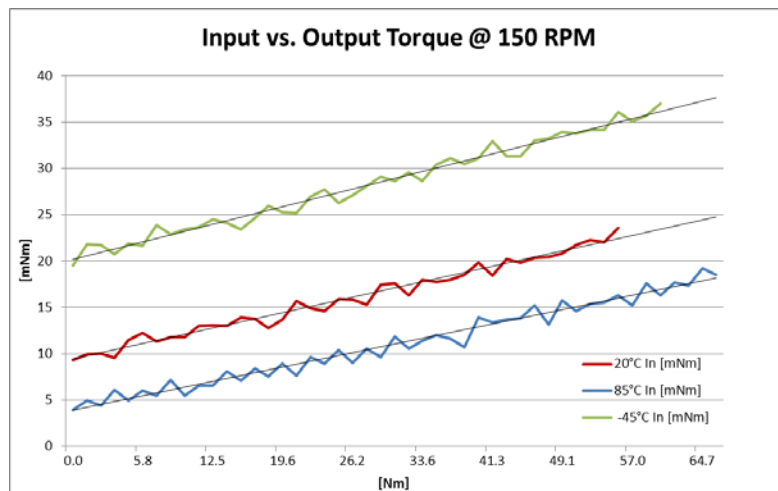


Figure 12. Input Torque vs. Output Torque

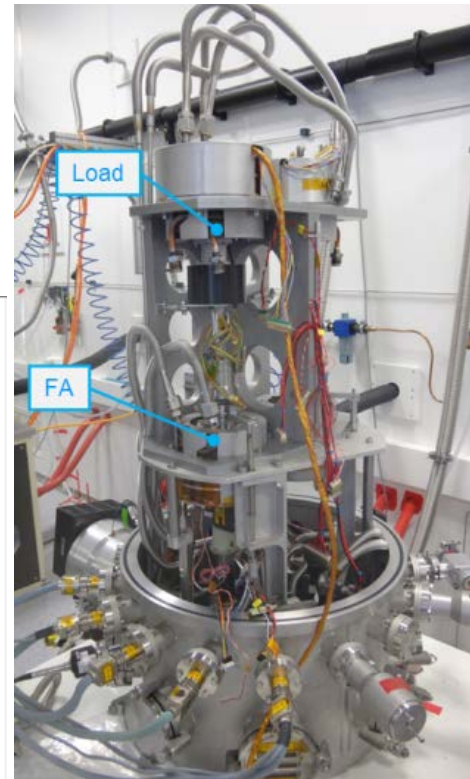


Figure 13. TV Test Setup

#### Hysteresis and Transmission Accuracy Test

Strain wave gears made by Harmonic Drive® AG are backlash free and have the highest position accuracy. Due to internal friction the gear shows a hysteresis loss. Therefore, a specific test setup was designed to derive the very small hysteresis of the Future Actuator configuration. The goal of the configuration was to exclude disturbance effects coming from outside the gearbox. The main contributor is the test motor and its attached gearbox and the second effect is the accuracy of the motor controller. Therefore, the motor was replaced with a mechanical hand-driven lever. The lever was moved along a grid-type disc (Figure 14) which ensured that the lever could be repeatedly positioned at specific positions. With this the input was position controlled and not speed controlled. The lever allowed to repeat the input position with a very high accuracy and the error was calculated based on the difference between the measured and theoretical position of the output flange. The encoder on the output side was a 28-bit reference encoder with enough resolution for this test. The test was repeated several times with different start directions. The test was then repeated at different input angles. All tests showed a very similar result, in the range of  $9 \times 10^{-6}$  rad.

The transmission accuracy test was performed with the same test setup used for the hysteresis test. For the test, the lever was rotated several times in the same direction about a specific angle. The deviation between the theoretical and the measured position then was calculated. This test was performed in both rotation directions and at different input angles.

The conclusion from the transmission accuracy test is that the accuracy is generally very high and the accuracy improves with the reduction of the actuation angle. For fine pointing angles the test has shown an average transmission accuracy of below  $2 \times 10^{-6}$  rad in the unloaded condition.

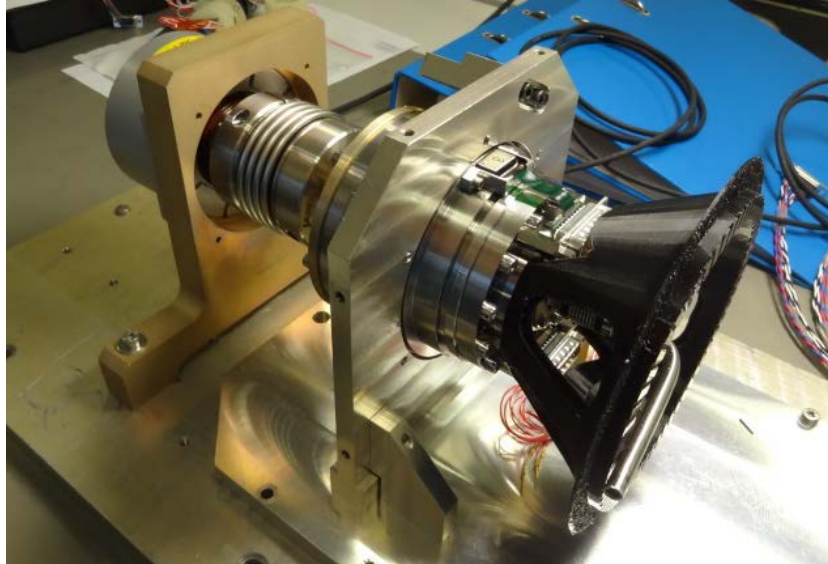


**Figure 14. Hysteresis Test Setup**

#### Stiffness Test

The stiffness of the actuator is important for the attached equipment. There are two contributors for the actuator stiffness: the gear stage for the rotational stiffness and the main bearing for the other stiffness directions. Due to the rotation symmetry of the actuator, four stiffness parameters remain: axial and radial translational stiffness, the bending stiffness and the rotational stiffness around the rotation axis. The stiffness test was performed with the SARA21 test rig and therefore the test could be easily performed. The test rig had to be reinforced due to the higher loads of the Future Actuator. The stiffness test itself confirmed the values resulting from the analysis performed during the development.

**Table 3. Future Actuator stiffness**

	Stiffness
Torsion	$> 2.5 \text{ E}+04 \text{ Nm/rad}$
Bending	$> 3.0 \text{ E}+05 \text{ Nm/rad}$
Radial	$> 9.3 \text{ E}+08 \text{ N/m}$
Axial	$> 1.4 \text{ E}+08 \text{ N/m}$

#### **Documentation**

Documentation makes a large contribution to the Future Actuator development cost efficiency. In the frame of the breadboard development the documentation was tailored to the needs and the important information. Key findings, test results and development steps were thoroughly documented but the development was not overloaded with standard documentation.

#### **Conclusion**

The Future Actuator development approach was entirely new within the mechanism domain of RUAG. It can be seen as a major success as it resulted in a very attractive new product which was developed by a small team, a small budget and within short duration. It thus demonstrated the suitability of the lean development approach. In a nutshell, the lean development approach can be summarized in the following sequence:

1. Define challenging development goals for the product including top level requirements
2. Prepare a basic concept and select key suppliers
3. Allow suppliers to bring in the best product with minimum restrictions
4. Build concepts around supplier components and refine requirements
5. Finalise the concept
6. Test the concept
7. Based on test result, initiate Phase 3 with the customer

Particularly, the early involvement of the suppliers was a key element of the development. Together with the early supplier involvement the technical requirements were kept open in order to allow the development of the best possible solution. This however required an intensive collaboration with the supplier and the openness to adapt the concept to the benefit of key components. It was important to stay as long as possible in the concept phase until the best possible solution was found. This is different from developments with a frozen milestone plan which does not allow such a flexibility.

The development with small teams allowed a fast and direct development but it required the regular consultation of the internal expertise to ensure maximum benefit of all existing know-how. General recommendations are: development tools as design thinking and concurrent engineering should be used whenever possible; and the documentation efforts should be reduced as far as possible but of course it has to be ensured that key information is documented.

Testing of critical technologies or elements should be performed as early as possible. The testing should be kept simple and limited to the mitigation of the identified risks. The test program should be defined flexible in order that modifications of the test program can be easily made during the tests. For developments like the Future Actuator internal funding should be preferred to external funding as the needed development flexibility might not fully be given in programmes having fixed milestones and customer expectations. For the Future Actuator design approach as presented in this paper, the final result would certainly not have been achieved with fixed and detailed requirements from the beginning.

The Future Actuator design is now being refined together with the main/launch customer based on the test results and updated customer needs. The next steps are the finalization of the design and the qualification program.

RUAG will make further use of the lean development approach for specific product developments. Further projects are already initiated and running.

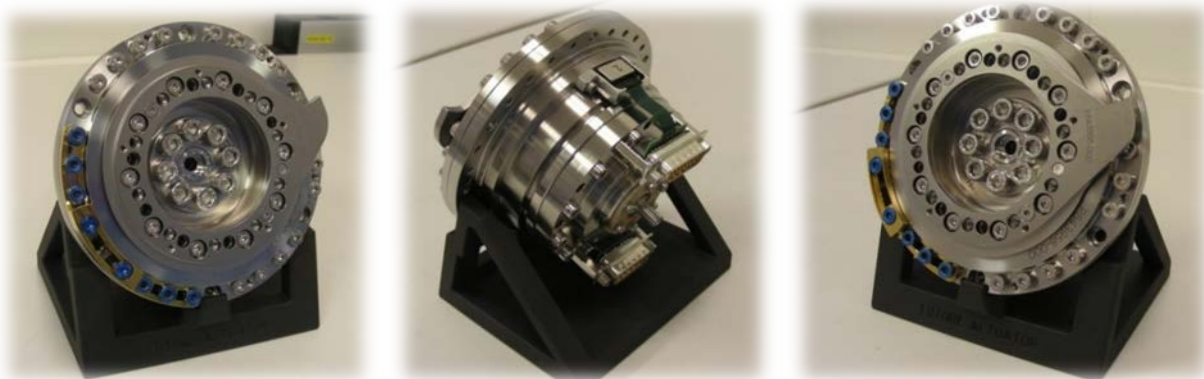


**Figure 15. RUAG's Future Actuator Breadboard Model**

## References

- [1] E. W. Roberts, '*A review of harmonic drives for space applications*' ESA-ESTL-TM-0103, 2012.
- [2] M. Jansson, H. Koenen, M. Brizuela, J.-L. Viviente and A. Merstallinger, *Harmles - Development of dry lubricated Harmonic Drive® gears for space applications*, Bilbao, Spain: Proc. '16th European Space Mechanisms and Tribology Symposium 2015', 2015.
- [3] E. W. Roberts, P. Bridgeman, M. Jansson, M. Schulke and A. Tvaruzka, *The performance and life of fluid-lubricated Harmonic® Drive gears*, Bilbao, Spain: Proc. '16th European Space Mechanisms and Tribology Symposium 2015', 2015.
- [4] E. W. Roberts, '*TV assessment of grease-lubricated compact harmonic drive gear boxes*' ESA-ESTL-TM-0031, 2006.
- [5] Klaus L. Schulte: *Kleine Geschichte der PT6*. K.L.S. Publishing, 2007.

